Maqarin Phase IV Report

Pitty, A and Alexander, R (editors).

A joint-funded international project report between NDA RWMD, Andra, CEA, SKB, Nagra and JNC

Table of Contents

Chapter 1

Introduction

W.R. Alexander, J.A.T. Smellie and A.F.Pitty

1.1 Background to the Jordan Natural Analogue Studies

Cement and concrete are extensively used in the construction of repositories for low- and intermediate-level radioactive wastes (L/ILW). In underground silos, like those in Sweden and Finland for example, much of the waste is conditioned with concrete (e.g. spent ion-exchange resins) and is packed in concrete containers (e.g. Figure 1.1)[1]. Even in many high-level radioactive waste (HLW) repositories, cement and concrete may be widely used. Instances include the paving of tunnels, shotcreting of tunnel walls, and injection and grouting of fractures. Consequently, in many repository designs, cement-based materials are expected to dominate the repository. In the Swiss L/ILW concept, for example, current designs envisage the use of up to 1.5 million tonnes of cement, approximately 85-90% by weight of the total repository. This will ensure the long-term maintenance of hyperalkaline conditions, predicted to suppress the solubility of key radionuclides in the waste (e.g. Hodgkinson and Robinson, 1987) and to enhance their sorption on the cement (e.g. Stumpf et al., 2004).

Models of cement evolution (e.g. Atkinson, 1985, Berner, 1987, 1990) predict that hydration of the cementitious material in the repository by groundwater will produce an initial stage of hyperalkaline (pH~13.5) leachates, dominated by alkali hydroxides, followed by a longer period of portlandite buffered (pH~12.5) leachates. Also, as the hyperalkaline porewater leaches out of the near-field, it may interact significantly with the repository host rock (e.g. Haworth et al., 1987). Where applicable, this may also apply to a bentonite backfill (e.g. Tajima et al., 2006). In consequence, those features for which the formation was originally chosen, such as low groundwater flux and high radionuclide retardation capacity, may deteriorate.

Crucially, these model predictions must be tested to assess the true significance of the predicted hyperalkaline leachate/host rock interaction. Traditionally, performance assessment (PA) modellers may have placed too much weight on laboratory data for the construction and testing of PA models. With only a few exceptions (see Alexander and McKinley, 1999, for examples), data from natural analogues and *in situ* experiments have been ignored (see additional comments in Alexander et al., 1997 and Smellie et al., 1997). The over-dependence on laboratory data is justified because this information is produced under well-understood, precisely controlled conditions, and modellers are confident about the results obtained. However, a repository is not like a laboratory, and processes must be addressed which are influenced by natural heterogeneities. These processes involve large degrees of uncertainty and usually operate over very long timescales. In consequence, laboratory data must be supplemented with information from *in situ* field experiments and from natural analogues.

[1] Although, as in this figure, the cementitious repository is generally in direct contact with the host rock, some disposal concepts (e.g. Sweden, Japan) use a bentonite layer to isolate the repository from the host rock.

Figure 1.1 An example of the multiple-barrier system in a cementitious repository (illustration courtesy of Nagra).

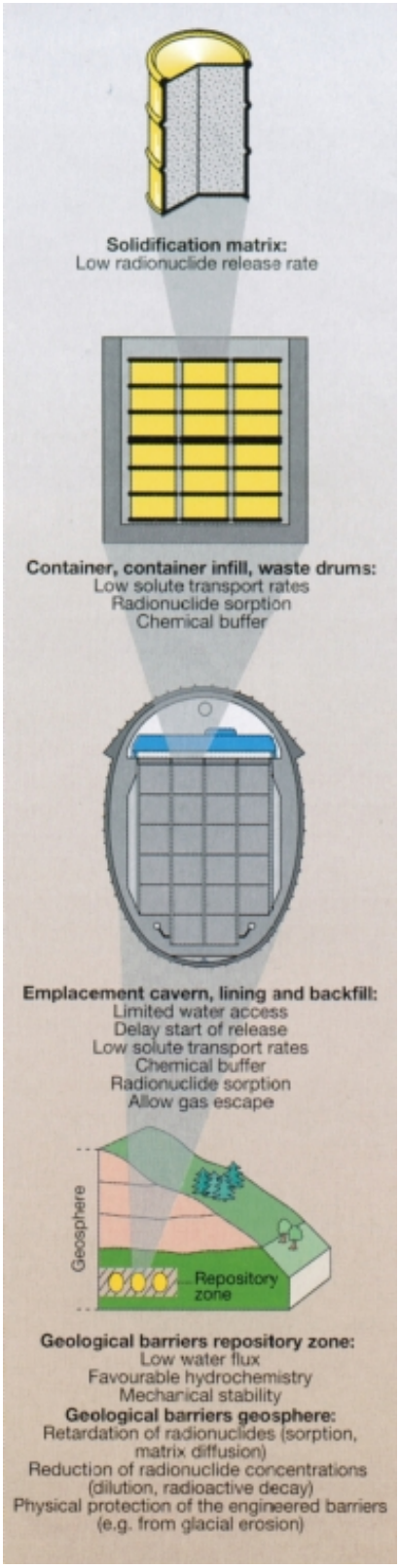

As emphasised in Alexander et al. (1998) “The advantage of natural analogues over short-term laboratory experiments is that they enable study of repository-like systems which have evolved over the geological timescales of relevance to a radwaste repository safety assessment (rather than the days to months usual in laboratory tests). However,

by their very nature, natural analogues often have ill-defined boundary conditions which may be better assessed under the well-constrained (if less relevant) conditions of a laboratory. Well designed, realistic *in situ* field experiments can bridge the gap between the laboratory and natural analogues by offering repository-relevant natural conditions with some of the constraints of the laboratory (and intermediate timescales). In short, combining information from the three sources (long-term and realistic, if poorly defined, natural analogues, medium-term, better constrained, *in situ* field experiments and short-term, less realistic but well defined laboratory studies) can provide greater confidence in the extrapolation of laboratory derived data to repository relevant timescales and conditions."

Increasingly, laboratory data of relevance have been produced (e.g. Chermak, 1992, 1993; Bateman et al., 1995, 1998; Wieland et al., 2004) and this information will be included where appropriate in this report. However, what little that has been done in URLs (e.g. Mäder, 2004; Mäder and Adler, 2004; Mäder and Traber, 2004; Mäder et al., 2006) has not yet been published comprehensively enough to allow full integration within this Report.

Before the more recent advent of *in situ* studies, Nagra, Ontario Hydro, SKB, UKHMIP, Nirex, ANDRA, CEA and JAEA, in collaboration with the University of Jordan, sought additional means of supporting the laboratory data. To test the models better, comparisons were drawn with observations of similar processes which have occurred in nature. This is the so-called natural analogue approach (see Miller et al., 2000 and www.natural-analogues.com for discussions on natural analogues).

Figure 1.2 Aerial photograph of the Maqarin area, northern Jordan. The Yarmouk River flows from right (east) to left (west) across the middle of the image.

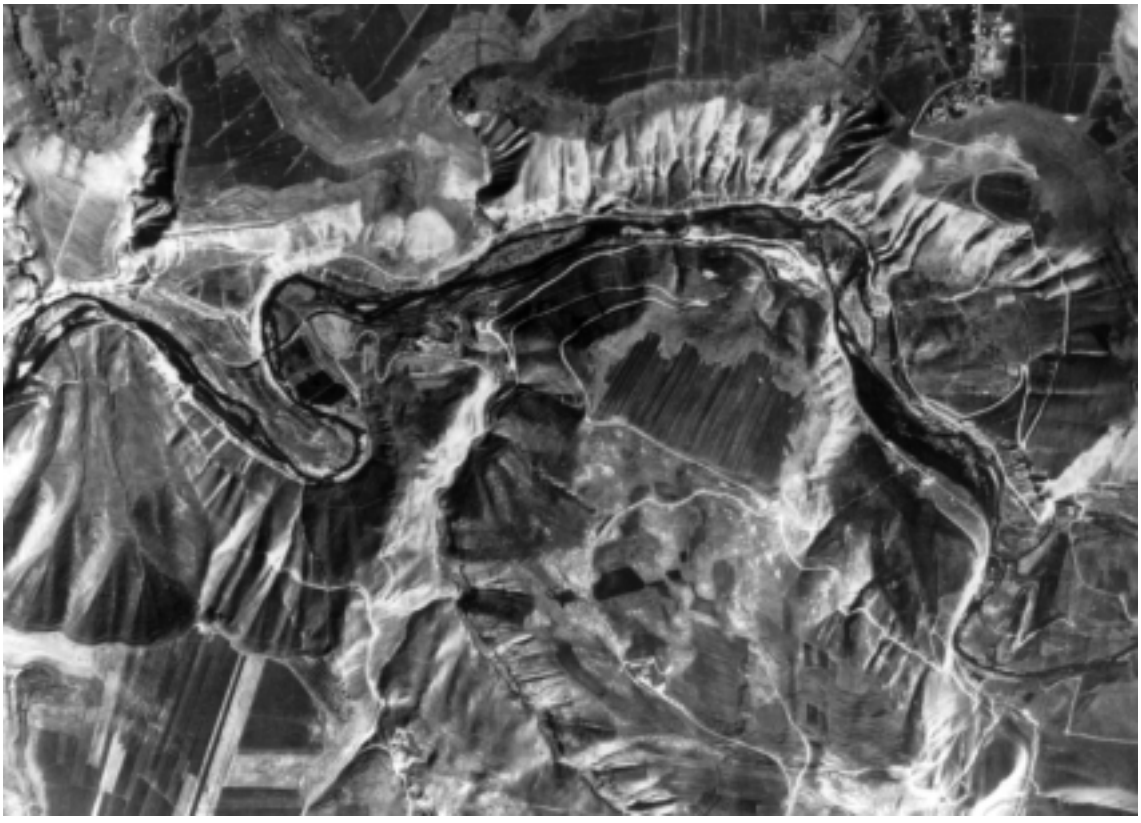

Several sites in Jordan (Figures 1.2 and 1.3) have been studied over the last 15 years (see, for example, Alexander, 1992; Linklater, 1998; Smellie, 1998; Milodowski et al., 2001; Kamei et al., 2005 and Trotingon et al., 2006). In northern and central Jordan, natural cements occur as a result of high-temperature, low-pressure metamorphism of kerogen-rich clay biomicrites (the Bituminous Marl Formation[2]). The rehydrated and recarbonated reaction products are analogous to the mineralogy of Portland cement. These offer an excellent natural analogue for cementitious repositories (see Figure 1.4).

Figure 1.3 Aerial photograph of the Daba and Khushaym Matruk areas of central Jordan

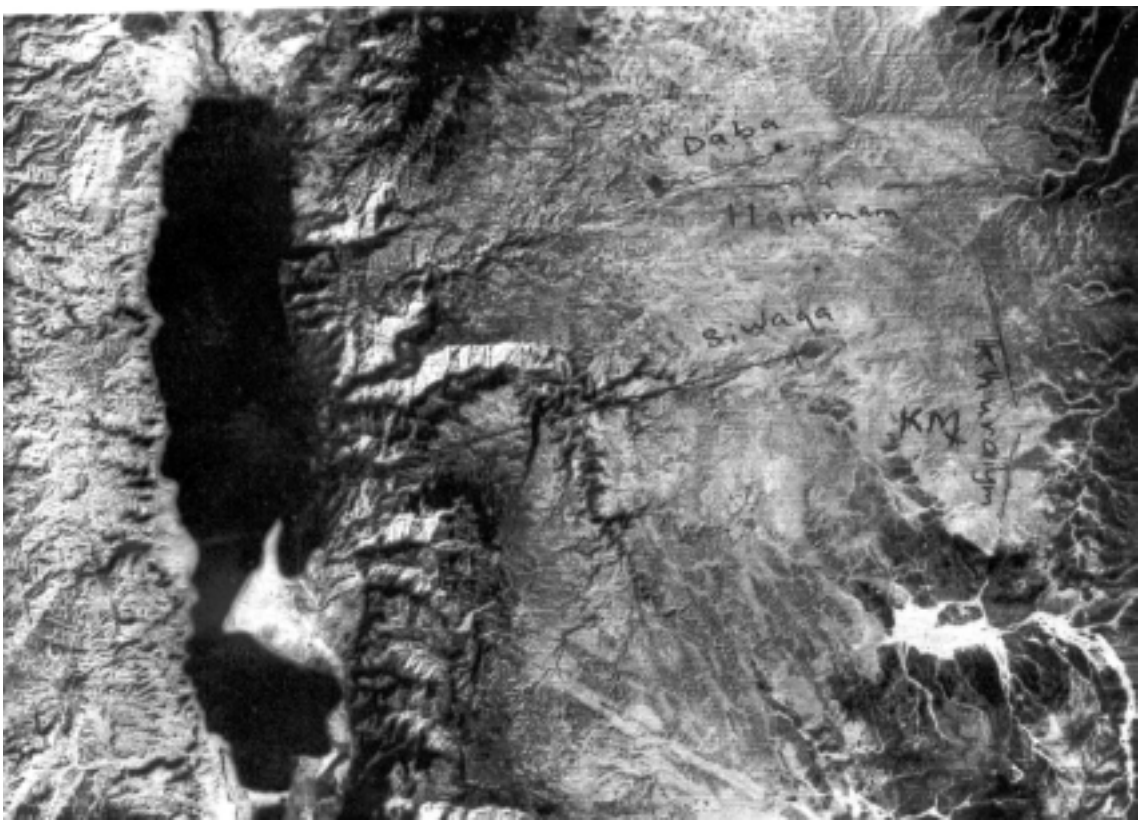

[2] Terminology has always been a problem in the project and so the main terms are clarified in Appendix 1.

Figure 1.4 Schematic representation of the production of the natural cements in Jordan

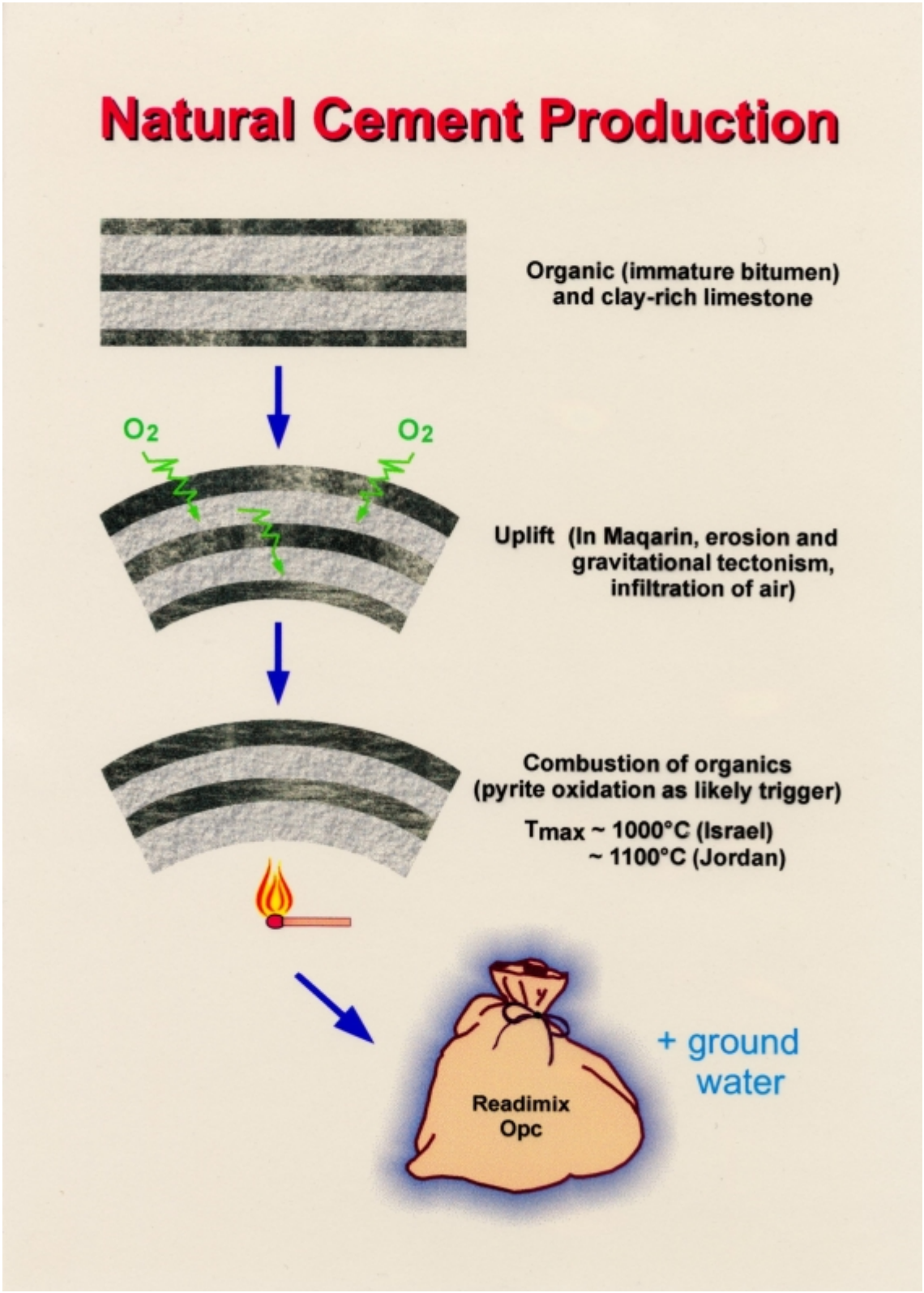

The Maqarin site in north-west Jordan may be unique, as hyperalkaline groundwaters in the area result from the interaction of normal (pH~7) recharge waters with these metamorphosed ‘cement’ zones. The result is similar water/rock reactions and mineralogy to that predicted for a cementitious respository environment. At least three different hyperalkaline groundwater environments have been identified in Jordan. These

appear to represent, by analogy, three different stages in the theoretical evolution of a cementitious repository (cf. Berner, 1987, 1990). These stages are:

- *Early Stage;* alkali hydroxide groundwaters (Western Springs, Maqarin – see Figure 1.2 and 1.5). The pH (maximum observed 12.9[3]) and the high Na/KOH content with relatively high Ca suggest that this site represents a slightly evolved (i.e. high pH, Na/KOH) leachate.

Figure 1.5 *Looking to the south-east to the Western Springs site at Maqarin, northern Jordan. Note the steep valley sides (about 32°) of the River Yarmouk in the right foreground. Unit B is basalt, lying on top of unit C, limestone, which lies on top of the cement-hosting horizon (somewhere between the 'C' and the road in this shot).*

- *Intermediate Stage;* portlandite-buffered system (Eastern Springs, Maqarin – see Figures 1.2, 1.6 and 1.7; Daba and Khushaym Matruk in central Jordan – see Figures 1.3, 1.8 and 1.9). A pH of ~12.5 and portlandite saturation reflect an intermediate-stage (i.e. lower pH, $Ca(OH)_2$ buffered) leachate.

[3] This is the highest ever reported for a natural groundwater.

Figure 1.6a *Part of the Eastern Springs system; the Railway Cutting site is next to Maqarin Station (constructed circa 1905). The thick, white deposits on the cutting wall are secondary phases (including calcite, vaterite, CSH) produced by precipitation from the hyperalkaline groundwaters. These flow from the cutting wall having passed through at least 500m of clay biomicrite from the ACZ. This site will be flooded by the impounding of a reservoir above the Unity Dam.*

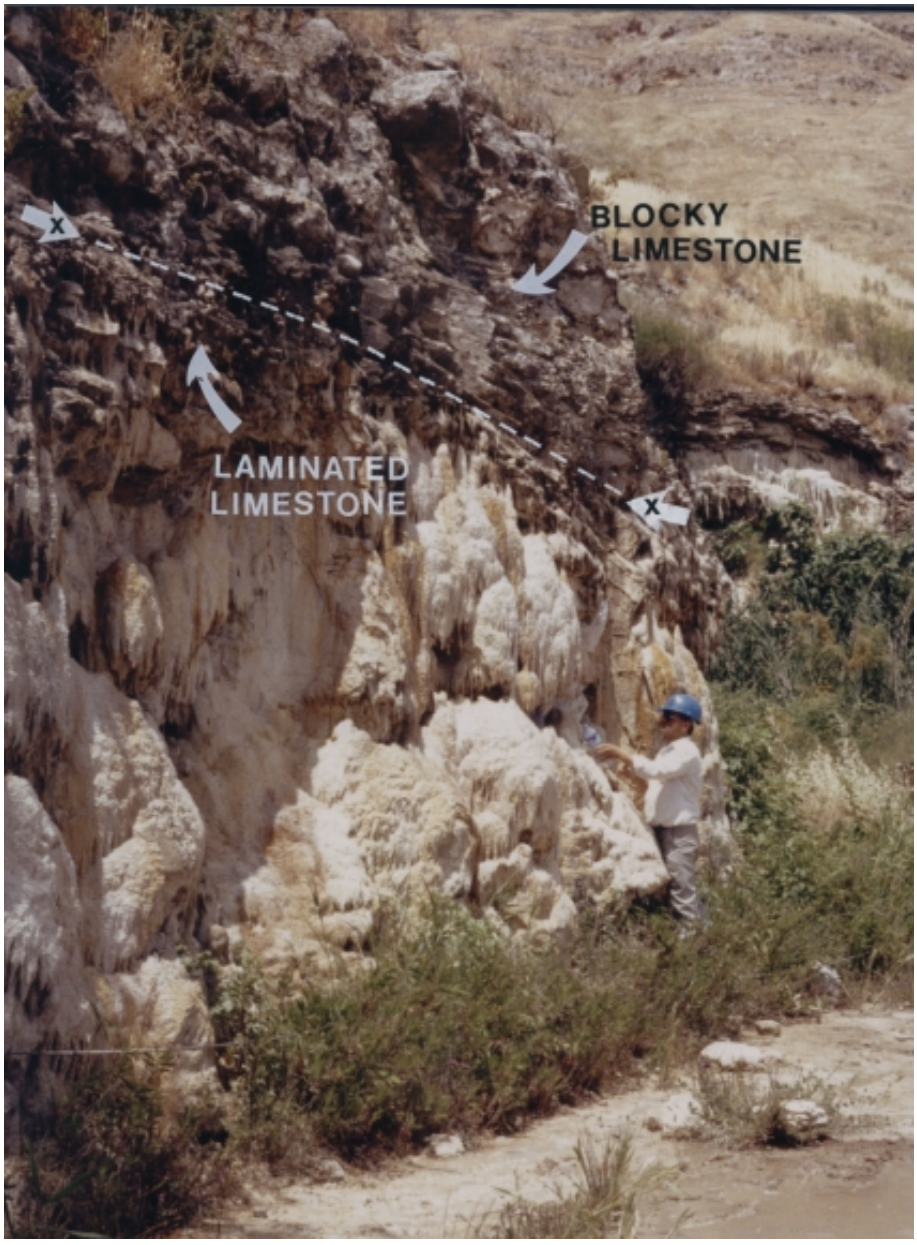

Figure 1.6b *Adit A-6, Eastern Springs. This drift was constructed in 1979 as part of the site exploration for the then planned dam (see Figure 1.7). As in Figure 1.6b, the thick white deposits are secondary deposits formed when the hyperalkaline groundwaters take up atmospheric CO_2 at the tunnel wall.*

Figure 1.7 *The Eastern Springs site, Maqarin (northern Jordan) in June 2004 after dam construction began. At the top left of the image is the remains of the tunnel (Adit A-6, Figure 1.6b) which hosted several of the seeps of the Eastern Springs. The hyperalkaline waters can be seen flowing down the excavated rock steps towards the valley floor.*

- *Late Stage;* lower pH, silica-dominated system (Daba and Khushaym Matruk). The present water table is at least one hundred metres below the cement zone, but the fossil mineral assemblage indicate a late-stage (pH 10-11) leachate in parts of both sites.

Figure 1.8 *The Khushaym Matruk site in central Jordan. The main area of investigation lies at the foot of the peak in the ridge in the distance.*

Figure 1.9 *The Khushaym Matruk site in detail. The harder outcrop in the middle of the view is the cement zone and the darker material below this is the Bituminous Marl Formation (i.e. clay biomicrite).*

Hyperalkaline groundwaters exist elsewhere, such as the ophiolite environments in Oman (Bath et al., 1987a, 1987b), the Philippines (Alexander et al., 2008), Cyprus (Milodowski et al, 2009) and in rift valley terrains like Kenya (Jenkins, 1936). However, these waters (maximum pH ~11) are produced by processes which are of little relevance to hyperalkaline cementitious systems. Significantly, they do reveal some features of a hyperalkaline environment, such as trace-element speciation and microbial populations (see McKinley et al., 1987, 1988). However, such sites do not represent processes in and around an OPC (Ordinary Portland Cement)-dominated cementitious repository as accurately as the Maqarin analogue.

1.2 Introduction to Phases I to III

In Jordan, the earlier Phase I-III studies sought to elucidate the complex reactions and processes expected to occur during the long-term evolution of a cementitious repository. The major areas of repository PA interest addressed include:

- characterisation of the 'cement' source term
- geochemical modifications and transport phenomena in the zone of interaction between the near-field leachates and host rocks of different composition, in particular the stability of CSH phases as a medium for pH buffering
- understanding the development and propagation of high-pH plumes through the host rock, including the implications of induced changes to the rock matrix and fracture porosity
- near-field colloid production
- zeolite stability studies
- microbiological implications
- testing of thermodynamic databases of radionuclides of interest to PA
- testing and development of PA modelling codes, including new coupled (geochemistry and transport) and microbiological codes.

In summary, the first three phases of the Maqarin project covered the following areas:

Phase I

The first phase of the work (reported in Alexander, 1992) focused on the source term, was to assess whether the Maqarin system was a good analogy of a cementitious repository. Unlike the source of other hyperalkaline waters studied to date (e.g. the ophiolite-fed groundwaters of Oman and Cyprus), the Maqarin source rock is a reasonable analogy to a man-made cement, since many common cement minerals are present in the source rock. Exemplifying the thoroughness of these source-term studies is the discovery of several new minerals. These include a previously unrecorded natural uranium mineral, the first observation of calcium selenium sulphide in terrestrial rocks, and the first description of natural calcium selenates and calcium strontium selenates. A new calcium-potassium selenide-sulphide was also discovered (Milodowski et al., 1992a, 1992b).

In addition to describing the source term, a predictive exercise to test the thermodynamic database (TDB) was carried out, along the lines of the original work in the Oman natural analogue study (cf Bath et al., 1987a, 1987b). Here the applicability of several TDBs to the hyperalkaline conditions, expected in a cementitious repository, was examined. A small-scale study of the viability of microbes in the hyperalkaline waters was also carried out. This showed that nutrient availability, and not the groundwater pH, was controlling

microbial activity. As this finding could have significant implications for a cementitious repository, microbiology was examined further in the Project's second phase.

Phase II

Having established the nature of the source rock in Phase I, Phase II (reported in Linklater, 1998) concentrated on defining the extent and degree of alteration of the host rock by the hyperalkaline leachates issuing from the cement zone (see, for example, Figure 1.10). This work began in Phase II and carried on through Phase III. A second phase of TDB testing was carried out in Phase II (Linklater et al., 1996), examining another set of TDBs. The results were similar to those of Phase I. As part of this work, trace-element speciation *in situ* was assessed, but with only limited success.

Figure 1.10 Example of fractures and joints in the ACZ (brown, top of photo) and the parent rock (black, bottom) in Adit A-6, sealed by secondary CSH (and locally zeolite) phases. Note hammer on left for scale.

Further microbiological work was pursued. Coombs et al. (1998) showed that up to 10^5 microbes mL^{-1} were present in the hyperalkaline groundwaters and ten times as many on fracture faces. Significantly, although the microbes are tolerant of the hyperalkaline conditions, only those which could exploit nutrient-rich conditions were detected (predominantly heterotrophs and sulphate reducing bacteria). A microbiology code was also tested, which estimated microbial populations in a range of environments, including radioactive waste repositories. This code over-estimates significantly the predicted microbial populations in the Maqarin hyperalkaline groundwaters (West et al., 1995).

Finally, two coupled codes (i.e. geochemistry/transport), which could be used to predict the extent of rock-water interaction in the hyperalkaline plume, were tested against observations at Maqarin. The codes' predictions of the types of secondary phases to be expected were generally in agreement with the field data. However, the physical extent of alteration was over-estimated (Chambers and Haworth, 1998).

Phase III

Phase III studies (reported in Smellie, 1998) examined the higher pH (up to a maximum of pH 12.9) groundwater system at the Western Springs site. Here the presence of Na/K-enriched $Ca(OH)_2$ groundwaters was confirmed. The new groundwater data, along with the existing information from the Eastern Springs, were used to test further the two coupled codes mentioned above. The results indicated the degree of applicability of the codes in a repository analogous environment. Those areas where further code development may be necessary were also identified.

In addition to more detailed study of the Western Springs groundwater, the presence of more siliceous rocks at the Maqarin site, such as basalt and chert, prompted studies of water/rock interactions which are relevant to repositories planned for crystalline host rocks. The reaction sequence is similar to that observed in the Eastern Springs system, thus validating further the conceptual model of hyperalkaline-plume development (Milodowski et al., 1998a).

An additional site of hyperalkaline water/rock interaction at Daba in central Jordan was also investigated. Here, the groundwater table is about 100 m deep and so hyperalkaline waters are not currently present. However, the site may represent the late stage of plume development, following exhaustion of the cements´ portlandite buffer capacity (Milodowski et al., 1998b). These features may have a bearing on disposal programmes for long-lived wastes (such as TRU) in cementitious repositories.

Geomorphological studies examined recent the geological evolution of the Yarmouk River Valley, including the identification of two major landslip events, one geologically older than the other. This sequence may explain the more hydrogeochemically evolved, older, Eastern Springs system compared to the less evolved, younger, Western Springs system. Additional objectives of Phase III included a literature review of zeolite minerals of relevance to the hyperalkaline plume. Colloid populations in the hyperalkaline groundwaters were also examined, and organic material in the rock and groundwaters studied. Finally, the stability of clay in the presence of hyperalkaline fluids was evaluated.

Much of this work was focused on the Maqarin sites along with some minor work at Daba and at Sweilih (near Amman). These studies showed that natural cements and associated hyperalkaline plumes in Jordan are excellent natural analogues for important processes and reactions which are expected to influence cementitious repositories over long periods of geological time (hundreds to thousands of years). However, even though the detail of the studies at these sites is unparalleled, important discrepancies do exist when compared to full-scale repository conditions. For example, the natural-cement mineralogy and leachate compositions at Maqarin are not directly comparable to industrial cements. Their evolved high-pH leachate products, when in contact with groundwaters of neutral pH, are an anology only. In addition, the Maqarin site is highly fractured and relatively transmissive. In consequence, the development of the high-pH plume (400-500 m in extent), studied in Phase III, is clearly much larger than would occur around a real repository. Furthermore, much of the hydrochemical data evaluated, and colloid and microbe data, too, relate to near-surface sub-oxic conditions. Such conditions would not occur in deep geological repositories[4]. Nevertheless, despite these reservations highly relevant PA-related information has been gathered. The more pertinent information from Phases I-III, based on Alexander and Smellie (1998), can be summarised as follows:

[4] Although it is of direct relevance to some of the shallower-repository concepts currently under consideration (e.g. McKinley et al., 2007)

- the conceptual model of a hyperalkaline plume in a generic host rock is largely consistent with observations at the site
- hyperalkaline pore fluid conditions, generated by minerals showing similarities to those in cements, are long-lived (> 1000's years) under Maqarin flow conditions
- hyperalkaline fluid/rock interactions generally have positive reaction volumes and thus fractures are sealed by secondary phases
- fracture sealing occurs extensively and over short timescales (tens to hundreds of years)
- the altered rock matrix (relevant to radionuclide retention) appears to be accessible to the diffusion of aqueous species (cm-length scale)
- sequences of minerals, predicted by coupled codes, are very close to those observed in the hyperalkaline alteration zones, even though the specific phases may not be predicted due to difficiencies in thermodynamic data
- repository-relevant thermodynamic databases provide conservative estimates of solubility, despite representation of the solubility-controlling phases being too simplistic
- the amounts of colloidal material generated under oxic conditions at the cement zone/host rock interface appears to be low
- microbes are present in hyperalkaline groundwaters, although their precise activity is elusive

1.3 Introduction to Phase IV

To date, most PAs have only used the available data in a qualitative manner and, in addition, many contain very conservative assumptions regarding hyperalkaline fluid-rock interactions. Consequently, the Phase IV studies aimed to constrain more critically many of these assumptions. The main objective, therefore, has been to provide high-quality quantitative and supporting data that will be directly relevant to safety and performance assessments for cementitious repositories. In addition, studies based at the Khushaym Matruk site in central Jordan, are relevant for planning repositories within clay-dominated host rocks[5].

As pilot studies for the Phase IV project, two separate fieldwork campaigns were undertaken, to the Eastern Springs area of Maqarin and to central Jordan (see Smellie, 2000, for details). The latter campaign focused only on the Khushaym Matruk site (see Rassineux, 2000, for details).

The purpose of the Phase IV project, initiated in 2000 and continued until 2006, included several topics of PA concern:

- detailed characterisation of the source term, i.e. the analogue cement-zone (ACZ),mineralogy, to strengthen the analogy with industrial cements. Additional data were required to constrain the paragenesis of the hydration products, to clarify the duration of the hydration, alteration and evolution of CSH minerals, and to quantify dissolution fluxes
- rigorous evaluation of the site-scale hydrostructural character at Maqarin to help determine solute flux rates through the bedrock; to establish the spatial and age relationships; to develop further the scenario of the episodic fracture formation, sealing and reactivation which characterises the site

[5] Although this remains to be proven, Khushaym Matruk may also represent a diffusive-transport dominated system, in comparison with the advective-transport dominated system at Maqarin.

- quantify microbial activity and assess its implications in hyperalkaline environments
- detailed study of clay-mineral stability in the presence of hyperalkaline waters as an analogy of a clay-based repository host rocks and for the use of bentonite as a backfilling material.

Seven main objectives were identified, together with numerous tasks to be fulfilled. The objectives focused on open questions remaining from Phases I-III:

(A) definition of path lengths and description of flow pathways
(B) dating the system (including the near-field cement hydration and the longevity of C-S-H phases)
(C) rock-matrix diffusion
(D) source-term definition and cement-alteration characteristics
(E) clay-leachate interaction
(F) coupled-code modelling and data organisation
(G) microbial studies.

The objectives and the content of the different tasks planned in Phase IV are outlined in Table 1.1.

However, following changes in the national programmes of several of the funding organizations, some objectives had to be either shelved or modified during the course of Phase IV.

Table 1.1 Phase IV main objectives

Task No.	Activity	Justification
Objective 1: Pathlengths and flow paths		
A1	Fracture mapping and flow system definition	Evaluate fracture patterns (geometry, frequency and relative timing of generation/reactivation), their significance for flow and structural controls on disposition of combustion zones. Provides context for smaller length scale analyses.
A2	Investigation of fracture-filling phases	Examine composition and paragenesis of the fracture-filling phases, including the relationship of mineralogy to fracturing. Supports conceptual model, Tasks C and D1.
A3	Hydrogeology	Interpretation of hydraulic and tracer tests provides information to specify site context for groundwater sources/sinks, flow path lengths and transport times.
A4	Investigation of rhenium	To evaluate the spatial distribution of rhenium concentrations in groundwaters and mineral phases as an analogue for technetium.
Objective 2: Constraining timescales		
B1	Age of the cement-zone hydration	Maximum hydration age ‘sets the clock’ for the kinematics of CSH, CASH and zeolite phases.
B2	Longevity of CSH Phase	Combine data on phase dating relationships and flow field evaluations to allow timescales of different plume environments to be assessed (and hence variation in rock mass transport properties). Combines with A2 and D1.

Objective 3: Rock Matrix Diffusion		
C	RMD	Investigate potential for radionuclide retardation and the way that CSH & CASH phases modify hydro properties.
Objective 4: Source term		
D1	Origin of Na/KOH and Mineralogy	Identify physical position of K/Na in cement to confirm model of early evolutionary phase. Review and reassessment of earlier data. New analytical study of mineralogy and paragenesis of cement and alteration zones.
D2	Cement alteration: Leaching	Understanding of evolution of the alkaline plume in relation to alteration in the cement zone (leaching) and comparison with man-made cement.
D3	Cement alteration: Magnetic properties	Derivation of fossil temperature profile by use of mineral magnetic properties. To evaluate use of technique and better understand iron speciation/redox.
Objective 5: Clay/leachate interaction		
E	Kusham Matruk sampling and analytical work	To find clays that would be appropriate to study and investigate stability of smectites under hyperalkaline conditions.
Objective 6: Modelling		
F1	Integration of site data	Provide the context for detailed studies; presentation and integration of site-scale information. Continuation and extension of Tasks A1 and A3.
F2	Identify data and availability	Pre-modelling study of precise aims, data availability, limitations and methodologies, evaluate uncertainties.
F3	Simulate quantitatively the subsystem	Hypothesis testing: evaluate solubility & kinetic controls; speciation; modelling of evolution of transport properties; constrain fluxes, evaluate retention of trace elements during alteration.
F4	Archivation and organisation of data	Enable easy access to all data.
Objective 7: Microbiology		
G1	Total number of microbes	To obtain the total number of native viable and non-viable microbes present.
G2	Culturing	Identify physiological groups and numbers.
G3	Uptake of organic carbon	Determine whether viable high pH microbes are active.
G4	Surface attachment	Find out if the viable native microbes attach to surfaces.
G5	Fossil microbes	Look for traces of former microbial growth

1.4 Phase IV Report

The structure of this Report reflects the nature of the tasks which were eventually accomplished and, thus, differs somewhat from Table 1.1.

In Chapter 2, the tectonic setting, geology and hydrogeology of the Maqarin site are updated. The latest data have improved the conceptual model of the site and its evolution. The concluding studies at the Adit A-6 site, which has now been obliterated by the construction of the Unity Dam (see Figure 1.7) are reported, along with new data on matrix diffusion.

In Chapter 3, the Maqarin hydrochemistry is likewise updated and the final analyses of Adit A-6 samples included. The regional hydrochemistry is described, with a concluding section on the hyperalkaline groundwater/host rock alteration.

Chapter 4 covers the cement zone, the source of the hyperalkaline leachates. The primary (cement slag) mineralogy is updated, followed by descriptions of the hydration phase mineralogy and the secondary cement phases. In addition, laboratory experiments on trace element leaching are reported. Finally, accumulated knowledge on the cement zone is synthesised.

Chapter 5 begins with an overview of all previous microbiological studies at Maqarin. The main part of the chapter then focuses on the *in situ* activity of the microbes in the hyperalkaline groundwaters.

In Chapter 6, the new site at Kyushaym Matruk is covered in detail for the first time, with the main field campaign described first. New data are then presented on the site mineralogy, primary and potential secondary clay minerals, isotope geochemistry and organic matter characterisation. This new information is then synthesised, and current undestanding of the site reviewed. The main areas of uncertainty, which require further study, are also noted.

In the concluding text, Chapter 7, the main findings from the two sites (Maqarin and Khushaym Matruk) are summarized, and the main quantitative and qualitative PA conclusions from each presented. Open questions are also raised, to which some solutions proposed.

Finally, extensive data tabulation, and much of the detailed supporting information, has been placed in the Appendices.

Chapter 2

Tectonic Setting, Geology and Hydrogeology of Maqarin

P.J.Degnan, E.Salameh, H.Khoury, A.E.Milodowski, U.K.Mader and M.White

2.1 Introduction

The geological objectives at the outset of the Phase IV work programme were to:

- investigate whether information was available from satellite and aerial imagery, in order to place the Adit A-6 studies and other local data into a wider site context
- undertake detailed fracture mapping, in order to produce fracture network models that would be suitable for incorporation into flow simulation models (together with hydraulic test data)
- re-examine the published literature for northern Jordan, north-east Israel and southern Syria, to ascertain if structural insights from other areas could be applied to the Maqarin area
- examine whether there is a relationship between the observed fracture patterns and the spatial distribution of metamorphic zones in the Bituminous Marl and Chalky Limestone Formations.

All of the above objectives were achieved with the exception of the second. In this instance, although extensive fracture mapping and a limited number of hydrogeological tests were undertaken at the site, it was not possible with the limited resources available to construct discrete fracture network or continuum flow models. However, the observations of fracture characteristics have proved to be invaluable in providing a structural history of the site that is consistent with the regional tectonics. This understanding, combined with the results of the hydrotests, support a model of hyperalkaline plume transport dominated by fracture flow.

In the following sections, the regional tectonic setting of north Jordan is presented first (Section 2.2). The stratigraphic sequence observed at Maqarin is then summarised in Section 2.3, followed by a brief analysis of satellite images and aerial photographs taken over the site. The results of fracture mapping in Adit A-6, and at outcrop scale, is then provided (with the results tabulated in Appendices 2.1 and 2.2), followed by the results of a small-scale surface- based resistivity survey. In Section 2.4 the regional hydrogeological setting is briefly described (with the data and methodology presented in Appendix 2.3) and an interpretation of the local hydrogeology is presented. This is based on transient pressure analysis measured in boreholes drilled in Adit A-6 and equipped with monitoring equipment. In the concluding part of this Chapter (Section 2.5), the integrated local geological and hydrogeological understanding developed during the Phase IV studies is used to introduce a series of three- dimensional models. These models are presented at the site scale and an embedded Adit A-6 model has also been produced. The models are available on a CD ROM that accompanies the Report. With its use, various features like topography, water-table elevation, lithostratigraphy, and the

location of boreholes, adits and hydrochemical sampling points, can be visualised interactively by sectioning or rotating the modelled volume. Instructions for the use of the software, along with a description of the development of the model, are presented in Appendix 2.4 and the full model in Appendix 2.5.

2.2 Regional Tectonics

Jordan is a country situated in close proximity to active and dormant plate boundaries. The complex tectonic history of the region has shaped a diverse landscape, reflecting varied geological deformation and sedimentation. The earliest tectonic event of relevance to the Maqarin study is recorded in structures that formed in a regional stress field that affected northern Jordan and parts of Syria, Lebanon and Israel sometime between the Late Maastrichtian and Miocene (Quennell, 1958). This compressive-stress regime was initially orientated east-south-east – west-north-west. It resulted in low-amplitude, long-wavelength folds and allowed shallow marine sediments to accumulate in broad troughs on a continental margin. With time, this stress field intensified and rotated clockwise towards a south-east – north-west orientation. This situation appears to have lasted until the Miocene. As well as creating new structures such as fractures, it affected earlier folding by deforming pre-existing north-north-east - orientated fold-hinge lines, as seen for example at Maqarin[6]. Also during the Miocene, a final adjustment in the compressional stress orientation then occurred with the continued clockwise rotation of the stress field towards a north-north-west – south-south-east direction.

The stage of late-Mesozoic to early-Cenozoic deformation may have been related to far-field effects caused by subduction of Tethyan Ocean micro-plates and several episodic collisions of their associated continental terranes along previously passive margins. There are several alternative plate-tectonic interpretations for this stage in the history of the eastern Mediterranean (e.g. Robertson and Dixon, 1984; Dercourt et al., 1986; Robertson et al., 1991). Debate centres on plate movement vectors, relative plate configurations and the nature of the subducted crust in several of these areas (i.e. oceanic versus thinned continental crust). Many of these issues are still unresolved, although the field-based evidence for a consensus position is growing.

The stress regime in Jordan changed significantly in the Oligo-Miocene with the rifting and then sea floor spreading of the Red Sea, splitting the Arabo-Nubian shield and causing the rotation of the African and Arabian plates. The initiation of the Dead Sea Fault System, between the Arabian plate and the Sinai microplate, was a result of these plate movements. Geological evidence indicates the system has been active since at least the mid-Miocene (Horowitz, 1987). Since this time, and up to the present day, the Dead Sea Fault System has been the major tectonic structure closest in proximity to the Maqarin site in northern Jordan. The Dead Sea Fault System runs for almost 1,000 km from the Gulf of Aqaba in the south, northwards to the East Anatolian Fault in Turkey and the frontal thrusts of the Tauros/Zagros mountains. The Dead Sea fault is a left-lateral transform accommodating strike-slip movement caused by the differential convergence of the Arabian and African plates with Eurasia. It was formed by the faster movement of the Arabian plate relative to Africa, and as a consequence of the opening of the Red Sea and the subduction of remnant oceanic crust along the leading edge of the Arabian margin. The Arabian plate is presently being pushed northwards at a rate of 18±2 mma^{-1} (McClusky et al., 2000) with relative motion between Arabia and Africa of about 5 - 10

[6] At Maqarin, a broad antiformal fold axis swings from the north-north-east to the south-south-west on the Jordanian side of the Yarmuk valleyand then further towards the east on the Syrian side (see Section 2.5).

mma^{-1}. Although dominated by strike-slip displacement, the Dead Sea Fault System is complex and comprises a number of strands accommodating transpressional movements at restraining bends, as observed in Lebanon (Griffiths et al., 2000). Also, there are transtensional elements, as observed along the Dead Sea rift margin of Jordan and the pull-apart Ghab Basin in western Syria. The evolution of the Dead Sea plate boundary, either as a continuous deformation event or partitioned into two discrete phases associated with Red Sea sea-floor spreading, remains conjectural (Beydoun, 1999).

Although the dominant present-day stress field in northern Jordan is strike-slip, with an inferred north-south orientated maximum horizontal compressive stress, mantle upwelling centred on, and adjacent to, the Red Sea is occurring. This may have resulted in locally highly variable stress vector orientations that have affected the Maqarin area. The clearest large-scale expression of this stress variability is seen in the timing and orientation of volcanic centres forming the Harrat Ash Shaam basalt field (see Tarawneh et al, 2000). This type area of “Plateau Basalt” probably developed along crustal weaknesses in south-western Syria, north-eastern Jordan and into north-western Saudi Arabia.. The volcanic vents and associated dykes are principally orientated north-west – south-east and may relate to the exploitation and reactivation of older structures that trend parallel to the Red Sea. Basalt-dominated eruptions have occurred during various phases of activity from the Miocene through to the Holocene (Llani et al., 2001) and there may have been eruptions in the southern Syrian fields as recently as ten thousand years ago. The earliest phases of volcanism appear to correlate with activity along the Red Sea ocean-floor spreading system - up to 22 Ma BP. After a period of quiescence between 22 and 13 Ma BP, volcanic activity resumed. This has continued until recently and appears to relate to recent movements of the Dead Sea Fault System (Ibrahim et al., 2002), rather than Red Sea activity.

In summary, the regional tectonic history appears to comprise:

- Originally east-south-east – west-north-west then more north-west – south-east - orientated compression relating to closure of Neotethyan ocean basins. This formed broad fold structures that parallel the Syrian Palmyride fold belt. The structures associated with this stress field are of probable late Cretaceous and Lower Tertiary age
- North-east – south-west - orientated extension, forming dilational north-west – south-east structures and related to Red Sea rifting during the Oligocene and later sea-floor spreading, possibly still affecting the region today and superimposed on the effects of the Dead Sea Fault System
- North-south transverse fault movement, due to the relative displacement of the Arabian plate with the African plate along the Dead Sea Fault System. Active faulting has been occurring since the Miocene and a north-south orientated, maximum horizontal stress vector is implied, except in areas of transpression and transtension where there is local complexity.

Each of these phases of tectonic activity is likely to have left a structural record in the Maqarin area.

2.3 Local Geology

2.3.1 Introduction

The Maqarin study area is located in the Yarmouk River valley at the Syrian-Jordanian border, 16 km north of the provincial town of Irbid .The local rock units comprise Cretaceous-Tertiary shallow-marine carbonate strata, overlain by Quaternary basalts, soils and alluvium. The east-west - trending Yarmouk River Valley (see Figure 1.2) is a relatively recent geomorphological feature, having incised through some 400 m of the Irbid Plateau, almost down to sea level. Although there is clear evidence for east-west fractures present at Maqarin, this is not a dominant structural orientation and there is no direct evidence that the development of the Yarmouk valley has been structurally controlled by large-scale tectonic faulting, including tectonism associated with the Dead Sea Rift Valley system (Pitty, 1998). A more complete description of the Yarmouk River valley and its associated geomorphology, together with local stratigraphic and structural information for the Maqarin site, has already been described in previous phases of the natural analogue project (Alexander 1992, Linklater 1998, Smellie, 1998). Consequently, the stratigraphy and new structural information are only briefly reviewed in the following section.

2.3.2 Stratigraphy and general structure

A generalised stratigraphic column is presented in Figure 2.1 and Figure 2.2 shows the general geology of the Maqarin area. The oldest stratigraphic unit at the site is the Upper Cretaceous Amman Formation. However, it does not outcrop in the immediate vcinity of Maqarin. The formation comprises thinly bedded limestones, cherty limestones and cherts with a local total thickness of 90 m.

The Amman Formation is conformably overlain by the Bituminous Marl Formation, also of Upper Cretaceous age. This unit reaches a thickness of 220 m locally. It comprises clay biomicrites with a high organic (immature kerogen; see Smellie, 1998) content and in some locations includes large limestone concretions (to 180 cm diameter) containing thin chert bands. The formation outcrops along the base of the Yarmouk River valley for a distance of 1.5 km to the east of Maqarin and also outcrops within the core of a local antiformal structure. The upper part of the formation, together with the lower part of the overlying Chalky Limestone Formation, is the horizon within which pyrometamorphism has occurred, resulting in natural cement zones. These are referred to as the Analogue Cement Zone (ACZ) in this Report. In isolated areas, which appear to be decimetric in scale and shaped as irregular “pods”, the rocks were metamorphosed at high temperature but low pressure and then brecciated. The extent of these rocks and the nature of the contacts have been described by Khoury and Nassir (1982) and in previous reports produced by the Maqarin natural analogue study group (Alexander, 1992; Linklater, 1998; Smellie, 1998).

The main lithostratigraphic unit exposed at Maqarin is the Chalky Limestone Formation, with a thickness of 300 – 390 m. It outcrops along both sides of the Yarmouk River valley and conformably overlies the Bituminous Marl Formation. It is dated as Lower Tertiary in age and comprises three members:

- *Lower Chalky Limestone Member*: The lower 50 m of this 190 m thick unit consists of thick-bedded homogenous limestone. Locally, the lower parts are organic-rich

and are also part of the ACZ in places. The overlying beds comprise thinner-bedded white micritic and crystalline limestone.

- *Chert Chalky Limestone Member*: This unit is 30-40 m thick and consists of chalk limestone beds with numerous thin chert beds.
- *Upper Chalky Limestone Member*: The unit is 170 m thick and is similar in lithology to the lower member. However, it is softer and less resistant to weathering.

Figure 2.1 Regional lithostratigraphic correlation chart (from Khoury et al., 1998)

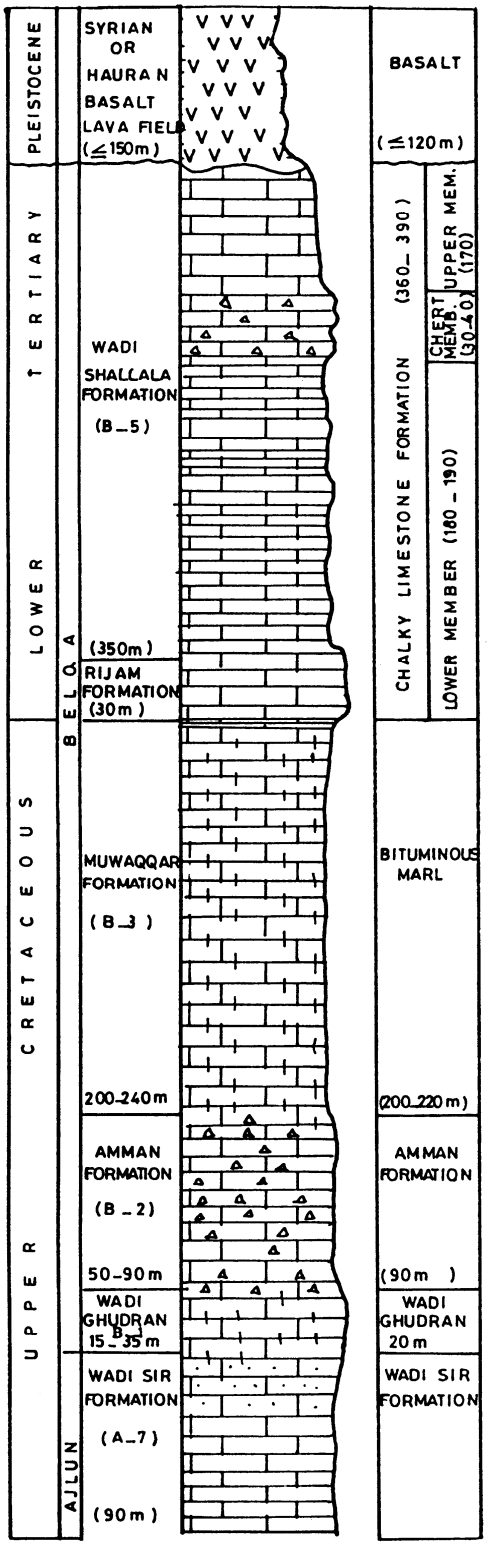

Figure 2.2 The general geology of the Maqarin area. ES = Eastern Springs locality; WS = Western Springs locality.(from Smellie,1998). Note that newly generated cross-sections of the site are available in Appendices 2.4 and 2.5.

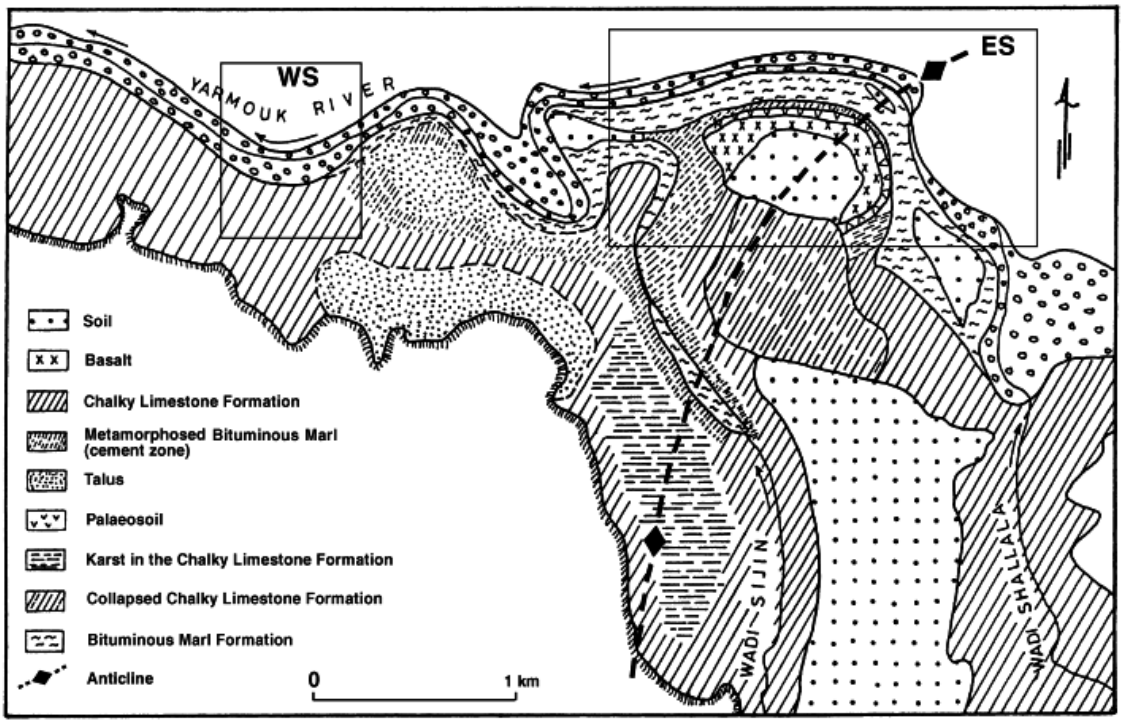

Generally, all the above stratigraphic units strike east-west with a low (<5°) dip to the north. The Amman Formation shows two distinctive structures locally; a north-south trending broad antiformal fold and an east-south-east – west-north-west - trending depression along which the Yarmouk River flows for a distance of about 550 m (Figure 2.2). Mapping of the structural contour lines, based on boreholes drilled into the Amman Formation, show the antiform trending north-north-east – south-south-west in its southern part This changes to north-east – south-west on the Syrian side of the river. On the south-eastern limb, strata dip at 18-20° before becoming horizontal after approximately 2 km. On the opposing flank, the dips are gentler and towards the north-west. Other than extensive fracturing (described below) and the above structures, the area appears to be little affected by deformation. However, some large-scale faulting has been inferred (Harza, 1978) and observed in previous phases of the Project (e.g. Smellie, 1998). New observations reported below demonstrate that small-scale displacements are prevalent, on the basis of slickenfibres and other movement indicators.

Igneous rocks (basalt) of the Jebel Druze-Wadi Hauran volcanic province are present in the area. They form a series of layered lava flows unconformably overlying the sedimentary strata. They outcrop mostly on the Syrian side of the valley where they are seen to have flowed over an extensive broad plain from a line of low-lying volcanic vents. The lava flows infilled the palaeotopography, including drainage channels now dissected by the Yarmouk valley (Figure 2.3). The basalts locally have a maximum thickness of 100 m and thin to the east and south. They are referred to as the Hauran Basalts and have been dated at 5.0 to 3.5 Ma. A much younger basalt flow is present in the lower reaches of the Yarmouk River (0.48 – 0.35 Ma), and is referred to as the Raqqad Basalt. There is a basalt outcrop present on the Jordanian side of the valley, on the west side of Wadi Shallala and close to Adit A-6. It directly overlies a palaeosol of 3 m thickness. The assignation of this basalt has not been established, but it appears to be *in situ* and not transported (as postulated in previous reports).

Figure 2.3 View of basalt flow infilling a steep-sided palaeo-drainage channel, now incised by the Yarmouk River, on the Syrian (north) side of the valley (approximately 3 km downstream from the Maqarin site).

2.3.3 Interpretation from satellite imagery and aerial photographs

Two satellite-based earth observation systems and a sequence of aerial photographs support the information collected from previous phases of field-based geological interpretations at the Maqarin site. They also aid identification of further exploration targets,. These images were used to investigate larger-scale geological and geomorphological structures in the vicinity of Maqarin. Satellite imagery was obtained by the British Geological Survey and comprised Landsat Thematic Mapper and SPOT imagery. The Landsat system has a spatial resolution of 30m per pixel. It is multispectral, comprising 7 component bands and, although all of the multispectral bands respond differently to different features, bands 3 (red: 0.63-0.69 μm), 4 (reflective infrared: 0.76-0.90 μm) and 5 (mid-infrared: 1.55-1.75 μm) were selected for use because they best discriminate the local geology. The SPOT imagery, on the other hand, is panchromatic (i.e. it has only one band, a greyscale), but it does have the advantage of a 10 m spatial resolution. Therefore, it was therefore decided to merge the two image datasets to make use of the combined spectral qualities of the Landsat Thematic Mapper and the spatial qualities of the SPOT-derived data. The merged high-resolution multichromatic image shown in Figures 2.4 and 2.5 were used for interpretation. The corner co-ordinates for the image are: upper left x:220873.1250, upper left y:241536.8750, lower right x: 236373.1250, lower right y:230006.8750. Units: metres. Spheroid: WGS 84.

Figure 2.4 Preliminary interpretation of the Maqarin site using combined Landsat and SPOT imagery. The trace of the Yarmouk river (the Jordanian-Syrian border) is shown in green. Scars attributable to landslips are coloured blue and interpreted fault/fracture lineaments are indicated in red.

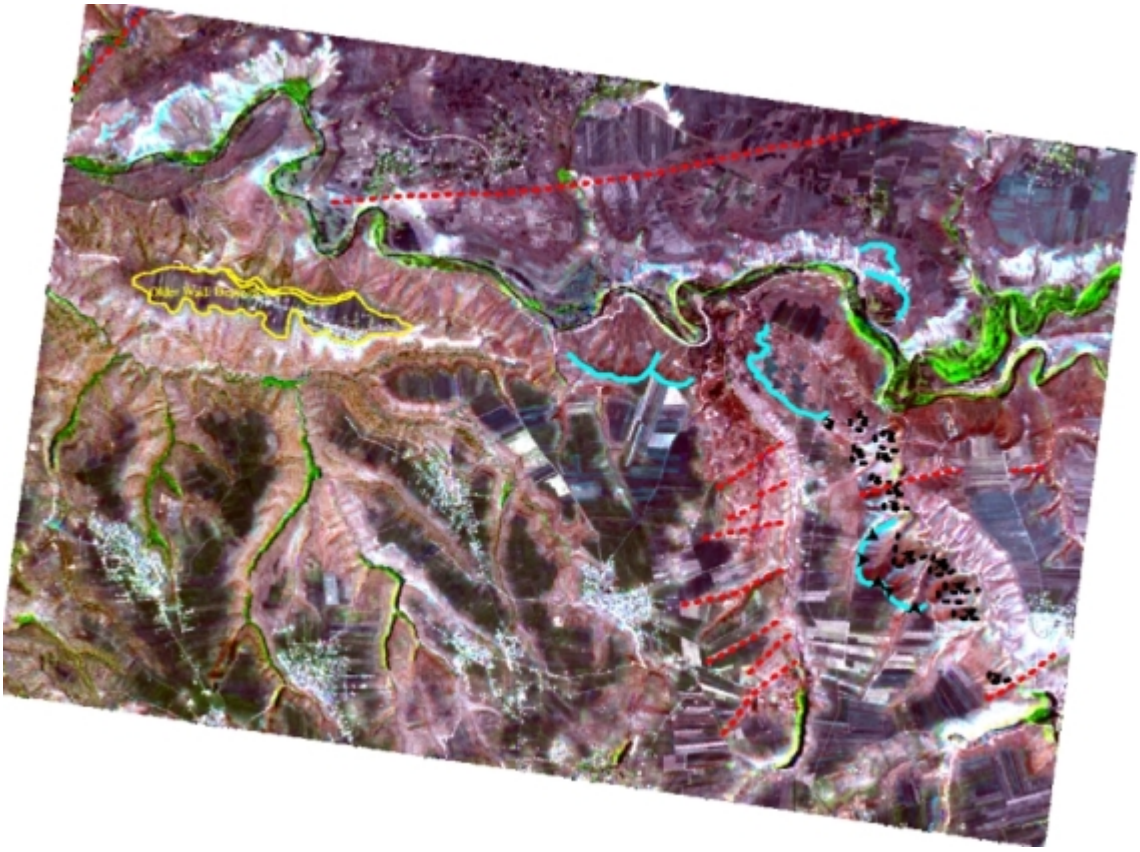

In addition to the satellite images, aerial photographs of the area were obtained, on behalf of the project partners, by the University of Berne (see, for example, Figure 1.2). The quality of the images is good, and they were analysed using x3-magnification stereoscopes.

Features of note from the interpretation of both the satellite and aerial images include the following:

- A region of enclosed elliptical depressions is present to the south of the detailed-study area, on the west side of Wadi Sijin. They may be karstic sink holes and dolines, or the result of mass movement of rock by block-gliding (Pitty, 1998). The features are several metres to several tens of metres in extent., and are highly localised in a 150 ha area of the Chalky Limestone Formation. Possibly, they formed in relation to a strong lithological control exhibited by the particular horizon outcropping at this site. The evidence in the field suggests that they are mass-movement features, related to cambering (Pitty, 2000), and associated with carbonate dissolution. These processes are locally significant and may exert a strong control on the regional and local groundwater system. It is noted in Chapter 3 that two depressions are present in the immediate vicinity of Adit 6.

Figure 2.5 Same image as previous Figure 2.4, but focused on the immediate Maqarin study area.

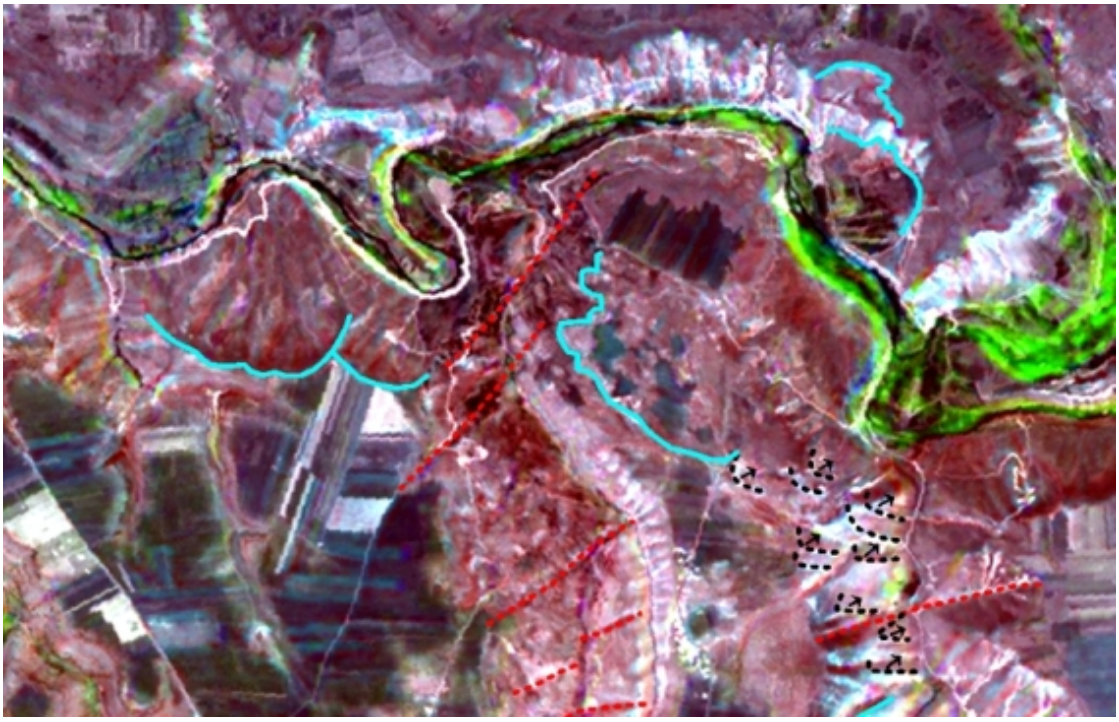

- Interpretation of the combined satellite imagery initially suggested that the deeply incised nature of the Yarmouk valley developed as a result of major land slipping and mass wastage. Pitty (1998) used this hypothesis to explain certain of the drainage diversions in the main valley. It was also noted that the effects of landslides triggered by seismic events elsewhere in the Yarmouk Valley and on the southern shore of Lake Tiberias. It has been suggested that catastrophic collapse of valley walls, possibly initiated by earthquakes, could be a causal factor in the combustion of the organic-rich horizons. Scallop-shaped margins on both sides of the valley, where the ca. 35° slope meets the plateau, appear to overlap in the satellite images, suggesting a chronology of major land slip events. In the field, however, the ground-based observations indicate that retreat of the valley sides is a more gradual erosional process, at least at the present day. This is based on the fact that although there is a great deal of talus present, and possibly minor rockslide deposits, there are no significant remnant mass flow debris deposits of material along the valley floor[7]. Nor has rafting of whole sections of relatively intact material down the valley slopes occurred. Rather, the recent deposits are dominated by poorly sorted talus with clast size ranging from gravel grade to boulders. Small-scale listric fractures are, however, observed in road sections above the Adit A-6 and along the margins of the adjacent wadis, Sijin and Shallala. The late-stage listric fractures have an east-west (valley-parallel) orientation in the Yarmouk valley and indicate that, in the past, some gravitational collapse and local slippage has occurred. Consequently, and as expected, erosion is certainly an important and active process. It has resulted in approximately 400 m of down-cutting in the river valley since its formation. Although the valley sides are steep, erosion is not, however, presently evident on the massive scale envisaged from the preliminary satellite image interpretation. The overlapping rims at the top of the valley coalesce and appear to be retreating gradually rather than by discrete landslip events.

[7] Although this may have been washed away by the periodic floods which sweep down the river valley.

- Gently eastward-dipping strata are observed in Wadi Shallala and a gentle antiformal structure can be recognised in both the satellite imagery and the aerial photographs. These data are consistent with the structural observations for a north-east plunging fold, clearly visible on the Syrian side of the valley (Bender, 1974; Harza, 1978). However, on the Jordanian side, the hinge line is not apparent from the imagery, although it has been mapped in the field, based on the dips of exposed strata.
- North-east – south-west lineaments of several hundreds of metres length are present in the satellite images and are visible in the aerial photographs. They represent one of the dominant structural sets mapped in the field (Section 2.4).
- A significant lineament, trending east-north-east, is observed on the Syrian plateau (Figure 2.4). This feature can be traced for several kilometres and was observed in both the satellite and aerial imagery. Access to the Syrian side of the valley was not possible during the Phase IV investigations and so the nature of this lineament cannot be assessed.

2.3.4 Fracture characteristics

Fracture mapping was carried out at several localities, both within Adit A-6 and in its immediate vicinity (i.e. within 3 km). In addition to observations in the Adit (within the first 130 m of the entrance), the principal mapped locations were: (i) a road cutting along Wadi Shallala (Waterfall Road cutting in Figure 2.6); (ii) a road cutting 150 m west of Maqarin Station; (iii) a bench cutting 5-10 m above and immediately to the east of the Yarmouk river bridge (which is almost directly below Adit 6) and (iv) a small alluvial terrace above the Bituminous Marls but situated 200 m east of the river bridge and off the road. In addition, several other localities were spot-checked for their dominant fracture orientations. This ensured that the main sample sites were representative of the general area and not being masked by local complexity or measurement bias. As a result of the mapping and analysis, it is possible that the fracture mapping is statistically biased by the dominant east-west orientation of the investigated outcrops, formed by the valley and by many of the road cuts. Mapping in Adit A-6 and in Wadi Shallala and Wadi Sijin was, however, orthogonal to the faces mapped at these main sites. In addition, an element of censoring is clear, caused by the scale of the field mapping and the incomplete exposure of the fractures. In general, hairline (and smaller) joints were not recorded, nor were any large linear features that could not be recognised at outcrop-mapping scale (such as those that might be recognised only from aerial or satellite observations).

Several hundred fracture measurements were made in the Bituminous Marl and Chalky Limestone Formations and the data are collated in Appendix 2.1. Where possible, the observations undertaken in the field comprised the following:

- fracture orientation as dip and strike
- frequency/spacing
- measurement of exposed fracture-trace length
- whether the fractures terminated at bed boundaries or within beds
- whether the fractures cut-across earlier structures
- whether there are kinematic indicators present (providing a slip sense)
- whether the fractures are currently open (with measurable aperture) or relatively sealed
- whether the fractures contain a mineral infilling

Figure 2.6 Main fracture mapping locations

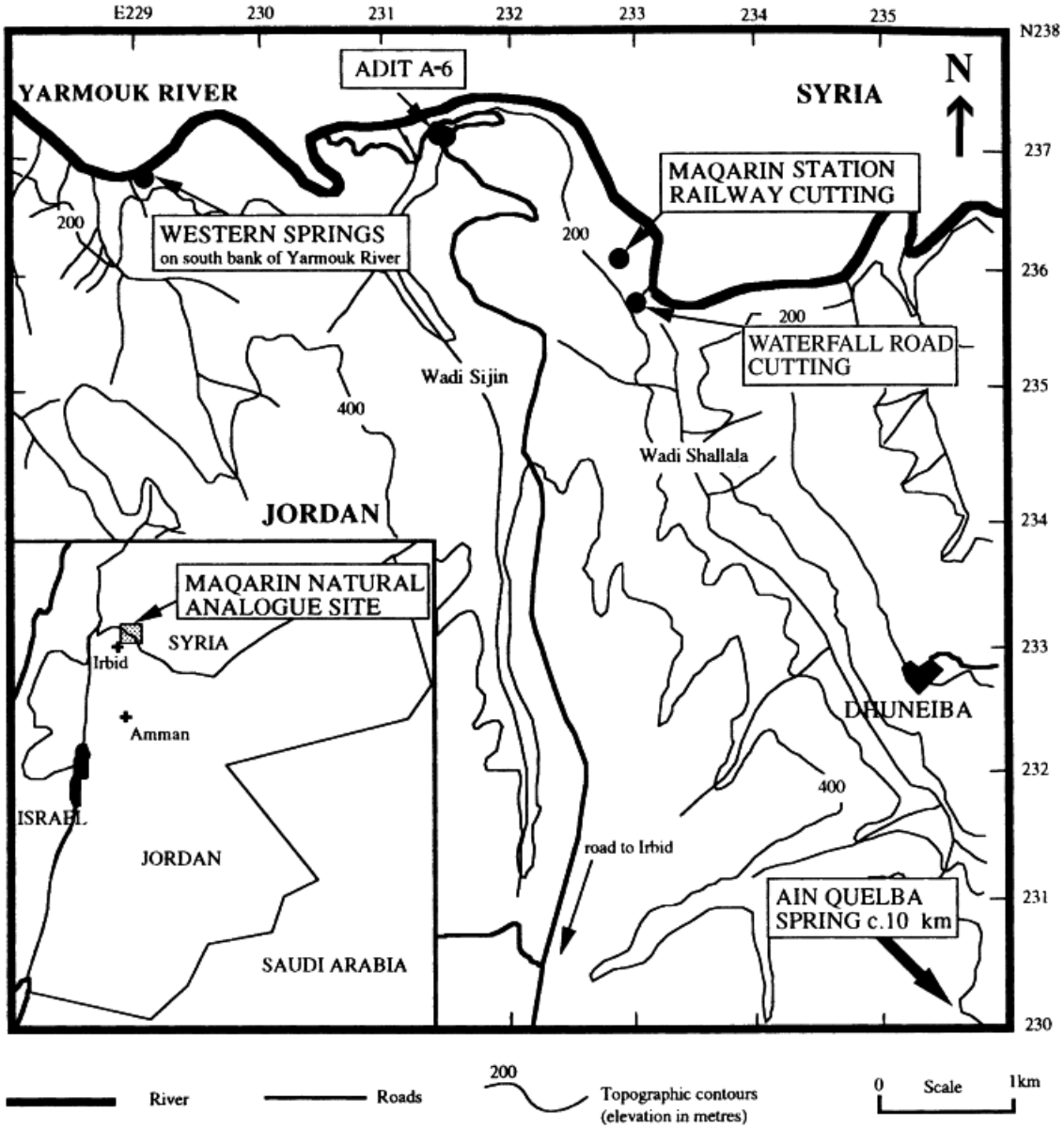

In the case of mineralised fractures, the dominant vein mineral and the presence of any accessory minerals was recorded, as was the nature of the mineralisation (e.g. deposition over several events or during a single episode).

Based on strike orientations, there are two major fracture sets present at Maqarin. A typical illustration of the nature of fracturing in the Chalky Limestone Formation is shown in Figure 2.7. By far the most significant set, in terms of the number of measured fractures, is orientated north-south (340° to 020°). A second set is present, with a north-west – south-east trend, with much less frequent fractures orientated north-east – south-west and broadly east-west (Figure 2.8). As can be observed on the rose diagram, the north-south and north-west – south-east azimuth data merge, but statistically these are discrete sets. Most of the observed fractures have steep to vertical dips (70-90°). These fracture sets are attributed to the prevailing regional and local stress fields at the time of their formation.

Figure 2.7 Typical fractures in Chalky Limestone Formation outcrop along Wadi Shallala road cutting adjacent to the Yarmouk River valley (looking NW towards the river).

Most fractures appear to be straight-forward dilational features. However on several fracture surfaces, there are slip indicators such as slickenfibre development (Figure 2.9) and pinnate joints forming at approximately 30° to the main fracture planes. There are also “small-scale steps” caused by micro-failures that represent the movement sense as the fractures were formed by shear strain. The kinematic indicators show a latest sense of movement that is largely almost pure strike-slip, with both dextral and sinistral movements observed. However, at Wadi Shallala, a fracture trending to 310° and dipping 40° to the north-east has slickenfibres, indicating a normal sense of displacement. This is cut by a later high-angle, north-south calcite vein. Elsewhere, as on the bench cut above the river, multiple reactivation of fractures is observed, with up to four generations of calcite forming crack-seal veins.

The north-south orientated fractures indicate that flow anisotropy is likely and the fractures are potentially significant pathways for flow. Unloading of the rock strata at bounding free surfaces, observed where road cuttings have incised the valley slopes, has produced stress relief along bedding-parallel horizons. This has generated a facoidal-type fabric in certain thin-bedded horizons of the Bituminous Marl and Chalky Limestone Formations. Stress-relief has also created voids for seepage along horizontal planes and at intersections with high angle joints. This is clearly displayed at the mineral springs site 100 m to the west of the Maqarin Station railway cutting (Figure 2.10).

Figure 2.8 *(a) Rose diagram showing strike orientations of fracture sets measured at Maqarin during Phase IV studies (n=586); (b) Stereonet showing poles to fracture planes and 2% per 1% area contour interval (n=586).*

(a) *(b)*

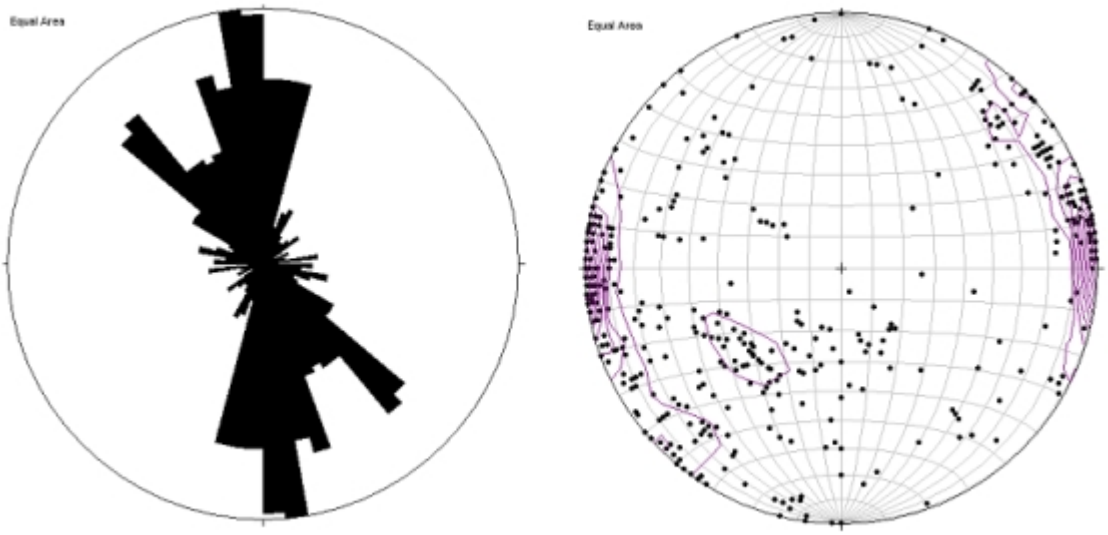

Figure 2.9 *Slickenfibres on fracture plane indicating shear movement (dextral strike-slip).*

Figure 2.10 Travertine formed by alkaline seepage from the rock-face cutting near Maqarin Railway Station. Note the hammer in middle foreground for scale.

A common observation in the field is that the north-south orientated fractures appear to form regularly spaced regions of greater and lesser intensity within members of the Chalky Limestone. The fracture-frequency histograms confirm this where logged. Where pink, mottled Chalky Limestone was observed in road cuttings or slopes, it was interpreted as a partially baked limestone, rather than a primary sedimentary colouration or due to weathering (Figure 2.11). There is greater fracture intensity in such exposures than at the adjacent sides, where there is a rapid transition to a more typical cream-coloured limestone in areas of lesser fracture frequency. This transition suggests that the combustion zones may have had a pre-existing structural control that limited the lateral extent of the intense pyrometamorphism (Figure 2.12). Furthermore, the vertical nature of the dominant fracture sets at Maqarin would have facilitated the ingress of oxygen down to the Bituminous Marl Formation to maintain any combustion and also acted as "chimneys" allowing heat to be transmitted vertically upwards into the Chalky Limestone Formation.

In addition to the main fracture sets described above, another distinctive fracture orientation is aligned east-west[8]. These fractures are seen in the road cuttings, especially high level (>200 m above sea level (a.s.l) road cuttings, and at outcrop higher up the valley sides within the Chalky Limestone Formation. They are also present on a smaller scale in Adit A-6. From field observations, the east-west striking fractures may represent two generations. One generation, measured along the valley floor, is high-angle and relates to the "older" tectonics of the area, being very similar to the north-south orientated fractures in nature and observable extent.

[8] An example of a similar low-angle listric fault, but striking north-south, was observed in Wadi Sijin, i.e. parallel to the wadi sides.

Figure 2.11 Cooling joints formed in baked pink, mottled limestone of the Chalky Limestone Formation

Figure 2.12 Transition from partially baked Chalky Limestone (pink) to less intensively fractured zones in the unaltered Chalky Limestone Formation, suggestive of a structural control on the lateral extent of combustion. 20 cm long rule for scale (left of foreground).

However, other east-west fractures appear to be much more recent. This latter set sometimes has joint planes that are listric or low angle (<40°) and dip towards the north (Figure 2.13). They clearly cross-cut more linear fractures orientated north-south. Usually

these fractures are open with apertures of at least several millimetres and sometimes much wider. In places, gypsum is observed filling the fractures, but generally they are barren. On the main road in the area leading down to the valley bottom, breccia-filled zones have been observed adjacent to a low angle east-west joint (possibly fault) surfaces (Figure 2.14). The listric and low-angle fractures are interpreted to represent rock failure during gravitational collapse of the valley sides and are postulated to be very recent features. However, whether they relate to ancient catastrophic landslip events, of which there is no evidence in the very recent past (1000 years or so), or the effects of more localised gradual displacement is unclear.

Fracture mapping was also carried out in Adit A-6. A total of 113 fractures were identified in the 130 m section logged within Adit A-6 (Appendices 2.1 and 2.2). The fractures represent the dominant features observed in the roof of the adit, at the scale of mapping. Fractures with trace lengths less than approximately 10 cm, or fractures that did not intercept the Adit roof or upper walls, were ignored. The Adit is orientated north-south and so a much greater cross- section of features, aligned at an angle to this orientation, were sampled than from many of the road-cutting exposures.

Figure 2.13 Listric fracture surface cutting older north-south orientated fractures. Hammer for scale (arrow).

Figure 2.14 Brecciated zone within low-angle, east-west fracture planes, possibly representing rock failure during slip associated with gravitational collapse of valley sides. Field of view approximately 3 m.

The fracture logging in Adit A-6 identified the following types of fracture fills:

- ***Calcium-Silicate Hydrates (CSH) (undifferentiated)***. This is typically a white gel-like filling material, which previous petrographical studies (e.g. Milodowski et al., 1992a, 1992b, 1998a, 1998b) have shown to be CSH. Observations using a portable infrared mineral analyser (PIMA) on selected representative samples were used to aid the identification of CSH but were unable to resolve the type of CSH mineral present.
- ***Early Calcite***. This is well-crystallised but xenomorphic translucent white-to-grey vein calcite that formed before pyrometamorphism. It is the earliest mineralisation observed in veins.
- ***Ettringite/Thaumasite (undifferentiated)***. This is typically fine cross-fibre vein mineralisation which is tentatively identified on visual examination and comparison with previous material which has been studied in detail. Previous petrographical analysis and XRD data on selected samples has confirmed the mineralisation to be ettringite, thaumasite or a solid-solution between the two end members. Field PIMA observations were used on selected samples in the field to aid mineral identification. However, ettringite and thaumasite cannot be differentiated by visual field observations alone.
- ***Jennite***. Jennite is only identified for a limited number of fractures where detailed mineralogical data (petrography, XRD, EPMA) have been obtained for fracture infill or similar infill from nearby fractures. Elsewhere, the jennite (if present) was logged as CSH.
- ***Tobermorite***. Tobermorite veining is locally well-developed, and produces distinctive 'waxy' and 'honey-coloured' massive and fibrous monominerallic fillings. Selected representative samples have been analysed by XRD and petrographical

analysis, and shown to be tobermorite *sensu stricto*. Possibly, some fine tobermorite mineralisation has not been recognised and may have been logged as CSH.

- ***Gypsum***. Fine white gypsum coatings are distinguishable in some cases. Field PIMA observations were used to confirm the identification on selected representative samples but, possibly, some gypsum has been misidentified as Ettringite/Thaumasite and vice versa.
- ***Late Calcite (Travertine)***. Late calcite (or calcium carbonate) precipitates usually accompany features associated with active high-pH groundwater discharge. This is typified by coatings of fine white tufa (travertines). These form the latest mineralisation on fracture surfaces.

Some fractures, which were dry at the time of observation, contain relatively recent tufa-like carbonate coatings, indicating that they probably carried recent high-pH groundwater but have since become 'drained' or sealed. There does not seem to be a preferred orientation for fractures with specific mineralisation, although certain mineralisation is concentrated in specific areas of the Adit (such as gypsum close to the Adit entrance).

In summary clearly there are two main fracture sets present at Maqarin. It appears that the fracture orientations are partitioned into discrete sets that record multiple episodes of deformation during different stress regimes. They are generally at a high angle to the horizontal lithostratigraphic layering. The main trend is north-south and this set, together with north-west – south-east and limited north-east – south-west variants, correspond to the expected patterns based on the regional tectonic history described in Section 2.1. It seems that fracturing was produced early on, due to an east-south-east – west-north-west compressive stress field. This rotated later, as indicated by the more north-south orientated fractures. The local spread of variation may also relate to local stress complexity caused by the development of an antiformal structure present at Maqarin. The fractures belonging to all these sets are commonly in-filled with calcite, often representing several generations of reactivation. In Adit A-6 many fractures have mineralogical infills related to the hyperalkaline zone development that certainly post-dates this calcite mineralisation. East-west - orientated fractures that are open, or have gypsum mineral fills, are attributed to rock failure associated with periodic mass-movement of the valley sides.

2.3.5 Geophysical survey

Ground-surface resistivity measurements were carried out to establish the lithostructural character of the upper 150 m of bedrock above Adit A-6. These data were used to confirm the geological profiles previously constructed and reported, which are based on extrapolation of information from wells drilled in the 1950's and 1960's (reported in Smellie, 1998).

A total of six profiles were measured in 1999, three in a north-south direction and three in an east-west direction. The spacing of the current electrodes, and hence depth of interpretation, was limited by the topography of the measured site, a relatively flat plateau of arable land (400 x 400 m) directly above the locations of Adits A-6 and A-7 (Figure 2.15). Beyond this area, the topography falls steeply at 35° and more down the valley sides to the north, west and east while to the south it rises to another level. Extending the electrodes to these steep slopes would have resulted in difficulty interpreting the results, so this was not undertaken.

Figures 2.16 to 2.21 show the interpreted geology along the traverses, supported by information extrapolated from well-logging data in existing boreholes in the immediate

area. Since the rock types in the area are well-known from surface observations, together with results from investigation boreholes and in the adits, the main lithological units chosen for interpretation from the resistivity survey were restricted to basalts, Bituminous Marl, Chalky Limestone, hillslope debris and soils. The results of the survey and the previous extrapolations of borehole information were used in the integrated geological models presented in Section 2.5.

Figure 2.15 Location of ground-resistivity traverses (1-6), from Smellie (2000).

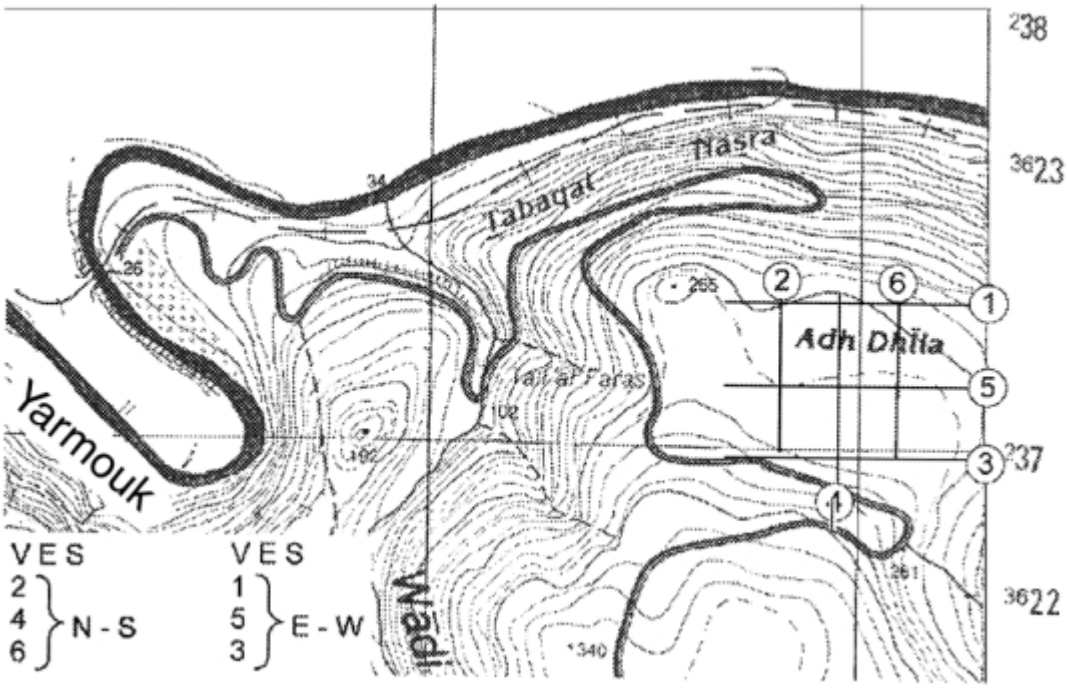

Figure 2.16 Geological profile along E-W ground-resistivity traverse 1 (Profile 1; VES-1 of Smellie, 2000)

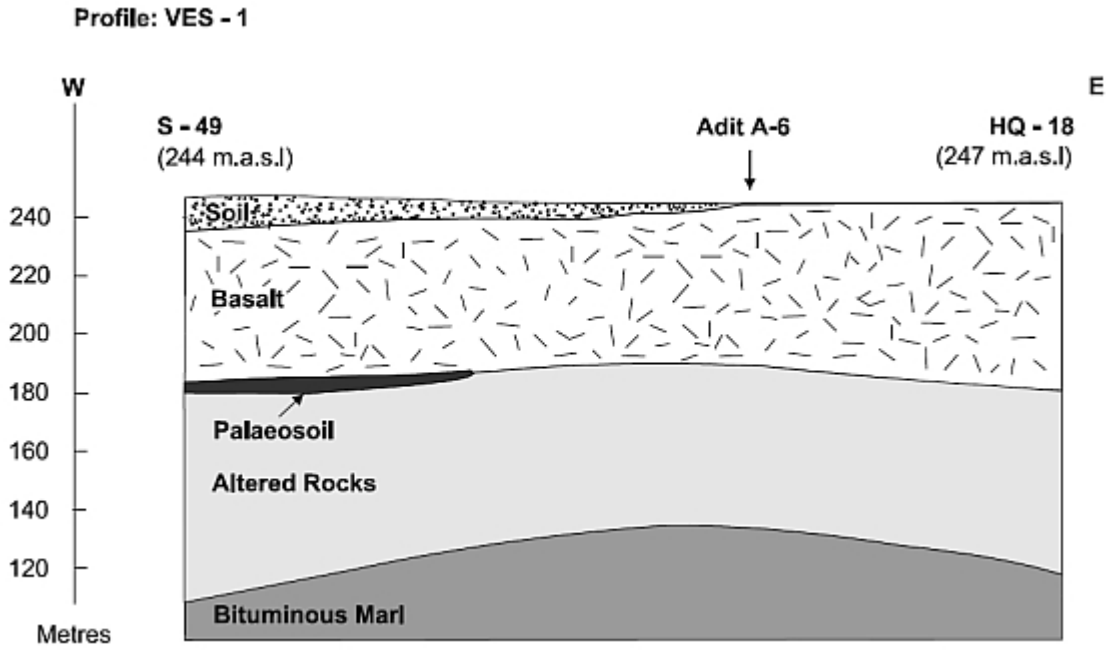

Figure 2.17 Geological profile along N-S ground-resistivity traverse 2 (Profile 2; VES-2 of Smellie, 2000)

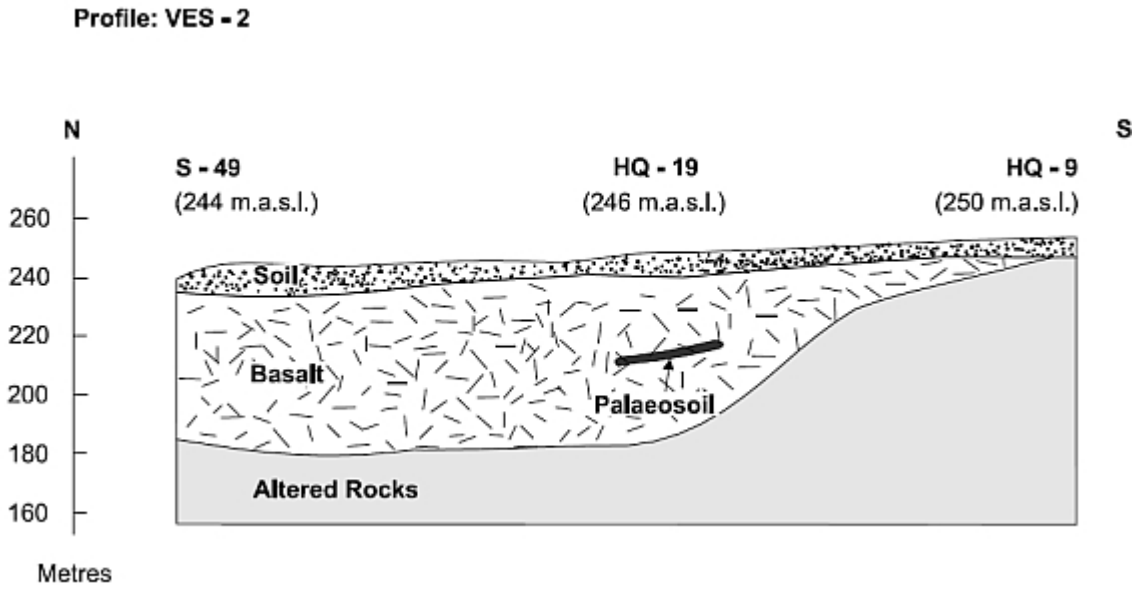

Figure 2.18 Geological profile along E-W ground-resistivity traverse 3 (Profile 3; VES-3 of Smellie, 2000)

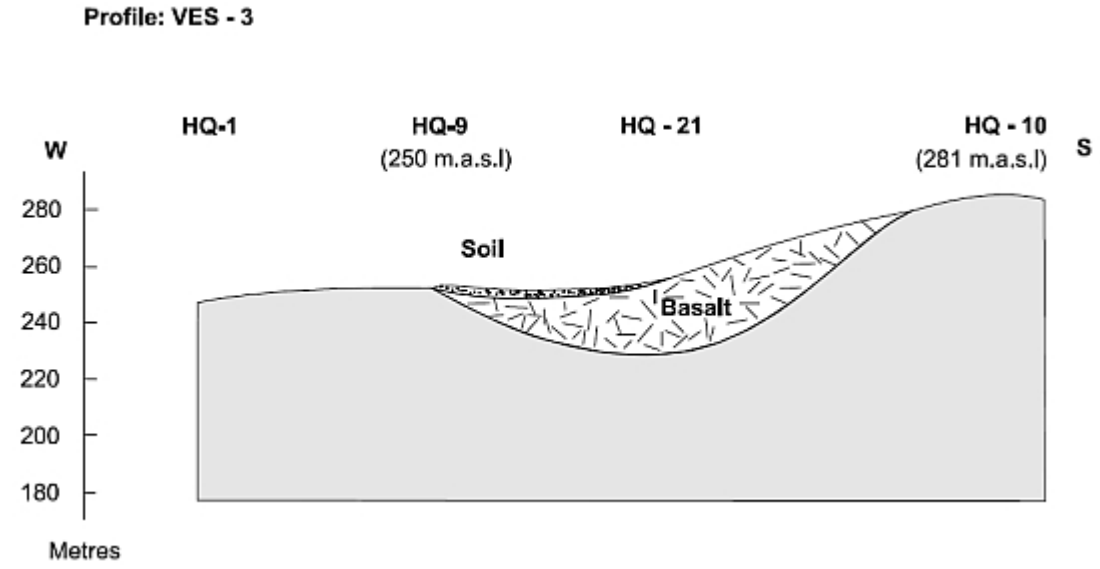

Figure 2.19 Geological profile along N-S ground-resistivity traverse 4 (Profile 4; VES-4 of Smellie, 2000)

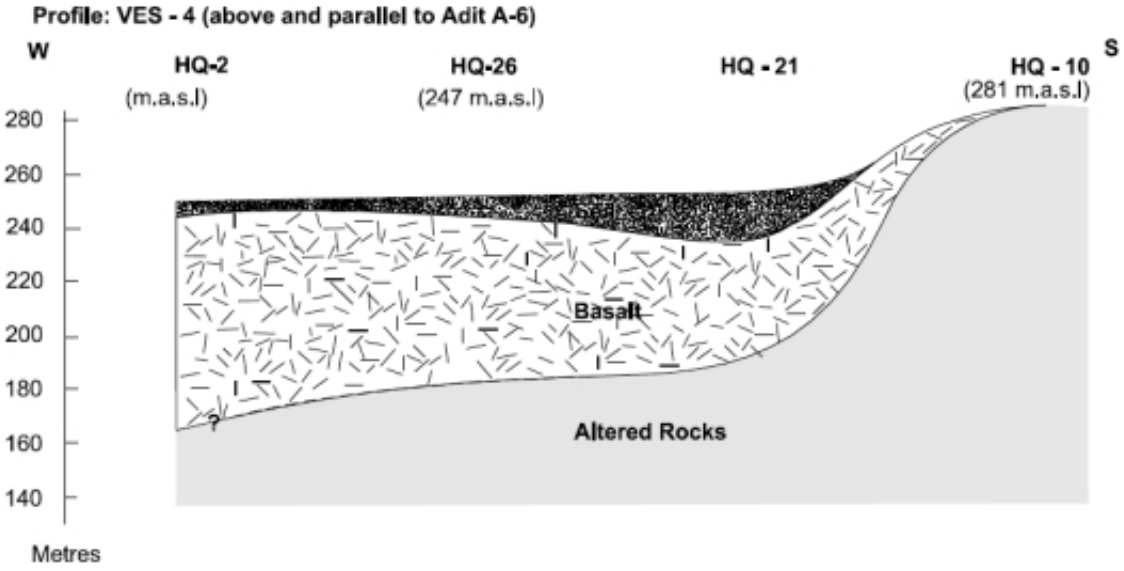

Figure 2.20 Geological profile along E-W ground-resistivity traverse 5 (Profile 5; VES-5 of Smellie, 2000)

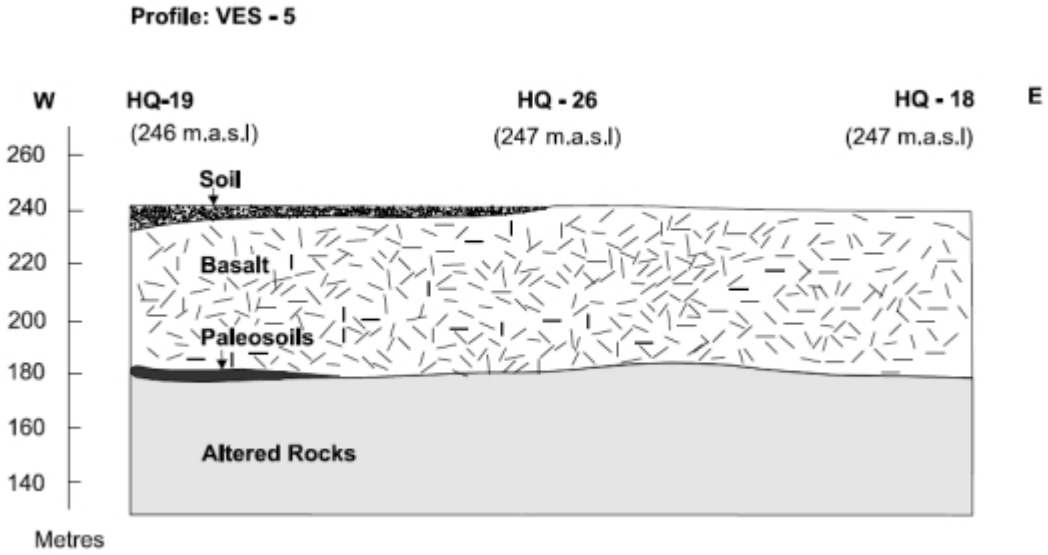

Figure 2.21 Geological profile along N-S ground-resistivity traverse 6 (Profile 6; VES-6 of Smellie, 2000)

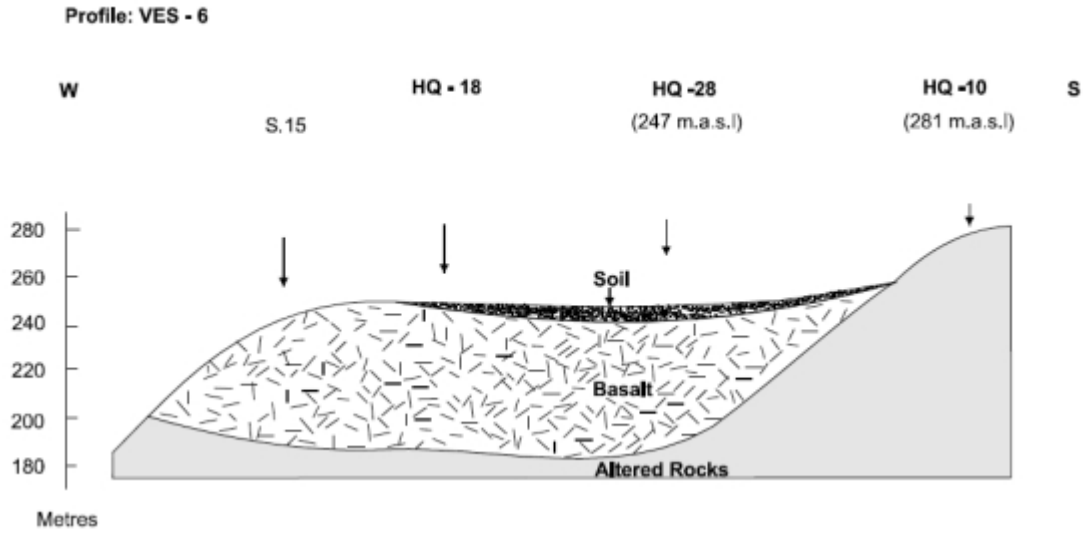

2.4 Hydrogeology

2.4.1 Regional hydrogeology

The Yarmouk River catchment extends from the highlands and plateaux areas of north-east Jordan and southern Syria in the east, to the Jordan Valley in the west. The Irbid Plain lies to the south of the Yarmouk. Here it comprises two stepped regional platforms, one at approximately 350-450 m above sea level, and one further south at an elevation of approximately 600 m. The Ajlun Mountains rise up, to the south of these platforms. To the north of the Yarmouk valley, within Syria, the topography forms an extensive basalt plateau, at the similar altitude to that of the limestone platforms, to the south. The Yarmouk River is the major tributary of the River Jordan and drains an area of approximately 6,800 km^2. The average rainfall in the area is approximately 450 mma^{-1}.

For water-supply purposes, there are two main aquifers in the area, the shallow Chalky Marl and the deeper Amman Formations. The Chalky Marl has hydraulic conductivity ranging from 10^{-5} to 10^{-8} ms^{-1}. It forms a locally perched system as it generally has little or no contact with the deeper aquifer, especially in the lower reaches of the Yarmouk River system. The Chalky Marl receives its recharge from local precipitation and locally contains some karstic features. The hydrogeological unit corresponding to the Amman Formation, on the other hand, is largely confined and, at least in parts, artesian. The formation receives its recharge from the highlands, and also laterally from basalt to the northeast. It has a permeability of 10^{-5} to 10^{-7} ms^{-1}.

2.4.2 Hydrogeology of Adit A-6

The hydraulic characterisation of the rock present in Adit A-6 at Maqarin was a key objective for Phase IV studies. During 1999, a number of hydraulic single-borehole tests were conducted in probe holes drilled from Adit A-6, to assess the hydraulic transmissivity and storativity of the parent rock and the ACZ.

The short-length probe holes were drilled in the Adit (hole numbers D1to D8) using standard single-barrel diamond drilling equipment. The holes were orientated with approximately 15º dip from the horizontal, inclined in towards the Adit (Figure 2.23 and 2.24). The test holes are free-standing without casing and well screen. No well-development activities have been carried out. Camera inspection indicates clean holes were produced with smooth surfaces and only rare breakouts. Nevertheless, due to the drilling process in relative soft-rock formations, with clay content of 2-5%, a substantial amount of debris might have been left in the disturbed zone, causing some skin effects. Single- and double-packer systems were used to close off specific test intervals, which vary in length between 0.75 and 1.47 m in D1, D2, and D6. The average borehole radius is 3.5 cm and the effective casing radius for the closed-off intervals ranges between 0.00658 cm and 0.00887 cm, depending on the interval volume. Pressurization of the test interval was performed with a hand pump, but this was not a reproducible initial condition. Therefore, a series of repeat slug tests could not be performed to evaluate the viability of conventional slug-test theory. However, a number of shut-in slug tests and pump tests were carried out. Also, the drill holes were monitored for pressure fluctuations over long periods between activities in the Adit (Figure 2.25). The methodology of the testing, and the data handling that was carried out, is presented in Appendix 2.3 and the results are presented below.

Figure 2.22 Locations and orientations (in the horizontal plane) of short-length probe holes drilled in Adit A6. Distances shown along bottom are from the Adit entrance to the north (left in figure). The shaded area represents the transition to the ACZ.

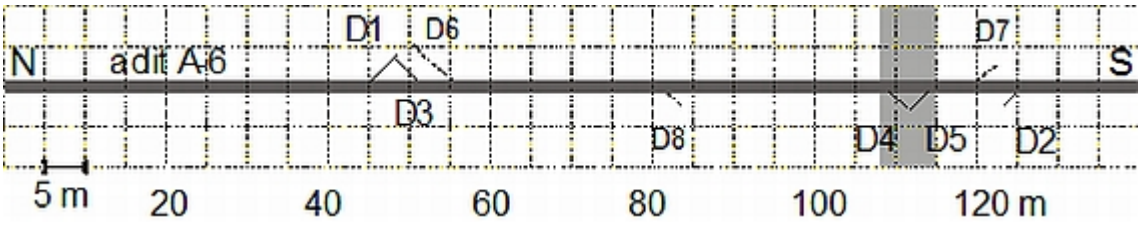

Figure 2.23: Drilling boreholes for hydraulic testing and core sampling in Adit A-6.

Figure 2.24 *Visualisation of the boreholes drilled from Adit A-6. Adit entrance is to the right-hand side of the figure. The 3D visualisation includes the true elevation of the start of the boreholes and therefore they appear to be floating above the Adit – which is visualised by a line along the Adit floor.*

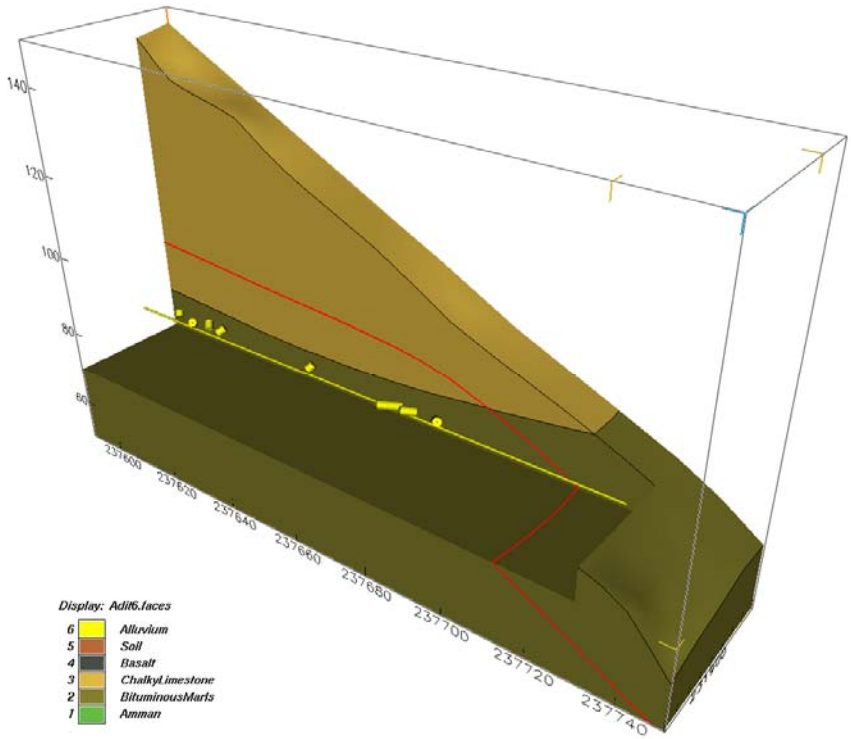

Figure 2.25 Monitoring equipment installed in probe hole in Adit A-6.

Table 2.1 Evaluation of hydraulic properties at Maqarin

Hydraulic Test	Test Interval	Method	μ or α	T [m²/d]	T [m²/s]	S.E.$_T$ [m²/d]	S	S.E.$_S$	P_0 [bar]	Q [ml/min]	Comments
shut-in, pressure pulse	D2-2	Bredehoeft & Papadopulos, 1980 (manual)	0.2	1.30E-07	1.50E-12		7.00E-07		6.99		no complete recovery
	D2-2	Cooper et al., 1967 (automatic)		1.60E-07	1.85E-12	1.07E-08	3.50E-07	5.52E-08	6.99		no complete recovery
shut-in, pressure pulse	D1-3	Bredehoeft & Papadopulos, 1980 (manual)	0.01	1.42E-06	1.64E-11		6.42E-08		0.759		no complete recovery
	D1-3	Cooper et al., 1967 (automatic)		1.56E-06	1.81E-11	5.36E-09	4.02E-08	6.77E-10	0.759		no complete recovery
shut-in, pressure pulse	D1-4	Bredehoeft & Papadopulos, 1980 (manual)	0.0001	3.54E-06	4.10E-11		6.42E-10		1.057		no complete recovery
	D1-4	Cooper et al., 1967 (automatic)		2.73E-06	3.17E-11	1.09E-07	7.80E-09	2.04E-09	1.057		no complete recovery
shut-in, pressure pulse	D1-6	Bredehoeft & Papadopulos, 1980 (manual)	0.1	2.83E-06	3.29E-11		6.42E-07		2.963		
	D1-6	Cooper et al., 1967 (automatic)		3.24E-06	3.75E-11	3.63E-08	5.45E-07	1.52E-08	2.963		
shut-in, pressure pulse	D6-2-20A	Bredehoeft & Papadopulos, 1980 (manual)	5	3.86E-07	4.47E-12		2.74E-05		7.38		
	D6-2-20A	Cooper et al., 1967 (automatic)		6.43E-07	7.44E-12	5.81E-08	2.98E-05	3.02E-06	7.38		
shut-in, pressure pulse	D6-2-20B	Bredehoeft & Papadopulos, 1980 (manual)	10	9.66E-07	1.12E-11		5.48E-05		5.06		
	D6-2-20B	Cooper et al., 1967 (automatic)		6.07E-07	7.03E-12	2.23E-07	7.44E-05	2.92E-05	5.06		
constant rate injection	D1-Q2	Cooper & Jacob, 1946; confined, (semi-automatic); early time fit 1 (16 to 80min)		3.93E-04	4.55E-09		2.76E-06			7.6	no 'quasi steady state' reached
	D1-Q2	Cooper & Jacob, 1946; confined, (semi-automatic); early time fit 2 (92 to 265min)		1.35E-04	1.57E-09		1.43E-03			7.6	no 'quasi steady state' reached
	D1-Q2	Hantish & Jacob, 1955; confined, leaky (automatic)		2.05E-04	3.27E-09	5.49E-05	1.12E-04	5.56E-05		7.6	no 'quasi steady state' reached

Slug Test and Pumping Test Results

A summary of the results from the shut-in slug tests and constant-rate injection testing is presented in Table 2.1 Examples of normalized head ($H(t)/H_0$) versus log-time plots for the shut-in slug tests are found in Figure 2.26. A plot of the type curves used for manual

curve matching is presented in Figure 2.27. Examples of plots including the automatic curve match are shown in Figure 2.28.

Transmissivity (T) values, derived from slug tests in D1, range between 1.64E-11 and 3.75E-11 m^2s^{-1} using the manual type curve fitting approach, and range between 1.81E-11 to 4.10E-11 m^2s^{-1} using the automatic procedure (Table 2.1). From the single-slug test in borehole D2 a transmissivity of 1.50E-12 m^2s^{-1} and a storativity parameter of 7.00E-07 is derived using the manual type curve fitting approach. For comparison, the automatic fitting procedure yields a transmissivity of 1.85E-12 m^2s^{-1}. Transmissivity parameters from both approaches are in good agreement. Differences in the test results from D1-3, D1-4, and D1-6 are expected, due to incomplete recovery of the response data, and due to significant differences in the initial displacement. The storativity parameter (S) derived from tests D1-3 and D1-6 ranges between 6.42E-08 and 6.42E-07 and between 4.04E-08 and 5.45E-07 for automatic and manual procedures, respectively. The test results from D1-4 are not included in this range of storativity values as they are associated with a significant standard error (Table 2.1), especially for the storativity parameter with 26%. For the repeat test D1-6, the transmissivity value increased by a factor of two compared to D1-3. Hydraulic parameters derived from both procedures (automatic and manual) are in good agreement.

In addition to the slug tests, a constant-rate injection pumping test was carried out in probe hole D1 and the test design and the methodology is also presented in Appendix 2.3. For an ideal injection test, the rate of injection stays constant and the pressure in the test interval increases during injection. The pressure build-up is rapid at first and then decreases and asymptotically approaches zero pressure build-up. Cooper and Jacob (1946) derived a graphical method to analyze the pressure-time response data by using an abbreviated Theis equation for non steady-state flow.

Figure 2.26 Examples of normalized head ($H(t)/H_0$) versus log-time plots for the shut-in slug tests

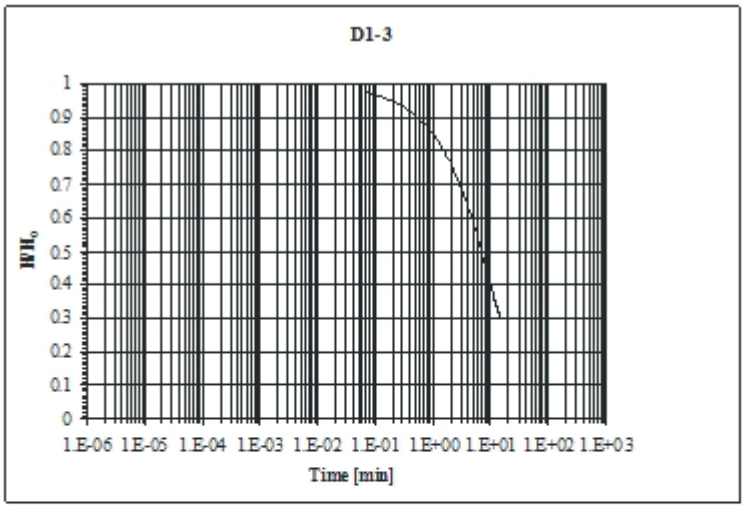

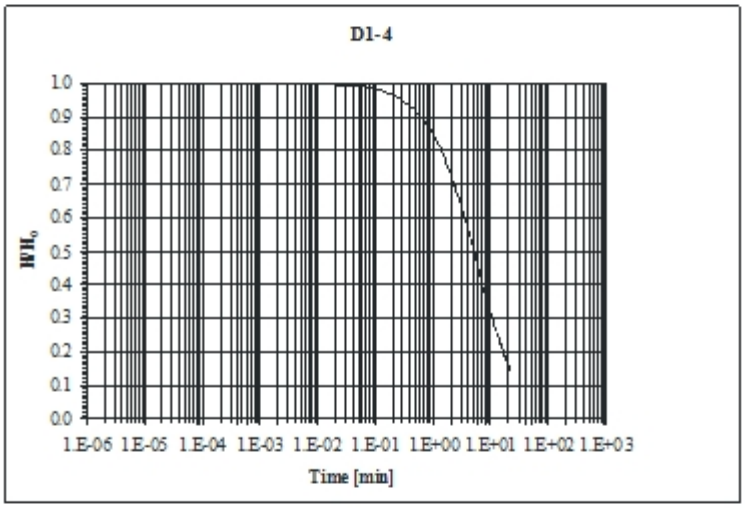

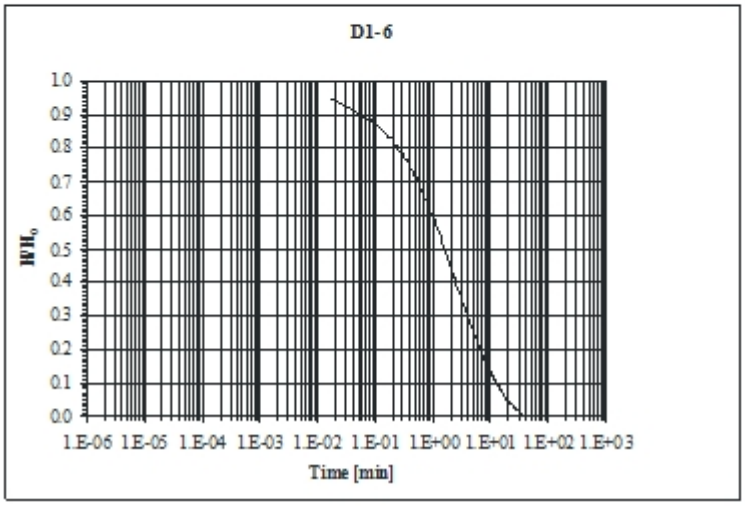

Figure 2.27 Cooper-Bredehoeft-Papadopulos type curves used for manual curve matching (in Figure 2.26)

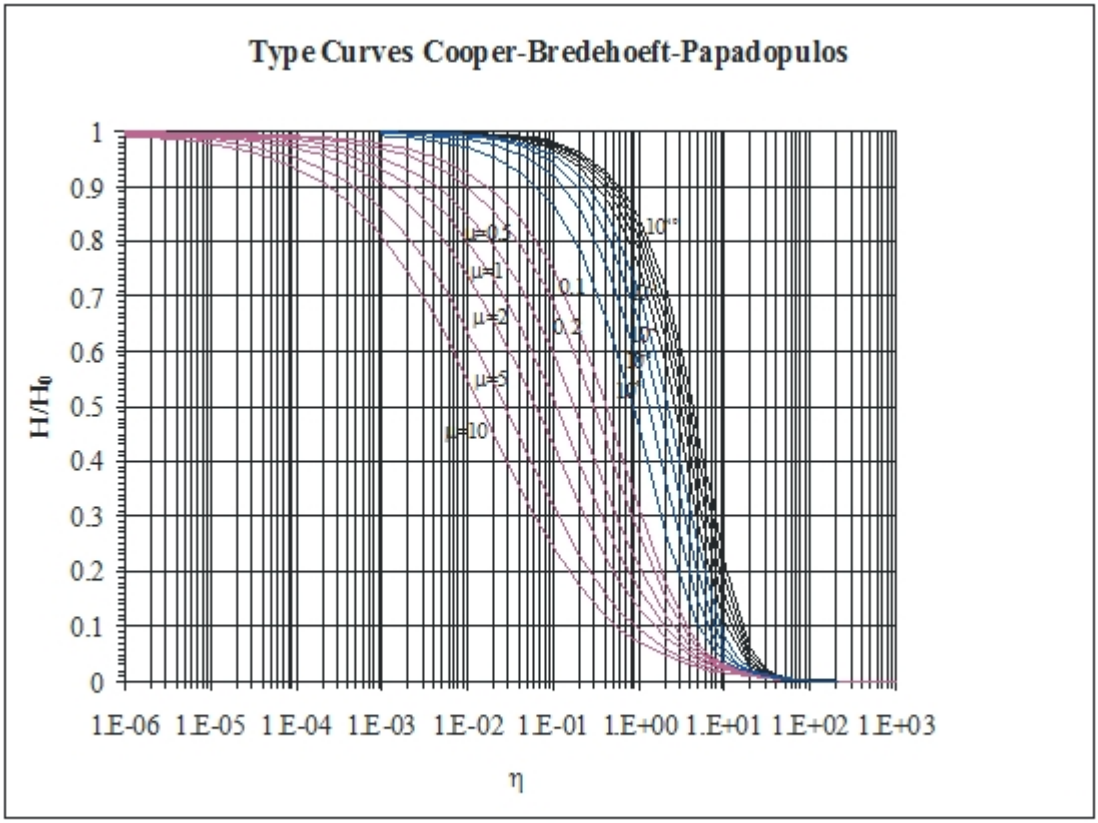

Figure 2.28 Examples of plots including the automatic curve match

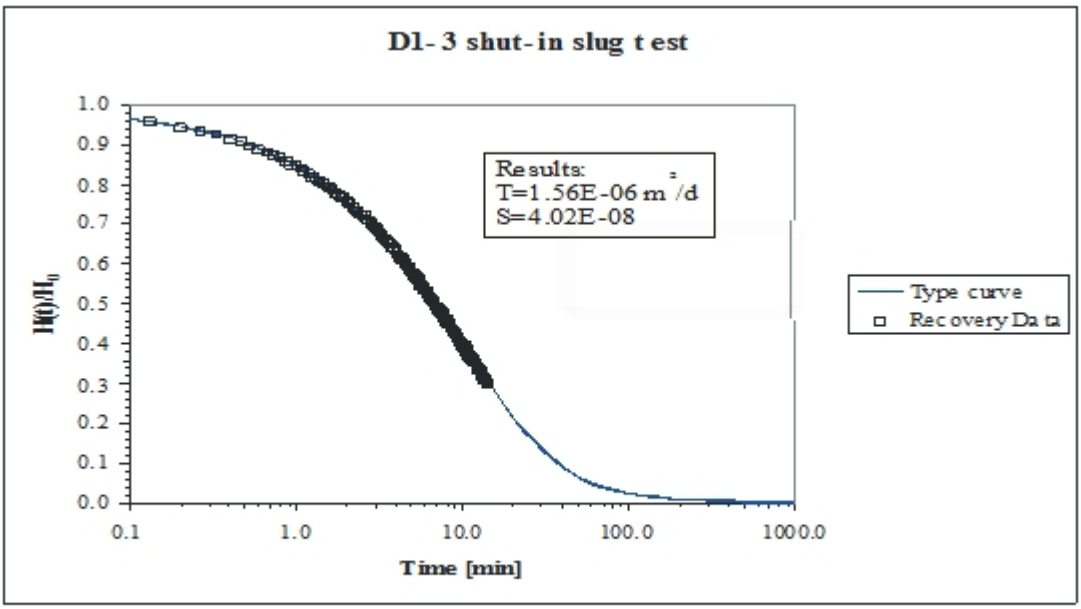

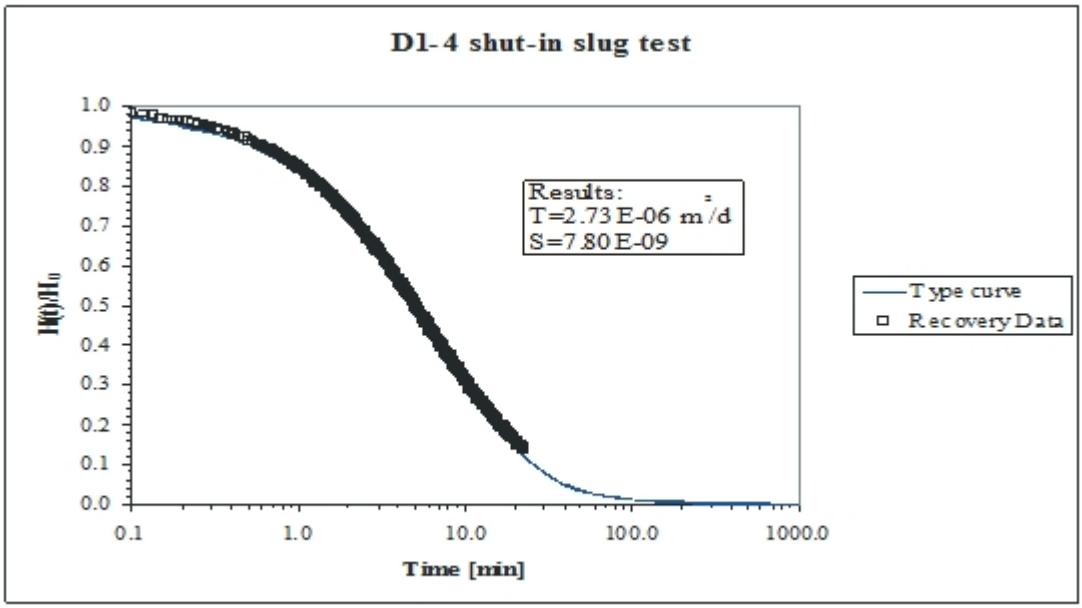

In the probe hole, the recorded response data do not following the idealised pressure build-up curve during the early test - it is slower than expected (Figure 2.29). This appears to be due to incomplete filling-up of the test interval and tubing with water prior to test initiation. On the diagnostic plot log ($p-p_0$) vs. log time, the duration of the well-bore storage effect is estimated at about 16 minutes (Figure 2.29a). This first portion of the response data set is not used for estimating hydraulic parameters of the surrounding rock formation.

Using the straight-line analysis after Cooper and Jacob (1946), the response data between 16 and 80 minutes were analysed, resulting in a transmissivity of 4.55E-11 m^2s^{-1} (Figure 2.29b). A sudden pressure drop following the straight-line segment suggests the

influence of a structural heterogeneity which might be an open fracture or small cavity. The estimated extent of the cone of depression at t = 80 minutes is 0.21m, based on calculations with average hydraulic parameters. Afterwards the pressure build up continues in a linear fashion with a slightly steeper slope compared to the previous line segment. Analysis of the second line segment yields a transmissivity of 1.57E-11 m^2s^{-1} (Figure 2.29b), which is about three-times lower than the result from the first line segment. The constant-rate injection test was terminated after 265 minutes by which time the extent of the cone of depression was approximately 0.39m.

A number of problems and uncertainties are associated with the tests carried out at Maqarin. For the shut-in slug tests the main issues are:

- equipment compressibility
- trapped air
- head disturbances prior to test initiation
- formation heterogenities and/or drilling-induced disturbances
- estimation of H_0 and t_0
- no repeat tests with identical initial displacement
- incomplete recovery of response data

The implications of all issues are discussed in Appendix 2.3 and are not repeated here. It is difficult to evaluate to what degree the derived hydraulic parameters are affected by those uncertainties and induced errors. Incomplete recovery of response data prior to test initiation is considered a major issue for repeat test D1-4 (Table 2.4), and formation heterogeneity (e.g. fractures) is influencing the response data of test D6-2-20A.

The main problems and uncertainties associated with the transient-pump test carried out at Maqarin are:

- well-bore storage effects due to incomplete water fill-up of the test interval
- formation heterogenities and/or drilling-induced disturbances
- no response data from observation wells
- insufficient duration of the constant-rate injection test

A major issue is the heterogeneity of the surrounding rock formation with disturbed zones and possible fractures in the near vicinity. In order to distinguish between near-well effects, the undisturbed rock matrix, and structural boundaries, the duration of future transient pump tests needs to be extended.

Figure 2.29 (a) Upper plot is a log-log diagnostic plot to estimate the end of well- bore storage effects for the injection test D1-Q2. (b) The lower plot is a straight-line analysis of the early and late time-response data from the same constant rate injection test.

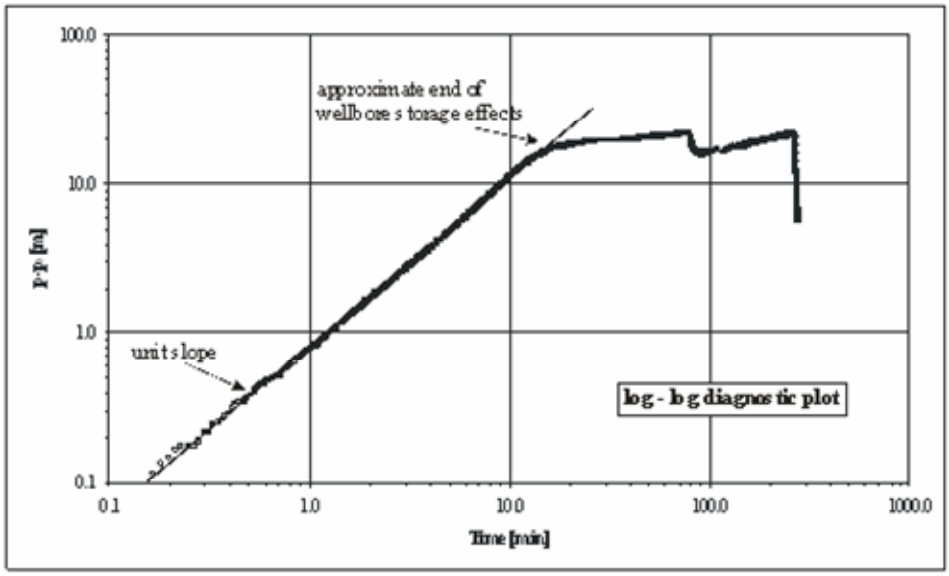

.

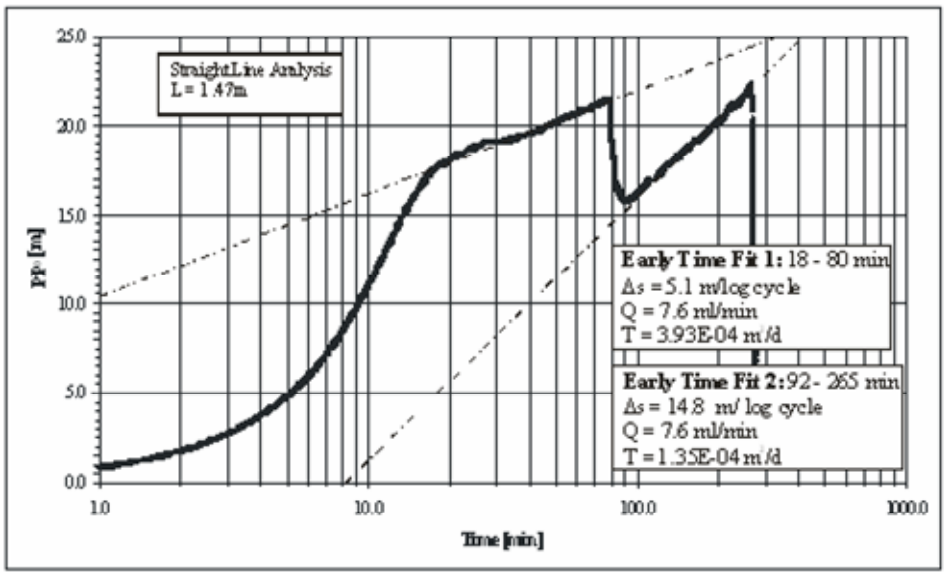

.

In summary, the shut-in slug tests suggest that the fracture transmissivity of the Bituminous Marl parent rock (as tested in probe holes D1 and D6) is between 4.47E-12 and 4.1E-11 m^2s^{-1}. The altered and metamorphosed equivalent is slightly tighter, with a shut-in slug test providing a value of approximately 1.5E-12 m^2s^{-1}. The injection test was only carried out in the parent rock and the test responses indicate a higher transmissivity than that obtained from the slug test at about 3E-9 m^2s^{-1}.

2.5 3D Modelling of the Maqarin Site

2.5.1 Introduction

Based on an integrated understanding of the geology and hydrogeology of the Maqarin site, developed over the entire four phases of research, a series of three-dimensional stratigraphic/hydrogeological models was constructed to support interpretations and to illustrate the geological understanding of the area. The geological models include a site-scale model and a nested model of the volume immediately surrounding Adit A-6. The visualisations have been developed with explicit representations of many of the boreholes and the adits at the site and they have been made available as electronic files on a CD ROM with this report. They are encrypted so that they can be distributed and installed on an unlimited number of PCs. Instructions on use and the background to the development of the models is presented in Appendix 2.4. The geological models enhance an understanding of the geology of the Maqarin area through the visualisation of the interpretations, particularly by allowing users interactively to rotate, slice and peel the modelled volume. The EarthVision geological modelling system was used to construct the model (Version 4.0.2, Dynamic Graphics, 1997). It was developed using standard isopach mapping for most of the geological horizons.

In constructing the EarthVision geological model (hereafter, the Geological Model) the large amount of newly aquired data presented above (Sections 2.3 and 2.4) was combined with information collected during previous phases of work. This provides a new three-dimensional interpretation of the stratigraphy and the geometry of the water table. In undertaking this modelling for Phase IV, the major elements for inclusion were:

- Significance of the topography and geology to the north of the Yarmouk River Valley (i.e. in Syria)
- Visualisation of the water-table model and refinement of previous hydrogeological understanding, incorporating a critical assessment of all of the available well-log data
- Development of an Adit Scale Model for visualisation of mineralogical and fracture data collected in Adit A-6, together with borehole paths, locations of palaeomagnetic samples and geological contacts
- Association of hydrochemical data with sampling locations
- Visualisation of borehole paths and mine workings
- Visualisation of the lithostratigraphy of Borehole S14

The finalised model is highly consistent with the available mineralogical, structural and hydrogeological data presented in section 2.3 and elsewhere, as will be described in Appendix 2.4. However, some local inconsistencies in the source data are noted

2.5.2 Integrated understanding

The series of integrated models of the Maqarin natural analogue site, developed within the EarthVision framework, illustrate several aspects of structural geology, hydrogeology, hydrochemistry and also the location of sampling points. The two key aims of the geological models are, first, to place the detailed information into a broader regional context. Secondly, spatial variability of the data is investigated, such as the location of certain fracture types and the correlation with particular fracture orientations in Adit A-6.

The two key components of the geology investigated in this project were the structure of the top of the Bituminous Marl Formation surface and the nature of the water table. In the

field, a gentle antiformal fold is recognised in this surface on the face of the Syrian side of the Yarmouk Valley. The data from the boreholes and geological maps support the presence of the antiformal structure trending north-east to south-west. However, the dips of the surface along limbs, as mapped from the borehole data, are quite irregular. This may be due to the presence of small faults across the hinge of the anticline, or due to the inaccuracy of the available data. Putative faults are not interpreted in the geological models developed here, as there were not sufficient data from the field to constrain their presence. However, local evidence of small-scale faulting has been observed in the field which collectively might be result in the measurable displacement of marker horizons.

A method has been developed for estimating the elevation of the water table based on the topography. Confidence has been demonstrated in this method by applying it to different amounts of input data with little change in the result. However, the method is only suitable for estimating the general level of the water table. Locally, recharge mounds or perched water tables may exist, and these could be affected by local fracturing and variations in lithology.

The water-table elevation along Adit A-6 is particularly affected by variations in the local geology. At the back of Adit A-6, which is completely dry, the water table is lower than the regional level. This is thought to be due to reduced infiltration through the palaeosols and basalt which are present at the surface above the far end of the Adit, and increased infiltration through fractures that are present towards the entrance to the Adit. The increased fracturing may be associated with the folding, pressure-release jointing (see above), and possible faulting of the top Bituminous Marl Formation (see above) or due to percolation through karstic features identified previously (see Figure 2.14 in Khoury et al., 1998). Indeed, there could be a causal relationship between the depressions and the fractures, with locally enhanced dissolution due to increased fracture intensity. Alternatively, the increased seepage towards the front of the Adit could simply be due to increased fracture frequency and dilation caused by stress relief from gravitational collapse at the free bounding surface (the valley side) – see also comments in Section 3.6.

A series of visualisations have been prepared that illustrate the investigations and mapping in Adit A-6. These include visualisations of the fracture mineralogy, the location of palaeomagnetic samples, the geometry of boreholes drilled from the Adit, the lithological logging of boreholes, and sampling of groundwater chemistry (see the examples in Appendix 2.4). The real value of these visualisations is in the ability to disseminate information and for all participants to have interactive access to the data, using the encrypted viewer.

In order to estimate of water-table elevation, a flow model would need to be developed that incorporates the unsaturated and saturated zones. This modelling would need to draw on the detailed understanding of the geological structure, as is presented in this Report. This includes the demonstrated interaction between the lithology, geological structure and possible presence of perched water tables. In addition, hydrogeological modelling would also need to account for the presence of the Adit. Data on the water budget, annual fluctuations in recharge and site-specific water retention models would also be required. However, acquiring this level of detail was not feasible within the Phase IV work programme. Nevertheless, it has been demonstrated that karstic features and the pervasive fracturing at the Maqarin site do control groundwater pathways. However, the limited evidence from the slug tests, and the direct observations of fracture filling, shows that the hyperalkaline plume induced secondary mineralisation also seals these pathways.

2.6 Conclusions

The Phase IV geological and hydrogeological studies support a number of important conclusions:

- The structural framework observed at the Maqarin site, comprising fractures, a large-scale fold and limited evidence of faulting, are all consistent with the regional tectonic understanding.
- The main fracture set at Maqarin is orientated approximately north-south and is close to vertical. The fracture frequency varies and there appear to be areas of greater fracture intensity adjacent to broad tracts where less fracturing is present. Some field evidence suggests that the ACZs are especially concentrated in domains where the presence of increased fracturing permitted the ingress of oxygen. This provided an accessible pathway for the combustion front to access other parts of the rock mass.
- The Yarmouk River is deeply incised, with steep valley sides.. Geomorphological and structural evidence (low-angle and listric faulting strike-parallel to the valley) indicates that gravitational collapse along the valley sides is prevalent, although there has been no catastrophic mass movement recently. Rather, at the present time, there appears to be gradual retreat of the valley sides in the vicinity of the study area. The nature of the topography has generated instability in the rock mass. In particular, low-angle east-west striking fractures, together with preferentially orientated pre-existing fractures, have opened and re-sealed over several generations. This is clearly evident from the crack-seal calcite and multiple generations of other mineral precipitates, including those derived from the ACZ.
- Mineral dissolution, transport and re-precipitation depend on the presence of pathways and groundwater with suitable chemical characteristics. At the present-day Maqarin site, there is enhanced infiltration of meteoric waters down from the overlying plateau towards the front of Adit A6. This supply of groundwater is facilitated by one or a combination of factors. These include increased fracture intensity, due to the combustion zone underlying the axial trace of the major fold in the area, the presence of karstic dissolution features overlying the Adit, and/or the increased prevalence of open fractures due to the gravitational instability close to the valley sides.
- Appendix 2.1 provides data on the frequency of sealed versus unsealed fractures. In Chapter 7, these data are combined with work from previous Phases of the Project, to assess the SA implications of these fracture and joint fills.

Chapter 3

Hydrogeochemistry

J.A.T. Smellie, E. Salameh, I.D. Clark and A.E. Milodowski

3.1 Introduction

Initially, hydrogeochemistry was not considered to be an integral part of Phase IV (see Chapter 1) since it was widely covered in the earlier studies, particularly those in Phase III (Smellie, 1998). However its potential relevance to Phase IV became increasingly obvious as work proceeded, and the necessity for a programme of sampling and analysis was therefore established. Identified areas of interest included:

- To establish seasonal variations
- To characterise additional seepage points discovered in Adit A-6
- To provide potential support for interpretation of the hydraulic flow systems at the regional, site and adit scales

The locations selected for sampling included all sites in Adit A-6 (drilled and seepage locations), two sites at the Eastern Springs (one previous and one new location), one previous site at the Western Springs, and four regional springs used for domestic purposes. Major sampling campaigns were carried out in April/May, 2000 (end of wet period), November, 2000 (end of dry period), in January/February, 2001 (transition period) and January, 2002 (beginning of wet period). Individual strategic locations of importance were sampled on a more regular basis. The samples from the first two campaigns were analysed for a fairly complete suite of major ions, trace elements and environmental isotopes. The two subsequent sampling campaigns were analysed for a less complete suite of major ions and selected trace elements in addition to environmental isotopes. Furthermore, samples collected earlier in November 1999 from four springs used for municipal water supplies, and the full set of samples from the November 2000 campaign, were analysed for $^{37}Cl/^{35}Cl$ to test the potential contribution of these data to the hydrochemical interpretation.

3.2 Background

3.2.1 Regional hydrogeology and hydrogeochemistry

To understand better the Maqarin area as a NA of a cementitious repository, a hydrochemical survey of the regional groundwaters in northern Jordan was carried out during Phase III. This produced detailed information about the general hydrochemical evolution in the area. Furthermore, the aim was to obtain specific geochemical information about the recharge conditions in the Maqarin area, and to define an input composition of 'normal' pH groundwater infiltrating into the Analogue Cement Zone (ACZ) which then subsequently evolved to high-pH groundwater. This input composition was intended to provide the source term for modelling the rock/water interaction in the Western Springs area. In Phase IV, additional information on the origin and type of the

various waters in the Maqarin area has been examined, with reference to the regional surface and sub-surface flow systems of northern Jordan.

Surface water at Maqarin is restricted mainly to the Yarmouk River. The main source of this water is the basalt aquifer covering the flanks of the Yarmouk River and extending far into Jordan and Syria. The chemical composition of the river base flow is relatively stable with a TDS ranging between 400 and 500 mgL^{-1}. More recent surveys (University of Jordan; February, 2002) show increased salinity due to the discharges of domestic waste water and irrigation return flows (Table 3.1).

The results of more than 30 analyses collected at different times and years show that the general geochemical trends are: Na > Ca; Mg > K; Ca + Mg > Na + K; Cl > SO_4; Cl > Na and Ca + Mg > HCO_3 + CO_3. The Yarmouk River water is saturated with oxygen, contains around 30 mgL^{-1} NO_3, and it is undersaturated with respect to calcite, dolomite, gypsum and halite. During periods of heavy run-off, the TDS drops to some 250 to 300 mgL^{-1} and the contents of alkalis, bicarbonate and chloride increase, but without major changes in the ionic ratios.

Table 3.1 Composition range of the Yarmouk River water chemistry

Electric Conductivity	**pH**	**Ca**	**Mg**	**Na**	**K**	**HCO_3**	**CO_3**	**SO_4**	**Cl**	**NO_3**
(μScm^{-1})		**mgL^{-1}**	**$mgL^{-1}L$**	**mgL^{-1}**	**mgL^{-1}**	**mgL^{-1}**	**mgL^{-1}**	**mgL^{-1}**	**mgL^{-1}**	**mgL^{-1}**
300-700	6.8-9.0	30-62	119-33	40-86	2-5.5	153-260	0.0-24	36-82	54-90	31
*1019	5.99	46.6	32.6	110	6.0	281	0.0	72.0	120.3	31

* Lower row of values represent February 2002 survey for comparison (University of Jordan, unpublished data).

The occurrence and chemistry of the subsurface groundwaters in the region reflect closely the geology and structural patterns. As presented in Chapter 2, the geology of northern Jordan consists of a succession from Triassic through Quaternary sediments, partly overlain by basalt flows of Oligocene to Holocene age. The different stratigraphic units generally dip towards the north-northwest, towards the Yarmouk and Jordan River valleys. The stratigraphically oldest units outcrop to the south in the area of the Zarqa River Valley whereas, in the Maqarin area, the sequence includes younger, late Cretaceous to Tertiary formations.

Structurally, northern Jordan is dominated by a synclinal structure between the Ajlun Highlands and the Golan Heights which influences the alignment of the Yarmouk Valley. The Ajlun Highlands further act as a divide for groundwaters discharging westward through tributary wadis directly into the Jordan Rift Valley and groundwaters which discharge eastward into the south-east - north-west oriented flow system of the Ramtha-Irbid-Yarmouk area (Bajjali et al., 1997).

Thus, four regional hydrostratigraphic units dominate in northern Jordan (Figure 3.1):

1 The deep Ajlun Group (A_1-A_6) is a low-yield artesian aquifer system consisting mainly of dolomitic limestone with intercalated marl and marl sequences. There is also geochemical evidence for subsurface gypsum.

Figure 3.1 Regional geology and major groundwater flow paths in northern Jordan (from Smellie, 1998).

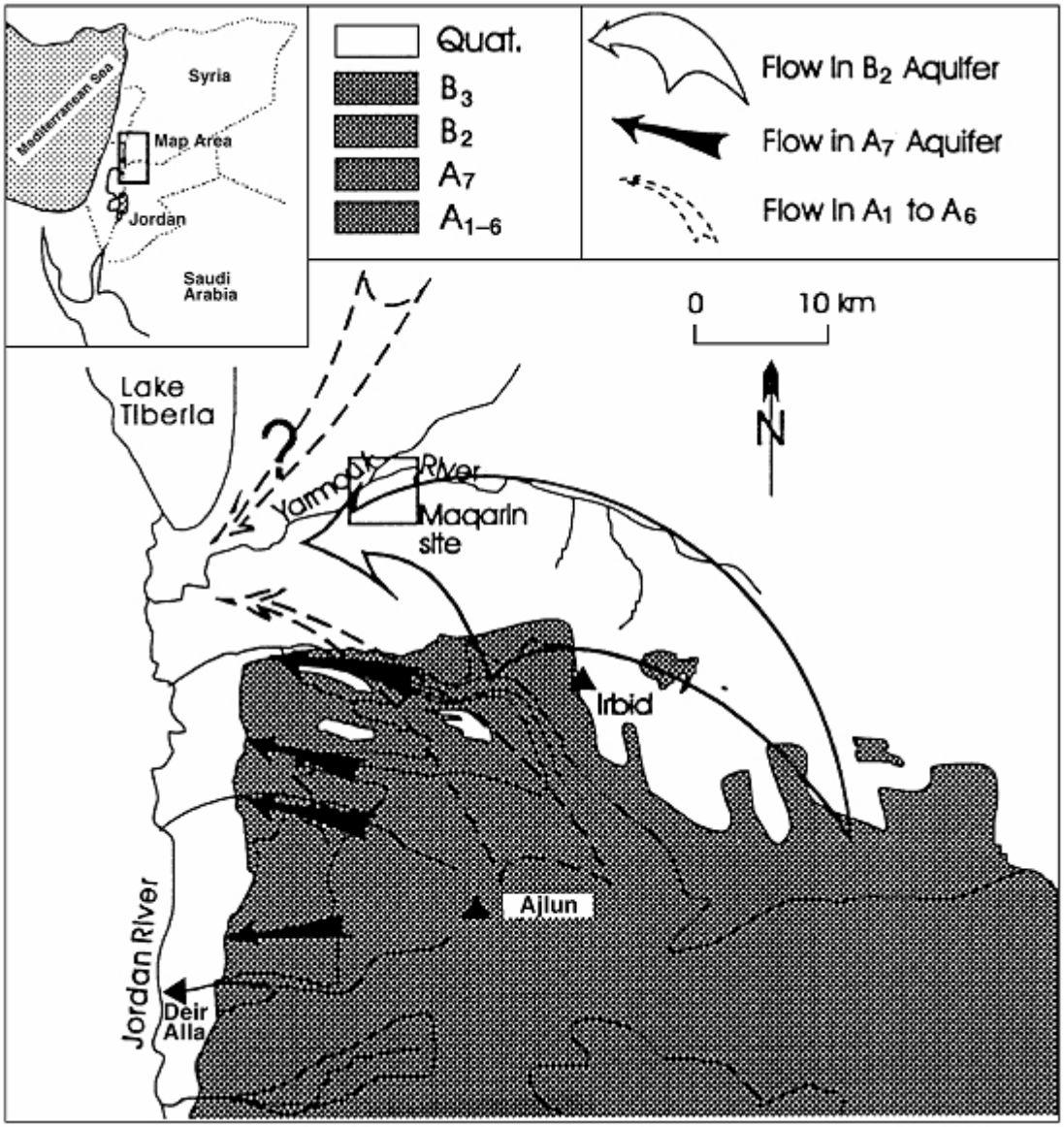

2 The overlying Wadi es Sir Formation (A_7) is a marly dolomitic limestone, outcropping in the Ajlun Highlands and in deeply incised wadi channels on the East Bank of the Jordan Rift Valley. Groundwaters (A_7-aquifer) are mainly developed by wells along the eastern boundary of the northern Rift Valley.

3 The overlying marly limestone Amman Formation hosts a highly productive artesian aquifer in the upper B_2 stratigraphical unit (B_2-aquifer). This B_2 unit outcrops south of Irbid towards the Zarqa River valley. In the Mukheiba area, 25 km to the west of Maqarin, the B_2 aquifer yields thermal waters with temperatures up to 52°C (Bajjali et al., 1997).

4 The overlying $B_{4,5}$ shallow, phreatic and karstified aquifer within the Chalky Limestone Formation is not shown in Figure 3.1. Waters tend to be restricted to natural springs, extensively used for domestic purposes.

The Amman Formation is overlain by the organic-rich marls and chalks of the Muwaqqar (B_3) Formation (referred to as the Bituminous Marl Formation at Maqarin) which generally acts as an aquitard. On top of the Muwaqqar Formation, the Tertiary limestone

sequences of the Rijan and Shallala Formations form local aquifers in northern Jordan (B_4 and B_5 aquifers). At Maqarin, these sediments comprise the Chalky Limestone Formation and are partly overlain by basalt flows of Oligocene and Holocene age.

At Maqarin, two groundwater sources occur: a) from the deep Amman Formation B_2-aquifer, and b) from the overlying Bituminous Marl Formation B_3-aquitard. The Amman (B_2) Formation hosts groundwaters that are under artesian pressure throughout most of the lower Yarmouk River basin. These can recharge overlying strata by connecting fracture systems in this area. The deeper Ajlun Group (A_1 to A_7) also hosts regionally confined aquifers that emerge as seepages in the lower Yarmouk Valley.

Since the groundwater of the Amman Formation mostly is confined, it does not discharge (unmixed with other waters) at any known surface localities. Samples from the B_2 aquifer were obtained during 1980 and 1981 in the course of an investigation campaign at the Maqarin dam site. The temperature of the water ranged, at that time, from 24.5^o to 29^{o}C. The chemical composition of the different borehole groundwaters varied widely (Table 3.2), but was stable within each individual borehole. This behaviour was attributed to: a) different groundwater pathways and pressures within the aquifer, b) the different natural seepage patterns, c) the overlying aquifers, and d) the ground-surface elevations at certain localities in addition to various mixing processes.

Table 3.2 Composition range of the Amman Formation groundwater chemistry

TDS	**pH**	**Ca**	**Mg**	**Na**	**K**	**NO_3**	**HCO_3**	**OH^-**	**CO_3**	**SO_4**	**Cl**
mgL^{-1}		***mgL^{-1}***	***$mgL^{-1}L$***	***mgL^{-1}***	***mgL^{-1}***	***mgL^{-1}***	***mgL^{-1}***	***mgL^{-1}***	***mgL^{-1}***	***mgL^{-1}***	***mgL^{-1}***
240-685	6.6-8.5	8-104	0-56	24-105	1.6-22.3	0-5.8	42.7-409	0.0	0-24	5-161	39-168

* In all samples, a weak to strong H_2S odour was detected during sampling.

The groundwater of the Amman Formation is recharged along its outcrops further to the south in Ajlun-Irbid area, and to the north in Syria (Figure 3.1). Even the groundwater in the Amman Formation itself, however, is a mixture of different aquifer groundwaters, which seep upwards from deeper-lying aquifers (i.e. the Ajlun Group: A_1 to A_7), where piezometric heads are higher than that of the Amman Formation. Therefore, the water quality in the Amman Formation differs from place to place, according to the presence of joints, fissures and other flow channels connecting one or more of the underlying aquifers with the Amman Formation.

The groundwater chemistry (Table 3.2) of the Amman Formation is generally that of a Na-Ca-HCO_3 type, gradually increasing in sulphate and sulphide content down-gradient as a result of gypsum dissolution and sulphate reduction. Finally, further down-gradient, the groundwater changes to a Ca-Na-(Mg)-HCO_3- SO_4-Cl type as a result of continuous water-rock interactions including dissolution of halite relicts and ion-exchange processes within the clayey portions of the aquifer. The groundwater is slightly under-saturated in respect to calcite (SI of -0.10 to -0.58), and generally over-saturated with dolomite (+0.77 to +0.54. One sample was found to be undersaturated with dolomite -0.45), moderately under-saturated with gypsum (-1.68 to -1.93) and strongly undersaturated with halite (-6.57 to -7.07) (Table 3.3).

Table 3.3 Saturation indices for the Amman Formation groundwater

Well No.	Calcite	Dolomite	Gypsum	Halite
S-62	-0.58	-0.45	-1.93	-6.84
NRA-WS	-0.31	+0.64	-1.68	-6.57
S-4	-0.21	+0.54	-1.86	-7.07
S-36	-0.15	+0.62	-1.93	-6.94
S-37	-0.10	+0.77	-1.92	-7.00

Phase III recorded that the major input groundwater to the Maqarin area is from the B_3-aquitard in the Bituminous Marl Formation which overlies the Amman Formation. It is typically of neutral pH. It covers a wide range in composition from dilute Ca-Mg-(Na)-HCO_3-(Cl)-type groundwaters, with TDS contents of 348–545 mgL^{-1}, to strongly mineralised Na-Ca-SO_4-Cl-type groundwaters with TDS contents between 1077–2161 mgL^{-1} (Table 3.4). Unfortunately, no isotopic data are available for these groundwaters and most of the pH-measurements are only semi-quantitative. B_3-groundwaters with accurate pH measurements are in equilibrium with calcite, which is as would be expected, since the groundwaters in the overlying formation have also reached calcite equilibrium. Under certain circumstances, the mixing of two calcite-saturated groundwaters with strongly different ionic strengths might result in a calcite undersaturation of the mixture. If such a process takes place between infiltrating dilute groundwaters from the overlying Rijam Formation/lower part of the Lower Chalky Limestone Member (B_4-Aquifer), and strongly mineralised formation water of the Bituminous Marl Formation, remains a matter of speculation due to the limited quality of the groundwater analyses.

Low-mineralised B_3-groundwaters have Na/Cl ratios higher than evaporated precipitation indicating a different source for Na. Such a source might be Ca-Na cation exchange on clay minerals in the clay biomicrites. This could also explain the slightly elevated K^+ and, in parts, the Mg^{2+} concentrations observed (Table 3.4). Such a process would be consistent with the low NO_3 concentrations (i.e. no significant anthropogenic input of fertilisers), the different ion ratios which exclude an admixture of known Amman B_2-type or deeper groundwaters. Carbonate dissolution[9] is responsible for the Ca^{2+}, HCO_3^- and, in parts, Mg^{2+} concentrations and sulphate probably comes from gypsum dissolution. At calcite equilibrium these groundwaters are undersaturated with respect to dolomite and gypsum.

[9] Further carbonate dissolution would decrease the PCO_2. Although PCO_2 is not given in Table 3.4, it should be noted that radiocarbon modelling, with hand calculations and with NETPATH, indicated that the high PCO_2 values were probably due to subsurface inputs of CO_2 in the Rift Zone.

Table 3.4 Average chemical composition of the Bituminous Marl Formation groundwaters in the Maqarin area (B_3-aquitard; Abdul Jaber, 1982, 1989; Phase III unpublished data from E. Salameh, 1996).

		Maqarin B3 : Low mineralised			Maqarin B3 : Highly mineralised		
		Average	**Stdev**	**n**	**Average**	**Stdev**	**n**
pH		6.92	0.28	30	6.87	0.12	3
Eh (mV)		–	–		–	–	
T (^oC)		20.0	0.0	30	20	0	3
Cond ($\mu S/cm$)		893.0	35.8	3	–	–	
TDS (calc.)	mgL^{-1}	459.9	64.8	30	1548.7	555.7	3
Na	mgL^{-1}	49.0	17.5	30	151.8	76.0	3
K	mgL^{-1}	7.4	4.3	30	11.9	9.1	3
Mg	mgL^{-1}	27.0	7.8	30	44.9	23.7	3
Ca	mgL^{-1}	81.3	20.1	30	309.3	148.1	3
Mn	mgL^{-1}	0.035	0.013	3	–	–	
Fe_{tot}	mgL^{-1}	0.027	0.004	2	–	–	
Zn	mgL^{-1}	0.007	0.005	3	–	–	
Cu	mgL^{-1}	0.001	0.000	2	–	–	
Ni	mgL^{-1}	0.003	0.002	2	–	–	
Cl	mgL^{-1}	63.3	21.5	30	220.3	139.3	3
SO_4	mgL^{-1}	73.5	34.9	30	604.7	282.0	3
NO_3	mgL^{-1}	1.9	1.4	26	24.9	29.6	3
HCO_3	mgL^{-1}	318.9	99.6	30	368.2	144.5	3

Similar processes are thought to account for the mineralisation in the highly mineralised B_3-groundwaters. Again, simple mixing with known deep groundwaters (i.e. from the Amman Formation) can be excluded, based on the observed ion/ion ratios, and also mixing with known high-pH groundwaters. Such highly mineralised groundwaters might, however, represent mixtures of young carbonate groundwater with very old formation water of the Bituminous Marl Formation. Measured pH and alkalinity values indicate that these highly mineralised groundwaters are in equilibrium with calcite, but undersaturated with respect to dolomite and gypsum.

The groundwaters of the overlying Chalky Limestone Formation were also reviewed as potential input to the Bituminous Marl Formation groundwaters in the Maqarin area. Different water samples have been collected from the $B_{4/5}$ shallow, phreatic and karstified aquifer over the last 15 years, mainly from springs, i.e. Ein Turab, Quelba, Aqraba and Khreiba. Average ranges of chemical composition are given in Table 3.5.

Generally, the water of these springs originates from precipitation over the surrounding uplands comprising the $B_{4/5}$ units. These waters, however, are characterised by relatively high contents of nitrates (0.35 to 0.71 $meqL^{-1}$), compared with the natural range of 0.25-0.35 $meqL^{-1}$ in the area as a whole. Two sources of nitrate were considered: a) due to agricultural activities, and b) due to leakages from cesspits and septic tanks used for the disposal of domestic waste water from nearby villages. These contaminated waters, therefore, may have infiltrated to reach the $B_{4/5,}$ groundwaters and from there join the aquifer. This hypothesis, however was not supported by the hydrochemical modelling carried out in Phase III, and further ruled out by present Phase IV studies (see section 3.5.2)

The water of the Quelba, Khreiba and Ein Turab springs is of Na-(Ca)-HCO_3 type , showing that the origin of the water is precipitation which has not had enough time to react completely with the calcareous aquifer. The Aqraba spring water differs because of increased amounts of sulphate and chloride from interaction processes with the aquifer

rocks, and also the high nitrate content of 0.64 and 0.71meqL^{-1} suggesting some contamination.

Groundwaters in the $B_{4/5}$ aquifer are undersaturated with respect to gypsum and halite and over- or undersaturated with respect to calcite and dolomite, depending on the mixing processes of recharge water with the older water in the aquifer and on the ratio of waste water joining the aquifer. The spring waters are, in certain periods of the year, under- or oversaturated with respect to calcite and dolomite, undersaturated with calcite and oversaturated with dolomite, or the contrary. Saturation indices are: calcite -1.58, dolomite -2.06, gypsum -1.97 and halite -6.45.

Table 3.5 Ranges of chemical composition of Rijam-Shallala aquifer ($B_{4,5}$) in mgL^{-1}

pH	Ca	Mg	Na	K	NO_3	HCO_3	SO_4	Cl
6.8-8.16	66-128	27.0-40.8	10.4-41.4	0-4-3.2	6-45	202-408	1.9-112	20.3-78.4

3.2.2 Maqarin hydrogeology and hydrogeochemistry

The geological setting of the localities investigated at Maqarin (Eastern Springs and Western Springs; see chapter 1), in contrast to the regional and discharge features of northern Jordan described above suggests shallow, locally recharged groundwater systems. At the Eastern Springs, where more data are available, there is evidence of rapid recharge and discharge features. Topographically, there is a depression directly above the Eastern Springs site (i.e. overlying Adit A-6) which allows surface run-off to accumulate and to percolate rapidly down along soil cracks to the underlying rock formation. Moreover, the underlying surface of the Bituminous Marl Formation (B_3-unit) is characterised by two depressions where the percolating waters subsequently accumulate (Figure 3.2). These correspond to the recharge access points which, in this hydrogeologically restricted area, represent the high permeability recharge zones from where the recharged waters flow laterally and downwards in all directions.

Figure 3.2 Topographic depressions A and B at the top of the Bituminous Marl Formation showing the groundwater flow and discharge patterns of the water body overlying this unit. The contours are m above sea level (asl) (E. Salameh, modified after Harza, 1980).

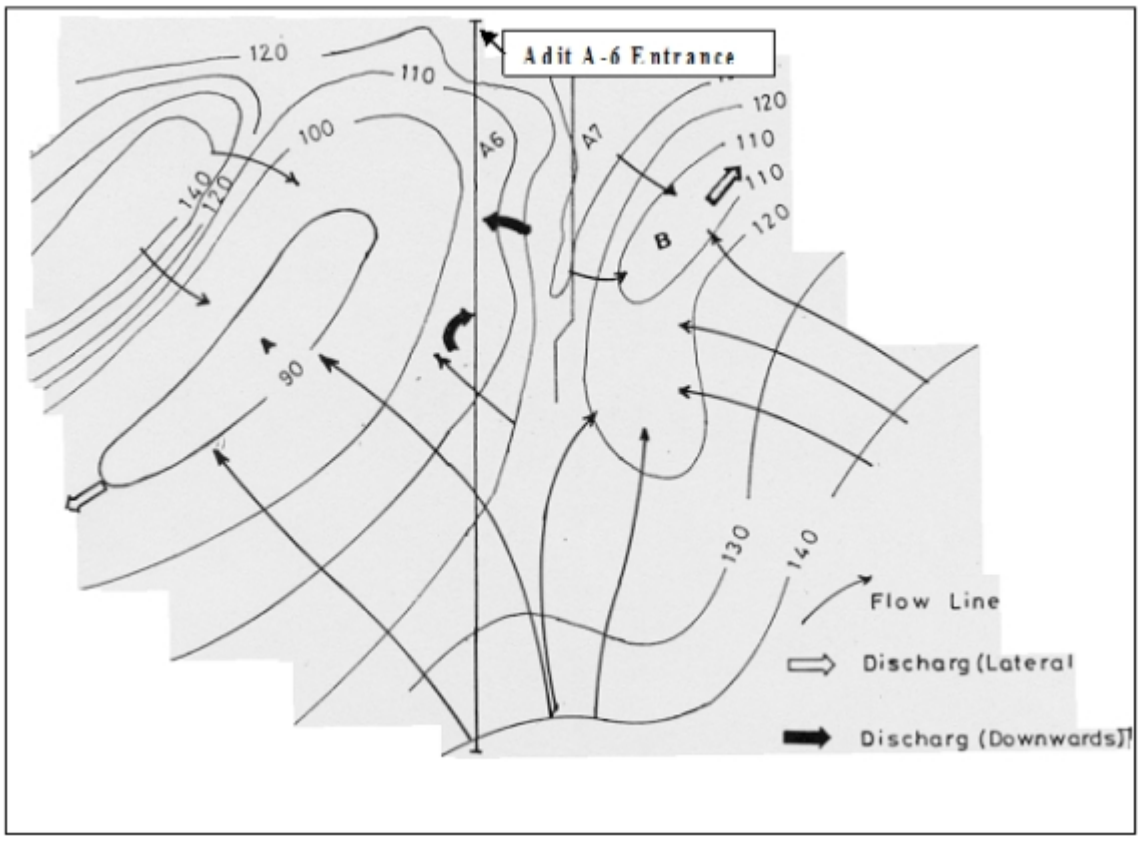

Although the phreatic groundwater table illustrated in Figure 3.2 shows flow lines in all directions, the main discharge sites of this perched groundwater body are downward to the Adit A-6 where the $B_{4/5}$-unit is exposed, and laterally north-eastwards to the Eastern Springs and west-south-west to Wadi Sijin. The other flow directions correspond in some cases to discharge sites characterised only by slight seepages, and others where discharge joins up with groundwater flow directions from other sources.

During these recharge and discharge cycles, groundwater interacts with the ACZs within the Bituminous Marl Formation parent rock. This results in the formation of the hyperalkaline groundwaters which characterise the Adit A-6 seepages and at the various localities to the north, east and west of Adit A-6. Figure 3.3 shows a geological and hydrogeological N-S cross section along Adit A-6, further illustrating the accumulation points of surface runoff, the percolating recharge pathways through the overlying soil cover to the basalt, the Chalky Limestone Formation ($B_{4/5}$-unit) and the Bituminous Marl Formation (B_3-unit). The main cement-zone area (ACZ), traversed by Adit A-6, is within the B_3-unit, close to the interface with the overlying $B_{4/5}$-unit.

Figure 3.3 Geological and hydrogeological cross-section along Adit A-6. Length of Adit is 776 m, with elevations of 100.6 m asl at the entrance and 114 m asl at the maximum excavation distance to the south (E. Salameh, modified after Harza, 1980).

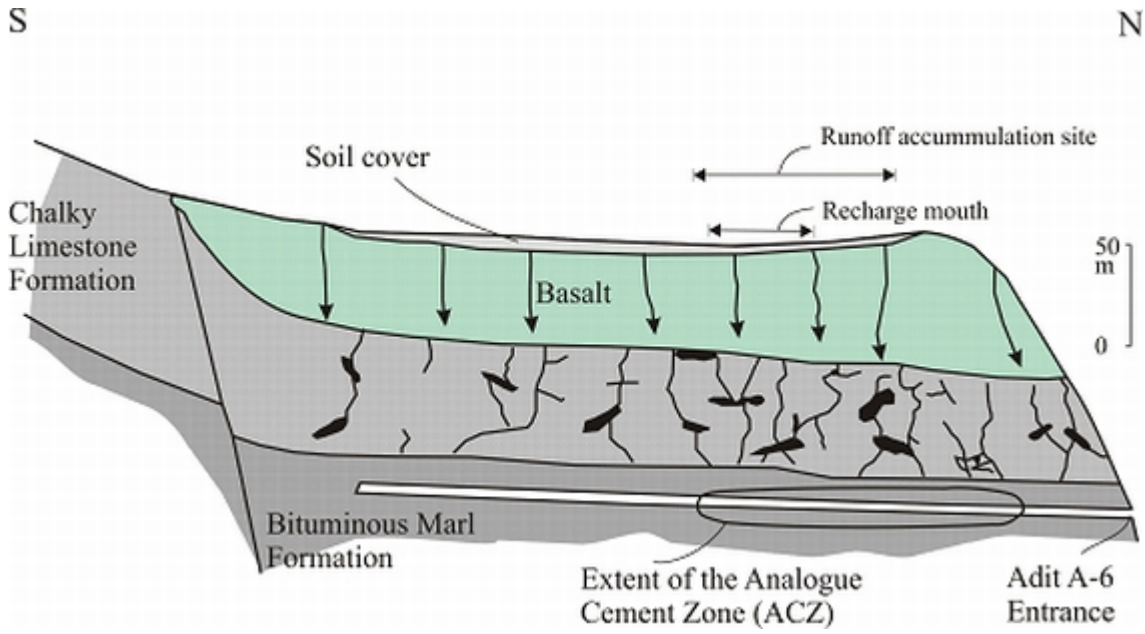

The situation at the Western Springs is less clear because of the lack of outcrop and borehole information, but geologically and conceptually it is believed to show close similarities with the Eastern Springs localities (Figure 3.4). Local recharge is rapid and facilitated by surface karst features in the Chalky Limestone Formation such as dolines which are tens of metres in diameter. Percolation continues through the ACZ at, and near the surface of, the underlying, generally impermeable, Bituminous Marl Formation where there is mixing with older regional groundwaters moving northwards. This neutral pH, mixed groundwater interacts in the ACZ producing the hyperalkaline groundwaters which percolate into the clay biomicrites along discrete fractures. Much of the water, however, appears to percolate down slope, initially at the interface of the biomicrite and the hill-wash sediments and later the colluvium until seepages occur near the level of the Yarmouk River. Travertine precipitation has resulted in cementation of both colluvial and alluvial deposits in the valley bottom at these seepage localities.

Figure 3.4 Schematic diagram of the hydrogeological situation in the Western Springs area. Discharge seepages at the bottom of the Yarmouk River valley occur mostly at the colluvium – cemented alluvium interface (from Smellie, 1998).

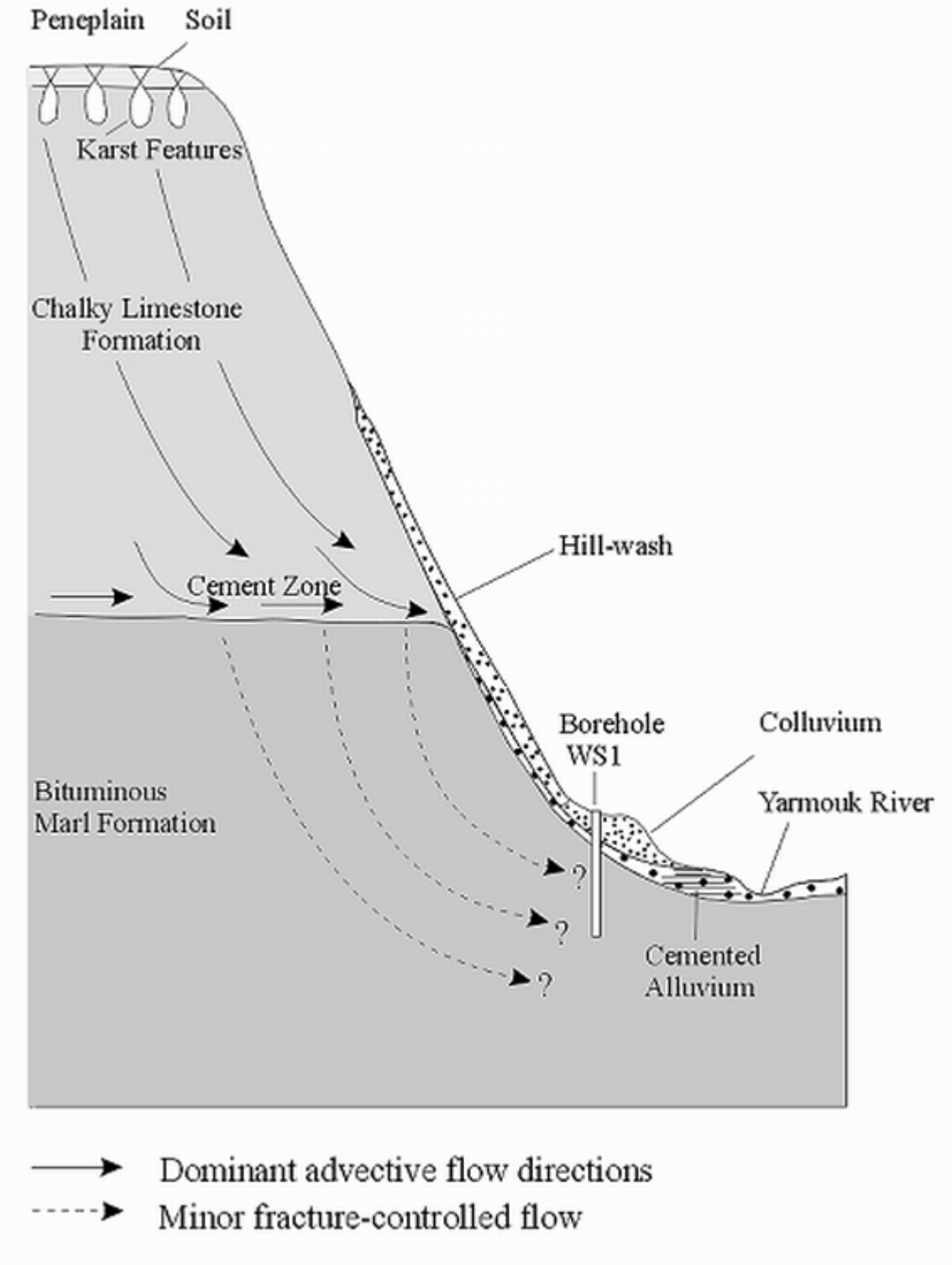

With respect to the hydrochemistry of the groundwaters, the major localities sampled at the two Maqarin sites during Phases I-III are shown in Figure 3.5. These include the Western Springs seepage localities at the Yarmouk River, a series of seepage points in the Eastern Springs area along railway and road cuttings into the Bituminous Marl Formation, and at various seepage points along Adit A-6. Immediately following the wet

period, some seepage localities are reactivated at the banks of the Yarmouk River, due north of Adit A-6.

Figure 3.5 Location of the Maqarin area in relation to the major wadis and the sampling sites (Note: Wadi Sijin M23 site refers to the Phase IV study).

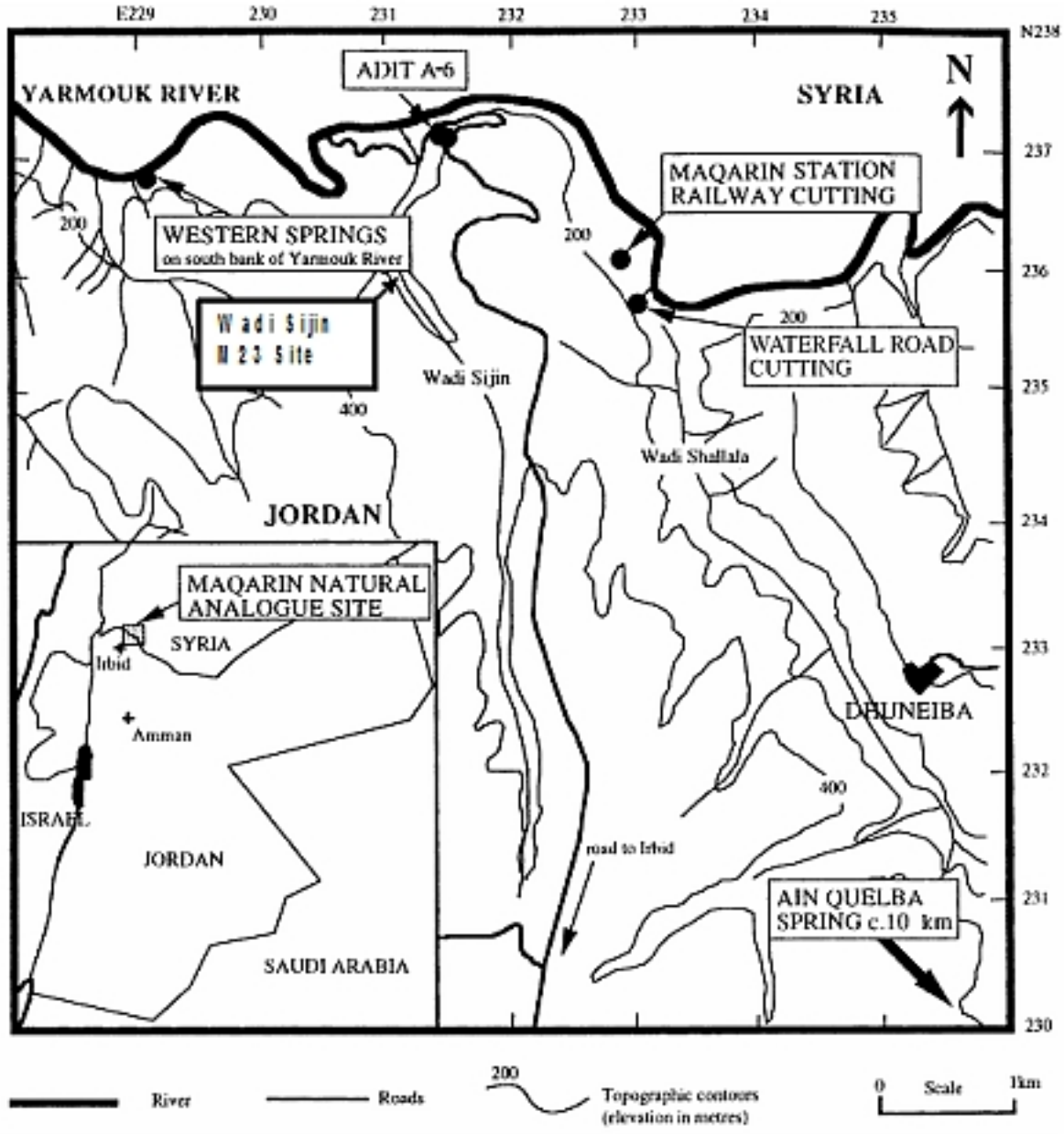

Table 3.6 Average chemical composition of high-pH groundwaters from the Eastern Springs area at Maqarin (B_3-Aquitard) (from Smellie, 1998).

		Adit A-6			**Railway Cutting**		
		Average	**Stdev.**	**n**	**Average**	**Stdev.**	**n**
pH		12.56	0.09	5	12.7	0.1	3
Eh	mV	239	63	4	197	66	2
T(Wa)	oC	23.94	1.8	5	24.9	1.7	3
Cond.	µS\cm	5165	1081.9	2	7220	nd	1
TDS							
(calc)	mgL^{-1}	1474.8	193.5	5	1687.4	106.1	3
Li	mgL^{-1}	0.394	0.332	5	nd	nd	0
Na	mgL^{-1}	47.1	3.5	5	38.6	6.9	3
K	mgL^{-1}	13.4	3	5	18.3	1.7	3
Mg	mgL^{-1}	0.1	0	5	0.1	0.1	3
Ca	mgL^{-1}	603.4	104.4	5	683.3	104.5	3
Sr	mgL^{-1}	7	1.7	5	10.6	0.3	3
Mn	mgL^{-1}	nd	nd	0	nd	nd	0
Fe_{tot}	mgL^{-1}	nd	nd	0	nd	nd	0
NH_4	mgL^{-1}	0.2	nd	1	0.13	nd	1
Ba	mgL^{-1}	0.033	0.008	5	0.047	0.006	3
Zn	mgL^{-1}	0.047	0.017	4	0.023	0.023	3
Cu	mgL^{-1}	nd	nd	0	nd	nd	0
Ni	mgL^{-1}	nd	nd	0	nd	nd	0
F	mgL^{-1}	0.323	0.055	5	0.329	0.023	3
Cl	mgL^{-1}	58.9	6.3	5	70.7	2	3
Br	mgL^{-1}	0.258	0.081	4	0.313	0.051	3
SO_4	mgL^{-1}	285.4	13	5	288	3.6	3
NO_3	mgL^{-1}	7.3	9.2	5	7.6	0.1	3
HCO_3	mgL^{-1}	nd	nd	0	nd	nd	0
CO_3	mgL^{-1}	1.98	0	5	1.98	0	3
OH	mgL^{-1}	435	111.9	5	551	22.3	3
Al	mgL^{-1}	0.16	0.028	2	0.15	nd	1
P	mgL^{-1}	0.003	nd	1	0.006	nd	1
Si	mgL^{-1}	1.14	nd	1	0.19	0.06	3
O_2	mgL^{-1}	4	0	2	11	nd	1
TOC	mgL^{-1}	3.9	1	2	1.6	0.2	3
$\delta^{18}O$	‰	-4.5	0.3	5	-4.9	0.8	3
$\delta^{2}H$	‰	-23	1.7	5	-24.2	4.4	3
^{3}H	TU	1.2	0.4	2	1.5	nd	1
$\delta^{34}S$	‰	-0.5	-1.1	4	-1.1	nd	1
$\delta^{18}O(SO_4)$	‰	12.2	9.8	4	9.8	nd	1

* CO_3 = from vacuum extraction of sample MQ1 (Adit A-6, 06/04/90); nd = not determined.

The conceptual geological and hydrological similarities between the Western and Eastern Springs are not reflected in the respective groundwater chemistries (cf. Tables 3.6 and 3.7) which are significantly different. Basically, interaction of neutral pH groundwaters in the ACZ has produced two chemically distinct hyperalkaline groundwaters: Eastern

Springs waters, which are of Ca-OH-SO_4 type with relatively low K and Na, and the Western Springs waters of Ca-K-Na-OH-SO_4-type, but more mineralised, with significantly higher concentrations of K, Na and SO_4.

The Phase I-III studies also showed that the groundwaters from the two areas also differ significantly in their trace element chemistry (Alexander, 1992; Linklater, 1998; Smellie, 1998). In particular, the Western Springs groundwaters were found to exhibit very high concentrations of Cr (up to 7 mgL^{-1}) compared to the Eastern Springs groundwaters (up to 0.95 mgL^{-1}). In fact, the very high concentration of Cr in the Western Springs imparts a characteristic pale yellow colour to the groundwaters in this area due to its presence as chromate species. In addition, these earlier studies showed that the Western Springs groundwaters are enriched in NH_4^+, Li, B, Zn, Mo, Se, Re and U by up to an order of magnitude relative to the Eastern Springs.

Some doubt persisted over the course of the Phase I and Phase II studies as to the origin of the high K^+, and Na^+ observed at the Western Springs locality. These alkali metals were observed as major elements in very unusual alkali and alkaline earth sulphide minerals such as oldhamite (CaS) (containing minor K in solid solution). A previously unknown copper-potassium-sodium-sulphide-selenide mineral ($Cu_{10.2}K_3Na_{0.2}Se_{7.7}S_{2.3}$) was also present within the primary metamorphic mineral assemblage (Milodowski et al., 1992a, 1992b, 1998a; Table 3-9, see section 3.5.1 below). These two minerals were observed to be highly reactive (i.e. very soluble), dissolving rapidly during the early stages of hydration of the marbles. Conceivably, therefore, the dissolution of these minerals, during the early stages of the hydration of the metamorphic rocks, might produce high K^+ and Na^+ concentrations in the groundwaters. Furthermore, these minerals are also Se-rich. This could possibly account for the correspondence of high concentrations of Se with high concentrations of K^+ and Na^+ observed in the Western Springs area. However, these sulphide-selenide minerals are only present as trace phases, occurring as inclusion phases within primary metamorphic calcite and calcium silicates. Consequently, it was unclear whether such trace minerals could realistically account sufficiently for the mass of K^+ and Na^+ in the groundwaters in the Western Springs.

Other potential sources for K^+ and Na^+ can also be ruled out for the Western Springs, for example: a) fertilisers (K-source) would be accompanied by far more NO_3 than observed, b) marine aerosols could not have lost so much Na by cation exchange or any other process, and c) probably leaching of the basalts can be neglected as the inventory of K-minerals would be too low. Moreover, the hydrogeochemical modelling carried out provides no support for these observations. Quite simply, it can be attributed to different stages of water/rock interaction.

Table 3.7 Average chemical composition of high-pH groundwaters from the Western Springs area at Maqarin (from Smellie, 1998).

		Average	Stdev.	n
pH		12.66	0.16	11
Eh	mV	173	59	4
T(Wa)	oC	24.1	2.1	11
Cond.	µS\cm	10210	nd	1
TDS				
(calc)	mgL^{-1}	3590.1	1029	11
Li	mgL^{-1}	0.3	0.3	10
Na	mgL^{-1}	122.6	47.2	11
K	mgL^{-1}	474.8	253.4	11
Mg	mgL^{-1}	0.1	0	5
Ca	mgL^{-1}	995.2	158.1	11
Sr	mgL^{-1}	14.1	4.1	11
Mn	mgL^{-1}	nd	nd	0
Fe_{tot}	mgL^{-1}	nd	nd	0
NH_4	mgL^{-1}	3.6	2.4	11
Ba	mgL^{-1}	0.028	0.009	11
Zn	mgL^{-1}	0.023	0.013	10
Cu	mgL^{-1}	0.08	0.014	2
Ni	mgL^{-1}	nd	nd	0
F	mgL^{-1}	0.764	0.248	11
Cl	mgL^{-1}	47.1	13	11
Br	mgL^{-1}	nd	nd	0
SO_4	mgL^{-1}	1283.8	491.7	11
NO_3	mgL^{-1}	28.3	13.1	11
CO_3	mgL^{-1}	1.2	0	11
OH	mgL^{-1}	600.5	110.7	11
Al	mgL^{-1}	0.1	nd	1
P	mgL^{-1}	0.1	0.1	6
Si	mgL^{-1}	0.4	0.3	8
O_2	mgL^{-1}	0.4	0.3	7
TOC	mgL^{-1}	6.6	3.2	10
$\delta^{18}O$	‰	-4.1	0.5	6
$\delta^{2}H$	‰	-19.1	2.5	6
^{3}H	TU	0.5	0.5	3
$\delta^{34}S$	‰	-2.6	0.1	2

* CO_3 - from vacuum extraction of sample MQ1 (Adit A-6, 06/04/90)

Irrespective of their origin, however, the occurrence of high K^+ and Na^+ concentrations in the Western Springs seeps, compared with lower concentrations in the Eastern Springs groundwaters, is significant to the repository analogue. It follows that the Western Springs groundwaters represent the early pore volumes of water leaving the cement zone (somewhat analogous to Region 1 in cement terminology), and that the Eastern Springs groundwaters represent subsequent pore volumes (somewhat analogous to Region 2) from a more highly leached cement zone.

The main hydrogeochemical conclusions from the Phase I-III studies were:

- Most of the neutral pH groundwaters which interact with the ACZs at Maqarin have recharged locally, following short transport pathways along fractures from the overlying formations.
- The recharged dilute bicarbonate groundwaters, represented by samples from Ain Quelba spring, and location M18 (Eastern Springs borehole) are therefore the probable precursor to the high pH groundwaters. These are modern (tritiated) groundwaters from local flow systems in the carbonate bedrock. No significant mixing of groundwaters from the underlying, confined Amman Formation B_2-aquifer has occurred.
- Interaction of neutral pH groundwaters with the ACZ has produced two chemically distinct hyperalkaline groundwaters: the Eastern Springs groundwaters of Ca-OH-SO_4-type and the Western Springs groundwaters of Ca-K-Na-OH-SO_4-type.
- The minor amounts of tritium measured in the hyperalkaline groundwaters are attributable to mixing with local bicarbonate groundwaters (^{3}H currently ~ 4 TU). Mixing with up to 50% bicarbonate waters has only a minor influence on pH. Accordingly, unmixed hyperalkaline groundwaters are considered to be ^{3}H-free and older than at least 40 years.
- In addition to high K^+ and Na^+, the Western Springs groundwaters contain high concentrations of NH_4^+, Li, B, Zn, Mo, Se and U compared to groundwaters in the Eastern Springs area.
- The δ^{18}O and δ^2H composition of samples of hyperalkaline groundwaters show a range of up to 3‰ for δ^{18}O and 9‰ for δ^2H. This is probably attributable to variations in the bicarbonate groundwater precursors, variations in the degree of hydroxide alteration, and to secondary mixing with bicarbonate groundwaters near the point of discharge.
- The δ^{18}O and δ^2H composition of the hyperalkaline groundwaters from the higher pH Western Springs is considered to have an evolved signature from a more depleted meteoric water precursor. Secondary mixing with up to 30% bicarbonate groundwaters may have taken place in the discharge area.
- Measurement of ^{36}Cl in the hyperalkaline groundwaters demonstrated that there was no thermonuclear ^{36}Cl in these waters. This is consistent with the interpretation of the ^{3}H data, indicating recharge prior to 1950. The age of the hyperalkaline groundwaters cannot, with the currently available data, be constrained to better than >40 years.
- Hydrogeochemical modelling suggests that the observed differences in groundwater composition between the Eastern and Western Springs localities can be attributed to different stages of water/rock interaction. There is no convincing evidence that the high Na^+, K^+ and SO_4^{2-} concentrations at the Western Springs locality are due to initial differences in metamorphic composition of the ACZ, variable infiltration conditions, or anthropogenic contamination.
- Aqueous speciation calculations show that the hyperalkaline groundwaters are strongly undersaturated with respect to silicate minerals. There will thus be a tendency for these waters to dissolve silicate and aluminosilicate minerals upon contact.
- Low carbon dioxide fugacity values result in a strong tendency to absorb atmospheric carbon dioxide when in contact with the air. This results in the observed widespread precipitation of, for example, calcite, aragonite and vaterite associated with the Eastern and Western Spring seepages. The observed mineral species of the thaumasite-ettringite solid-solution series are the most likely

candidates for controlling the abundances of both dissolved silica and sulphate in the high pH groundwaters.

- Laboratory support studies (Bateman et al., 1995, 1998 and Chapter 4) show that high concentrations of K and Na can be leached from samples of the ACZ. Corrected for a volumetric water-to-rock ratio of 1, their concentrations correspond with those measured in the Western Springs groundwaters. Accordingly, this supports the analogue that the Western Springs groundwaters represent the early pore volumes discharging from the ACZ (cement Region 1), and that the Eastern Springs groundwaters represent later, more evolved (cement Region 2), discharge.

3.3 Phase IV Sampling and Analysis

For the Phase IV studies, the emphasis was initially to focus on Adit A-6 where a drilling programme was planned for hydrogeological characterisation (see chapter 2). This programme was co-ordinated to fulfil the objectives of hydraulic measurements to determine groundwater-flow directions, and also for groundwater sampling. One disadvantage of the Phase I-III sampling campaigns was that only oxidising groundwaters (i.e. non-repository relevant conditions) could be collected from the various seepage localities. With the Phase IV borehole programme there was the possibility of sampling under more representative reducing groundwater conditions deeper into the host bedrock. Unfortunately, several of the boreholes drilled in the parent rock and the ACZ were hydraulically tight and only small amounts (if any) of groundwater could be sampled. Additionally, the ACZ was extremely hard and drilling to around a metre depth was the best that could be managed with the equipment available. Nevertheless, to mimimise oxidation of the groundwaters, which were percolating and accumulating, the boreholes were sealed. Nearby travertine precipitates were used and tubing, inserted through the seals, was fitted with a simple adjustable clamp to allow periodic sampling.

Figure 3.6 *M22 strong seepage (left); several dripping stalactite sources were channelled by plastic sheeting into PVC bottles. M19 weak seepage locality (right). Both sites in Adit A-6.*

The sampling sites in Adit A-6 also included new seepage localities that had been detected much deeper into the gallery. Sampling from these seepage points was usually directly into PVC bottles positioned under the dripping stalactites (e.g. M22 site; Figure 3.6). Depending on the flow rate, this could take from some minutes to several hours and was obviously not anoxic. In the absence of any focused dripping, plastic sheeting was shaped into a funnel to collect drops from a greater area. For some of the very weak single-drop seepages (e.g. M19; Figure 3.6), overnight collection was necessary. Sampling protocols are described in detail in appendix 3-1.

Most of the Adit A-6 sampling localities are schematically shown in Figure 3.7.

Figure 3.7 *Schematic illustration of Adit A-6 showing areas of intense formation of stalactites/stalagmites and most of the sampled seepage localities in the Bituminous Marl parent rock and in the Analogue Cement Zone (ACZ). (D =borehole; M =seepage point; lower numbers refer to metres from the Adit entrance).*

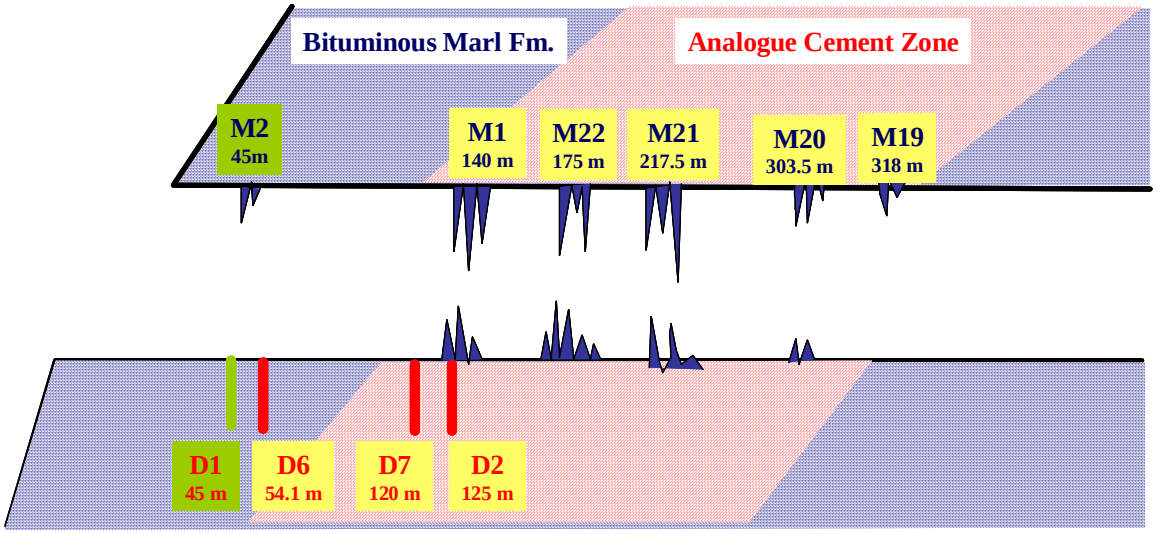

To complete the site-scale campaign, two of the earlier Phase I-III site-scale locations (Figure 3.5) were resampled (M3: Eastern Springs Maqarin Railway Cutting and M5: Western Springs) with the addition of a new site in Wadi Sijin (M23 Site). Furthermore, as in previous phases of sampling (see section 3.2) four nearby municipal water supplies (Aqraba, Ein Turab, Khreiba and Quelba) were also included. These provide a better understanding of the neutral-pH, regional-groundwater input to the Maqarin area.

High-pH groundwaters were sampled initially in April/May 2000 at M1/D2, D5, D6, D7, M22, M21 and M20 and lower-pH groundwaters at M19. Later, in November 2000, low pH values were recorded at localities M20 and M21, in addition to M19. This underlined the importance of periodic sampling to assess seasonal fluctuations.

3.4 Analytical Results and Interpretation

3.4.1 Sampling and analytical data

As referred to above, major groundwater sampling campaigns were undertaken in May 2000, November 2000 and January 2001 for chemistry and isotopes. Additional campaigns were undertaken by the University of Jordan for hydrochemical data in

January 2001, February 2001, September 2001, November 2001 and January 2002. Note that the hydrochemical data, presented and discussed here, are a synthesis of analyses from the University of Jordan, the British Geological Survey and the University of Ottawa[10]. The groundwater data sets are presented in Appendix 3.2. The analytical techniques used, and the uncertainties involved, are given in Appendix 3-1.

In some cases, discrepancies occur, probably due to analytical problems with hyperalkaline waters. In this interpretation, field pH values have been used in order to have a consistent data base. Admittedly, as is often the case in hyperalkaline systems, some problems were experienced in calibrating the pH electrodes, and readings as high as pH 13.8 were noted in the Eastern Springs samples. However, these values are not reflected in the chemistry of the samples and are, therefore, assumed to be too high. Nevertheless, while the absolute values may be in question, the data are reproduced here, since the trends are useful in interpreting contributions from various sources.

3.4.2 Seasonal variations

3.4.2.1 Introduction

Seasonal variations in the discharges from Adit A-6 have been apparent since the onset of research at Maqarin. Evidence includes high-water marks from calcite precipitate along the Adit wall, as well as variations in measured pH at some seepage locations. Sufficient data have been collected sufficiently often to develop a conceptual model of recharge to the Adit seepages (see Section 3.6).

The most striking parameter reflecting variations in geochemistry on a seasonal basis is pH. Field values are plotted over the Phase IV sampling period for Adit A-6 sites in Figure 3.8. A significant spatial variation exists between the monitoring locations, with seepages at the south end of the ACZ having the strongest component of neutral pH groundwater (M19), and the locations on the northern boundary of the ACZ (M22, D2 and D5) having the highest pH. Values exceeding the pH of a portlandite saturated solution (pH 12.56, blue line in Figure 3.8) are considered to be too high. The temporal trends of these high pH sites appear to be realistic, although an increase in pH for M22, D2 and D5 in January 2001 is not supported by increased Ca (discussed below). A pH-electrode and/or meter calibration error for these samples cannot be ruled out.

All locations show variation in pH over the monitoring period, and are consistent in showing increased pH in the January/February 2001 period, with a decline in pH through 2001 and 2002. The four municipal water-supply springs also show a variation in pH, from a high near 8 to a low near 6.5.

3.4.2.2 Sampling locations M19, 20, 21 – low and variable pH inflows

Due to increased precipitation in the Yarmouk catchment, during the autumn of 2000, the sampling sites M19, 20 and 21 showed increased flow. This was followed by a period of

[10] April/May 2000 and December 2000 analyses of major ions and trace elements on the Western and Eastern springs samples were carried out by the British Geological Survey (BGS), U.K.
April/May 2000 analysis of major ions and trace elements on the four domestic wells were carried out by the University of Ottawa, Canada.
Electric conductivity, pH and temperature measurements and major ion analysis were carried out during the January 2002 campaign on the Adit A-6 and four domestic springs by the University of Jordan, Amman.
Oxygen-18 and deuterium (University of Ottawa and BGS) and the chlorine isotopes ($^{37/35}$Cl) and tritium (University of Waterloo) were carried out in Canada on all samples from the April/May 2000 campaign.
Oxygen-18 and deuterium isotopes (University of Ottawa) and tritium (University of Waterloo) were carried out on all samples from the January 2002 campaign.

decreased recharge and a return to more fully rock-equilibrated values in January, 2001. Subsequent monitoring over the 2001 and 2002 period shows a more gradual decrease in pH, suggesting an increase in a rapid inflow component.

While the marked variations in pH for M20 and M21 suggest a two component mixing scenario, the major ion data are inconsistent. The high pH for both samples in May 2000 (Appendix 3.1) is supported by high Ca, indicating a strong $Ca(OH)_2$ component. The high pH samples from January 2001 (appendix 3.1.2) for both locations, however, are not supported by an increase in any major cation, and the anion-cation balance for these analyses indicates a 40 to 50% discrepancy. This may be due to Ca loss during analysis by precipitation of $CaCO_3$ (note elevated bicarbonate in these samples), and is observed in other samples as well (M22 and D7). However, pH at the most alkaline locations (e.g. M22 and D2; Figure 3.8) is greater than can be generated by the chemistry of these waters (maximum of around 12.6). If the pH meter was consistently reporting too high values, then the January 2001 pH anomaly is exaggerated. Nevertheless, as noted above, the trends in the pH values are still useful indicators of seasonal fluctuations.

This rapid fluctuation suggests a two-component flow system involving a highly permeable, rapidly recharged flow system, and a low-permeability flow system with rock-equilibrated groundwater. This conceptualisation was briefly mentioned in Section 3.2.2, and is discussed in more detail below, in Section 3.6.

Figure 3.8 *Field pH variations between 2000 and 2002 for monitoring locations in Adit A-6 and for the four carbonate springs in the Maqarin region. The horizontal blue line (at pH 12.56) indicates a $Ca(OH)_2$ saturated solution, which in this system represents a realistic upper limit for pH. Values exceeding this level are considered to be an artefact of electrode sensitivity at very high pH.*

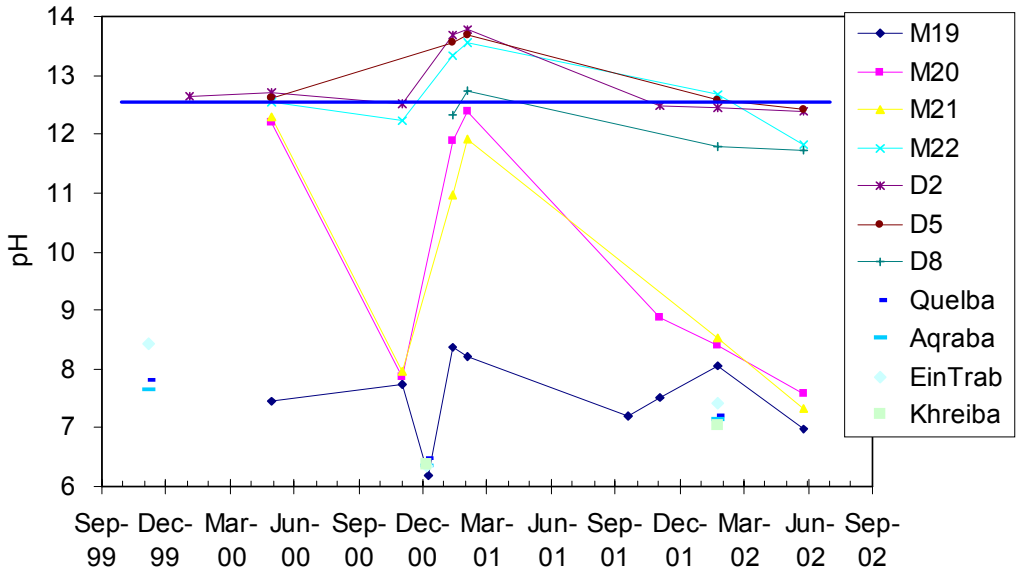

The M19 location shows variations in major ion geochemistry that closely correlate with pH (Figure 3.9). This demonstrates simple mixing between rock-equilibrated water (but not the ACZ, due to insignificant OH^-) and rapidly recharged low-pH water that has not attenuated carbonate acidity through weathering. Principal events over this period include a drop in pH in November 2000, which is closely matched by decreases in rock-derived ions including Ca, SO_4 and K. By contrast, the strong increase in Cl and Na

indicates that these components are surface derived. A surface-derived source of Cl is consistent with Phase II and III conclusions, but is contrary to the interpretation of ^{37}Cl isotope data. A baseline source of Cl from the Chalky Limestone Formation is possible, although it is unlikely to be from the ACZ (because it varies inversely with pH).

The source of Ca-SO_4 salinity in M19 appears to be derived from dissolution of gypsum (note the close stoichiometric correlation for Ca and SO_4), probably associated with the Chalky Limestone. Alternatively, gypsum may also be derived from the ACZ. However, there is no indication of high-pH groundwater from the ACZ. The modest increase in pH from 6.2 to 8.4 observed over the monitoring period can be attributed to limestone weathering. Thus, discharge at M19 can be attributed to mixing between a slow-moving, rock-equilibrated Ca-SO_4 groundwater with pH near 8, and a rapidly recharged Na-Cl surface water with low pH near 6[11]. Potassium is assumed to be derived from the overlying basalt (although a fertiliser source cannot be ruled ou).

Figure 3.9 Temporal monitoring of pH and major ions at locations M19, M20 and M21. Horizontal blue line indicates pH of a Ca-OH saturated water.

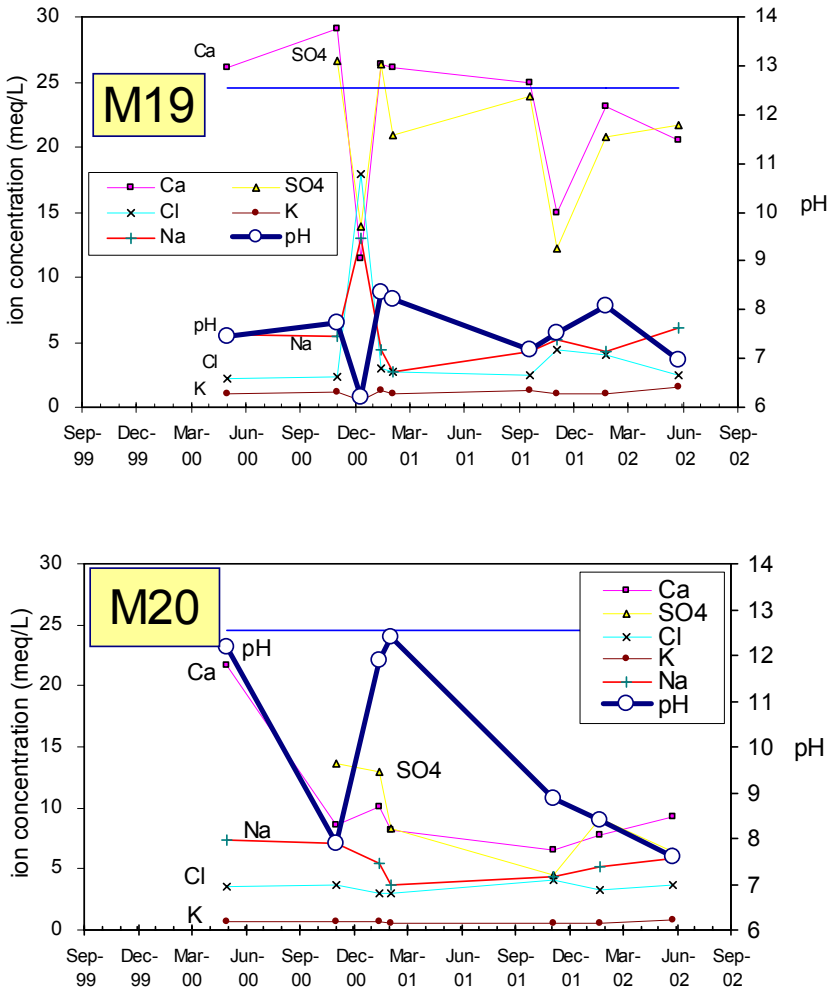

[11] Such contrasts between slow and rapid recharge are commonly reported for karst environments.

Locations M20 and M21 include a Ca-OH component derived from the ACZ, consistent with their location further north of M19 and within the ACZ. These groundwaters also carry a Ca-SO_4-(K) rock-derived (and neutral pH) component which, although less than that observed in M19, is similar to that sampled at M22.

The presence of the low-pH, rapidly circulating component seen in M19 may be present in M20 (November 2001). The very diagnostic trends for M19 taken in December 2000 (sharp decrease in pH and rock-derived ions Ca and SO_4 and increase in Cl and Na) are not readily observed elsewhere. This is due to the low ion concentrations, although the November 2001 sample comes close to representing this component in M19 (Figure 3.9). For this period, M20 also shows a decrease in pH, Ca and SO_4, but with an increase in Cl.

3.4.2.3 Locations M22, D2 and D7

The high-pH Ca-OH groundwater from the ACZ, the third mixing end member, is best identified in M22 and the 'D' borehole sites (Figure 3.10) but is also observed for some of the sampling campaigns in M20 and M21 (Figure 3.9). The high pH values are matched by high Ca concentrations. Sulphate is much lower than Ca, but shows similar variation, indicating a component of Ca-SO_4 as observed in M19, 20 and 21. By contrast, Cl is poorly to inversely correlated with Ca and pH, indicating a source external to the ACZ.

The strong seasonal fluctuations observed in M19, 20 and 21 are not seen in M22 or the 'D' boreholes (Figure 3.10). These sites are consistently hyperalkaline, with only a minor variation in the Ca-SO_4 component. There is no evidence for a component of the neutral-pH, rapidly circulating groundwater observed in M19.

Figure 3.10 Temporal monitoring of pH and major ions at locations M22, D2 and D7. Horizontal blue line indicates pH of Ca-OH saturated water.

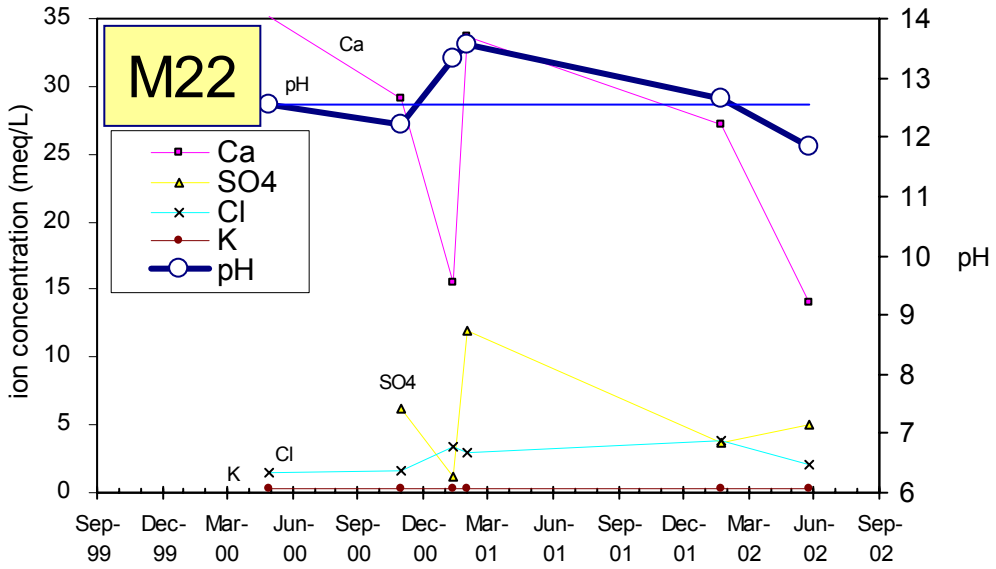

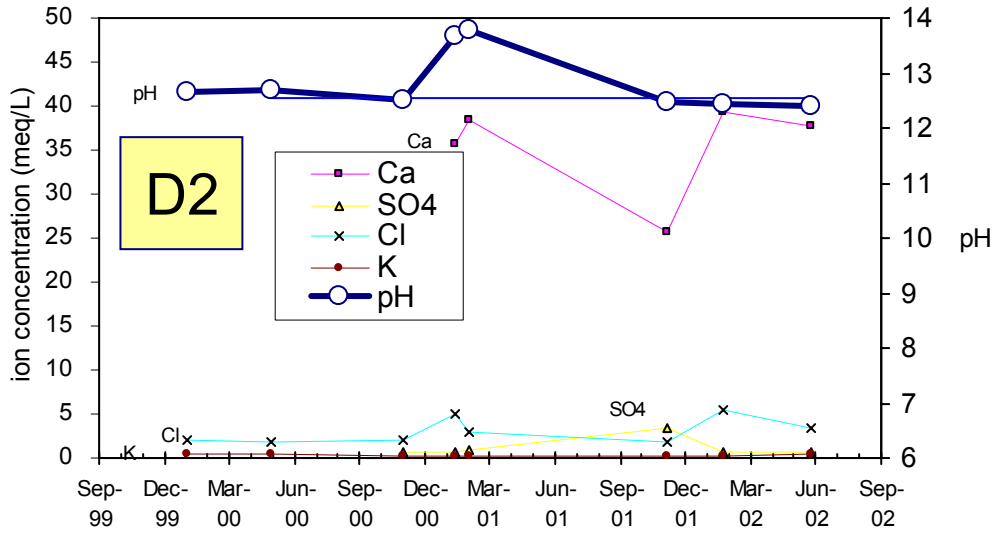

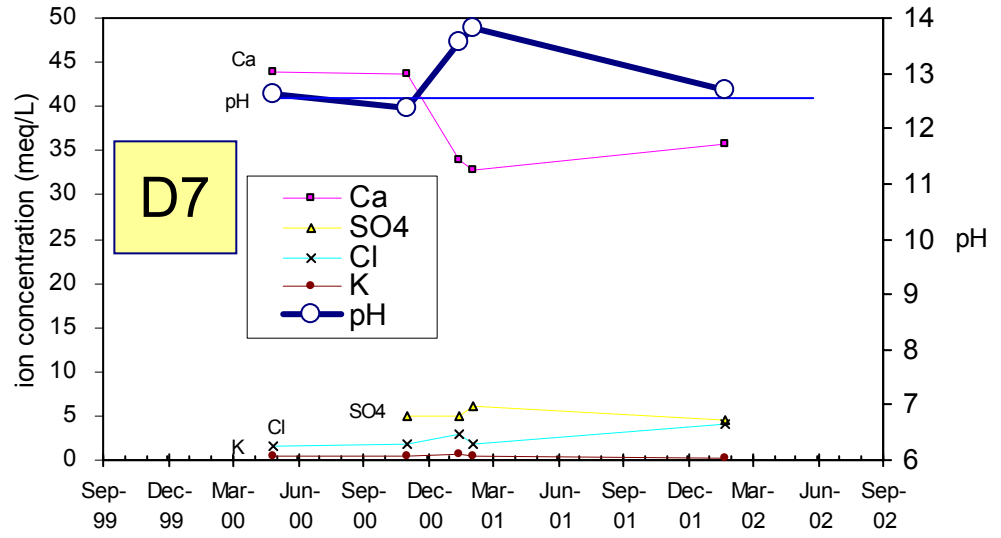

3.4.3 Tritium

The variations observed in the temporal monitoring data indicate that all seepages have more than one component to discharge. Tritium analyses show that groundwaters dominated by a high pH component from the ACZ have low but measurable tritium levels while groundwaters from the neutral pH (rapid recharge) component are apparently tritium-free (Figure 3.11). This seems counter-intuitive, considering that in most regions, modern precipitation now carries on the order of 5 to 15 TU of tritium. However, in low latitude regions, precipitation can today have low to no detectable tritium (Clark and Fritz, 1997). In Jordan, low-tritium precipitation has been analysed by the Jordan Water Authority, with values for the Irbid region averaging 7.3 TU between 1988 and 1991. Today, modern precipitation will be lower than this. The four municipal water-supply springs, which undoubtedly discharge recent precipitation, have tritium values between 3.2 and <0.8 TU.

Figure 3.11 Tritium concentrations in Maqarin Phase IV samples and in the municipal water-supply (carbonate) springs of Aqraba, Ein Turab, Kreiba and Quelba.

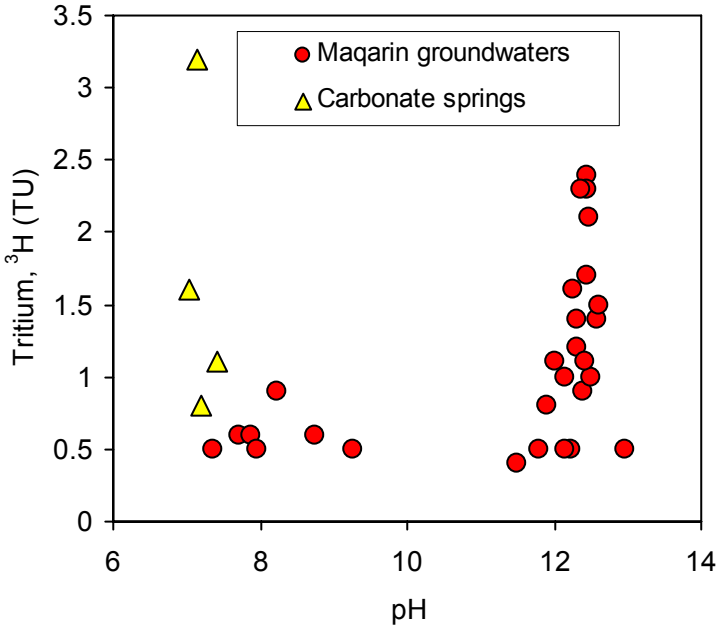

In Figure 3.12, the tritium contents of the M19, 20, 21 and 22 locations are plotted with pH and sampling campaign. The association of tritium with the slow, rock-equilibrated groundwater component is evident for all sites. In particular, the neutral groundwaters of M19 have tritium levels below detection. For the high-pH site, M22, only the sample collected during the wettest period is tritium-free. Similarly for M20 and M21, only the high pH samples (dry period) contain measurable tritium.

This association of tritium with slowly circulating groundwater in the ACZ provides an age constraint on this water. It can be attributed to recharge during the period of thermonuclear bomb testing in the 1960s and 70s when global precipitation had high levels of anthropogenic tritium. In earlier phase studies at Maqarin, the low levels of tritium measured in Adit A-6 groundwaters were attributed to modern inputs, and that the tritium-free groundwaters of the Western Springs were recharged prior to atmospheric testing of thermonuclear bombs (1951 to 1976). These new data from Phase IV are still in agreement, with the confirmation that modern components of recharge are once again tritium-free. Therefore, the tritium-bearing groundwaters from the Eastern Springs area are several decades old, recharged during the era of bomb testing.

Figure 3.12 Tritium contents at locations M19 to M22. The left-hand plot shows variations with pH for these four sites and, in the right-hand plot, the temporal variation. Values that are below analytical detection are plotted at 0 TU.

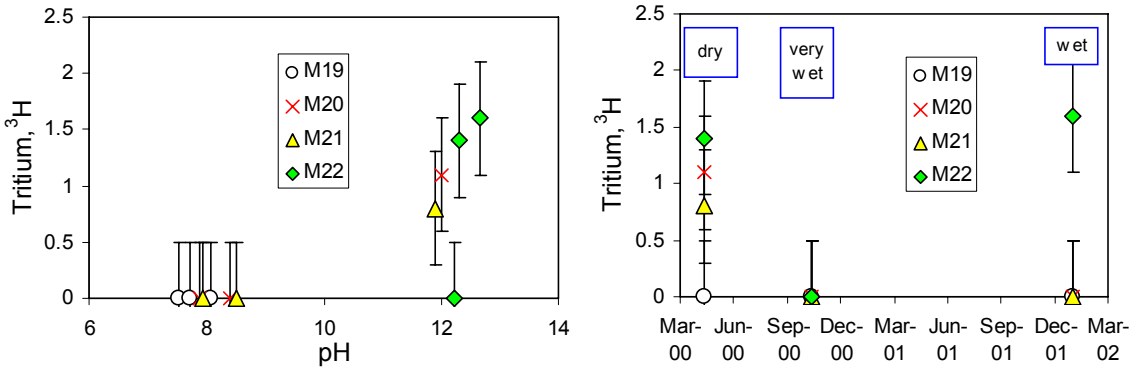

3.4.4 Oxygen-18 and deuterium

In the Phase I-III studies, it was shown that the Eastern Springs had an isotopic signature that showed no indication of ^{18}O enrichment through reaction with hydroxide, whereas the higher pH seepages at the Western Springs were relatively ^{18}O-enriched. The Phase IV isotope data are plotted against pH in Figure 3.13. No distinction s apparent for $\delta^{18}O$ between high and low pH groundwaters in the Adit A-6 samples. This is consistent with the Phase II observation that the Eastern Springs (Adit A-6 sites) represent a later-stage discharge from the ACZ, where more soluble KOH and NaOH components have been leached, leaving a $Ca(OH)_2$ dominated solution. In Phase III, it was observed that the Western Springs experienced ^{18}O enrichment due to fractionation between water and portlandite.

Figure 3.13 Oxygen-18 vs. pH in Phase IV groundwater samples from the Eastern and Western Springs. Sample dates shown for those with significant seasonal variation.

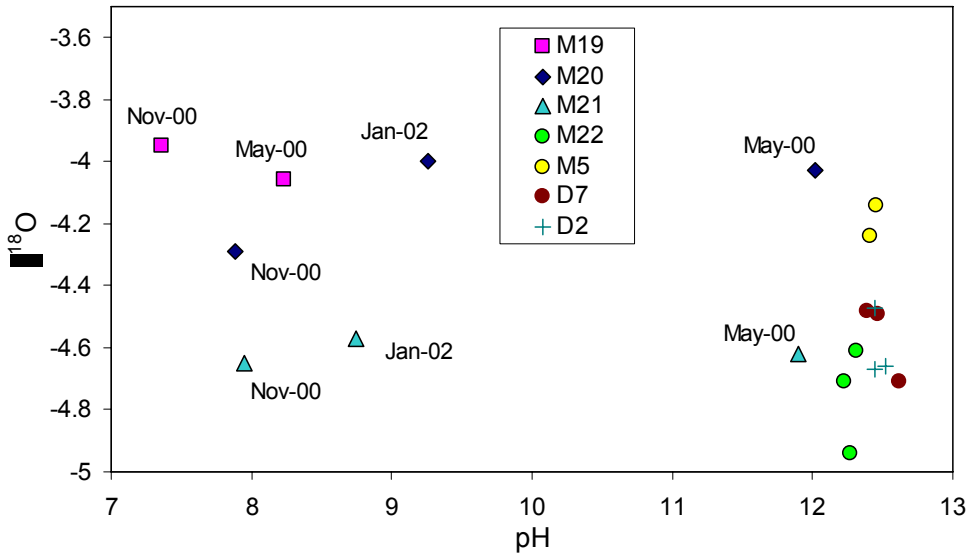

The $\delta^{18}O$ - $\delta^{2}H$ relationship in Figure 3.14 shows an ^{18}O enrichment for samples from the Western Springs (M5), but also for the M19 and M20 locations. No seasonal variations are apparent for the remainder of the samples, although there is some variability.

Comparing the $\delta^{18}O$ - $\delta^{2}H$ data by sampling location in the Eastern Springs **(**Figure 3.14), the high pH locations plotting close to the local meteoric water line indicate no significant $\delta^{18}O$ enrichment during recharge. There is, however, clear enrichment for M19 and seasonally for M20, i.e. locations that have a significant component of rapid infiltration water. This appears to be an evaporation trend representing an artefact of surface runoff in arid regions. The absence of an evaporative enrichment in the data for the exclusively high pH seeps (D2, D7, M21 and M22) reflects the dominant recharge mechanism of these groundwaters by low-permeability infiltration from surface. The Maqarin groundwaters show little variation in ^{18}O between the May and November 2000 sampling periods (Figure 3.13). They are also distinctly different from the more depleted B_2 aquifer groundwaters (Figure 3.14) which are shown to recharge at a higher elevation (Bajjali et al., 1997). This supports the conclusion that both the Eastern and Western Springs groundwaters are locally recharged by direct infiltration through the overlying strata.

Figure 3.14 *$\delta^{18}O$ vs. $\delta^{2}H$ diagram for Maqarin Phase IV groundwaters, shown with the Northern Jordan Meteoric Water Line ($\delta^{2}H$ = 7 $\delta^{18}O$ +16 ‰).*

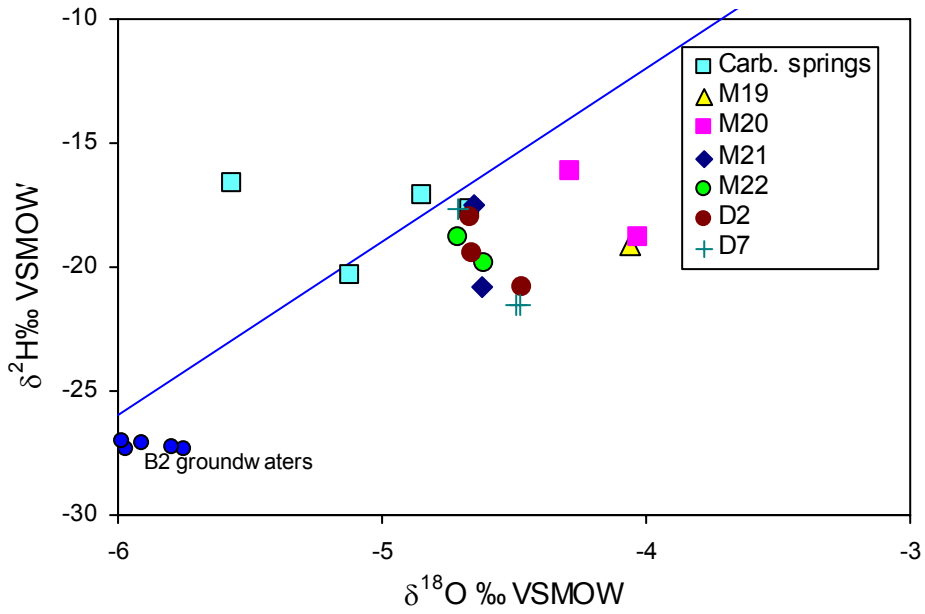

3.4.5 Principal Components Analysis – PCA

Identification of mixing end members in complex geochemical settings is facilitated by the use of codes that simultaneously examine the variability of a fixed number of components (i.e. geochemical and isotopic parameters). Here, the M3 program (Multivariate Mixing and Mass balance calculations) by Laaksoharju et al. (2000) was used.

In addition to mixing, geochemical reaction will also contribute to the range of values measured in a given set of samples. For this reason, PCA calculations seldom account for all of the variability in selected isotope and geochemical parameters. However, to have meaningful results, it is expected that at least 70% of the variability in a given data set can be accounted for by the PCA on the basis of pure mixing.

The object of this exercise was to account for the variability in the isotope and geochemical values, measured in the different waters from the Adit A-6 (spatial and temporal variations) due to mixing. From this, it was anticipated that the numbers and geochemical/isotopic characteristics of different sources of recharge in Adit A-6 could be identified.

PCA yields better results when a minimum of parameters is used. This constrains the amount of variability that needs to be accounted for by the analysis. Selection of geochemical and isotopic parameters should focus on conservative species to minimise the effects of geochemical reaction. The parameters used in this exercise are given in Table 3.9. Note that this exercise was limited by the fact that samples from the May, 2000 sampling campaign were not analysed for sulphate, although tritium and stable isotopes were analysed. These samples, despite their importance in the temporal analysis, could not be included in the PCA analysis unless the missing sulphate data were added by mass and charge balance calculations. This has not been done in this analysis.

The first and second principal components account for over 85% of the variation in the samples, making this a statistically valid analysis (70% is acceptable). The values for the first and second principal components for each sample are plotted in Figure 3.15. The different sample sites are identified by colour/shape codes and labelled accordingly. Sample data and identifications on the PCA output diagram are provided in Figure 3.16.

Figure 3.15 Principal components analysis using M3 Multicomponent Multivariat Mixing program analysis (after Laaksoharju et al., 2000)

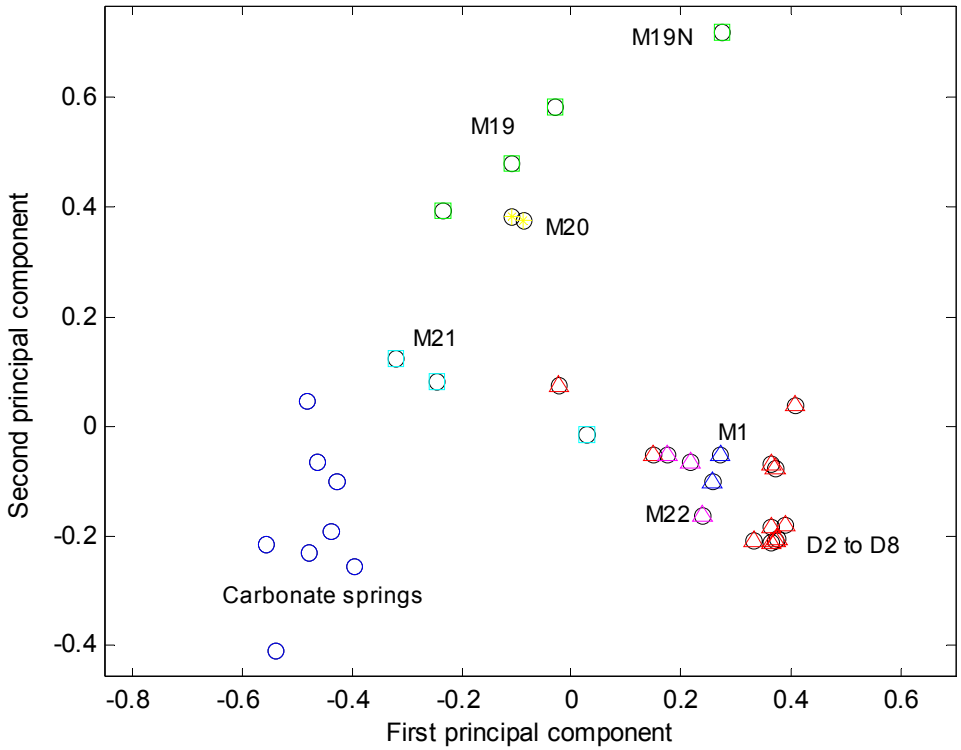

Table 3.8: Principal components analysis data set

Sample *site*	Date	PCA iden-tifier	pH	^{3}H	^{18}O	Ca *mgL^{-1}*	OH *mgL^{-1}*	HCO_3 *mgL^{-1}*	Cl *mgL^{-1}*	SO_4 *mgL^{-1}*
D2	May 2000	1	12.45	1	-4.47	908	640	0	67	750
D2	Nov 2000	2	12.52	1	-4.66	951	683	0	73	28.8
D2	Jan 2002	3	12.44	1.7	-4.67	786	496	0	193	28.8
D5	Jan 2002	4	12.58	1.4	-4.72	676	684	0	145	308
D6 (1)	May 2000	5	12.46	2.4	-4.42	923	548	0	69.8	299
D6 (1)	Nov 2000	6	12.16	1	-4.58	497	294	0	66.3	208
D6 (2)	May 2000	7	12.47	2.1	-4.46	904	548	0	69.8	103
D7	May 2000	8	12.46	2.3	-4.49	878	553	0	58.3	368
D7	Nov 2000	9	12.38	2.3	-4.48	872	587	0	66.1	243
D7	Jan 2002	10	12.62	1.5	-4.71	656	750	0	61.1	295
D8	Jan 2002	11	11.79	0.5	-4.53	93	111	0	62.1	264
M1	May 2000	12	12.38	0.9	-4.41	745	437	0	52.2	224
M1	Nov 2000	13	12.30	1.2	-4.58	722	459	0	54.7	301
M19	May 2000	14	8.23	0.9	-4.06	521	0	188	80.6	1248
M19	Nov 2004	15	7.73	0.6	-4.50	581	0	259	71.9	1280
M19	Jan 2002	16	7.36	0.5	-3.95	463	0	79	145	997
M19N	Jan 2002	17	11.50	0.4	-3.94	363	57	0	279	1000
M20	Nov 2000	18	7.88	0.6	-4.29	173	0	27	130	656
M20	Jan 2002	19	9.26	0.5	-4.00	155	0	77	116	435
M21	May 2000	20	11.90	0.8	-4.62	273	138	0	74.5	108
M21	Nov 2000	21	7.95	0.5	-4.65	126	0	149	77.3	272
M21	Jan 2002	22	8.75	0.6	-4.57	88	0	79	63.6	158
M22	May 2000	23	12.32	1.4	-4.61	702	435	0	51.6	171
M22	Nov 2000	24	12.22	0.5	-4.71	582	392	0	55.1	296
M22	Jan 2002	25	12.27	1.6	-4.94	672	335	0	106	575
Kreiba	Jan 2002	26	7.03	1.6	-5.12	82	0	278	33.7	15.4
Aqraba	May 2000	27	8.16	3.2	-4.91	90	0	234	79	34
Ein Turab	May 2000	28	8.05	1.1	-5.12	60	0	159	23	7
Aqraba	Jan 2002	29	7.15	3.2	-5.57	51.20	0	249.49	74.20	74.88
Ein Turab	Jan 2002	30	7.42	1.1	-4.85	41.20	0	157.99	26.98	37.92
Khreiba	May 2000	31	8.18	1.6	-5.09	97	0	240	28	12
Quelba	May 2000	32	8.03	0	-5.02	69	0	187	23	9
Quelba	Jan 2002	33	7.20	0	-4.67	21.00	0	211.06	26.98	15.36

Figure 3.16 PCA analysis showing the clear distinction between the neutral pH of the karst spring groundwaters, and the Adit A-6 low and high pH groundwaters. For sample identification, see Figure 3.15.

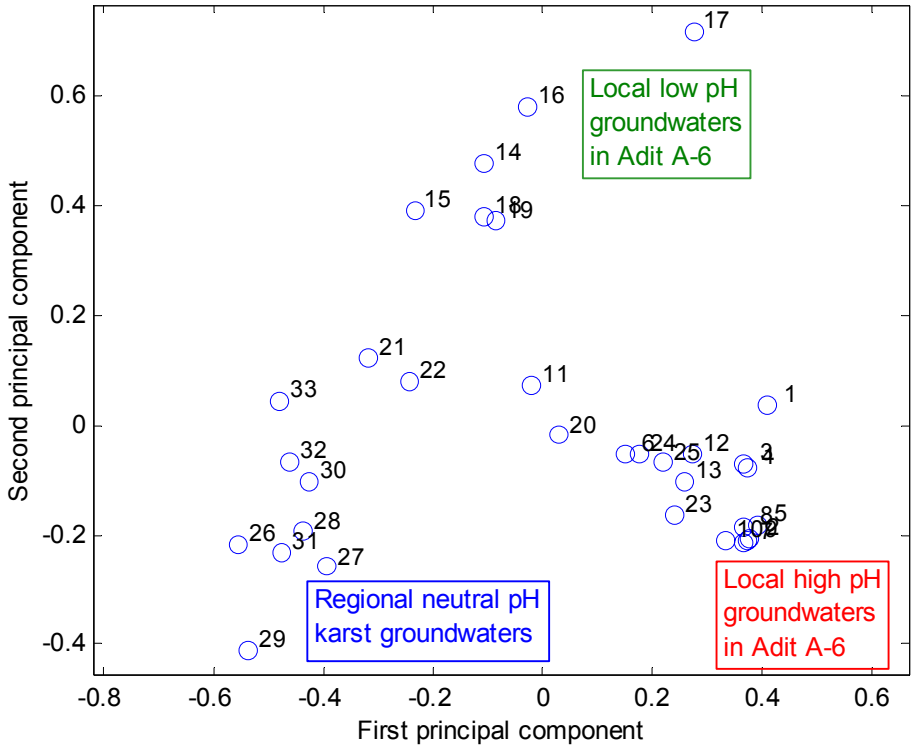

The PCA supports the observations, discussed above, in that several distinct water types are contributing to discharge in Adit A-6. The M3 program weighs each of the different geochemical parameters in the two principal components to highlight differences between sample types. The spatial presentation of the PCA analysis allows trends to be observed between the mixing end members. The following points can be summarised:

- The most distinguishing parameter for the M19 samples is their high Ca-SO_4 content, which separates them from the carbonate springs. The source of this component could be the overlying $B_{4/5}$ Chalky Limestone Formation, or from residual sulphate from ACZ material leached of portlandite which may be found along the southern boundary of this zone. Isotope analysis of the SO_4 component will be required to distinguish the source of this component.
- The borehole samples D2 to D8 are most representative of the high-pH leachate from the ACZ, and must represent the high pH end-member. Sulphate in these waters is elevated and variable, but does not reach the levels observed in the M19 waters. The clustering of these data points suggests that most samples are not mixed with other water types. However, D6 and D8 do show mixing with a groundwater that is also mixing with M19, probably the neutral pH fast-recharging water.
- The two neutral pH samples for M20 (sample site with highly variable pH) plot close to the M19 range, indicating that this discharge is a mixture between the Ca-SO_4 water and the high-pH seepage.
- M21, a sample site also with highly variable pH, is clearly mixing between the high pH Ca-OH water from the ACZ, and a neutral pH water which is mixing with in the M19 system. This neutral pH water is close to the carbonate-springs water type,

and it can be proposed that this is the rapidly circulating water observed in M19 (December 2000 – not included in the PCA due to missing parameters).

- The carbonate spring samples, found within the region of Maqarin, do not appear to be involved in the mixing scenarios for the Adit A-6 samples. A closer evaluation of their hydrogeological setting may support this interpretation.

3.4.6 Summary

The Adit A-6 inflows vary from hyperalkaline, $Ca(OH)_2$ solutions, discharging from the north to central ACZ (M22 and borehole sites), to neutral-pH solutions discharging from the southern margin of the ACZ (M19). Intermediate sites (M21 and M22) show marked seasonal variations in pH.

Integration of geochemical and isotopic data shows clear mixing trends in the Adit A-6 groundwaters. Mixing occurs between a hyperalkaline, $Ca(OH)_2$ seepage that dominates discharge in the northern end of the ACZ. A second mixing component is a neutral pH $Ca\text{-}SO_4$ groundwater derived by direct infiltration through, and equilibrating with, the overlying $B_{4/5}$ limestone and basalt. This component is observed in all roof seepages, increasing in relative importance from M22 towards the south at M19. A third mixing component is a rapid to flash infiltration, low-pH groundwater that is highly seasonal and is likely derived from rapid runoff in the overlying catchment and infiltrating to the Adit through open fissures. This component shows no evidence for rock interaction through weathering reactions.

M19 shows strong seasonal variations in pH that indicate a two-component flow system. This includes a rock-equilibrated, base-flow water with elevated pH that carries a seasonally variable, rapidly infiltrated water with low pH. The same pattern is observed in the regional municipal water supply springs, and is typical of groundwater flow in karstic limestone[12].

- The rock-equilibrated, base-flow component has a $Ca\text{-}SO_4$ geochemical facies from gypsum dissolution, possibly from the $B_{4/5.}$
- The base-flow component carries elevated K, indicating leaching from the overlying basalts.
- No $Ca(OH)_2$ component from the ACZ is observed.
- The seasonal flux of low-pH, direct infiltration is commonly observed in karst environments and here is a regional event also observed in the municipal water supply springs and is very dynamic, with rapid response time.
- The low-pH component carries elevated Na-Cl, probably derived from surface deposition of marine aerosols.
- Tritium is not detected in either the base flow or rapid-infiltrating component. Tritium in modern precipitation in this region has returned to low natural levels.
- $\delta^{18}O$ and $\delta^{2}H$ show a degree of evaporation in the recharge waters not observed in the $Ca(OH)_2$ waters.

M22 and the 'D' series sites are dominated by $Ca(OH)_2$ discharge with high pH.

- Only minor variation in pH is observed.
- A minor and variable $Ca\text{-}SO_4$ component is present in M22, and at even lower concentration in the 'D' borehole sites.

[12] In most karst river waters, solution often tends to be concentrated beneath valley floors (e.g. the cross-sections beneath the Tennessee River, discovered when dam foundations were excavated). It is therefore reasonable to suppose that the pre-basalt palaeoriver, flowing E to W across the Adh Dhlla bench, had similar solutional effects on the calcareous strata beneath i.e. above the Adit.

- There is no evidence for a component of the rapid infiltration observed in M19.
- Stable isotopes do not show the evaporation effect observed in M19, nor the hydroxide-exchange effect observed in the NaOH/KOH Western Springs.
- The low tritium contents consistently found in these discharges are remnants from thermonuclear tests and constrain ages to a few decades. Modern recharge in the region now has tritium levels close to the level of detection.

M20 and M21 are intermediary sites with strong seasonal variations in pH that show mixing between the high-pH seepage of the 'D' boreholes, the neutral-pH Ca-SO_4 base flow of M19 and the low-pH rapid infiltration of M19.

- The pH is highest in the late winter samples of 2000 and 2001 and lowest in the wet period of November 2001, indicating response to infiltration of neutral pH water.
- M20 contains a greater component of the Ca-SO_4 groundwater observed in M19 than does M21, and has a closer association with M19 according to PCA results.
- M21, situated closer to the M22 and the 'D' sites, shows a greater degree of mixing with these $Ca(OH)_2$ waters.

The regional municipal water-supply springs, while important to show the geochemical and isotopic character of regional precipitation and groundwaters, show no association with the inflows in Adit A-6.

- The regional springs show a two-component flow, including a rock-equilibrated component with neutral to elevated (8) pH and a flash-infiltration component with low (<7) pH.
- These springs show no geochemical association with the Adit A-6 infiltration, lacking in particular the Ca-SO_4 component, and with lower Na-Cl facies.
- Stable isotopes show no indication of evaporation, and their relative depletion in ^{18}O suggests a higher elevation of recharge for at least the Aqraba and Kreiba springs.

3.5 Water-Rock Interaction

The original intention within the Phase IV hydrogeochemistry programme was to conclude with geochemical modelling of the important water-rock reactions on the site scale, to complement similar modelling approaches carried out on a regional scale and reported in the Phase III studies (Chapter 4 in Smellie, 1998). Unfortunately, this has not been possible because of resource and time constraints. On the positive side, the mineralogical input from fracture-filling and host-rock investigations has been a major accomplishment of the Maqarin natural analogue project and details of this are outlined below in section 3.5.1. In section 3.5.2, these mineralogical data have been used to help explain the chemical differences between groundwaters from the Eastern and Western Springs.

3.5.1 Mineralogy of the Maqarin site

The mineralogy and petrology of the Maqarin site is described in detail in Chapter 4. Pyrometamorphism of the clay biomicrite of the Bituminous Marl Formation has produced a complex assemblage of high-temperature minerals, many of which are reactive with water and bicarbonate/carbon dioxide. Consequently, hydration and carbonation reaction associated low-temperature alteration by groundwater, has resulted in the formation of an equally complex assemblage of secondary crystalline and amorphous phases. The primary metamorphic and secondary minerals, identified from the Maqarin site during Phases I-IV, are summarised in Table 3.9. The wide variety of secondary minerals found

as alteration products of the ACZ and precipitated as fracture fillings from hyperalkaline groundwaters in the ACZ and parent rock are summarised in Table 3.10. These two tables indicate the relative importance of these minerals in terms of their qualitative abundance. A more detailed discussion of the sources and sinks for chemical components in the Maqarin groundwaters is provided in Chapter 4 and Milodowski et al. (1992a, 1992b; 1998a, 1998b). The principal features of rock-water interaction, that may explain the differences in chemistry between the Eastern and Western Springs, are summarised below.

Table 3.9: Primary metamorphic minerals from the Marble Zone, Maqarin site.

Mineralogy	**General Formulae**	**Abundance**
Carbonates		
Calcite	$CaCO_3$	MAJOR
U-Ca-oxycarbonate?	Ca:U = 2:1	TRACE
Simple Oxides		
Lime	CaO	MINOR to TRACE
Periclase*	MgO	TRACE
Haematite or ferric oxide	α-Fe_2O_3	MINOR to TRACE
Magnetite (?)	Fe_3O_4	MINOR to TRACE
Maghemite (?)	γ-Fe_2O_3	
Ferrites, Aluminates And Mixed Oxides		
Ca-aluminate	Undefined	MINOR
Calcium ferrite,	$CaFe_2O_3$	MINOR
Brownmillerite	$Ca_2(Al,Fe)_2O_5$	MINOR
Multiple element ferrites	$(Ca,Ba,Cr,Al,Ti,Mg,Zn,Mn)Fe_2O_3$ Undefined	TRACE
Apatite Group		
Fluorapatite	$Ca_{10}(PO_4)_6F_2$	MAJOR
Francolite	$Ca_{10-x-y}(Na,K)_xMg_x(PO_4)_{6-z}(CO_3)_zF_{0.4z}F_2$	MAJOR
Ellestadite	$Ca_{10}(SiO_4)_3(SO_4)_3O_{24}(Cl,OH,F)_2$	MAJOR
Silicates		
Larnite	β-Ca_2SiO_4	MAJOR
Wollastonite	$CaSiO_3$	MINOR
Anorthtite	$CaAl_2Si_2O_8$	MINOR
Rankinite (?)*	$Ca_3Si_2O_7$ (significant Zn substitution for Ca)	TRACE
Diopside-hedenbergite	$Ca(Al,Fe)Si_2O_6$	MINOR
Complex Silicates And Silicates With Other Oxyanions		
Spurrite	$Ca_5(SiO_4)_2(CO_3)$	MAJOR
Parraspurrite	$Ca_5(SiO_4)_2(CO_3)$	MAJOR
Calcium silicate (unknown mineral)*	$Ca_5(SiO_4)_2(SO_4)$	MAJOR
Ba-Ca-sulphate-silicate	Undefined	TRACE
Ba-Ca-Zr-Mo-silicate	Undefined	TRACE
Elements		
Graphite	C	MINOR to TRACE
Sulphides And Selenides		
Oldhamite	CaS to $CaS_{0.9}Se_{0.1}$	TRACE
Cu-K-Na-Selenide	$Cu_{10.2}K_3Na_{0.2}Se_{7.7}S_{2..3}$ (approx.)	TRACE
Krutaite*	$CuSe_2$	TRACE

Note: *denotes new species discovered during Phase IV

Table 3.10: Secondary minerals from the Marble Zone, Maqarin site.

Mineralogy	General Formulae	Abundance
Carbonates		
Calcite	$CaCO_3$	MAJOR
Aragonite	$CaCO_3$	MINOR to TRACE
Vaterite	$CaCO_3$	MINOR to TRACE
Strontianite	$SrCO_3$	MINOR to TRACE
Ankerite	$Ca(Mg,Fe)(CO_3)_2$	TRACE
Kutnahorite	$Ca_{0.75}(Mn,Mg)_{0.25}(CO_3)_2$	TRACE
Complex Carbonates		
Hydrotalcite	$MgAl_2(CO_3)(OH)_{16}.4H_2O$	MINOR to TRACE
Simple Oxides		
Haematite or ferric oxide	α-Fe_2O_3	MINOR to TRACE
Maghemite (?)	γ-Fe_2O_3	MINOR to TRACE
Simple Hydroxides		
Brucite	$Mg(OH)_2$	MINOR to TRACE
Portlandite	$Ca(OH)_2$	MAJOR
Gibbsite	α-$AlOH_3$	MINOR to TRACE
Goethite	α-FeO.OH	MINOR to TRACE
Iron oxyhydroxide	undifferentiated	MINOR to TRACE
Sulphates		
Gypsum	$CaSO_4.2H_2O$	MAJOR
Bassanite	$CaSO_4.0.52H_2O$	?
Anhydrite	$CaSO_4$	MINOR to TRACE
Barite	$BaSO_4$	TRACE
Celestite (celestine) [3]	$SrSO_4$ [3]	TRACE
Barytocelestite	$(Ba,Sr)SO_4$	TRACE
Calcian barytocelestite	$(Ba,Ca,Sr)SO_4$	TRACE
Hashemite	$BaCrO_4$ to $BaSO_4$ [complete solid-solution]	TRACE
Cd-sulphate	undefined	TRACE
Pb-sulphate	undefined	TRACE
Cu,Zn-sulphate	undefined	TRACE
Complex Sulphates		
Ettringite [1]	$Ca_6Al_2(SO_4)_3(OH)_{12}.25H_2O$ [1]	MAJOR
Thaumasite [1]	$Ca_6Si_2(SO_4)(CO_3)_2(OH)_{12}.24H_2O$ [1]	MAJOR
Jourovskite	$Ca_3Mn(CO_3)(SO_4)(OH)_6.12H_20$	TRACE
Silica Minerals		
Quartz	SiO_2	MINOR
Opal-CT	SiO_2	?
Opal-A	$SiO_2.nH_2O$	?
Apatite-Group		
Hydroxyapatite	$Ca_{10}(PO_4)_6(OH)_2$	MAJOR to MINOR
Fluorapatite	$Ca_{10}(PO_4)_6F_2$	MAJOR to MINOR
Francolite	$Ca_{10-x-y}(Na,K)xMg_y(PO_4)_{6-z}(CO_3)_z(OH)_2F_{0.4z}F_2$	MAJOR to MINOR
Ellestadite	$Ca_{10}(SiO_4)_3(PO_4)_3O_{24}(Cl, F, OH)_2$	MAJOR to MINOR
Fluorellestadite [3]	$Ca_{10}(SiO_4)_3(PO_4)_3O_{24}(F)_2$ [3]	MAJOR to MINOR
CSH and Cash Phases		
Afwillite	$Ca_3Si_2O_4(OH)_6$	MAJOR to TRACE
Tobermorite(s) [2]	$Ca_5Si_6O_{16}(OH)_2.2\text{-}8H_2O$ [2]	MAJOR
Jennite	$Ca_9H_2Si_6O_{18}(OH)_8.6H_2O$	MAJOR
Birunite	$Ca_{15}(CO_3)_{5.5}(SiO_3)_{8.5}SO_4.15H_2O$	MINOR to TRACE

CSH(I) hydrogel [4]	amorphous Ca:Si = 0.8-1.5 [4]	MAJOR
CSH(II) hydrogel [4]	amorphous Ca:Si = 1.5–2 [4]	MAJOR
CSH hydrogel [4]	amorphous, undefined/variable Ca:Si = <0.8 [4]	MAJOR
Tacharanite [5]	$Ca_{12}Al_2Si_{18}O_{15}(OH)_2.3H_2O$ [5]	MAJOR
CASH hydrogels	variable compositions between tacharanite and zeolite compositions	MAJOR
Zeolite Group [7]		
Mordenite	$CaNa_2K_2Al_2Si_{10}O_{24}.7H_20$	MAJOR to TRACE
Dachiardite	$(CaNa_2K_2)_5Al_{10}Si_{38}O_{96}.25H_20$	MAJOR to TRACE
Henlandite	$(CaNa_2)Al_2Si_7O_{18}.6H_20$	MAJOR to TRACE
Epistilbite [7]	$Ca_3Al_6Si_{18}O_{48}.16H_20$	MAJOR to TRACE
Yugarawaralite	$Ca_2Al_4Si_{12}O_{32}.8H_20$	MAJOR to TRACE
Laumontite	$Ca_4Al_8Si_{16}O_{49}.16H_20$	MAJOR to TRACE
Wairakite	$Ca_4Al_{16}Si_{32}O_{96}.16H_20$	MAJOR to TRACE
Leonhardite	$Ca_4(Al_8Si_{16}O_{48}).14H_20$	MAJOR to TRACE
Clay Minerals		
Volkonskoite.	Cr-substituted smectite	MINOR to TRACE
Other Phases		
Apophyllite [6]	$KCa_4Si_8O_{20}(OH,F).8H_2O$ [6]	MAJOR to TRACE
U-Ca-silicate	unidentified and undefined	TRACE
Ca-Cr-silicate hydrogel	unidentified and undefined	TRACE

Notes:

[1] A complex solid-solution is observed between ettringite and thaumasite mineralization;

[2] Tobermorites of variable hydration states are present (including 14 Å tobermorite (sometimes formerly referred to as 'plombierite') with 8 H_2O; 11Å tobermorite with 4 H_2O; 9 Å tobermorite with 2 H_2O)

[3] New species found during Phase IV

[4] CSH hydrogels from Maqarin can host significant Al content.

[5] Includes non-crystalline CASH hydrogels with similar composition to tacharanite

[6] Apophyllite analyses from Maqarin are significant deficiency in K^+ site occupancy (up to 25 %) compared to ideal apophyllite stoichiometry, indicating probable major lattice substitution of K^+ by NH_4^+.

7 'Zeolites' at Maqarin are tentatively inferred on the basis of micochemical composition (EPMA, EDXA and ATEM). Most appear to be amorphous CASH 'hydrogels' of zeolitic composition and only epistilbite has been confirmed by XRD as a crystalline zeoloite

3.5.2 Mineralogy and its relevance to understanding hydrochemical processes at Maqarin

One of the most important aspects of the Maqarin groundwaters, as an analogue for studying the potential evolution and interactions of cement porewater in a radioactive waste repository, is an understanding of the origin of the high K^+ and Na^+ concentrations in the Western Springs, compared to the Eastern Springs. Do the Western Springs represent an analogue of the 'early' hyperalkaline cement pore fluid (i.e. with NaOH/KOH dominated leachates of pH>13). In comparison, do the Eastern Springs represent a more evolved, 'later' cement-pore fluid (i.e. much lower NaOH/KOH, $Ca(OH)_2$ buffered with pH around 12.5)?

The only primary metamorphic phase in the ACZ previously identified, in which K and Na are significant constituents, was a previously unknown copper-potassium-sodium-sulphoselenide mineral ($Cu_{10.2}K_3Na_{0.2}Se_{7.7}S_{2.3}$) occurring in close association with oldhamite (CaS) (Milodowski et al., 1992a, 1992b). Oldhamite is the more common and was also observed to contain minor K^+ in solid-solution. However, both of these minerals only occur as rare grains up to 10 μm in diameter, with an abundance in thin section that is typically less than 2.5 grains cm^{-3} (i.e. equivalent to a concentration of less than about

50 ppm). Consequently, the dissolution of these two trace minerals is unlikely to be able to account for the high concentrations of K^+ and Na^+ in the Western Springs groundwaters. The Phase IV study identified a new calcium sulphosilicate phase ($Ca_5(SiO_2)_2SO_4$), containing between 0.3-3.3 wt.% K_2O and up to 0.3 wt.% Na_2O in solid-solution, as part of the primary metamorphic assemblage of the ACZ. This mineral was unrecognised in earlier studies, or was misrepresented as spurrite or paraspurrite. It is a major component of some spurrite-brownmillerite-rich marbles, forming over 30 % of the rock volume. As such, it represents a major potential source of K^+ and Na^+ encountered in the groundwaters.

Detailed petrographical analysis (cf. Chapter 4) reveals that oldhamite and copper-potassium-sodium-sulphoselenide are highly reactive with water and, along with lime (CaO), are the first phases dissolved in the earliest stages of hydration of the ACZ. The newly discovered potassic $Ca_5(SiO_2)_2SO_4$ also appears to be a very reactive phase, possibly similar in reactivity to larnite. It is readily replaced by thaumasite at a relatively early stage in the groundwater leaching sequence. Along with oldhamite and potassium-sodium-sulphoselenide, potassic $Ca_5(SiO_2)_2SO_4$ is now only preserved in relicts of unhydrated or partially hydrated ACZ in samples examined from Adit A-6 and boreholes in the Eastern Springs area. In contrast, the other major metamorphic calcium silicate minerals such as spurrite, paraspurrite and ellestadite alter more slowly. They are replaced at a later stage in the leaching sequence by thaumasite, ettringite, CSH, calcium carbonates and other secondary products. SEM-EDXA and EPMA microchemical observations clearly demonstrate that potassium and sodium are not incorporated into the thaumasite replacing potassic $Ca_5(SiO_2)_2SO_4$. These elements must, therefore, be removed in solution by the groundwater leaching during the hydration process.

The formation of apophyllite ($KCa_4Si_8O_{20}(OH,F).8H_2O$), as one the earliest fracture filling and matrix secondary minerals in marbles from the Adit A-6 area, also provides evidence that high-K groundwaters were produced during the early stages of retrograde alteration of the ADZ in the Eastern Springs area. The apophyllite is notably deficient in potassium – EDXA, indicating that up to 25 % of the K^+ sites are occupied by an undetected ionic species. The most obvious candidate species that would account for this is NH_4^+, since: it has a similar ionic size and charge to K^+; neither nitrogen nor hydrogen are detected by EDXA; and it is known that significant amounts of NH_4^+ can substitute for K^+ in apophyllite and other potassium silicate minerals such as potassic feldspars, micas and illite (e.g. Marriner et al., 1991). This implies that high concentrations of NH_4^+, as well as K^+, should also be anticipated in the groundwaters during the early stages of leaching and hydration of the ACZ(s). Thermal (evolved gas) analysis carried out during Phase II showed that large amounts of ammonia (comparable to at least 0.5 % by volume of CO_2 produced and about 10 % by volume of SO_2 produced) can be liberated by incomplete combustion of organic matter during heating of the parent rock to between 300-600°C (Milodowski et al., 1998a). Therefore, it is feasible that ammonia could potentially have been evolved during pyrometamorphism of the Bituminous Marl Formation. It is then incorporated into potassium-bearing minerals as NH_4^+ or forms soluble ammonium salts, such as $(NH_4)_2SO_4$, by condensation with SO_2/SO_3 also produced during combustion. These phases would represent a potentially important source of NH_4^+ present with K^+ in mineralising groundwaters, during early stages of retrograde hydration of the metamorphic rocks of the ACZ.

The major differences in hydrochemistry between the Western Springs and Eastern Springs can now be readily explained by the mineralogical observations described above. The correspondence of high concentration of K^+, Na^+ and SO_4^{2-} in the

groundwaters in the Western Springs can best be explained as representing groundwater discharging from a part of the ACZ that is undergoing the early stages of hydration. The mineralogical observations show that high K^+, Na^+ and SO_4^{2-} concentrations should be produced during early hydration of the ACZ containing very reactive potassium-rich $Ca_5(SiO_2)_2SO_4$ as a major metamorphic mineral. Other primary metamorphic phases, such as spurrite, paraspurrite and ellestadite hydrate, react more slowly and their alteration is important in the later stages of the alteration sequence. However, these phases also contain very little K^+, Na^+ and much lower SO_4^2. Consequently, the concentrations of these elements would be expected to be much lower in groundwaters during the later stages of hydration. Therefore, the much lower concentration of K^+, Na^+ and SO_4^2, observed in the Eastern Springs, is consistent with later-stage leaching of (the remaining) less reactive calcsilicate minerals in the ACZ. The presence of much higher concentrations of Se and Re in the Western Springs groundwaters is also consistent with this model. Detailed petrographic studies (cf. Chapter 4) show that Se and Re are both hosted within traces of oldhamite, copper-potassium-sodium-sulphoselenide and krutaite, which also rapidly dissolve during early hydration. Although the abundance of these phases is too low to account realistically for major K^+ and Na^+ in the Western Springs groundwaters, they are probably important sources of trace elements, such as Se and Re. The close correspondence of high K^+, Na^+ and SO_4^{2-} with high concentration Se and Re, in the Western Springs, is also consistent with the simultaneous leaching of major potassium-rich $Ca_5(SiO_2)_2SO_4$ and the trace minerals oldhamite, copper-potassium-sodium-sulphoselenide and krutaite ($CuSe_2$).

The higher pH of the Western Springs can also be explained by the dissolution of lime and probably also portlandite, accompanying the alteration of potassium-rich $Ca_5(SiO_2)_2SO_4$ and sulphoselenides. This occurs during the earliest stages of the retrograde hydration of the metamorphic rocks. As these early-reacting minerals become depleted during the later stages of alteration, the pH will become progressively more buffered by the slower hydration of larnite, spurrite/parraspurrite and other calcsilicates, and by the dissociation of CSH alteration products. These phases, which react later in the alteration sequence, dominate the extensively altered marbles wherever they have been observed in the Eastern Springs area.

The high Cr in the Maqarin groundwaters can be explained by the dissolution of minor calcium aluminate, brownmillerite and calcium ferrites. These primary metamorphic phases contain significant Cr (up to 2 wt% Cr_2O_3 in some brownmillerite grains). Calcium aluminate, brownmillerite and calcium ferrites are less reactive than the primary metamorphic potassium-rich $Ca_5(SiO_2)_2SO_4$ and trace sulphoselenides. They appear to react during the mid-stages of the retrograde hydration and alteration sequence. However, since they are only relatively minor components, they would be expected to become exhausted (as sources of Cr and other transition metals) more rapidly than the more abundant slower-reacting major calcium silicates and silicophosphates as hydration progressed. Thus, the much higher Cr content that is observed in the Western Springs, compared to that of the Eastern Springs, is consistent with the groundwaters of the Western Springs representing leaching of the metamorphic zone at an earlier stage in the alteration process, before depletion of the primary Cr-rich metamorphic minerals. In contrast, the Eastern Springs groundwaters can be interpreted as discharging from more extensively altered metamorphic rocks, from which the Cr-rich primary minerals have already been extensively leached.

Finally, in agreement with the hydrochemical modelling carried out in Phase III, it is no longer necessary to consider contamination from sewage, or the application of fertiliser in arable fields area above the site, in explaining the enhanced concentration of NH_4^+ (and

K^+) in the Western Springs groundwaters. These possibilities had been considered in previous studies (cf. Alexander, 1992; Linklater, 1998; Smellie, 1998). The mineralogical considerations outlined above, and in Chapter 4, show that NH_4^+ can be inferred to be present in early-stage groundwater hydration of the ACZ. This is suggested by the formation of probable ammonium-bearing apophyllite as an early secondary phase. In addition, mineralogical studies also show that abundant ammonium can potentially be produced during pyrometamorphism. This may condense as soluble salts (e.g. $(NH_4)_2SO_4$) or be incorporated into the potassium-bearing metamorphic minerals. Any such NH_4^+-bearing phases would be very soluble and would, therefore, be leached (along with K^+) during early hydration and ACZ leaching.

In summary, careful consideration of the mineralogical evidence of rock-water interaction, and of the paragenesis of the alteration sequences observed at Maqarin, now provides strong evidence. This demonstrates that the hydrochemistry of the Western Springs (with higher pH and high concentrations of K^+, Na^+, SO_4^{2-}, Cr, Se, Re and other trace elements) reflects the early stages of leaching of the ACZ. In contrast the Eastern Springs (with lower pH and markedly lower concentrations of these species) reflect discharge from a more evolved system, in which the ACZ has been more extensively leached.

However, detailed examination of the site makes it clear that the ACZ of the Eastern Springs is not being leached as one, homogeneous body, but rather as small, fracture-isolated pods of the main body (see Figure 1.10, for example). Thus, the current hydrochemistry is typical of the group of pods currently being leached[13]. To examine the leaching process further, an investigation of the accessibility of the ACZ cement material along the lines of that described in Appendix 3.3 for the Bituminous Marl parent rock, would be necessary. Here, a profile is taken across a fracture and into the matrix and a few samples have been analysed for the natural-decay series distribution (in the whole rock), to sketch the accessibility of the matrix to groundwater reaction. A similar pilot study was previously carried out on ACZ samples and indicated very poor accessibility to the ACZ matrix (Hyslop, 1998), although the measured matrix diffusivities of $10^{-11}m^{-2}s^{-1}$ (Stone, 1998) are not unusually low. In both studies, the authors stressed the preliminary nature of the work. Clearly, a more focused study on the ACZ matrix accessibility would be needed before any further comment might be made on cement leachability.

A clearer appraisal is also required of the analogy between the accessibility/leaching behaviour of the ACZ material and the various industrial cements/concretes foreseen for use in a repository. This information could also be dovetailed with the data on the Maqarin site tectonics (Smellie, 1998, and Chapter 2), to provide a detailed analogy of the likely long-term behaviour of a cementitious repository in a tectonically active host rock.

3.6 Integrated Understanding

Understanding the hydrochemical evolution of the groundwaters collected in Adit A-6 depends on the local structural geology and its hydraulic response to seasonal infiltration variations in recharge. The residence (reaction) times of these recharging infiltrating waters with the host rocks and the geochemistry of the host rocks are also equally

[13] This has also been observed at most of the sites examined, including Daba, Khushaym Matruk and Sweileh.

important. There is now sufficient information to develop a conceptual model for Adit A-6 at the Eastern springs site in Maqarin.

Figure 3.3 schematically illustrates the location of the 776 m-long Adit A-6 in the Bituminous Marl Formation (B_3). This formation is succeeded by the overlying Chalky Limestone Formation ($B_{4/5}$) and finally the Quaternary basalt flows. A thin soil horizon covers the basalt surface, immediately above Adit A-6.

The topography overlying Adit A-6 is flat and the thin soil cover is intensively fissured, with some cracks as wide as 20 cm and penetrating to a few metres depth. The cracks form meshes 0.70 to 2.00 m apart and may reflect the presence of karst cavities and openings in the underlying $B_{4/5}$ unit. These karstic features may have resulted from the spontaneous combustion and the associated reduction of volume of the B_3 and partly $B_{4/5}$ units. Alternatively, such shrink-swell phenomena are typical of many semi-arid soils, regardless of the substate. Larger fissures, in this location, are probably due simply to pressure-release jointing, following incision of the Yarmouk valley.

The basalt flows are highly permeable from tensional fracturing initiated during rapid cooling of the lava and later tectonic movement. As mentioned, below the basalt the $B_{4/5}$ unit is characterised by karst features, namely an interconnected system of pressure-release jointing (up to several metres in depth). Some cavities contain basalt fragments/boulders which have fallen in from the overlying basalt following dissolution. The presence of basalt boulders at greater depths within the limestone, together with the recording of large drilling water circulation losses, were documented by Harza (1980) during the preliminary drilling investigation phase of the Unity Dam Project.

In fact, some large-scale features were observed in the now exposed[14] slopes in the vicinity of Adit A-6 (see Figures 3.21 and 3.22). Here, the karstic depression is approximately 20-25 metres deep and 20 metres long at its mouth. Below the $B_{4/5}$ unit lies the Bituminous Marl Formation (B_3) (i.e. clay biomicrite) which hosts the Adit A-6. The thickness of B_3 above the ceiling of the Adit is around 20 m at its entrance, (A-6 bottom elevation 100 m asl Figure 3.21), and 7 m at a distance of 80 m inside the Adit. It is then absent between 120 m to 280 m, but then increases gradually to 23 m at the end of the Adit, at about 776 m from the entrance (A-6 bottom, 114 m asl).

[14] Construction of the Unity Dam began in 2004 and a large area around Adit A-6 has been cleared for construction purposes.

Figure 3.21 Exposed Bituminous Marl Formation in the area around Adit A-6 (view looking south from Syria). The entrance to Adit A-6 can be seen at the extreme right, half way up the exposed rock face. Immediately above the Adit is the Chalky Limestone Formation and a lighter, funnel-shaped patch above, and to the left of the Adit entrance is an infilled karstic feature. For scale, note the army guard post in the left foreground and the Adit entrance are both about 2m high. Image courtesy of W.R. Alexander.

Figure 3.22 Close up of the karstic feature near Adit A-6. For scale, note the white hut, extreme right side of middle ground, which is about 2m high. Courtesy of W.R. Alexander.

Figure 3.3 also shows an approximately 250 m length of the Adit within the water table of the B_3 unit. This corresponds to the main area of the ACZ and consequently includes the main inflow points of hyperalkaline fluids into the Adit. Pre-existing fracturing of the rocks has played a major role in facilitating combustion and channelling groundwaters which have subsequently reacted to form the high pH waters. The restriction of combusted biomicrite and associated hyperalkaline waters to the most fractured parts of the Adit coincides with the axis of the regional north-north-east - south-south-west trending Maqarin anticline (see Chapter 2).

In addition, two depressions exist at the top of the B_3 unit at distances of about 200 m east and west from the Adit A-6, and a distance of approximately 200 m south from the entrance of the Adit (Figure 3.2). These act as accumulation zones for recharging waters from higher up in the overlying rock formations, and then as the main discharge sites

downward into Adit A-6 and laterally west-south-west to Wadi Sijin and north-east towards the Eastern Springs.

In summary, the geomorphological, lithological and hydrostructural setting of Adit A-6 facilitates the initial surface/near-surface collection/retention of precipitation waters. Subsequently, it then channels this recharge water through the different rock units, following fracture and joint systems. Finally, it reappears as groundwater seepages (fresh and hyperalkaline types) within a restricted 250 m length of the Adit.

Figure 3-23, focusing on this approximately 250 m length of the Adit, attempts to illustrate that, during recharge conditions, two mechanisms are in operation:

- rapid (fast-track) recharge and filling of the $B_{4/5}$ karst cavities with fresh water, and
- slow-track recharge with only partial filling of the cavities with hyperalkaline waters which have resulted from longer residence (i.e. reaction) times. Seasonal variations would therefore be registered quickly by fast-track filling (and emptying) of the connected karst cavities. This appears as a pulse of fresh water entering the Adit, following significant precipitation. Slow-track recharge might therefore be expected not respond to precipitation, but provide a continuous slow and steady accumulation/release of hyperalkaline water to and from the partly filled cavity reservoirs which eventually seeps into the Adit.

The rapidly, downward-percolating recharge water (fast-track channel or cavity flow) does not seem to have enough time to react fully with the rock matrix. This is especially the case at the peripheries of the recharge mouths, a few tens of metres inside the Adit ,and at around 300 m from the Adit entrance (Fig 3.23). It is important that the fast-track recharge water, coming from the surroundings of the Adit (> 100 m diameter), becomes slow-track recharge. This transition is due to distance, decreasing fracturing, and an increasing horizontal-flow component, instead of vertical flow and unsaturated flow. It contrasts with the saturated flow in the immediate vicinity of the recharge mouths.

Figure 3.23 Fast and slow track recharge in the vicinity of Adit A-6 (cf. also Figure 3.3).

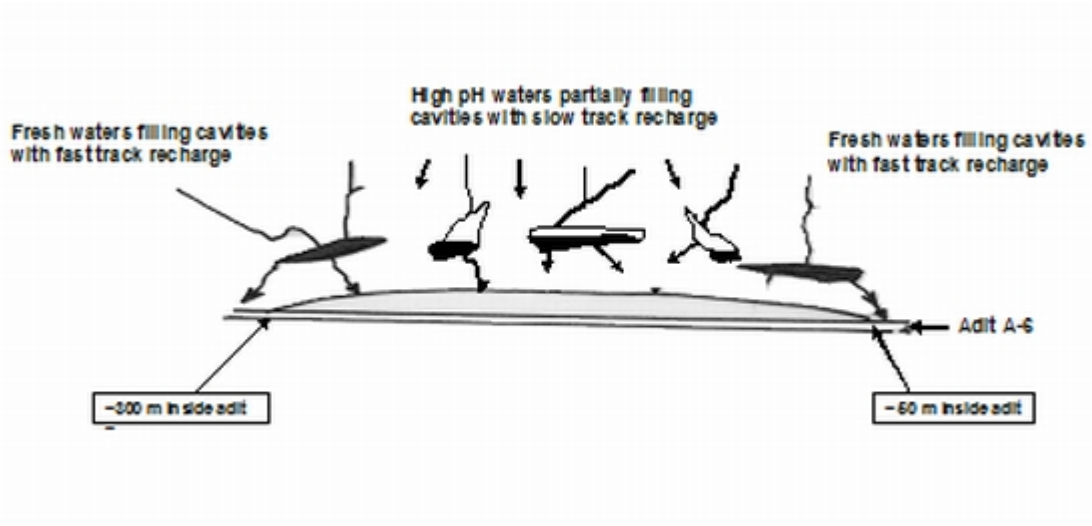

In summary the following points can be emphasised:

- The presence of the topographic depression overlying the seepage area in Adit A-6 facilitates surface runoff water to accumulate and to percolate rapidly downwards along soil cracks. This network of soil cracks, situated at the ground surface above Adit A-6 and its surroundings, overlies karst channels, openings, and fissures (cf. Figures 3.21 and 3.22).

- The surface of the $B_{4/5}$ unit (the bottom of the basalt) forms a topographic depression above Adit A-6, possibly along the axis of the pre-basalt Yarmouk palaeoriver. This means that the downward percolating water through the basalt, which originates from a relatively large catchment area (at least $36x10^4$ m^2, from west, east and south) accumulates at the surface of the $B_{4/5}$ unit overlying Adit A-6.
- The surface of the underlying B_3 unit shows two depressions (recharge mouths) which concentrates the downward percolating water through the $B_{4/5}$ unit. The formation of these recharge mouths, approximately overlying adits A-6 and A-7, depends on the accumulation of run-off water in the topographic depressions in the surface area overlying them.
- The main discharge sites of this perched groundwater body are downward to Adit A-6, where the $B_{4/5}$ unit is exposed, and laterally to the Eastern and Western springs.
- Therefore, once the fast-track recharge water reaches the centres of the recharge mouths, it percolates downwards into Adit A-6.
- At the periphery of the recharge mouths (dry area or temporary wet area to about 300 m inside Adit A-6), the fast-track water enters the Adit forming fresh water seepages. After the depletion of this fresh water, due to seepages and mixing processes, the same location starts discharging hyperalkaline water originating from the slow-track recharge and prolonged water-rock interactions.
- The main conditions involved in the change from fresh to hyperalkaline-water discharge are the ratio of fast-track recharge, compared to the slow-track recharge, and the volume and extent of the stored, perched-groundwater body.
- The amount and intensity of fast- and slow-track recharges differ from one precipitation event to another. Some precipitation events produce no surface or very limited surface run-off, but persistent slow recharge (low-intensity precipitation lasting for days). Others (storm rains) produce pronounced run-off and resultant fast-track recharge, but no slow-track recharge.
- It seems that moderate fast-track recharge does not alter significantly the flow regime in Adit A-6.

This conceptualisation of events, within and surrounding Adit A-6 during seasonal variations in precipitation frequency and volume, can be linked with the main chemical and isotopic signatures derived from long-term chemical monitoring of the seepage waters into the Adit (see Section 3.4). The hydrochemical evaluation emphasised the importance of both reaction and multiple-flow mixing mechanisms to explain the analytical data, which reflect the complex hydraulics and geological history of the Adit A-6 site area. The result is that no discrete end members have been preserved. All seepage water may incorporate some degree of mixing. Nevertheless, there is clear evidence from some seepage waters of relatively fast-track or slow-track recharge conditions. For example, M19 shows marked seasonal variations in pH that indicate a two-component flow system. This includes a rock-equilibrated baseflow with elevated pH, that includes a seasonally variable, rapidly-infiltrated (fast-track) water with near-neutral pH. The same pattern is observed in the regional carbonate springs, and is typical of groundwater flow in karstic limestone.

In contrast, other seepages have remained virtually unaffected, maintaining a stable, slow-track baseflow recharge of hyperalkaline waters (i.e. D2-D8). Other samples have more marked mixing components; for example M20 and M21 are intermediary sites with pronounced seasonal variations in pH. These show mixing between the hyperalkaline seepage of the ‘D’ drillholes, the neutral pH Ca-SO_4 baseflow of M19, and the low-pH, fast-track infiltration of M19.

Tritium, ^{18}O and ^{2}H data also support the slow-track infiltration model (e.g. some ‘old’ measured tritium present, and no ^{2}H depletion is indicated, which may suggest evaporation). In contrast, rapid, fast-track infiltration waters show below-detection tritium (reflecting present-day absence of atmospheric tritium) and some deuterium depletion, perhaps suggesting surface-evaporation effects prior to infiltration. This contrast between “fast-track” and “slow-track” flow is generally known by karst specialists as ‘conduit flow’ and ‘seepage flow’.

Chapter 4

The Analogue Cement Zone (ACZ)

A.E. Milodowski, L. Trotignon, H. Khoury, E. Salameh, N. Arnal, P. Bienvenu, C. Bulle, S.R. Chenery, N. Crouzet, L. Fontanini, E.S. Hodgkinson, U. Mäder, J. McKervey, H. Peycelon, S. Pontremol, F. Rassineux, J. Raynal, J. Rose and D. Vandamme

4.1 Introduction

4.1.1 General

In the Maqarin area, unusual zones of marble occur as discontinuous 'lenses' and 'pods', hosted within the organic-rich cherty, phosphatic limestone and clay-biomicrite beds of Upper Cretaceous-Lower Paleocene age. The marbles belong to the sanadinite and pyroxene hornfels facies of high-temperature and low-pressure thermal metamorphism, and are associated with in situ spontaneous combustion of the organic-rich sedimentary strata. The metamorphic rocks are mainly exposed on the south bank of the Yarmouk river[15] and occur in an unusual brecciated unit, which can be traced from Wadi Sijin eastward to the Unity dam and then to about 1,900 m towards Wadi Shallala to the southeast. The marbles are highly fractured, and groundwater circulating through these rocks interacts with the high-temperature minerals to produce localised hyperalkaline Ca(±Na,K)-OH-SO_4-type groundwater (pH >12.5) systems.

Secondary mineralisation formed during the retrograde hydration and alteration of the marbles is very common, filling voids, fissures, fractures and joints. The rocks are highly heterogeneous in texture, colour and composition and have been investigated previously by Khoury and Nassir (1982) and Milodowski et al. (1992a, 1992b; 1998a, 1998b).

4.1.2 Background and objectives of the Phase IV studies

The primary mineralogy and subsequent low-temperature alteration of the pyrometamorphic marbles constituting the ACZ were originally examined during the Phase I studies of the Maqarin Natural Analogue Site. The objectives during Phase I were to define the degree of the cement analogy – i.e. just how close were the natural cements (and their groundwaters) to industrial cements (and their leachates)? In addition, the sources and sinks of radionuclide analogue elements in the primary and secondary cement phases were examined. These observations were compared with thermodynamic model predictions of solubility-governing phases, in order to test and validate model codes and thermodynamic databases being developed for repository performance assessment (Alexander, 1992). Although the nature of the secondary alteration products was examined, the paragenesis of alteration was not evaluated in any detail. A small

[15] Limited outcrop exists on the north bank, directly across the river from Maqarin Station but, due to the massive nature of the ACZ here, no hyperalkaline waters have been observed (W.R.Alexander, pers comm, 1998).

amount of additional work was carried out in Phases II and III on the hydration and carbonation of the marbles (Linklater, 1998; Smellie, 1998), but further data were required to constrain the paragenesis of the hydration products and to understand fully the hydration, alteration and evolution of CSH minerals within the ACZ. This was an important objective to be addressed in the present (Phase IV) study programme (see Chapter 1).

The hyperalkaline porewaters leached during the early stages of cement hydration in a cementitious repository are anticipated to contain high concentrations of NaOH and KOH. Na and K will be progressively leached as cement alteration proceeds. It is predicted that the porewaters will become Ca-OH dominated, with the pH buffered over a longer period of time by portlandite ($Ca(OH)_2$) and calcium silicate hydrate (CSH) mineral solubility. The interaction of Na-K-OH groundwaters may significantly modify the mineralogy and physical properties of the repository host rock, prior to interaction with later $Ca(OH)_2$-dominated porewaters. A key aspect of the natural analogue studies is to understand the origin and behaviour of Na and K in the hyperalkaline groundwaters at Maqarin. Equally, the difference in geochemistry between the 'Na-K-rich' Ca-K-Na-OH-SO_4 hyperalkaline groundwaters of the Western Springs area, and the 'Na-K-poor' Ca-OH-SO_4 groundwaters of the Eastern Springs area, must be explained.

A prime objective of this study was, therefore, to compare the natural Ca-K-Na-OH-SO_4 groundwaters of the Western Springs with early industrial cement leachates, and the Ca-OH-SO_4 groundwaters of the Eastern Springs to more evolved cement leachates (cf. Region 1 and 2 of Berner, 1987, 1990). Some tentative data on the presence of Na-K-rich minerals in the cement zone were provided at the end of Phase I (Milodowski et al., 1992a, 1992b), but this was not followed up. The Phase I studies suggested that K and Na in the hyperalkaline groundwaters may be derived from leaching of trace alkali and alkali-earth sulphide minerals closely associated with oldhamite (CaS_2), which was identified as a trace mineral. These sulphides are known to be highly reactive with water and extremely soluble, and Phase I observations indicated that these are amongst the earliest phases to dissolve or react in the ACZ. However, these minerals are only trace components of the primary metamorphic assemblage. In studying the leaching of K and Na from the cement zone, the mineralogical distribution and budget of these elements must be understood more fully. Equally, the relative paragenesis of alteration processes, affecting the primary sources of K and Na in the cement zone metamorphic rocks, requires clarification. The crucial question is not just simply the identification of the Na-K phases, but rather the determination of their physical position in the cement and their reactivity. Only then can their analogue 'value' be properly assessed.

Many trace elements have been examined at the Maqarin sites throughout Phases I-III, mainly as analogues for radionuclides in a cementitious repository. However, Re, Mo and Cr have not yet been studied in detail. Therefore, Re, has been thoroughly examined in Phase IV as a direct analogy of fissiogenic Tc, and as a valuable indicator of redox conditions in the groundwaters. Mo was also studied because of its close association with Re at Maqarin, and Cr because it is directly analogous to Cr in cementitious chemotoxic waste, and because of its great abundance in these natural systems.

The alteration behaviour of the ACZ, and its influence on the hyperalkaline groundwater chemistry at Maqarin also required further clarification. Therefore. a series of laboratory leaching experiments were conducted on samples of the primary marbles and bituminous clay biomicrite host rock. These experiments are described in Sections 4.6 and 4.7, below. The leaching studies were undertaken to:

- characterise the source term directly.

- Compare the leaching of the Maqarin ACZ and Portland cement, in order to investigate the analogy between the behaviour of natural and artificial cements placed in identical leaching conditions, and thus to evaluate better the link between these two types of materials.
- To constrain better the leaching fluxes under the field conditions at Maqarin, to attempt to quantify the analogy between the Maqarin source-term and an industrial cement source-term, and to contribute to a simplified model of the source-term release.

As part of the characterisation of the ACZ at Maqarin, the fossil-temperature profile, related to the combustion event(s), was mapped. This was achieved by studying the perturbation in the magnetic properties of minerals, caused by the combustion metamorphism, along a traverse from cement to unaffected Bituminous Marl in Adit 6 (Section 5.5). The variation in magnetic properties was correlated with the mineralogy. The aims of the palaeomagnetic study were to:

- Evaluate if magnetic properties of rocks could be used as a field tool at cement outcrops.
- Evaluate the spatial extent of the temperature gradient at the end of combustion and to correlate this with dating information, where available.
- Evaluate the spatial correlation between thermal perturbation and clay content of the marl. This association is useful for understanding the altered-clay profiles from the Khushaym Matruk site in central Jordan.

4.1.3 Analytical methods

The analytical methods are presented in Appendix 4.

4.2 Primary Mineralogical Characteristics of the 'Near-Field Cement Zone'

4.2.1 General

Thermally metamorphosed rocks, formed by the spontaneous combustion of the organic-rich cherty limestones and clay biomicrites, similar to those of the Maqarin area, are found in several other parts of Jordan where the combustion of organic-rich upper Cretaceous and lower Tertiary strata has occurred near outcrop. For example, they are developed on a very large scale in the Daba-Siwaqa area of central Jordan, where the marbles are locally worked for ornamental stone. They also occur in the Sweileh area, west of Amman (Heihmbach and Rosch, 1980; Nassir and Khoury, 1982; Khoury and Nassir, 1982; Khoury and Salameh, 1986; Linklater, 1998; Smellie, 1998).

Irregular and discontinuous lenses of these unusual metamorphic rocks also occur within the statigraphically equivalent Hatrurim Formation in Israel and in the West Bank, Also referred to as 'The Mottled Zone', these occurrences have been described in detail by numerous authors (for example, Bentor et al., 1963a, 1963b; 1972; Gross et al., 1967; Kolodny et al., 1971; Kolodny and Gross, 1974; Gross, 1977; Kolodny, 1979; Ron and Kolodny, 1992). Although there is evidence of retrograde alteration and hydration in all of

these areas, it is only at the Maqarin site that contemporary hyperalkaline groundwaters associated with this alteration have been reported.

Note that all the raw data are presented in Appendix 4.

4.2.2 Mineralogy and petrology

The marbles belong to the sanidinite and pyroxene hornfels facies (Winkler, 1976; Treiman and Essene, 1983) and are strongly coloured, with a wide range of shades of brown, red, pink, violet, grey, green and black. Some of the mineralogical characteristics of the rocks are similar to those encountered in the low-pressure, high-temperature contact-metamorphic aureoles around shallow igneous intrusions. The rocks are highly fractured, and secondary mineralisation is very common in voids, fissures and fractures. Polygonal (hexagonal) columnar microjoints on a spacing-scale of 5-15 mm are common (e.g. Figure 4.1). These probably formed as a result of contraction on rapid cooling from high temperature after the combustion event. Virtually all of the marbles examined show at least some partial retrograde low-temperature hydration and alteration, which often proceeds initially by alteration along the polygonal joints.

A large number of unusual high- and low-temperature minerals have previously been identified in the marbles (ACZ) and adjacent HDZ developed in the enclosing country rocks (see Milodowski et al., 1992a, 1992b, 1998a, 1998b). Many of the minerals are analogous to those found in Ordinary Portland Cement (OPC) clinkers and hydrated OPC paste. Some of these unusual minerals are unique to these metamorphic rocks in Jordan and Israel. The primary metamorphic minerals described from Maqarin during Phases I-III (Alexander, 1992; Linklater, 1998; Smellie, 1998), supplemented with new information from Phase IV, are listed in Table 4.1.

The most abundant primary minerals found in varying proportions within the ACZ, identified on the basis of bulk X-ray diffraction (XRD) analysis, backscattered scanning electron microscopy (BSEM) with energy-dispersive X-ray microanalysis (EDXA), and/or quantitative electron probe microanalysis (EPMA) are: calcite ($CaCO_3$); larnite (β-Ca_2SiO_4), spurrite ($Ca_5(SiO_4)_2(CO_3)$) or paraspurrite ($Ca_5(SiO_4)_2(CO_3)$), a calcium silicosulphate mineral ($Ca_5(SiO_4)_2(SO_4)$); the apatite-group minerals – fluorapatite ($Ca_{10}(PO_4)_6F_2$), francolite ($Ca_{10-x-y}(Na,K)_xMg_x(PO_4)_{6-z}(CO_3)_zF_{0.4z}F_2$) and ellestadite ($Ca_{10}(SiO_4)_3(SO_4)_3O_{24}(Cl,OH,F)_2$); brownmillerite ($Ca_2(Al,Fe)_2O_5$), calcium ferrite ($CaFe_2O_3$) and various calcium aluminate(s) whose composition(s) cannot be defined by EPMA because of their extremely fine grain size.

The calcium sulphate-silicate mineral $Ca_5(SiO_4)_2(SO_4)$ has not been recorded previously as a natural mineral. This mineral was identified during the most recent Phase IV investigations on the basis of quantitative EPMA. Its composition is very close to the synthetic phase $Ca_5(SiO_4)_2(SO_4)$, described by Lea (1970) and Hewlett (1998) as a stable phase in the experimental system CaO-$CaSiO_3$-$CaSO_4$.

Confirmation of its identification from bulk XRD analyses is difficult because many of the other calcium silicate, silicophosphate and silicocarbonate minerals (and their alteration products) have coincident principal diffraction lines. This obscures the definitive diffraction lines for $Ca_5(SiO_4)_2(SO_4)$.

However, a number of minor lines, and shoulders on the diffractions lines of the other major calcium silicate minerals are consistent with the diffraction spacings listed in the Joint Committee on Powder Diffraction Standards (JCPDS) database reference pattern for $Ca_5(SiO_4)_2(SO_4)$. Although it has not been reported previously as a natural mineral, $Ca_5(SiO_4)_2SO_4$ is known from lime kiln deposits formed at temperatures around 1100°C

(Price, 1972). It forms under abnormal conditions (i.e. in kiln rings) in Portland Cement kilns and its phase composition can be significantly affected by small amounts of K_2O (Hewlett, 1998). The formation of this phase in the ACZ is consistent with the temperatures that might be postulated for combustion metamorphism events at Maqarin. According to Hewlett (1998), it forms as part of the subsolidous (950 °C) phase assemblage during calcium sulpho-aluminate clinker manufacture.

The principal rock types within the ACZ are:

- Calcite-marble.
- Larnite-calcite-marble.
- Larnite-spurrite (or paraspurrite)-calcite-marble.
- Larnite-spurrite (or paraspurrite)- $Ca_5(SO_4)(SiO_4)_2$-brownmillerite-marble.
- Ellestadite (or francolite/fluorapatite)-calcite-marble.
- Ellestadite-larnite-spurrite (or paraspurrite)-brownmillerite-calcite-marble.

Calcite marbles have formed by the metamorphism of the relatively pure limestone parent rock. Larnite-calcite, larnite-spurrite (or paraspurrite)-calcite, and larnite-spurrite (or paraspurrite)- $Ca_5(SO_4)(SiO_4)_2$ (± brownmillerite) marble assemblages are the result of the metamorphism of cherty limestones and cherty clay biomicrites. Ellestadite (or francolite/fluorapatite)-rich rocks are the metamorphic equivalent of phosphatic micrite and phosphatic cherty limestone parent rocks.

Many of these rocks possess a strongly developed planar fabric, defined by elongated grains of calcite, reflecting the bedding fabric of the original parent rock. Some marbles contain discrete patches of recrystallised calcite that preserve the outlines of original calcareous bioclasts, mainly foram tests (cf. Figure 4.2). The calcite grains are enclosed within a groundmass of interlocking xenomorphic groundmass of calcium silicates, phosphates and aluminates.

Fine-grained red haematite (α-Fe_2O_3) and fine-grained black iron oxides - possibly magnetite (Fe_3O_4) or maghemite (γ-Fe_2O_3), graphite (C), lime (CaO), wollastonite ($CaSiO_3$), anorthite ($CaAl_2Si_2O_8$) and diopside-hedenbergite ($Ca(Al,Fe)Si_2O_6$) are also present as minor to trace components in many of the marbles. The leaching of lime, although only a minor to trace component, is a potentially important buffer controlling the chemistry of calcium hydroxide (portlandite)-saturated hyperalkaline groundwaters discharging from the ACZ. Traces of possible periclase (MgO) were found in some samples.

Traces of an anhydrous Zn-rich calcium silicate were identified, with a few grains which were large enough to yield quantitative EPMA chemical data. It was found to have the formula $Ca_2Zn_{0.9}Si_2O_7$. If the Zn is considered to be substituting in the lattice for Ca, then it has a molar (Zn+Ca)/Si ratio of 1.44 which is close to rankinite ($Ca_3Si_2O_7$). This material could alternatively be a mixture of wollastonite ($CaSiO_3$) and Zn oxide. Other trace silicate minerals found within the marbles include an undefined Ba-Ca-sulphate-silicate and an undefined Ba-Ca-Zr-Mo-silicate.

Traces of primary metamorphic sulphide and selenide minerals are present in the ACZ, particularly in the more phosphatic (apatite and ellestadite) marbles. Oldhamite (CaS) – known previously only from experimental systems (Fincham and Richardson, 1954; Larimer, 1968; Helz and Wyllie, 1979), meteorites (Keil, 1968; Larimer, 1968; Blander, 1971; Skinner and Luce, 1971; Graham et al., 1977) and metallurgical slags (Butler, 1977; Scott et al., 1986) - was first identified during Phase I, and was again observed in samples examined during Phase IV. Oldhamite is readily detected by

cathodoluminescence (CL) microscopy, as it characteristically displays extremely strong bright-blue, blue-violet and greenish luminescence (Marshall, 1987). Its identification in the marbles from Maqarin is the first record of the natural terrestrial occurrence of oldhamite.

Krutaite ($CuSe_2$) and a Cu-K-Na-selenide (with a composition approximating to $Cu_{10.2}K_3Na_{0.2}Se_{7.7}S_{2.3}$) were found in close association with oldhamite and all three occur as tiny (<1-5 μm) inclusions within the recrystallised patches of calcite, as pseudomorphs of calcareous microfossils. The inclusions form an 'inner rim' that probably delineate the internal chamber walls within the original microfossil skeleton (see also Section 4.5). Sulphur-rich hydrocarbon is sometimes observed filling microfossil chambers in the parent limestones (see also Chapter 6). Therefore, the sulphide and selenide inclusions in the calcite pseudomorphs probably formed by reaction of the calcite with elemental or organic S and Se, released from hydrocarbons during its incomplete combustion within the restricted microenvironments provided by the test chambers.

The ellestadite- and apatite-rich marbles also contain trace amounts of an unidentified Ca-U-rich mineral (probably a carbonate or oxycarbonate) with a Ca:U ratio of 2:1. This mineral occurs as small (<20 μm), subhedral poikiloblastic crystals that appear to have crystallised late in the metamorphic phase and at the expense of the apatite-group minerals. Uranium was possibly derived from apatite in the original phosphatic parent rock.

Table.4.1 Primary metamorphic minerals from the Marble Zone, Maqarin site

Mineralogy	**General Formulae**	**Abundance**
Carbonates		
Calcite	$CaCO_3$	MAJOR
U-Ca-oxycarbonate?	Ca:U = 2:1	TRACE
Simple Oxides		
Lime	CaO	MINOR to TRACE
Periclase*	MgO	TRACE
Hematite or ferric oxide	α-Fe_2O_3	MINOR to TRACE
Magnetite (?)	Fe_3O_4	MINOR to TRACE
Maghemite (?)	γ-Fe_2O_3	
Ferrites, Aluminates and Mixed Oxides		
Ca-aluminate	Undefined	MINOR
Calcium ferrite,	$CaFe_2O_3$	MINOR
Brownmillerite	$Ca_2(Al,Fe)_2O_5$	MINOR
Multiple element ferrites	$(Ca,Ba,Cr,Al,Ti,Mg,Zn,Mn)Fe_2O_3$	TRACE
	Undefined	
Apatite Group		
Fluorapatite	$Ca_{10}(PO_4)_6F_2$	MAJOR
Francolite	$Ca_{10-x-y}(Na,K)_xMg_x(PO_4)_{6-z}(CO_3)_zF_{0.4z}F_2$	MAJOR
Ellestadite	$Ca_{10}(SiO_4)_3(SO_4)_3O_{24}(Cl,OH,F)_2$	MAJOR
Silicates		
Larnite	β-Ca_2SiO_4	MAJOR
Wollastonite	$CaSiO_3$	MINOR
Anorthtite	$CaAl_2Si_2O_8$	MINOR
Rankinite (?)*	$Ca_3Si_2O_7$ (significant Zn substitution for Ca)	TRACE
Diopside-hedenbergite	$Ca(Al,Fe)Si_2O_6$	MINOR
Complex Silicates and Silicates with Other Oxyanions		
Spurrite	$Ca_5(SiO_4)_2(CO_3)$	MAJOR

Parraspurrite	$Ca_5(SiO_4)_2(CO_3)$	MAJOR
Calcium silicate (unknown mineral)*	$Ca_5(SiO_4)_2(SO_4)$	MAJOR
Ba-Ca-sulphate-silicate	Undefined	TRACE
Ba-Ca-Zr-Mo-silicate	Undefined	TRACE
Elements		
Graphite	C	MINOR to TRACE
Sulphides and Selenides		
Oldhamite	CaS to $CaS_{0.9}Se_{0.1}$	TRACE
Cu-K-Na-Selenide	$Cu_{10.2}K_3Na_{0.2}Se_{7.7}S_{2..3}$ (approx.)	TRACE
Krutaite*	$CuSe_2$	TRACE

Note: *denotes new species discovered during Phase IV

Figure 4.1 BSEM image showing columnar hairline microjoints in calcite- ellestadite-brownmillerite-spurrite marble, with hydration alteration evident as narrow zones of duller material seen in the adjacent wallrock. Sample M15P (cf. Milodowski et al., 1992a, 1992b)

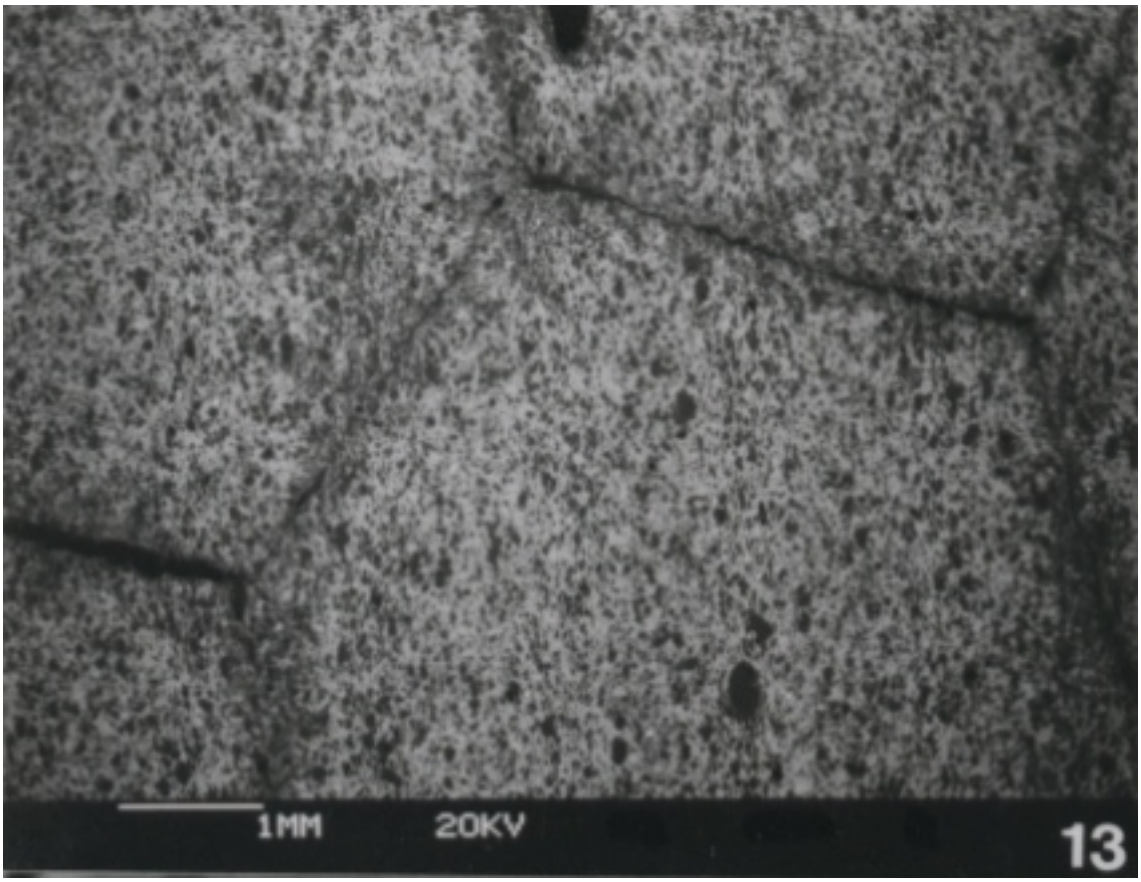

Figure 4.2 *BSEM image showing planar in calcite-ellestadite marble. Some of the recrystallised calcite (dark grey) can be seen to form lens-shaped pseudomorphs after former bioclasts from the original limestone parent rock Ellestadite-spuriite-rich matrix is seen as lighter grey areas. Sample M15P (cf. Milodowski et al., 1992a, 1992b)*

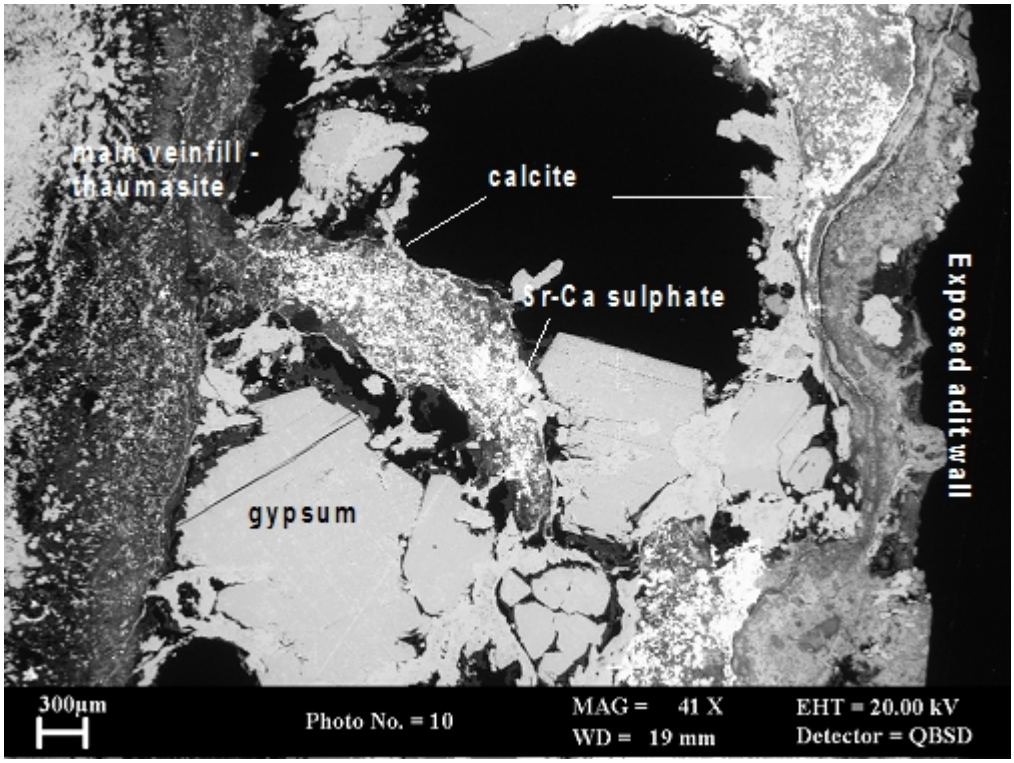

4.3 Hydration and Alteration of the ACZ

4.3.1 General

Prior to Phase IV, mineralogical information on the alteration characteristics of the Maqarin metamorphic rocks was based largely on source-term characterisation studies undertaken during Phase I (Milodowski et al,, 1992a, 1992b). Further detailed petrographical analyses on new samples studied during Phase IV show similar alteration characteristics to those seen in Phase I. This section presents a compilation of the alteration characteristics observed during Phase I to Phase IV, with emphasis on the alteration of the ACZ.

Low-temperature hydration and retrograde alteration of the ACZ have produced a complex assemblage of secondary minerals. A wide variety of simple and complex carbonate, oxide, hydroxide, sulphate, phosphate, silica minerals, zeolitic minerals, calcium silicate hydrate (CSH), calcium aluminosilicate hydrate (CASH) and other silicate phases have been identified from the Maqarin site (summarised in Table 4.2). These phases have been identified by combining XRD analysis and microchemical compositions determined by EMPA, EDXA and/or ATEM undertaken during Phases I-III (Milodowski et al, 1992a, 1992b, 1998a, 1998b) with new analyses undertaken in Phase IV.

The alteration of the metamorphic rocks and secondary mineral formation is the result of very complex interplay between different alteration processes, including (see also Figure 10.5 in Clark and Fritz, 1998):

- Hydration of the high temperature metamorphic minerals by interaction with groundwater.
- Carbonation reactions resulting from the interaction of HCO_3^{2-}, from the percolating bicarbonate-type groundwater, with the primary high-temperature metamorphic minerals.
- Carbonation reactions resulting from the interaction of HCO_3^{2-}, from the percolating bicarbonate-type groundwater, with secondary portlandite, CSH, CASH, calcium silicosulphates, and calcium aluminosulphates.
- Sulphatisation reactions resulting from the interaction of aqueous SO_4^{2-} with primary high temperature minerals such as lime, and with secondary portlandite, CSH and CASH phases. The aqueous SO_4^{2-} is derived through the interaction and dissolution of primary and secondary sulphate minerals in bicarbonate-type groundwaters.

The secondary mineral assemblage is also highly variable, and depends to some extent on the primary mineralogy of the metamorphic rocks. The major secondary alteration minerals are: portlandite ($Ca(OH)_2$), which is often at least partially replaced by secondary carbonates; crystalline CSH mineral, including 9Å, 11Å and 14Å tobermorite ($Ca_5Si_6O_{16}(OH)_2.2\text{-}8H_2O$), jennite ($Ca_9H_2Si_6O_{18}(OH)_8.6H_2O$), afwillite ($Ca_3Si_2O_4(OH)_6$ and tacharanite ($Ca_{12}Al_2Si_{18}O_{15}(OH)_2.3H_2O$); amorphous CSH hydrogels with compositions corresponding to CSH(I) (Ca:Si = 0.8-1.5), CSH(II) (Ca:Si = 1.5-2), and low-Ca CSH gel (Ca:Si = <0.8); poorly crystalline calcium-rich zeolitic and CASH hydrogels, which give only very weak and poorly defined XRD lines, and that are identified largely on the basis of microchemical composition; apophyllite ($KCa_4Si_8O_{20}(OH,F).8H_2O$); the sulphates gypsum ($CaSO_4.2H_2O$), ettringite ($Ca_6Al_2(SO_4)_3(OH)_{12}.25H_2O$) and thaumasite ($Ca_6Si_2(SO_4)(CO_3)_2(OH)_{12}.24H_2O$) and phases representing a solid-solution between ettringite and thaumasite; and calcite ($CaCO_3$) and apatite minerals.

Brucite ($Mg(OH_2)$) and hydrotalcite ($MgAl_2(CO_3)(OH)_{16}.4H_2O$) are locally important where dolomitic limestones have been pyrometamorphosed, and reflect the high magnesium content of the parent rock. The other polymorphs of $CaCO_3$, aragonite and vaterite, also commonly accompany calcite in the altered rocks. Vaterite is an unusual and very rare mineral that is more normally associated with boiler-scale deposits. However, it has been recorded previously from partially hydrated larnite nodules from contact metamorphosed chalk in Northern Ireland (McConnell, 1960), and also as an alteration product in similar pyrometamorphic rocks from the Hatrurim Formation of Israel (Gross, 1977). The most highly altered and leached rocks are almost entirely replaced by calcite, gypsum, ettringite or thaumasite. Gibbsite ($\alpha\text{-}AlOH_3$) was occasionally observed as the dominant vein-filling phase in some microfractures at the margins of the ACZ, and in the adjacent Bituminous Marl Formation parent rock (Milodowski et al., 1992a, 1992b).

A large number of other secondary phases occurs only in volumetrically very minor to trace amounts (Table 4.2), but may be significant as sources and sinks for trace elements (e.g. U, Cr, Cd, Pb, Ba, Sr).

4.3.2 Paragenesis of the alteration products

The earliest evidence of alteration of the metamorphic zone rocks is best preserved in partially hydrated relicts of the primary marble zone. Hydration was initiated by groundwater percolation through columnar joints and other fractures (e.g. Figure 4.1). Fine-grained microcrystalline calcite and aragonite, sometimes accompanied by traces of

barite, celestite, baritocelestite, calciocelestite, barite and hashemite intergrown with the carbonate minerals, often form a very thin coating lining these microfractures and appear to be the earliest secondary alteration phases.

The carbonate minerals may result from the direct interaction of bicarbonate in the groundwater with the primary metamorphic zone minerals (principally, larnite, spurritite, paraspurrite and $Ca_5(SiO_4)_2(SO_4)$). Tobermorite, or a CSH(I)-type hydrogel, is the earliest secondary mineral seen to have precipitated in these fractures. It forms gel-like globules or radiating fibrous aggregate masses that are now largely replaced by, and included within, coarser crystals ettringite (Figure 4.3).

As the secondary vein mineralisation develops, thaumasite may be deposited on top of, or occasionally replaces, earlier-formed ettringite (Figure 4.2). The relationship between ettringite and thaumasite is not always clear and, in some cases, multiple generations and alternations of ettringite and thaumasite may be present (Figure 4.5). Afwillite is also present as an alteration product in these early veins in partially hydrated marble zone rocks (Figure 4.5). It appears to have nucleated within, and partially replaces, earlier-formed thaumasite and ettringite. Occasionally, thick veins (up to 15 mm) of apophyllite are found cutting the altered marble zone rocks.

Apophyllite appears to be a relatively late-stage alteration product. It is found both as a vein fill and as part of the matrix alteration assemblage in the most extensively altered metamorphic zone rocks. Petrographical observations indicate that the apophyllite may replace earlier-formed CSH minerals and ettringite-thaumasite mineralisation (Figure 4.6). Previous analyses of apophyllite indicated that it is deficient in K, and that up to 25 % of the K may be substituted by NH_4^+ (Milodowski et al., 1992a). The apophyllite may also be growth zoned, with the development of Sr-rich bands (Figure 4.6), indicating the periodic enrichment of Sr in the reacting groundwaters.

The earliest primary minerals to show evidence of alteration are the trace sulphide-selinide phases: oldhamite, krutaite and other K-Na-Cu-Se sulphides. These occur as tiny inclusions within recrystallised calcite matrix of the marbles, and as lime, which was only seen to be preserved as inclusions isolated from hydration in more coarsely crystalline calcite. The sulphoselenide minerals appear to dissolve very rapidly. They are even corroded and removed from marbles that show only very minor evidence of alteration along microfractures, leaving euhedral mouldic dissolution cavities within the host minerals (usually calcite; Figure 4.7). Lime is much more abundant than the sulphoselenides but it is also very rapidly hydrated to form fine-grained portlandite. Complete hydration and alteration of the matrix of the marbles produces an assemblage dominated by calcite, portlandite, ettringite and thaumasite. This may or may not be accompanied by apophyllite and poorly crystalline CSH, and minor Fe oxides. These alteration products are typically extremely fine-grained (grain size typically <10 μm, and often <1 μm) and complexly intergrown with each other. This makes the individual phases very difficult to resolve under the optical microscope or by SEM.

After the alkali earth and alkali metal sulphoselenides, the next most reactive primary metamorphic mineral is $Ca_5(SiO_4)_2(SO_4)$. However, unlike the trace sulphoselenides, this phase is a major mineral component of the larnite-spurrite (or paraspurrite)-$Ca_5(SO_4)(SiO_4)_2$-brownmillerite-marble, which is one of the main rock types present within the ACZ. Consequently, the alteration of $Ca_5(SiO_4)_2(SO_4)$ has a major effect on the overall mineralogical fabric of these marbles. $Ca_5(SiO_4)_2(SO_4)$ is intergrown with spurrite and paraspurrite and in the hydrated rocks is seen to alter much more rapidly than any of the other silicate and oxide phases. It is often only seen as corroded relicts within a groundmass of fine- grained ettringite, thaumasite, portlandite and/or CSH minerals

(Figure 4.8). These are alteration products mixed with relatively unaltered brownmillerite and weakly altered spurrite and paraspurrite. Larnite also reacts on exposure to water, to produce CSH alteration products. It appears to be significantly less reactive than $Ca_5(SiO_4)_2(SO_4)$ but more reactive than spurrite, paraspurrite or ellestadite, which only display hydration alteration to secondary minerals in the late stages of alteration, represented by the most highly altered marble-zone rocks.

The latest stages of alteration in the ACZ are evident in the walls of Adit 6 and appear to be related to carbonation of earlier-formed secondary CSH, thaumasite and ettringite. These result from continuing percolation by, and interaction with, background bicarbonate groundwater. They form fine-grained calcite, and possibly also aragonite and vaterite, and amorphous silica and gypsum (e.g. Figure 4.9). Also, where the rocks are exposed in the walls of Adit 6, dehydration and decomposition of thaumasite has occurred, to form secondary calcite and gypsum, with traces of celestite or calciocelestite (Figure 4.10).

The overall paragenesis of the alteration and hydration of the ACZ and secondary mineral formation are summarised in Table 4.3.

Table.4.2 Secondary minerals from the ACZ, Maqarin

Mineralogy	General Formulae	Abundance
CARBONATES		
Calcite	$CaCO_3$	MAJOR
Aragonite	$CaCO_3$	MINOR to TRACE
Vaterite	$CaCO_3$	MINOR to TRACE
Strontianite	$SrCO_3$	MINOR to TRACE
Ankerite	$Ca(Mg,Fe)(CO_3)_2$	TRACE
Kutnahorite	$Ca_{0.75}(Mn,Mg)_{0.25}(CO_3)_2$	TRACE
COMPLEX CARBONATES		
Hydrotalcite	$MgAl_2(CO_3)(OH)_{16}.4H_2O$	MINOR to TRACE
SIMPLE OXIDES		
Hematite or ferric oxide	α-Fe_2O_3	MINOR to TRACE
Maghemite (?)	γ-Fe_2O_3	MINOR to TRACE
SIMPLE HYDROXIDES		
Brucite	$Mg(OH)_2$	MINOR to TRACE
Portlandite	$Ca(OH)_2$	MAJOR
Gibbsite	α-$AlOH_3$	MINOR to TRACE
Goethite	α-FeO.OH	MINOR to TRACE
Iron oxyhydroxide	undifferentiated	MINOR to TRACE
SULPHATES		
Gypsum	$CaSO_4.2H_2O$	MAJOR
Bassanite	$CaSO_4.0.52H_2O$	?
Anhydrite	$CaSO_4$	MINOR to TRACE
Barite	$BaSO_4$	TRACE
Celestite (celestine) [3]	$SrSO_4$ [3]	TRACE
Barytocelestite	$(Ba,Sr)SO_4$	TRACE
Calcian barytocelestite	$(Ba,Ca,Sr)SO_4$	TRACE
Hashemite	$BaCrO_4$ to $BaSO_4$ [complete solid-solution]	TRACE
Cd-sulphate phase	Undefined phase	TRACE
Pb-sulphate phase	Undefined phase	TRACE
Cu,Zn-sulphate phase	Undefined phase	TRACE
COMPLEX SULPHATES		
Ettringite [1]	$Ca_6Al_2(SO_4)_3(OH)_{12}.25H_2O$ [1]	MAJOR
Thaumasite [1]	$Ca_6Si_2(SO_4)(CO_3)_2(OH)_{12}.24H_2O$ [1]	MAJOR
Jourovskite	$Ca_3Mn(CO_3)(SO_4)(OH)_6.12H_20$	TRACE
SILICA MINERALS		
Quartz	SiO_2	MINOR
Silica gel	$SiO_2.nH_2O$	MINOR to TRACE
Opal-CT	SiO_2	NOT KNOWN
Opal-A	$SiO_2.nH_2O$	NOT KNOWN
APATITE-GROUP		
Hydroxyapatite	$Ca_{10}(PO_4)_6(OH)_2$	MAJOR to MINOR
Fluorapatite	$Ca_{10}(PO_4)_6F_2$	MAJOR to MINOR
Francolite	$Ca_{10-x-y}(Na,K)xMg_y(PO_4)_{6-z}(CO_3)_z(OH)_2F_{0.4z}F_2$	MAJOR to MINOR
Ellestadite	$Ca_{10}(SiO_4)_3(PO_4)_3O_{24}(Cl, F, OH)_2$	MAJOR to MINOR
Fluorellestadite [3]	$Ca_{10}(SiO_4)_3(PO_4)_3O_{24}(F)_2$ [3]	MAJOR to MINOR
CSH and CASH PHASES		
Afwillite	$Ca_3Si_2O_4(OH)_6$	MAJOR to TRACE
Tobermorite(s) [2]	$Ca_5Si_6O_{16}(OH)_2.2\text{-}8H_2O$ [2]	MAJOR

Jennite	$Ca_9H_2Si_6O_{18}(OH)_8.6H_2O$	MAJOR
Birunite	$Ca_{15}(CO_3)_{5.5}(SiO_3)_{8.5}SO_4.15H_2O$	MINOR to TRACE
CSH(I) hydrogel [4]	amorphous Ca:Si = 0.8-1.5 [4]	MAJOR
CSH(II) hydrogel [4]	amorphous Ca:Si = 1.5–2 [4]	MAJOR
CSH hydrogel [4]	amorphous, undefined/variable Ca:Si = <0.8 [4]	MAJOR
Tacharanite [5]	$Ca_{12}Al_2Si_{18}O_{15}(OH)_2.3H_2O$ [5]	MAJOR
CASH hydrogels	Highly variable compositions between tacharanite and zeolite compositions	MAJOR
ZEOLITE GROUP[7]		
Mordenite	$CaNa_2K_2Al_2Si_{10}O_{24}.7H_20$	MAJOR to TRACE
Dachiardite	$(CaNa_2K_2)_5Al_{10}Si_{38}O_{96}.25H_20$	MAJOR to TRACE
Henlandite	$(CaNa_2)Al_2Si_7O_{18}.6H_20$	MAJOR to TRACE
Epistilbite [7]	$Ca_3Al_6Si_{18}O_{48}.16H_20$	MAJOR to TRACE
Yugarawaralite	$Ca_2Al_4Si_{12}O_{32}.8H_20$	MAJOR to TRACE
Laumontite	$Ca_4Al_8Si_{16}O_{49}.16H_20$	MAJOR to TRACE
Wairakite	$Ca_4Al_{16}Si_{32}O_{96}.16H_20$	MAJOR to TRACE
Leonhardite	$Ca_4(Al_8Si_{16}O_{48}).14H_20$	MAJOR to TRACE
CLAY MINERALS		
Volkonskoite.	Cr-substituted smectite	MINOR to TRACE
OTHER PHASES		
Apophyllite [6]	$KCa_4Si_8O_{20}(OH,F).8H_2O$ [6]	MAJOR to TRACE
U-Ca-silicate	unidentified and undefined	TRACE
Ca-Cr-silicate hydrogel	unidentified and undefined	TRACE

Notes:

[1] A complex solid-solution is observed between ettringite and thaumasite mineralization;

[2] Tobermorites of variable hydration states are present (including 14Å tobermorite (sometimes formerly referred to as 'plombierite') with 8 H_2O; 11Å tobermorite with 4 H_2O; 9Å tobermorite with 2 H_2O)

[3] New species found during Phase IV

[4] CSH hydrogels from Maqarin can host significant Al content.

[5] Includes non-crystalline CASH hydrogels with similar composition to tacharanite

[6] Apophyllite analyses from Maqarin are significant deficiency in K^+ site occupancy (up to 25 %) compared to ideal apophyllite stoichiometry, indicating probable major lattice substitution of K^+ by NH_4^+.

[7] 'Zeolites' at Maqarin are tentatively inferred on the basis of micochemical composition (EPMA, EDXA and ATEM). Most appear to be amorphous CASH 'hydrogels' of zeolitic composition and only epistilbite has been confirmed by XRD as a crystalline zeolite

Table 4.3 Summary paragenesis of alteration and mineral formation of the ACZ at Maqarin

Stage	Process	Primary minerals alteration	Secondary mineral formed
1	Early ingress of calcium bicarbonate type ground water into the Metamorphic Zone. Direct interaction between HCO_3^- from groundwater with primary metamorphic calcium silicate and calcium sulphosilicates Dissolution of soluble sulphate and interaction between aqueous sulphate and primary metamorphic calcium silicates and calcium sulphosilicates	Dissolution and hydration of lime. Dissolution of traces of oldhamite, and K-Na-Cu-Se-sulphide phases	Portlandite Calcite, ±aragonite, ±vaterite Barite, ±baritocelestite, ±celestite, ±calciocelestite, ±hashemite
2	Major early hydration of major calcium sulphosilicate component Production of sulphate-rich groundwater	Alteration and hydration of $Ca_5(SiO_4)_2(SO_4)$	Tobermorite, CSH hydrogels Precipitation of ettrinigite and replacement of tobermorite and CSH hydrogel by ettringite Precipitation of thaumasite (often in complex relationship with ettringite
3[1]	Reaction of sulphate-rich groundwater with primary metamorphic minerals and secondary CSH minerals		
4	Early-to-late hydration of marbles	Alteration and hydration of larnite	Tobermorite, CSH hydrogels
5	Late-stage hydration of marbles	Alteration and hydration of spurrite, paraspurrite and ellestadite	Tobermorite, CSH hydrogels, apatite
6	Carbonation of secondary CSH minerals, thaumasite and ettringite by bicarbonate groundwaters		Calcite, gypsum, silica gel
7	Interaction with moisture atmospheric CO_2 on exposure to air		Calcite, gypsum, silica gel produced by breakdown of CSH and thaumasite.

Note:

[1] Sulphate reaction processes occurring in Stage 3 may also accompany, interact with, or overlap with alteration during Stage 4 and Stage 5.

Figure 4.3 *BSEM image showing early hydration alteration along a microfracture in calcite-ellestadite-spurrite-brownmillerite marble. Early-formed fibrous tobermorite (t) is enclosed and partially replaced by later blocky euhedral crystals of ettringite (et). Sample M15P (cf. Milodowski et al., 1992)*

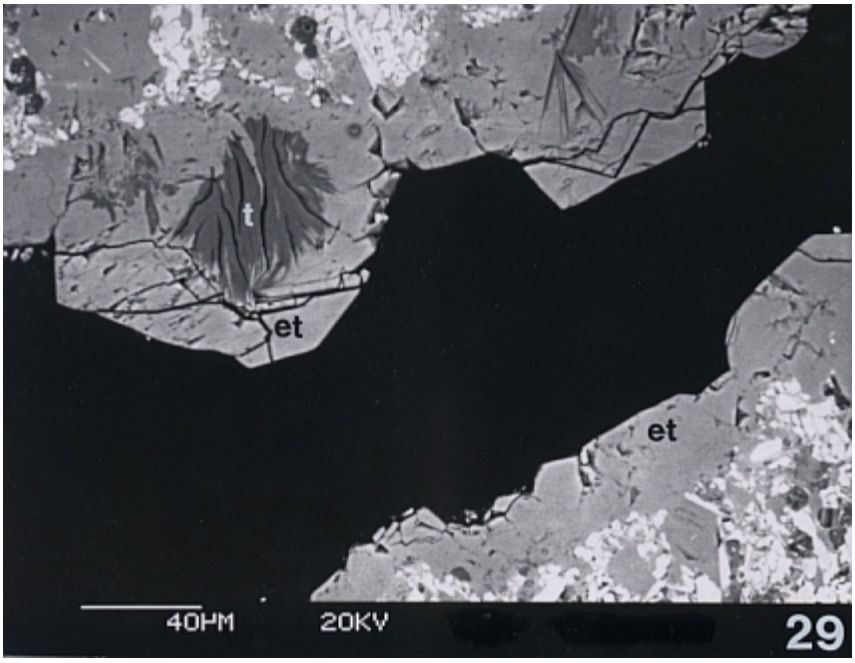

Figure 4.4 *BSEM image showing vein alteration in partially altered calcite- ellestadite-spurrite-brownmillerite marble. Ettringite (et) rests on early euhedral fracture lining calcite (mid-grey), which directly coats the fracture walls. Thaumasite (t), showing desiccation cracking, encloses the earlier-formed ettringite. Sample M15P (cf. Milodowski et al., 1992)*

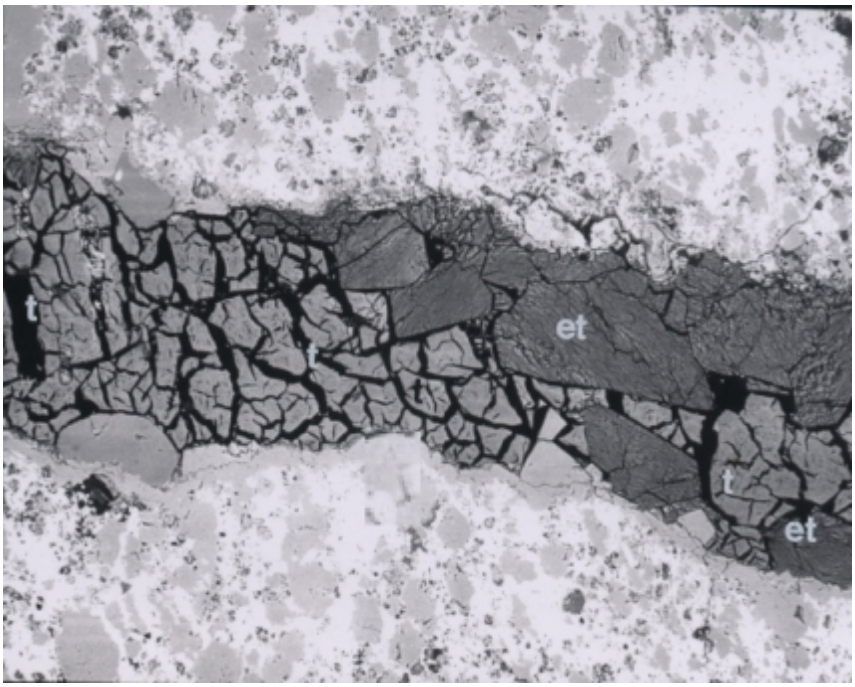

Figure 4.5 *BSEM image showing vein alteration in partially altered calcite- ellestadite-spurrite-brownmillerite marble. Ettringite (et) rests on earlier thaumatite (tm). Late-stage fibroradiate afwillite (af), has nucleated within microfractures in the ettringite and replaces ettringite along the fibrous intergcrystalline grain boundaries. Sample M33P (cf. Milodowski et al., 1992)*

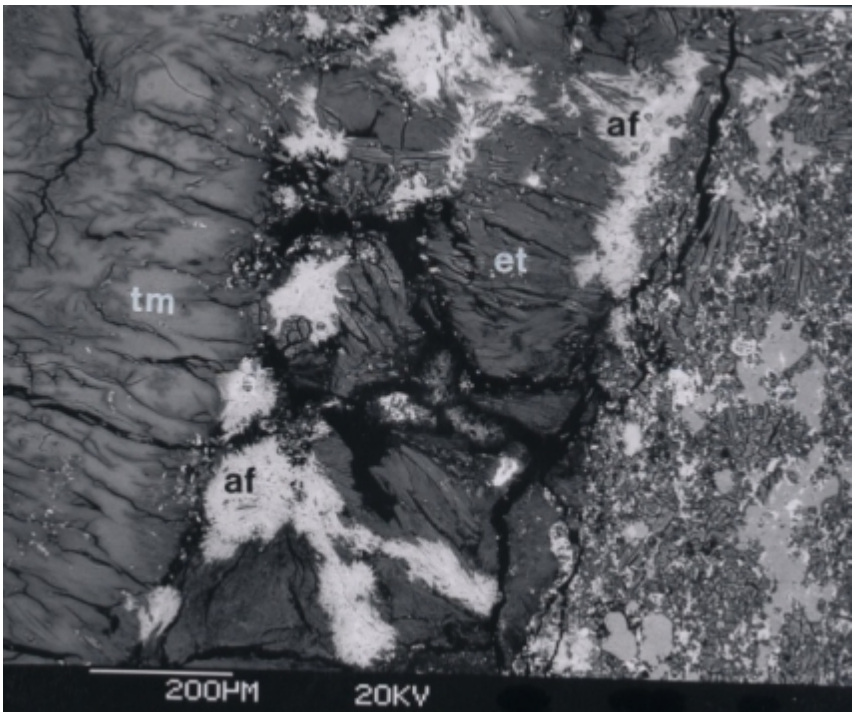

Figure 4.6 *BSEM image showing fibrous ammonium-bearing apophyllite vein filling displaying zonation with brighter Sr-rich apophyllite. The apophyllite has nucleated on and replaced earlier CSH and ettringite-thaumasite mineralisation (porous region close to fracture wall). Sample M17P (cf. Milodowski et al., 1992)*

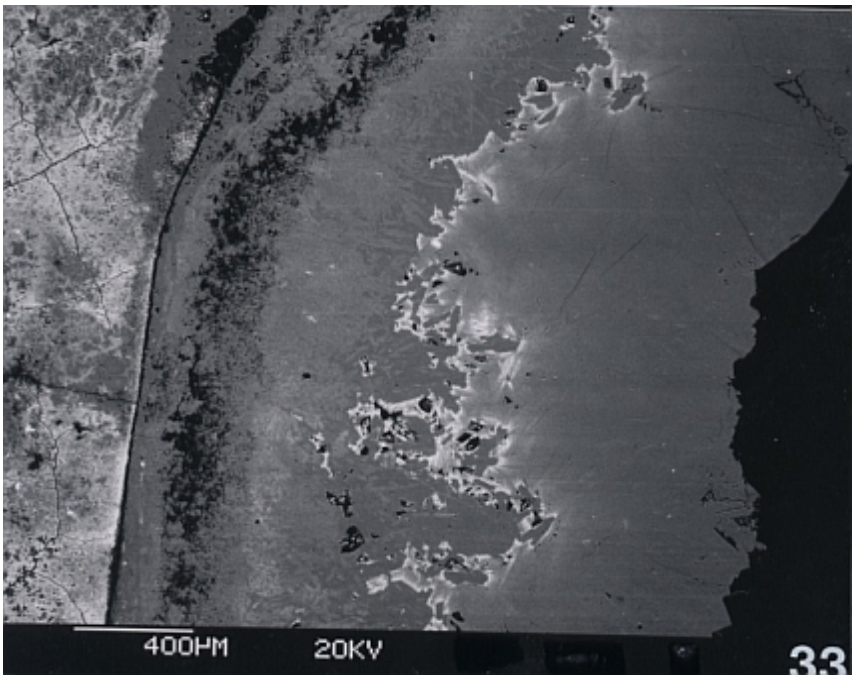

Figure 4.7 *BSEM image showing tiny crystal of oldhamite (mid grey), enclosed by thin bright rim of Cu-K-S-Se mineral, within calcite matrix of weakly hydrated marble. The Cu-K-S-Se phase has partially dissolved to leave a cavity (black). Sample M00-1-12*

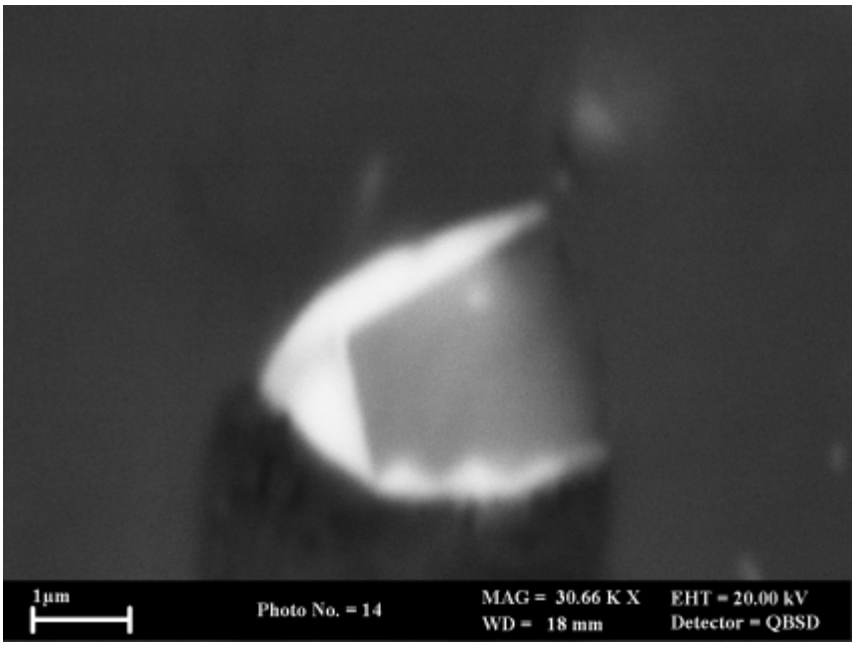

Figure 4.8 *BSEM image showing altered marble with corroded relicts of K- bearing $Ca_5(SiO_4)_2(SO_4)$ (light grey) in a matrix of secondary thaumasite (dark grey). Tiny bright grains are brownmillerite and calcium ferrite. Sample M00-1-47*

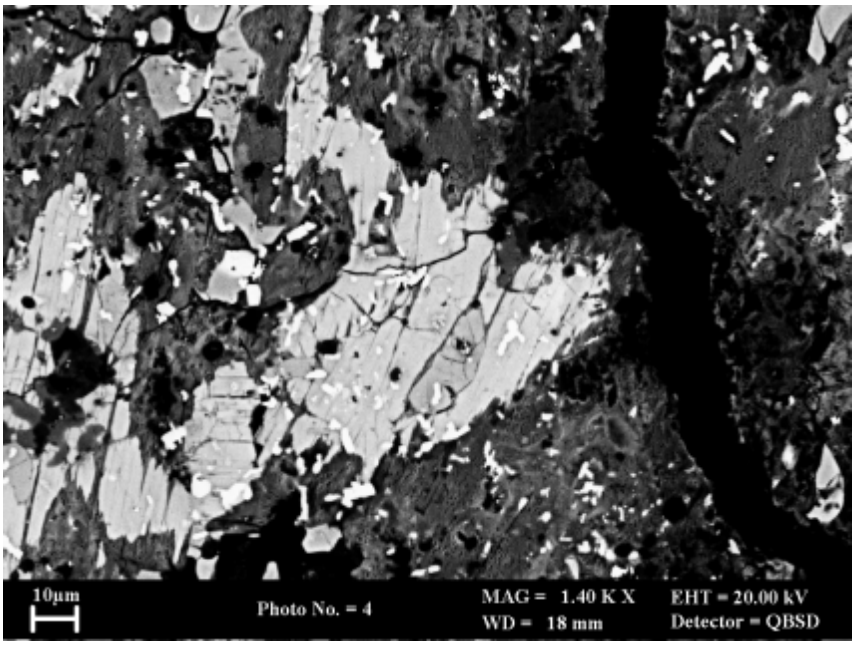

Figure 4.9 *BSEM image showing a fracture in calcite-rich marble. The earliest fracture-filling phase is fibrous thaumasite. This is overgrown by calcite rhombs and finally by coarser, well-cleaved gypsum crystals which have grown with their main cleavage in crystallographic continuity/orientation with the length of some thaumasite fibres. Both calcite and gypsum may have formed following a rise in the bicarbonate content of the waters and corresponding destabilisation of the thaumasite. Sample M00-1-5*

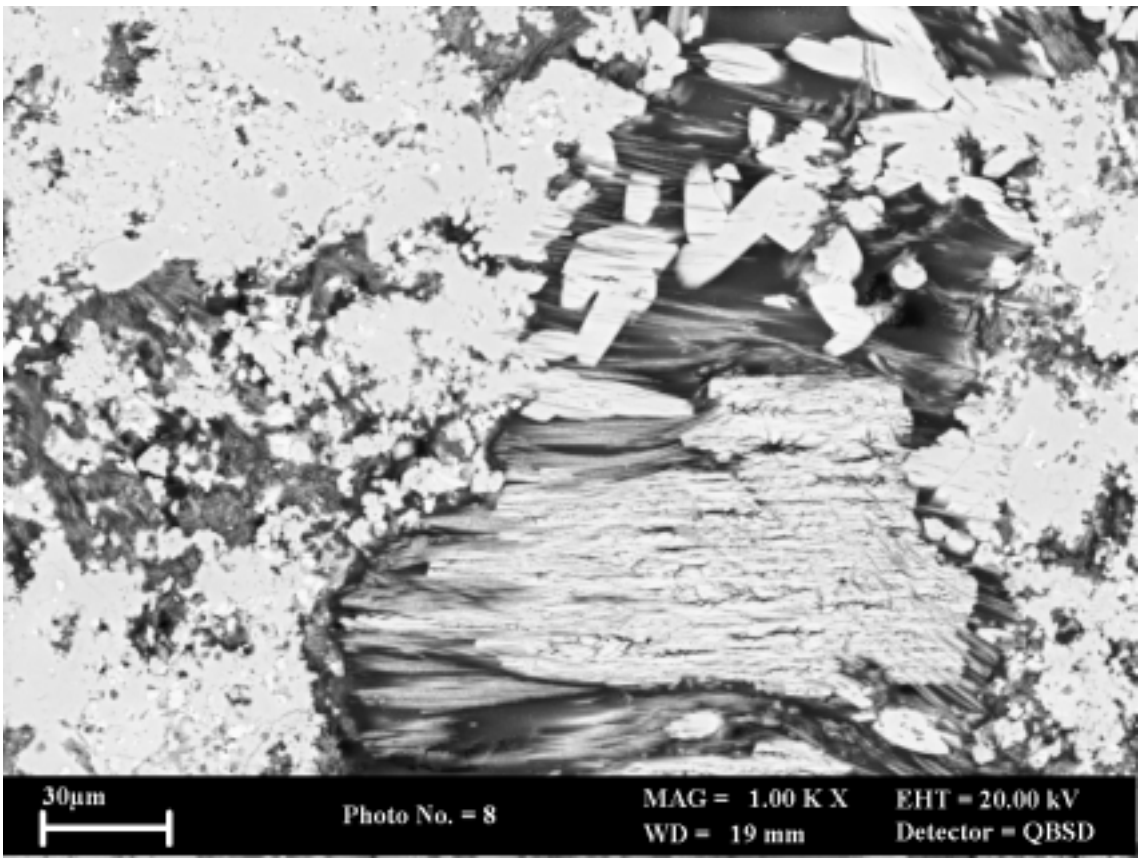

Figure 4.10 *BSEM image showing a fracture which has been exposed at the surface of the Adit. The outer surface is on the righ- hand side, and the main part of the fracture fill is to the left (thaumasite). In the intermediate area shown are thin rinds of calcite, some siliceous gel and late, coarse sparry gypsum overgrowing some of the earlier calcite rinds (slightly brighter phase within the gypsum). The extremely bright, fine grained phase is a Sr-Ca carbonate. If the calcite, siliceous gel and gypsum are alteration products of thaumasite exposed to the CO_2- rich atmosphere, it makes sense that the Sr-C carbonate phase, which occurs early (Stage x) in the paragenesis, is preserved. Sample M-00- 1-5*

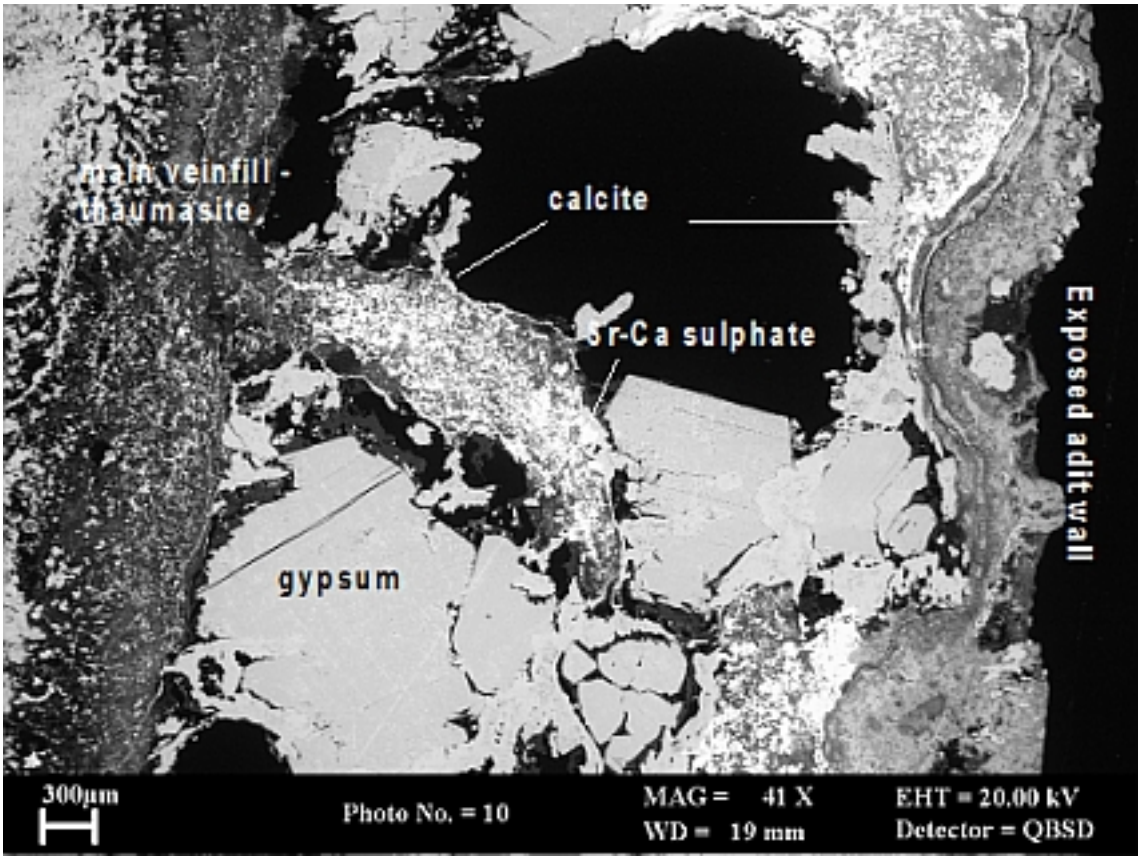

4.4 Investigations on Re, Mo, Cr, Se and Other Trace Elements

4.4.1 Introduction

In Maqarin, trace metals are leached from the ACZ and clay biomicrite and get trapped in a variety of secondary phases (sulphates, chromates, ettringite-thaumasite, CSH, zeolites, clay minerals, carbonates, etc). Significant concentration levels of several trace metals are also detected in groundwaters. Since Phase I of the project (Alexander, 1992), great attention has been paid to the levels of metals (such as Cr, Ni, Se, U and Th) in the groundwaters and to the identification of minerals hosting these metals. Such observations yield interesting guidelines to predict the behavior of such metals in hyperalkaline systems, and provide valuable tests for thermodynamic databases used in geochemical modelling. They also help to understand water-rock interactions in Maqarin and/or, by analogy, in analogue cementitious environments.

The presence of Re in Maqarin groundwaters was recognised during Phase I (Milodowski et al., 1992), but the behavior of Re in Maqarin was not examined in detail. It was proposed to investigate on this element during Phase IV because:

- Re resembles fissiogenic Tc chemically, at least in oxidation states IV and VII (Brookins, 1986; Xiong and Wood, 1999, 2001, 2002; Kim and Boulègue, 2003). Knowledge of Re behavior in Maqarin may therefore be used to help predictions of Tc behavior in hyperalkaline environments.
- Re is a sensitive redox indicator, in particular to trace redox conditions during sediment burial, e. g. in black shales (Colodner et al, 1993; Crusius et al., 1996; Crusius and Thomson, 2000; Peucker-Ehrenbrink and Hannigan, 2000) of the diverse rock-masses in Maqarin (biomicrite, analogue cements, chalky limestone, basalt) and the complex and not totally constrained ground-water flow pattern (see Chapter 2). Here, perhaps, Re could be used as a tracer.

Table 4.4 *Extract of the periodic table of elements showing the position of Re with respect to other neighbouring transition elements*

Cr	Mn	F
Mo	Tc	Ru
W	Re	O

Re (Z=75; see Table 4.4) is a transition element present at a low concentration in the earth crust (~0.0005 ppm crustal abundance). The two naturally occurring isotopes are ^{185}Re (37.4 %) and ^{187}Re (62.6 %), the latter decaying to ^{187}Os with a half life of 45.6×10^9a. Oxidation states from –I to +VII are possible for Re in laboratory conditions or under low temperature geological environments (Xiong and Wood, 1999), but the redox states 0, +IV and +VII are usually found to be the most stable redox states for Re in the environment (Brookins, 1986; Xiong and Wood, 1999; Kim and Boulègue, 2003). Sulphide phases are potential important scavengers for Re(IV) (Wharton et al., 2000) and ReS_2 is thought to be a solubility controlling phase in sulphur-bearing environments (Xiong and Wood, 2001). Important controlling phases in sulphur-free environments are Re and $Re(IV)O_2$. Re_2O_7 is highly soluble in aqueous solution; this oxide is in addition volatile at temperatures above ~270-300°C. As is shown below, this volatility had probably some influence on the spatial distribution of Re around combustion zones in Maqarin. Major aqueous species of Re are $Re(VII)O_4^-$, $Re(IV)(OH)_4(aq)$ and $Re(IV)O(OH)_3^-$. Re(IV) complexes with HS^- or polysulphide ions in the neutral to mildly alkaline region are plausible, although not proven. Under the ReO_4^- aqueous form, Re is most probably not controlled by the solubility of a pure Re phase but more likely by anion exchange reactions or anion substitution (perhaps with sulphates).

It was also decided to combine this investigation on Re with detailed observation and analysis of several other redox sensitive elements on which research had already been performed in previous phases of Maqarin project (see Linklater, 1998; Smellie, 1998):

- Cr, which is one of the 'major' trace elements in Maqarin. This study was prompted by the fact that Cr is often contained in industrial analogue cements, either as naturally occuring trace or as a waste (Bénard, 2004).
- Se, because of Se isotopes contained in radwaste.
- Mo, because of the frequent Mo-Re association observed in reducing environments (Mo(IV), Re(IV) in sulphides) and also because of radioactive Mo isotopes in radwaste.
- W, because of its potential association with Re or Mo.

Finally, because the analytical methods were often multi-elemental, interesting data was simultaneously acquired on many other elements, present as traces or minor elements : e.g. Ti, V, Mn, Fe, Ni, Cu, Zn, Ga, As, Rb, Sr, and Y

The results presented here concern

i analyses of groundwaters and metal speciation.
ii investigations on the solid phase, including bulk and micro-analyses of trace metals.
iii leaching experiments performed on columns of Maqarin natural analogue cement and biomicrite.

4.4.2 Analytical methods

All analytical methods are presented in Appendix 4.

4.4.3 Data on groundwaters for Cr, Re, Mo and Se

Datasets for groundwaters and spring waters sampled during Maqarin Phase IV are reported in Appendix 3.1. The sampled waters group mainly hyperalkaline waters (from both the Eastern and Western Springs) but also one occurrence of neutral groundwater sampled in Adit A-6 (M19 fracture seep site, 318 m from entrance). The ranges for Cr, Re, Mo and Se concentrations in these samples are respectively (0.0 to 5.2 mgL^{-1}), (0.6 to 6.5 μgL^{-1}), (10 to 260 μgL^{-1}) and (100 to 1100 μgL^{-1}). As was already recognized in earlier works, the M5 (Western Springs) location groundwater contains high concentrations of Cr, Mo and Se; it also presents the highest values for Re. The other hyperalkaline waters have Cr, Se and Re concentrations in a quite narrow range, whereas Mo concentrations are more variable. Figures 4.11 and 4.12 show the evolution of Re against Mo, NO_3^-, SO_4^{2-} and Se concentrations. These graphs show that the Re concentration detected in most hyperalkaline waters seems independent of Mo and SO_4^{2-} concentrations whereas some better correlation is found with NO_3^-. The data indicate that, for low concentration samples, the variations of Se and Re concentrations are not clearly correlated. The Re and Cr trend shows an inverse correlation for these low-metal, hyperalkaline waters.

Some speciation calculations were performed in order to evaluate whether observed Re concentrations in groundwaters could be linked to a specific mineral control. The speciation code CHESS (Van der Lee, 1998) was used in this purpose. The thermodynamic database was completed to include data for Re species given in Brookins (1986), Xiong and Woods (2001) and Kim and Boulègue (2003) (i.e. ReO_4^-, $Re(OH)_4(aq)$, $ReO(OH)_3^-$, Re metal, ReO_2, ReS_2). Calculations performed on groundwater data from

M19 enabled the redox conditions in these waters to be constrained and to show that Re in these waters is probably controlled by ReS_2.

Figure 4.11 *Groundwater analyses: correlation between Re and Mo, Re and nitrate. Blue diamonds: Nov. 2000 field samples (groundwaters + springs). White squares: May 2000 field samples (groundwaters + springs)*

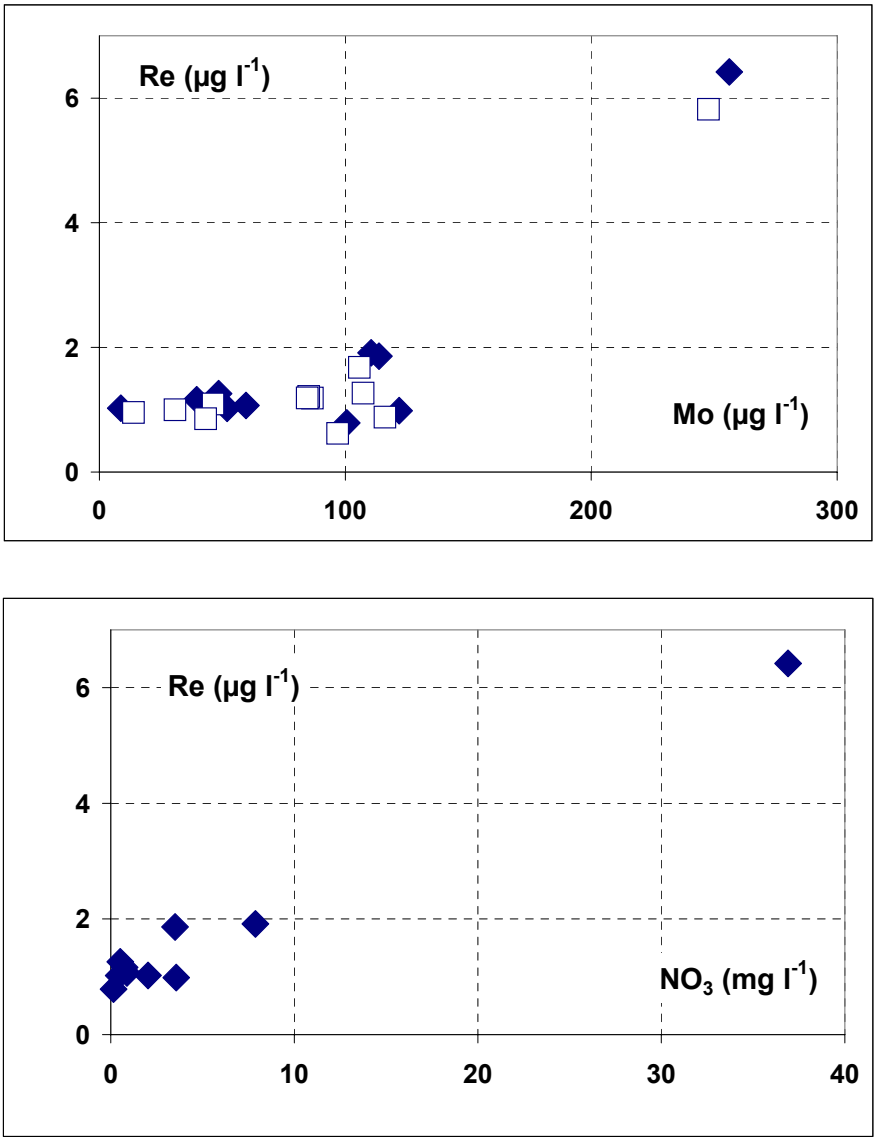

Figure 4.12 Groundwater analyses: correlation between Re and sulphate, Re and Se. Blue diamonds: Nov. 2000 field samples (groundwaters + springs). White squares: May 2000 field samples (groundwaters + springs)

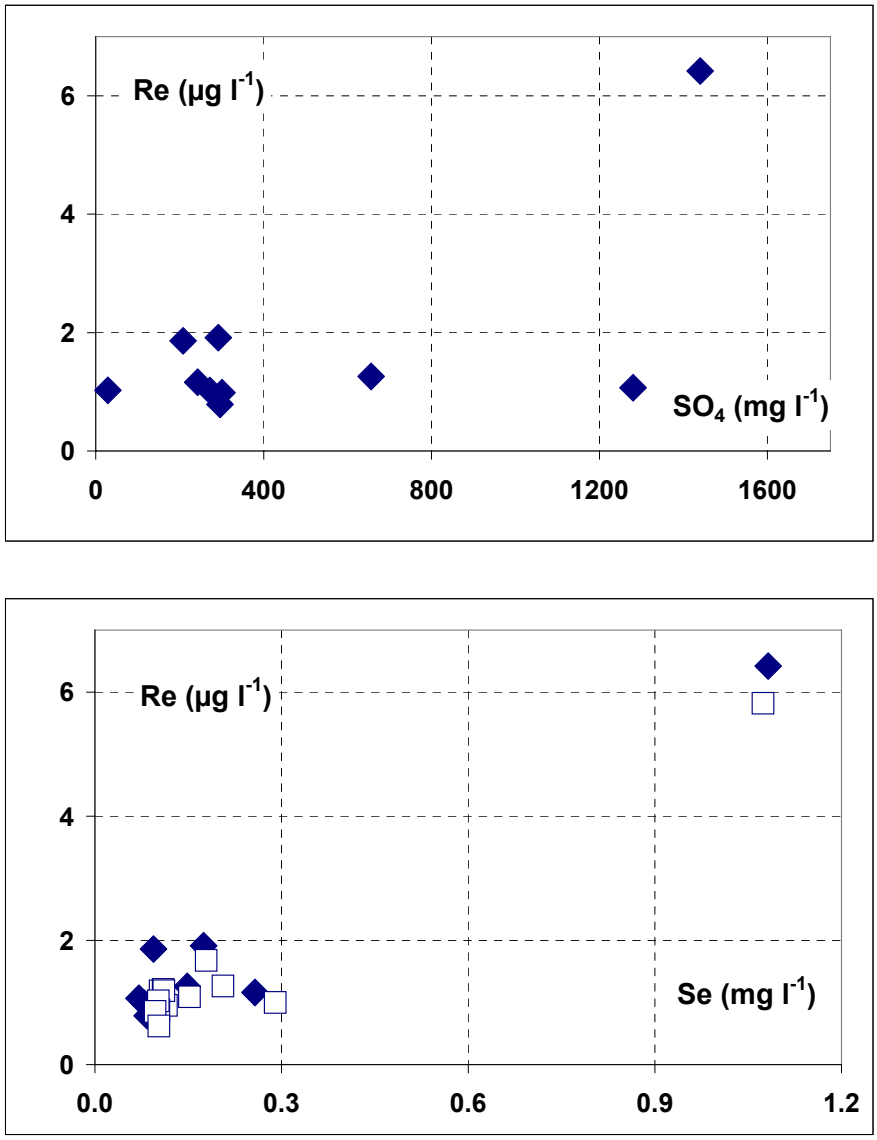

The saturation index (SI) of several significant minerals in redox buffering (haematite, goethite, pyrrhotite, troilite, coffinite, uraninite) were indeed simultaneously close to a SI of 0 when a Eh(25°C) = -260 mV was assumed. The water is also in equilibrium with quartz, calcite and gypsum. In these conditions the saturation index of ReS_2 is found to be slightly positive (Table 4.5). This, in addition to the fact that sulphide minerals are present in the biomicrite, makes this phase a plausible candidate for Re control. Further investigations on the redox of groundwaters were conducted using Cr data, demonstrating that the M19 water was close to equilibrium with $Cr(OH)_3$ (Figure 4.13).

Re control by solubility in hyperalkaline waters could not be elucidated; these waters seem in partial redox equilibrium. The best hypothesis (Re in VII oxidation state and controlled by Re metal) yielded a very negative Eh(25°C) (-0.52 V). This value is however not consistent with field measurements: e.g. Clark *et al*., 1992 and Milodowski et al., 1998a give a Eh range between+ 0.10 V and + 0.30 V for almost all hyperalkaline samples.

Table 4.5 Saturation indices of M19 groundwater computed under the assumption of pH = 8 and Eh = -0.26 V at T = 25°C

ReS2	0.6	Pyrrhotite	-0.1	Uraninite	0.8
Se	0.8	Magnetite	-0.2	Gypsum	-0.02
Hematite	0.4	Goethite	-0.3	Quartz	-0.03
Troilite	0.01	Coffinite	0.01	Calcite	-0.03

The concentration of dissolved oxygen (DO) in several water samples has also been measured in previous field campaigns (Milodowski *et al*., 1998a, 1998b). The very low flow rate of most of the seepages means that DO values are in most cases influenced by contact with the atmosphere during sampling. In rare instances, however, the flow was sufficient to collect and measure rapidly DO, which gave values in the order of several mgL^{-1}. Although these field measurements were performed under difficult conditions and should be taken with caution, the presence of a significant concentration of DO in dripping waters cannot be discarded. However, as noted above, in chapter 5 and in Pedersen et al. (2004), the activity of microorganisms in the hyperalkaline spring waters of Maqarin show that these microorganisms are adapted to conditions with no or little dissolved oxygen. In addition, nitrate respiration is strongly suggested, which supports again the anaerobic state of the groundwaters in Maqarin. . This apparent disequilibria was also noted in Milodowski et al. (1992a) and, in fact, is not uncommon for natural groundwaters where true redox equilibrium is rare (e.g. Lindberg and Runnels, 1984). Although available information is contradictory and requires further field investigations, it seems that the hyperalkaline porewaters are probably in an anoxic to sub-oxic state but that the groundwaters are not necessarily reducing. Therefore, Re in the groundwaters was probably oxidised and controlled by dilution processes.

Previous investigations (Clark et al., 1992) establish the presence of Cr(VI) species in the groundwaters. Comparison of total dissolved Cr in groundwaters with the $Cr(OH)_3$ solubility limit is effectively consistent with this observation (Figure 4.13). Indeed, the total dissolved Cr concentration in these hyper-alkaline waters exceeds by more than one magnitude order the solubility of $Cr(III)(OH)_3(s)$. In addition, Eh-pH diagrams for Cr, Mn and Fe (Figure 4.13) were constructed using the geochemical tool JCHESS (Van der Lee and De Windt, 2000). The diagrams were constructed for a temperature of 25°C and taking into account activities of major ionic species (Ca^{2+}, SO_4^{2-}, Na^+, K^+). Total concentrations for Cr (10^{-5} mol L^{-1}), Fe (10^{-6} mol L^{-1}) and Mn (10^{-7} mol L^{-1}) were also assumed to represent the measured values in the hyperalkaline waters. In the Eh-pH region corresponding to Maqarin hyperalkaline waters, shown as a cross-hatched area on the diagrams of Figure 4.13, Cr(VI) dissolved species are dominant. In addition, mineral buffering of Eh and redox-sensitive species is suggested through a mineral assemblage grouping chromite, haematite, possibly different Mn(II,III,IV) oxides, and Ca-ferrite[16]. The observation of discrete Cr containing Fe-oxide type phases in Maqarin analogue cements (Milodowski et al, 1992a) is consistent with the choice to include chromite $FeCr_2O_3$ as one of the indicator mineral phases. It also agrees with the modelling work of Tweed et al (1992) on Cr in these groundwaters, even though pure chromite has never been reported.

[16] As noted by Tweed et al. (1992), although ferrite phases are of little relevance to a analogue cementitious repository due to their high formation temperatures, they have been reported in the ACZ at Maqarin (Milodowski et al., 1992a, 1992b), reflecting the high temperatures of formation of the ACZ.

Figure 4.13 *A- Speciation diagrams. (A): comparison of $Cr(OH)_3$ solubility (after Rai et al, 1987) and total dissolved Cr measured in groundwater samples (Appendix 3.1). Equilibrium with respect to $Cr(OH)_3$ is plausible for M19 water whereas existence of Cr(VI) species is suggested for M3 and M5 waters, in agreement with field observations. (B) (C) (D): simplified Eh-pH diagrams for Cr, Fe and Mn computed at 25°C for a Cr(tot) = 10^{-5} mol L^{-1}, Fe(tot) = 10^{-6} mol L^{-1} and Mn(tot) = 10^{-7} mol L^{-1} (Eh scale in V). Other major ions of the solution (Ca^{2+}, SO_4^{2-}, Na^+, K^+) were set at their computed activity from a previous CHESS speciation run (Van der Lee, 1998). The shaded area corresponds to the Eh-pH location of hyperalkaline waters from field measurements (Clark et al., 1992)*

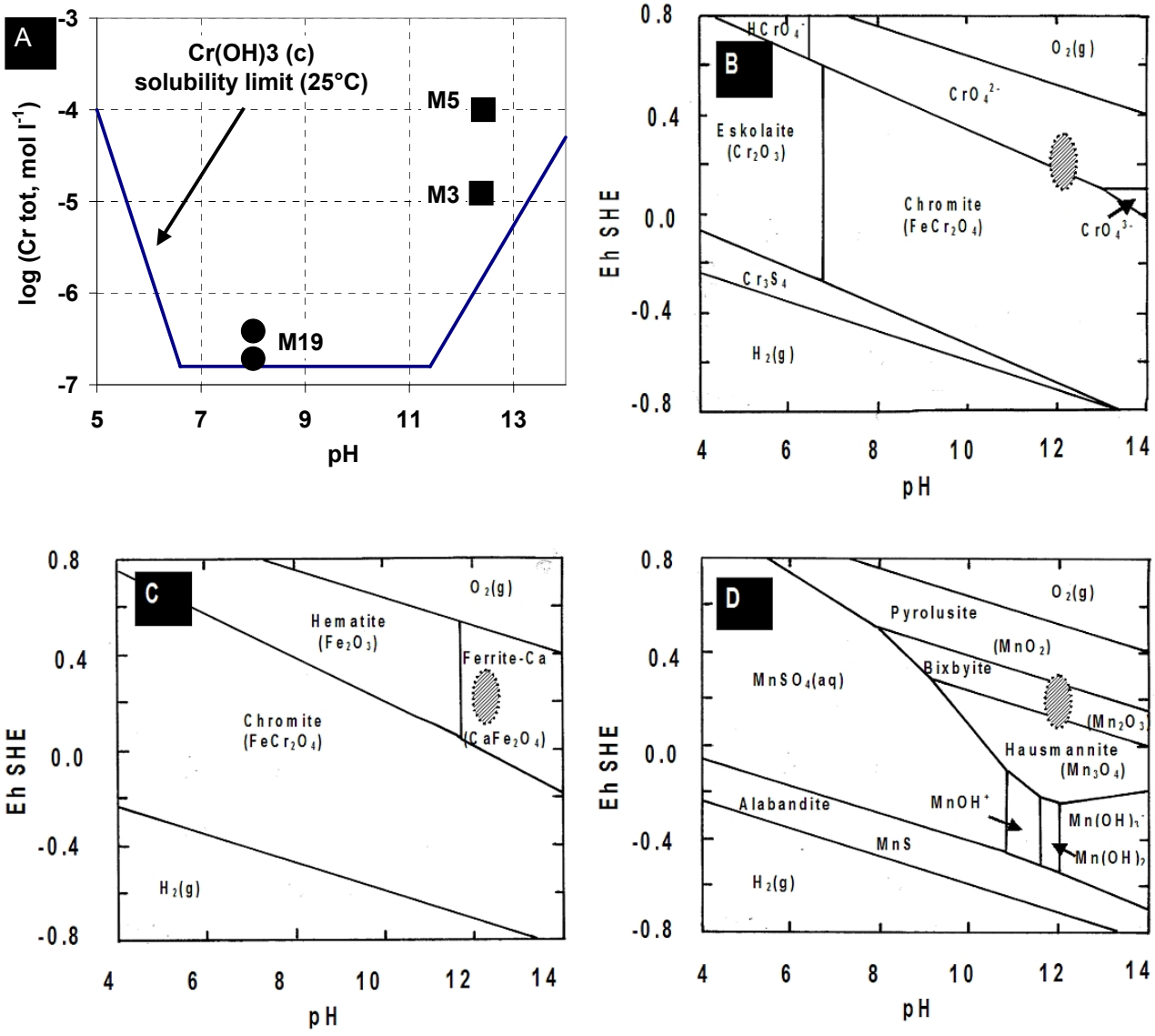

Table 4.6 Identification of rock samples for trace element analyses

N°	Identification	Description	Comment	BGS	UT2A	LARC
1	M00-1-23	Bituminous marl, Adit A-6, 50 m	Hand crushed - Agate mortar	X	X	X
2	M00-1-26	Vein fillings in Bituminous Marl Formation, Adit A-6, 100 m	Hand crushed - Agate mortar	X	X	X
3	M00-1-24	Basalt from just above Adit A6	Machine crushed - Agate mortar	X	X	X
4	M00-1-4	Relatively unaltered Metamorphic Zone marble, Adit A6, at 256 m depth (at point of adit branching)	Machine crushed - Agate mortar	X		X
5	M99-1-33d TZ (2)	111.5 m, Adit A-6, brownish to reddish-grey baked marl/clay biomicrite with veinlets and green secondary coatings	Hand crushed - Agate mortar	X	X	X
6	M99-1-33b TZ (4a)	113.5 m, Adit A-6, strongly altered metamorphic rock with red and white alteration products/colouration	Hand crushed - Agate mortar	X	X	X
7	DD-M99-2/4	Whole core subsample of largely orange-brown, ellestadite-rich Metamorphic Zone, from between 154-160 cm in borehole DD-M-99-2, Adit A-6	Fragments	X		
8	M99-1-41	Altered and hydrated metamorphic zone rocks (ACZ), Adit A-6, 140 m distance	Fragments	X	X	
9	M99-1-43a	Altered and hydrated metamorphic zone rocks (ACZ), Adit A-6, 130 m distance, 0.5 m above adit floor (west wall)	Fragments	X		X
10	M99-1-33b TZ (-2)	104 m, Adit A-6, Bituminous Marl, black and wet	Hand crushed - Agate mortar	X		X

4.4.4 Investigations on the solid phase

4.4.4.1 Basic data on solid samples

Solids selected for this study were sampled in May 1999 and in Spring 2000. These rock samples include (Table 4.6) :

- one sample of unaltered biomicrite (not combusted, baked or altered) collected in Adit A-6 at 50 m from the entrance of the Adit.
- two samples of biomicrite collected closer to the combustion front in Adit A-6 (104 m and 111,5 m from the Adit entrance).
- mineral filling collected from a fracture at 100 m from Adit A-6 entrance.
- a basalt sample collected above Adit A-6 at the main basalt outcrop along the road.
- samples from the ACZ showing various grades of reaction.

This selection was done in order to cover typical rock types encountered on the site and susceptible to release Re to ground waters. A brief description of the samples is given in Table 4.7. The characterisation of several of these samples was completed using XRD and other techniques, in particular for samples M00-1-23, M00-1-4, M99-1-41 and DD-M99-2/4 in connection with leaching experiments (see sections 4.6 and 4.7). Some other samples were also characterised in the framework of magnetic investigations (see section 4.5). Sample M00-1-26 (vein fillings) was shown to consist mainly of gypsum and calcite.

4.4.4.2 Bulk analyses of trace metals in the samples

In this exploratory investigation, the reliability of bulk analyses was a greater priority than the number of data. This is why several of the samples were analysed in parallel by three independent laboratories using their own protocol (BGS (UK), CEA/LARC (Cadarache), UT2A (Bordeaux University), see appendix 4 for details). About 15 g of each sample was ground in an agate mortar and carefully separated in three equivalent sub-samples that were distributed to the laboratories in tight polycarbonate tubes. Between each sample, the mortar was washed with water, ethanol and then decontaminated by grinding Fontainebleau sand (99 % quartz) and then washed again with water and ethanol. For several very hard samples (basalt, some analogue cements), a grinding machine was used. The splitting of samples between the different laboratory is reported in Table 4.6. In all cases, direct mineralisation by appropriate acid mixtures was found to be more reliable than other protocols using alkaline fusion.

Metals analysed in common by the different laboratories were Mo, W and Re (Table 4.7). LARC (Cadarache) also analysed Cr, Mn, Fe, Cu, Zn and Sr on several of the samples (Table 4.8). The major difficulty encountered in comparing results produced by the different laboratories is related to the initial drying protocol of the samples: UT2A (no drying), BGS (drying at 40°C), LARC (drying at 105 °C). Indeed, water content of several samples is very high (> 30% for 2 samples). The reference chosen to normalise concentration data was taken as the BGS drying protocol, because this laboratory analysed all of the samples. The concentrations given by the other laboratories were recomputed to a drying state equivalent to that of BGS. Another difficulty considered was that, despite care in preparing and distributing the samples, concentrations might fluctuate, due to heterogeneities between the different fractions analysed by the laboratories. However, except for one or two samples, results obtained by the different labs show an excellent consistency (Table 4.7).

Mo: most values range between 1 and 35 mg kg^{-1} (= µg g^{-1} = ppm). This concentration range is compatible with values given in Milodowski et al. (1992a). Analytical means were at that time less sensitive and a < 25 ppm is often quoted. The high value (~160 ppm) found by UT2A on sample M99-1-41 was verified and confirmed. It probably corresponds to a concentration fluctuation, suggesting a heterogeneous distribution of Mo in dispersed phases. Except for this value, excellent consistency is found between results. Analogue cements (20 to 35 ppm) present larger concentrations than the biomicrite (~10 ppm) and fracture fillings or strongly altered products (~3 ppm). Strong concentration variations occur along Adit A-6, from the marl to the ACZ. These result suggest that strong Mo concentrations, found in the hyperalkaline waters, are probably linked to leaching the ACZ.

Table 4.7 Summary of results for Mo, W and Re analyses on bulk rock samples

Identification	Mo	Mo	Mo	W	W	W	Re	Re	Re	mass loss at 40°C
	mg/kg	mg/kg	mg/kg	mg/kg	mg/kg	mg/kg	mg/kg	mg/kg	mg/kg	%
	BGS	UT2A	LARC	BGS	UT2A	LARC	BGS	UT2A	LARC	BGS
M00-1-23	9.7	8.8	8.5	0.21	0.27	0.21	0.15	0.090	0.11	12.30
M00-1-26	1.6	1.8	1.6	0.19	0.15	<0,2	0.06	0.038	<0,1 (~0,05)	27.20
M00-1-24	1.4	0.9	1.3	0.16	0.27	<0,2	<0.010	0.011	<0,1	0.50
M00-1-4	21.4	n. a.	20.0	0.21	n. a.	<0,2	1.21	n. a.	1.00	1.30
M99-1-33d TZ (2)	10.6	7.8	9.1	0.30	0.54	0.32	0.05	0.098	<0,1	8.90
M99-1-33b TZ (4a)	2.4	2.4	3.5	0.24	0.63	0.26	<0.010	0.016	<0,1	26.70
DD-M99-2/4	25.9	n. a.	n. a.	0.55	n. a.	n. a.	0.09	n. a.	n. a.	0.50
M99-1-41	26.8	161.6	n. a.	0.39	0.40	n. a.	0.06	0.020	n. a.	1.00
M99-1-43a	33.5	n. a.	33.0	0.31	n. a.	0.29	0.04	n. a.	<0,1 (~0,03)	4.90
M99-1-33b TZ (-2)	20.8	n. a.	17.9	0.32	n. a.	0.42	<0.01	n. a.	<0,1	10.20

Table 4.8 Bulk rock analyses for selected metals and Sr (LARC, Cadarache)

Identification	Description	Cr[17]	Mn	Fe	Cu	Zn	Sr
		mg/kg	mg/kg	mg/kg	mg/kg	mg/kg	mg/kg
M00-1-23	Bituminous marl, Adit A-6, 50 m	330	29	6600	31	150	1600
M00-1-26	Vein fillings (mainly calcite + gypsum)in Bituminous Marl Formation, Adit A-6, 100 m	37	1	300	25	2200	2400
M00-1-24	Basalt from just above Adit A6	200	1200	80000	47	110	860
M00-1-4	Relatively unaltered unhydrated Metamorphic Zone marble, Adit A6, at 256 m depth (at point of adit branching)	490	33	10000	51	120	1700
M99-1-33d TZ (2)	111.5 m, Adit A-6, brownish to reddish-grey baked marl/clay biomicrite with veinlets and green secondary coatings	1080	28	12000	62	100	1200
M99-1-33b TZ (4a)	113.5 m, Adit A-6, strongly altered metamorphic rock with red and white alteration products/colouration	550	28	14000	18	290	440
DD-M99-2/4	Whole core subsample of largely orange-brown, ellestadite-rich Metamorphic Zone, from between 154-160 cm in borehole DD-M-99-2, Adit A-6	n. a.	n. a.	n. a.	n. a.	n. a.	n. a.
M99-1-41	Altered and hydrated metamorphic zone rocks (ACZ), Adit A-6, 140 m distance	n. a.	n. a.	n. a.	n. a.	n. a.	n. a.
M99-1-43a	Altered and hydrated metamorphic zone rocks (ACZ), Adit A-6, 130 m distance, 0.5 m above adit floor (west wall)	400	48	11000	62	300	900
M99-1-33b TZ (-2)	104 m, Adit A-6, Bituminous Marl, black and wet	480	34	15000	42	200	3500

[17] These values compare well with the data of Loop and Hall (1992).

W: most values range between 0.1 and 0.4 ppm. Variations between different types of rocks (such as analogue cement, basalt, and biomicrite) are often of the same order of magnitude as fluctuations observed for a given sample analysed by the three different laboratories. No clear correlation can be found between W concentration and other data. W seems more concentrated in the analogue cements than in the initial biomicrite.

Re: although measured concentrations are distributed over a two orders of magnitude range (< 0.01 ppm to ~1 ppm; Note that the natural abundance of Re in the Earth crust is about 0.0007 ppm), consistent data was provided by the different laboratories. Basalt has a very low concentration. Unaltered biomicrite (M00-1-23) has a Re concentration around 0.1-0.15 ppm whereas biomicrite samples having undergone baking show significantly lower concentrations (M99-1-33b TZ(4a) or M99-1-33b TZ(-2) for example). Note that palaeotemperature profiles derived from the magnetic investigations (section 4.5) are in good agreement with this observation (Re(VI) is volatile above ~270°C, which corresponds well to distance > 104 m from Adit A-6 entrance). The Re concentration in unaltered biomicrite corresponds to the range of concentration observed in blackshales (0.05 to 0.2 ppm). Most altered analogue cements show Re concentrations somewhat lower than the initial biomicrite (0.03 to 0.09 ppm) whereas one analogue cement sample, showing signs very slight alteration, has by far the highest Re concentration of all samples (~1 to 1.2 ppm).

Se: Se data on rocks were acquired in parallel analysis runs in connection with leaching experiments (see below). Two analogue cement samples were analysed (M99-1-41 and M00-1-4), yielding respectively 15 ppm and 10 ppm of Se. However, these values should be considered with caution. Previous data (Milodowski et al., 1992a, 1992b) give Se concentrations for the biomicrite in the range of 140 to 260 ppm and for analogue cements in the range of 20 to 120 ppm. Analyses performed in Phase II (Milodowski et al, 1998a) give Se concentrations in the biomicrite around 50 ppm. Se is thus suspected to have been mobile during the combustion process, probably due to volatile Se species.

Fe, Mn, Cr, Cu, Zn, Sr: although the data set is not very extensive, several interesting features can be noted. The iron concentration of the analogue cements is roughly 1.5 to 2 times the iron concentration in the biomicrite. A similar increase is noted for Cr, Cu and to a lesser extent Zn. In contrast, Sr does not seem to follow this pattern. Also, marked fluctuations of Cr concentration seem to exist at the vicinity of the combustion front (a complete profile of metal concentrations along Adit A-6 is presented in section 4.5, on magnetic investigations).

In summary, several important results are found from bulk analyses of several trace elements in these samples:

- *two main (potential) source terms for Re were identified:* (i) the Cretaceous biomicrite (M00-1-23) with a concentration level of 0.1 to 0.15 ppm. This source term may explain a base level of Re in most groundwaters collected around Maqarin. (ii) a analogue cement sample presenting a low alteration grade (M00-1-4) with a high concentration of Re (~1 to 1.2 ppm). This source term may explain the high concentration level of Re in the Western Springs.
- baked biomicrites (samples M99-1-33b TZ(4a), M99-1-33d TZ(2) or M99-1-33b TZ(2)) have lost a large part of the initial Re of the biomicrite. One of the explanation for this loss could be linked with an oxidation reaction associated

with combustion, leading to the formation of volatile Re(VII). The combustion front appears to be linked to an oxidation process (see Section 4.5); the temperature profile derived in this Chapter is consistent with the volatility of Re(VII) after 104 m in Adit A-6 (T > ~250 °C). Movements of organic matter inside the porosity of the biomicrite at the vicinity of the combustion front, although they are suspected (see Section 4.5), cannot account for high enrichments of Re in the analogue cement M00-1-4. The best hypothesis accounting for high local Re enrichments is Re(VII) volatility, making possible Re transport in the vapour phase. The exact process causing Re reconcentration is not known (such as condensation, salt precipitation after water evaporation, or sorption). Possibly, part of Re remained at valence VII after reconcentration.

- the lower concentration level of Re in hydrated analogue cements, compared to the analogue cement M00-1-4, is consistent with the hypothesis that Western Springs hyperalkaline waters, with high dissolved Re, represent younger leachates than Eastern Spring groundwaters. In addition, this would support the hypothesis of VII valence for Re in analogue cements.
- the level of Re in sample M00-1-26 (fracture fillings) is not negligible. XRD has revealed that these fillings were mainly constituted of calcite and gypsum. This supports again the valence VII for Re, SO_4^{2-} being substituted by ReO^{4-}.
- enrichment or depletion factors of several trace elements, between the original biomicrite and analogue cement samples, are noteworthy. That for Fe is ~1.5 - 2. Except for samples having probably undergone alteration, a similar factor is found for Cr and Cu. For Mo, enrichment factors are generally between 2 and 3. For Re, they may go up to 10, although marked depletions are also observed. These observations are probably due to general mass losses in the rocks (CO_2, organics) and also to the mobility of several elements during the combustion process. In the case of Re, which is volatile when in the the VII valence state, a redeposition process is possible after cooling of the combustion zone. This could explain why analogue cement samples show weak alteration signs and very high Re concentrations.

4.4.4.3 Investigations of Cr using microanalytical techniques

Three samples were selected Cr analysis: an unhydrated analogue cement (M00-1-4, Adit A-6, 256 m), a hydrated analogue cement (M99-1-41, Adit A-6, 140 m) and biomicrite (M00-1-23, Adit A-6, 50 m). These materials were also used for column leaching experiments (see section 4.7) and their major element and mineralogic characterisation is given in this section. These three samples are a subset of samples analysed for trace elements (see above in this section). The characterisation of Cr localisation and speciation in these samples was carried out using several techniques (see Appendix 4 for details):

- SEM/EDX as a reconnaissance tool, in order to identify phases with high concentrations of Cr (detection limit ~2000 ppm)
- XANES/µXANES in order to characterize the oxidation state of Cr in the samples (~10 ppm detection limit). The µXANES technique facilitated visualisation of the heterogeneous distribution of Cr(III) and Cr(VI) at the micrometer scale.

- EXAFS in order to characterize the crystalline sites occupied by Cr. The interpretation of EXAFS spectra is still provisional, because Cr is hosted by several different phases.
- Nuclear Microprobe (PIXE) enabled analysis of heavy elements (Z > 20) with a far better detection limit than SEM/EDX and µm lateral spatial resolution. However, the shape of the interaction volume between the proton beam and the sample is that of a ~30 µm long and ~2 µm diameter tube, preventing the accurate analysis of very small grains.
- LA-ICPMS maps and profiles for ^{52}Cr and several other elements were also performed

SEM-EDX analysis confirmed that the biomicrite sample (M00-1-23) is composed of a matrix rich in Ca and Mg in which foraminifera tests are dispersed (Figure 4.14). Fe and S are the major elements detected in the tests suggesting the presence of pyrite. According to the chemical analysis of various tests it appears that chromium is also detected by SEM-EDX and micro-SXRF. A positive, but not systematic, spatial correlation exists between Cr-Fe and S amounts whereas Cr and Ca are inversely correlated as shown by chemical maps obtained with synchrotron-based micro-X-ray fluorescence (Figure 4.14 E-F). The Cr distribution in the biomicrite looks simple, with one or two main Cr-bearing products, containing also Fe or Fe and S, located in fossil tests. The calcite matrix, in contrast, is depleted in Cr.

Table 4.9 *Simplified mineralogical model of the different rock samples derived from chemical and XRD analyses. For the two cement samples, silica was supposed to be associated with larnite and ellestadite. Careful SEM-EDX observation of the samples showed however that a significant part of the silica was combined in ill-defined Ca-Al-Si-K-S gels and phases as well as, to some extent in sample M00-1-4, in ettringite-thaumasite solid-solutions. A large part of the silica was grouped as larnite, one of the identified phases*

Mineral\Sample	**M00-1-4 Unhydrated cement**	**M99-1-41 Hydrated cement**	**M00-1-23 Biomicrite**
Calcite (*)	65.0	39.8	71.0
Ettringite	5.0	20.8	–
Ellestadite (**)	<1.0	19.8	–
Brownmillerite	4.0	5.6	–
Larnite	13.6	14.0	–
Gypsum	< 1	–	–
Fluorapatite	3.2	–	6.4
Monocarboaluminate	6.8	–	–
Kaolinite	–	–	10.0
Pyrite			2.4
Chalcedony			4.0
Organic matter			6.0
Total	97.6	100	99.8

Figure 4.14 *Top and middle: SEM image of a foraminifera test surrounded by the Ca-rich matrix. Chemical Maps of the foraminifera test and the embedding matrix obtained with SEM-EDX: A) BSE image, B) Fe Kα, C) Ca Kα, D) S Kα. Bottom: Synchrotron-based micro-X-ray fluorescence (µ-SXRF) E) Ca and F) Cr maps of the foraminifera test and the embedding matrix*

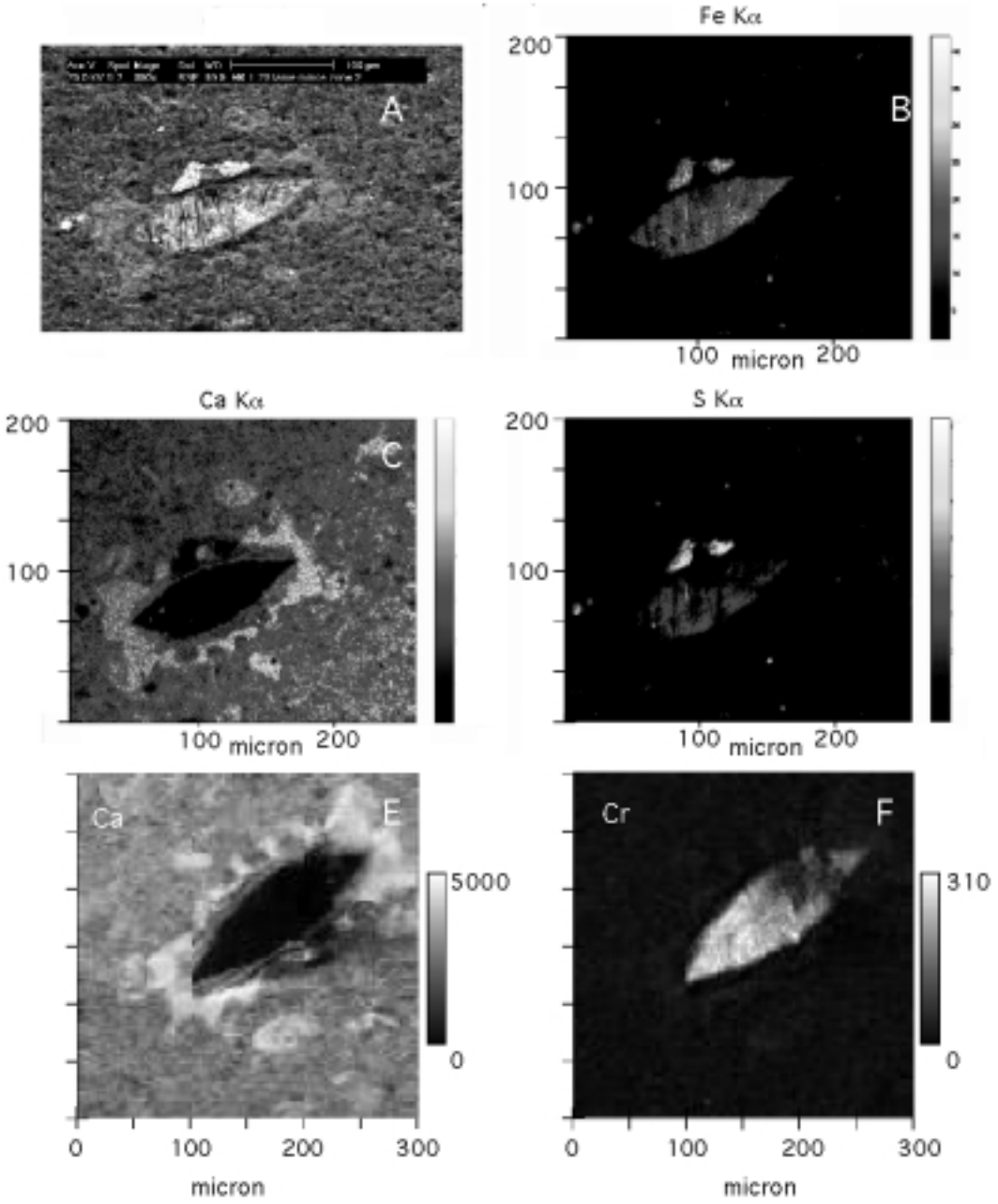

The texture of the M00-1-4 analogue cement sample, as revealed by SEM-EDX analyses, appears to be complex (Figures 4.15 and 4.16). This material is similar to a sponge skeleton of carbonate (calcite, aragonite) containing inclusions of various minerals from a submicron size to more than 50 µm in diameter (Figure 4.16). The sample is crossed by rare fractures partly filled with a thaumasite ($(Ca_3Si(OH)_6\ 12\ H_2O)_2\ (CO_3)\ (SO_4)\ .\ 2\ H_2O$)-ettringite ($(Ca_3Al(OH)_6\ 12\ H_2O)_2\ (SO4)_3\ .\ 2H_2O$) product and a potassium Ca-Al-Si-S phase. Pores of the carbonate network are generally filled with a variety of Ca-Si-Al gel-like phases, thaumasite-ettringite and a Ca-Al-Si-

S-unidentified potassium containing phase. Larnite crystals are rarely found and, as noted by Milodowski et al. (1992a, 1992b, 1998a, 1998b), the major Ca-Si bearing phases appear to be gels and ill-defined, often amorphous, phases. These probably correspond to CSH-type phases. This is why the phase reconstruction given in Table 4.9 is, for the analogue cements, simplified and has been elaborated by sharing silicon between two minerals (larnite, ellestadite). Apatites and ellestadite crystal are identified by EDX and are often observed as crystals from 5 to 20 μm size in small clusters. Oldhamite (CaS), previously reported in Maqarin analogue cements (Milodowski et al., 1992a, 1992b) is found as rare ~10 μm diameter grains. A variety of other mineral phases, usually of small size (< 1 μm to 5 μm in diameter) is observed. These mineral grains usually contain as major cations Ca, S, Si and Fe in variable proportions accompanied by numerous trace elements (Cr, V, Ti, Mn, Ni, Cu, Zn, Se, etc). Cr is detected by EDX in several mineral phases but could not be quantified because of the small size of most grains, because of their variable composition and also due to the relatively high detection limit of the EDX system (~2000 ppm) increasing the statistical errors. However, the minerals can be classified qualitatively according to their Cr content : very low Cr content (calcite, thaumasite, oldhamite), variable Cr content (Si-Ca-Al-S gel phases, Ca-Fe-S rich grains, apatite) and higher Cr content (ellestadite, K-bearing Ca-Si-Al-S phase). Cr distribution in this sample thus appears complex and controlled by several host phases. The highly heterogeneous distribution of Cr is confirmed by micro-SXRF. A micro-SXRF Cr Kα fluorescence line-scan (Figure 4.15) confirms that the concentration of Cr in the thaumasite-ettringite fractured zone is low whereas distinct rich spots are measured in the matrix.

Figure 4.15 BSE SEM image of the unhydrated analogue cement M00-1-4 in a fractured zone. The fracture contains a thaumasite- ettringite type precipitate. Micro Cr SXRF transverse scan of the unaltered analogue cement (sample M00-1-4) across a fracture (ettringite-thaumasite vein). Cal.: calcite; Ap.: apatite; Tha.: thaumasite type phase

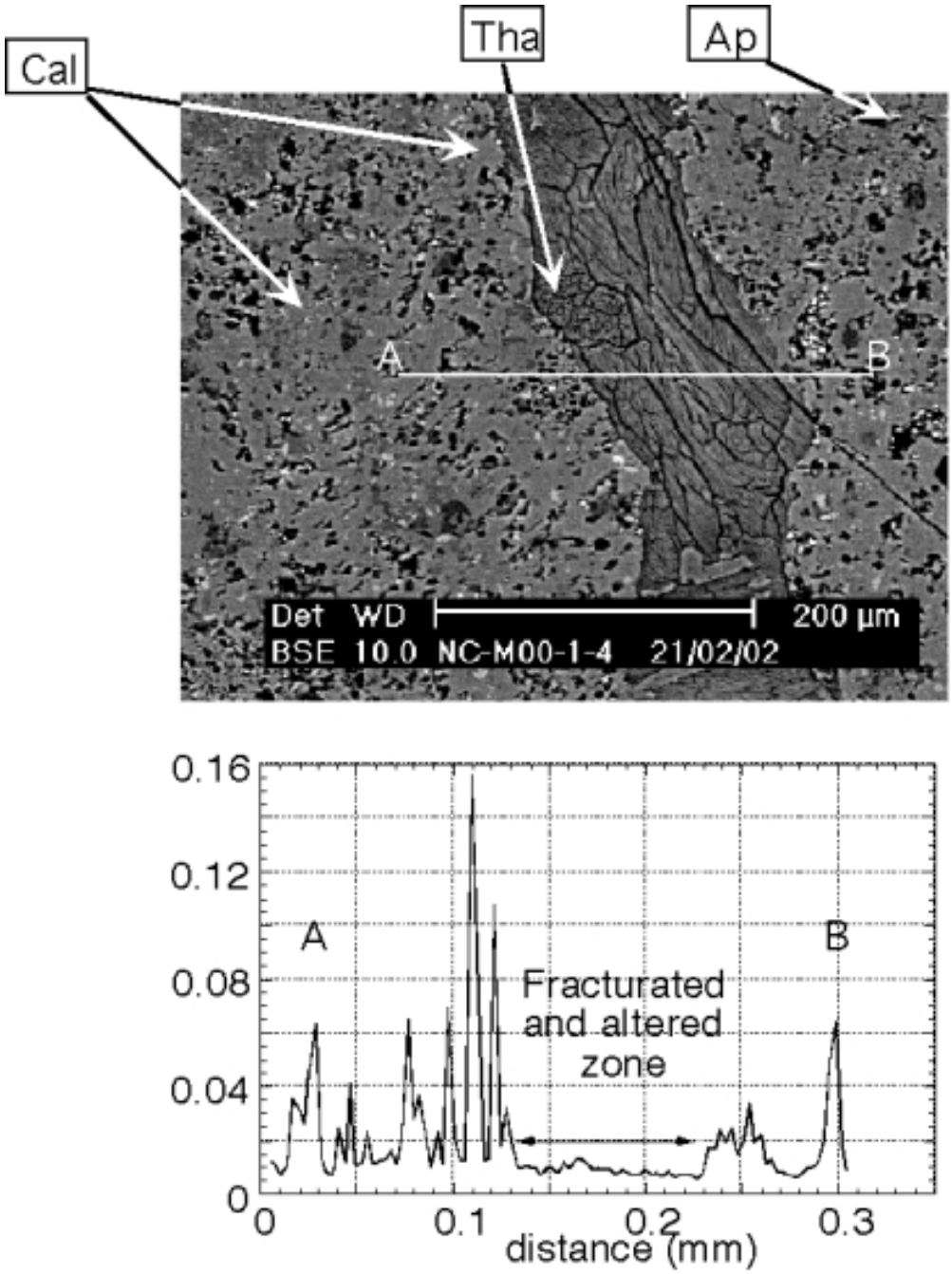

Figure 4.16 *SEM BSE aspects of a polished cross-section of sample M00-1- 4. Top: large-scale images showing the porous calcite (C) matrix, the fracture partly filled with thaumasite (T). The major potassium bearing phase is found the porous matrix (K1) or as a partly dissolved phase in the fracture (K2). Middle: Small Fe-S rich grains; dark vacuoles are filled with gel-like materials. The round grain on the right is a calcium sulphide. Bottom: pores in the matrix skeleton filled with thaumasite type products and surrounded by Fe-S rich grains. These large pores are thought to be remnants of fossil tests, initially filled with glauconite and iron sulphide*

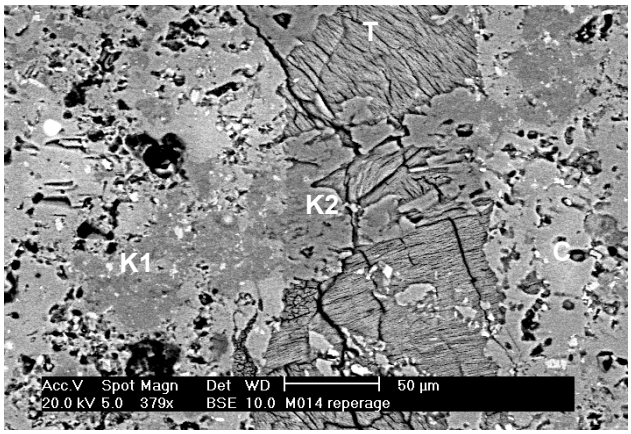

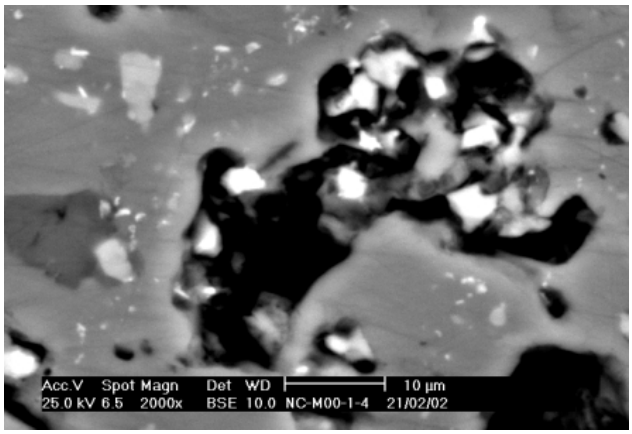

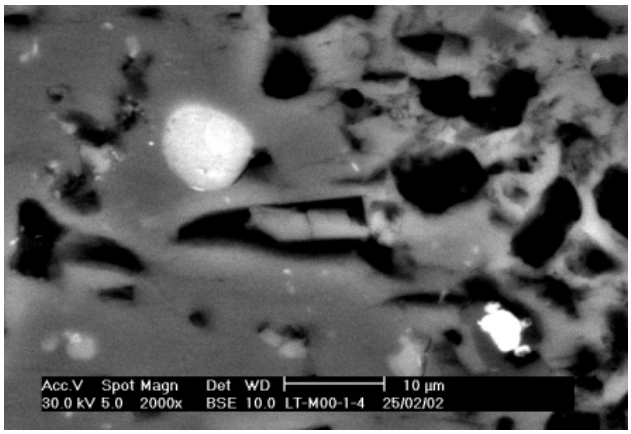

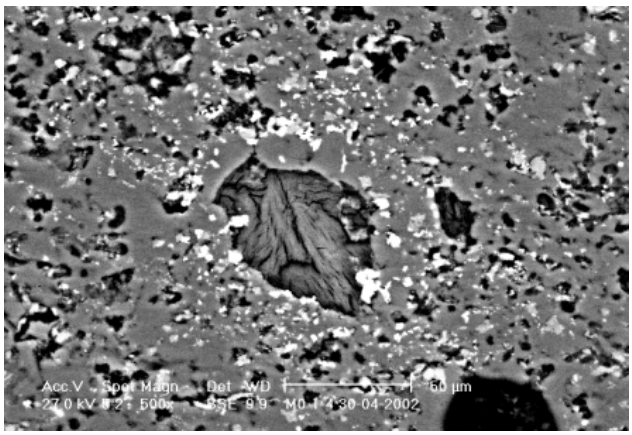

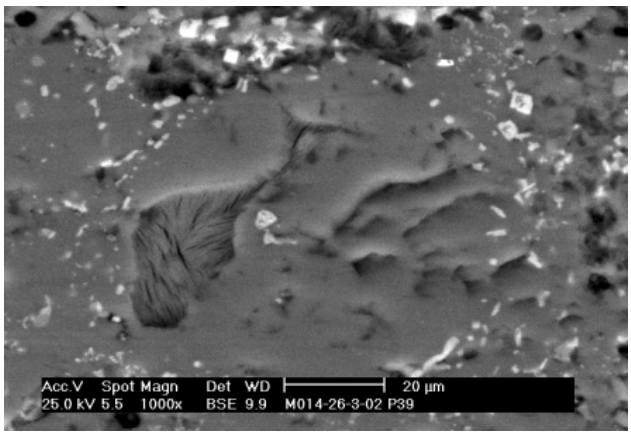

Table 4.10 Evaluation of the Cr(VI)/Cr(III) ratio in the studied samples

Samples	Area of the pre-edge	Cr(VI)/Cr(tot)
Reference compounds	0.022	0%
	0.242	20%
	0.488	50%
	0.630	90%
	0.722	100%
Biomicrite	0.024	0.2%±2,6
Fresh analogue cement	0.028	0.4%±2,6
Hydrated analogue cement	0.171	11.4%±2,6

Sample M99-1-41 (hydrated analogue cement) displays a thorough vein network, filled with ettringite products, surrounding pockets of partially hydrated analogue cement (Figure 4.17). Thaumasite type end members were also observed in fractures. Calcite is present in the analogue cement matrix but at a lower level than in sample M00-1-4 (unhydratedanalogue cement). A Ca-P-Si-S-Al phase is detected; this could correspond to a solid solution between pure ellestadite and apatite type end-members. Red colours are probably due to very finely dispersed iron oxides such as haematite (Milodowski et al., 1992a; Vandamme et al., 2003). Cr was rarely detected with SEM-EDX, indicating a lower level of local accumulation compared to the unhydrated analogue cement sample.

Bulk Cr K edge XANES of the three samples with different reference compounds are presented in Figure 4.18. The analysis of the pre-edge region (5985-6000 eV) allows the characterization of the Cr(VI)/Cr(tot) ratio. The quantification of the pre-edge was performed after the deconvolution of the pre-edge region into a linear combination of Gaussian peaks and an arctangent step function as done in Szulczewski et al. (1997). The area of this pre-edge peak in a Cr spectrum is quantitatively proportional to the amount of Cr(VI) in the sample. A calibration curve correlating the area of the pre-edge peak and the Cr(VI)/Cr(tot) ratio was constructed using reference samples of known Cr(VI)/Cr(tot) ratios.

Table 4.11 details the area of the pre-edge for the reference samples and the three studied samples and provides the corresponding Cr(VI)/Cr(III) ratios. Cr from the biomicrite and the unaltered analogue cement is mainly in the Cr(III) form. This result shows that the Cr was not oxidised before the formation of the analogue cement through combustion. The very significant point is that 11.4 ± 2.6 % of the Cr is in the Cr(VI) valence state in the hydrated analogue cement. Even if this information should be considered as an average redox state of Cr in the altered analogue cement, Cr(III) has been partly oxidised during long-term alteration. This result is crucial to predict the long-term transfer of Cr.

Cr in the biomicrite is mainly in the Cr(III) form and SEM-EDX and micro-SXRF revealed that Fe- and Cr-oxides can be considered as plausible Cr-bearing phases. Cr concentration in the carbonate matrix is very low (Figure 4.15) and micro-XANES spectra recorded in the calcite matrix were too noisy to be analyzed. Micro-XANES spectra recorded in various foraminifera tests always exhibit same features as the bulk-XANES spectrum of biomicrite. Therefore the Cr speciation within fossil tests, where this element has accumulated, is homogeneous and does not vary from test to test.

The Cr(VI)/Cr(tot) ratio variation at the micron scale in the unaltered analogue cement (M00-1-4) has been determined along a 300 µm line crossing the fracture (Figure 4.19). The Cr(VI) and Cr(tot) profiles are not strongly correlated. For example, point #1 and point #2 correspond to high Cr concentrations, but the Cr(VI) intensity in point #1 is lower than in point #2. The difference between both profiles is illustrated by the Cr(VI)/Cr(tot) profile (Figure 4.10). In the case of point #1 the Cr(VI)/Cr(tot) ratio is lower than 7 % whereas it reaches 40% in point #2. Micro-XANES spectra have been recorded for both points (Figure 4.20) and the Cr(VI)/Cr(tot) ratio is confirmed (7% and 49% respectively).

Figure 4.17 *BSE SEM image and EDX spectra of two ROI's of the altered analogue cement. The area illustrates the location of the Cr(VI)/Cr(tot) chemical map presented in Figure 4.22. Large ettringite-filled veins are clearly visible in grey on this micrograph of a polished section of the sample*

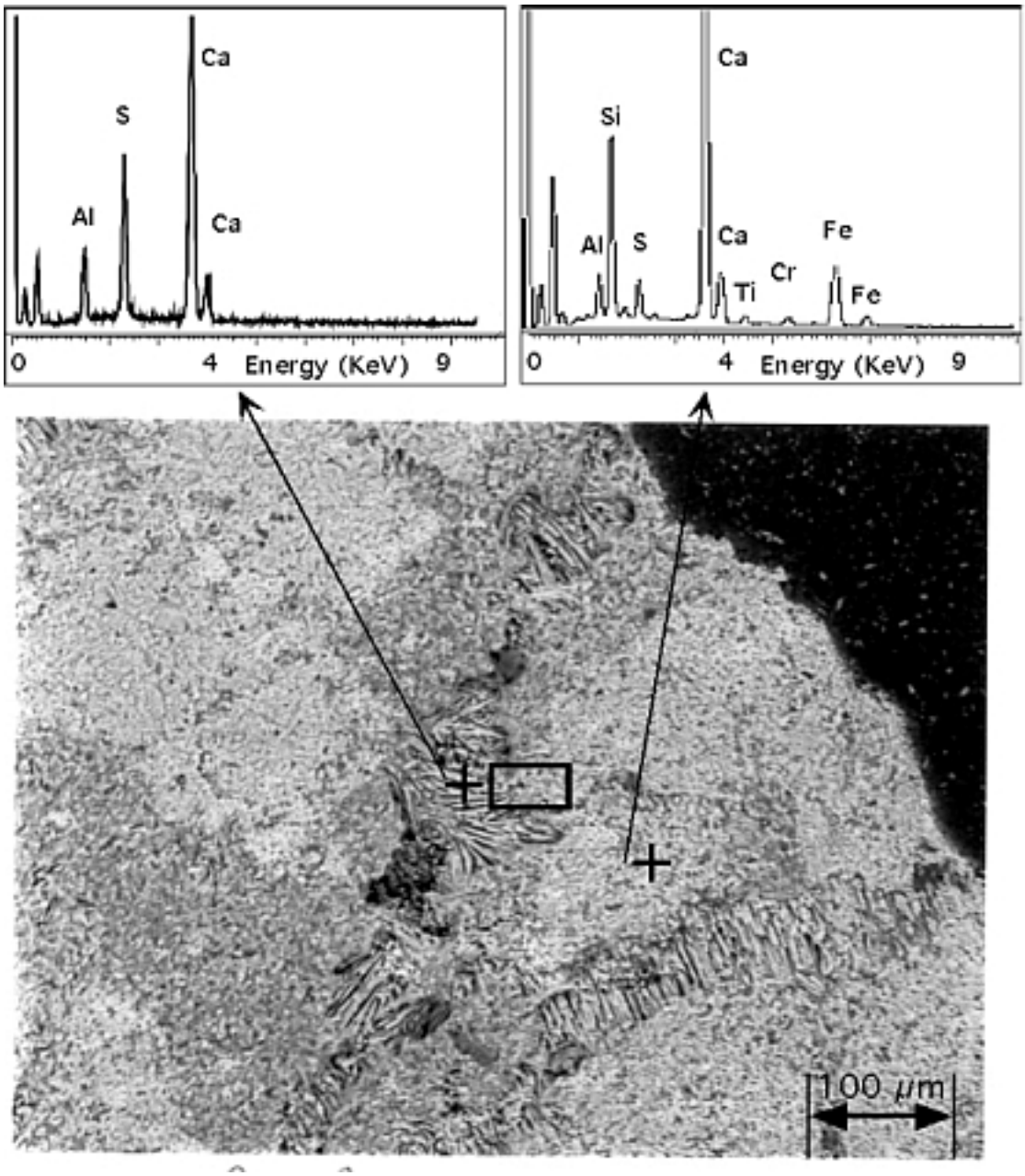

Figure 4.18 XANES spectra of the three Maqarin samples compared with spectra of different reference compounds (chromite, stichtite (Cr-hydrotalcite), fuschite (Cr-muscovite), Cr(OH)3, C3A+Cr(VI) (= (CaO)3Al2O3 hydrated in presence of Cr(VI))

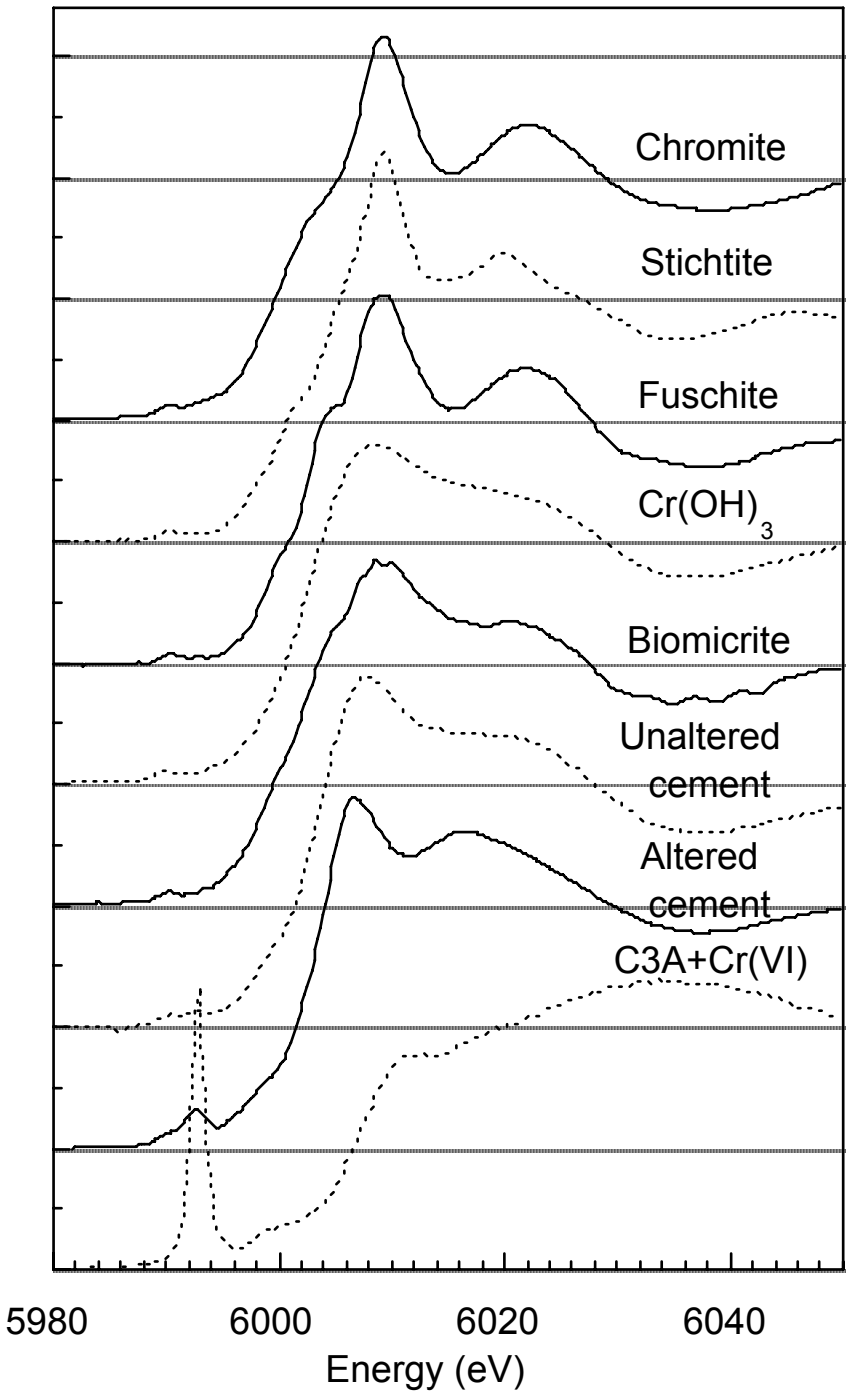

Table 4.11 Evaluation of the Cr(VI)/Cr(III) ratio in the studied samples

Samples	Area of the pre-edge	Cr(VI)/Cr(tot)
Reference compounds	0.022	0%
	0.242	20%
	0.488	50%
	0.630	90%
	0.722	100%
Biomicrite	0.024	0.2%±2,6
Unhydrated analogue cement	0.028	0.4%±2,6
Hydrated analogue cement	0.171	11.4%±2,6

Therefore, for two points separated by less than 10 µm, the content of Cr(VI) can change drastically. The analysis of the Cr(VI)/Cr(tot) profile reveals that the Cr(VI) fraction in the fractured zone is high, since the average Cr(VI)/Cr(tot) reaches ~50% whereas, in the less fractured areas, this ratio is approximately 20-30 % lower. Bulk-XANES of the unaltered sample presented in Figure 4.19, revealed a very low average Cr(VI)/Cr(tot) ratio (< 1%) in the bulk of the sample. Therefore the line scan (Figure 4.19) is not representative of the unaltered analogue cement bulk, but corresponds to analogue cement at a low alteration grade, due to the vicinity of the fracture. The alteration grade is, however, clearly lower than in the more 'thoroughly' altered analogue cement sample. This result indicates the importance of coupling bulk-XANES with micro-XANES analysis.

The analysis of the altered analogue cement sample indicates a similar trend to that seen in the fractured zone of the unaltered analogue cement. Figure 4.21 presents the evolution of the Cr oxidation state along a 0.8 mm line scan in a fractured zone, where it crosses two fractures. This line scan also reveals the extremely high heterogeneity of the Cr concentration. However the behavior of the Cr(VI) is more difficult to describe than for the weakly altered zones (such as in the fractured zone of the unaltered analogue cement (Figures 4.15 and 4.19). Even if the Cr(VI)/Cr(tot) ratio is high in the two fractures (average Cr(VI)/Cr(tot) for zones 1 and 3 are 0.34 and 0.26 respectively), rich Cr(VI) zones can be found between large fractures (rich Cr(VI) zone in the 0.68-0.78 mm zone (zone 4b: mean Cr(VI)/Cr(tot) = 0.32).

As noted above, there appears to be an inverse correlation between the Cr(VI)/Cr(tot) ratio and the Cr concentration and this has been visualised on a 2D chemical map. This map (Figure 4.22) was acquired with an unprecedented spatial resolution: 1x1 μm^2 at the border between a fracture and the matrix (Figure 4.17). The inverse correlation between the Cr(VI)/Cr(tot) ratio and the Cr concentration is clearly shown around points #1 and #2. The spatial distribution of Cr at the micron scale is highly heterogeneous. Notably, going from the fracture into the matrix, the evolution of the Cr(VI)/Cr(tot) ratio is not monotonous, but very irregular. EXAFS spectra (not shown here) were also recorded for the sample M00-1-4 at the Cr (K) absorption threshold. The preliminary interpretation and modelling of these spectra was carried out using both linear combination of standard spectra and direct numerical methods. An octahedral environment for Cr(III), close to that of CrO(OH), is proposed with Cr(III) and Fe(III) octahedra in a neighbour position. Cr-Fe distances of 2.98 Å and 3.5 Å correspond to edge and double corner sharing octahedra, respectively.

Figure 4.19 *Unaltered analogue cement - A) Cr(VI), Cr(tot) profiles and B) Cr(VI)/Cr(tot) line scan. The weighted average of the Cr(VI)/Cr(tot) is presented (dark line) for the fractured zone("moving rectangle average" based on the average of 20 points). The location of the line scan of the unaltered analogue cement is presented in Figure 4.15*

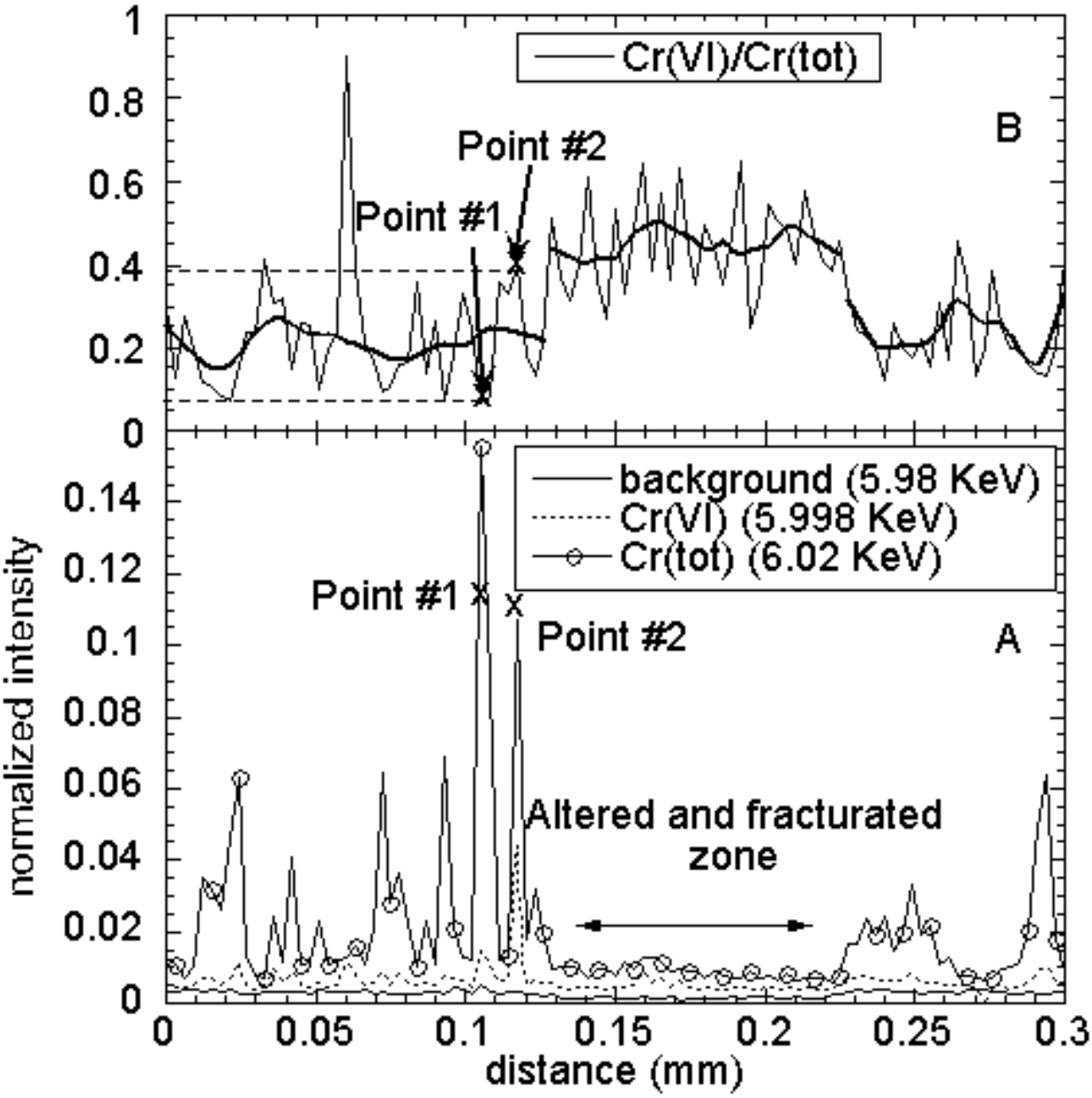

Figure 4.20 Micro-XANES spectra of point #1 and point #2 of the line scan presented in Figure 4.19

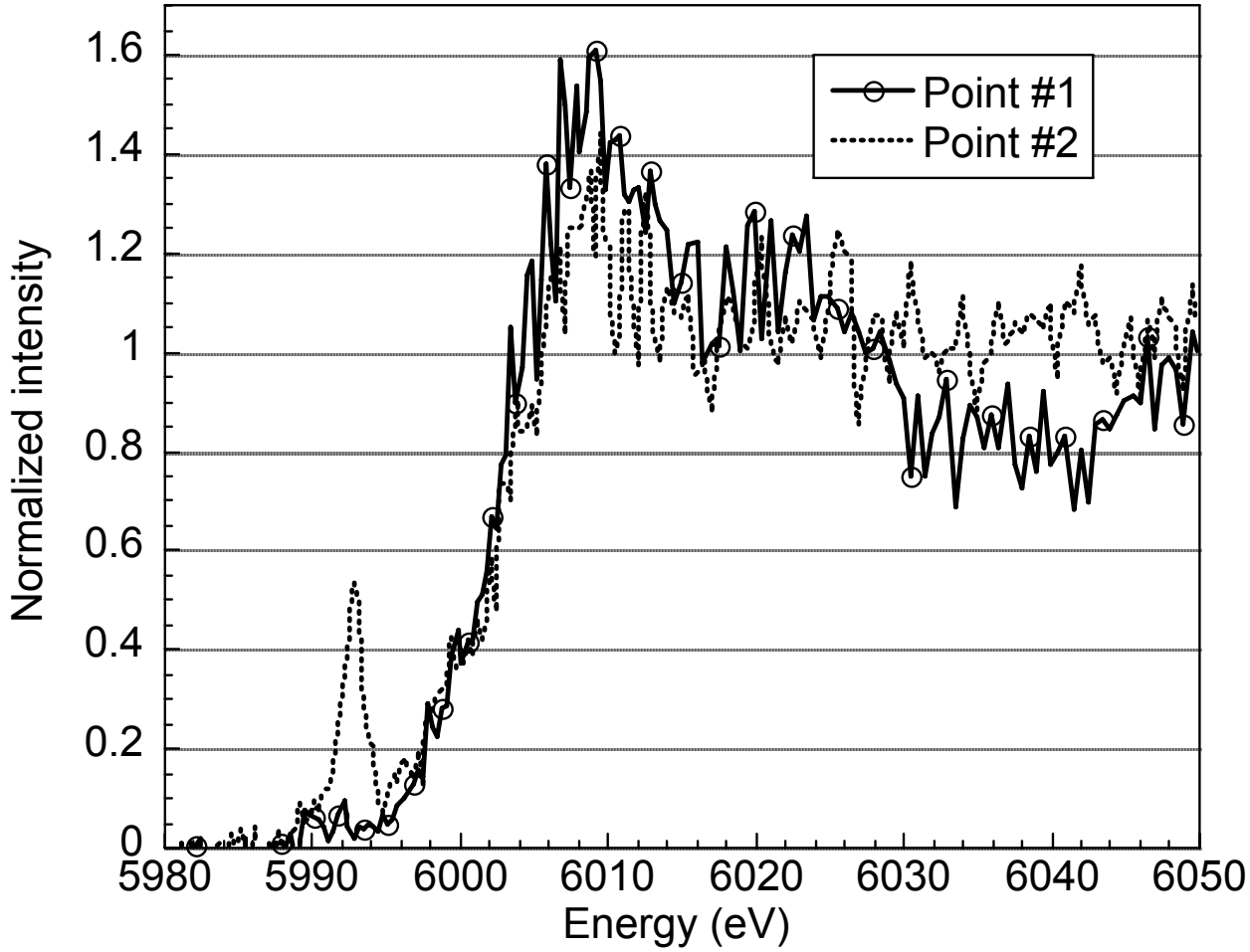

Nuclear microprobe (PIXE) analyses of sample M00-1-4 were performed in the Laboratoire Pierre Süe (CEA-CNRS) (Figures 4.23 to 4.27). These analyses were performed either on points, as linear profiles or as 2D maps. Because the analysed volume has the shape of a 2 µm diameter vs 25 to 40 µm length cylinder (depending on the X-ray energy and on the material properties), reliable analyses of single phases or mineral grains were difficult. Only for the minerals presenting large crystals (i.e. calcite, thaumasite and the large K-bearing phases) could point analyses be linked to the actual composition of the phase. Figures 4.23 and 4.24 show spot analyses performed on calcite, thaumasite and the unidentified K-bearing Ca –Si-S phase). PIXE analyses (see Figures 4.25 and 4.26) show the following points :

- the Cr distribution in analogue cement M00-1-4 is highly heterogeneous, as is Fe, Cu and Ni
- the spatial distribution of Zn seems less heterogeneous
- a good spatial correlation is found between Cr and Fe
- Cu and Se are spatially correlated, confirmating previous results of Phase I (Alexander, 1992)

Figure 4.21 Altered analogue cement (M99-1-41): A) Cr(VI), Cr(tot) profiles and B) Cr(VI)/Cr(tot) line scan. The weighted average of the Cr(VI)/Cr(tot) is presented (dark line) ("moving rectangle average" based on the average of 20 points). Zones 1 and 3, with low Cr(tot) and high Cr(VI)/Cr(tot) correspond to large fractures and zones 2 and 4 (4b) correspond to the matrix zone

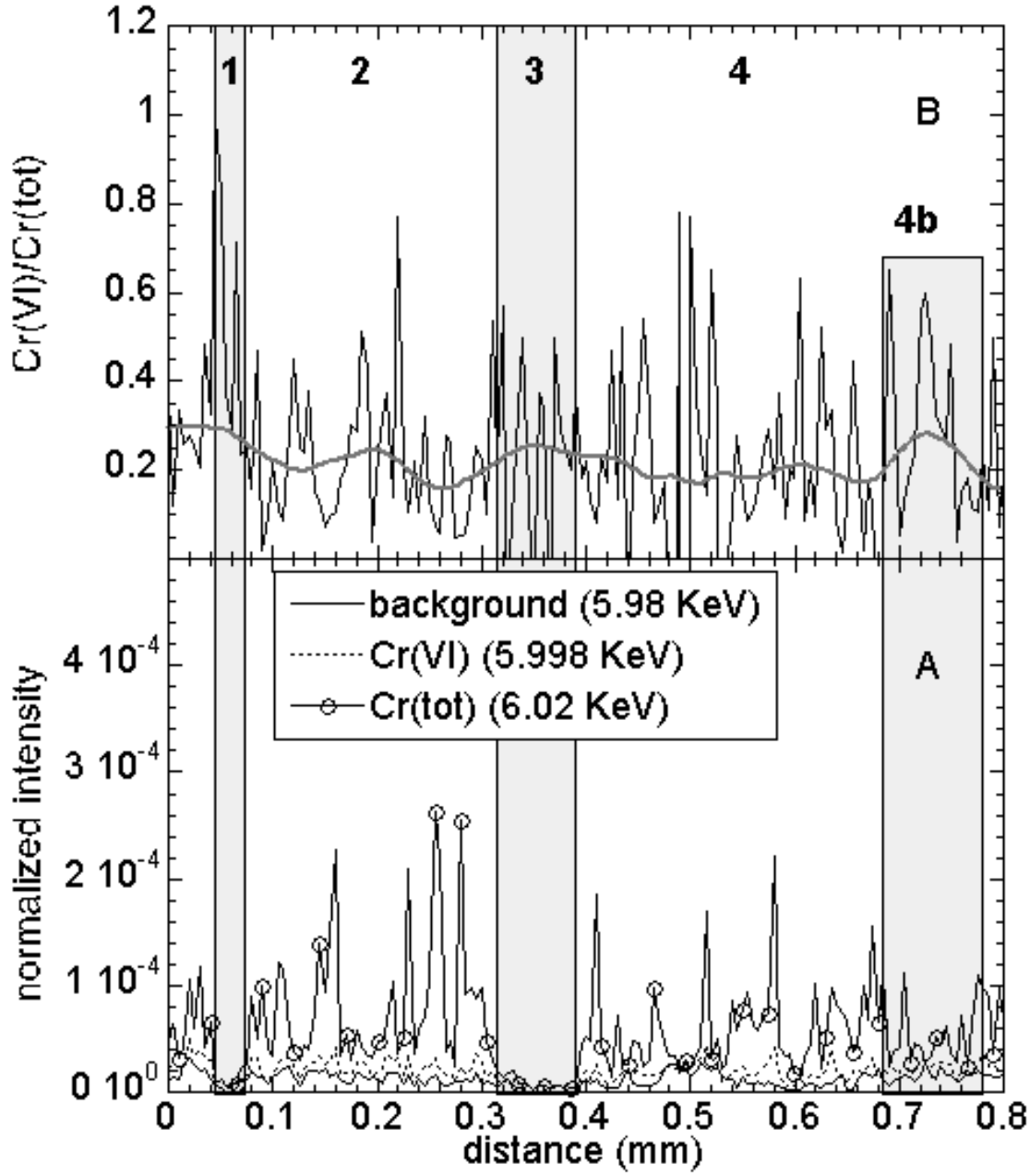

Due to a careful SEM reconnaissance, a PIXE profile was run on the same line along which μXANES data were recorded in sample M00-1-4 (Figure 4.15). Parallel representation of μXANES information and PIXE analyses are reported in Figure 4.27. A good agreement was found between total Cr (μXANES) and Cr (PIXE). Differences may be assigned to the different shapes of the analytical volume. There were also difficulties in superimposing, with μm precision, two profiles measured on two different machines with different specimen holders, stages and binocular systems. The comparison between the Cr(VI) (μXANES) and Fe (PIXE) profiles

suggests that very high Cr(VI) peaks correspond to lower Fe concentration regions. Finally, the last figure clearly shows the parallel between the Cr(VI) (µXANES) and the vanadium (PIXE) profiles.

ICP-MS laser ablation data obtained on sample M00-1-4 (Figures 4.28 to 4.30) confirmed the spatial association of Cr and Fe.

Figure 4.22 *Cr and Cr(VI)/Cr(tot) chemical maps in the hydrated analogue cement. The location of the map is presented in Figure 4.15 The Cr(VI)/Cr(tot) ratio determined from the Cr(VI)/Cr(tot) map for points #1 and #2 is compared with the Cr(VI)/Cr(tot) ratio determined from the XANES*

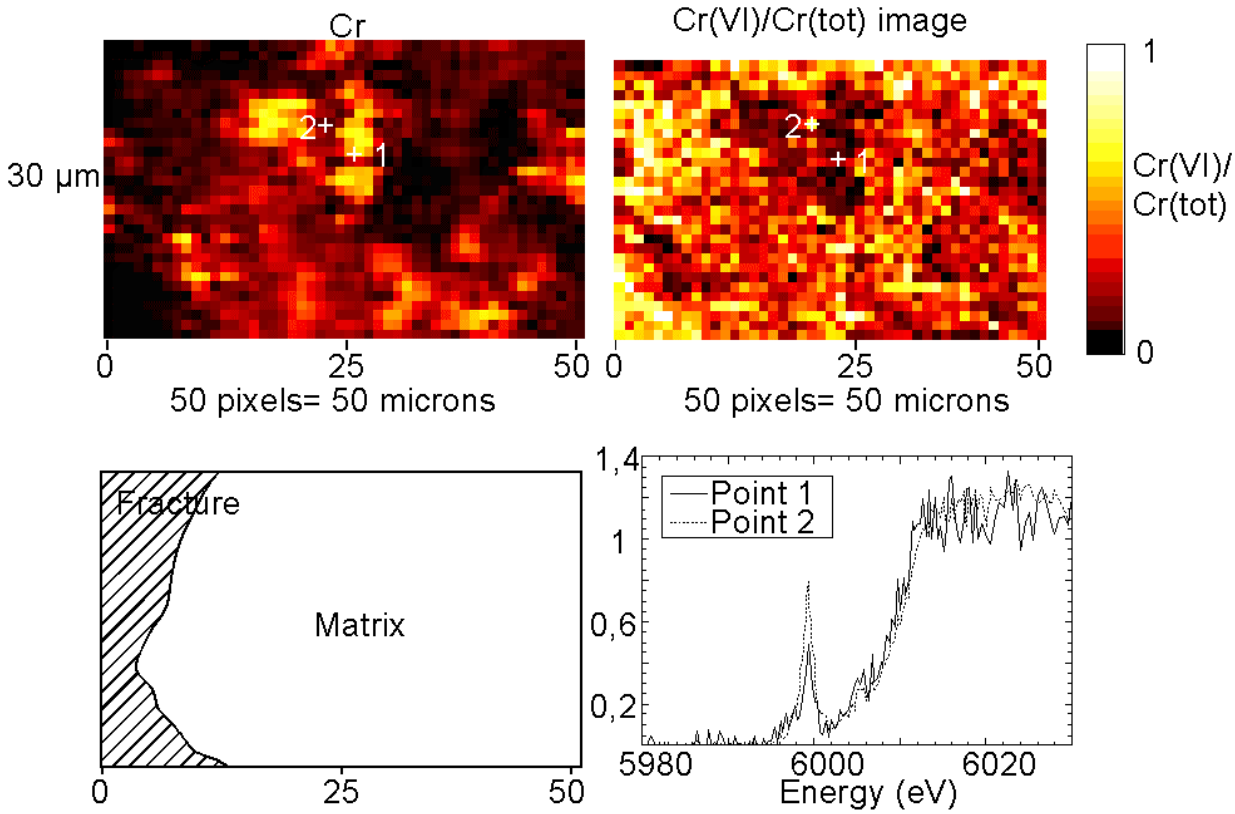

Figure 4.23 *Sample M00-1-4. PIXE (3.5 MeV protons, 350 pA) spectra of calcite (top, 0.2 μC), thaumasite (middle, 0.2 μC) and the potassium-rich phase (bottom, 0.48 μC) situated in the fracture (labelled K2 in Figure 4.16). Calcite contains around 1500 ppm Sr. The presence of Ga, Se and Rb is observed in the K-rich phase*

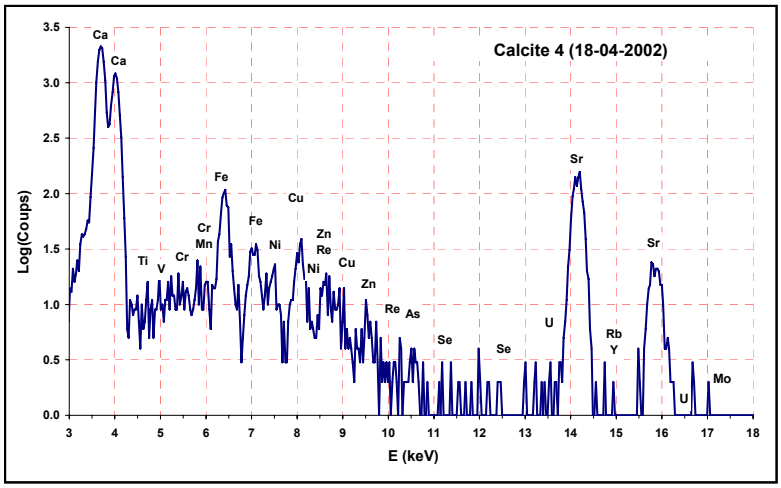

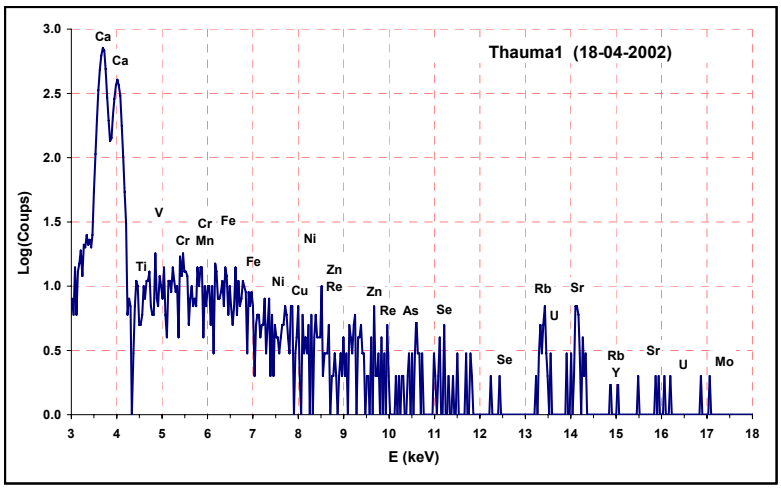

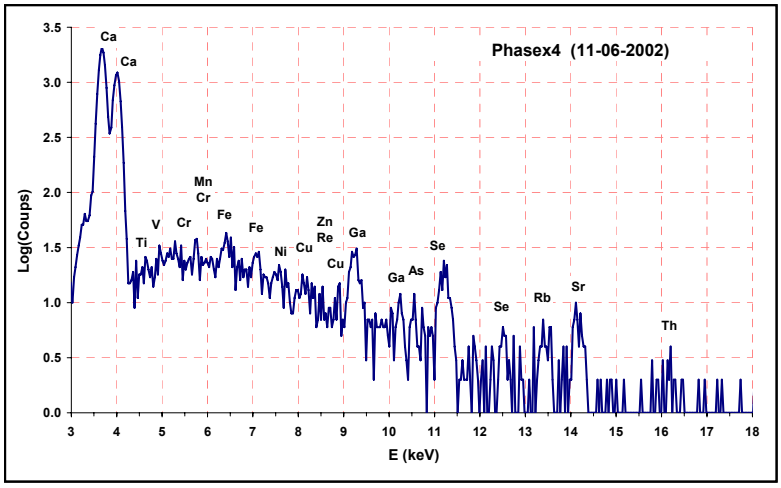

Figure 4.24 *Sample M00-1-4. PIXE spectra of the potassium rich phase (top) located in the matrix (labelled K1 in Figure 4.16) and of a Fe-S rich grain (bottom). The K rich phase located in the matrix (see Figure 4.28) contains Fe (Ni, Zn etc) rich inclusions: this appears clearly on the spectrum. Some Mo is also detected. In the Fe-S rich grain, several metals and heavy elements are present: Ti, V, Cr, Ni, Zn, Re(?), As, Se, U(?), Rb(?), Y, Mo(?). Because of a significant Zn concentration, Re cannot be defined*

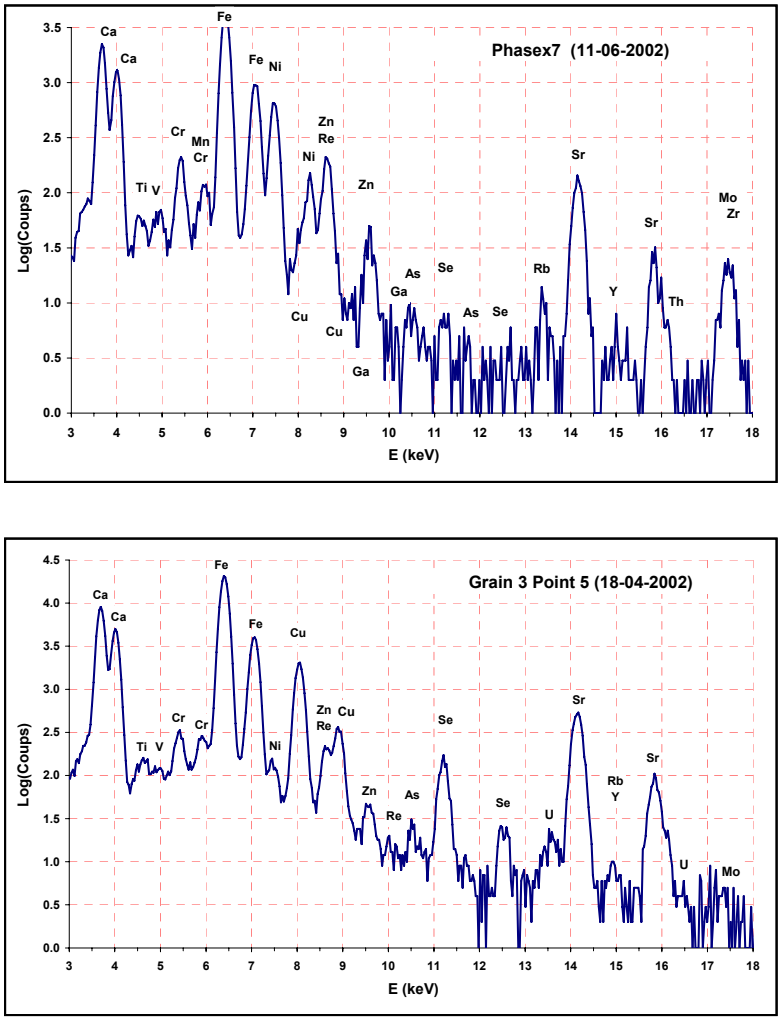

Figure 4.25 Element distribution maps (Fe, Zn, Cr, Ni, Se and Re) obtained by PIXE on sample M00-1-4. The analysed section contains several Fe rich grains. The signal for Re is very weak. Visual correlation with other elements is not convincing. (PIXE, incident protons of 3.5 MeV, total charge 6.42 µC)

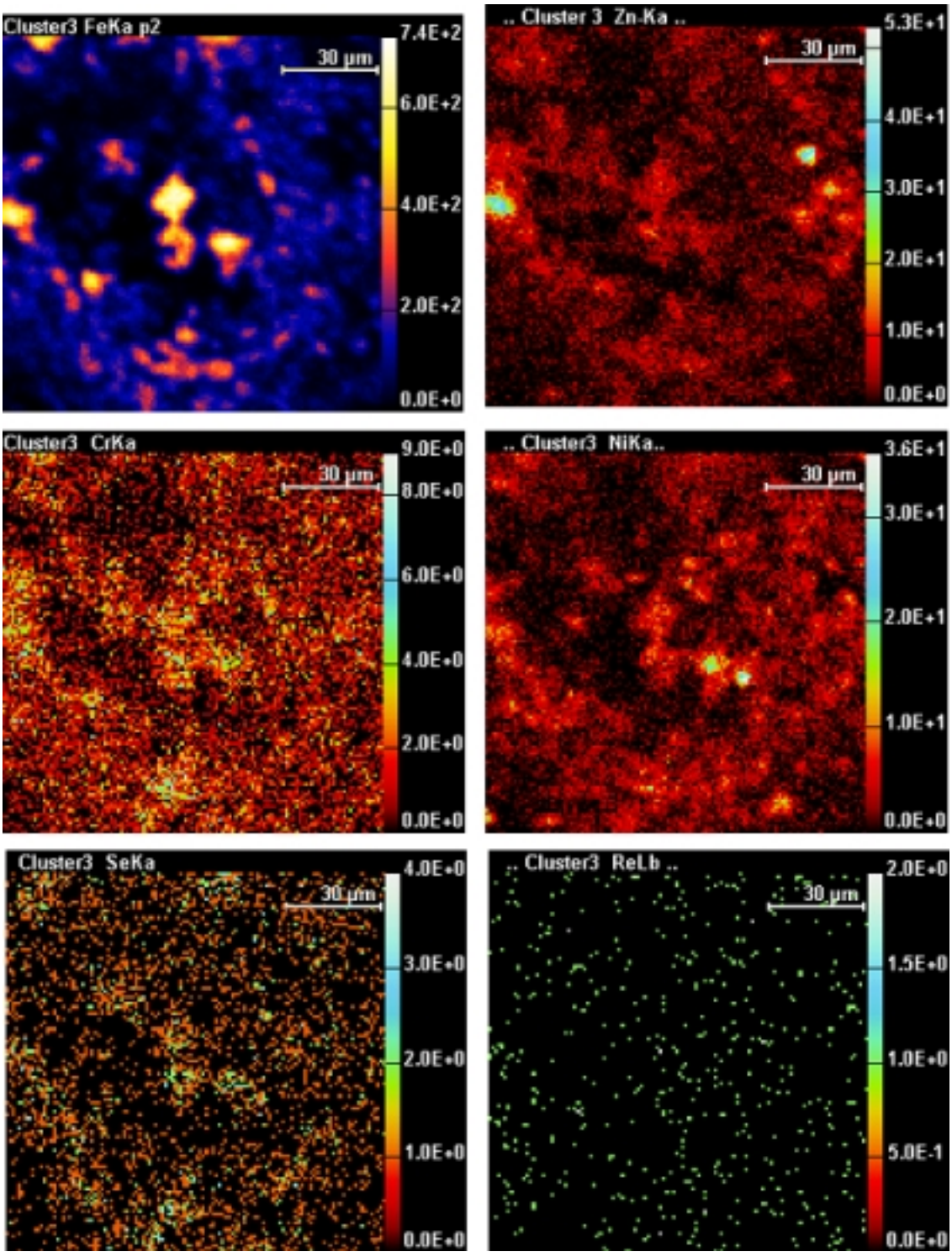

Figure 4.26 *Sample M00-1-4. PIXE profile (3 MeV protons, 3.5 μC) across the thaumasite-rich fracture (this profile is superposed to the μXANES line shown in Figure 4.15)*

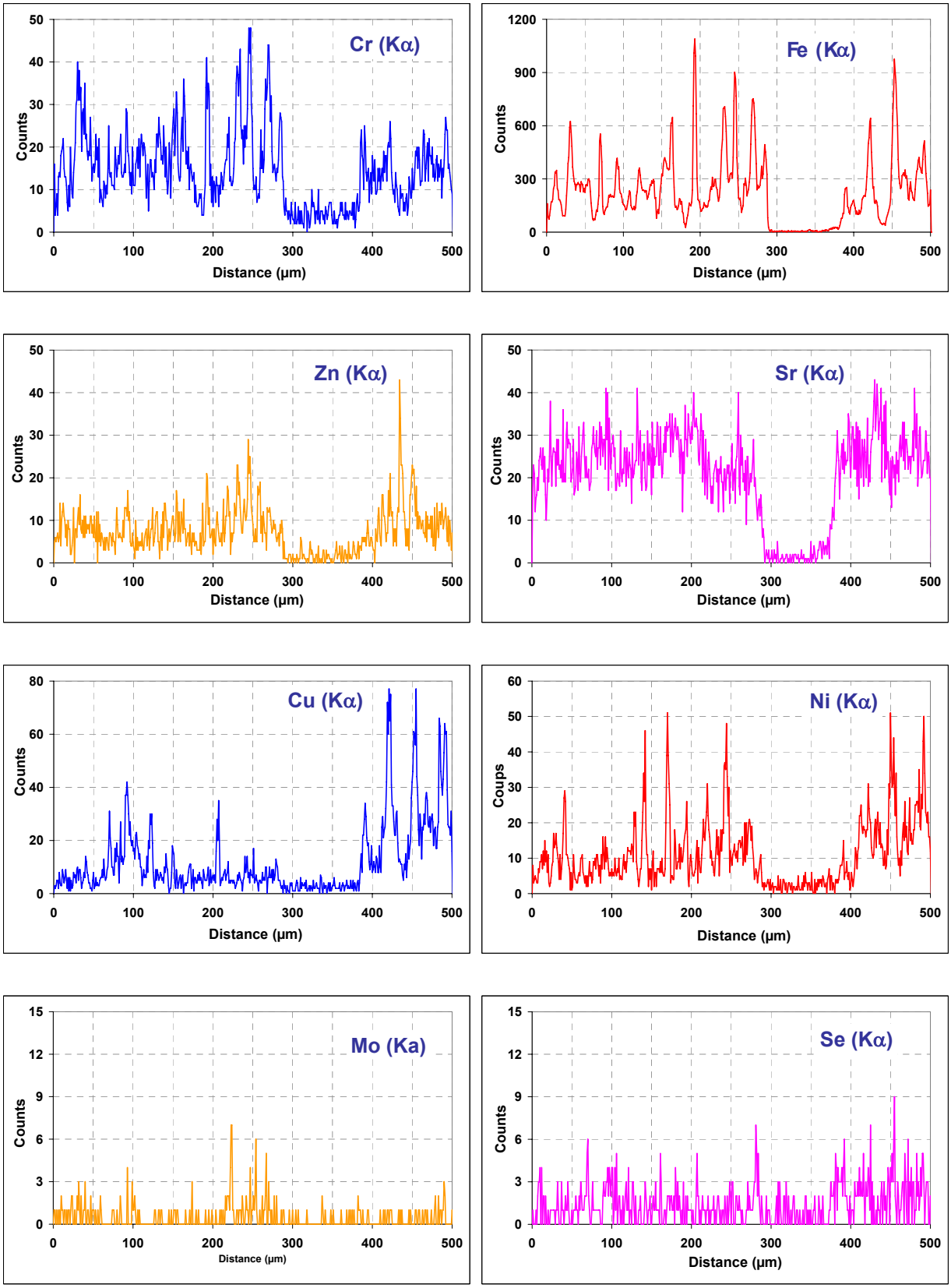

Figure 4.27 Sample M00-1-4. Superposition of PIXE data and μXANES data in the common section of profiles shown in Figures 4.19 and 4.26

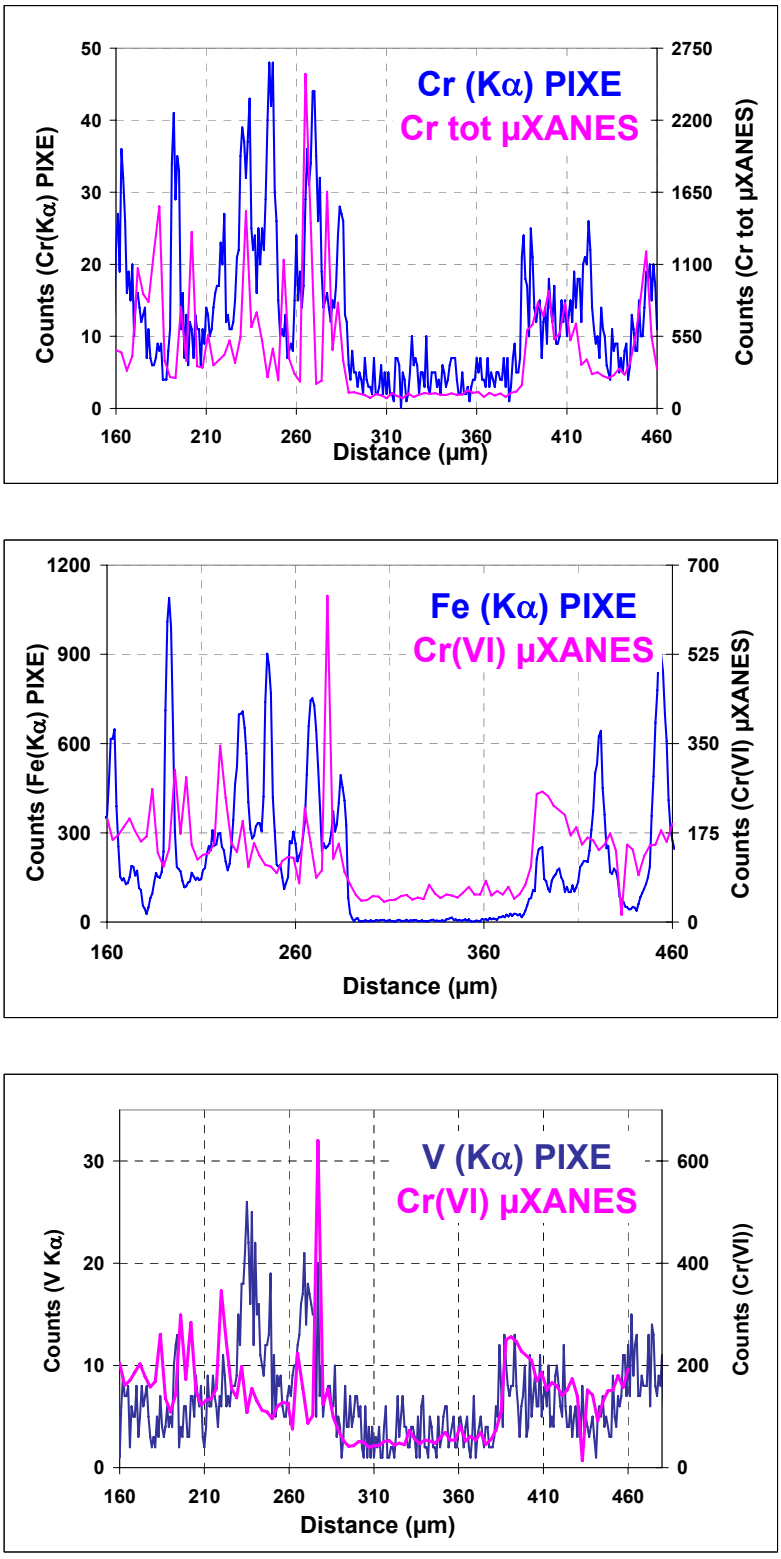

Figure 4.28 *Sample M00-1-4. ICP-MS LA profiles obtained on several isotopes. Top: comparison of the 187Re and 185Re spatial profiles (note the mounting resin is situated from 0 to 600 µm). These profiles demonstrate that part of the Re is effectively found in small grains. Bottom: Profiles for 57Fe, 53Cr, 95Mo and 187Re. The inclusion resine is situated from 0 to 500 µm. The thaumasite rich fracture is about 100 µm wide and located at ~1200 µm. The good spatial correlation between Fe and Cr is clearly seen. The 187Re profile suggests some Re accumulation in the thaumasite fracture. 95Mo and 187Re are clearly not correlated*

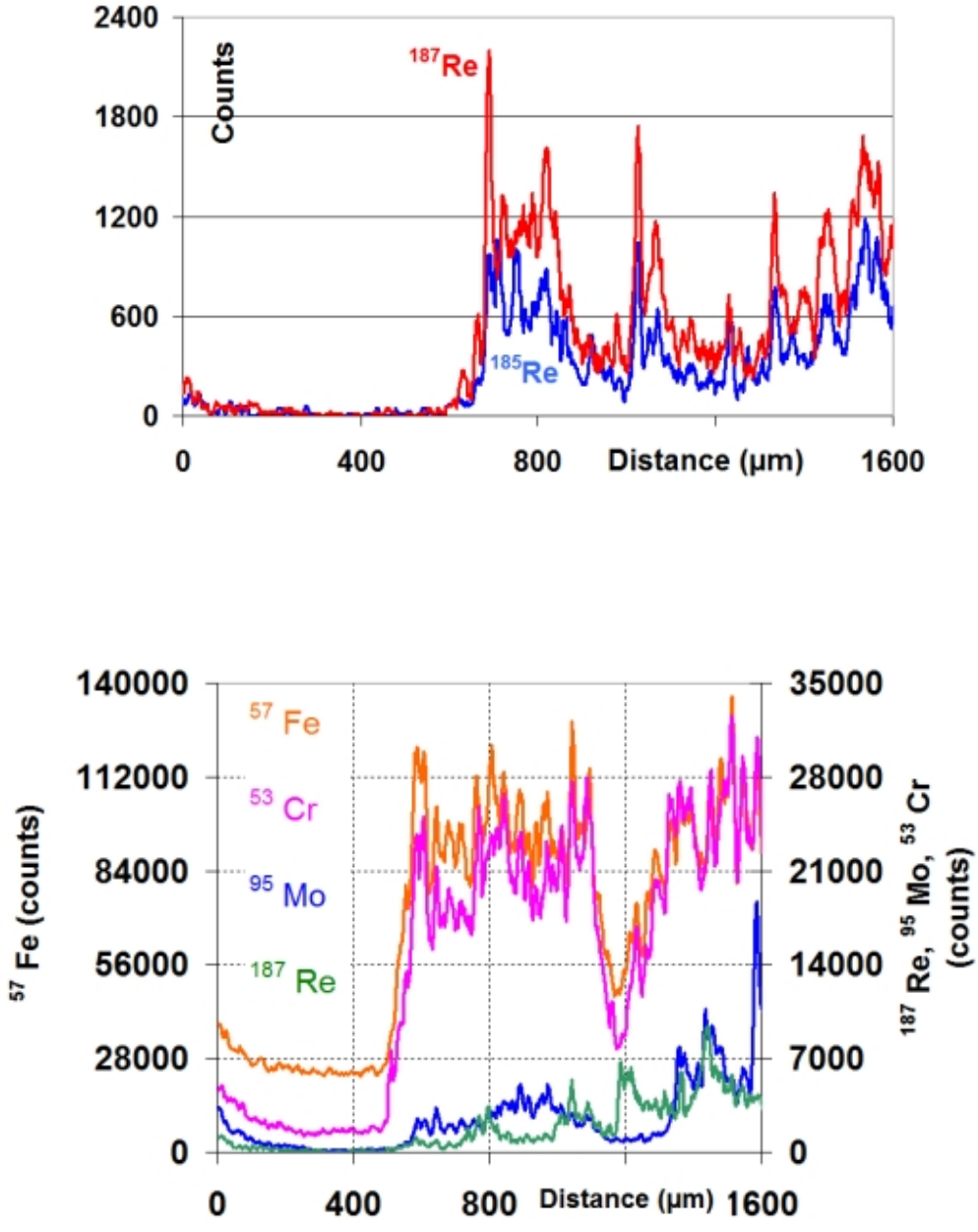

Figure 4.29 *Visualization of the Fe-Cr correlation (top, left). The representation of 187Re as a function of 53Cr shows that R- rich grains are also C-rich. In addition, the existence of a low Re phase is suggested, with a distinct Re-Cr correlation. A similar conclusion can be drawn from the 187Re-95Mo representation (bottom, left): Re-rich grains are poor in Mo. However, a low Re phase with a distinct Re-Mo correlation is strongly suggested (different colours correspond to different line profiles)*

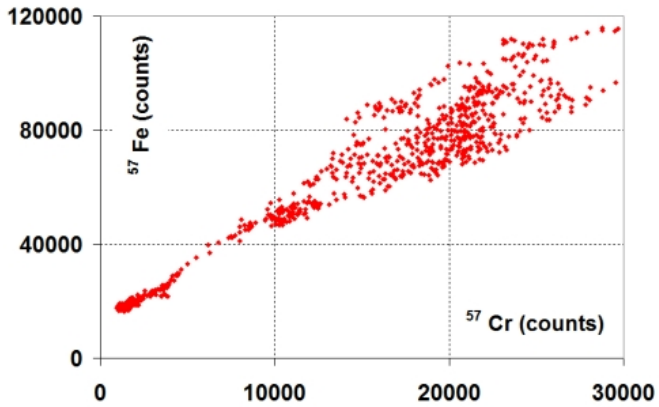

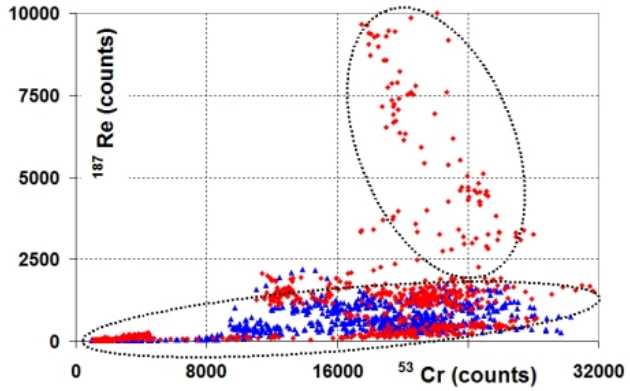

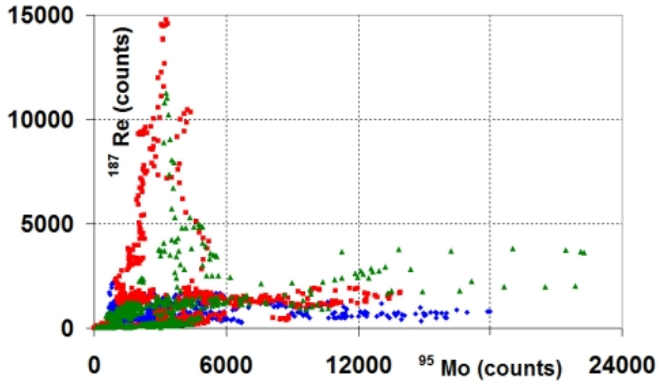

Figure 4.30 *Sample M00-1-4. ICP-MS-LA map. A SEM image of the sample after analysis shows the successive lines. The mounting resin is on the right. The thaumasite rich fracture, clearly visible on the 53Cr map, crosses the analysed region. Local fluctuations in the concentration of several elements (Sr, Fe, Al) reveal that, in addition to the thaumasite fracture, large scale (> 100 µm) heterogeneities (possibly due to combusted fossil tests) probably affect the sample*

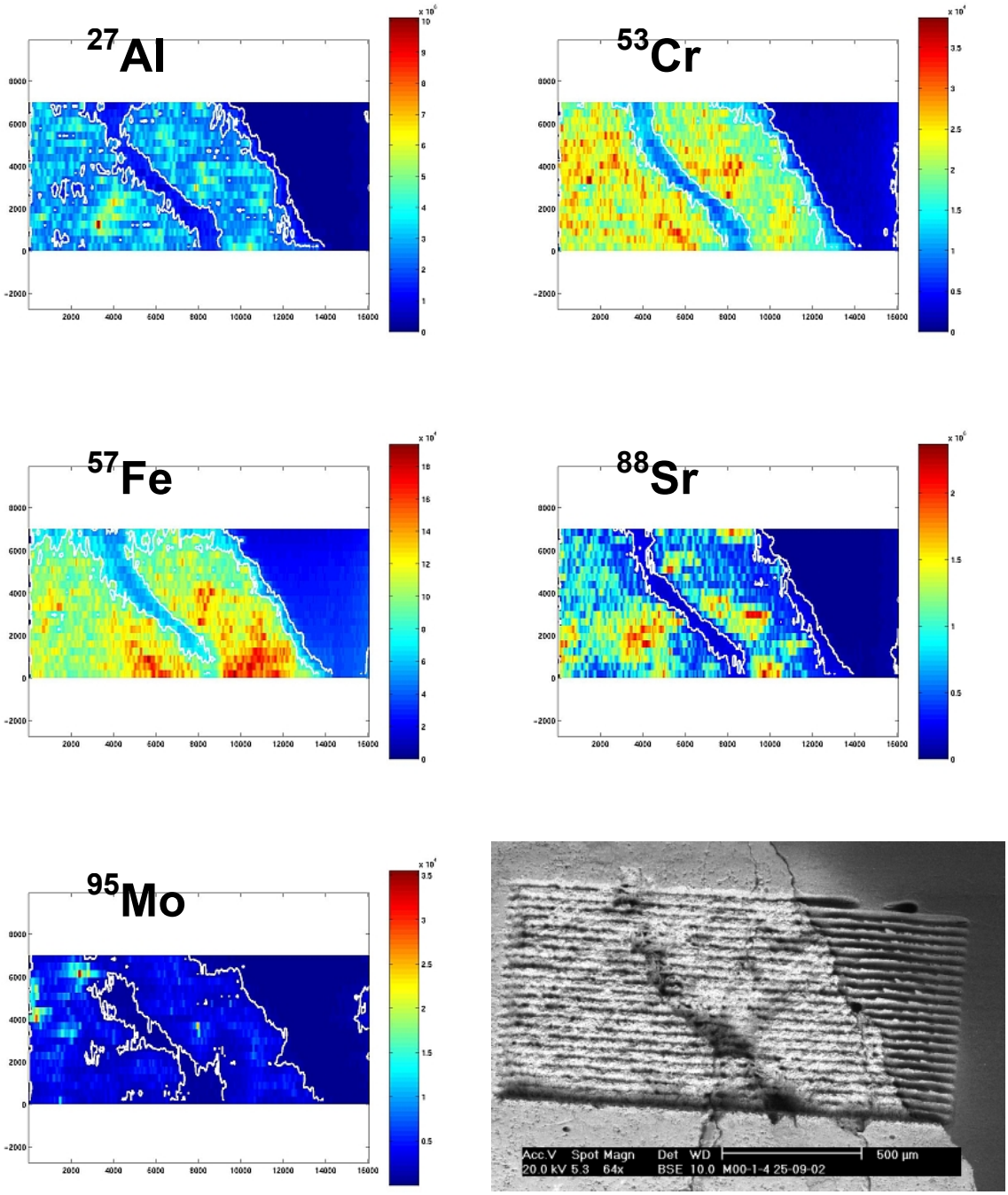

4.4.4.4 Investigations of Re using microanalytical techniques

Investigations were focused on the sample containing the highest bulk concentration in Re (M00-1-4; composition given in section 4.7). A reconnaissance examination was carried out on a polished section of this rock (avoiding contact of the sample with water during the whole preparation). In a first stage, SEM/EDX observations and analyses were done and revealed the complex and heterogeneous structure of this material (Figure 4.16). As noted above and in Milodowski et al. (1992a,b), the basic structure of this biomicrite is that of a microporous calcite mass and the pores are filled with phases of complex and variable composition, such as Ca-Al, Ca-Al-Si-S, K-Ca-Al-Si-P-S gels, thaumasite-ettringite, and apatite. A K-rich phase was also identified, tightly intermingled with the calcite matrix (EDX spectrum given in Figure 4.15). A prominent feature of the sample is a ~100 µm wide fracture containing mostly a thaumasite type phase and also some crystallised Ca-silicates. Remnants of the K-rich phase (or crystals of a secondary K-bearing phase of similar composition) are also found in the fracture. In addition, different phases occurring as small (from < 1 µm to < 10 µm) grains or crystals can be observed in the rock matrix either around gel-containing vacuoles, or as inclusions in the carbonate matrix. The elemental SEM images and EDX maps presented in Figures 4.31 and 4.32 give a synthetic view of the distribution of major elements, especially Si, K, S and Fe. Among the tiny minerals, rare and discrete round shaped calcium sulphides (already recognised during Maqarin Phase I; Milodowski et al., 1992a, 1992b) were identified. Other grains are most often enriched in metals, such as Fe, Zn, Ni, Cr and Se, with Fe as a major constituent. Among these small phases, several Ca-Fe-S rich grains were the only minerals in which Re could be detected by EDX (less than 10 occurrences on about 4 cm^2 sample explored; e. g. spectrum on Figure 4.33). Detection of Re in these grains was, however, very difficult because:

- the detection limit of the EDX analyser was not very good (> 2000 ppm)
- several peak overlaps occurred that prevented good detection of Re lines: Si-Kα over Re-Ma, Zn-Kα over Re-Lα, as well as interference with As and Ga lines in the 10 to 11 keV range
- Re migration and evaporation occurred under the electron beam, because the Re lines rapidly vanished upon successive analyses of the same grain

The EDX elemental map for Re (Figure 4.32) is not considered as a sufficient indication of Re presence in the grain shown. It is suspected that differential background levels between different minerals are responsible for the weak signal observed on the Fe-S rich grain.

Nuclear microprobe analyses (PIXE) were also performed on the same sample (see appendix 4 for analytical settings). Although this technique has a much better detection limit (~10 to 100 ppm) than SEM/EDX, energy lines interference especially from the Zn-Kα line, remained a strong handicap. In addition, as noted above, the analysed volume by the PIXE technique has the shape of a ~2 µm diameter and ~30 µm length cylinder, causing dilution of the signal for analyses performed on very small grains (1 to 3 µm diameter). Finally, Re migration under the proton beam was also suspected. The prior SEM reconnaissance enabled, however, the PIXE analyses to be performed on well recognised mineral phases and data on several other elements (e.g. Fe, Cr, Sr, Se and Mo) was acquired. In Figure 4.25, a multi-element map, performed on a cluster of small Fe-Ca-S grains, is shown.

Figure 4.31 EDX chemical map obtained on a selected area of sample M00- 1-4 (see Figure 4.16, top right). These maps clearly show the location of the K-rich phases (inside the matrix or in the fracture), the location of sulphur (ettringite-thaumasite in the fracture, CaS phase, Fe-S-rich grains), the dispersion in the matrix of iron-rich grains and phosphates, the occurrence of Al in discrete and large pores. The K-rich phase located in the fracture (K2 in Figure 4.16) does not contain Fe-rich grains and is thought to be secondary with respect to the K-rich phase inside the porous matrix

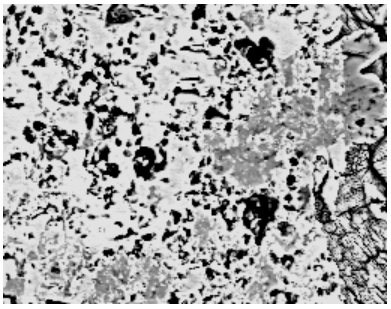
BSE

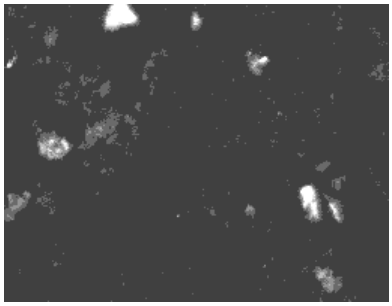
Al Ka

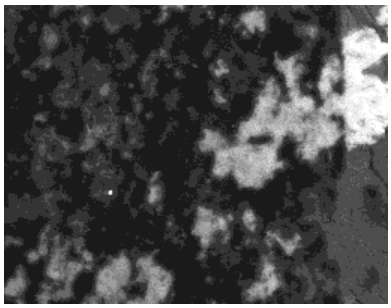
Si Ka

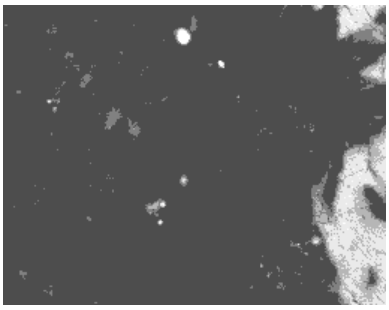
S Ka

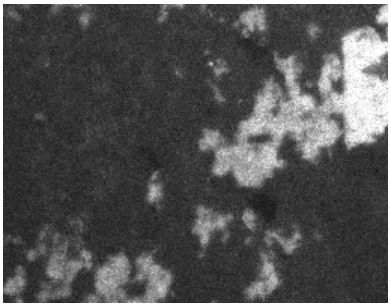
K Ka

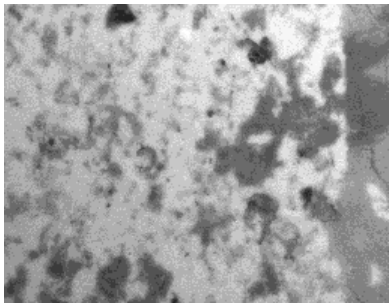
Ca Ka

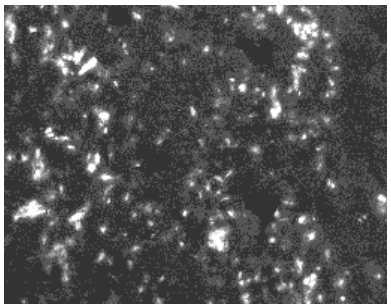
P Ka

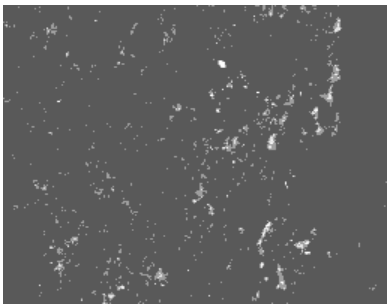
Fe Ka

Figure 4.32 SEM BSE image of Fe-S rich grains around a pore filled with thaumasite (top). The EDX chemical maps of one single grain (below) show that the grain also contains Cr, Ni, Zn and K. The interference between Zn Kα and Re Lα lines makes difficult the mapping of Re. The slightly higher yield of the Re Lβ region on the grain is not sufficient to prove presence of Re because this could be caused by a higher background level of the spectrum of the grain, compared to surrounding minerals

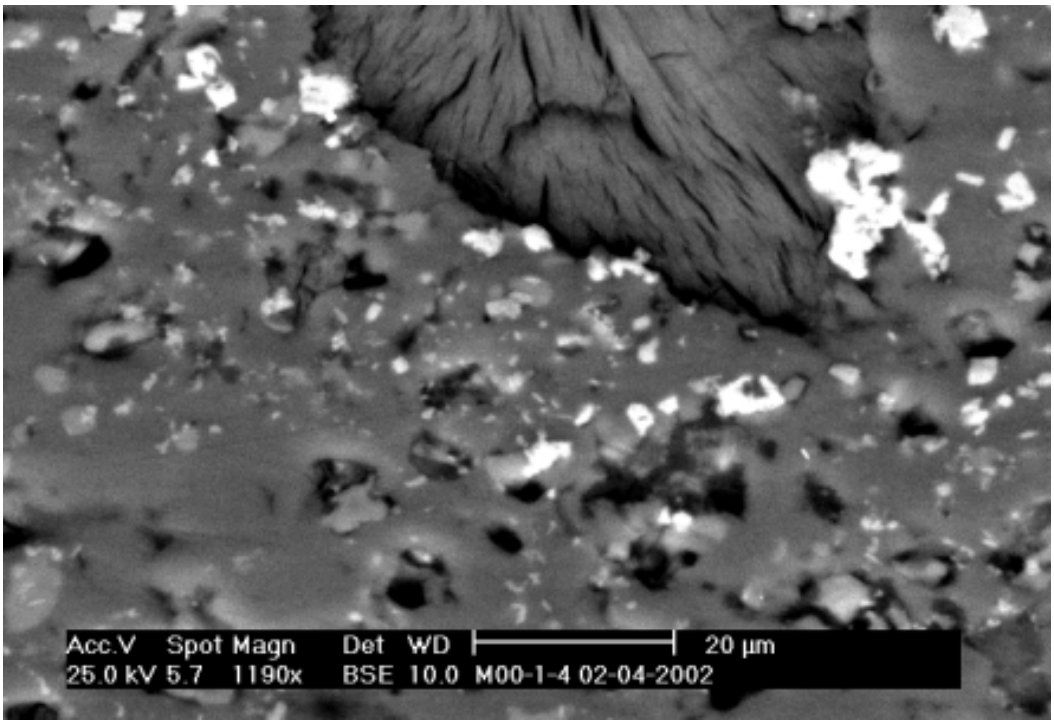


BSE

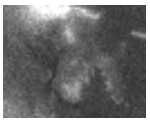
Al Kα

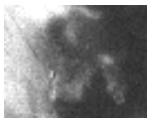
Si Kα


S Kα


K Kα

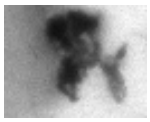
Ca Kα


Cr Kα

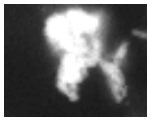
Fe Kα

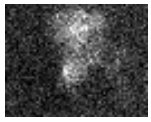
Ni Kα

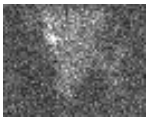
Zn Kα/
Re Lα


Re Lβ

Figure 4.33 *EDX spectrum of an individual Fe-S rich grain found in sample M00-1-4. This spectrum shows that, in addition, this type of grain probably contains Ca. In this spectrum, the absence of the Zn Kb line shows that the 8.65 keV line can be attributed to the Re La line. This is consistent with the presence of the Re Lb lines between 10.0 and 10.3 keV. Successive analyses of this grain showed that Re was progressively lost under the beam*

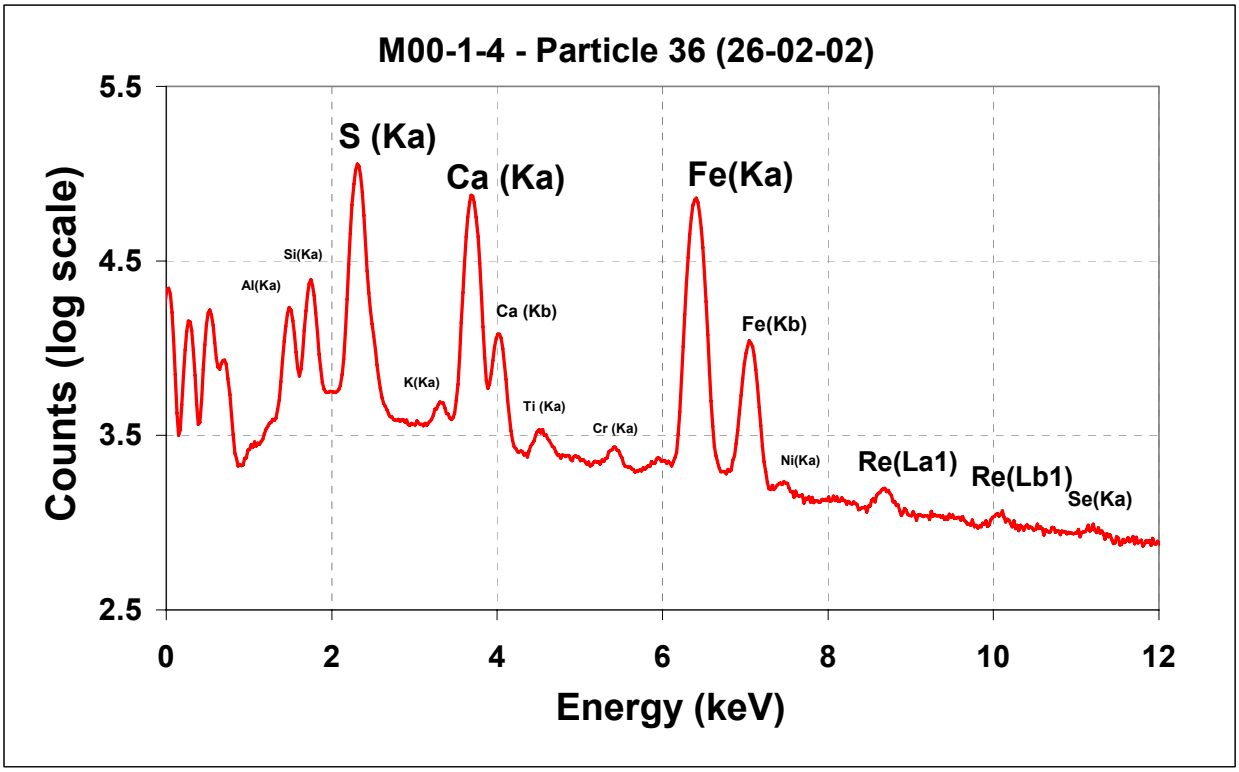

Laser ablation ICP-MS (see appendix 4 for analytical details) was then attempted on two polished sections of sample M00-1-4. This technique is destructive and the sample is locally vaporised by the incident laser beam. Because of the heterogeneous nature of the sample, strong fluctuations may occur in the vaporisation rate and in the signal. The laser beam is moving along successive and adjacent lines in order to explore large portions of the sample (~ 1 mm^2) and draw 2D isotope maps or 1D profiles. Memory effects are sometimes observed along lines because of gas mixing and circulation in the vaporisation chamber. The first important result was the clear confirmation of the presence of Re in the sample (Figures 4.28 and 4.34). Re is also confirmed to be in localised mineral grains, but Re is also present, although at a lower concentration level, in at least one other phase. This is suggested by the drawing for the two Re isotopes of contours with level values in the ratio of their isotopic abundances. These contours draw regions of similar shape for the two isotopes. Maps (Figure 4.35) suggest that this other phase, where Re is also present, is one of the major phases of the analogue cement sample.

Figure 4.34 *Sample M00-1-4. ICP-MS LA analysis along a profile. Signal for 187Re is reported as a function of signal for 185Re. The pink line corresponds to the natural ratio of the two Re isotopes. The good agreement between the data points and the theoretical line demonstrates that Re is effectively detected*

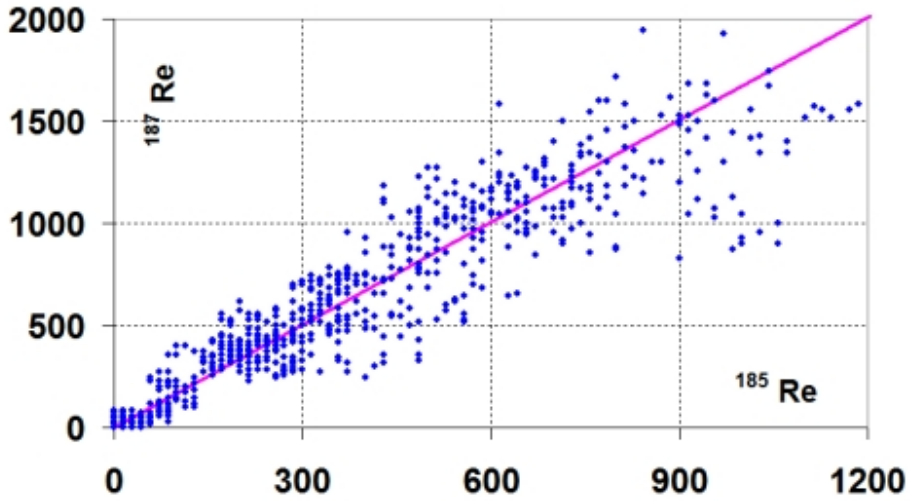

Several SIMS images were performed on the same sample, in zones where a preliminary SEM/EDX reconnaissance was done. However, due to the low spatial resolution of the SIMS acquisition mode (around 20 µm resolution) and due to the big differences in detection limits between these two techniques, EDX elemental maps could not easily be compared to SIMS maps, except for some major elements (Al, Si, K). Out of 6 mapping trials, in only one was Re detected at a significant concentration. It is, however, difficult to specify precisely whether the observed intensity corresponds to the high range or low range of intensities measured using ICP-MS LA. In this map (Figure 4.36), a correlation exists between the Cr and Re spatial distributions but not for all concentrated spots. This correlation is consistent with the ICP-MS LA data (Figure 4.29) showing that high Re spots are also rich in Cr. The high Re line shaped structure corresponds on the SEM image to a very thin fracture. This suggests that, due to its vaporisation, Re could perhaps have been trapped and sorbed in the fracture network of the analogue cement. In this case, Re distribution could also include, in addition to specific mineral host phases, sorbed or surface condensed Re compounds. This could also explain part of the lability of Re from unhydrated analogue cements.

4.4.4.5 Investigations of Mo, Se and other elements using microanalytical techniques

During SEM investigations of sample M00-1-4, due to the poor detection limit of the EDX system, Mo could only be detected in rare discrete grains. One of these grains (Figure 4.37) could be analysed both using EDX and PIXE probes. In this case the mineral grain is probably a Ca-molybdate. PIXE profiles obtained on Mo also show spots with higher Mo concentration but no correlation is found with other elements. ICP-MS LA analyses (Figures 4.29 and 4.30) confirm that high concentration Mo grains probably coexist with other Mo

containing phases. Simultaneous analysis of several Mo isotopes could help to clarify this point.

Figure 4.35 *Sample M00-1-4. ICP-MS LA maps for 185Re (top) and 187Re(bottom) (see Figure 4.30). The rare Re-rich particles are clearly visible. In addition, the low intensity, white contours drawn on the two maps have been given respective intensities that follow the 187Re/185Re natural ratio. The fact that on the two maps these contours draw very similar shapes strongly supports the existence of a widespread phase containing a low level of Re concentration*

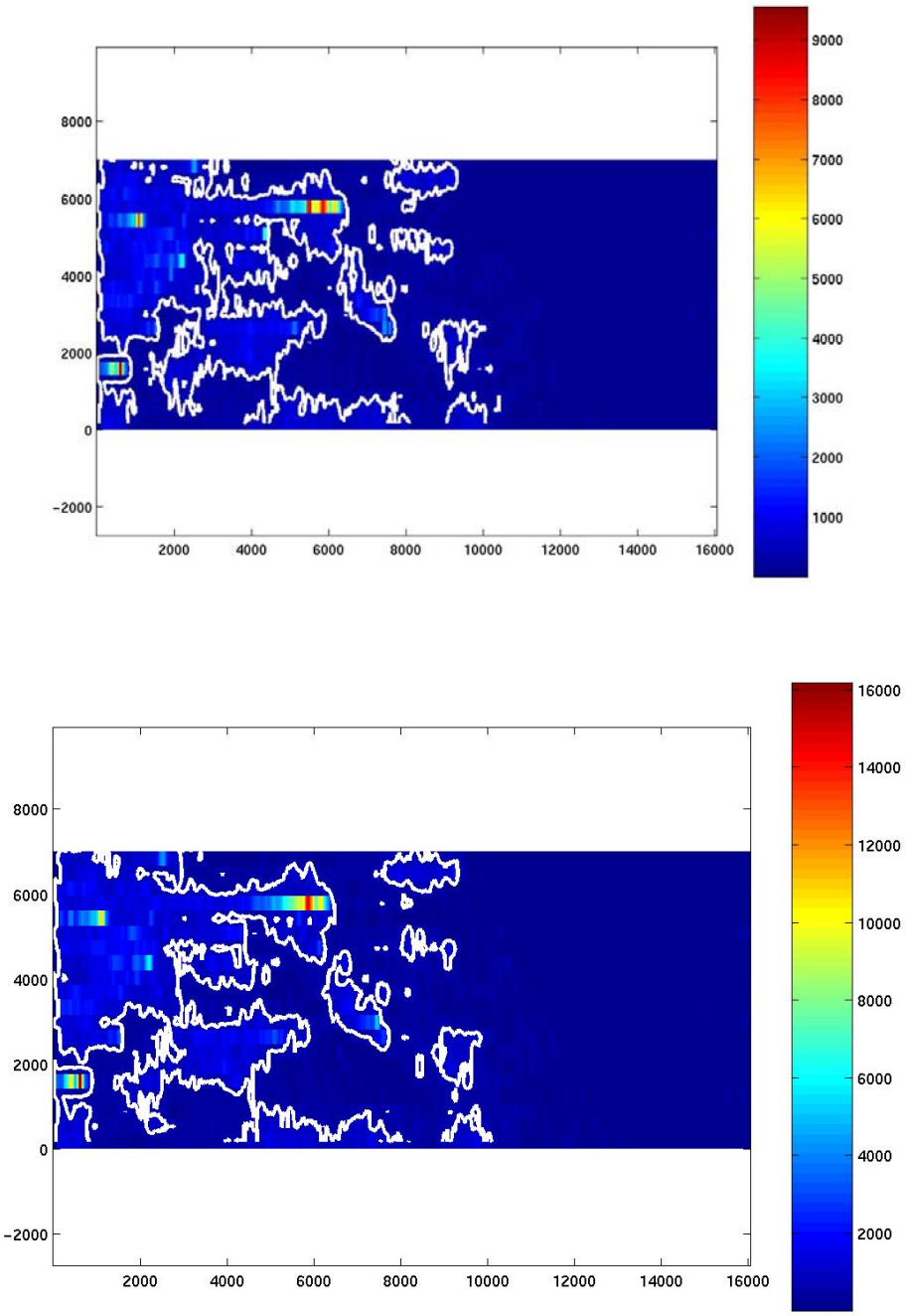

Figure 4.36 *Sample M00-1-4. SIMS maps for Cr, Fe, Mo and 187Re. The width of the maps is about 250 µm. The spatial resolution is about 20 µm. A clear correlation is seen between the Re-rich regions and several Cr rich spots. This is consistent with ICP- MS LA data shown in Figure 4.29. At present, the unambiguous link between ICP-MS LA data and SIMS data is, however, not easy to ascertain, because respective detection limits and volumes of investigation are not the same*

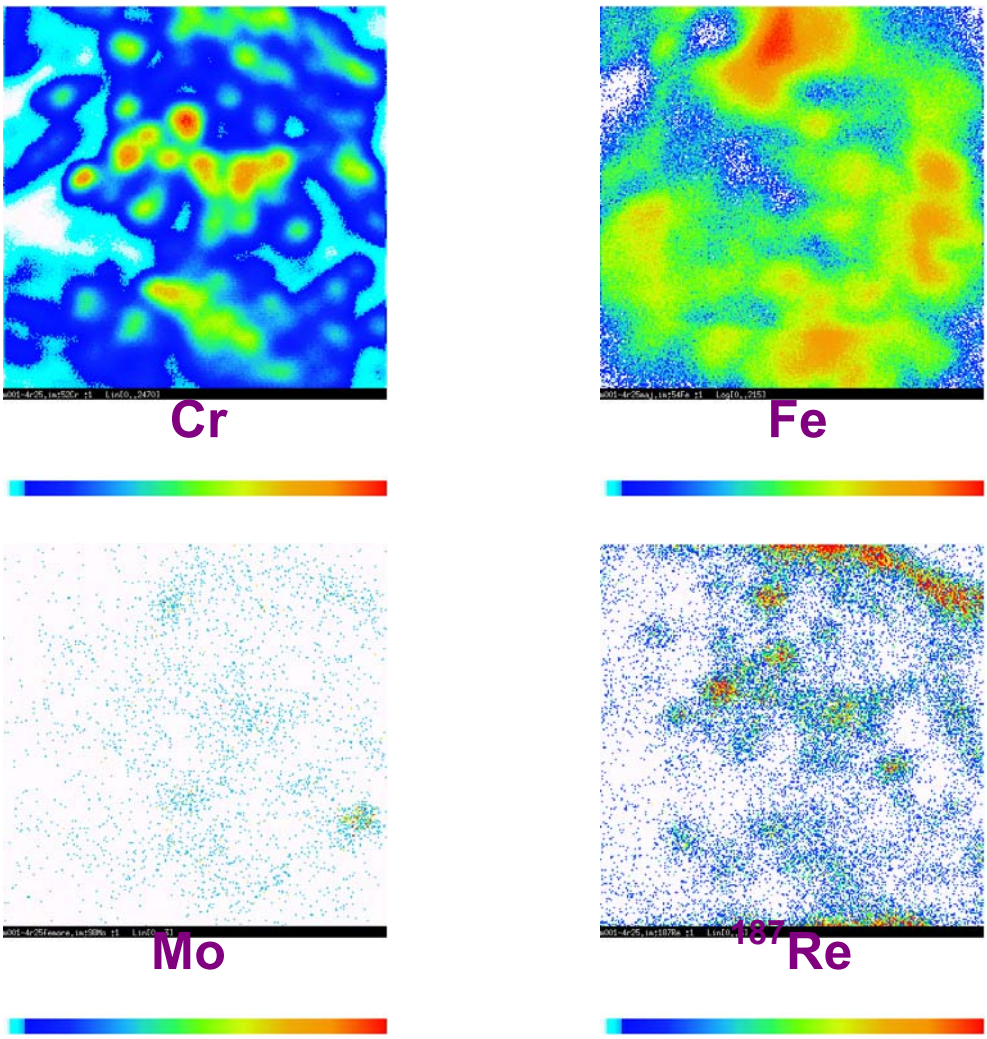

Figure 4.37 *Observation by SEM of a Mo rich grain. This grain (< 2 µm diameter) is found on the edge of a pore filled with thaumasite. The surrounding matrix is calcite. Due to the very small size of the grain, influence of the surrounding matrix on the spectra (SEM-EDX left, PIXE right) could not be avoided. The grain is assumed to be a Ca-molybdate phase*

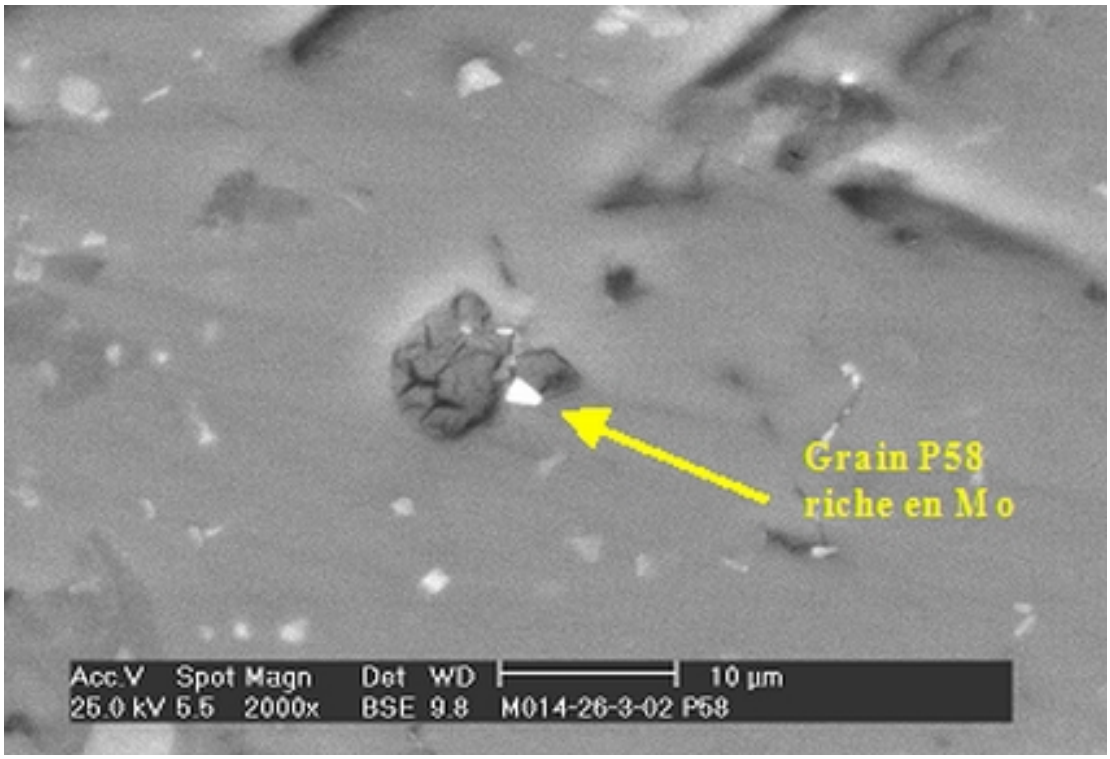

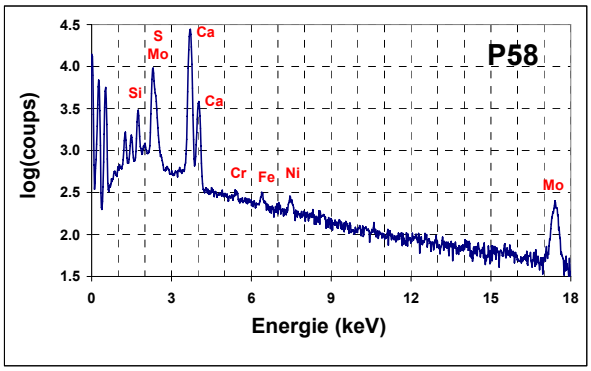

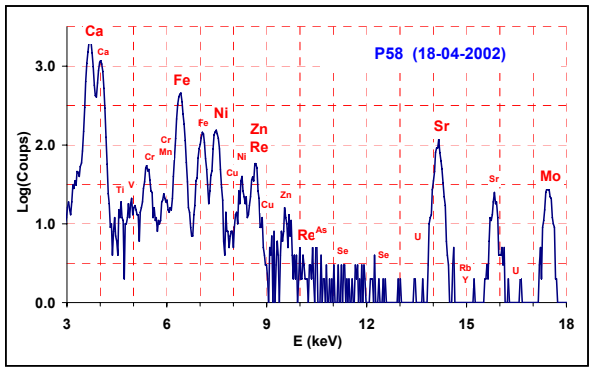

During SEM investigations of sample M00-1-4, Se was occasionally detected in small Fe-S-rich grains, containing also V, Cr, Ni, Cu, Zn, As and Re (Figure 4.33). ICP-MS LA trials on the ^{77}Se and ^{82}Se isotopes gave poor and noisy results. PIXE spectra of individual grains confirmed the SEM observations on Fe-rich grains. In addition, PIXE spectra of calcite showed undetectable concentration levels of Se whereas some other major phases showed irregular values. The number (< 7) of datapoints is too small to draw firm conclusions. However, in agreement with the observations of Milodowski et al. (1992a, 1992b), it seems that thaumasite contains low levels of Se, whereas higher concentrations are observed in the K-rich phases (see Figures 4.23 and 4.24). Several PIXE profiles confirmed the

existence of a spatial correlation between Cu-rich and Se-rich grains (Figure 4.26), in agreement with previous observations of Maqarin samples (Milodowski et al., 1992a, 1992b). Generally, difficulties in detecting Se support the idea that Se has a low concentration level in sample M00-1-4. Other noteworthy observations concerning several trace elements were also made during these investigations:

Sr: is present at significant levels (>1500 ppm) in calcite and in most unhydrated phases of sample M00-1-4. In contrast, very low Sr levels are observed in thaumasite and in the K-rich phase located inside the fracture (this is not the case for the K-rich phase inside the matrix porosity). This suggests that Sr could help to elucidate early alteration patterns in Maqarin analogue cements (see also the discussion in Chapter 6).

Rb: is detected in the K-rich phases and also in thaumasite (Figure 4.23 and 4.24). Rb could also be potentially useful in tracing analogue cement-alteration stages.

Ga: was detected in the K-rich phase found in the fracture of sample M00-1-4 (Figure 4.23). From semi-quantitative ICP-MS runs, Ga is found to be present at much higher levels in the basalt (~20 ppm) than in other rock types (~2 ppm). Ga is also found at a significant level in one vein filling (M00-1-26, ~14 ppm). Ga could potentially be a tracer of waters having percolated through (or being brought with) the basalts before interacting with analogue cements.

4.4.5 Leaching experiments

The temporal evolution of Cr concentration in the column leachates confirms the much higher availability of Cr in the altered analogue cement sample M99-1-41 (Figure 4.38). The released concentrations are initially as high as 1000 µg L^{-1}, decreasing nearly exponentially to about 50 µg L^{-1} after 400 hours leaching. In contrast, the measured concentrations for the unaltered sample (M00-1-4) remain around, or less than, 10 µg L^{-1}. An evaluation of the fraction of total Cr mobilised shows that about 1.2 % of total Cr is leached out from the altered analogue cement in 400 hours whereas, for the unaltered sample, the leached fraction during the same time amounts to about 0.08 %. Assuming that the empirical exponential law for the release of Cr by the altered analogue cement is valid (no further oxidation of Cr during the test assumed), the total mobile fraction of Cr is about 15 % (+/- 5 %), in good agreement with the total initial Cr(VI) content of the material (Table 4.10). The release of Cr by the biomicrite, leached by water in equilibrium with portlandite (Figure 4.39), is low but higher than for the analogue cement M00-1-4.

The leaching of Re from the different materials confirms that fresh unaltered analogue cements (M00-1-4) provide a massive and rapid input of Re to groundwaters (Figure 4.38). Roughly, about half of the Re contained in the powdered M00-1-4 sample was leached out in 450 h. Biomicrite is also shown to release some Re.

Cr, Se and Mo released by analogue cement M99-1-41 are in constant ratio (Figure 4.38). A preferential release of Cr over Mo is observed during the leaching experiment (Mo/Cr ~0.026 in leachates, compared with Mo/Cr ~0.042 in the solid). Mo/Cr ratios in hyperalkaline waters range from 0.01 to 0.1. The preferential release of Cr over Se cannot be confirmed because of the high variability of the Se content in the solid experiment (Se/Cr in hyperalkaline groundwaters ranges from 0.05 to 0.15).

Initial release of Re from sample M00-1-4 is clearly faster than Mo release, but the leachates then approach a Mo/Re ratio close to bulk rock composition (Figure 4.40). Se release from

sample M00-1-4 initially decreases and increases again at longer times (Figure 4.40, top). The Se/Mo ratio in leachates from sample M00-1-4 progressively reaches the range observed for sample M99-1-41 (Figure 4.40, bottom).

Comparison of Re and Mo leaching rates from the biomicrite show that Re is preferentially leached (Figure 4.40, middle). Se preferential release over Mo cannot be confirmed because of the variability of Se content in the biomicrite.

4.4.6 Discussion and summary of results

The main results obtained during these investigations may be summarised as:

- the element Re is confirmed to be present in hyperalkaline groundwaters at levels from 0.8 to 6.6 µg L^{-1}
- the main source terms for Re in Maqarin are
  i) unaltered analogue cements (up to 1.2 ppm Re)
  ii) the biomicrite (~0.1-0.15 ppm Re).
- The combustion process has caused important remobilization of Re, probably due to volatile compounds of Re. Thermally altered biomicrite is depleted in Re around the combustion front
- in unaltered analogue cements, Re is present in at least two main phases
  i) small Fe-S rich grains with high Re concentration
  ii) a major phase with low Re concentration.

The redox state of Re in these phases is not known. The small Fe-S rich grains almost certainly also contain Ca as a major element. These grains could be (Ca)Fe sulphides or possibly (Ca)Fe sulphates. The possibility for Re being present as a sorbed species in the porosity of the analogue cement is not excluded. Good correlation between Re and nitrate in groundwaters also suggests that anionic Re species could be trapped in a phase hosting nitrate.

- the neutral M19 water is likely to represent a reducing groundwater equilibrated with the biomicrite. The speciation study assigns an Eh ~-0.26 V to this water and suggests solubility control of Re by ReS2.
- Re in hyperalkaline waters is probably not solubility controlled by a pure Re phase. Some potential Re trapping in sulphate bearing secondary phases is found (sample M00-1-26), suggesting partition of Re between solution and sulphates.
- investigations suggest that Cr is mostly in the III valence state in unaltered analogue cements and is progressively converted to the VI valence state upon analogue cement hydration. Thermodynamic calculations suggest that the redox state of hyperalkaline waters in Maqarin is in equilibrium with Fe/Cr oxides, ferrites[18] and perhaps Mn oxides. The influence of the surrounding biomicrite, rich in organic matter, is not evidenced.
- the leaching experiments confirm that Re is leached preferentially over several metals (Cr, Mo, Se) from the unhydrated analogue cement. This observation supports the hypothesis that the Western Springs in Maqarin are characterised by recently hydrated analogue cement bodies.

[18] However, as noted in Tweed et al. (1992), ferrites are highly unlikely to be present in such a low temperature system and this result is simply an indication of the inappropriateness of the thermodynamic database utilised for the calculation.

A simplified scheme is proposed in Figure 4.41 to represent the major features of Re transfer in Maqarin. The interpretation of data is complex because the biomicrite is both a potential source and sink (because of reducing capacity) for Re.

The origin and kinetics of Cr oxidation in Maqarin analogue cements is interesting. The results presented here suggest that Cr(III) immobilised in a analogue cementitious environment is, over a long time scale, prone to be at least partially oxidised to Cr(VI) and then exposed to be leached and transported in the environment. This conclusion is also supported by field observations in Maqarin where leaching of Cr(VI) from the ACZs is clearly visible along water pathways (Clark *et al*., 1992)[19]. The fact that the Cr(III) oxidation is triggered by the analogue cement-water interaction is shown on one side by the comparison between the bulk-XANES of the two analogue cement samples and on the other side by the micro XANES observation around the fracture zone in the unaltered analogue cement sample. Cr(III) oxidation seems, however, to occur at the microscopic scale in an heterogeneous fashion, producing patterns with adjacent Cr(III) or Cr(VI) rich zones at less than 10 µm distance. It appears thus that Cr(III) oxidation likely occurs *in situ* at the scale of individual mineral grains.

At least, two main reaction pathways can be proposed to account for the oxidation of Cr(III) to Cr(VI):

i) interaction with dissolved oxygen from percolating water
ii) redox reaction with manganese III or IV oxides.

Notably, both pathways may interfere or be catalyzed by biological processes (bacterial aerobic or anaerobic respiration (Lovley, 1993); Francis and Tebo, 2002; Desjardin et al., 2002). It is known that Cr(III) oxidation to Cr(VI) by dissolved oxygen is a slow process, especially at pH under 9 (Schroeder and Lee, 1975; Eary and Rai, 1987; Richard and Bourg, 1991). Cr(III) oxidation may, however, be catalyzed at the MnO_2-water interface (Eary and Rai, 1987; Rai et al., 1989; Fendorf and Zasoski, 1992). Manceau and Charlet (1990, 1992) and Weaver and Hochella (2003) observe that several Mn(IV) oxides (birnessite, ramsdellite) and even Mn(III) oxides (feitknechtite, β MnOOH, hausmannite and γ Mn_2O_3) are able to convert Cr(III) to Cr(VI) by surface catalysed oxidation.

Previous investigations (e.g. Loop and Hall, 1992) on the Maqarin site show that the Mn content of the biomicrite and metamorphic rocks usually lies below 100 ppm. Pure Mn(IV) oxides have never been observed in this environment. This does not exclude the presence of Mn(III, IV)-bearing phases, although Mn seems to be present most often at the II (or III) valence in mineral phases. Localized kutnahorite (Mn^{2+} analogue of dolomite and ankerite) was previously identified by Khoury and Nassir (1982) in Maqarin. Mn at low concentration (< 100 ppm) was also detected in calcite, CSH phases, portlandite, ettringite, thaumasite and zeolite. In calcite, Mn is most likely present as Mn^{2+}, substituting for Ca^{2+}. In minerals like ettringite and thaumasite Mn may be behaving like Fe^{3+}, and indeed jouravskite ($Ca_3Mn(CO_3)(SO_4)(OH)_6.12H_2O$), which is the Mn analogue of ettringite in which Mn^{3+} occupies the same role as Al^{3+}, was identified as an alteration product at Maqarin (Milodowski *unpublished data*). The oxidation state of Mn in other phases is less clear. Fine= grained ferrites, or Fe-oxide phases associated with the marbles, contain small amounts of Mn of the order of 0.2 to 1 wt %, along with Cr, Zn, Ti, Al, Mg and Ba. Possibly, Mn will be present as Mn(III) or Mn(IV) in these phases. This information leads to the conclusion that

[19] Green, chromate-rich, groundwaters can be seen at several localities, including Wadi Sidjin, midway between the Eastern and Western Springs.

pure MnO_2 is not likely to be an oxidant for Cr(III) in the Maqarin analogue cement. However, the most probable host phase for Mn(III, IV), micrometer-size, ferrite-type and Fe-oxide phases, is also a host phase for Cr(III). This makes interaction between the two elements possible without strong transport limitations. The only limitation is the presence of water that is necessary for these reactions to occur.

The second oxidation pathway involves reaction between Cr(III) and dissolved oxygen. Although surrounding aquifers in the biomicrite seem to be well buffered in a reduced state, the penetration of oxygen in fractured analogue cements cannot be discounted, mainly due to the seasonal water cycle. Eh-pH diagrams (Figure 4.14) show that at pH ~12 and in the presence of dissolved oxygen, Cr(VI) species should be dominant and stable in solution. Unfortunately, attempts to examine trace element speciation in the highly aggressive groundwaters at Maqarin have so far proved unsuccessful (see Alexander, 1992 and Linklater, 1998 for details). Kinetic limitations reported at lower pH for the oxidation of Cr(III) by DO (Schroeder and Lee, 1975; Eary and Rai, 1987; Richard and Bourg, 1991) could therefore be removed at higher pH and produce visible effects on long time scales as shown by the Maqarin natural analogue. Such a hypothesis requires experimental confirmation.

Both hypotheses have important implications for the industrial use of analogue cements as an immobilisation matrix for Cr or with respect to the release of Cr by leached analogue cements. In particular, the content and speciation of Mn in these analogue cements is predicted to have a potentially crucial role in the stability of Cr within this matrix. Maqarin analogue cements are a tool that will enable further investigations in this direction, by looking carefully, at the grain scale, at the speciation changes of Fe and Mn upon hydration. One important point to elucidate is whether Mn and Cr found as diluted elements (< 10,000 ppm) in host phases like iron oxides, spinels or ferrites are, in the presence of water, able to react together. This is observed in the laboratory for pure Mn oxide suspensions in presence of dissolved Cr (Weaver and Hochella, 2003). The possibility for DO to oxidise significantly Cr(III) blocked in a analogue cement matrix is also of practical importance for the performance assessment of degrading chemotoxic waste containing concrete.

Even if Cr(VI) is more soluble than Cr(III), secondary trapping of leached Cr occurs *in situ* because of fixation of Cr(VI) in several mineral phases (e.g. Cr(VI) in gypsum, Cr(III) and Cr(VI) in ettringite, and Cr(VI) in hashemite). Therefore, the release of Cr(VI) is not only driven by diffusive phenomena, as secondary minerals can block or retard Cr(VI) transfer. The highly variable Cr(VI) profiles presented in Figures 4.19 and 4.21 confirm this hypothesis. Recently, Rose et al. (2003) also indicated that Cr(VI) may be less mobile than predicted by models based on diffusion control release.

Figure 4.38 *Leaching experiments. Top: Cr concentration in leachates of analogue cement columns M99-1-41 and M00-1-4 (log scale in concentration). Middle: Re concentration in leachates of analogue cement columns and the biomicrite column (M00-1-23). Bottom: linear correlation between Mo, Cr and Se release from sample M99-1-41*

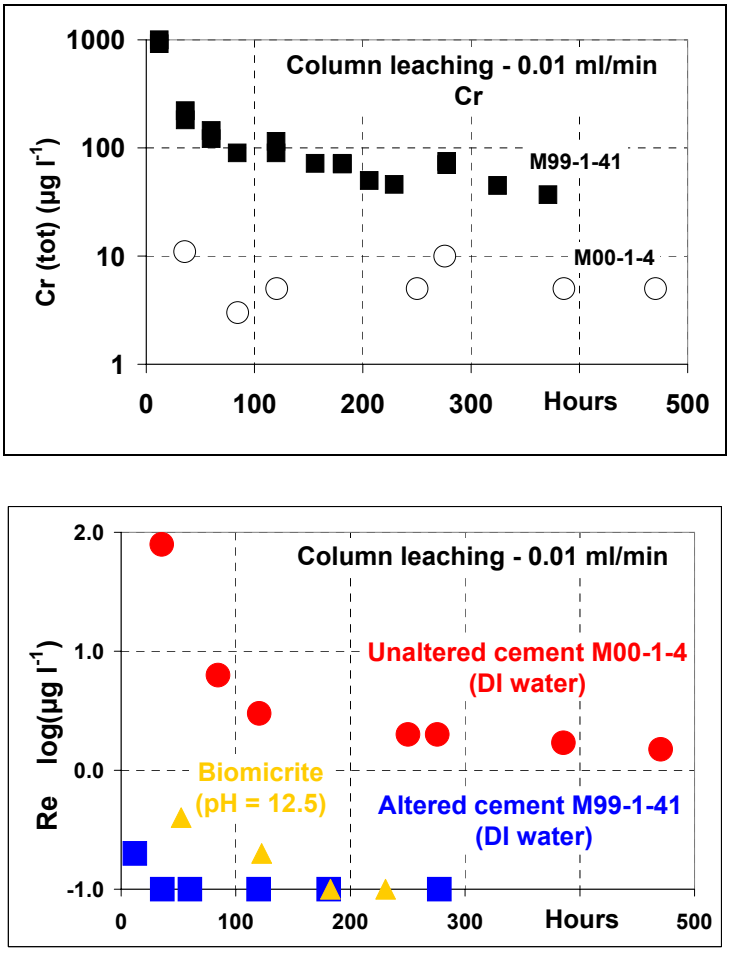

Figure 4.39 *Column-leaching experiments. Top: Cr, Zn and Fe release by the biomicrite column. Middle: Re and Mo release by the biomicrite column. Bottom: preferential release of Re over Mo from the biomicrite leached by high pH water. Due to uncertain data on Se content in the biomicrite, the preferential release of Se over Mo cannot be ascertained. A line was drawn assuming 200 ppm Se in the biomicrite*

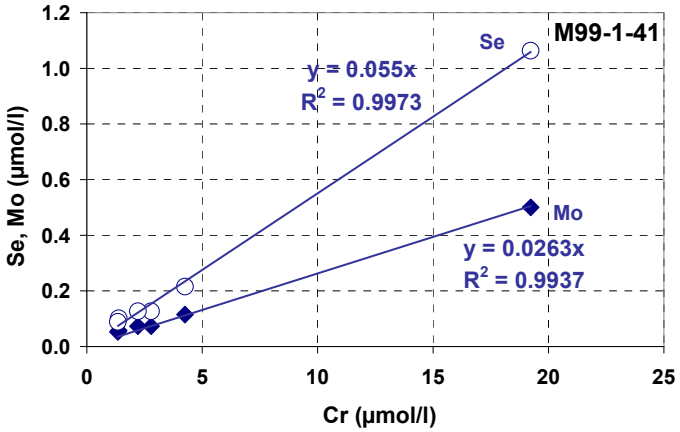

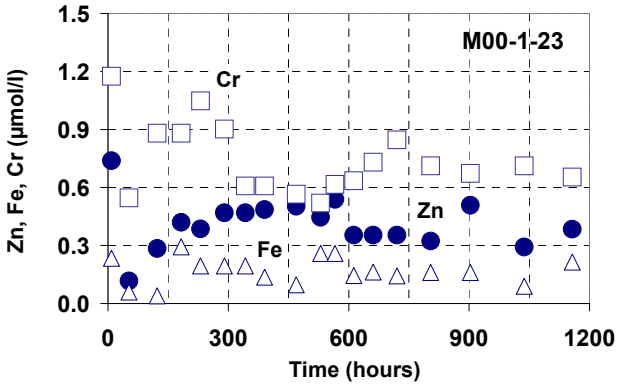

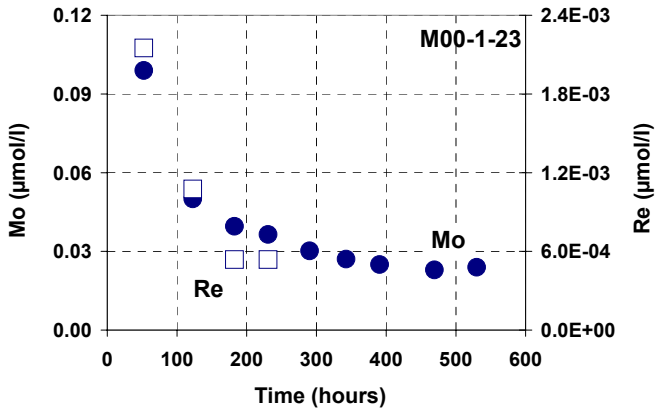

Figure 4.40 *Column-leaching experiments. Top: Compared releases of Re, Mo and Se by sample M00-1-4. Middle: Mo-Re correlation in leachates showing initial preferential release of Re. Bottom: Se- Mo correlation in the leachates showing the different behaviour of analogue cement M99-1-41 and M00-1-4*

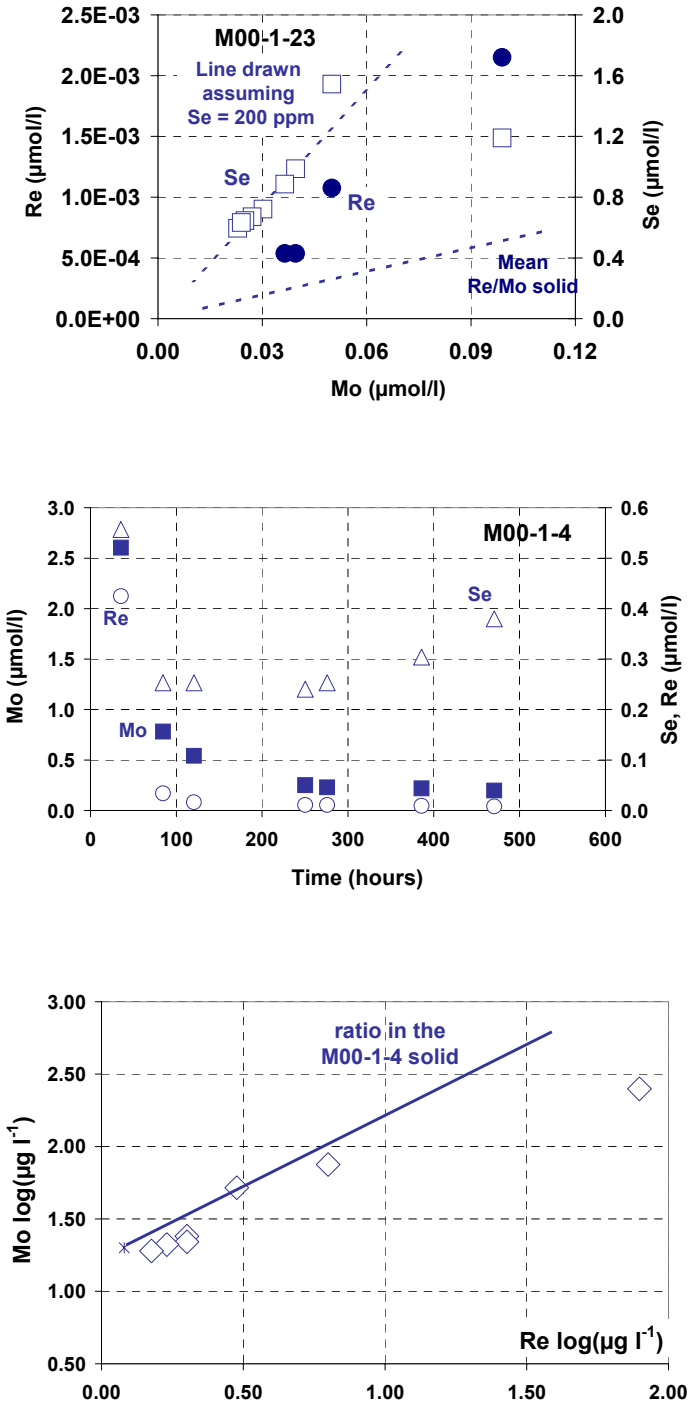

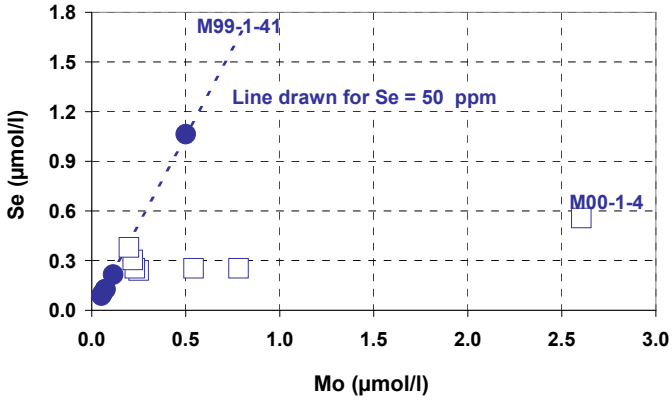

Figure 4.41 *Simple scheme presenting main Re sources and sinks in Maqarin. Two major Re pools are present: i) the Re present in the biomicrite (probably as Re(IV) in sulphides); ii) the Re trapped and concentrated after combustion in some regions of the analogue cement bodies (due to volatile Re compounds); at least two types of mineral phases host Re in analogue cements: small and rare Fe-S grains with high Re concentration and a major phase with low Re concentration. The redox state of Re in these minerals is not known. A large halo of weakly baked biomicrite seems to be depleted in Re. Leaching experiments have shown that Re can be rapidly leached from unaltered analogue cement bodies (see also Western Springs M5 groundwaters). Re is also leached out of the biomicrite by high pH waters. Re sinks are: i) outflowing waters, ii) several analyses suggest that sulphate bearing phases (gypsum?) could trap some of the leached Re*

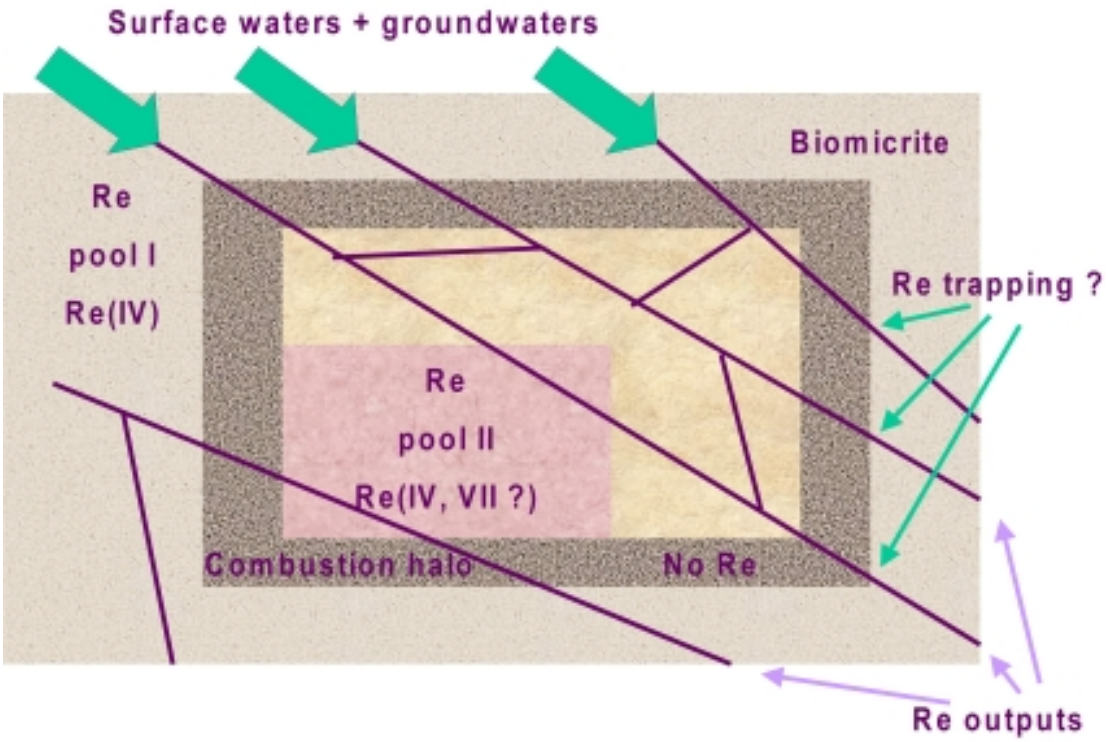

4.5 Magnetic Investigations across the Combustion Front in Maqarin (Adit A-6)

4.5.1 Introduction

Previous investigations conducted on different combustion-metamorphosed sediments have shown the occurrence of a magnetic anomaly at the vicinity of, or within, the metamorphosed body (Cisowski and Fuller, 1987; Ron and Kolodny, 1992). The magnetic anomaly arises from the transformation of sedimentary sulphides to magnetic iron oxides (mainly maghemite and magnetite) under the effect of heat. As such studies had not been conducted in Maqarin or Khushaym Matruk, they were proposed in Maqarin Phase IV project with three main objectives:

- to obtain more information on the combustion phenomenon itself by reconstructing a palaeotemperature profile. This information is important to interpret several features, e. g. clay accumulation in Khushaym Matruk or redox fronts in Maqarin. In Maqarin and Khushaym Matruk, the opportunity was given to sample material, from the ACZ to the biomicrite, along transects that were nearly perpendicular to the combustion front. The sampling line is relatively short in Khushaym Matruk (~10 m) but quite long in Maqarin (more than 100 m). The magnetic characterisations were coupled to mineralogical investigations.
- to test the feasibility of dating the combustion event by using palaeomagnetic information. Such a dating has been attempted in other sites (e.g. Ron and Kolodny, 1992). Oriented samples were collected from the Khushaym Matruk site for this purpose (see section 6.3.4).
- to use the magnetic signature of the combustion halo as a prospecting tool for buried ACZs. This was in particular intended for exploring the Western Springs site in Maqarin where the ACZ shows no visible outcrop. Inverse modelling of the magnetic anomaly should help to map the invisible analogue cement body. This possibility to use a magnetic survey to map analogue cement bodies could, however, be difficult in Maqarin, due to the presence of basalt flows above some of the ACZs.

This section presents results obtained on the Maqarin site. Magnetic investigations performed on the Khushaym Matruk site are presented in section 6.3.4, but the discussion in section 4.5.4 will also refer to some of the results obtained in Khushaym Matruk.

4.5.2 Samples: description and characterisation

The samples collected along Adit A-6 were taken from the west wall, at about 1.5 m above the floor. To minimise the effects of tunnel-induced artefacts, the samples were collected after removal of the first few centimetres of the rock surface. This is especially important in the ACZ where a mixed carbonate/CSH coating develops on the wall surface (Figure 4.41). The profile was collected in several campaigns from May 1999 to May 2002 (Smellie, 2000). Table 4.12 lists the studied samples with their visual aspect. The above mentioned samples were not oriented. A small series of oriented samples (small plugs) were also collected during the field campaign of November, 2000 (Table 4.13).

Figure 4.42 View of Adit A-6 showing typical thick carbonate travertine precipitates on the tunnel wall (consists of calcite, aragonite vaterite and minor CSH (Milodowski et al., 1998a)

4.5.2.1 Magnetic characterisations

The following quantities were measured during magnetic characterisations :

- Specific magnetic susceptibility χ ($m^3\ kg^{-1}$)
- Saturation remnant magnetisation **Mrs** ($mA\ m^2\ kg^{-1}$)
- Saturation magnetisation **Ms** ($mA\ m^2\ kg^{-1}$)
- Coercitive field **Hc** ($kA\ m^{-1}$)
- Remnant coercitive field **Hcr** ($kA\ m^{-1}$)

In addition, the remnant magnetisation of the samples was characterised using following quantities:

- Natural remnant magnetisation **NRM** (direction, intensity)
- Isothermal remnant magnetisation **IRM** (intensity).

4.5.2.2 Mineralogical and geochemical characterisations

Samples were subjected to thermal analysis (thermogravimetry, heat flow measurement, evolved gas analysis) in order to characterise the evolution of several compounds along the profiles: carbonates, organic matter, gypsum, sulphides and clay minerals.

Specific elements were analysed on whole rock because of their importance in magnetic mineralogy: Ti, V, Cr, Fe, Ni, Zn, Sr.

Several samples or separated fractions were also characterised using FTIR spectroscopy, X-ray diffraction and Scanning Electron Microscopy coupled to an EDX analyser.

Details on methods, techniques and significance of measured quantities are given in Appendix 4.

4.5.3 Results

4.5.3.1 Magnetic characterisation of Adit A-6 samples

The evolution of the magnetic susceptibility along the profile (Figure 4.43 and Table 4.14) confirms the existence of a strong anomaly, as was foreseen from previous investigations on similar systems (e.g. Cisowski and Fuller, 1987). The intensity of the anomaly is very high for a sedimentary rock and in the same order of magnitude as the susceptibility for a basalt. The anomaly is located between 95 m and 113.5 m in Adit A-6 and displays two major maxima, at 109 m (4.8×10^{-6} m^3 kg^{-1}) and 105 m (2.46×10^{-6} m^3 kg^{-1}). Slightly negative values that are observed between 50 m and 90 m suggest that paramagnetic components of the rock are very weak and are consistent with the diamagnetic signature of calcite. In the deeper part of the profile, low and positive values are obtained, suggesting the existence of paramagnetic or ferrimagnetic minerals in the ACZ (e.g.clays, haematite).

The same profile for saturation remnant magnetisation (Figure 4.43) also displays a strong anomaly with the same location and aspect as the susceptibility anomaly. These data support the hypothesis of ferromagnetic minerals (e.g. magnetite, maghemite, pyrrhotite) being the carrier of the remnant magnetisation. To obtain more detail, the evolution of susceptibility with temperature was studied (see Figures 4.44 and 4.45). For samples before 80 m, the susceptibility and its variations with temperature are very weak and do not provide any further information. For the sample at 90 m, no significant signal is observed under Ar atmosphere, whereas under air, during the cooling period, formation of a susceptible phase is noted under 550°C.

Table 4.12 List of samples collected in Adit A-6 for magnetic investigations (unoriented samples)

Sample Reference	Sampling Date	Distance from Adit entrance (m)	Comment
M99-1-33b TZ -3	May 1999	50	Grey, homogeneous marl

M01-A6-U1	Feb. 2001	70	Grey, homogeneous marl
M01-A6-U2	Feb. 2001	80	Grey, homogeneous marl
M02-A6-H1	May 2002	85	Marl (grey and black)
M01-A6-U3/M02-A6-H2	Feb. 2001	90	Marl (grey and black)
M02-A6-H3	May 2002	95	Brown black marl
M02-A6-H4	May 2002	100	Black to dark grey marl
M99-1-33b TZ -2	May 1999	104	Brown marl
M01-A6-U4	Feb. 2001	105	Grey marl, veins with white fillings
M01-A6-U5	Feb. 2001	106	Dark grey marl
M01-A6-U6	Feb. 2001	107	Grey beige marl
M01-A6-U7	Feb. 2001	108	Pale grey, hard marl, slightly baked
M99-1-33b TZ -1	May 1999	109	Beige baked marl (hard)
M99-1-33b TZ 1	May 1999	110.5	Pale grey marl (fossil tests present)
M99-1-33b TZ 2	May 1999	111.5	Pale grey baked marl
M99-1-33b TZ 3a	May 1999	113	Pale grey baked marl; less fossil tests
M99-1-33b TZ 3b	May 1999	113.3	Beige pink baked marl
M99-1-33b TZ 4a	May 1999	113.5	White orange altered material
M99-1-33b TZ 4b	May 1999	114	Altered analogue cement (white pink red)
M99-1-33b TZ 5	May 1999	115	White altered analogue cement (no more fossils)
M99-1-33b TZ 6	May 1999	118	White altered analogue cement
M99-1-43 a	May 1999	130	Altered analogue cement pink beige
M99-1-41	May 1999	140	Altered analogue cement pink beige
M00-1-4		256	Unaltered analogue cement (pink with dark spots)

Table 4.13 List of oriented samples collected in Maqarin Adit A-6

Sample reference	Sampling Date	Distance from Adit entrance (m)	Comment
M00-1-27	Nov 2000	115.1	White pink altered analogue cement
M00-1-28	Nov 2000	114.1	Pink totally baked marl
M00-1-29	Nov 2000	112.85	Grey baked marl
M00-1-30	Nov 2000	112.15	Dark grey baked marl
M00-1-31	Nov 2000	112.15	Grey baked marl; fissures with white fillings
M00-1-32	Nov 2000	99	Grey marl
M00-1-33	Nov 2000	98.85	Grey marl; fissures with white fillings

For further samples (105 m, 106 m, 107 m, 108 m, 109 m and 110,5 m), the signal is sufficiently strong to give access to the Curie temperature Tc. For samples 105 m, 106 m and 107 m, Tc is clearly 580 $\pm$ 5 °C whereas for samples 108 m, 109 m and 110.5 m, the susceptibility versus T curves indicate a composite signal with Curie temperatures between 580°C and 620°C (e.g. sample 108 m, Figure 4.44). Low temperature (0°C to –195°C) susceptibility was measured, to search for the crystallographic Verwey transition at –150$\pm$5°C characteristic of pure magnetite. This characteristic transition was, however, not observed (Figure 4.45). Therefore, the ferromagnetic minerals responsible for the anomaly are not pure magnetite. Other magnetic phases explaining the observations could be minerals from the maghemite family or substituted magnetites. Making the assumption that the mineral responsible for the anomaly is maghemite, a profile of equivalent concentration in maghemite can be drawn from saturation magnetisation Ms (Figure 4.46). This yields maximum mineral concentrations in the order of 0.5 wt %, compatible with the total Fe content of the biomicrite of around 1 %.

For verification of the nature of this magnetic phase, a chemical and physical separation was performed on samples 105 m and 108 m. The X-ray diffraction spectrum of the magnetic

fraction of sample 105 m indicated haematite (not previously detected magnetically because of its weak magnetic signature). Neither magnetite nor maghemite could, however, be confirmed by the XRD spectrum, probably because of their low concentration in the separate and because of line interference with calcite and haematite.

Figure 4.43 Evolution with distance along Adit A-6 of the magnetic susceptibility (red) and of the saturation remnant magnetisation (black) of samples

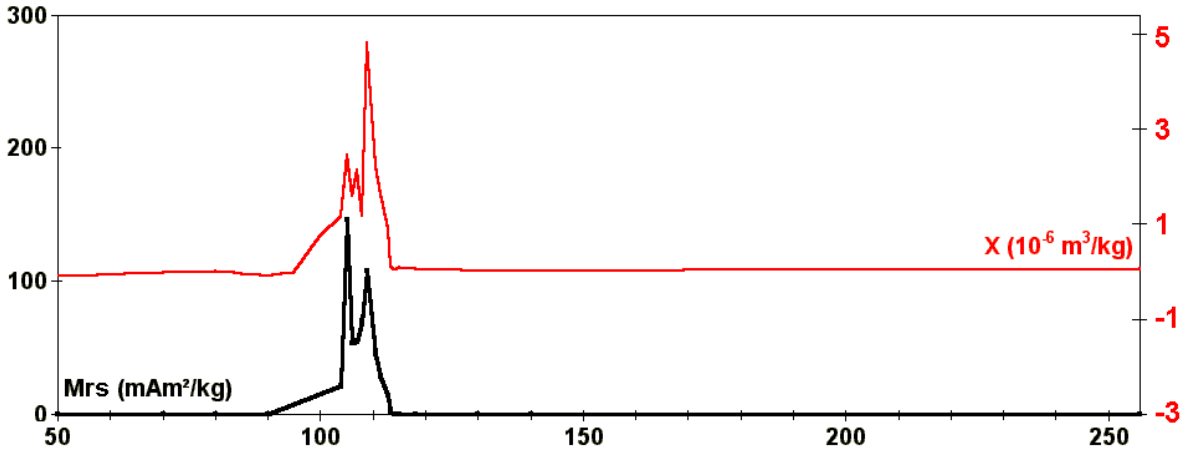

4.5.3.2 Correlation with SEM investigations

SEM investigations conducted on the magnetic extractions (105 m, 108 m) and on polished sections of these samples confirmed the presence of Fe-oxide type minerals. These iron oxides are present as framboidal aggregates (Figure 4.47) around 20 µm in diameter, with individual particles around 0.5 µm size. These aggregates are often found within foraminiferal tests together with other mineral phases (probably clay type minerals). EDX analyses show that these iron oxide framboids contain several trace elements, including Ni, Zn, Cr, Ti, Cu and V (Figure 4.48). Chemical analyses of bulk samples were therefore carried out on the samples (Table 4.15).

Previous observations of the intact biomicrite (e.g. Milodowski et al., 1992a, 1992b; 1998a, 1998b) have shown that pyrite is frequently found as framboidal aggregates within fossil tests. This suggests that the magnetic iron oxides found in samples 105 m and 108 m are directly inherited from these sulphide aggregates. Combining magnetic data from Table 4.15, a Day diagram (Day et al., 1977) was built (Figure 4.49).

Table 4.14 Magnetic parameters for samples collected in Adit A- 6 (non oriented samples)

Sample Reference	Distance from Adit entrance (m)	Hc (kA/m)	Hcr (kA/m)	Mrs (mAm²/kg)	Ms (mAm²/kg)	X(m^3/kg)
M99-1-33b TZ -3	50	nd	nd	nd	nd	-9,52E-08
M01-A6-U1	70	12,17	0	0	0,19	2,17E-08
M01-A6-U2	80	52,71	0	0	1,98	4,45E-08
M02-A6-H1	85	nd	nd	nd	nd	1,86E-09
M01-A6-U3/M02-A6-H2	90	187,70	0	0	0,87	-5,85E-08
M02-A6-H3	95	nd	nd	nd	nd	5,61E-09
M02-A6-H4	100	nd	nd	nd	nd	7,60E-07
M99-1-33b TZ –2	104	12,98	33,71	21,11	80,20	1,20E-06
M01-A6-U4	105	29,98	55,33	145,90	374,60	2,46E-06
M01-A6-U5	106	19,62	38,77	35,86	174,60	1,61E-06
M01-A6-U6	107	19,30	37,37	55,48	163,20	2,13E-06
M01-A6-U7	108	12,44	22,91	70,05	269,15	1,17E-06
M99-1-33b TZ -1	109	17,79	32,93	108,02	307,93	4,80E-06
M99-1-33b TZ 1	110.5	16,78	34,39	44,92	138,66	2,21E-06
M99-1-33b TZ 2	111.5	14,10	26,59	28,06	88,00	1,65E-06
M99-1-33b TZ 3a	113	12,47	26,35	13,66	42,86	8,96E-07
M99-1-33b TZ 3b	113,3	nd	nd	nd	nd	nd
M99-1-33b TZ 4a	113,5	11,59	68,71	1,63	4,22	1,07E-07
M99-1-33b TZ 4b	114	24,60	4,93	0,13	2,59	4,84E-08
M99-1-33b TZ 5	115	2,82	6,83	0,11	2,94	8,15E-08
M99-1-33b TZ 6	118	45,40	6,70	0,08	2,86	5,84E-08
M99-1-43 a	130	88,40	0	0,07	0,21	2,63E-09
M99-1-41	140	-10,26	0	0,02	-1617,51	4,26E-09
M00-1-4	256	2,63	19,99	0,20	6,79	6,21E-08

Figure 4.44 High-temperature susceptibility of several samples of the profile, showing the Curie transition

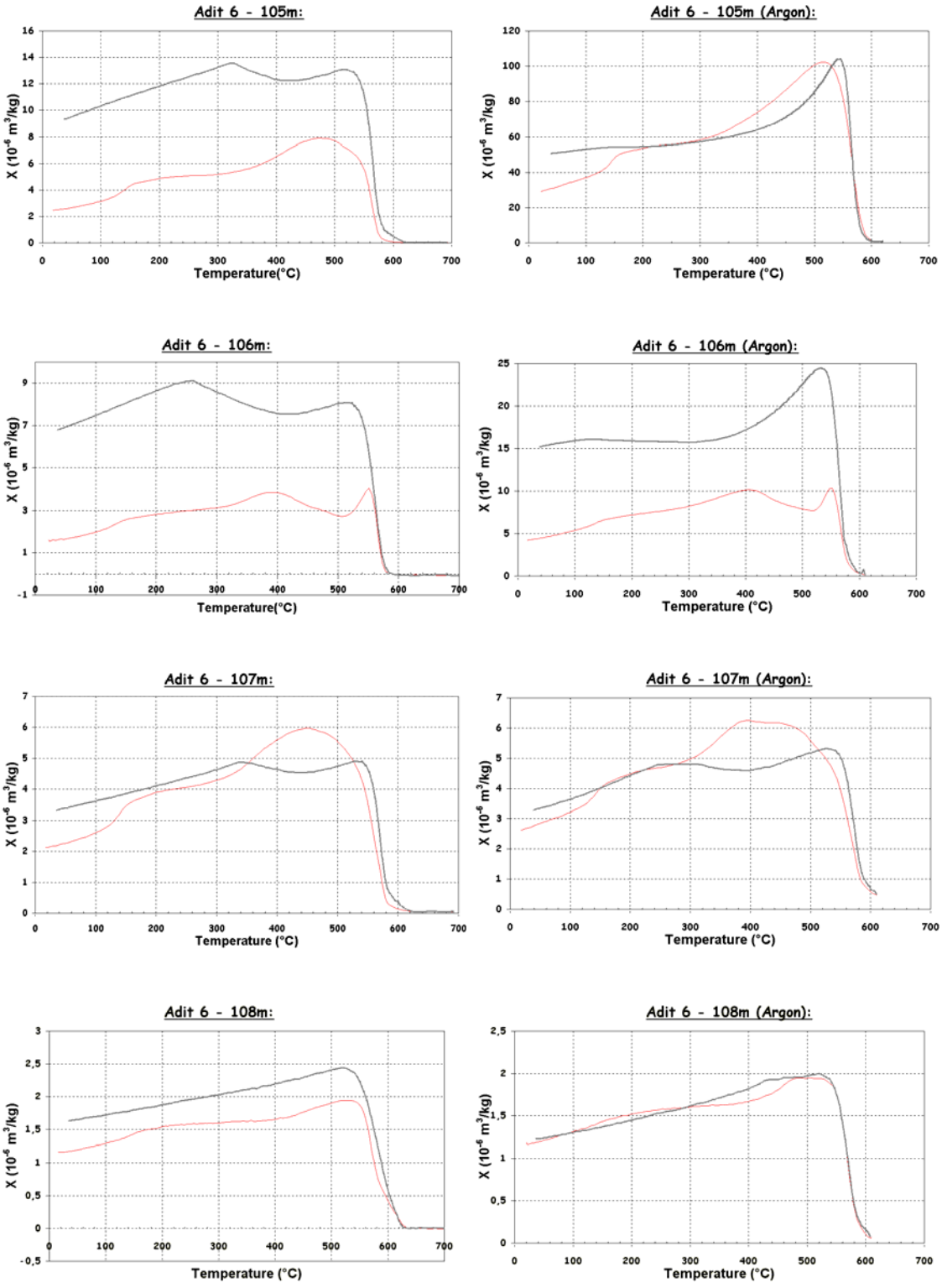

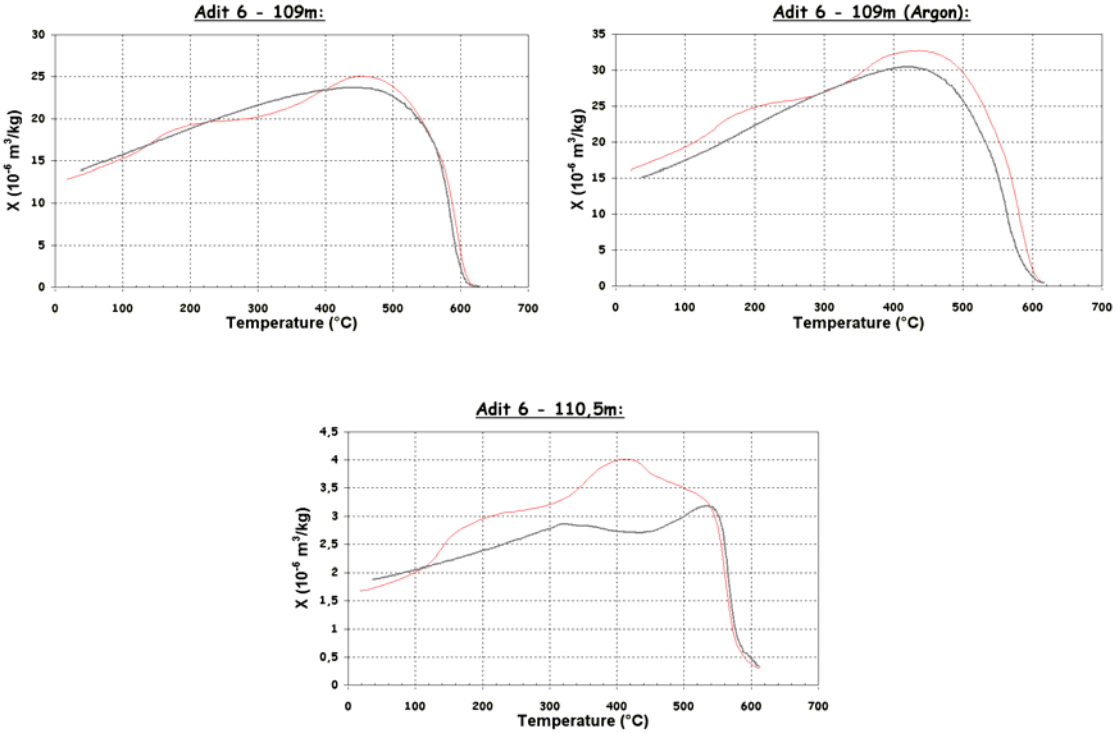

Figure 4.45 Low-temperature susceptibility of samples 106 and 107 m. The absence of a low-temperature transition excludes pure magnetite

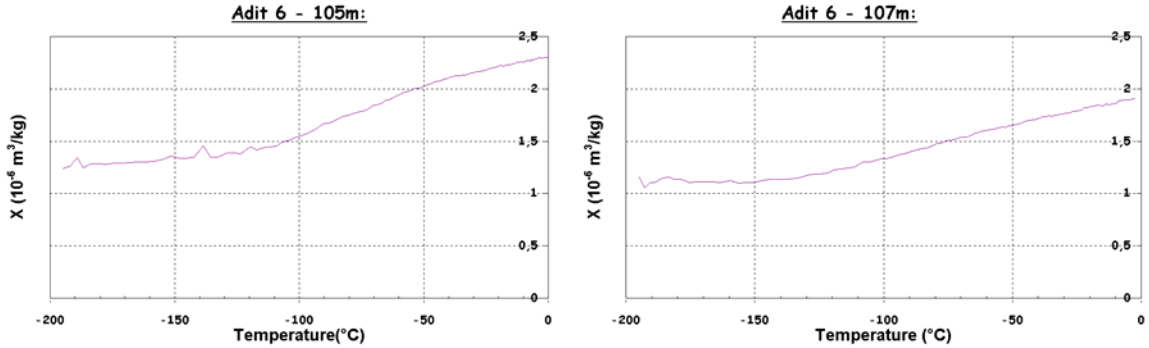

Although Day diagrams are normally used for magnetite, the distribution of the data points clearly suggests that the magnetic grains are pseudo-single-domain. That means that they should be present as small (< 1 µm) magnetic grains interacting one with each other. This distribution is consistent with the SEM observations (Figure 4.47), showing that the iron-rich grains are gathered in clusters, inherited from the pyrite framboids.

On Figure 4.50, the coercivity of several samples (104 m to 113.3 m) is compared to the same quantity for reference minerals (pyrrhotite, magnetite, goethite, haematite). This clearly shows that the behaviour of the samples is close to that of a magnetite-type mineral.

The difficulty in reaching saturation indicates the presence of haematite in the magnetic mineral fraction. In summary, the combined magnetic and chemical investigations have shown that a significant magnetic anomaly exists across the combustion front in Adit A-6. This magnetic anomaly, located between 95 m and 112 m from the Adit entrance, exhibits

two marked maxima at 105 m and 109 m. The investigations have shown that the origin of the anomaly are pyrite framboids, thermally pseudomorphosed and transformed to iron oxides.

Figure 4.46 Equivalent concentration of maghemite along Adit A-6 deduced from the magnetic anomaly

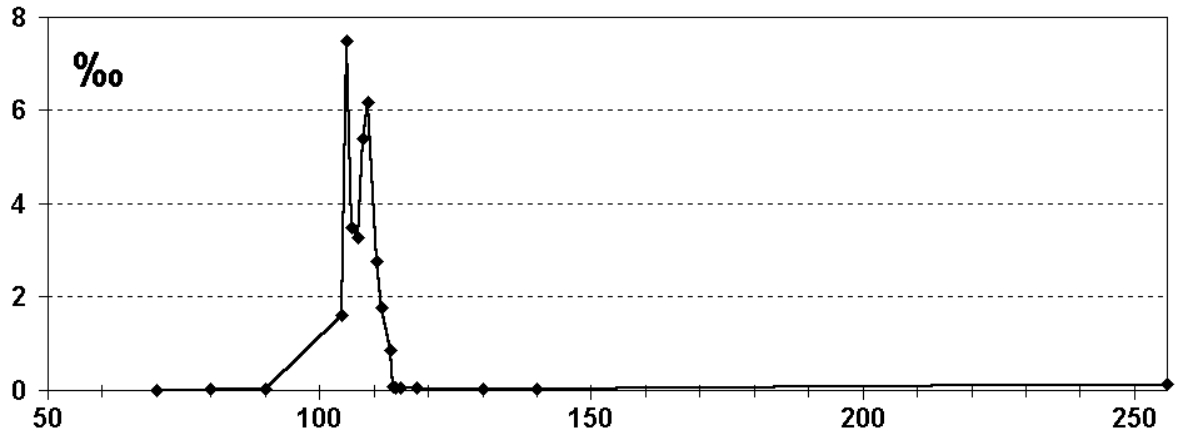

These iron oxides are mostly haematite and a magnetic iron oxide with properties suggesting a chemically substituted maghemite. These findings are in good agreement with data published by Ron and Kolodny (1992) on combustion-metamorphic rocks in Israel which have formed similarly to the Maqarin ACZ rocks.

4.5.3.3 Results from thermal analysis

Further characterisations were conducted on the profile samples using chemical analysis, thermal analysis, thermogravimmetry and Fourier transform IR spectroscopy. The objective was a better understanding of the spatial organisation of the magnetic anomaly within the combustion front. The results of thermal analyses are given in Figures 4.51 to 4.53. The thermal analysis of the biomicrite displays two major exothermic events (centered at ~320°C and at ~440°C) and one major endothermic event (centered at ~790°C). These events are correlated with important mass losses. By using the evolved gases analysis (EGA) (Figure 4.52) and previous investigations performed in Maqarin Phases II and III, it was possible to interpret the associated transformations (Table 4.16). The two important exothermic events observed on the intact marl (sample 50 m) are linked to the oxidation of two types of organic matter. As shown by EGA, these two kinds of organic matter (OM1 and OM2) have different signatures:

- for OM1 (exothermic event at 320°C), a strong H_2O and a medium CO_2 release are observed, together with low SO_2 and possibly CH_4 (or NH_3 ?) releases.
- for OM2 (exothermic event at 440°C), a strong CO_2 and a moderate H_2O releases are observed, together with SO_2. This signal corresponds to the signal observed previously by Geyer et al. (1998) on the Maqarin biomicrite.

It is observed in Figure 4.51, that the heat flux peak relative to OM2 decreases first when going from the unaltered biomicrite to the combustion front (i.e. the ACZ). It is also seen that the characteristic temperature for the heat flux peak relative to OM1 increases from ~315°C (sample 50 m) to ~400°C (sample 104 m). The organic matter OM1 disappears between samples at 105 m and 108 m.

The evolution along Adit A-6 of the magnitude of the three main heat flux peaks is summarised in Figure 4.53. A marked zoning is displayed in this representation:

- for $x \leq 80$ m: the three signals are stable
- for 85 m < x < 90 m: strong decrease of OM1 and OM2; OM2 disappears almost completely
- for 90 m < x < 105 m: OM1 displays a local maximum and then disappears
- for 100 m < x < 110 m : the decarbonatation peak shows a maximum
- for x > 112 m: the decarbonatation peaks diminishes strongly

For x > 110 m, the water loss peak at ~130°C, attributed to gypsum or ettringite is strongly increasing in magnitude.

The sample at x=85 m gives a specific response, with only one broad exothermic peak for OM and an endothermic peak corresponding to gypsum.

4.5.3.4 Results from FTIR spectroscopy

Figures 4.54 and 4.55 compare the IR absorbance spectra of different samples in the wave number intervals 3800-2700 cm^{-1} and 1200-400 cm^{-1}. Major absorption bands observed are quoted and interpreted in Appendix 4.

Geyer et al. (1998) concluded that the organic matter in the Maqarin biomicrite had a low aromatic carbon content. The same was observed in Khusaym Matruk (central Jordan) (see Chapter 6 of this Report), showing that the organic fraction of the biomicrite is an immature kerogen. Because the IR spectra shown here were recorded on total rock, most weak absorption bands, characteristic of organic matter, are masked by the very intense absorption bands of calcite and clay minerals. The pattern shown by the 2927 cm^{-1} and 2856 cm^{-1} bands can be attributed to aliphatic carbon (M. Elie, pers comm., 2007), although spectra for bitumen material containing aromatic carbons and containing these two bands are given in Van der Marel and Beutelspacher (1976). This doublet disappears almost completely for x > 80 m. It is thus possible to associate OM2, identified using thermal analysis, with this aromatic-poor immature kerogen fraction of the organic matter. The other fraction, OM1, was not detected using IR spectroscopy.

The group of absorption bands between 3700 and 3620 cm^{-1} is characteristic of kaolinite (Van der Marel and Beutelspacher, 1976). This is in good agreement with the data of Milodowski et al (1998a,b) who reported 1-5wt% kaolinite (although <1wt% was more usual) in samples from Adit A-6. The evolution of these bands from 50 to 110 m shows that a halo, containing a significantly higher concentration of kaolinite, exists from 90 to 100 m in Adit A-6. By comparing spectra of a pure reference kaolinite acquired in conditions normalised to our reference conditions (see appendix 4 on experimental conditions), it seems that the kaolinite reaches ~10 % wt concentration in the 90 m and 100 m samples which are the most concentrated. This is consistent with a low (< 1 % wt%) content in the 50 m sample. .

The wave number interval 1200-400 cm^{-1} shows the decarbonation after 113 m as well as the strong increase of carbonate around 106 m. The normalised absorbance of several characteristic bands have been plotted against distance from the entrance of Adit A-6 in Figure 4.56. The zones are in good agreement with those derived from thermal analysis :

- for x < 85 m: kerogen is present and mineral phases have average values.
- around x = 85 m: strong decrease in kerogen content
- from 90 to 105 m: a halo enriched in kaolinite is observed. The XRD of sample at 100

m confirms the presence of kaolinite.

- between 105 and 113 m: a marked enrichment in carbonates is noticed. However, this apparent enrichment could be partly due to the fact that, in this section of the profile, organic matter is totally destroyed.
- a massive drop in carbonate content is observed after 113 m. The higher absorbance at 875 cm^{-1} for sample 114 m could be partly due to the contribution of thaumasite.

Figure 4.47 Top and middle: SEM observations on a polished section of sample M01-A6-U7 (Adit A-6, 108 m). BSE image of a fossil test containing magnetic products and Ca distribution map. Middle: Detail showing Fe distribution and the product of Fe and Ni counts. Bottom: Sample M01-A6-U4 (105 m) BSE image of fossil test with iron oxides and glauconitic products; image of a separated fossil test showing pseudomorphosed sulphur framboids

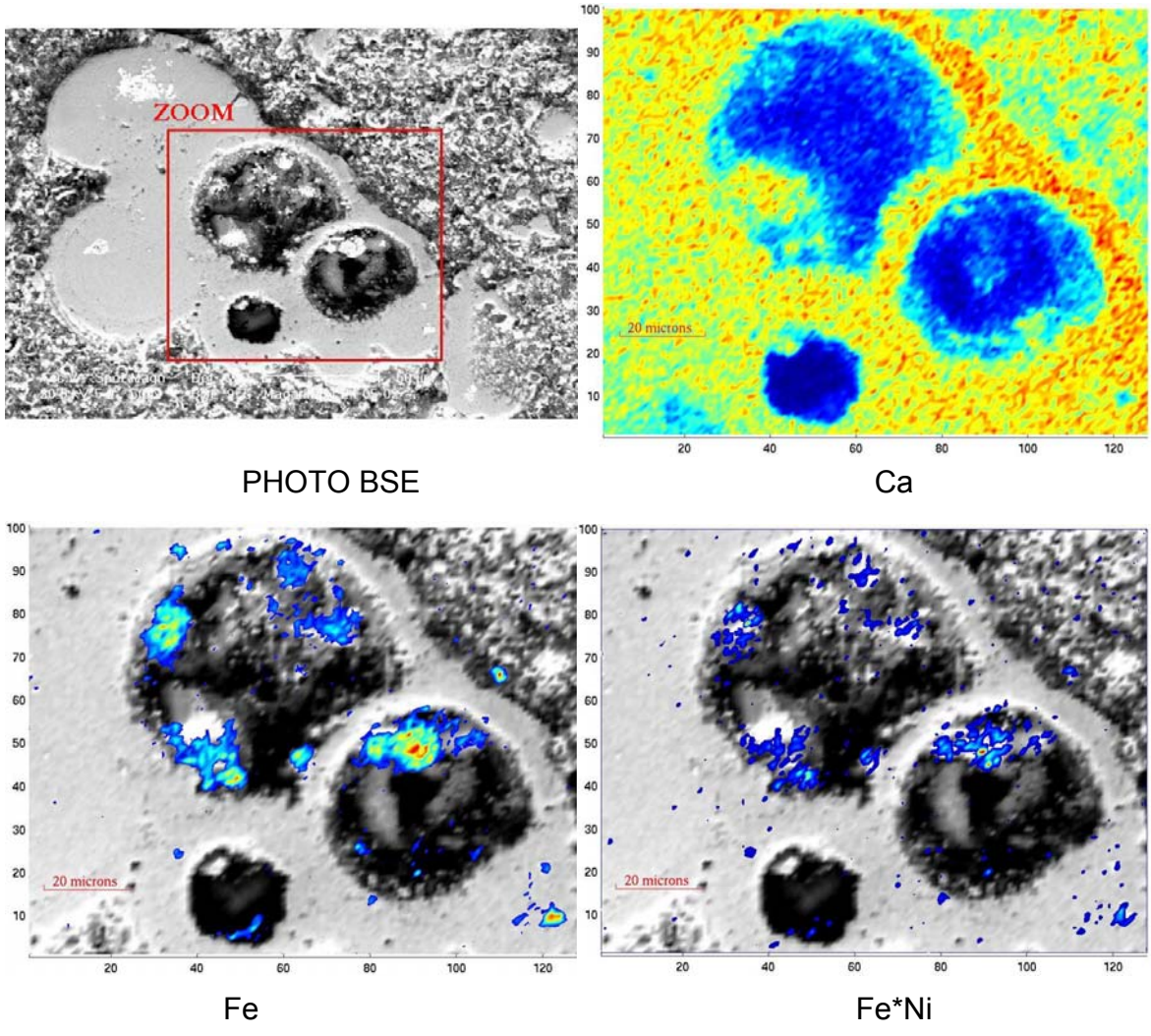

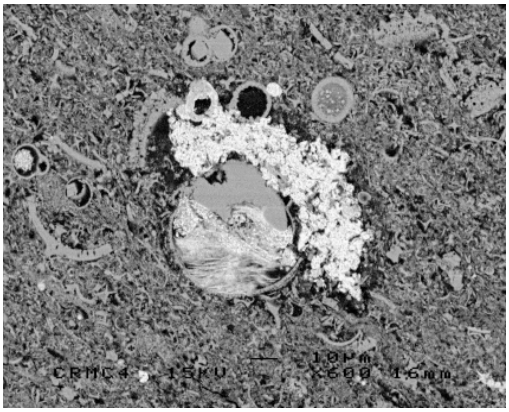

Glaucony

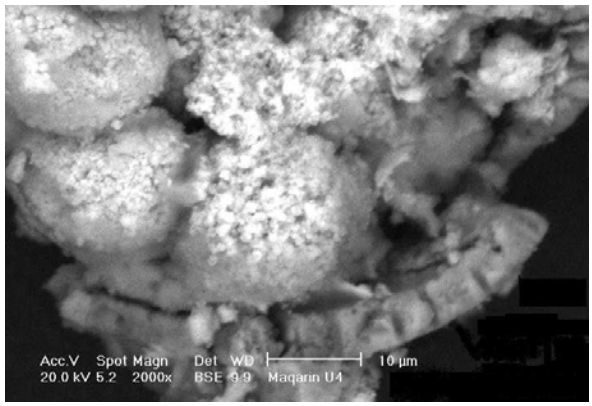

Foraminifera

Figure 4.48 SEM-EDX spectrum obtained on a separated magnetic fraction (iron oxide framboids) on sample U7 (108 m)

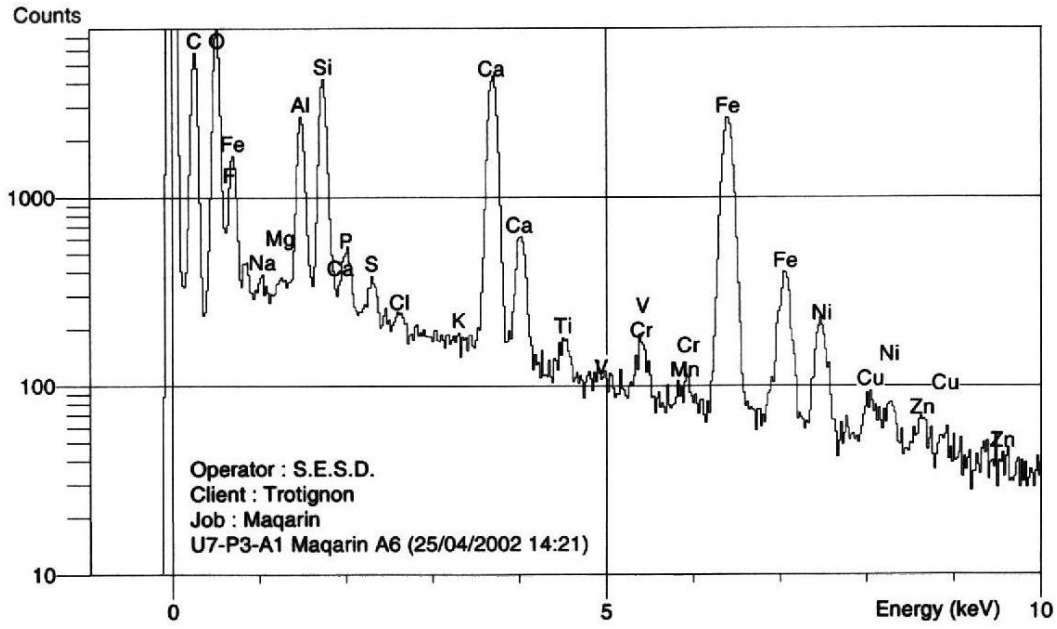

Some further information was derived from IR spectroscopy :

- at around 113-114 m, the mineral aragonite is present in significant quantities in the strongly baked biomicrite. This region is at the interface of what can be qualified as a baked biomicrite and hydrated cements. Bands characteristic of the mineral vaterite (White, 1974) or an amorphous calcium carbonate (Russell and Fraser, 1992) are also suspected. The XRD spectrum of sample 113.5 m confirms the presence of aragonite. The presence of vaterite is not confirmed because of many line interferences with calcite and thaumasite. Aragonite has been described previously (Milodowski et al., 1992a, 1992b; 1998a, 1998b) in association with fractures in the biomicrite which have reacted with hyperalkaline waters and the white travertine precipitates found on the tunnel walls (Figure 4.42). These are the sites of active hyperalkaline seeps which contain aragonite and vaterite (Milodowski et al., 1998a).
- a sulphate phase is detected in samples after 113 m, the observed bands corresponding to the hemihydrate of $CaSO_4$. As the samples were dried at 105°C

before the measurements, this corresponds to the probable presence of gypsum in these samples. Significant amounts of gypsum have been described previously by Milodowski et al. (1992a,b; 1998a,b) and is likely a byproduct of pyrite oxidation.

- weak and broad absorption bands at 962 and 1109 cm^{-1} were attributed to ettringite and/or thaumasite (Barnett *et al*., 2002). These bands are detected after sample 113 m.
- as already noted for thermal analyses, the sample at 85 m has a specific pattern, showing the presence of gypsum and total depletion in kaolinite. The XRD spectrum of sample at 85 m confirms the presence of gypsum.

Figure 4.57 compares the normalised IR absorbance at 875 cm^{-1} of the profile samples with the mass loss derived from thermogravimetry between 560°C and 1000°C. A relatively good agreement is found between these two series of measurements, confirming in particular the increase of carbonate content between 100 and 110 m followed by a sharp decrease beyond 113 m.

Table 4.15 Chemical analyses of Adit A-6 samples

Sample Reference	Distance from Adit entrance (m)	Ti (ppm)	V (ppm)	Cr (ppm)	Fe (ppm)	Ni (ppm)	Zn (ppm)	Sr (ppm)	Fe(II) (ppm)
M99-1-33b TZ -3	50	n.d.	n.d.	330	6600	n.d.	150	1600	n.d.
M01-A6-U1	70	825	81	213	7414	78	218	3760	4819
M01-A6-U2	80	825	81	213	9093	115	246	2044	8006
M02-A6-H1	85	675	71	152	7694	301	591	1310	4431
M01-A6-U3/M02-A6-H2	90	1274	100	332	10771	121	258	1735	10727
M02-A6-H3	95	1124	128	242	13149	105	201	1683	6063
M02-A6-H4	100	1124	116	283	14758	169	275	3385	14691
M99-1-33b TZ -2	104	1049	123	305	18045	143	236	3850	8861
M01-A6-U4	105	750	76	262	11401	133	320	8717	4664
M01-A6-U5	106	675	105	282	9932	161	380	3088	6996
M01-A6-U7	108	525	48	422	7834	117	310	920	1088
M99-1-33b TZ -1	109	1049	67	302	13499	92	293	4404	1088
M99-1-33b TZ 1	110.5	600	37	319	7974	126	231	1120	1166
M99-1-33b TZ 2	111.5	n.d.	n.d.	1080	12000	n.d.	100	1200	n.d.
M99-1-33b TZ 3a	113	600	38	194	7554	128	280	1114	933
M99-1-33b TZ 4b	114	675	81	168	9233	179	214	3127	700
M99-1-43 a	130	n.d.	n.d.	400	11000	n.d.	300	900	n.d.
M00-1-4	256	n.d.	n.d.	490	10000	n.d.	120	1700	n.d.

Chemical data for metals and Sr (Table 4.15) were plotted against distance (Figure 4.58). The Fe(tot) and Fe(II) profiles display strong variations within the 85 m to 113 m interval. For x < 100 m, Fe is predominantly present as Fe(II), suggesting that sulphide minerals (pyrite) are still present. A marked decrease in Fe(II) content is observed between 100 m and 110 m. Between 85 m and 104 m, Fe(tot) displays a marked and regular increase from about 8000 ppm to about 18000 ppm. This maximum is followed by a marked decrease and fluctuations between 108 m and 113 m. The Fe(tot) in the ACZ ranges between 10000 and 12000 ppm. The elements Zn, Cr and Ni show similar profiles, displaying marked

fluctuations and suggesting a local accumulation of Zn and Ni around x = 85 m and 106 m. A pronounced local accumulation of Cr is identified at 111.5 m The mean concentrations of Zn, Cr and Ni slightly increase from the marl to the analogue cement. Ti and V have very similar profiles, showing higher concentrations above 85 m and important fluctuations between 105 and 113 m. The specific magnetic susceptibility and the saturation remnant magnetisation have been plotted alongside the iron profiles in Figure 4.58. The first magnetic anomaly (~105 m) is clearly linked with the redox front of iron, whereas the second magnetic anomaly (~109 m) corresponds to an iron accumulation situated in the oxidised zone. A significant correlation between the location of magnetic anomalies and the profile of strontium concentration is also observed.

Figure 4.49 Day Diagram on which datapoints from Adit A-6 and Khushaym Matruk are plotted

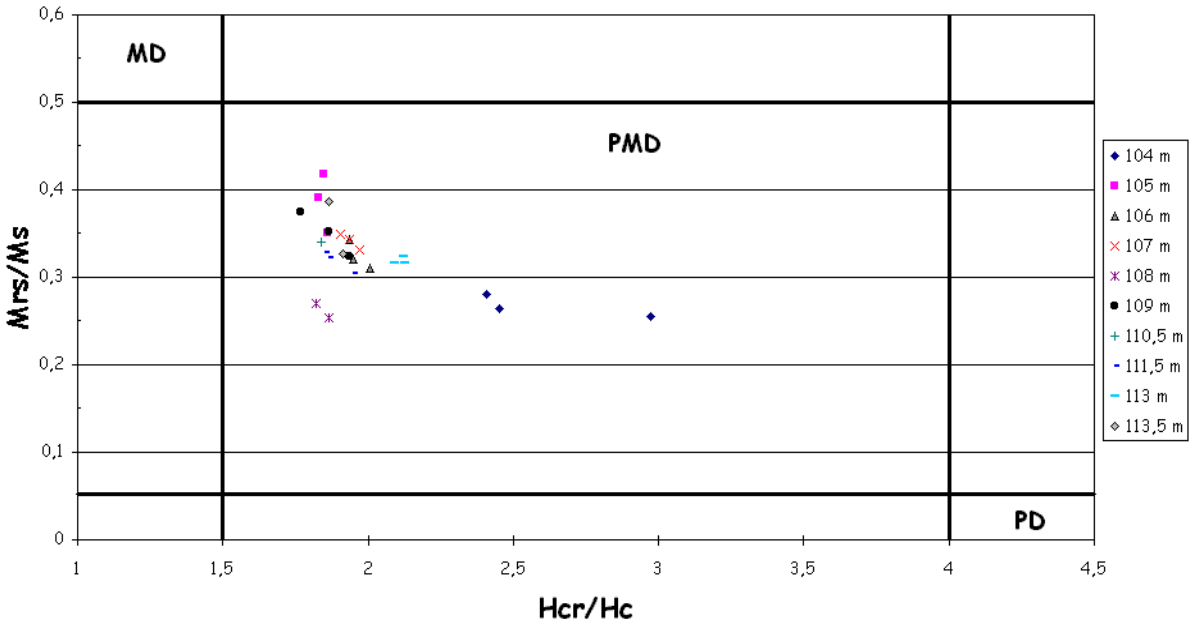

Table 4.16 Description of main thermal events observed during the thermal analysis of Adit A-6 samples

Temperature (°C)	Description	Interpretation
~80°C	Weak endothermic	Water loss from clays
~130°C	Weak to medium, endothermic	Water loss from sulphates (gypsum)
~320°C	Strong to medium exothermic	Oxidation of organic matter (OM1)
~440°C	Strong to medium exothermic	Oxidation of organic matter (OM2) and of pyrite
~520°C	Weak exothermic	Oxidation of organic matter (OM3)
~790°C	Strong endothermic	Decarbonation of calcite

Figure 4.50 Comparison of coercivity of reference mineral phases with Adit 6 samples. The field at saturation is normalized to 1

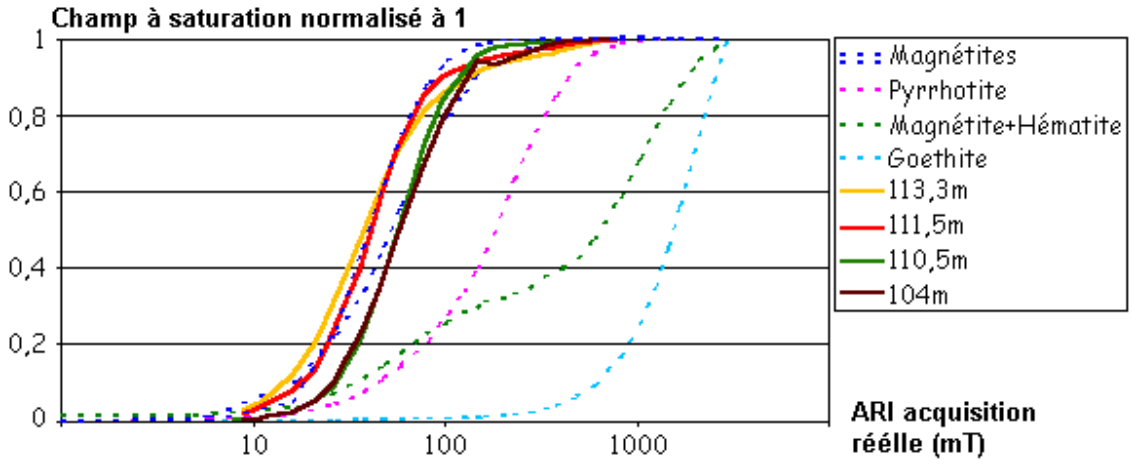

Figure 4.51 Thermal analysis and thermogravimetry of samples along Adit A-6 from abscissa 50 m to 118 m

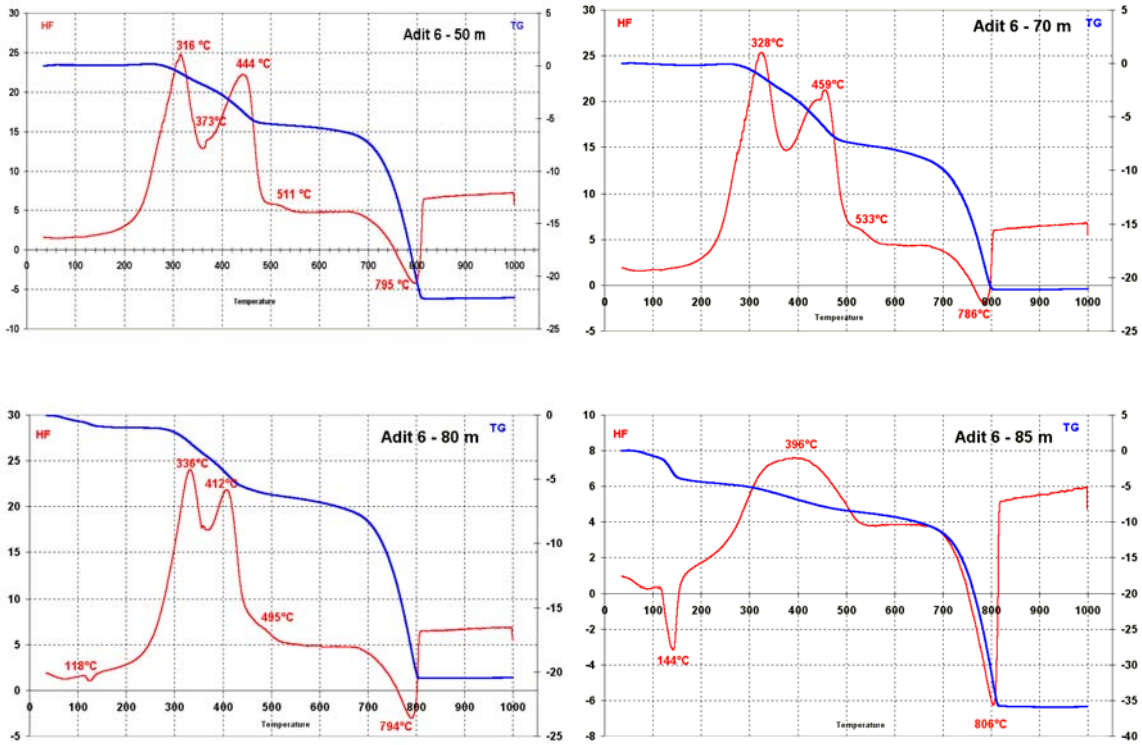

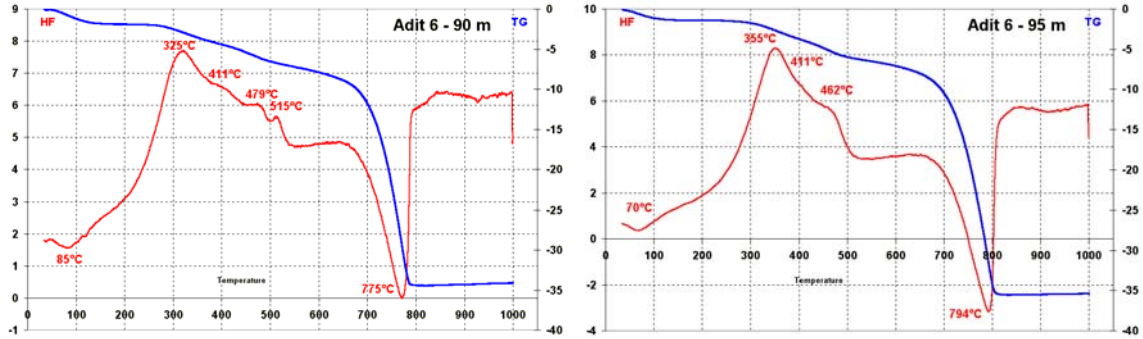
HF
TG
Adit 6 - 90 m
325°C
411°C
479°C
515°C
85°C
775°C
Temperature

HF
TG
Adit 6 - 95 m
355°C
411°C
462°C
70°C
794°C
Temperature

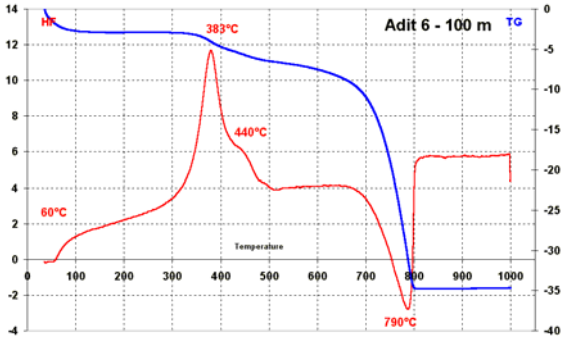
HF
TG
Adit 6 - 100 m
383°C
440°C
60°C
790°C
Temperature

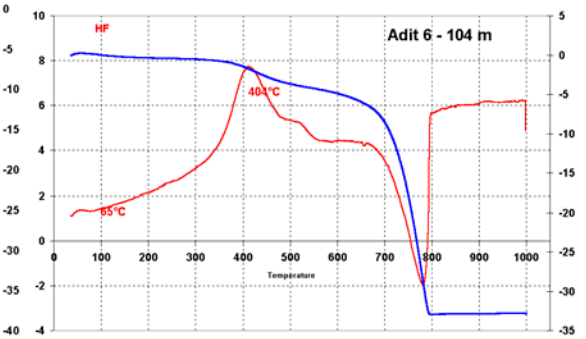
HF
Adit 6 - 104 m
404°C
65°C
Temperature

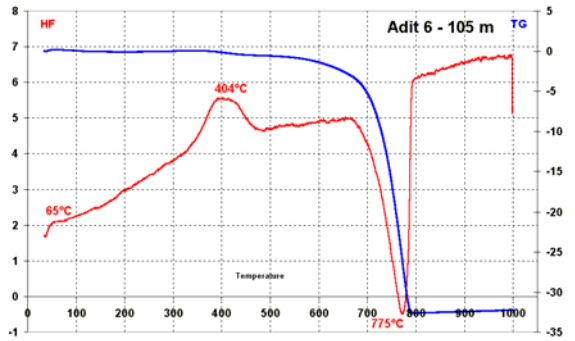
HF
TG
Adit 6 - 105 m
404°C
65°C
775°C
Temperature

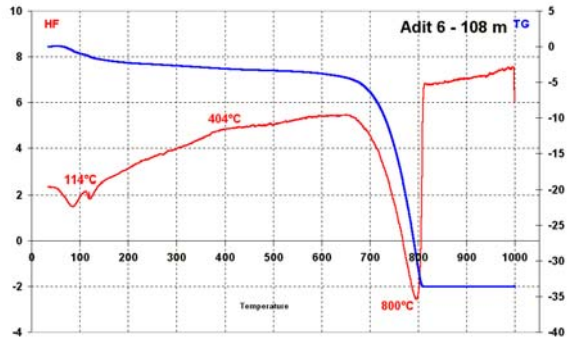
HF
TG
Adit 6 - 108 m
404°C
114°C
800°C
Temperature

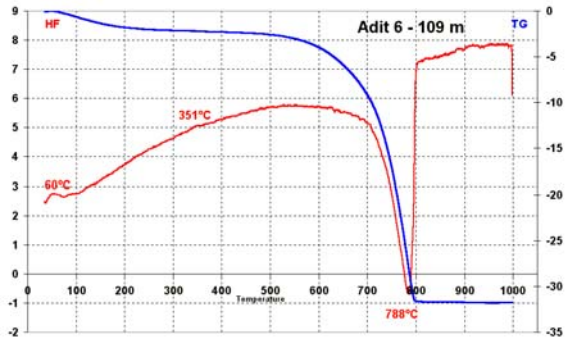
HF
TG
Adit 6 - 109 m
351°C
60°C
788°C
Temperature

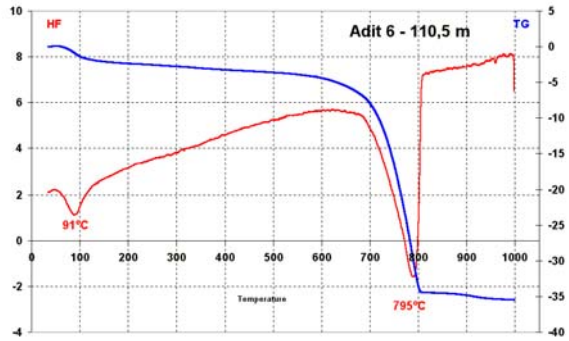
HF
TG
Adit 6 - 110,5 m
91°C
795°C
Temperature

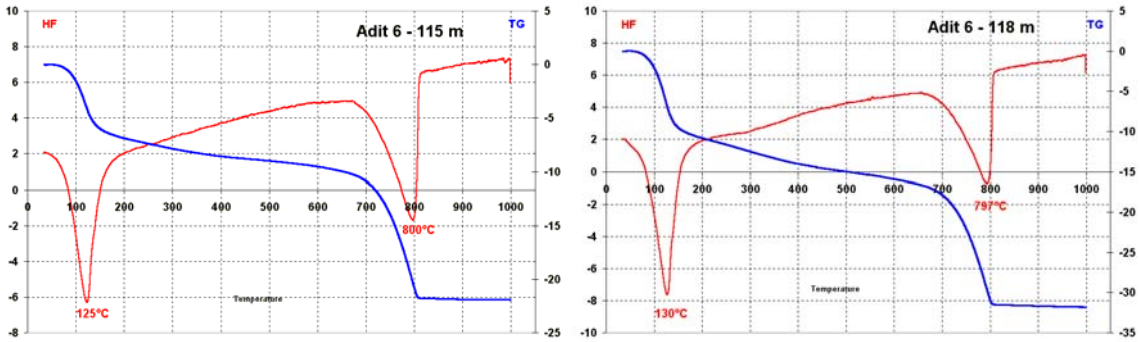

Figure 4.52 *TG/Thermal analysis with evolved gas analysis for sample M01-A6-U1 (Adit A-6 70 m). The different signals have been expanded for better legibility of the figure. Heavy dotted green : TG; light dotted green : DTG; red : DTA; purple : CO_2; blue: H_2O; dark green : SO_2; bright green : CH_4 or NH_3*

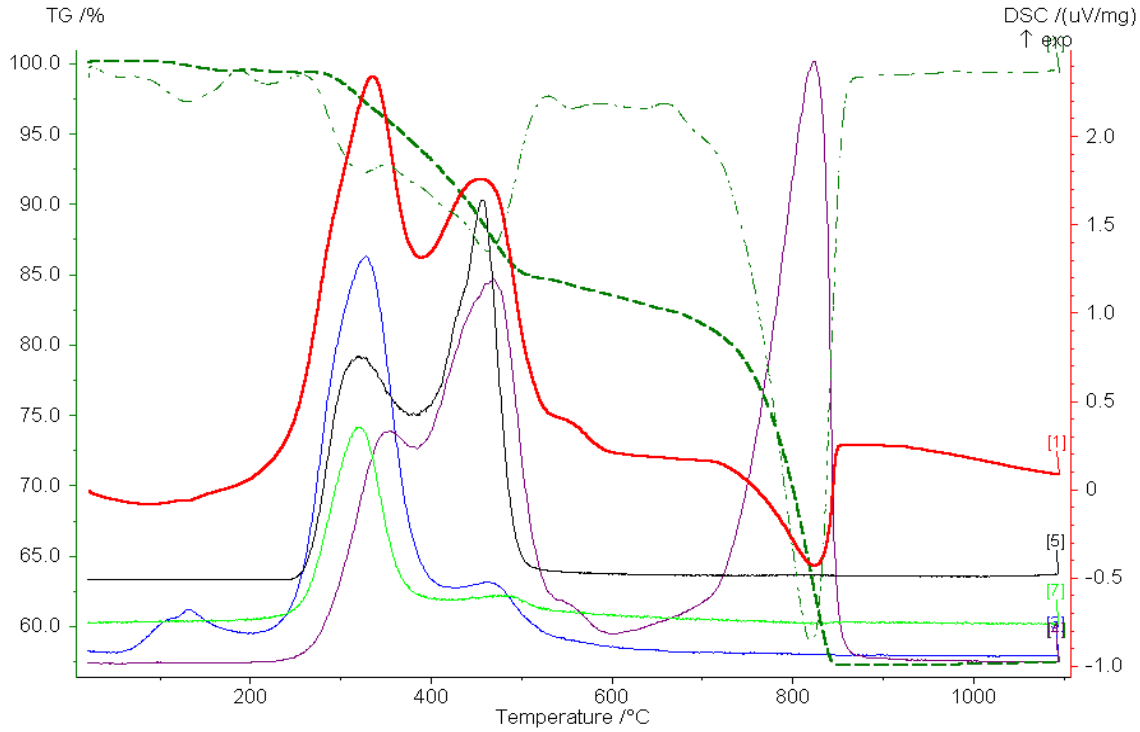

Figure 4.53 Evolution along Adit A-6 of specific heat fluxes measured on samples during thermal analysis (OM1 : organic matter 1 at ~330°C; OM2 : organic matter 2 at ~440°C; Calcite at ~790°C)

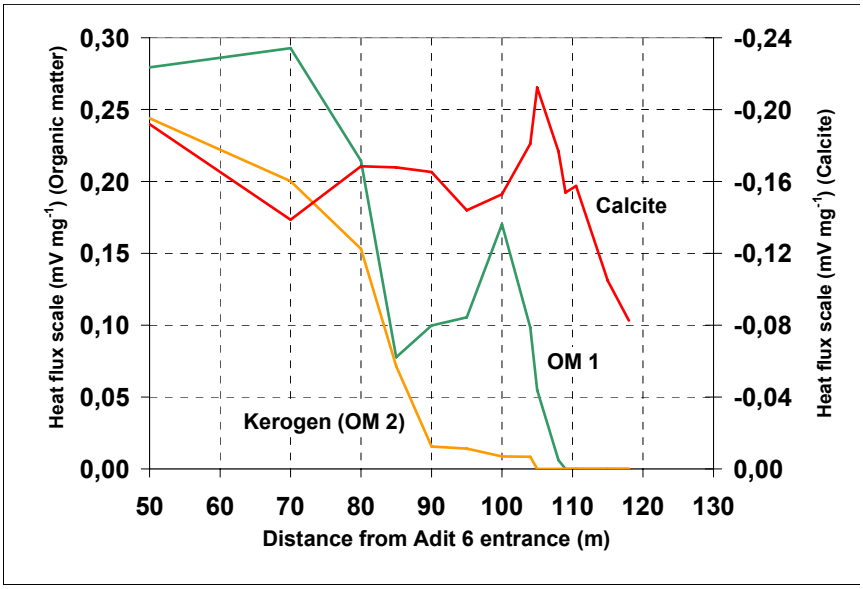

4.5.4 Synthesis and discussion

In this discussion, reference will also be made to several results obtained in Khushaym Matruk. The magnetic investigations conducted on samples collected in Maqarin along Adit A-6 and in central Jordan (Khushaym Matruk) confirmed the existence of a significant magnetic anomaly between the analogue cement bodies and the unaltered marl. This finding is consistent with previous investigations on combustion metamorphism (Cisowski and Fuller, 1987; Ron and Kolodny, 1992). The sampling and characterisation in Maqarin of a complete profile of about 100 m in length, from unaltered micrite to wihtin the analogue cement body, gives new insight on the spatial organisation of the combustion halo and therefore on the combustion process itself.

The magnetic anomaly observed in Maqarin is found to be double, exhibiting two distinct maxima (for both susceptibility and remnant magnetisation) at ~105 m and ~109 m from Adit A-6 entrance, respectively. Combined mineralogical and magnetic characterisations show that

- the magnetic minerals are inherited from sulphide minerals (pyrite). These sulphides are found in the biomicrite, as framboids, within fossil tests. This observation is consistent with findings by Ron and Kolodny (1992) on the Mottled Zone Formation of Israel, which is very similar to the ACZ at Maqarin.
- the measured Curie temperatures, the order of magnitude of other magnetic parameters and the geochemical characterisations clearly suggest that the 105 m anomaly is due to magnetite-type iron oxides, whereas the 109 m anomaly originates from maghemite type oxides.
- the rock mass affected by the combustion process, between unaltered biomicrite and analogue cements, extends for about 30 m (from ~85 m to ~115 m from Adit A-6 entrance). Several geochemical markers have been identified within this span. These

include degradation of the different fractions of the organic matter, local accumulation of kaolinite, local recarbonation, iron(II)/iron(III) redox front, aragonite marking at 114 m, and correlated fluctuations of the concentration level of several trace elements. Several of these correlations are still not fully understood, such as the correlation between Sr concentration and magnetic anomalies.

A synthetic sketch combining several physico-chemical data, as well as the colour of samples, is presented in Figure 4.59.

The observation made on the organic matter are particularly noteworthy. Thermal analyses clearly show that this organic matter is composed of several different fractions. However, the kerogen fraction of this organic matter called OM2, (Figure 4.53) appears to have disappeared from the combustion halo before the other main fraction (OM1) although OM2 is stable at higher temperatures. One hypothesis, which could explain this observation, is that the rock surrounding the combustion front was sufficiently heated so that the kerogen became mobile due to the viscosity drop before being in contact with the oxidant. Rheologic data on industrial bitumen (C. Toncelli, *pers comm.,* 2001,) indicate a viscosity drop of 6 to 8 orders of magnitude between 25°C and 150°C. A viscosity of about 10^{-3} Pa s (~viscosity of water at 25°C) is expected at about 200°C. However, movements of kerogen are plausible at lower temperatures because of mixture phenomena with water. The aspect of the 85 m sample, showing heterogeneous grey and black patterns, with a lustrous sheen on fractures, suggests indeed mobilisation of organic matter around this position in Adit A-6. Such a migration process of kerogen could play a significant role in the sustaining or stopping of the combustion process itself. Although the triggering phenomenon causing the combustion phenomenon to start is still not identified (basalt flow, land slip, pyrite oxidation – or a combination of processes – see discussion in Smellie, 1998), it may be assumed that the combustion process is sustained by continuous and sufficient supply of oxygen from the surface. Such a movement of part of the organic matter could indeed open up the porous network to oxygen ingress, causing the immobile fraction of organic matter to combust and to drive the process further. Another simultaneous process to be taken into account is the volume reduction caused in the metamorphosed zone by carbon dioxide loss (such shrinkage patterns are clearly seen in the ACZ at Khushaym Matruk). Conversely, large subvertical discontinuities such as those observed at the Maqarin site (see Chapter 2) could act as sinks for the organic matter and lower the combustion yield, eventually arresting the process.

Magnetic investigations conducted at Khushaym Matruk (see Chapter 6) give results in good qualitative agreement with observations made at Maqarin. In particular, a comparable susceptibility anomaly exists at about 1 or 2 metres below the top of the profile (at the probable base of the analogue cement). The order of magnitude of the susceptibility is consistent with values measured in Maqarin. However, several differences are noted between the two sites :

- only one susceptibility maximum was measured in Khushaym Matruk whereas the iron profile displays clearly two distinct peaks, one of which corresponds to the χ maximum. This point has to be clarified by further measurements. It could also be linked to the very high concentrations of Cr and V in Khushaym Matruk, potentially leading to a different magnetic mineralogy.
- the organic matter at Khushaym Matruk, characterised by thermal analysis, displays a different decomposition spectrum, with only one major exothermic peak. In addition, the organic matter content seems to be lower than at Maqarin.

- the spatial extension of the combustion halo seems smaller in Khushaym Matruk, but the spatial extension of the sampled profile is also smaller. It is thus not excluded that otherwise unaltered biomicrite samples from the base of the trench in Khushaym Matruk may have been influenced by the combustion event (see, for example, the spatial extent of kaolinite distribution in Maqarin)

Using available information and new data acquired during this study, an attempt was made to reconstruct the temperature profile along Adit A-6 at the moment when combustion stopped. This profile is built from a series of data points as follows :

- **X = 50 m:** unaltered biomicrite; the temperature is assumed to be 30 +/- 10 °C
- **X = 85 m:** limit between mobile/immobile organic matter; considering viscosity data, this point was set at 100 +/- 30 °C. Notably, however, this temperature point is subject to significant uncertainty, as this temperature was estimated using data relating mostly to bituminous organic matter, and not the kerogen which is actually present.
- **X = 105 m and X = 110 m:** magnetic anomalies; data obtained in Khushaym Matruk suggest a temperature range of 200 to 350 °C for the magnetic mineralisation. The point X = 105 m was assigned a lower range temperature of 200 +/- 30°C and the point X = 110 m the upper range temperature of 350 +/- 30°C.
- **X = 114 m:** the temperature is assumed to be 700 +/- 30°C, corresponding to the decarbonation of calcite.
- **X = > 114 m:** the temperature is assumed to reach 1100 +/- 50 °C somewhere in the ACZ, corresponding to the maximum characteristic temperature of Maqarin analogue cements, deduced from mineralogy (in particular, the presence of C2S larnite (see Alexander and Smellie (1998), Appendix 1).

This reconstructed temperature profile is plotted in Figure 4.60. In order to check the consistence of this temperature profile further, a simple heat transfer model was used. The heat transfer processes accompanying the combustion process are complex. They are accompanied by gas and fluid (water, organic material) movements, porosity variations, and other changes. Moreover, the heat source is mobile and the geologic medium presents heterogeneities, as in faulting and variations in organic matter content. A very simple model was therefore applied with spherical and a cylindrical symmetry. The heat source is supposed to be located inside a spherical and cylindrical volume of radius R1 and the temperature profile has reached a stationary state. The temperature inside the heat source volume is assumed to be constant (T1 = 1100°C). The temperature far from the spherical heat source is T0. The Fourier equations in spherical (left) and cylindrical coordinates (right) are respectively :

$$\nabla^2 T = \frac{1}{r^2}\frac{\partial}{\partial r}\left(r^2 \frac{\partial T}{\partial r}\right) = 0 \qquad \nabla^2 T = \frac{1}{\rho^2}\frac{\partial}{\partial \rho}\left(\rho \frac{\partial T}{\partial \rho}\right) = 0 \quad \text{equation 4.1}$$

where T is temperature, r the spherical radial coordinate, and ρ the cylindrical radial coordinate. The general solutions of these equations are:

$$T = T_0 + \frac{A}{r} = T_0 + (T_1 - T_0)\frac{R_1}{r} \qquad T = T_1 + A\ \ln\left(\frac{\rho}{R_1}\right) \quad \text{equation 4.2}$$

The integration constant A may be expressed using the expression of the heat flux through a spherical interface (or cylindrical interface):

$$Q = -4\pi r^2 \lambda \nabla T \qquad Q = -2\pi \rho\lambda \nabla T \qquad \text{equation 4.3}$$

where λ is the thermal conductivity (W K^{-1} m^{-1}) and Q the total heat flux. The expressions of A are therefore in spherical or cylindrical geometry:

$$A = \frac{Q}{4\pi\lambda} \qquad A = \frac{Q}{2\pi\lambda} \qquad \text{equation 4.4}$$

Although these models are very simplistic, an attempt was made to plot the temperature data with respect to the inverse distance to the hypothetical heat source (spherical model) and to fit the temperature data with a logarithmic function (cylindrical model).

In order to plot the graph given in Figure 4.61 (spheric model), it was assumed that:

(i) the long axis temperature T0 was close to 20°C
(ii) the origin of radial coordinates was situated somewhere at a distance X0 > 114 m in Adit A-6.

For X0 < 123 m, excellent fits are found (r^2 > 0.95). For X0 > 118 m, the T0 parameter is negative and the solution has to be rejected. The best spherical solution corresponds to X0 = 117.2 m (r^2 = 0.995), which provides following numerical result:

$$T = 20.3 + \frac{2207}{r} = T_0 + (T_1 - T_0)\frac{R_1}{r} \qquad \text{equation 4.5}$$

where r = 117.2 – X, X being the distance along Adit A-6. This means that the equivalent radius of the spherical heat source is of the order of 1 m and that, taking λ = 2 W K^{-1} m^{-1} (a typical range for carbonates), the equivalent heat source Q is in the range of 55 kW.

The cylindrical model was fit by a least squares procedure (Figure 4.52). As for the spherical model, the fit was done on 5 data points from X = 50 m to X = 114 m. The resulting equation is :

$$T = 1100 - 111.7 \ln\left(\frac{\rho}{0.004}\right) \qquad \text{equation 4.6}$$

The modelled cylindrical heat source has now a very small radius because it is supposed to have an infinite extension in the z direction. The power of the linear heat source is calculated to be 1.4 kW m^{-1}.

The above figures could help to evaluate the duration of the combustion process. By using typical combustion enthalpies and organic matter content of the biomicrite, it is possible to evaluate an order of magnitude of the time necessary to combust 1 m^3 of marl. In the second model, because the heat source has an infinite volume extension, it was chosen to limit its length to 100 m. Assuming an oxidisable organic carbon content of 6% and an energy yield of 350 kJ mol^{-1} for the combustion process, leads in both cases to a duration of the combustion process of about 50 years to produce 10 000 m^3 of analogue cement.

The real shape and the temporal evolution of the combustion front are not precisely known at the time combustion was active. In addition, the combustion front was moving. Field observations in Maqarin and Khushaym Matruk show rather large scale analogue cement bodies (radius > 10 m) and the interface between analogue cement and biomicrite seems to have curvatures less than 0.1 m^{-1}. The combustion front, therefore probably had a panelled,

or slab, shape. The use of a field susceptometer could help in the mapping of this fossilised combustion front. More precise modelling of the combustion phenomenon should therefore take into account these parameters and compare the reconstructed temperature profile with the temperature distribution computed around a moving and heating planar volume of finite dimensions. The numerical values obtained from the two simple models can be used as an initial range for constructing this more elaborate model.

Figure 4.54 Comparison of infrared absorption spectra of several Adit A-6 samples in the wave--number range 3800 to 2700 cm^{-1}

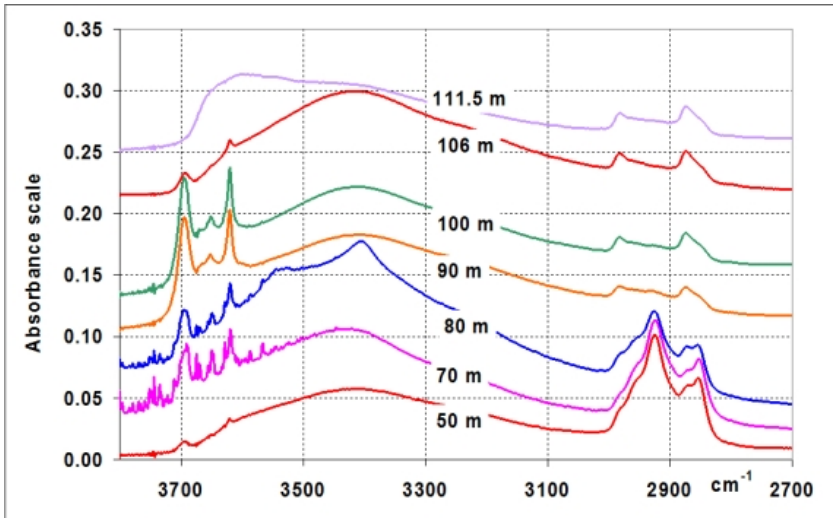

Figure 4.55 Comparison of infrared absorption spectra of several Adit A-6 samples in the wave-number range 1200 to 400 cm^{-1}

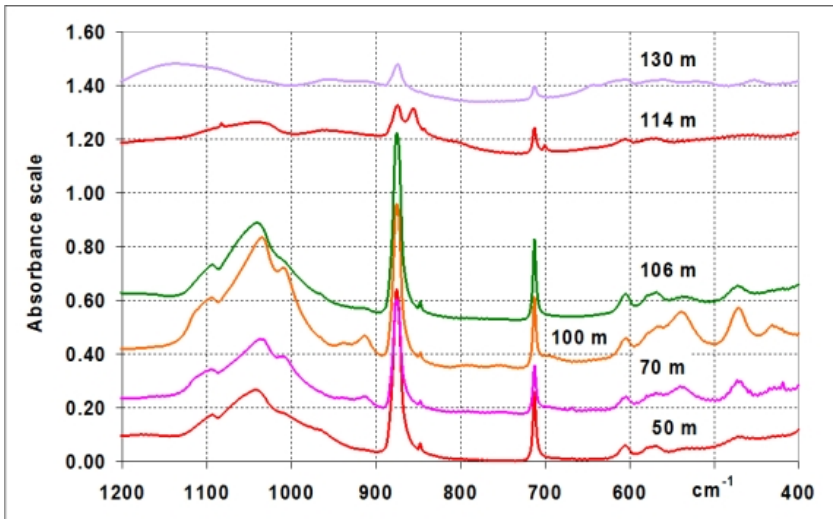

Figure 4.56 Evolution with distance along Adit A-6 of the normalised IR absorbance of specific absorption bands (kerogen (yellow), kaolinite (red), apatite (pink), calcite (blue)). Aragonite is observed as a point source, around 113m

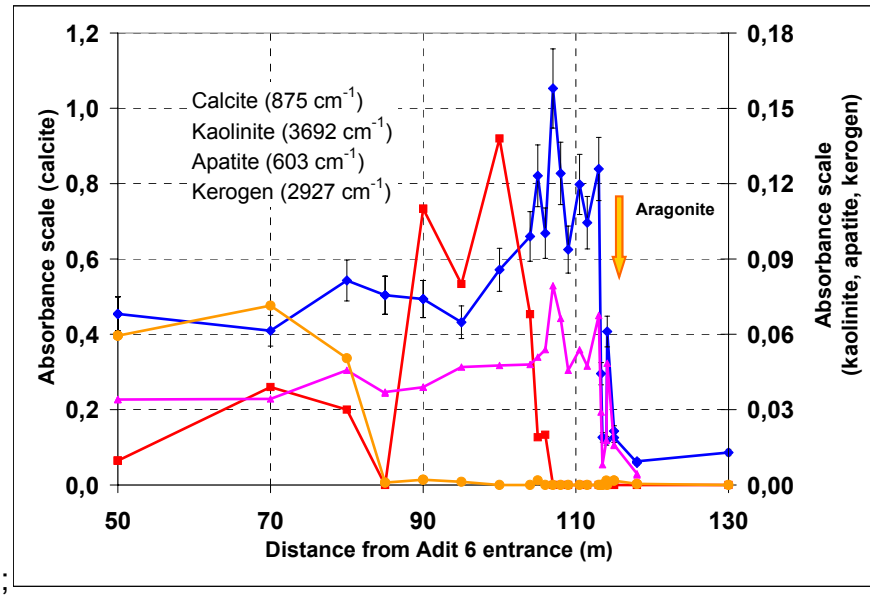

Figure 4.57 Comparison of mass loss and absorbance at 875 cm-1 along Adit A-6 (left). Comparison of magnetic susceptibility and IR absorbance for calcite (right)

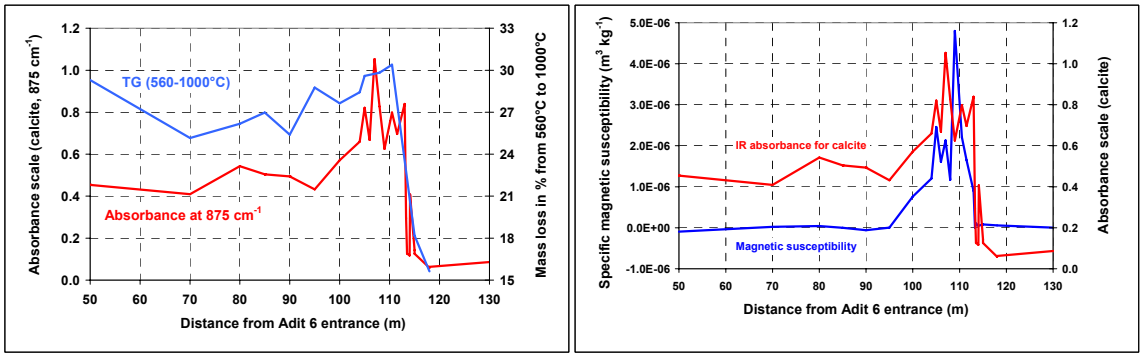

Figure 4.58 Chemical analyses of metals (Fe, Fe(II), Ti, V, Cr, Ni, Zn) and Sr along Adit A-6. Magnetic signals are also plotted in the bottom figures

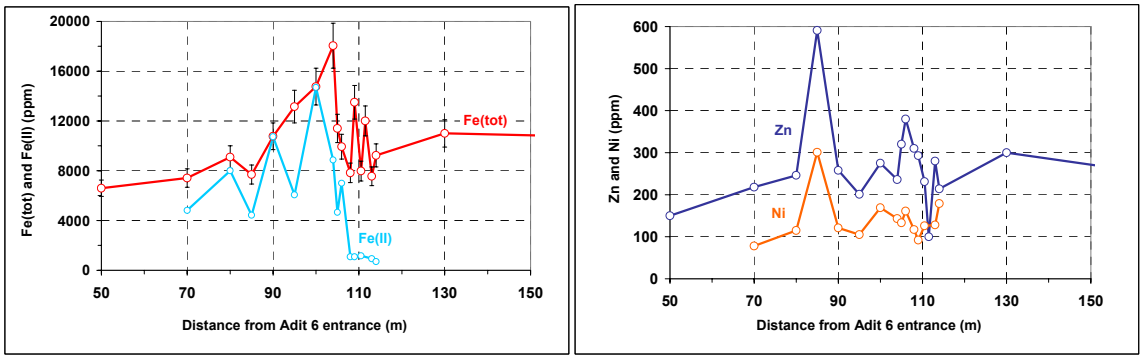

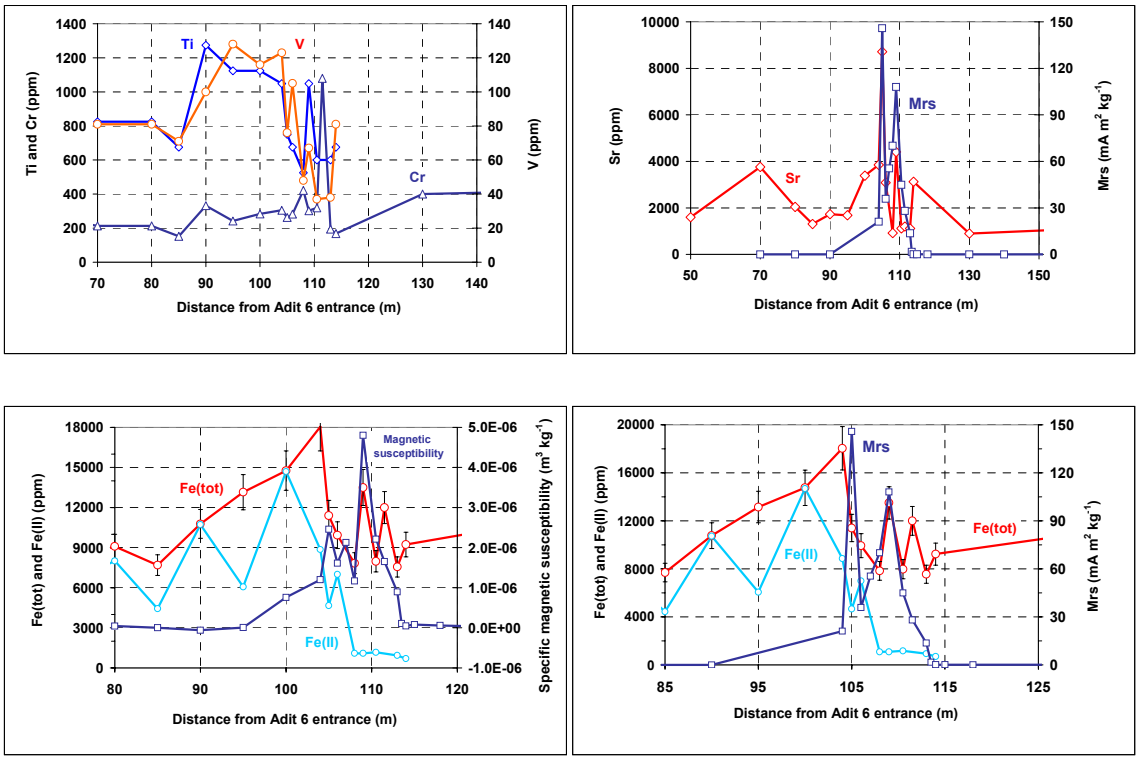

Figure 4.59 Synthetic diagram of the Maqarin combustion profile, representing chemical, magnetic, mineralogical and colour information in parallel

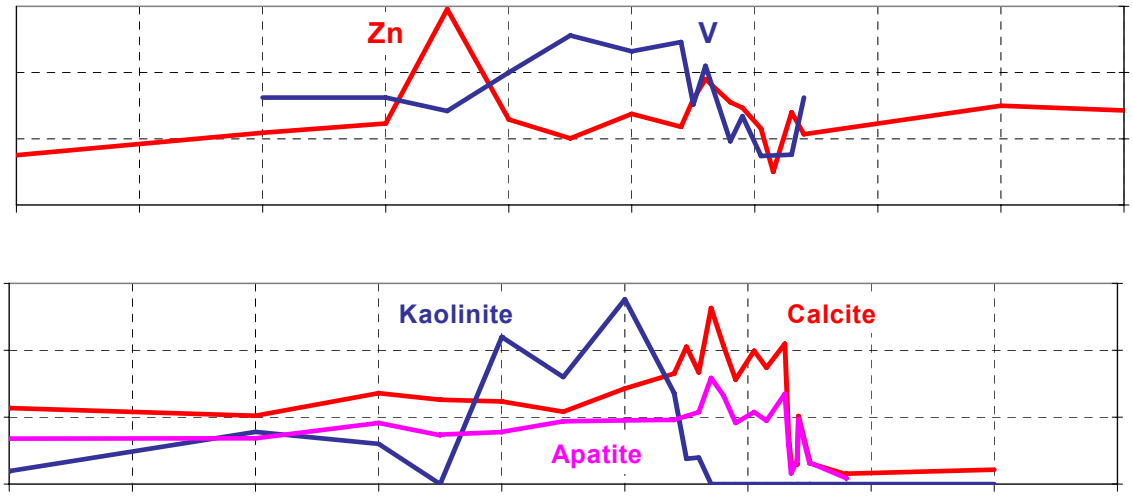

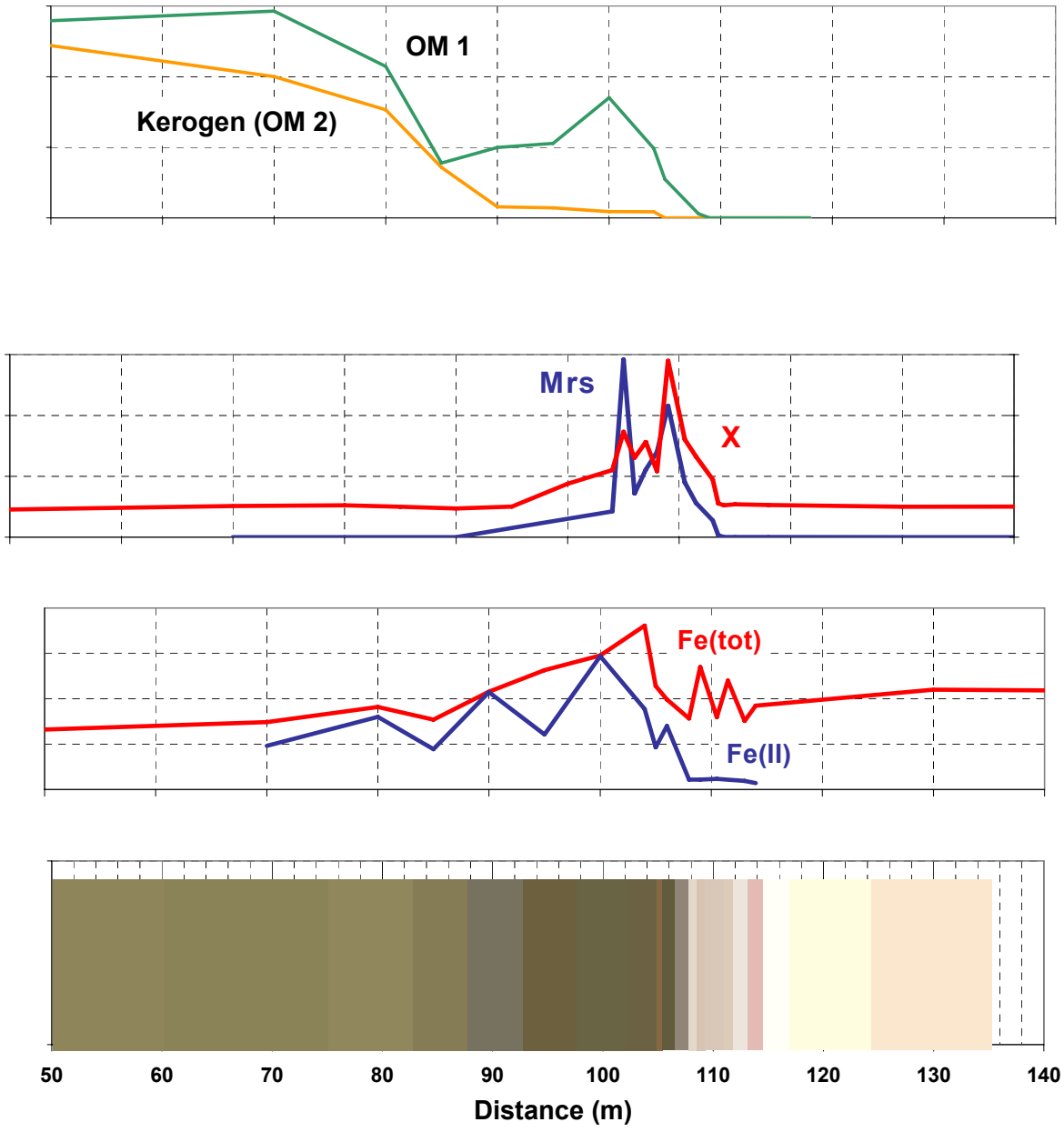
OM 1
Kerogen (OM 2)
Mrs
X
Fe(tot)
Fe(II)
50
60
70
80
90
100
110
120
130
140
Distance (m)

Figure 4.60 *Reconstruction of a plausible temperature profile corresponding to the end of the combustion process (3-D model with spherical heat source)*

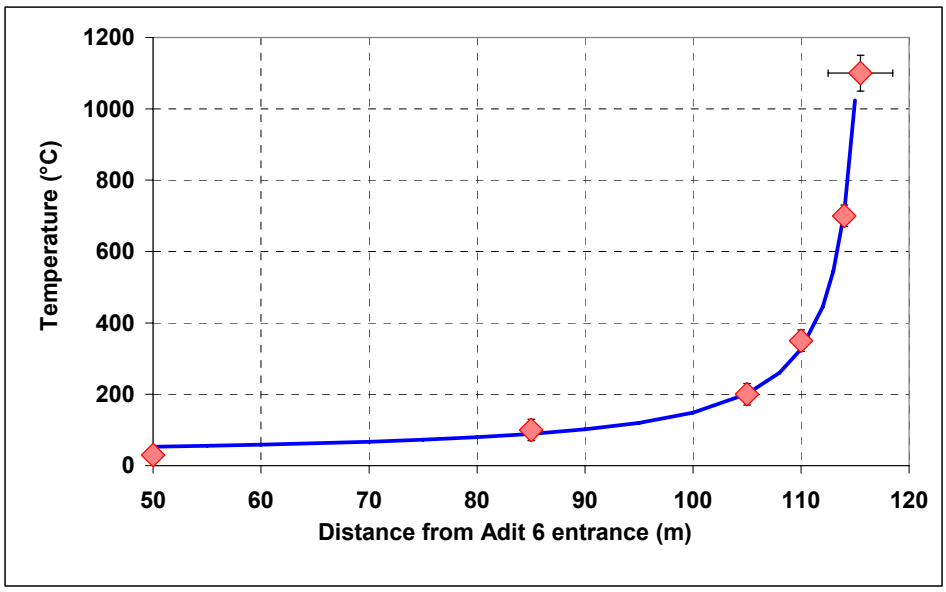

Figure 4.61 *Plot of the temperature as a function of the inverse distance to the heat source (3-D model with spherical heat source)*

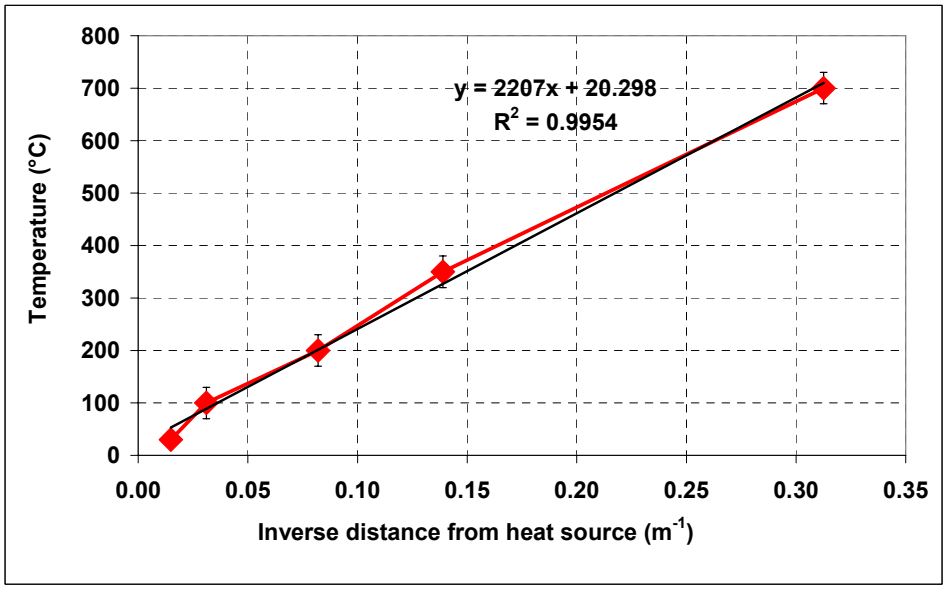

Figure 4.62 Reconstruction of a plausible temperature profile corresponding to the end of the combustion process (2-D model with wire-form heat source)

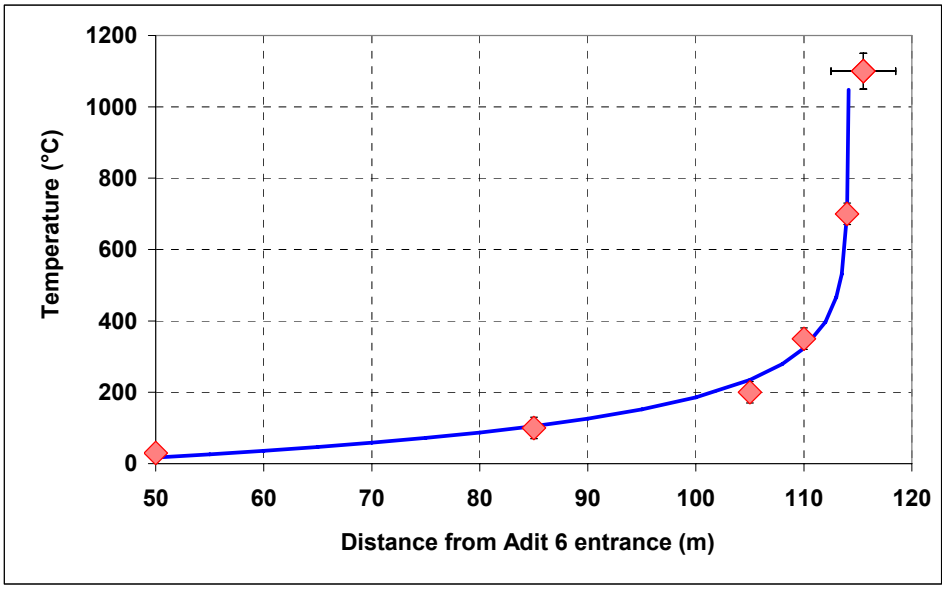

4.5.5 Conclusion

The investigations presented in this Section demonstrate, as is consistent with zones of combustion metamorphism studied in other countries, the existence of a strong magnetic anomaly. The magnetic minerals are formed by pseudomorphosis of pyrite framboids encapsulated in fossil tests. Detailed investigation of this anomaly made it possible to model the palaeo-combustion front in the A-6 Adit at Maqarin. This study suggests that the thermally enhanced mobility of the some fraction of the organic matter could have played an important role in sustaining the combustion process. In addition, the information allows the extent and shape of the palaeotemperature profile along Adit A-6 to be estimated. Although this site has now been obliterated (see Chapter 1), existing samples in the project archive (stored at BGS) could be analysed for palaeotemperature indicator minerals, so allowing the modelled profile to be tested (quasi-validation of the model).

This step will be important as it will allow the effects of the combustion metamorphism on the biomicrite to be disentangled from any subsequent hyperalkaline alteration. In conjunction with the existing data on kaolinite in these samples (see Milodowski et al., 1998a, 1998b and Figure 4.56), this could provide unique information on clay/hyperalkaline leachate interaction of direct relevance to a repository SA.

The paleomagnetic studies conducted in Kushaym Matruk are only preliminary (see also Chapter 6). They suggest that the combustion phenomenon occurred in Kushaym Matruk during a period of inverse orientation of the magnetic field (based on a limited set of samples) and that the characteristic temperature of the magnetic record was in the 200 to 350°C range.

The information and knowledge collected from this combined magnetic and mineralogical investigation can be used in several ways :

- they contribute to the general background information putting in perspective the relative

effects of combustion and hyperalkaline fluid effect. The reconstruction of the temperature profile proposed in Maqarin show that modifications affecting both minerals and organic matter have occured at distance up to about 20 m of the combustion front. This background information will be very useful for the study in Khushaym Matruk where the distribution and alteration of clay minerals near the ACZ is used as a proxy for the analogue cement/clay interface. Further, as with the Maqarin site, this should help assess whether any observed clay alteration is due to thermal effects or simply due to the influence of the hyperalkaline from the ACZ.

- in future, the magnetic anomaly will be invaluable in mapping the shape of the combustion front or to detect buried ACZs (e. g. at the Western Springs).
- the continuation of palaeomagnetic measurement on larger sample numbers will provide useful information on dating the combustion process.

4.6 Applying a Standardised Leaching Protocol to Maqarin Analogue Cement: Implications for the Natural Analogue Approach

4.6.1 Introduction

An important process studied in Maqarin is the long-term effect of hyperalkaline fluids on a sedimentary formation. The knowledge of the analogue cement source term and of the water-rock interactions occuring within the ACZ or along the fracture paths is therefore of prime importance. What are the equilibrium controls? What is the role of kinetics? The leaching studies were also conducted in relation to other investigations, specifically the study of the migration of several metallic elements (such as Re, Mo, Se and Cr, see Section 4.4) and also for cross-checking with field data on hydrogeochemistry (see Chapter 3). This will help to understand better what tracers may be used to quantify mass transfer at Maqarin and also provide knowledge on the geochemical controls of several radionuclide analogues in a hyperalkaline medium. A further motivation for these experiments was the possibility to put in perspective the analogue concept for the analogue cement source term itself. Although industrial analogue cements and Maqarin analogue cements exhibit clear mineralogical common points, they are also differences, as in carbonate and phosphate content, for example. Are the consequences of these differences on the leaching process quantifiable? And what are the consequences for leachate/host rock interactions?

A specific leaching experiments, a constant pH leach test, using a protocol (Adenot, 1992) used for evaluating the leachability of industrial analogue cements was therefore undertaken. The following Sections describe this protocol and the results of this particular investigation, give a first interpretation, and discuss the application of these results in the framework of the natural analogue approach.

4.6.2 Leaching test at constant pH in a diluted solution

The analytical methods are presented in Appendix 4.

4.6.3 Results

The sampled solutions have been analysed by ion chromatography for Ca^{2+}, K^{+}, Cl^{-}, NO_3^{-} and SO_4^{2-}. The solid sample was investigated using two different techniques :

- mineralogical profiles by performing XRD on alteration layers scraped from the surface of the sample after the experiment
- investigation of a polished cross section of the sample by SEM/EDX

The experiment was conducted over 228 days. The evolution of Ca^{2+}, SO_4^{2-} in solution and of HNO_3 uptake have been plotted as a function of the square root of time and normalised to the surface area of the sample (Figure 4.63). The uptake of HNO_3 displays a linear trend throughout the experiment. Over the first 70 days, the release of Ca^{2+} follows a parallel release at a rate exactly half of the HNO_3 uptake.

Figure 4.63 Evolution with the square root of time of the cumulative releases of Ca^{2+}, $SO4^{2-}$ and the uptake of HNO_3^{-} by the cement sample

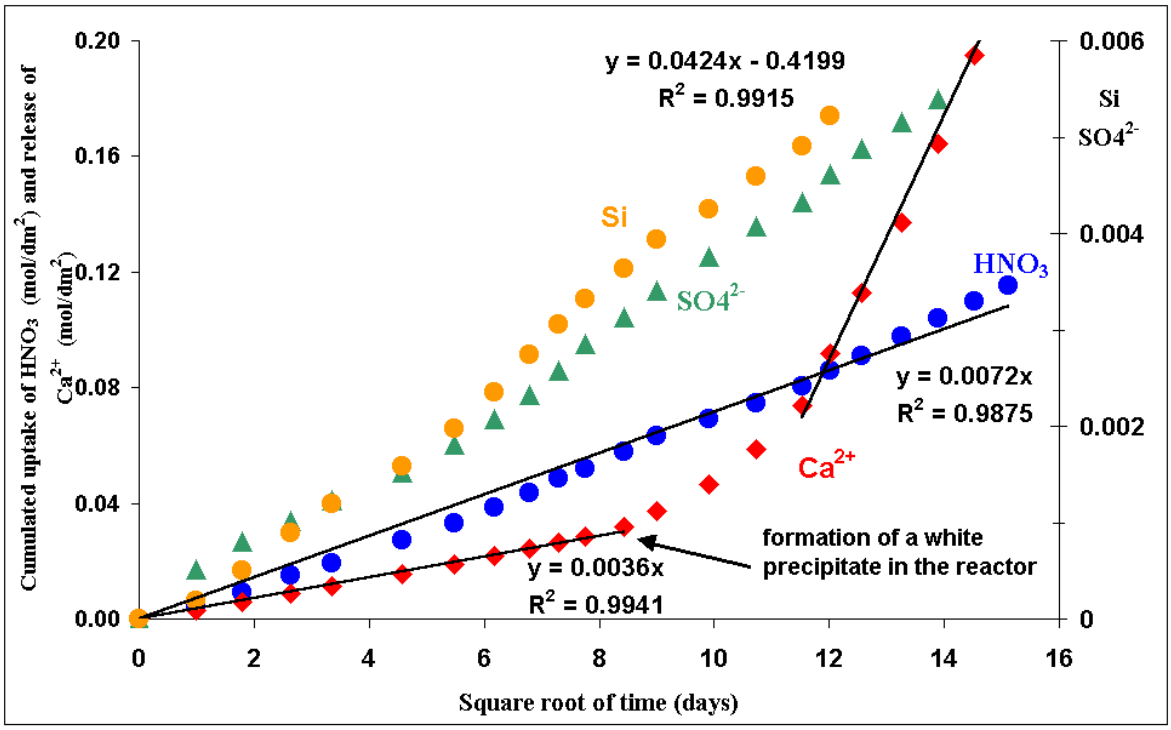

This behaviour has already been described for industrial analogue cement pastes (Adenot, 1992) and is attributed to calcium leaching. After about 70 days, a precipitate has been observed in the reactor and the release of Ca^{2+} increases by a factor of about 10 and then maintains a linear trend as a function of $t^{1/2}$. The releases of Si and SO_4^{2-} follow a nearly linear trend with $t^{1/2}$ throughout the experiment; the release rates increase a little after about 35 days leaching. The molar ratio of Si and SO_4^{2-} in the leachates increases progressively from less than 0.2 at the start to about 1.1 after about 35 days and then keeps close to this value (Figure 4.64). Note that the solution data for K^{+} and Cl^{-} were corrupted by a KCl leak from the control pH electrode.

The optical observation of a polished cross section of the analogue cement sample (Figure 4.65) reveals the existence of a ~500 µm thick alteration layer. This layer is underlined on its

internal edge by a white, discontinuous rim of about 50-100 µm thickness. The heterogeneous structure of the pristine material is also clearly visible as large ettringite veins and texture/colour details from less than 50 to about 500 µm.

The SEM observations of the sample (Figure 4.66) reveal several other features:

- the alteration layer has a complex internal structure, displaying a highly porous external edge (~200 µm thick) and a progressive gradient towards pristine analogue cement.
- the internal zone of the altered layer (~600 µm depth) is underlined by a thin fracture.
- ettringite veins reaching the outer surface have been severely attacked to depths up to 500 µm. The dissolution of ettringite along these channels is, however, not complete.

Figure 4.64 Evolution of the Si/SO_4^{2-} molar ratio in the leachates. The initial low value of this ratio is linked with rapid ettringite dissolution

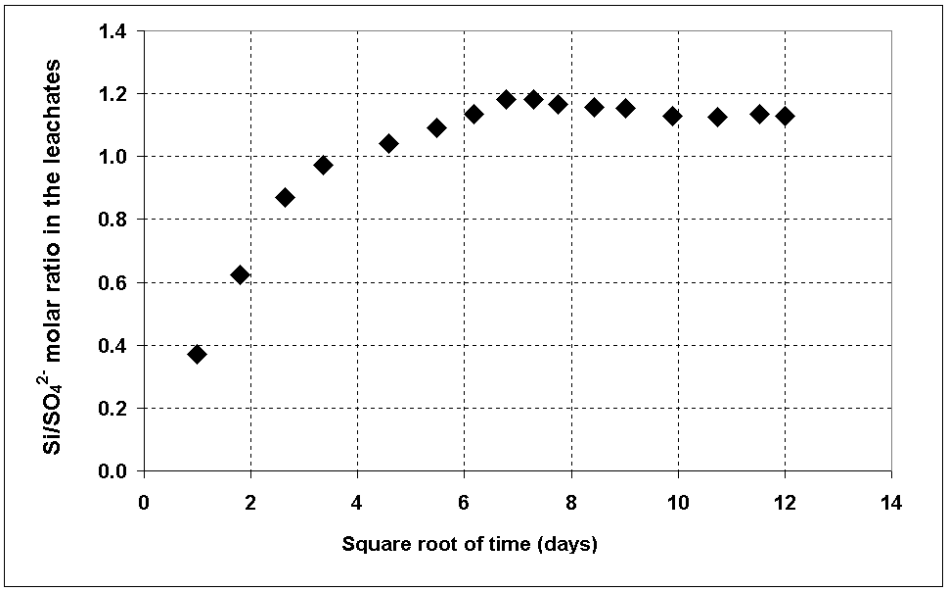

Figure 4.65 *Polished cross-section of the leached cement sample observed using a binocular microscope. An alteration layer of about 600 µm thickness is observed at the cement/water interface. The internal part of the alteration layer is underlined by a white rim. The photograph on the left also shows a large, and several small, ettringite veins crossing the sample. The yellow rectangle shows the zone where EDX maps and analyses were performed (see Figure 4.66)*

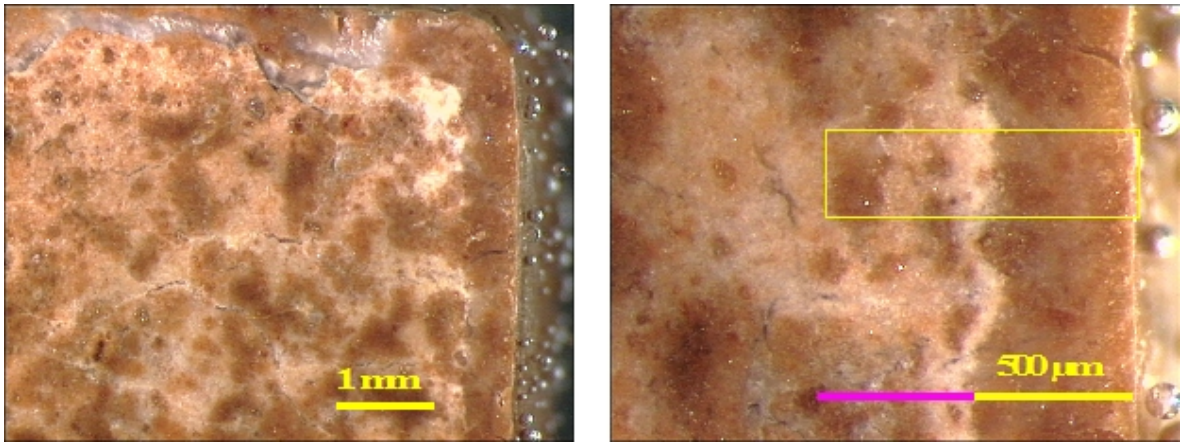

Figure 4.66 *Top: BSE image of the polished cross section of the leached cement showing the alteration layer. A porous external zone of about 200 µm is visible. The internal part of the layer is marked by a thin fracture line at about 600 µm from the solution interface. Bottom: BSE images of the alteration layer at different scale showing the dissolution of the ettringite filling along fractures*

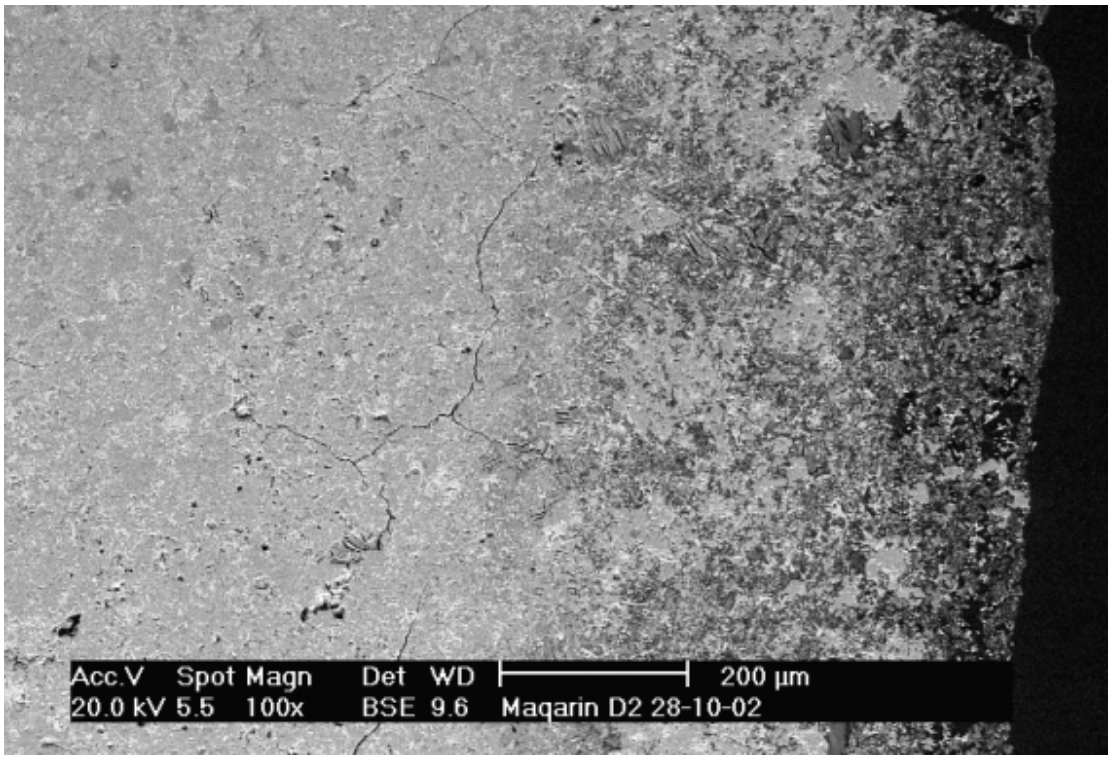

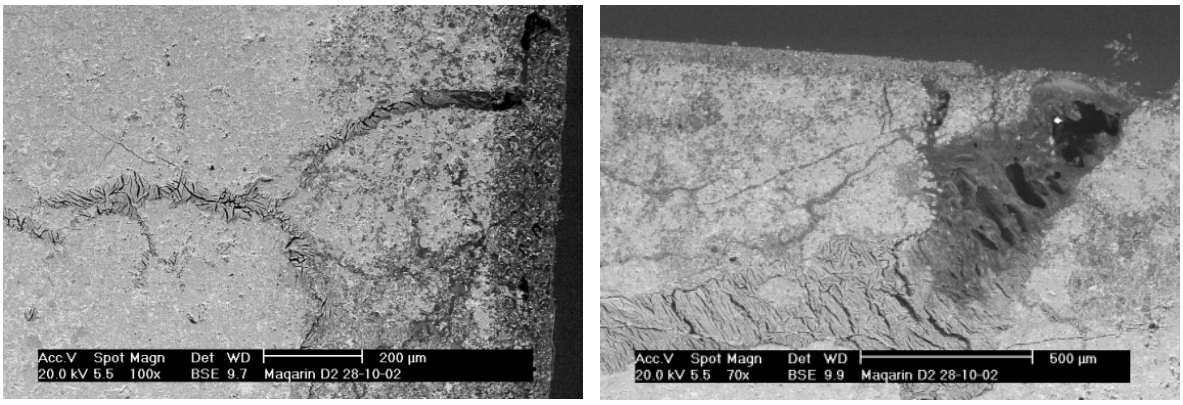

Figure 4.67 *Composite SEM-BSE image of the cement zone were EDX maps and profiles were acquired. Variations of texture are correlated with porosity and chemistry trends. The cement water interface is on the right here. Individual scale bars represent 100 µm*

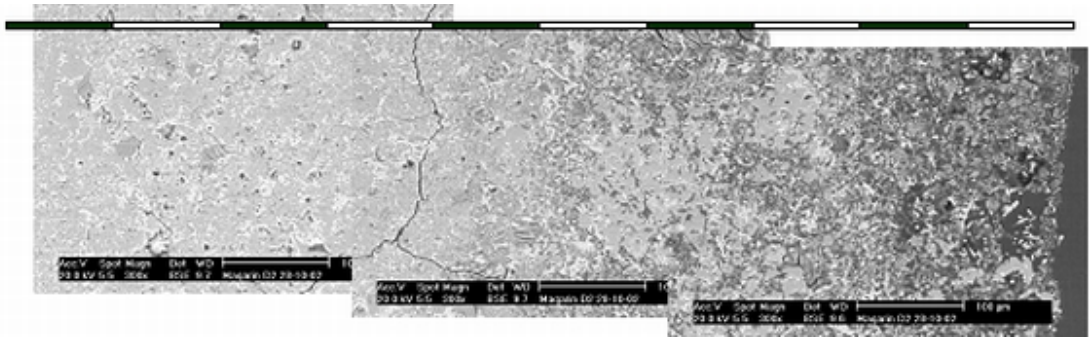

Figure 4.68 *Qualitative elemental profiles (SEM-EDX) for C, O, P, Al, Ca, Si and S across the altered layer formed on the cement (see Figure 4.67). Note the cement/water interface is on the left here*

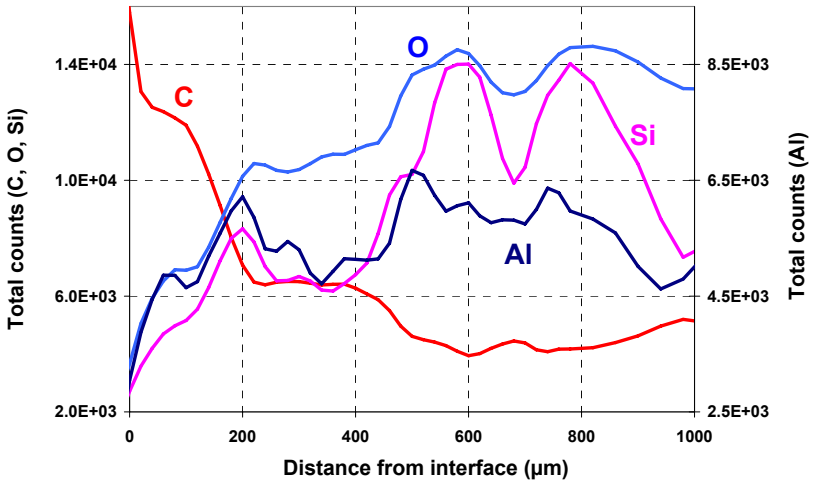

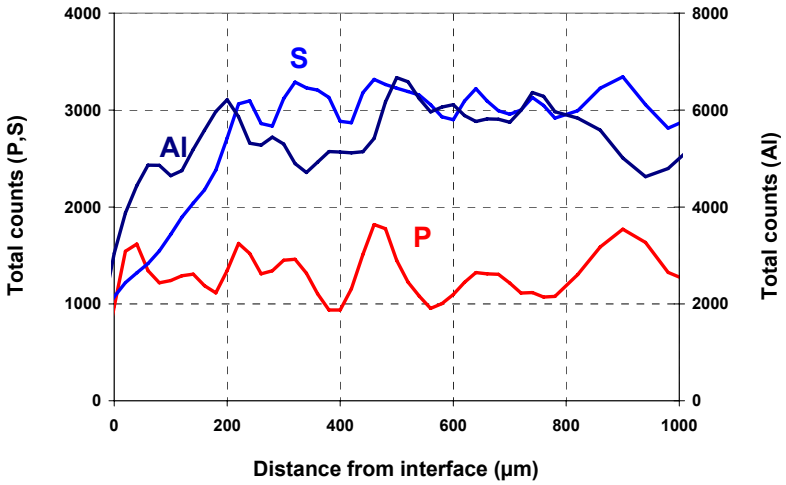

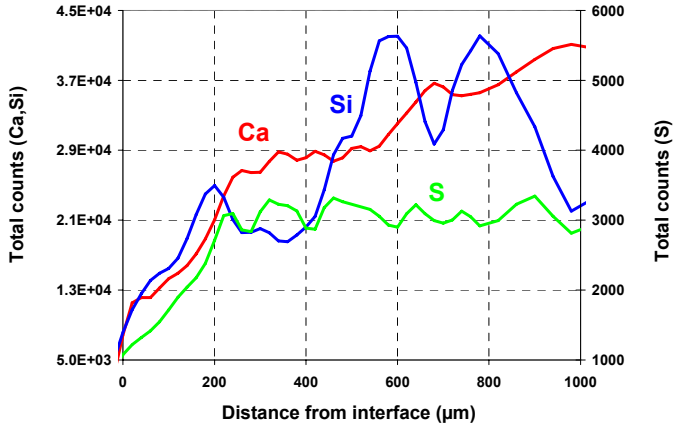

A qualitative chemical profile was performed using the EDX probe on the region shown in Figure 4.67. For this purpose, and with the aim of averaging composition fluctuations due to the material heterogeneity, total counts were accumulated on a window of 300 µm length and 25 µm width, moving perpendicularly to the sample interface by 20 µm steps. The qualitative elemental profiles obtained for C, O, Al, Si, P, S, Ca are shown in Figure 4.68.

The carbon profile is due to the combined contributions of (i) the epoxy resin used to impregnate the sample and (ii) C-containing mineral phases, such as calcite, and monocarboaluminate. The variations of C thus give partly access to the porosity distribution in the outer zones of the alteration profile:

- 0-30 µm : very high porosity (zone I)
- 30-200 µm : high porosity (zone II)
- 200-500 µm : medium porosity (zone III)
- > 600 µm : pristine analogue cement

This zonation can also be recognised on the other elemental profiles:

- O: the variations are the converse of C

- Si:
  - 0-200 µm: marked concentration gradient in two steps with a local maximum at 200 µm 200-~400 µm: plateau
  - 400-600 µm: increase. The maximum of Si observed at around 600 µm corresponds to the white rim observed under the binocular microscope. Fluctuations observed deeper seem to correspond to textural variations in the material
- Al :
  - 0-200 µm: marked concentration gradient in two steps with a local maximum at 200 µm 200-500 µm plateau with fluctuations;
  - >500 µm : higher plateau with fluctuations.
- S: marked increase from 0 to 200 µm and then plateau with fluctuations
- P: no marked gradient but fluctuations all along the profile
- Ca:
  - 0-30µm: steep increase
  - 30-200 µm: further steep increase
  - 200-550 µm: more gentle, but regular increase
  - > 600 µm: plateau with fluctuations.

These trends were confirmed by elemental EDX maps acquired from the interface to the pristine analogue cement (Figure 4.69). The profile of BSE intensity confirms that the total alteration profile extends to 600 µm. The Al, P and S maps show that these elements are, in the analogue cement matrix, not including ettringite veins, mostly located in phases of 10 to 20 µm grain size. This could explain, in part, the fluctuations observed on several elemental profiles. High Ca-low Si zones correspond to large calcite areas of around 100 µm diameter. Otherwise Ca and Si seem to be distributed as a fine grained material.

Mineralogical profiles could be derived from XRD analyses performed by a stepwise abrasion of the sample, following a technique described in Planel (2002). The profiles derived by this technique (Figure 4.70) give a qualitative representation of mineral abundances.

Figure 4.69 *Sample DD M99 2/1 Elemental EDX maps for Ca, Al, P, S, Si, C, Fe and BSE intensity map. These maps were acquired on the zone marked on Figure 4.67*

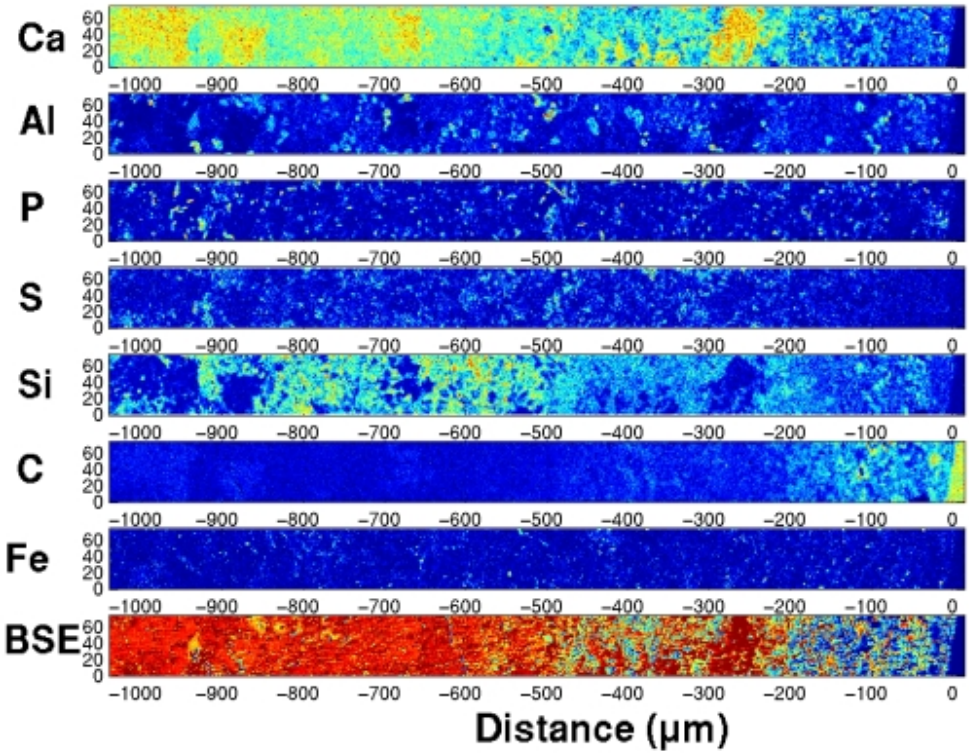

Figure 4.70 *Profiles of XRD peak intensity. These qualitative profiles were constructed by using XRD spectra acquired on successive layers of the cement sample. In some cases (e. g. ellestadite and apatite) peak interference could not be avoided*

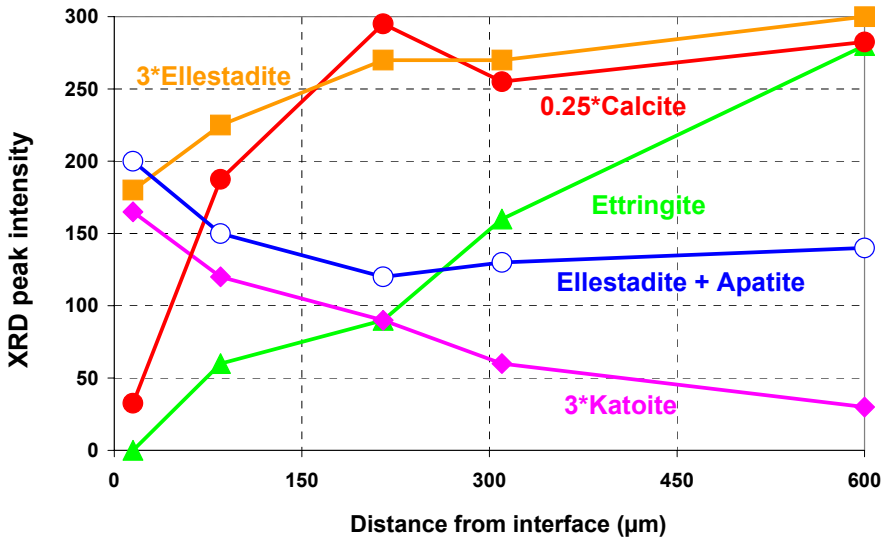

The following diffraction lines were selected to avoid interference as much as possible: ettringite (9.70 Å), katoite (5.07 Å), fluorellestadite (3.48 Å), calcite (3.05 Å). The peak at 2.8 Å is due to both fluorellestadite and apatite. Larnite lines could not be easily followed on the XRD diagrams. Katoite ($Ca_3Al_2[(OH)_4]_3$ belongs to the hydrogarnet family and represents the silicon-free end-member of the hydrogrossular solid solution. Peak height representative of the pristine analogue cement were assigned to the distance 600 µm on the profiles given in Figure 4.70.

The calcite profile exhibits a very sharp front between 0 and 100 µm and then a weak maximum around 200 µm. A dissolution front is found for ellestadite with a probable apatite precipitate as a secondary product. Katoite forms in the most altered zones of the analogue cement and is also possibly an alteration product of ellestadite as the profiles of these minerals match quite well (Figure 4.70) and the observed ellestadite contains some Al. The profile for ettringite increases linearly; it was, however, observed that ettringite was mostly located in large fractures intersecting the sample surface (Figure 4.66). The dissolution of ettringite is thus probably decoupled from the alteration of the analogue cement matrix.

The precipitate formed in the reactor at about 70 days and collected on a PTFE filter was characterised by SEM-EDX. Two major phases were found, a Ca-P-O phase (probably (OH,CO_3)-apatite) and a Si-Al-Ca-O-(Fe) phase (possibly a hydrogarnet phases).

A link between the chemical and mineralogical zonations allows the following interpretation (Figure 4.71):

- *Zone I (0-30 µm):* Calcite, larnite and ellestadite are dissolved. Apatite and hydrogarnet have precipitated. Very high porosity.
- *Zone II (30-200 µm):* The Ca-Si bearing phase (larnite?) and ellestadite are dissolved. Apatite and hydrogarnet (katoite) have precipitated. High porosity.
- *Zone IIIa (200-500 µm):* The Ca-Si bearing phase is dissolving. Medium porosity.
- *Zone IIIb (~600 µm):* Dissolution front for the Ca-Si bearing phase.

For ettringite, a separate subsystem has to be considered, i. e. dissolution along individual fractures intersecting the sample interface. The linear increase of ettringite concentration with depth (Figure 4.70) is probably due to the fact that open channels exist in these fractures and that the whole bulk of the ettringite fracture filling is not accessible at once at a given depth.

4.6.4 Modelling attempts

An attempt was made to reproduce the observations presented here using geochemical (CHESS, Van der Lee, 1998) and transport-chemistry coupled codes (HYTEC, Van der Lee et al., 2002). In a first step, a mineralogical model of the analogue cement was built. The mineralogical composition given in Table 4.17 represents a global composition, including the ettringite filled veins and the fine grained matrix with calcite, ellestadite and other phases and is based on the geochemical analysis of the sample (see Table A4.2.2.4 for details). It was assumed that the analogue cement matrix contained low concentrations of ettringite. No thermodynamic data exists for ellestadite; EDX analyses clearly showed that the ellestadite found in the studied analogue cement contained Si, S, P in similar concentrations and some fluorine. Some Al was also detected in the ellestadite but was discarded in the model mineral. An ellestadite of chemical formula $Ca_5(PO_4)(SiO_4)(SO_4)F$ was first assumed. Further computations using this formula led to high F concentrations in solution (> 3 mg L^{-1} whereas field data are < 0.5 mg L^{-1}) and also large quantities of fluorine CaF_2 were

predicted to precipitate upon analogue cement alteration, whereas this mineral phase is not reported in altered Maqarin analogue cements (see Milodowski et al., 1992a, 1992b; 1998a, 1998b). A fluorine-poor ellestadite was therefore assumed and a logK for the reaction was evaluated by using analyses of groundwaters collected in borehole D2 (pH ~12.5), representing long-term interaction between analogue cement and water, and observations that pH in small batch leaching experiments rapidly reached ~11.5 and slowly stabilised at 11.9 (20°C) after several days (unpublished data, see Figures 4.73 and 4.75). Because fluorine, phosphate and silica concentrations in alkaline groundwaters collected on the field during Phase IV, are very often below detection limit, a first estimate was made for the equilibrium constant by assuming for F, SiO_2 and PO_4 total aqueous concentrations of respectively 0.001 mg L^{-1} (5.2 10^{-8} mol L^{-1}), 0.15 mg L^{-1} (2.5 10^{-6} mol L^{-1}) and 0.001 mg L^{-1} (1.0 10^{-8} mol L^{-1}) in borehole D2. The value obtained (logK = -35) was then refined by studying the chemical equilibrium at 25°C between the minerals calcite-ettringite-ellestadite-monocarboaluminate-larnite and solution. It was found such a mineral assemblage buffered the pH of the aqueous solution at 11.90 $\pm$ 0.05. The equilibrium constant of ellestadite was adjusted to –31 so that a calcite-ellestadite-ettringite-monocarboaluminate assemblage put in contact with pure water would give an equilibrium pH ~11.5 at 25°C in simultaneous equilibrium with fluorapatite and hydroxylapatite. In order to obtain these results, it was necessary to assume that CSH phases, tobermorites and Si-hydrogarnet were unable to precipitate in the short term laboratory batch experiment. In a further modelling step, the larnite-calcite-ettringite-ellestadite-monocarboaluminate assemblage was reacted in closed system, leaving only three secondary phases precipitating under kinetic control: portlandite, CSH1.1 and Si-hydrogarnet. The composition obtained after a significant reaction progress approaches closely the groundwater composition collected in borehole D2 (Table 4.18).

$$Ca_5(PO_4)(SiO_4)(SO_4)(0.25\ F, 0.75\ OH) + 5.75\ H^+$$

$$<==> 5\ Ca^{2+} + HPO_4^{2-} + SiO_2(aq) + SO_4^{2-} + 2.75\ H_2O + 0.25\ F^-$$

Figure 4.71 Sketch representing the interpretation of major zones identified on the sample

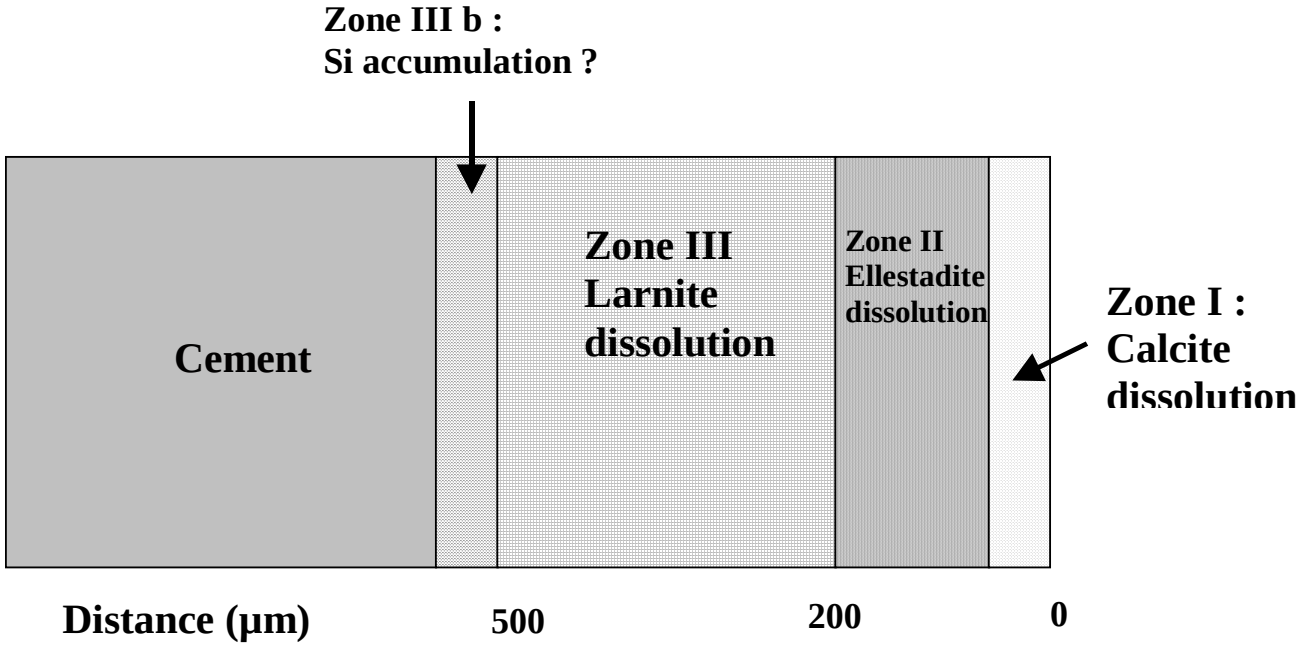

Table 4.17 Model mineralogical composition for the sample DD-M-99-2. Ellestadite formula $Ca_5(PO_4)(SiO_4)(SO_4)$ F. An alternative formula, with larnite instead of CSH1.1 also gives satisfactory results, although less precise on water content. This suggests that part of the larnite is hydrated. This model mineralogical composition is thus a very simplified representation of the actual mineralogical composition of this material (see sections 4.2 and 4.3 in this chapter)

Phase	Calcite	Brownmillerite	Ellestadite	Ettringite	CSH1.1	Monocarboaluminate
Wt %	24.2	4.6	15.9	35.6	17.2	2.36
Moles/100 g	0.242	0.019	0.032	0.028	0.125	0.004

Table 4.18 Comparison between predicted and observed groundwater composition (the studied cement sample was collected in borehole D2). This batch model considers that portlandite and CSH precipitation are kinetically limited. Concentrations are given in mol L^{-1}. The simulation was conducted at 25 °C

	Start of reaction	After significant reaction progress	Water sampled in borehole D2[20]
pH	11.9	12.47	12.45 to 12.6
mol l^{-1}			
Ca	$9.5\ 10^{-3}$	$2.38\ 10^{-2}$	2.25 to $2.36\ 10^{-2}$
SO_4 (aq)	$2.2\ 10^{-3}$	$3\ 10^{-3}$	$2.9\ 10^{-3}$
Si	3.6 10-^{3}	$3.7\ 10^{-5}$	$< 5\ 10^{-6}$ to 1.010^{-5}
Al	$3.6\ 10^{-5}$	$5\ 10^{-7}$	$7\ 10^{-7}$ to $3.6\ 10^{-6}$
F	$9\ 10^{-13}$	$1.8\ 10^{-13}$	$< 2.5\ 10^{-5}$
Saturation index			
Portlandite	-1.0	+0.3	+0.3
CSH 1.1	+2.4	+1.2	0 to +0.1
Si-hydrogarnet	+3.5	0	+0.2 to +0.3

The final pH indeed depends on the precipitation kinetics of portlandite and other secondary phases. For the results presented in Table 4.18, the precipitation rate constants for portlandite, CSH 1.1 and Si-hydrogarnet were fixed at $5\ 10^{-10}$, $4\ 10^{-11}$ and $1\ 10^{-11}$ mol $m^{-2}\ s^{-1}$, respectively. This closed system reaches a dynamic stationary state in which larnite progressively transforms into portlandite, Si-hydrogarnet and CSH 1.1 (Figure 4.72). The other phases are almost unaffected in such closed environment. The saturation index of portlandite at the stationary state keeps a slightly positive value. The driving force for the transformation of the larnite is the precipitation of CSH phases.

[20] It should be noted, however, that these data are not generally representative of the Maqarin groundwaters (see Alexander, 1992; Linklater, 1998; Smellie, 1998).

Figure 4.72 *Simulation of the dissolution of larnite in a closed system. Secondary phase formation (CSH, portlandite and hydrogarnet) is limited by kinetics. The CSH precipitation kinetics drives the pH evolution*

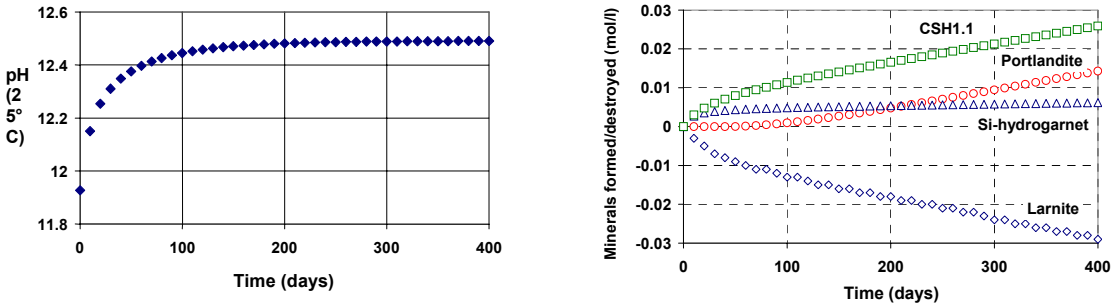

Figure 4.73 *Cement DD M99 2/1 – Evolution of pH in a small batch test (1 g of powdered cement in 10 ml of water). The batch was kept out of atmospheric contact between pH measurements. The maximum pH of about 11.9 (note the log time-scale) is reached in about 1 day*

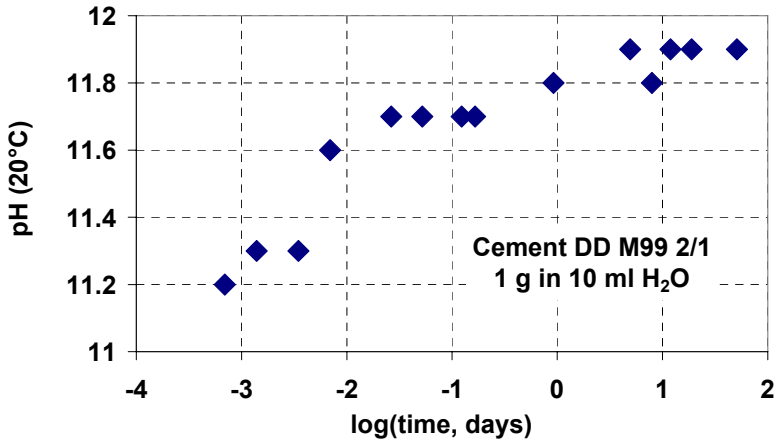

This first step in modelling clearly suggests that the formation of CSH phases from a larnite analogue cement is kinetically rate limited. This could account for the discrepancy between field pH (~12.5) and pH measured in small batch experiments over a duration of about 2 months (pH ~11.9, see Figure 4.73). This is why it was assumed that, in the diffusive experiment, the CSH phases were not able to precipitate at all. Therefore, for this first modelling attempt, a simple equilibrium model was built. Another aspect to take into account is the heterogeneous distribution of mineral phases in the analogue cement and also possible artifacts in the experimental protocol. Water reaching the surface of the sample has simultaneous access to veins of pure ettringite and to the analogue cement matrix containing mostly calcite, ellestadite, monocarboaluminate, brownmillerite and the CaSi bearing phases. The precipitation of secondary phases may thus proceed in several different ways:

- alteration inside the analogue cement matrix due to the aggressive action of the pH front and the diffusion of released Ca, Si and other elements.

- precipitation of secondary phases in the external solution reservoir, due to the combination of elements released by the dissolution of the ettringite veins, and other elements released by the analogue cement matrix.
- precipitation of secondary phases in the outer zones of the analogue cement matrix due to the inward diffusion of Al released in solution by ettringite dissolution[21].

Several observations support to these assumptions:

- formation of apatite and hydrogarnet type phases in the solution reservoir (outside the sample).
- shape of the katoite profile at the surface of the sample, suggesting the influence of a penetrating Al diffusion front (or reflecting the alteration of ellestadite?).
- shape of the calcite profile, compatible with equilibrium diffusion-dissolution-reprecipitation processes.

In this equilibrium model, only the analogue cement matrix was considered and the ettringite veins were not described. The analogue cement matrix is assumed to be made up of 4 mineral phases, calcite, ellestadite, monocarboaluminate and larnite in relative proportions consistent with chemical analyses. The porosity was assumed to be constant (0.1) as was the effective diffusion coefficient of aqueous species. At $2x10^{-11}$ m^2 s^{-1}, it is very similar to $3x10^{-11}$ m^2 s^{-1} as measured in biomicrite from Maqarin by Stone (1998).

Main results of the simulation are presented in Figure 4.74. The diffusion coefficient was adjusted in order to obtain a retreat of the larnite dissolution front of about 400 µm in 200 days. The ellestadite dissolution front is then located at about 200 µm from the solid/solution interface and the calcite dissolution front at less than 50 µm. The calcite concentration also exhibits a smooth maximum just behind the front. Phosphates (apatites) are predicted to precipitate from 0 to 200 µm, using phosphates released by ellestadite. It was however observed in the experiments that phosphates precipitated outside the sample in the reactor. The comparison between spatial profiles of major elements obtained by EDX (Figure 4.68) and similar profiles obtained by modelling (Figure 4.74) is encouraging. Some kinetic limitation probably exists on the dissolution of ellestadite as is shown by the spreading of the S front on the EDX profiles.

Several improvements are obviously needed in this modelling (in particular with respect to porosity variations). Nevertheless, the change of diffusion regime that is apparent in solution data has still no clear explanation. The marked increase in calcium release, coupled to the formation of precipitate in the reactor, could be linked to a sudden and pronounced opening of porosity in the outermost parts of the profile. This lead to an accelerated dissolution of calcite and release of insoluble particles by a sudden loss of cohesion of the most altered external layer. This hypothesis is supported by the observation that calcite dissolution is more extensive in the outermost layers of the profile than predicted by modelling.

4.6.5 Implications for the natural analogue approach in Maqarin

Although coupled code modelling studies have been carried out in Phases I-III on leachate/host rock interaction (see Alexander, 1992; Linklater, 1998; Smellie, 1998), this

[21] As noted in section 4.1, most of the ACZ has seen some form of shrinkage, following combustion and mass loss so reaction is often along such zones.

section represents the first attempt to model the actual hydration of the cement. This work, and the data from the leaching experiment presented here, raises several important issues in connection with the use of natural analogues for analogue cements and the relationships between field and laboratory observations of water/rock interactions.

Figure 4.74 *Main results of the 1-D simulation with Hytec. Top: spatial profiles of mineral phases accross the alteration profile in the matrix. Bottom, left: spatial profiles of pH and aqueous Si, Ca; right: spatial profiles of Ca, S and Si in the solid phase*

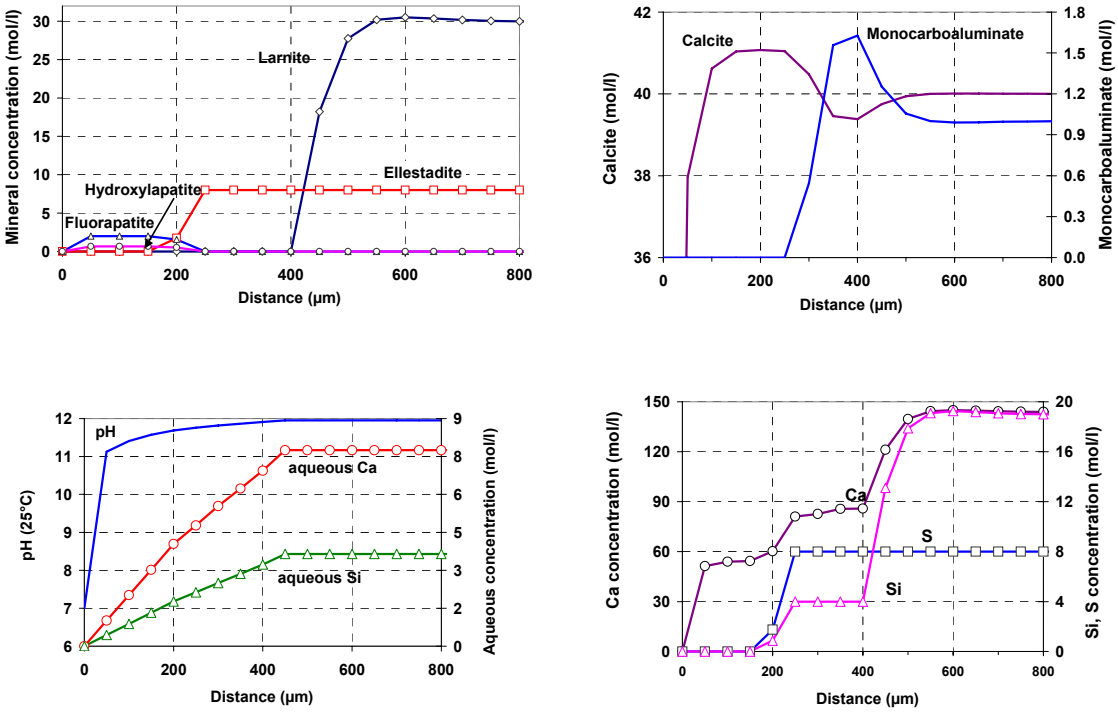

The same conceptual models are valid for describing the leaching of both analogue cement pastes and natural analogue cements. However, note the unhydrated natural analogue cement is closer to a clinker phase assemblage than to an actual analogue cement paste in which CHS phases are present initially and unhydrated calcium silicate is scarce.. The heterogeneous nature of the natural sample (e.g. ettringite veins) also makes the leaching regime more complicated at the scale of observation of our sample. The influence of phosphate minerals also complicates the geochemical scenario and causes precipitation outside the sample. The complete modelling of such a heterogeneous system presents conceptual challenges that could not be solved at once and still persist.

Another important finding, related to the Maqarin site, is that inconsistency between field and laboratory data (e.g. pH) could be linked to the kinetic limitation of the precipitation of portlandite and CSH phases during larnite (C2S) hydration. Such a limitation is probably not encountered in industrial analogue cements where C3S hydration rapidly produces CSH phases. This could mean that CSH precipitation at Maqarin could be temporally and spatially more spread out than in the case of the alteration of an industrial analogue cement. This could also mean that the high pH in Maqarin groundwaters is a sign of long residence time. This is supported by the observations of Clark et al. (1998) that the hyperalkaline water is

effectively ^{3}H-free and that some seepages in Adit A-6 that show seasonal variations with oscillations between ph ~6-8 and pH ~11.9 (see the Chapter 3), the latter value being very close to the observed pH in short-term batch runs.

4.7 Column Leaching Experiments Performed on Analogue Cements and Marl: Study of Major Elements

4.7.1 Introduction

Column leaching tests were performed on three different materials: an unaltered analogue cement (M00-1-4, Adit A-6, 256 m), an altered analogue cement (M99-1-41, Adit A-6, 140 m) and on an unaltered biomicrite (M00-1-23, Adit A-6, 50 m). The cement leaching experiments are novel within the project, but biomicrites have been leached (and the data modelled) previously by Bateman et al. (2000).

These leaching experiments were initially designed to study the release of Cr, Mo, Se and Re from the analogue cements and the biomicrite. As such, they provide information to be correlated with the solid state investigations devoted to these metals (section 4.4). Their results also have to be compared with groundwater data (Chapter 3). In this section, the evolution of major elements leached from the different columns is discussed.

4.7.2 Characterisation of the materials

The three materials were characterised using several techniques: wet chemical analyses, XRD, FTIR spectroscopy, thin sections, SEM/EDX investigations, TG-DTA (details in appendix 4). The chemical analyses are reported in Table 4.19. The results given by XRD are summarised in Table 4.20. Other investigations (optical microscope, SEM/EDX) gave complementary information:

- sample M00-1-23 is a fined-grained biomicrite corresponding well to the description given by Milodowski et al. (1992a, 1992b). The presence of pyrite as framboidal clusters within fossil tests is clear.
- sample M99-1-41 (altered analogue cement) displays a thorough vein network, filled with ettringite surrounding pockets of partially altered analogue cement. Thaumasite-type end members were also observed in fractures. Calcite is present in the analogue cement matrix. A Ca-P-Si-S-Al phase was also detected. This could correspond to a solid solution between ellestadite and apatite-type end-members. The pink colour of the material suggest the presence of haematite-type iron oxides.
- sample M00-1-4 (fresh analogue cement) is similar to a sponge skeleton of carbonate (calcite, aragonite) containing inclusions of various minerals from a submicron size to more than 50 µm in diameter. The sample is crossed by occaisonal fractures filled with a thaumasite (ettringite) product. In some regions, the pores of the carbonate network seem to be filled with a unidentified K-containing phase (see section 4.4 for more details). Semi-quantitative EDX analyses indicate compositions compatible with that of CSH phases having C/S ratios betweeen 0.5 and 2.0.

From the chemical analyses and XRD spectra, an idealised mineralogical composition of the different samples was computed. For sample M00-1-4, CSH 1.1 was preferred to larnite to describe the Si containing phase.

Table 4.19 Bulk chemical analysis as oxide wt %

Compound (wt %)	M00-1-23 Biomicrite (Adit 6 – 50 m)	M99-1-41 Altered cement (Adit 6 – 140 m)	M00-1-4 Unaltered cement (Adit 6 – 256 m)
SiO_2	9.30	6.98	5.86
TiO_2	0.16	0.13	0.10
Al_2O_3	3.96	3.25	2.79
Fe_2O_3	1.61	1.59	1.39
MnO	0.01	0.03	0.01
MgO	0.34	0.21	0.25
CaO	46.08	45.45	49.66
Na_2O	0.25	0.09	0.09
K_2O	0.45	0.01	0.27
P_2O_5	2.40	2.37	1.58
CO_2 (*)	30 +/- 2	17 +/- 2	31 +/- 2
Org. C + H_2O (**)	7 +/- 3		
H_2O (***)		7 +/- 1	3.0 +/-0.5
Total (****)	101.5 (a)	77.1 (b)	93 (c)

(*) from mass loss between 640 and 910 °C in the TG

(**) from mass loss between 40°C and 550°C in the T

(***) from the mass loss between 40°C and 400°C in the TG

(a) variability in the organic C content on several analyses, sulphides not dosed

(b) SO4 not analysed; strong content in ettringite

(c) SO4 not analysed; gypsum, ellestadite and ettringite present.

Table 4.20 Bulk mineralogical analysis (by XRD)

Mineral phase	**M00-1-23 Biomicrite (Adit 6 – 50 m)**	**M99-1-41 Altered cement (Adit 6 – 140 m)**	**M00-1-4 Unaltered cement (Adit 6 – 256 m)**
Calcite $CaCO_3$	****	****	****
Aragonite $CaCO_3$			***
Gypsum $CaSO_4$-$2H_2O$			*
Fluorapatite $Ca_{10}(PO_4)_6F_2$	**	* (?)	**
Ettringite $Ca_6\ Al_2\ (SO_4)_3\ (OH)_{12}\ 26H_2O$		****	*
Larnite $Ca_2\ SiO_4$		**	**
Pyrite FeS_2	*(?)		
Kaolinite $Al2(Si_2O_5)(OH)_4$	**		
Ellestadite $Ca_{10}(SiO_4)_3(SO_4)_3(Cl,OH,F)_2$		**	* (?)
Carbonapatite		* (?)	* (?)
Monocarboaluminate $Ca_4\ Al_2\ (OH)_{12}\ (CO_3)\ 5H_2O$			*
Brownmillerite $Ca_2\ (Al,Fe)_2\ O_5$		*	*

*(?) : uncertain and very weak

* : very weak

** : weak

*** : medium

**** : strong.

4.7.3 Experimental set up and protocol

The experimental methods are presented in Appendix 4.

4.7.4 Results

As quoted in Table 4.21, the column leaching experiments of analogue cements M00-1-4 and M99-1-41 will respectively be referred as **experiments 1 and 2** and the leaching experiment of biomicrite by portlandite equilibrated water will be referred as **experiment 3**.

4.7.4.1 pH evolution

A preliminary batch-test was conducted at 25°C in which 1 g of powdered material was placed, in an air-tight vessel, in contact with 20 mL of deionised water and the pH was followed during 1 hour (Figure 4.75). Three distinct signals were observed. For the biomicrite sample, pH was constant at ~8.3, reflecting the calcite buffering in presence of atmospheric CO_2. For sample M99-1-41 (altered analogue cement), pH rapidly rose to ~11.9 and then stayed constant. This observation is consistent with what was found in a similar but longer (~3 months) batch test on a analogue cement collected in Adit A-6 (see Section 4.6). In contrast, for sample M00-1-4, a much slower increase of pH is observed: after 1 hour, pH reached 10.5 and still increased, but very slowly. This means that different pH buffering mechanisms are active in these two analogue cement samples. In particular, sample M00-1-4 has much higher calcite and lower ettringite contents than sample M99-1-41. Note that, as was described in Section 4.6, a pH above 12 could never be reached in these simple and short experiments, whereas *in situ* pH of hyperalkaline groundwaters at the Eastern Springs generally reaches 12.4 (buffering by portlandite).

The pH evolution at the outlet of the column for experiments 1 and 2 is shown in Figure 4.76. For sample M00-1-4, pH increases up to 10.5 in about 18 hours and, after 32 hours, a new rapid increase of pH was observed, up to 11. After 72 hours, pH diminished slowly and regularly all through the rest of the experiment. For sample M99-1-41, pH increased rapidly up to 11 and then more slowly, reaching 11.67 after 5 days. Then, pH decreased slightly and stabilised around 11.55 for the rest of the experiment. The pH electrode drift was smaller than the observed pH evolution.

For experiment 3 (addition of portlandite equilibrated water to biomicrite), pH was followed qualitatively at discrete times. It was observed that pH at the column outlet increased very rapidly to 11.7 and then remained above 12. Recomputation of pH values from speciation simulations agree with this observation, as discussed further below.

4.7.4.2 Evolution of major elements (experiments 1 and 2)

The evolutions of major elements leached from the two analogue cement columns (experiments 1 and 2) display marked differences (Figure 4.77). For analogue cement M00-1-4 (experiment 1), Ca and SO_4 concentrations first display a high concentration level (~9-12 mmol L^{-1}) during 100 hours and then a massive decrease, followed by a slow decrease in the mmol L^{-1} range. The Ca/SO_4 ratio initially less than 1 (Figure 4.78) increases up to 2 after 150 h and remains at that value up to about 400 h; a marked decrease of the Ca/SO_4 ratio is then noted. In contrast, for analogue cement M99-1-41 (experiment 2), Ca and SO_4 display a regular decrease with time, with a faster decrease for SO_4. The Ca/SO_4 ratio regularly increases from 1 up to values around 5 after 200 hours and then decreases. The Al and Si concentrations measured in experiment 1 are clearly correlated but noisy. The Si/Al ratio is between 1 and 2. The Si and Al concentrations for experiment 2 are also correlated and display in addition a marked decrease with time. The Si/Al ratio lies between 2 and 3.

4.7.4.3 Study of saturation indices (experiments 1 and 2)

Saturations indices of the water samples with respect to several mineral phases were computed using the CHESS geochemical tool (Van der Lee, 1998) and reported as a

function of time (Figure 4.79). For these computations, it was assumed that the solutions were in equilibrium with calcite. In addition, pH was set at 11 for experiment 1 and 11.5 for experiment 2 (see Figure 4.76). An initial stage corresponding to gypsum dissolution is clearly seen for experiment 1. This is consistent with mineralogical characterisations. A plateau is also seen for the saturation index of ettringite and monosulphoaluminate in experiment 1. In experiment 2, however, although ettringite is a major phase of the leached material, the saturation index for ettringite and monosulphoaluminate decrease continuously from about 0, reaching a plateau after about 200 hours at low undersaturation indices. A similar plateau is observed for experiment 1 but with more negative indices. Saturation indices of several Si-Al phases have also been represented. The total Al concentration behaves as if it was controlled by pure Al oxy-hydroxide phases (gibbsite experiment 1, diaspore in experiment 2). The saturation indices of leachates are consistent with the hypothesis of solution control by tobermorite (exp. 1) or CSH or laumontite (experiment 2). Finally, the hypothesis of withlockite precipitation ($Ca_3(PO_4)_2$), as secondary product of primary phosphate alteration, is a plausible hypothesis.

Table 4.21 Main characteristics of the three different column experiments

	Experiment 1	**Experiment 2**	**Experiment 3**
Material	M00-1-4	M99-1-41	M00-1-23
Inlet solution	DI water	DI water	Water in equilibrium with $Ca(OH)_2$
Flow rate	0.01 mL min^{-1}	0.01 mL min^{-1}	0.01 mL min^{-1}
Duration	380 hours	576 hours	1200 hours

Table 4.22 BET surface area measurements of the powdered samples

Sample	M00-1-23	M00-1-4	M99-1-41
BET surface area (m2/g)	10	5.5	6.1

It was also found that the saturation index of wollastonite ($CaSiO_3$) was close to 0 in the leachates from experiment 1. This finding will be further discussed in the modelling section below.

4.7.4.4 Observation of leached solids (experiments 1 and 2)

A limited number of observations could be performed on the columns.

Visual inspection of the head of the column shows red stained material. Observations conducted with the SEM on material extracted from column 1 (M00-1-4) showed a decrease of the calcite content and formation of unidentified calcium silicates and Si-Al-K containing grains at the head of the column. XRD spectra showed that ettringite and gypsum were removed from the column head at about 1 cm depth. On further column sections, only gypsum seemed to have been removed.

Figure 4.75 Evolution of pH over 60 minutes in a batch reactor where DI water is interacting with a small quantity of the different rock powders

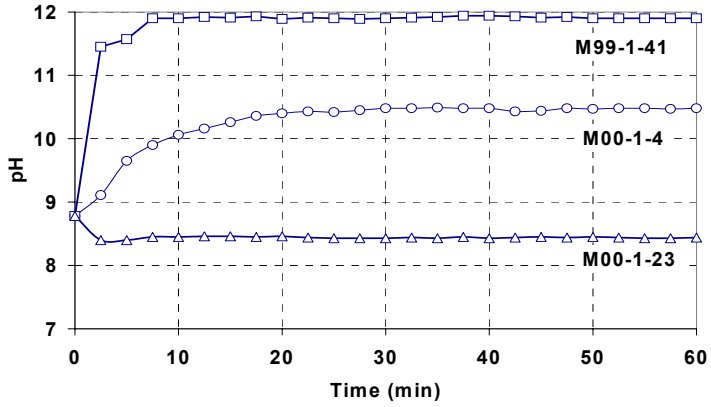

Figure 4.76 Experiments 1 and 2: pH evolution at the column outlet

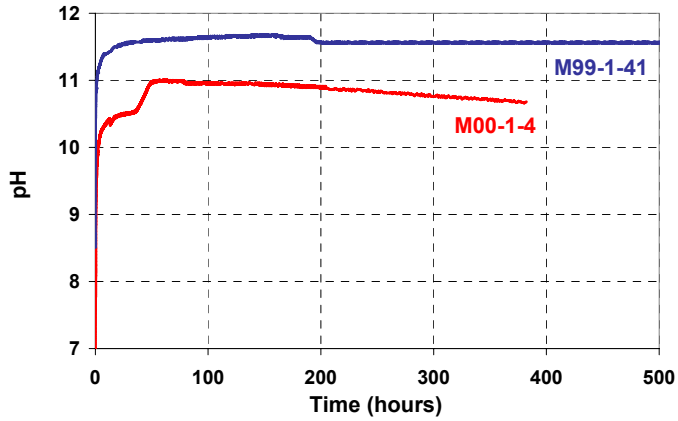

XRD spectra from material extracted from column 2 (M99-1-41) indicate that ettringite has been removed from about 1.5 cm at the head of the column. In deeper sections, the XRD spectra are similar to the initial spectrum of the analogue cement. An indurated zone was found in the middle of the column (about 4.5 cm from the head) suggesting reprecipitation and partial analogue cementation.

4.7.4.5 Hypotheses on processes occurring in experiments 1 and 2

Major elements evolution as well as saturation indices study and solid phase investigations clearly show that the analogue cement columns undergo important transformations during the experiments:

- strong dissolution processes affect gypsum and ettringite and also Si and Al-bearing phases.
- dissolution processes probably also affect calcite and phosphate containing phases.
- precipitation processes occur simultaneously, probably both at equilibrium and with kinetic limitations..

Figure 4.77 Experiments 1 and 2. Major evolutions observed in the column leachates

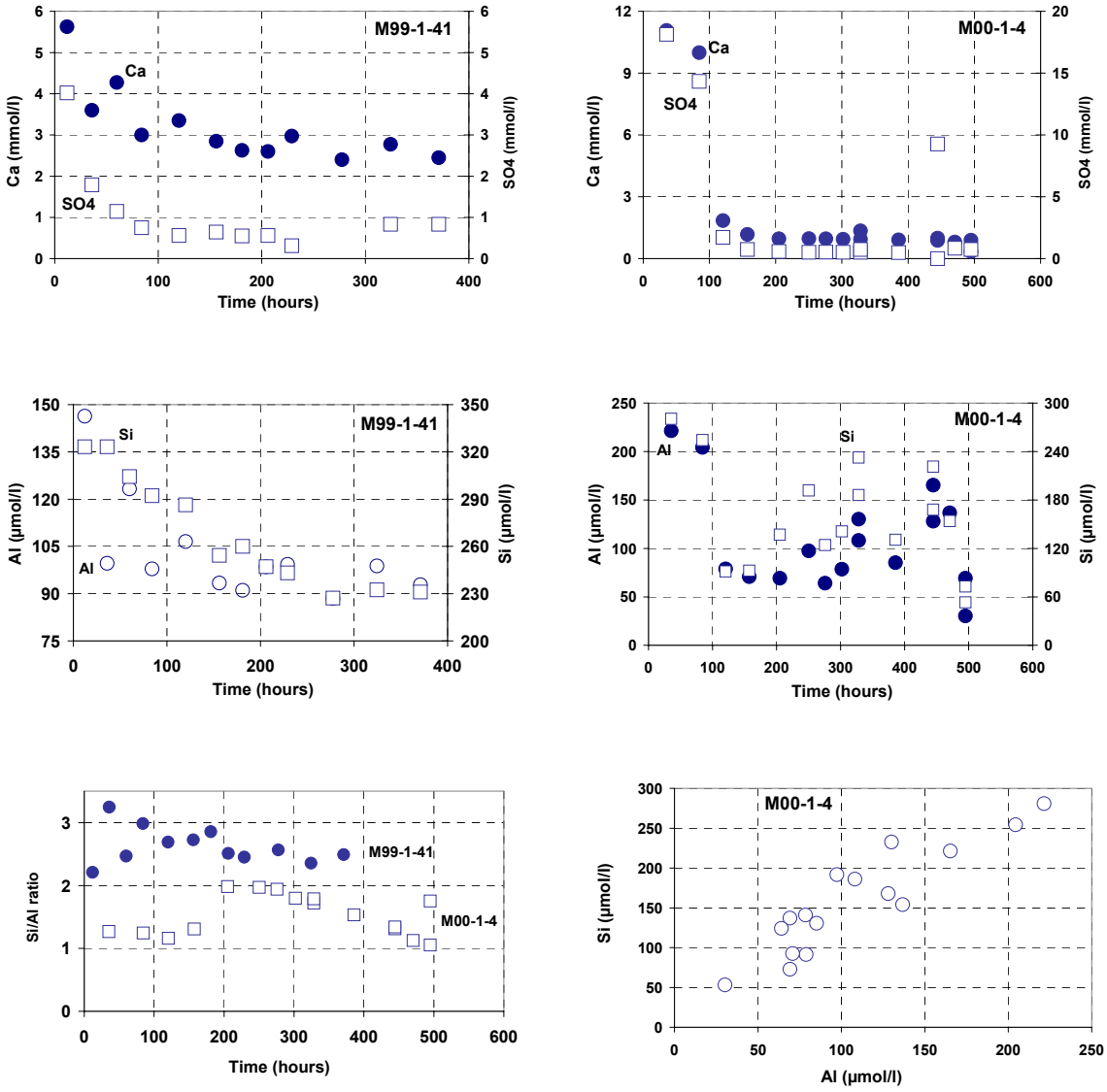

The high flow rate imposed during the experiments (0.01 mL min^{-1}, corresponding to a renewal of the pore volume in 2.5 hours) probably gives a limiting role to several dissolution/precipitation processes. The flow rate has been varied at the end of experiment 2 over the range 0.05 mL min^{-1} to 0.2 mL min^{-1}. It appears that the Si, Ca and Al-leached concentrations tend to be higher when flow rate increases which supports the hypothesis of rate limited precipitation of Ca, Si, Al-bearing phases. Another feature of the experiments could explain the observation made on the ettringite saturation index in both experiments. Although the powdered material filling the columns has been carefully calibrated, fine particles are present (see Figure 4.80). The very fast dissolution of these fines, presenting a high specific-surface area, could explain the rapid decrease of the saturation index of ettringite from values initially close to 0, by coupling surface area variations and dissolution processes. In addition, the precipitation of Al released by ettringite dissolution further pulls the saturation index towards negative values.

Figure 4.78 Evolution of the Ca/SO_4 molar ratio of leachates in experiments 1 and 2

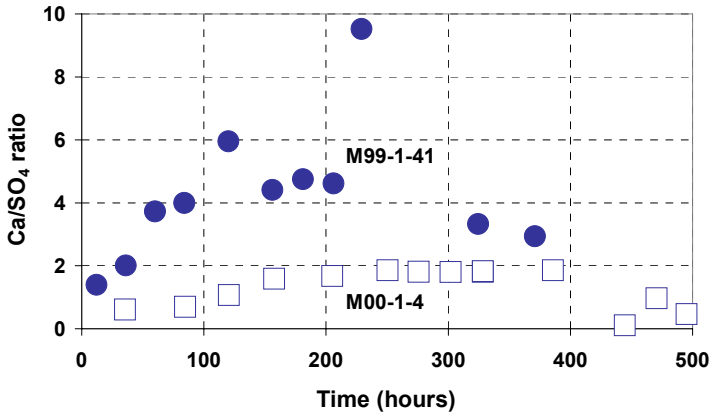

4.7.4.6 Evolution of major elements (experiment 3)

The temporal evolution of the concentrations of major elements at the outlet of column 3 is reported in Figure 4.81. Although the residence time of solutions in the column is short (< 3 hours), it appears that the calcium level increases quite slowly (during about ~500 h) at the outlet, reaching the equilibrium with portlandite in at least 300 h (Figure 4.82). A small decrease of calcium concentration is then noticed, followed by a plateau and then a further decrease after 1000 hours. The released sulphate concentration is significant in the first sample (~3.5 mmol L^{-1}) and then keeps a low and constant level (~0.01 mmol L^{-1}). Magnesium concentration decreases in about 100 h from ~20 µmol L^{-1} to a constant and low level (~0.1 µmol L^{-1}). Silicon exhibits two distinct plateaux, high concentrations (~900 µmol L^{-1}) before 100 h and then low concentrations (~10-20 µmol L^{-1}) during the rest of the experiment. Potassium concentration displays a progressive decrease on about 500 h, decreasing from about 1.5 mmol L^{-1} to 0.1-0.2 mmol L^{-1}. Sodium concentrations show a sharp decrease during the first 20 h (from 130 mmol L^{-1} to ~10 µmol L^{-1}); a slight increase is observed at ~500 h and the Na concentrations reach a plateau ~30 µmol L^{-1}. Al and total organic carbon (TOC) concentrations could not be measured on all aliquotes and trends can be observed on the first half of the experiment. Al increases rapidly up to a plateau level of ~600 µmol L^{-1}. TOC concentrations show a continuous and significant decrease between 150 and 600 h (Figure 4.82, first points missing). A good correlation is found between released K and TOC (Figure 4.81). Using speciation calculations, pH could be recomputed. The recomputed pH evolution of leachates (Figure 4.82) is consistent with the Ca evolution and thus with the portlandite saturation index. Leachates are found to be close to equilibrium with respect to diaspore and the CSH 1.1 phase. Solutions are initially undersaturated with respect to ettringite but the saturation index values have a trend towards equilibrium at long times. The leachates are markedly oversaturated with respect to monosulphoaluminate.

4.7.4.7 Observation of leached solids (experiment 3)

Few observations were done on the solid sample. A preliminary XRD investigation showed that the pyrite concentration decreased and the calcite concentration increased slightly at the head of the column (0-2 cm section). On XRD patterns, a broad dome corresponding to distances between 6 Å and 15 Å, is more developed on the tail sections (6-10 cm).

Figure 4.79 Experiments 1 and 2. Saturation indices of the leachates with respect to selected mineral phases

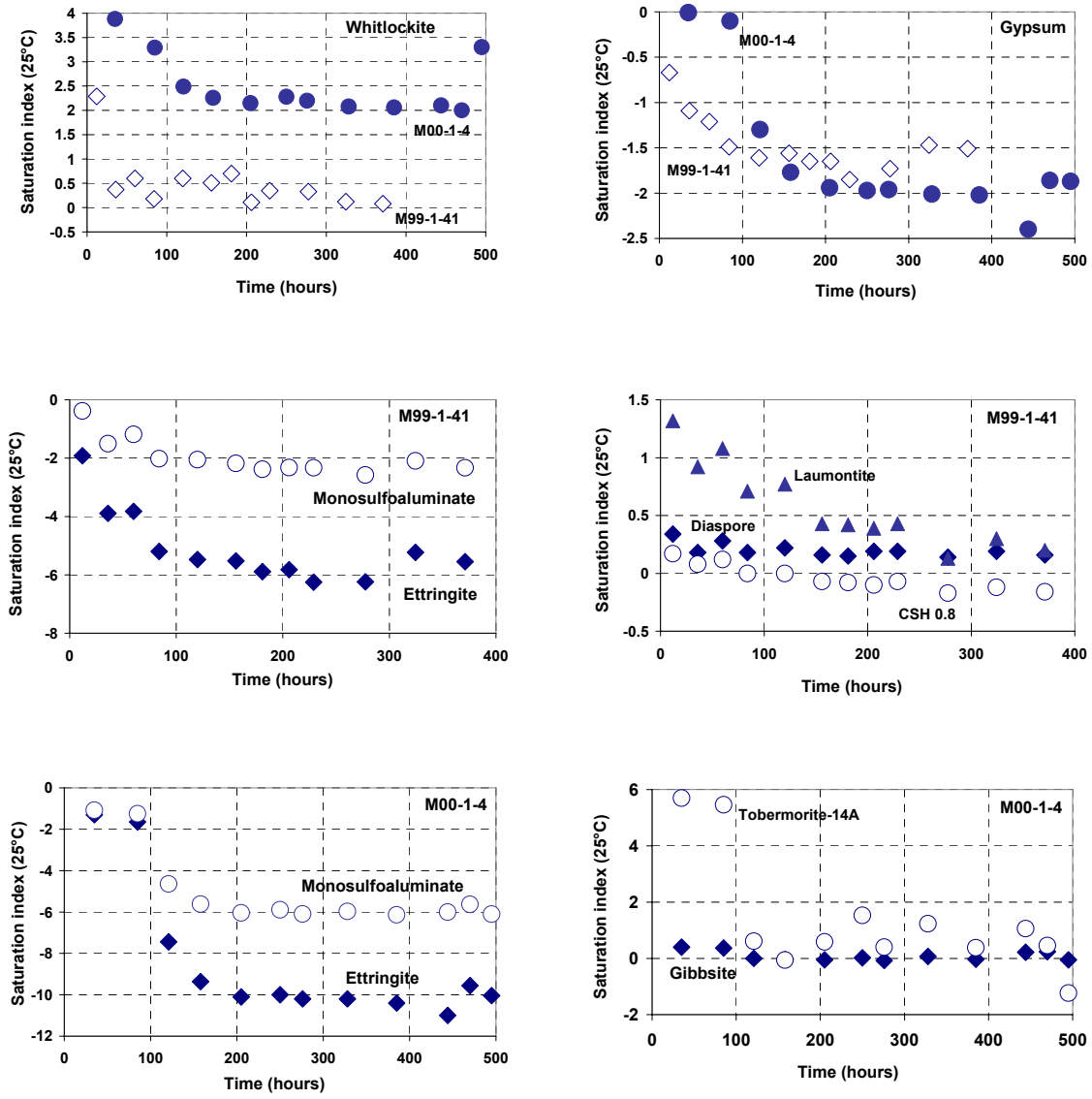

4.7.4.8 Hypotheses on processes occurring in experiment 3

The Ca, Si and Al concentration evolutions clearly show that strong interactions occur in the biomicrite column. At least 500 h are necessary until the pH of the input solution is reached at the outlet. Precipitation of secondary phases is probable as indicated by the saturation indices of diaspore and CSH 1.1. Dissolution processes affecting organic matter, kaolinite and probably pyrite (the input water is in equilibrium with atmospheric O_2) are active. The role of sulphate production by pyrite oxidation and on subsequent ettringite precipitation has to be explored. Also, the leaching out of organic matter by the hyperalkaline water is observed (cf Geyer et al., 1998) and could play a role in explaining the progressive increase of pH.

Figure 4.80 Grain-size distribution of powdered rock samples used in the column leaching experiments

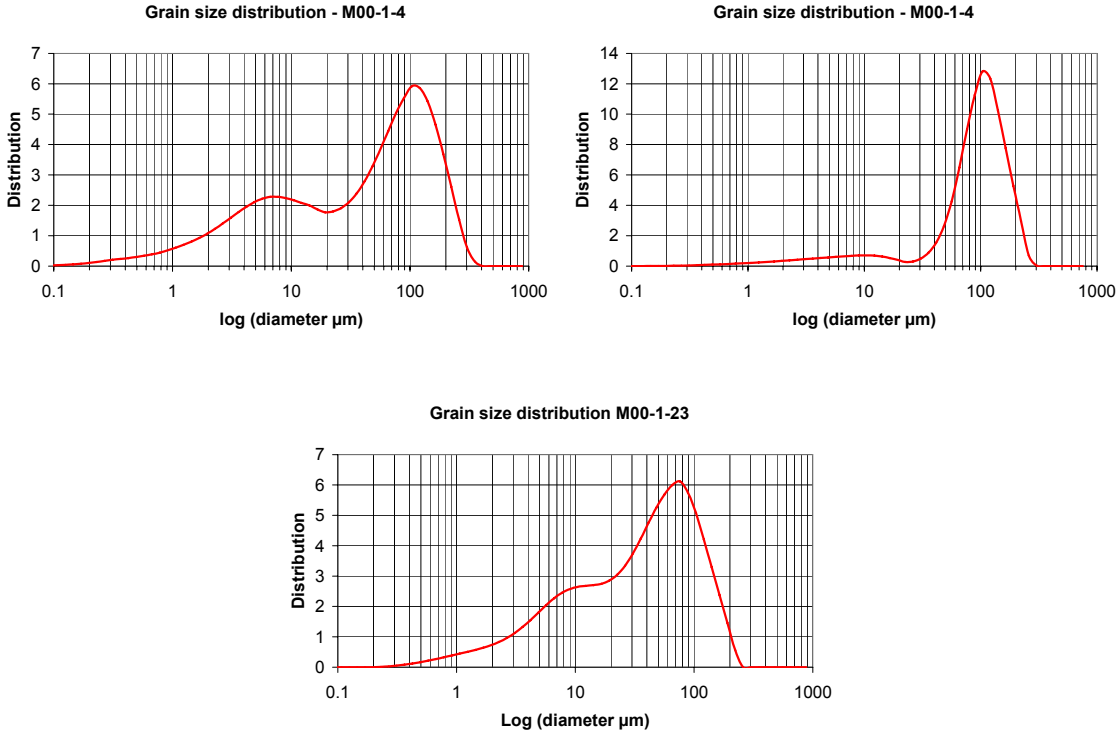

4.7.4.9 Modelling attempts of the column experiments

The modelling of these column experiments was attempted by using available information on the experimental conditions (flow rate, volume of columns, initial composition of rock) and on analysed liquid and solid samples. The simulation tool HYTEC (Van der Lee et al., 2002) was used to reproduce the results. Specifications of the model are given in Table 4.23.

The rather high flow rate will make surface reactions the rate-limiting step for the global release of elements. As will be seen below, this will give us access to several interesting features.

Experiment 1

The first objective was to reproduce the pH evolution with time as well as the Ca and SO_4 evolutions. After several trials is was found that :

- a model including calcite, ettringite and gypsum as primary minerals was able to reproduce quite correctly these features
- it was necessary to describe dissolution kinetics of minerals to account for observations. In particular, a dissolution front of ettringite was predicted to develop in the column only if a pH dependence was given in the rate law. More specifically, it was found that only a $[H^+]^{0.5}$ dependence was able to reproduce correctly the pH curve (see Figure 4.81)

Table 4.23 Summary of assumptions for the simulations of column experiments

	Experiment 1	**Experiment 2**	**Experiment 3**
Column composition	Calcite : 41 mol l^{-1} Ettringite : 0.05 mol l^{-1} Gypsum : 0.33 mol l^{-1} Tobermorite-14 : A 9 mol l^{-1}	Calcite : 41 mol l^{-1} Ettringite : 0.16 mol l^{-1} Larnite : 5 mol l^{-1}	Calcite : 44.7 mol l^{-1} Kaolinite 2.4 mol l^{-1} Chalcedony 0.2 mol l^{-1}
Selected secondary precipitates	Laumontite	Si-Hydrogarnet CSH 1.1	Tobermorite-11A, Si-hydrogarnet
Rate laws	Calcite: $r = 10^{-6}$ mol m^{-2} s^{-1}	Calcite: $r = 10^{-6}$ mol m^{-2} s^{-1}	Calcite: $r = 10^{-4}$ mol m^{-2} s^{-1}
	Ettringite: $r = [H^+]^{0.5}$ 1.4 10^{-1} mol m^{-2} s^{-1}	Ettringite: $r = [H^+]^{0.5}$ 0.6 10^{-1} mol m^{-2} s^{-1}	Chalcedony: $r = [OH^-]$ 2 10^{-3} mol m^{-2} s^{-1}
	Gypsum: $r = 10^{-4}$ mol m^{-2} s^{-1}	Larnite: $r = [H^+]$ 8 10^{3} mol m^{-2} s^{-1}	Kaolinite: $r = 10^{-7}$ mol m^{-2} s^{-1}
	Tobermorite-14A: $r = [H^+]^{0.5}$ 2 10^{-4} mol m^{-2} s^{-1}	Si-hydrogarne : $r = 3\ 10^{-9}$ mol m^{-2} s^{-1}	Tobermorite: $r = 10^{-7}$ mol m^{-2} s^{-1} Si-hydrogarnet: $r = 10^{-7}$ mol m^{-2} s^{-1}
	Laumontite: $r = 10^{-10}$ mol m^{-2} s^{-1}	CSH 1.1 : $r = 1.5\ 10^{-7}$ mol m^{-2} s^{-1}	

Comparison of the main output of this model with experimental results is given in Figures 4.82 and 4.83. However, several details are unsatisfactory, in particular the fact that the leachates are predicted to have equal initial Ca and SO_4 concentrations, which is clearly not the case in the experiment (Figure 4.78). Another mismatch is the time shift between the pH step (at about 50 hours, Figure 4.76) and the the Ca and SO_4 drop (about 90 hours, Figure 4.77). The existence of a specific source of sulphate ions may explain some of these discrepancies and is also in good agreement with SEM observations (see Section 4.4 and Milodowski et al., 1992a, 1992b). In this case, gypsum is not a primary phase but a secondary product precipitated by the combination of Ca released by ettringite and SO_4 released by this specific mineral source. For example, the alteration of the calcium silicosulphate mineral ($Ca_5(SiO_4)_2(SO_4)$), described earlier in this Chapter (Section 4.2), could trigger a sudden calcium and sulphate simultaneous release, causing gypsum to precipitate very rapidly.

Different trials were done in order to include in the column model the dissolution and precipitation of Si/Al/Ca bearing phases. The silicate bearing phases of sample M00-1-4 were represented by 14 Å tobermorite, in order to simulate the leaching of CSH phases observed in the porous calcite matrix. The dissolution rate of tobermorite was assumed to be dependent of pH with a $[H^+]^{0.5}$ dependence as for ettringite. Several possibilities were examined for the precipitation of secondary products, such as zeolites (laumontite, heulandite), hydrogarnet and gibbsite. However, no satisfactory fit could be found with the experimentally observed concentrations of Al and Si in the leachates. In addition, the fit to the pH evolution was slightly altered when silicate dissolution was included. Results on one sample simulation, combining 14A-tobermorite dissolution with secondary precipitation of Ca-heulandite (Table 4.23) are shown in Figures 4.84 and 4.85.

Experiment 2

The initial column material was simulated by a mixture of calcite, ettringite and larnite. The rate-law form adopted for calcite and ettringite was the same as in the modelling of experiment 1. The rate factor for ettringite was decreased, which is probably an indication of surface area differences between the two analogue cement powders. Best fits were found when larnite was given a dissolution rate law with a $[H^+]^1$ dependence. The rate factor was set in order to obtain the good pH level at the outlet of the column. A better fit between observations and predictions was obtained for the simulation of experiment 2 than in the case of experiment 1 (Figure 4.86). A noteworthy feature in Figure 4.87 is the precipitation of CSH in the middle of the column, where it was was partly cemented and clogged.

Experiment 3

Modelling of experiment 3 was more difficult than for the other experiments. Also, because of the lack of time, investigations could not be pursued in great detail. Attempts were conducted by simulating the biomicrite column by a mixture of calcite, chalcedony and kaolinite. Tobermorite was selected as a possible secondary product. The predicted pH evolution is compared in Figure 4.88 to the pH evolution evaluated from leachates composition. It was not possible to simulate correctly the sulphate elution, because of the complexity of processes involved (interactions between dissolved oxygen, pyrite and organic matter, and potential reprecipitation as gypsum). The column response was very sensitive to kinetic rate factors for kaolinite and chalcedony. More work is obviously needed for understanding this experiment as the underlying processes (high pH interactions with organic matter, in particular) are of some importance in PA.

Figure 4.81 Experiment 3. Evolution in the leachate chemistry

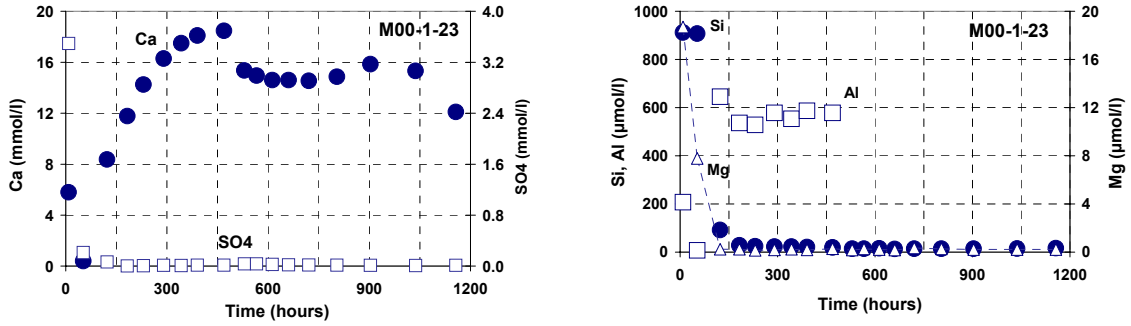

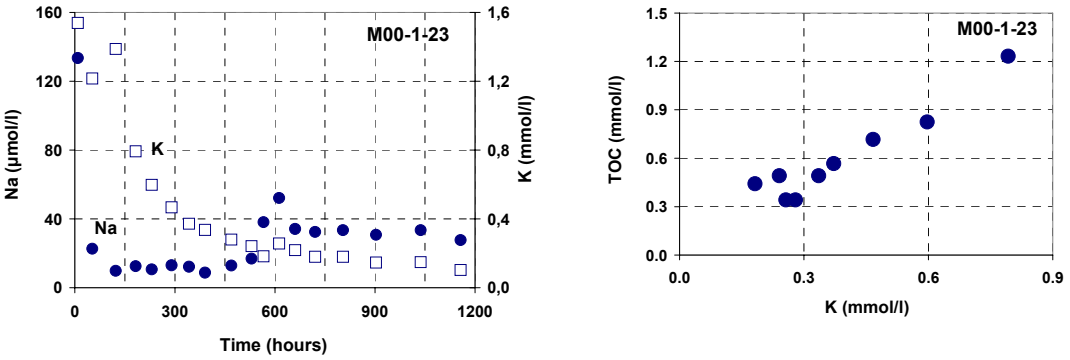

Figure 4.82 Experiment 3. Recalculated pH in leachates. Saturation index of the leachates with respect to selected mineral phases. Evolution with time of TOC in the leachates

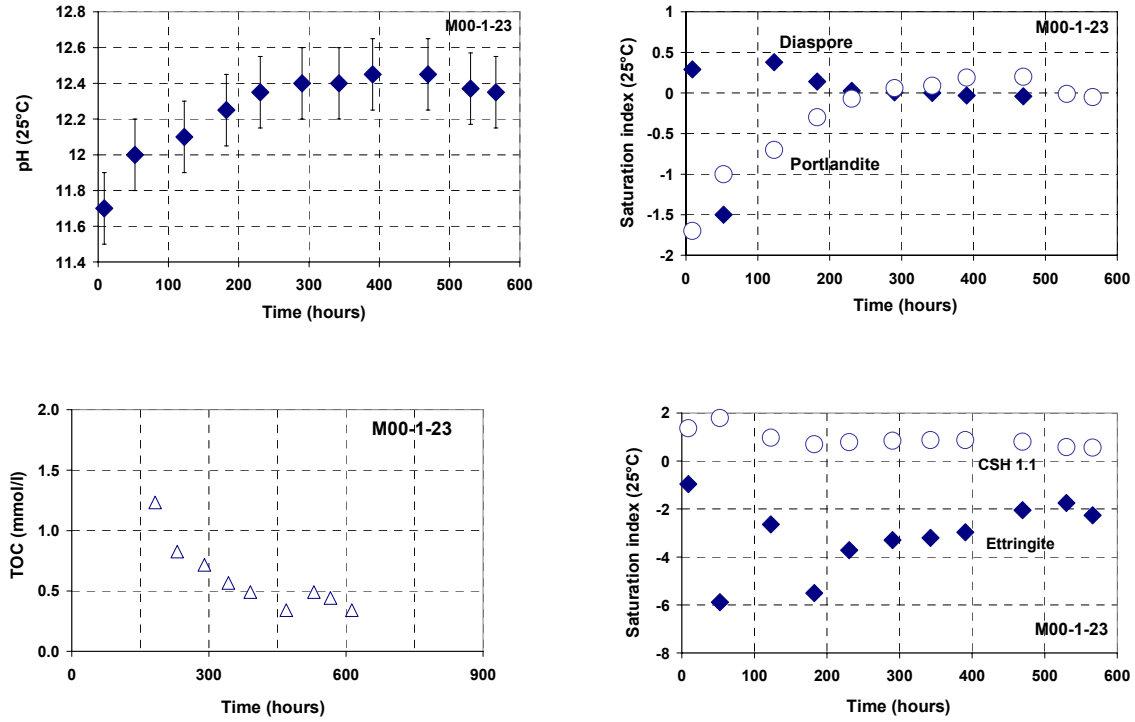

4.7.5 Discussion

The type of experiments presented here were not performed previously on analogue cement samples from Maqarin, whereas the biomicrite had already been examined in more detail. They aim at a better linking of field observations, with conceptual models of pH plume generation and reactive transport modelling. The experiments were conducted on powdered materials with high flow rates and this has to be taken into account in linking with the field data.

The pH evolutions observed in experiments 1 and 2 are qualitatively consistent with observations on small batches: pH > 12 cannot be reached in short term experiments. The

modelling attempts explain in part the range and evolution of pH by taking into account the simultaneous dissolution of calcite, ettringite and larnite or tobermorite. Therefore, this observation raises the important issue that the high pH (> 12.3), observed in the field in Maqarin, is most probably the sign of rather confined conditions or long residence times. Further experimental work is clearly needed to clarify this issue. The rate limited precipitation of CSH phases explains *pro parte* this slow increase of pH.

The marked initial release of sulphate in experiment 1 is most probably linked to the potassium-bearing Ca-Si-SO_4 phase identified on less altered analogue cements (See sections 4.2 and 4.4) and not to the presence of gypsum. Gypsum is thought to be a secondary precipitate and to limit sulphate availability in the present case.

Notably, due to experimental conditions, the release of several elements from the column was limited by the kinetics of ettringite dissolution. The modelling of experiments 1 and 2 gave some constraint on the dependence of ettringite dissolution rate law versus pH, a $(H^+)^{0.5}$ dependence being found. The observation of an ettringite dissolution front in the column is consistent with the existence of a pH dependence in ettringite dissolution rate law. The best adjustment between modelled and observed pH curves was found for an H^+ exponent of 0.5. Such a pH dependence in ettringite dissolution rate law could play an important role in the precipitation of secondary ettringite accross pH boundaries (at, for example, fractures in the biomicrite).

Experiment 3 was only a preliminary investigation on the interaction between biomicrite and high pH waters. This experiment proves the high reactivity of the biomicrite, with important mobilisation of organic matter. The modelling of this experiment is complex: the predicted behaviour seems to be very sensitive to the choice of rate law parameters for the respective sources of silicon and aluminium in the material. In addition, the interaction with organic matter seems to be fast and significant.

4.7.6 Conclusion

In addition to important information on trace element behaviour (see Section 4.4), the column experiments presented here contribute towards a better understanding of the evolution of hyperalkaline waters in Maqarin. They suggest several key parameters to be taken into account in the modelling of such systems:

- the rate-limited precipitation of CSH phases
- the pH dependence of ettringite dissolution (and probably precipitation)
- the competition in the availability of Al and Si from the biomicrite, as has been noted elsewhere (e.g. Steefel and Lichtner, 1994; Chambers and Haworth, 1998), is a critical issue for modelling the alkaline perturbation

Further experiments and modelling of this type is needed to understand how (and how fast) Maqarin groundwaters acquire their high pH. Such information will be useful to bracket better the extent precipitation of secondary CSH phases in the near field of a repository, by allowing a better direct comparison between the natural cements from Maqarin and the industrial cements used in radwaste disposal.

Figure 4.83 *Experiment 1: observed pH at the column outlet (red line). Modelled pH evolution: no pH dependence in ettringite dissolution kinetics (yellow), (H+)0.5 dependence in ettringite dissolution rate law (blue)*

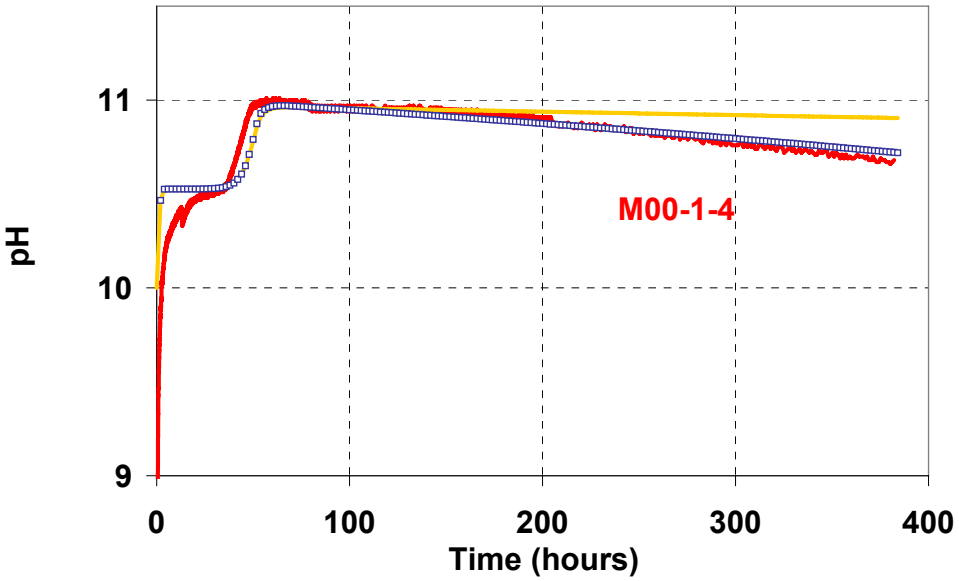

Figure 4.84 *Experiment 1. Comparison between experiment and simulation*

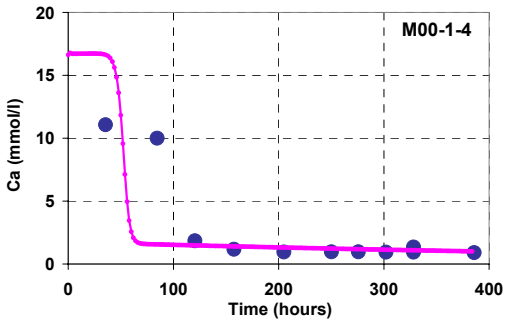

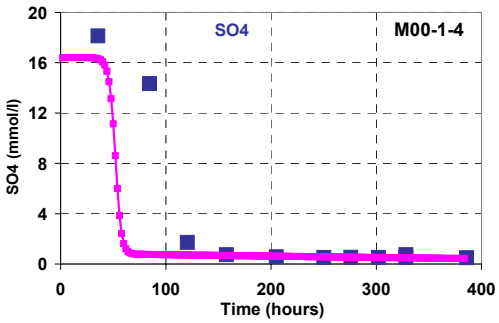

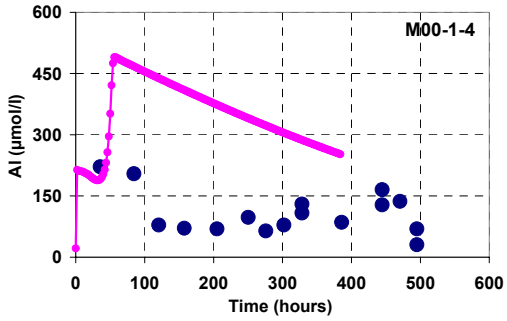

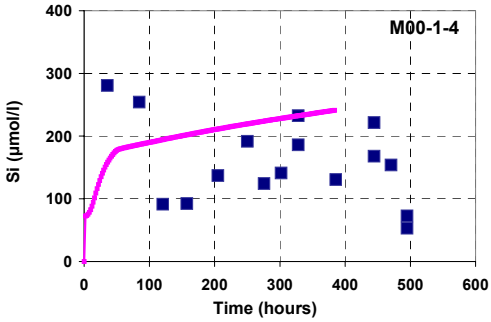

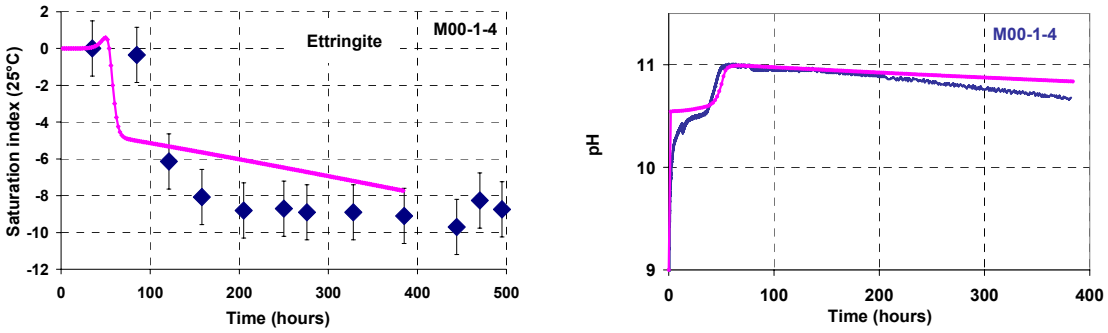

Figure 4.85 Experiment 1. Prediction of spatial profiles for pH, ettringite and precipitated heulandite

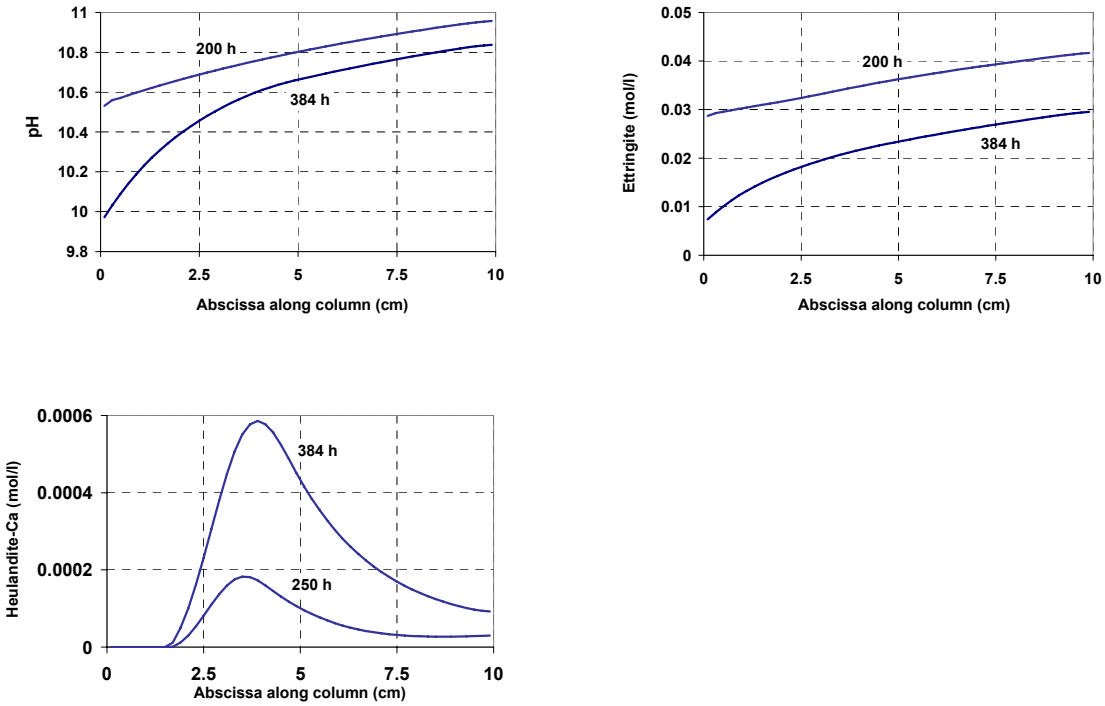

Figure 4.86 Experiment 2. Comparison between experiment and simulation

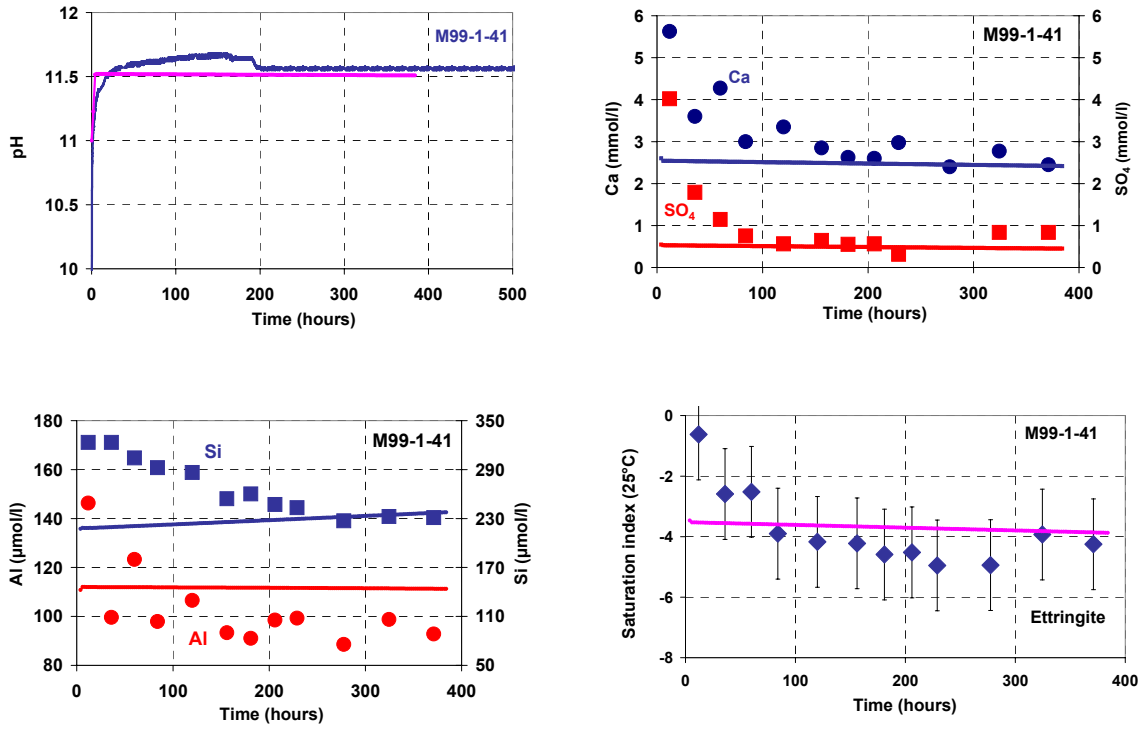

Figure 4.87 Experiment 2. Prediction of spatial profiles for pH, mineral phases, and aqueous Ca and Si

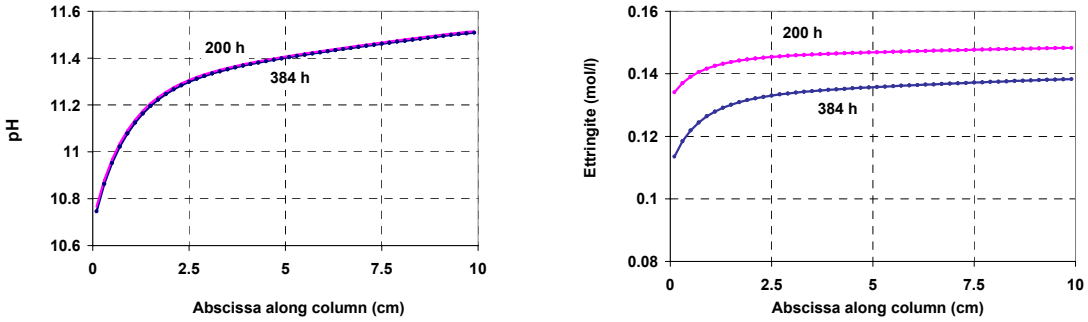

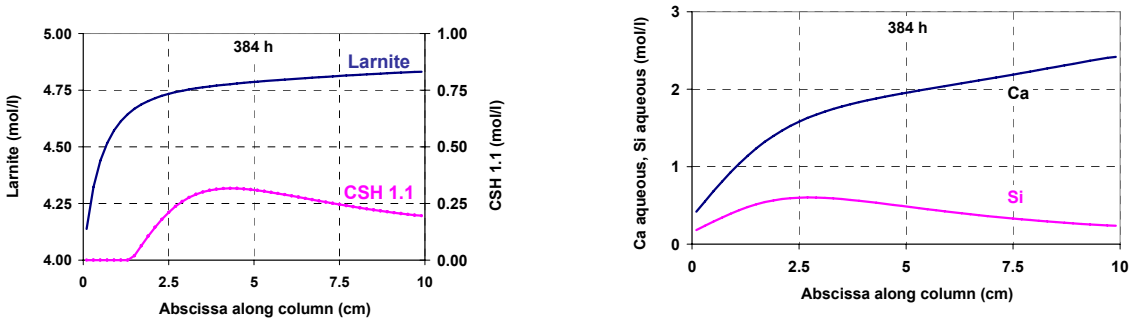

Figure 4.88 Experiment 3. Comparison between recalculated and simulated pH in the leachates

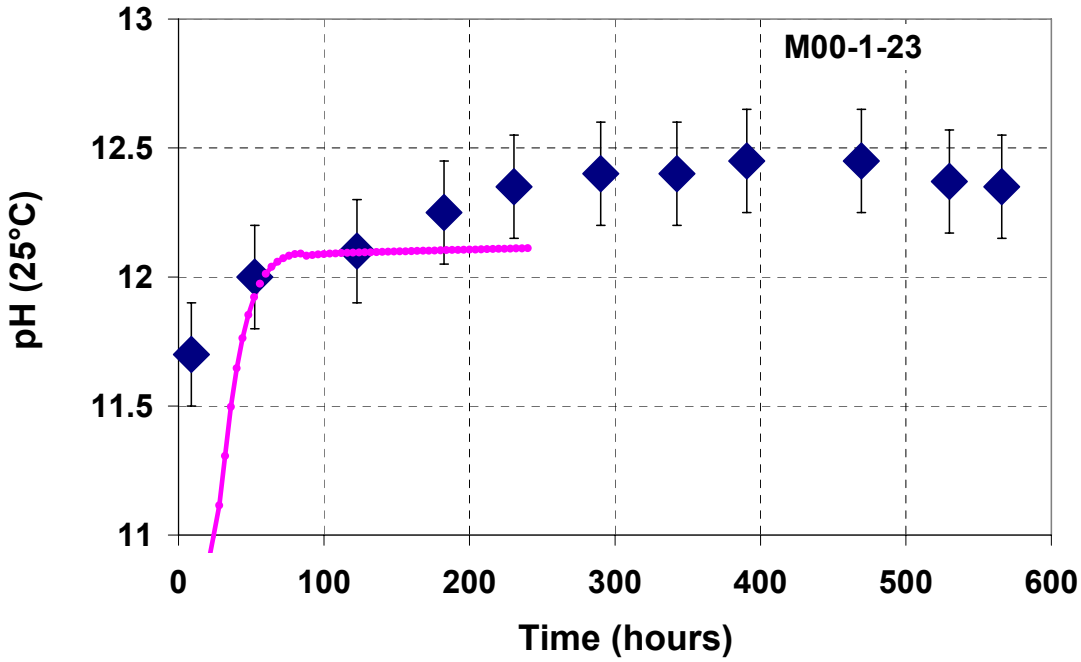

4.8 Conclusions

During Phase IV of the Maqarin Project, several studies focused on the analogue cement zone in order to complete and extend the initial effort undertaken on this subject during Phase I. Together with a more comprehensive description of the analogue cement source term, a better understanding of the alteration paragenesis is now available. A general geochemical classification of cement bodies is proposed, based on the initial characteristics of their parent rocks (limestones, cherty or cherty clayey biomicrites, phosphatic micrite). An update of observed mineralogical phases and of their genetic relationship has also been carried out.

4: The Analogue Cement Zone (ACZ)

One of the most salient finding of Phase IV is the identification, among major phases of the primary unhydrated cement bodies of the larnite-spurrite type, of a new calcium-silicate-sulphate mineral. Although this phase contains potassium as a minor constituent, it is a major source of potassium during hydration of cement bodies. The hydration of this $Ca_5(SiO_4)_2SO_4$ phase is also expected to release massive quantities of sulphate to solution and thus plays a key role in the precipitation of gypsum and in ettringite-thaumasite paragenesis. Future modelling of the hyperalkaline water evolution should therefore consider the respective influence of larnite, spurrite and $Ca_5(SiO_4)_2SO_4$ source terms. The alteration and hydration of $Ca_5(SiO_4)_2SO_4$ are shown to precede chronologically the alteration of larnite and spurrite and are responsible for the formation of a first generation of CSH phases in the paragenesis scheme. The leaching of this calcium-silicate-sulphate phase is thus thought to give the Maqarin Western Springs their specific geochemical signature of higher potassium and sulphate than the Eastern Springs.

Leaching experiments presented in Chapter 4 suggest that high pH values observed in the field (> 12.5) cannot be easily reproduced in the laboratory because of kinetic limitations in the precipitation of CSH phases during larnite hydration. This could mean that high pH values observed in Maqarin are the sign of relatively long residence times of groundwaters percolating through the cement bodies. Complex relationship between thaumasite and ettringite could be, in part, explained by slow and heterogeneous evolution of pH inside the cement zones.

By combining these observations, a more quantitative model of the alteration of the ACZ is possible and shows that:

- the Maqarin natural analogue includes a specific and massive sulphate source term which is not present at an equivalent level in industrial cements.
- kinetic limitations have to be considered in representing CSH precipitation in Maqarin. The correct time-scale associated with this process is not available and should be integrated with other time-dependent processes (e.g. transport and seasonal variations).

From the magnetic investigations conducted during Phase IV, a global picture of the ACZ, including the neighbouring thermally perturbated rocks, is now available. A significant local magnetic anomaly is found in the thermally altered biomicrite. The magnetic minerals are inherited from sulphide minerals, pseudomorphosed by the heat into maghemite-type iron oxides. The use of the magnetic anomaly as a qualitative dating tool for the combustion process was not attempted here, but could be a future development. In addition, the evolution of organic matter along the reconstructed temperature profile is complex and requires a more complete characterisation in order to discriminate temperature effects and high-pH groundwater effects (see also Chapter 6).

The investigations into the behaviour of rhenium are a direct continuation of Phase I investigations on trace element behaviour. In particular, the results here show that the combustion metamorphism has strongly modified the distribution of several elements, including Re, around the ACZ, creating a specific source term for this element. Unaltered cements are shown to contain up to 1.2 $\mu g\ g^{-1}$ Re to be compared to 0.15 $\mu g\ g^{-1}$ in the initial biomicrite. Thermally altered biomicrites seem, in contrast, to be Re depleted. Re localised in unaltered cements is rapidly leached and can be used as a tracer of recent cement alteration episodes. Preliminary data suggest that Re could be partially retained in

secondary fracture minerals (possibly gypsum and/or ettringite), although this point needs further investigation.

The study of chromium raises several important issues related to the redox state of the Maqarin groundwaters and also to the oxidation kinetics of Cr(III) to Cr(VI) under high pH conditions. The results presented here suggest that Cr(III) immobilised in a analogue cementitious environment is, over a long time scale, prone to be at least partially oxidised by dissolved oxygen to Cr(VI) and then exposed to be leached and transported in the environment. Cr(III) oxidation seems to occur at the microscopic scale in a heterogeneous fashion, producing patterns with adjacent Cr(III) or Cr(VI)-rich zones at less than 10 μm distance. Therefore, Cr(III) oxidation probably occurs *in situ* at the scale of individual mineral grains.

Chapter 5

Microbiology

K. Pedersen

5.1 Introduction

Microorganisms are an inherent part of groundwater and many geological formations, down to depths that greatly exceed the depths of existing and future radioactive waste repositories (e.g. Fredrickson and Fletcher, 2001). Microorganisms flowing in the groundwater will therefore enter the repositories. In addition, there will be microorganisms in the repositories that were introduced during the construction phase or that were associated with the disposed wastes. The possible interactions between microorganisms and repositories and radionuclides have been well-documented (e.g. Keith-Roach and Livens, 2002).

As noted in Chapter 1, cement and concrete will be major components in underground repositories for LILW, as well as in some repositories for HLW, and the porewaters and leachates will provide a high-calcium, hyperalkaline, repository environment. Microorganisms from high alkalinity environments, such as soda lakes, have been isolated, cultured and described (Grant et al., 1990; Duckworth et al., 1996; Jones et al., 1998). These environments are characterised by a low content of calcium and a high salinity, which is opposite to the typical cementitious repository environment with a high content of calcium and a (generally) much lower salinity. Indeed, naturally occurring hyperalkaline environments of repository relevance are very rare. Therefore, little can be deduced about possible microbial abundance and activity in hyperalkaline repositories from the literature.

However, the hyperalkaline springs of Maqarin represent a hyperalkaline, high-calcium environment that mimics deep, cementitious repositories and can be regarded as an analogue for microbial migration through a repository. Abundance of microbes in the alkaline springs of Maqarin relates to survival at, and adaptations to, the hyperalkaline conditions. Microbial activity may depend on degradation of organic material in the Bituminous Marl Formation underlying the cement zones.

5.1.1 Phase I-III results

International research teams have explored microbial life in the spring, seepage and groundwaters of Maqarin during four defined Phases stretching back over a decade.

Phase I of the Maqarin natural analogue project, initiated in 1989, included a microbiological study to establish the likely impact of microbes in hyperalkaline LILW repositories (West et al., 1992). One of the conclusions of that work was that sulphate-reducing bacteria (SRB) were present, in agreement with laboratory studies by the same authors. These had shown microbes, especially SRB, capable of growing in hyperalkaline environments containing repository structural materials (West et al., 1992).

During Phase II, which was initiated in 1991, extensive work was carried out on the microbiology of the springs (Coombs et al., 1994). The investigators concluded that diverse populations of microbes were present at all sites sampled and the unaltered, kerogen-rich biomicrites seemed to have the greatest potential for growth. However, it should be noted that all populations were only capable of exploiting nutrient-rich environments, which would indicate a need for a steady supply of nutrients and energy, and were seen to be clearly nutrient-limited in the Eastern Springs (West et al., 1995). Microbial tolerance for a pH of up to 11 was confirmed and appeared to be associated with SRB, which were found at all sampling sites.

In Phase III, which was initiated in 1993, the total numbers of microorganisms in seven alkaline water locations were analysed and the diversity of the microbes was explored using 16S ribosomal deoxyribonucleic acid (rDNA) gene sequencing and comparison. Combinations of culture media compositions were inoculated with spring, seepage and groundwater and incubated. For comparison, two neutral groundwater wells in the area were also included in the investigations. Planning and execution of the microbiological work in Phase IV was to a large extent based on Phase III results, conclusions and suggestions for continued work. In addition, there has been a significant addition of new information on the molecular databases on 16S sequences and so the Phase III molecular 16S results have been re-evaluated as a part of the Phase IV work. Consequently, the Phase III microbiology results have been merged here with the Phase IV results. This facilitates comparison between Phases III and IV microbiology data and gives the conclusions a more solid base.

The Phase IV work presented in this Chapter is the result of two field campaigns to the hyperalkaline springs of Maqarin with the first campaign taking place from November 24th to December 13th, 1999 and the second campaign from April 28th to May 13th, 2000.

5.2 Task Descriptions

During the first three Phases of the Maqarin investigations, proof for microbial *in situ* activity at pH 12-13 could not be presented, but it was established that some Maqarin microbes were tolerant of up to at least pH 11. The major task in Phase IV was to investigate if the microbes found in Maqarin were active at the *in situ* pH as this is more relevant to repository PA. Four sub-tasks were identified and executed to solve the main task.

5.2.1 Sub-task G1: Total number of microbes

Objective: To obtain the total numbers of unattached and attached viable and non-viable microbes in groundwater from Adit A-6 boreholes and at the Western and Eastern Springs.

5.2.2 Sub-task G2: Culturing

Objective: To obtain the total numbers of unattached and attached viable and non-viable microbes in groundwater from Adit A-6 boreholes and at the Western and Eastern Springs.

5.2.3 Sub-task G3: Assimilation of organic carbon sources by unattached microbes

Objective: To investigate if microorganisms flowing with alkaline groundwater in Adit A-6, and in the Western and Eastern Springs, were active *in situ*, i.e. could they assimilate various organic carbon compounds under *in situ* conditions in the groundwater emerging from the springs. Experiments were set up with ^{14}C and ^{3}H labelled carbon sources.

5.2.4 Sub-task G4: Assimilation of organic carbon sources by attached microbes

Objective: To study if microorganisms in Adit A-6 attached to surfaces and showed metabolic activity, i.e. if they assimilate organic carbon sources and metabolise them *in situ* at ambient pH (pH 12 to 13). Flow-through boxes/cylinders (FTB/C) were installed and left for periods of time. Surfaces in the FTB/C were removed and exposed to ^{14}C and ^{3}H labelled carbon sources. Assimilation of those organic carbon sources was analysed.

5.3 Materials and Methods

Materials and analytical methods are presented in Appendix 5.

5.4 Results

5.4.1 Groundwater chemistry

All sampled sites except M17 and M18 were hyperalkaline with a pH of between 12.1 and 12.7 (Table 5.1). The pH at M17 and M18 was close to neutral, 7.2 and 7.4 respectively, and there was lower conductivity. Compared to M17, M18 is believed to be a mixture with some hyperalkaline water (Milodowski, 1996), as indicated by its elevated calcium and alkalinity values compared with M17. The temperature varied from 16 °C to 27 °C in all groundwaters, depending on the site and season. In general, November temperatures were lower than May temperatures, and Adit A-6 boreholes had lower temperatures than did the ground-surface springs and seepages. Nitrogen was present as nitrate in the surface spring (M5 and M6) and seepage (M3 and M8) waters but below detection at the Adit A-6 sites and M18. Nitrogen was, however, present as ammonium and nitrite in most waters. There were high concentrations of calcium in all alkaline groundwater (480–1100 mgL^{-1}) and sulphate was generally high in these waters (270–1500 mgL^{-1}). Phosphate was not detected, except at M18. The Western Springs (M5 and M6) were characterised by higher alkalinity and concentrations of calcium, sulphate and chromium than seen at the Eastern spring seepage localities (M3 and M8) and the Adit A-6 boreholes (D3 and D6) and the Adit-6 seepage locality M1. Although no Eh data are available for the samples presented here, these waters are mostly sub-oxic to oxic (see Chapter 3 for detailed discussions on the groundwater chemistry; also Alexander, 1992; Linklater, 1998; and Smellie, 1998).

Table 5.1 Chemistry results sampled and analysed in November 1995 for M17, in 1996 for M6, M8 and M18 and in 1999 for M1, M3, M5, D3 and D6.

Component	Units	Method°	M1	M3	M5	M6	M8	D3	D6	M17	M18
Field pH		.	12.7	12.6	12.7	12.3	12.1	12.7	12.6	7.2	7.4
Conductivity 25°C	mS/cm	SSEN 27888	586	669	948	927	483	573	573	–*	203
Chloride, Cl	mgL^{-1}	SS 028120	54	71	35	48	53	63	67	46	163
Alkalinity, HCO_3	mgL^{-1}	SS 028139	1 700	1 900	2 300	2 200	1 400	1 600	1 600	79	630
Calcium, Ca	mgL^{-1}	CR-A2IM	666	742	993	1 100	480	648	646	87	460
Chromium tot, Cr	mgL^{-1}	CR-AIM	0.66	0.61	4.9	5.0	0.88	0.49	0.36	<0.01	<0.01
Iron, Fe	mgL^{-1}	FE-NI	0.20	<0.02	<0.02	0.12	<0.05	<0.02	<0.02	<0.01	0.8
Ammonium, NH_4	mgL^{-1}	SS 028134	<0.02	0.11	2.2	1.9	0.11	0.13	0.07	–	0.024
Nitrate, NO_3	mgL^{-1}	SS 028133-2	<1.0	9	6.6	8.1	2	<1.0	<1.0	–	<0.2
Nitrite, NO_2	mgL^{-1}	SSEN 26777	0.007	0.037	0.24	0.51	0.028	0.13	0.008	<0.04	0.018
Phosphate, PO_4	mgL^{-1}	SS 028126-2	<0.01	<0.01	<0.01	<0.01	<0.01	<0.01	<0.01	<0.02	0.01
Sulphate, SO_4	mgL^{-1}	SS 028182	300	340	1 500	1 300	325	270	300	–	780

* – = not analysed. ° Methods and measurement uncertainty detailed on www.sis.se, the web site for the Swedish Standards Institute.

5.4.2 Total number of microbes

The total number of unattached cells for all campaigns is given in Table 5.2. The numbers obtained during November were generally higher than the numbers obtained during April/May, possibly because there was more precipitation preceding the autumn sampling campaigns compared with the spring campaigns. Rainfall may have induced more groundwater flow, which transports more microbes into the aquifer system. The total numbers in the neutral groundwater from the boreholes M17 and M18 exceeded the hyperalkaline waters ten- to a hundred-fold. The Adit A-6 sites tended to show higher numbers than the ground surface springs and seepages. The SDs (standard deviations) for the total number of unattached cells were in the range of 25–50%, with the highest SD seen for the lowest numbers. These relatively high SDs were due to the fact that some of the numbers counted were close to the detection limit for the method (1×10^3 cells/mL), which increased the uncertainty of the counts. The total number counts of attached cells are shown in Table 5.3. The numbers of attached cells did not differ significantly between the sampling periods, or between the number of days of exposure to groundwater.

Table 5.2 Total number of unattached cells for the sampled sites°.

Sampled site	Total number of cells (cells mL^{-1})				
	Phase III			Phase IV	
	November 1994	April 1995	November 1996	November 1999	May 2000
M1	–*	2.5×10^3	–	3.3×10^5	1.7×10^4
M3	–	2.0×10^4	–	7.8×10^3	7.0×10^3
M5	–	3.0×10^3	4.6×10^3	2.3×10^4	2.2×10^4
M6	–	–	2.4×10^4	–	–
M8	1.2×10^4	–	1.3×10^5	–	–
D3	–	–	–	6.9×10^4	n.s.
D6	–	–	–	4.3×10^5	1.6×10^4
M17	1.1×10^6	–	–	–	–
M18	6.4×10^6	–	–	–	–

* – = not sampled. n.s. = not sampled ° Methods and measurement uncertainty detailed on www.sis.se, the web site for the Swedish Standards Institute.

Table 5.3 Total number of attached cells, with standard deviation (SD) as error°.

Sampling site	Campaign	No. of sampling days	Total number of cells (cells cm^{-2})
M1	November 1999	7	1.8×10^5
D6	May 2000	54	1.2×10^5
M1	May 2000	56	1.1×10^5
M1	May 2000	5	8.4×10^4

° Methods and measurement uncertainty detailed on www.sis.se, the web site for the Swedish Standards Institute.

5.4.3 16S-ribosomal deoxyribonucleic acid diversity

A total of 82 clones were sequenced, distributed over six sample localities (Figure 5.1). The diversity of clones found in neutral waters was double that found in hyperalkaline groundwater. Of 37 sequenced clones, 15 unique sequences were found in the neutral water, but only eight unique sequences out of 35 sequenced clones were found in the hyperalkaline water. The majority of the sequences belonged to Proteobacteria. There was no overlap between clone libraries obtained from the hyperalkaline water compared with M17. Two hyperalkaline clones coincided with M18, which was believed to have a component of hyperalkaline water similar to M3 and M8. The 25 clones representing clone group JA21agh were closely related to a *Pseudomonas* sp. ML-124 (AF139998), isolated from Mono Lake (California, USA), a well-studied saline and alkaline (pH 10) environment. The relationship of JA21agh to ML-124 was supported 100% by both evolutionary distance and parsimony bootstrap analysis, and these sequences shared 97.5% identical sequence positions.

Figure 5.1 *Neighbour-joining tree showing the 16S rDNA relationships of the Maqarin clones to data available in the Genebank database. Bootstrap support of the branching topology of more than 75% from both evolutionary distance and maximum parsimony methods is indicated at the branching points of the tree by an open circle (O). The scale bar represents the number of nucleotide substitutions per position. Gr = phylogenetic groupings; EP = Epsilonproteobacteria; DP = Deltaproteobacteria; FM = Firmicutes; T7 = candidate division TM7; AC = Actinobacteria; DT = Deinococcus-Thermus; AR = domain Archaea.*

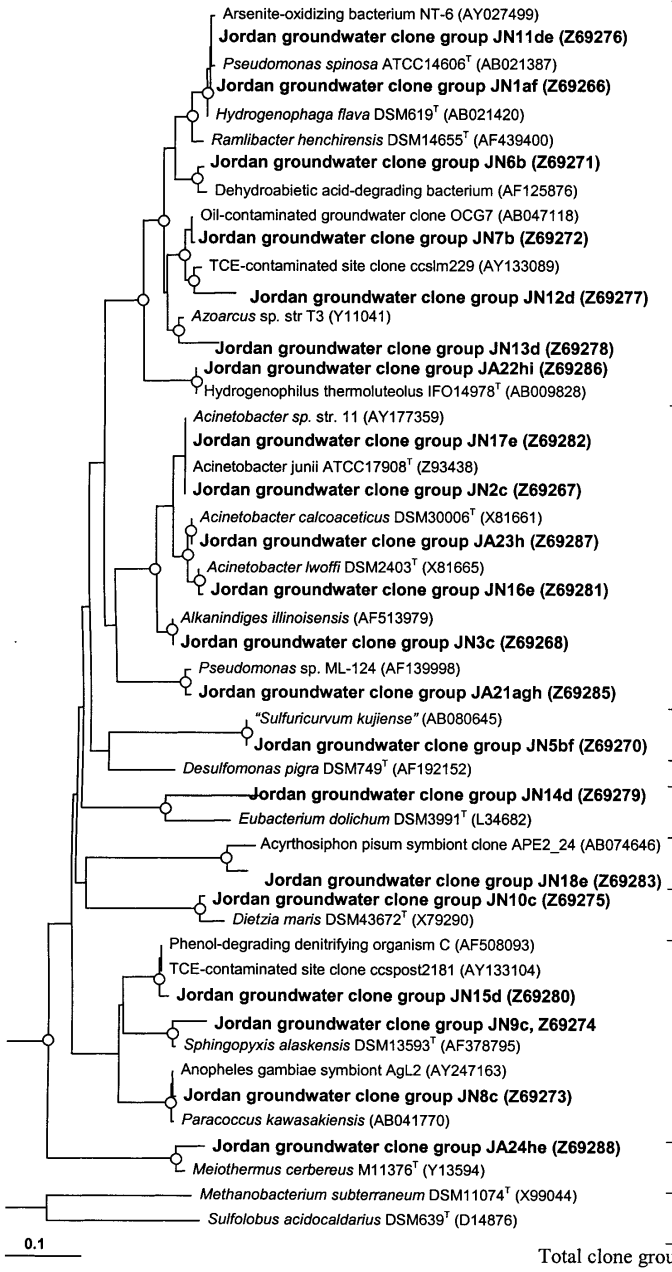

Gr		Alkaline				Neutral		Total
	M1	M3	M5	M8	M17	M18	
Betaproteobacteria					9		9
			9			1	10
				1			1
				2			2
					1		1
					1		1
		1	1				2
Gammaproteobacteria					2		2
					6		6
		2					2
					1		1
					1		1
	10	6	9				25
EP				3		9	12
DP							
FM					1		1
T7					1		1
AC					1		1
Alphaproteobacteria					1		1
					1		1
					1		1
DT		1					1
AR							
Total clone groups	1	4	3	3	13	2	26
Total clones	10	10	19	6	27	10	82

5.5 Cultivation

5.5.1 Introduction

The cultures from the 1996 campaign were filtered and stained in the AO direct counting (AODC) method. Enrichments to be sub-cultured were chosen where growth could be detected. Only a few of the cultures had grown and were sub-cultured in new medium (data not shown). They included glucose and lactate media inoculated with M8 water and the lactate medium inoculated with M1 water. Sub-cultures from M8 showed growth, but not so M1 sub-cultures. The pH of the cultures was monitored during incubation of the enrichment cultures and showed a decrease of approximately 0.5 units in the glucose-based medium and an increase of about 0.5 units in the lactate-based medium, compared with the sample water pH. The pH was initially high in the sub-cultures when using the Maqarin groundwater as water source, but subsequent preparations of synthetic media with a pH stable at around 12.5 were unsuccessful.

The total number of cells was used to calculate the number of generations produced (n) in the aerobic and anaerobic cultures obtained in 1999 and 2000. The numbers of generations (n) for the aerobic cultures, together with the pH values registered after the cultivation, are shown in Table 5.4. None of the cultures with CH_4 medium or H_2 medium inoculated in November 1999 showed visible growth. These media types were therefore not used in May 2000. Visible growth was obtained in several of the R2A cultures inoculated in November 1999. The R2A medium was not used in May 2000.

Table 5.4 *Number of generations (n) for aerobic cultures inoculated with alkaline groundwater and total number of cells at the end of the incubations. Cultures were inoculated in November 1999 and May 2000 with cell numbers and pH as indicated in italics following the name of the sampled localities, and cultured for about 300 and 150 days, respectively. The pH values in the culture vessels after inoculation are shown for each culture. Methods and measurement uncertainty detailed on www.sis.se, the web site for the Swedish Standards Institute.*

Medium	November 1999			May 2000		
	Cells mL^{-1}	n	pH	Cells mL^{-1}	n	pH
M1	*2.9×10^5*		*12.7*	*1.3×10^4*		*12.5*
R2A	1.2×10^6	2	11.5	–*	–	–
Glucose	1.2×10^6	2	11.0	2.7×10^5	4.3	8.0
Lactate	1.2×10^6	2	12.5	3.3×10^5	4.6	10.0
Acetate	8.8×10^5	1.6	12.5	4.3×10^5	5.0	11.0
Formate	8.2×10^5	1.5	12.0	3.8×10^5	4.8	11.0
M3	*7.4×10^3*		*12.6*	*5.5×10^3*		*12.5*
R2A	1.9×10^6	8.1	11.5	–	–	–
Glucose	2.0×10^6	8.2	10.5	8.7×10^5	7.3	10.0
Lactate	1.2×10^6	7.4	12.0	6.9×10^5	6.9	10.0
Acetate	7.6×10^5	6.8	12.0	5.8×10^5	6.7	9.0
Formate	1.2×10^6	7.3	12.5	3.1×10^5	5.8	10.0
M5	*2.1×10^3*		*12.6*	*1.7×10^4*		*12.6*
R2A	1.7×10^6	9.7	12.5	–	–	–
Glucose	1.3×10^6	9.3	10.5	2.3×10^5	3.7	11.0
Lactate	1.8×10^6	9.8	12.0	6.6×10^5	5.3	12.0
Acetate	1.2×10^6	9.2	12.0	4.2×10^5	4.6	12.0
Formate	1.1×10^6	9.1	12.0	6.6×10^5	5.3	12.0
D3/D6	*3.8×10^5*		*12.7*	*1.3×10^4*		*12.6*
R2A	1.2×10^6	4.3	10.0	–	–	–
Glucose	9.2×10^5	3.9	10.0	3.8×10^5	4.9	10.0
Lactate	1.0×10^6	4.0	12.0	2.1×10^5	4.1	10.5
Acetate	7.6×10^5	3.6	12.0	5.2×10^5	5.4	11.0
Formate	7.4×10^5	3.6	12.0	6.7×10^5	5.7	10.5

* – = not sampled

The pH values dropped by about two units for most of the May 2000 cultures, while staying closer to initial values in the November 1999 cultures (Table 5.4). There were two to four times more cultured cells in samples cultured from the November 1999 campaign than there were in those from the May 2000 campaign. The number of obtained generations (n) was higher in the November 1999 than in the May 2000 cultures for M5, and similar for M3 and D3 versus D6 between the campaigns, while it was lowest in M1 compared with all other cultures. The n depended strongly upon the number of cells in the groundwater used for inoculation. This suggests that there is an upper limit for the number of cells, which cannot easily be exceeded by growth, at or just above 1 000 000 cells per mL of the cultures. Sub-cultures from selected original cultures showed moderate growth with between three and five generations after about 190 days (data not shown).

The numbers of cultured cells in the anaerobic cultures were lower in M1 and D3 (Table 5.5) than those obtained for aerobic cultures. November 1999 cultures from M1 and D3 did not grow at all. The highest growth numbers and number of generations in anaerobic cultures were obtained from M5 cultures inoculated in November 1999. Otherwise, the number of

generations was approximately the same as obtained for aerobic cultures. The pH dropped by between one and two units for all cultures. The smallest drop was observed in the M5 November 1999 cultures, which also showed the best growth. The anaerobic sub-cultures multiplied for approximately four to seven generations from the start values (data not shown). The pH in these cultures dropped to values of about two to four units lower that the values observed in the respective sampled waters.

Table 5.5: Number of generations (n) for anaerobic cultures inoculated with alkaline groundwater and total number of cells at the end of the incubations. Cultures were inoculated in November 1999 and May 2000 with cell numbers and pH as indicated in italics following the name of the sampled localities, and cultured for about 300 and 150 days, respectively. The pH values in the culture vessels after inoculation are shown for each culture. Methods and measurement uncertainty detailed on www.sis.se, the web site for the Swedish Standards Institute.

Medium	**Electron acceptor**	**November 1999**			**May 2000**		
		Cells mL^{-1}	**n**	**pH**	**Cells mL^{-1}**	**n**	**pH**
M1							
Start values		2.9×10^5		12.7	1.4×10^4		12.5
R2A	–	3.2×10^5	0.1	10.0	–*	–	–
Glucose	Mn	2.8×10^5	–0.1	11.0	4.6×10^5	5.1	10.0
Lactate	Mn	2.1×10^5	–0.5	11.0	2.1×10^5	3.9	11.0
Acetate	Mn	1.2×10^5	–1.2	11.0	1.1×10^5	2.9	11.0
Formate	Mn	1.2×10^5	–1.2	11.0	2.2×10^5	4.0	11.5
Pyruvate	Mn	2.6×10^5	–0.2	11.0	5.3×10^5	5.2	10.5
Glucose	Fe	–	–	–	–	–	–
Lactate	Fe	–	–	–	5.0×10^5	5.2	11.5
Pyruvate	Fe	2.3×10^5	–0.4	11.0	2.2×10^5	4.0	11.0
Glucose	SO_4^{2-}	1.2×10^5	–1.4	11.0	1.6×10^5	3.6	10.5
Lactate	SO_4^{2-}	–	–	–	–	–	–
Pyruvate	SO_4^{2-}	1.9×10^5	–0.6	11.0.	1.5×10^5	3.5	12.0
TMA & methanol	SO_4^{2-}	1.2×10^5	–1.4	11.0	–	–	–
M5							
Start values		2.1×10^4		12.7	1.7×10^4		12.7
R2A	–	2.8×10^6	10.4	12.0	–	–	–
Glucose	Mn	2.9×10^6	10.5	12.0	1.2×10^5	2.9	11.0
Lactate	Mn	2.4×10^5	6.9	12.0	1.8×10^5	3.4	11.0
Acetate	Mn	3.3×10^5	7.3	12.0	1.5×10^5	3.2	11.5
Formate	Mn	1.3×10^5	6.0	12.0	1.7×10^5	3.3	11.5
Pyruvate	Mn	1.2×10^6	9.2	12.0	1.7×10^5	3.3	12.0
Glucose	Fe	–	–	–	–	–	–
Lactate	Fe	–	–	–	–	–	–
Pyruvate	Fe	8.0×10^5	8.6	11.0	2.7×10^5	4.0	12.0
Glucose	SO_4^{2-}	2.6×10^5	7.0	12.0	1.7×10^5	3.3	11.0
Lactate	SO_4^{2-}	4.0×10^5	7.6	12.0	2.2×10^5	3.7	12.0
Pyruvate	SO_4^{2-}	–	–	–	–	–	–
TMA & methanol	SO_4^{2-}	–	–	–	–	–	–

		D3 November 1999			D6 May 2000		
Start values		3.8×10^5		12.7	1.3×10^4		12.6
R2A	–	3.4×10^5	–0.2	11.0	–*	–	–
Glucose	Mn	6.5×10^5	0.8	11.0	5.8×10^5	5.5	10.5
Lactate	Mn	2.5×10^5	–0.6	11.0	2.3×10^5	4.2	11.5
Acetate	Mn	2.0×10^5	–0.9	11.0	1.2×10^5	3.2	11.0
Formate	Mn	3.2×10^5	0.3	11.0	4.6×10^5	5.2	11.0
Pyruvate	Mn	5.7×10^5	0.6	11.0	3.8×10^5	4.9	11.5
Glucose	Fe	–	–	–	3.1×10^5	4.6	11.0
Lactate	Fe	–	–	–	–	–	–
Pyruvate	Fe	2.0×10^5	–0.9	11.0	1.6×10^5	3.7	11.0
Glucose	SO_4^{2-}	1.8×10^5	–1.1	11.0	1.6×10^5	3.6	10.5
Lactate	SO_4^{2-}	–	–	–	–	–	–
Pyruvate	SO_4^{2-}	2.1×10^5	–0.9	11.0	1.7×10^5	3.8	11.5
TMA & methanol	SO_4^{2-}	1.7×10^5	–1.2	11.0	–	–	–

* – = not sampled. TMA = trimethylamine.

5.5.2 Assimilation of organic carbon sources by unattached microbes

The assimilation data appeared very scattered, which obscured trends. To overcome this problem, two criteria were set that had to be met in order for assimilation of the respective carbon source to be considered significant. First, all repetitions (N) of the uptake series and batches were plotted against time and the slope of the linear regression line through the data points was calculated. Second, the average assimilation per cell and hour was calculated for all samples (N) and subtracted from the start value for the killed controls. Assimilation was regarded as significant only for series and batches that had a positive slope and a positive average uptake per cell and hour.

The samples from Adit A-6 (M1, D3 and D6) all showed significant assimilations (Table 5.6). The anaerobic series assimilated more diversely than did the aerobic ones. All tested carbon sources scored significantly in the anaerobic tests, while in the aerobic series glucose and lactate were significant only with D6 groundwater. Glucose assimilation was also significant in the M3 series (data not shown). All M5 series were negative in one or both of the defined test criteria (data not shown). Glucose seemed to be the preferred carbon source, since assimilation was found to be significant in seven out of the eleven series investigated, followed by six acetate, three lactate and one leucine series assimilation (Table 5.6). The same trend was obtained using a balanced comparison excluding one of the glucose and the acetate series, tested pair-wise with different isotope configurations. This approach gave five glucose, five acetate, four lactate and one leucine assimilation series.

Table 5.6:. In situ assimilation of added carbon sources by unattached microorganisms in M1, D3 and D6 groundwater. The experiments were started on 5 December 1999 with 3.4 × 10^5 cells mL^{-1}(M1) and on 4 May 2000 with 1.7 × 10^4 cells mL^{-1}(M1) and run for 11 h and 6 h, respectively, as well as on 26 November 1999 with 3.4 × 10^5 cells mL^{-1} (D3) and on 4 May 2000 with 1.7 × 10^4 cells mL^{-1} (D6) and run for 7 h. The average slope of all results is shown as negative or positive and the assimilation is calculated per cell. N shows the number of bottles used for each experiment, excluding the four bottles used for each background determination. The pH of the groundwater used for the assimilations was 12.7 in November 1999 (M1), 12.5 in May 2000 (M1), 12.7 in November 1999 (D3) and 12.6 in May 2000 (D6). Data regarded as significant are shown in bold text. Methods and measurement uncertainty detailed on www.sis.se, the web site for the Swedish Standards Institute.

Carbon source	November 1999 (M1)			May 2000 (M1)		
	N	**slope***	**amol/ (cell h)**	**N**	**slope***	**amol/ (cell h)**
Aerobic series						
[^{14}C]-acetate	12	–	≤0	12	–	≤0
[^{3}H]-acetate	12	–	≤0	12	–	≤0
[^{14}C]-glucose	12	–	≤0	28	–	≤0
[^{14}C]-glucose (batch)	12	.**	.	28	+	≤0
[^{14}C]-lactate	12	–	0.021	12	–	≤0
[^{3}H]-leucine	12	–	≤0	12	–	≤0
Anaerobic series						
[^{14}C]-acetate	12	–	2.840	12	**+**	**0.066**
[^{3}H]-acetate	12	**+**	**0.004**	12	–	≤0
[^{14}C]-glucose	12	**+**	**2.348**	28	–	0.003
[^{14}C]-glucose (batch)	12	.	.	28	+	≤0
[^{14}C]-lactate	12	**+**	**0.505**	12	**+**	**0.141**
[^{3}H]-leucine	12	+	≤0	12	–	≤0
Carbon source	November 1999 (D3)			May 2000 (D6)		
Aerobic series						
[^{14}C]-acetate	12	–	≤0	12	–	≤0
[^{3}H]-acetate	12	–	≤0	12	–	≤0
[^{14}C]-glucose	12	–	≤0	28	+	≤0
[^{14}C]-glucose (batch)	.	.**	.	28	**+**	**0.020**
[^{14}C]-lactate	12	–	0.266	12	**+**	**0.001**
[^{3}H]-leucine	12	–	≤0	12	–	≤0
Anaerobic series						
[^{14}C]-acetate	12	**+**	**6.758**	12	**+**	**0.0289**
[^{3}H]-acetate	12	**+**	**0.001**	12	+	≤0
[^{14}C]-glucose	12	**+**	**18.59**	28	**+**	**0.330**
[^{14}C]-glucose (batch)	.	.	.	28	**+**	**0.600**
[^{14}C]-lactate	12	–	4.635	12	**+**	**0.094**
[^{3}H]-leucine	12	**+**	**0.001**	12	+	≤0

5.5.3 Assimilation of organic carbon sources by attached microbes

The assimilation data from attached microbes appeared less scattered than were those from the unattached series. However, for consistency's sake, the same approach as for unattached microbes was applied here (Table 5.7). Three acetate, two lactate, one glucose and one leucine assimilation series were regarded to be significant.

5.5.4 16S-ribosomal deoxyribonucleic acid accession numbers

Note that the nucleotide sequence data reported in this chapter appear in the EMBL, GenBank and DDBJ Nucleotide Sequence Databases under the accession numbers Z69266–Z69288, corresponding to JN1af–JN19e and JA21gh–JN24he, respectively.

5.6 Discussion

5.6.1 Alkaline environments

A combination of geological and climatic features gives rise to high surface-water alkalinity. Low-calcium-concentration environments are characterised by high concentrations of sodium carbonate. Ions, particularly sodium and chloride, concentrate owing to evaporation and this eventually results in a saline, high-pH environment. When the concentration of carbonate is greater than that of Ca^{2+} and Mg^{2+}, alkalinity rises, usually with Na^{+} as the dominant cation (Grant et al., 1990). Soda and desert lakes constitute the most stable, naturally occurring alkaline environments, with pH values exceeding 11.5. The most extensively studied soda lakes are those of the East African Rift Valley (e.g. Jenkins, 1936; Grant et al., 1990; Jones et al., 1998), but soda lakes are also found in Central Asia (Balashova and Zavarsin, 1980). Soda lakes are among the most productive naturally occurring aquatic environments in the world because of their almost unlimited supply of CO_2, high temperature and high daily light intensity. The predominance of microorganisms, particularly phototrophs (*Cyanobacteria*), is striking (Grant et al., 1990). Jones et al. (1998) recently reviewed the diversity of soda lakes and a phylogenetic study on soda lakes has been published by Duckworth et al. (1996).

Alkaline soda lakes with low calcium and high sodium concentrations have little in common with the environment that will develop in underground cementitious repositories. The water–cement interaction in the repository will cause leaching of calcium and thereby create a high-calcium, hyperalkaline environment. Naturally occurring high-calcium alkaline environments have only been found underground (Grant et al., 1990). High-calcium-concentration groundwater with a pH exceeding 11 has been identified in various locations worldwide, including in the former Yugoslavia and Oman (Barnes et al., 1978; Bath et al., 1987) as well as Jordan (Barnes et al., 1982). Only two of these sites, Oman and Jordan (McKinley et al., 1988; Bath et al., 1988; West et al., 1992, 1995; Coombs et al., 1994, Pedersen et al., 1997), have thus far been the subject of microbial studies and most of those reported have been performed as part of the Maqarin natural analogue project as the site is the more relevant for cementitious repositories.

In a high-calcium environment, the amounts of Ca^{2+} and/or Mg^{2+} present exceed that of carbonate. Normally, water rapidly becomes saturated with respect to Ca^{2+}, resulting in precipitation of calcite ($CaCO_3$) and inhibition of the genesis of alkaline brine due to the lack of carbonate. However, if the host rock contains either of the two primary minerals olivine or pyroxene, high-calcium alkaline groundwater can be produced. In near-surface zones, CO_2-containing water decomposes these minerals and Ca^{2+} and OH^{-} are released. Initially this will lead to calcite precipitation, but the carbonate soon becomes depleted, after which $Ca(OH)_2$-dominated brine is produced. The alkalinity will then be caused by OH^{-} which will be in equilibrium with solid $Ca(OH)_2$ in the absence of carbonate. In addition, these chemical

conditions are profoundly reducing in most cases (Bath et al., 1987; Grant et al., 1990). While of some interest to radwaste, the source rocks (usually olivine and pyroxene-containing ophiolites) are not directly relevant to cementitious repositories other than those constructed in the future using the specially formulated 'low-pH cements'. However, as this is beyond the scope of this study, it will not be discussed further here.

As noted in Chapters 1 and 3, in Jordan, at least three different sites with hyperalkaline groundwater have been identified. In the analogy they appear to represent three different stages in the theoretical evolution of a cementitious repository. The three stages are: (1) early, active, high-pH Na/KOH leachates (M5 and M6, Western springs, Maqarin) (Table 5.2); (2) intermediate, active, lower-pH $Ca(OH)_2$-buffered leachates (M1, D3 and D6, Adit A-6; M3, M8, Eastern spring seepages, Maqarin) (Table 5.2); and (3) late, inactive, lower-pH silica-dominated leachates (Daba and Khushaym Matruk, central Jordan). The last sites, because of an absence of water, could not be used for studies of active microorganisms.

5.6.2 16S-ribosomal ribonucleic acid diversity

The types of microbes in the Maqarin hyperalkaline groundwaters identified by 16S-rRNA sequencing (Fig. 5.1) could not be linked to species that have been reported from surface alkaline environments by Duckworth *et al.* (1996). These sequences are, however, from surface water environments with intensive solar radiation, which are high in carbonate and calcium concentrations and lower pH and which are consequently very different from the Maqarin localities. In Maqarin, it is plausible that microorganisms in the surrounding groundwater have adapted over a long time to the hyperalkaline conditions in the cement zone and hyperalkaline plume. The absence of deeply branching 16S rRNA species supports the assumption that the populations in Maqarin have adapted to the Maqarin environment in relatively modern evolutionary times. If this is true, it cannot be excluded that similar adaptations may occur in high-pH areas of future radioactive waste repositories.

5.6.3 Total number of cells

The objective of counting cell numbers was to obtain the total numbers of unattached and attached, viable and non-viable microbes in groundwater from Adit A-6 boreholes, the Western and Eastern springs and the boreholes M17 and M18. All data ranged within about three orders of magnitude from 2.5×10^3 to 6.4×10^6 cells mL^{-1} of groundwater (Table 5.2). The numbers were generally highest in November 1999. The database of total numbers of microorganisms in Fennoscandian Shield groundwater is large and comprises analytical data from more than 100 sites at depths down to 1500 m in deep crystalline bedrock (Pedersen, 2001). The numbers range from about 1×10^3 to 5×10^6 cells mL^{-1} of groundwater. The highest numbers tend to come from shallow sites. The data from the Maqarin hyperalkaline waters (Table 5.5) cluster around the lower part of the Fennoscandian Shield numbers, suggesting that microbial abundance and activity are lower in Maqarin compared with circum-neutral, crystalline groundwater.

The total numbers of attached cells did not exceed 1.8×10^5 cells cm^{-2} (Table 5.3), irrespective of whether the exposure to the hyperalkaline water was 1 or 8 weeks. There can be two explanations for this: first, that the attaching microbes were inactive and attached only as a result of surface interaction forces (cf Marshall, 1984). Attached microbes depend on transport of nutrients to the surface to be able to proliferate. The flow in the FTB/FTC may have been too low to allow growth of attaching microbes. Surfaces introduced in slowly

flowing Fennoscandian shield groundwater commonly collect about 10^5 attaching cells cm^{-2} within the first week. Thereafter, there is a slow growth and the numbers may increase to about 10^7 cells cm^{-2} after 8 weeks or more (Pedersen, 2001). This growth phase could not be observed in the M1 and D6 FTB/FTCs (Table 5.3).

Overall, the low total numbers of unattached cells, relative to Fennoscandian Shield groundwater, and the absence of attached cell growth, suggest that the microorganisms found in the investigated hyperalkaline waters are inactive, though not necessarily dead. Consequently, cultivation experiments were performed to assess the live/dead status of the microorganisms found in the hyperalkaline groundwaters of Maqarin (see below).

5.6.4 Cultivability

The objective of these cultivation experiments was to cultivate, at *in situ* pH, the main physiological groups of microbes expected to be present at Adit A-6 and the Western and Eastern springs using different carbon and energy sources. The first attempt, in 1996, to cultivate microorganisms from Maqarin was not very successful; only two out of 14 cultures grew. It was deduced that the concentrations of nutrients that had been applied were too high and in the next attempt, in November 1999, the concentration of organic carbon was lowered from one or a few gL^{-1} to 10–50 mgL^{-1}. This was an adaptation to the actual concentrations of organic carbon in the Maqarin hyperalkaline groundwaters, reported to be <10 mgL^{-1} (Geyer et al., 1998).

All aerobic cultures from the 1999 and 2000 campaigns increased in numbers and multiplied from two to, at the most, ten times (Table 5.4). These results show that at least some of the total numbers of microorganisms in the hyperalkaline waters were viable and able to grow. The pH remained high and close to the ambient values in the November 1999 cultures and in many of the May 2000 cultures, suggesting that the observed growth occurred at hyperalkaline pH. Most November 1999 cultures reached around 10^6 cells mL^{-1}, while most May 2000 cultures stopped at about 5×10^5 cells mL^{-1}, irrespective of the number of cells when culturing commenced, which varied from 2.1×10^3 cells mL^{-1} to 2.9×10^5 cells mL^{-1}.

The culture media used would most probably have produced numbers at least 100 times higher if inoculated with neutral pH lake or stream water. It appears as if the high pH put a limitation on the highest number that could develop in the cultures. A low highest obtainable cultivable number is not unique; for instance, the iron oxidising-bacterium *Gallionella ferruginea* never grows to numbers greater than 2×10^6 cells mL^{-1} when cultured in the laboratory (Hallbeck and Pedersen 1990). It is not clear why this is so, but it can be assumed that the cells expel signal substances that terminate growth at a specific concentration, which is defined by evolution. More cells than this number would result in "overpopulation" of the environment, which would pose a threat to the survival of the whole population. Therefore, the cultivation results suggest that there is a maximum number of cells that could be reached by growth in the hyperalkaline cultures, at between 5×10^5 and 1×10^6 cells mL^{-1}. Sub-culturing was done with the aim of enriching the microorganisms that adapted to the culture conditions. However, sub-culturing did not result in any values higher than this assumed maximum number. Instead, the numbers obtained were close to the ones obtained in the first cultures. Limited growth was therefore observed again.

Anaerobic growth was not obtained in the M1 and D3 cultures of November 1999 (Table 5.5). Possibly, this was because the number of cells in the hyperalkaline waters used for innoculation was equal, or almost equal, to the supposed maximum number of cells that can

be obtained by growth in the hyperalkaline cultures employed. Growth would then have been restricted directly at innoculation. The best anaerobic growth was obtained with M5 water in November 1999. R2A, glucose and also pyruvate showed good growth relative to the other investigated carbon sources in all tested waters. As with the aerobic cultures (Table 5.4), the overall numbers obtained in the anaerobic sub-cultures (Table 5.5) were, however, close to the ones obtained in the first cultures.

In general, the culturing task proved that microorganisms can be cultured under hyperalkaline conditions. Both aerobic and anaerobic conditions were found to support growth. However, although the obtained growth was significant, it was not vigorous.

5.6.5 Assimilation activity

The objective of the assimilation task was to investigate whether microorganisms flowing with hyperalkaline groundwater at Adit A-6 and the Western and Eastern Springs are active *in situ*, i.e. whether they could assimilate various organic carbon compounds under *in situ* conditions in the flowing seepage and groundwaters.

Cultivation of microbes from environmental samples is frequently carried out and the results obtained are useful. However, it is also commonly recognised that many microorganisms in the environment do not grow in cultures. In other words, a positive result from cultivation demonstrates that living organisms were present and that a negative cultivation result is not conclusive – there may have been organisms in the sample that just did not grow under the conditions offered (as was suggested to be the case by West et al., 1992, during the first Maqarin microbiology study). To circumvent this problem with the Maqarin samples, activity assays were employed. This methodology assumes that if microorganisms in a sample are living and active, they will assimilate introduced carbon sources, and this assimilation is not growth-dependent, as are cultures. Assimilation studies have previously been successfully performed with samples from deep groundwater (e.g. Pedersen and Ekendahl, 1992a, 1992b; Ekendahl and Pedersen, 1994).

Assimilation was more frequent under anaerobic than aerobic conditions (Table 5.6). This suggests that the microorganisms in the hyperalkaline waters of Maqarin are adapted to conditions with no or little dissolved oxygen. Some hydrochemical results (data not shown) have indicated large concentrations of dissolved oxygen, but the accuracy of the oxygen analysis was possibly disturbed by the slow flow of water. It is very difficult to sample for oxygen in very slowly flowing water because oxygen from the atmosphere easily mixes with the sample unless a fast flow flushes the sample container. In Maqarin, most of the water sampled was dripping rather than flowing fast, which adds a large uncertainty to the obtained oxygen readings. The presence of nitrite in the samples may indicate that anaerobic microbial nitrate respiration has been ongoing, either before the water reached the cement zone, or all along the flow path. Nitrate respiration is an anaerobic metabolic process that operates in the absence of oxygen and this suggests that the Maqarin aquifers are actually anaerobic, at least in places.

Both [^{3}H]-acetate and [^{14}C]-acetate were used in the assimilation tests. In several cases where [^{3}H]-acetate assimilation was negative, [^{14}C]-acetate resulted in positive assimilations. This is probably explained by the much higher concentration of [^{14}C]-acetate of 6490 nM, compared with that of 11 nM for [^{3}H]-acetate. The scintillation is about 500 times more sensitive to ^{3}H than it is to ^{14}C, due to the much shorter half-life of ^{3}H. However, this sensitivity can be masked by isotope dilution with naturally present acetate in the water

studied. The discrepancy between the two differently labelled acetates suggests that there may have been some acetate in the spring water.

The total number of cells per sample may also have had a significant influence on the assimilation results, assuming a constant percentage of viable cells in the different samples. The more viable the cells, the uptake will generally be greater. In our study, M1 November 1999 and M3 November 1999 cultures had higher total numbers of cells and also, more assimilation per cell of different sources. The same situation was observed for D3 compared with D6.

As a whole, the assimilation investigations strongly suggest that parts or all of the microbes in the studied Maqarin waters were viable and responded to introduced carbon sources by assimilation. The assimilations all occurred under hyperalkaline conditions, suggesting that microbial activity is possible under these extreme conditions, such as in the Maqarin hyperalkaline groundwaters (and, by implication, cementitious leachates).

An additional task of the assimilation studies was to investigate whether microorganisms at Adit A-6 would attach to surfaces and show metabolic activity, i.e. whether they assimilate organic carbon sources and metabolise them *in situ* at ambient pH (i.e. pH 12–13). As mentioned above, microorganisms did attach to the surfaces in the FTB/FTC systems, but they did not proliferate over time. The assimilation results were positive for all carbon sources tested with M1 water (Table 5.7). A comparison of these results with the results for unattached microorganisms (Table 5.6) revealed that the attached cells seemed to have been more active that the unattached ones. This result is consistent with what has previously been found in circum-neutral pH crystalline groundwater (Pedersen and Ekendahl, 1992a, 1992b; Ekendahl and Pedersen, 1994). Attachment to a surface is commonly looked upon as a more favourable state of living, compared with cells in a planktonic state, at least in systems with flowing water. This is because microorganisms will be exposed to more nutrients over time when attached in a flowing system, than when flowing with the water.

Table 5.7 *In situ assimilation of added carbon sources by attached microorganisms in M1 groundwater. The experiments were started on 7 December 1999 with 1.8 × 10^5 cells cm^{-2} and run for 7 h and on 1 May 2000 with 1.1 × 10^5 cells cm^{-2}, as well as on 6 May 2000 with 8.4 × 10^4 cells cm^{-2} and run for 6 h. The average slope of all results is shown as negative or positive and the assimilation is calculated per cell. N shows the number of bottles used for each experiment, excluding the four bottles used for each background determination. The pH of the M1 groundwater used for the assimilations was 12.7 in November 1999 and 12.5 in May 2000. Data regarded as significant are given in bold text. Methods and measurement uncertainty detailed on www.sis.se, the web site for the Swedish Standards Institute.*

Carbon source	November 1999			1 May 2000		
	N	**slope***	**amol/ (cell h)**	**N**	**slope***	**amol/ (cell h)**
Aerobic series						
[^{14}C]-acetate	6	**+**	**0.531**	6	**+**	**0.810**
[^{3}H]-acetate	6	+	≤0	6	+	≤0
[^{14}C]-glucose	6	**+**	**9.544**	6	–	≤0
[^{14}C]-lactate	6	–	≤0	6	**+**	**0.164**
[^{3}H]-leucine	6	–	≤0	6	+	≤0

Carbon source	6 May 2000		
	N	**slope***	**amol/ (cell h)**
Aerobic series			
[^{14}C]-acetate	6	**+**	**2.403**
[^{3}H]-acetate	6	–	≤0
[^{14}C]-glucose	6	+	≤0
[^{14}C]-lactate	6	**+**	**1.256**
[^{3}H]-leucine	6	**+**	**0.001**

* negative (–) or positive (+) value.

5.7 Conclusions

The types of microbes in the Maqarin springs, as identified by 16R rRNA sequencing (Figure 5.1), could not be tied to species that have been reported from surface alkaline environments. Of course, the Maqarin groundwaters are not typical of most such environments, i.e. surface waters with intensive solar radiation and that are low in carbonate and calcium. In Maqarin, it is plausible that microorganisms in the groundwater have adapted over a long time to the hyperalkaline conditions of the cement zone and hyperalkaline plume. The absence of deeply branching 16S rRNA species supports the assumption that the populations in Maqarin have adapted to the Maqarin environment in relatively modern evolutionary times. If this is true, it cannot be excluded that similar adaptations may occur in high pH areas of future radioactive waste repositories.

In this chapter, it has been shown that microorganisms in Maqarin could be cultured at low but significant numbers and that some were metabolically active under hyperalkaline conditions. However, the growth and activity found were not dramatic. Rather, slow growth to low numbers and a generally low metabolic *in situ* activity was found. This implies that

microbial activity will be low during the hyperalkaline phase of a repository. However, such repositories will not be sterile, so when the pH (slowly) falls with time, the microorganisms present may increase their activity.

The main microbiology conclusions from the Phase IV study are:

- The low total numbers of unattached cells, relative to Fennoscandian Shield groundwater, and the absence of attached cell growth, suggest that the microorganisms found in the investigated springs were inactive, but not necessarily dead;
- The culturing experiment proved that microorganisms could be cultured under hyperalkaline conditions, with both aerobic and anaerobic conditions supporting growth. However, while the obtained growth was significant, it was not vigorous;
- The assimilation investigations strongly suggested that parts or all of the microbes in the studied Maqarin springs were viable and responded assimilatory to introduced carbon sources. The assimilations occurred under hyperalkaline conditions, implying that microbial activity is possible under extremely high pH conditions, such as in the Maqarin groundwaters or in the porewaters and leachates of a cementitious radioactive waste repository. The attached cells seemed to be more active that the unattached.

5.8 Acknowledgements

Dr.Hani Khoury and Dr.Elias Salameh, University of Jordan, Amman, made this work possible due to the excellent organisation of the sampling campaigns. I would like to thank John Smellie, Conterra, Stockholm for carefully reading and commenting on the original manuscript. Proper English AB is acknowledged for proof reading.

Chapter 6

Khushaym Matruk

H. Khoury, L. Trotignon, I.Techer, M.Elie, E.Salameh, P. Bienvenu, P. Boulvais, A. Didot, I. Félines, L. Fontanini, S.Fourcade, L. Martinez, J.-C. Parneix, S.Ramirez-Martin, F. Rassineux, J. Raynal, D. Vandamme

6.1 Metamorphic Rocks in Central Jordan

6.1.1 Occurrences

The metamorphic rocks and the associated kerogen-rich biomicrites and travertines are widely distributed in two areas: Daba (Khan Az-Zabib) and Siwaqa (Figures 6.1 and 6.2). The northern boundaries of the first and second areas are located 25 km and 60 km south of Amman with the first area situated between E36^{o} 00' to 36^{o} 15' and N31^{o} 15' to 31^{o} 30' and the second area between E35^{o} 00' to 36^{o} 15' and N31^{o} 15' to 31^{o} 30'. Daba covers 662 km^{2} and Siwaqa covers about 660 km^{2}. Many tracks leading from the desert are easily reached from the Amman-Aqaba desert highway, making all parts of the two areas accessible by four- wheel drive vehicles, weather permitting.

Figure 6.1 Location of the Daba-Siwaqa areas

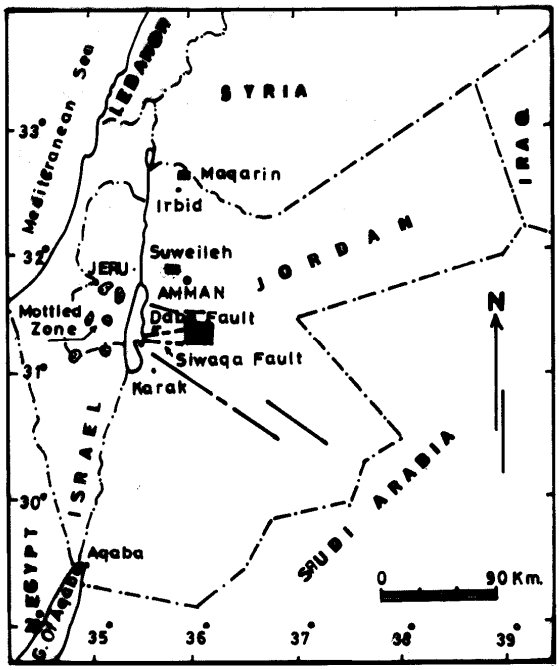

Figure 6.2 Distribution of the Analogue Cemen Zone in central Jordan

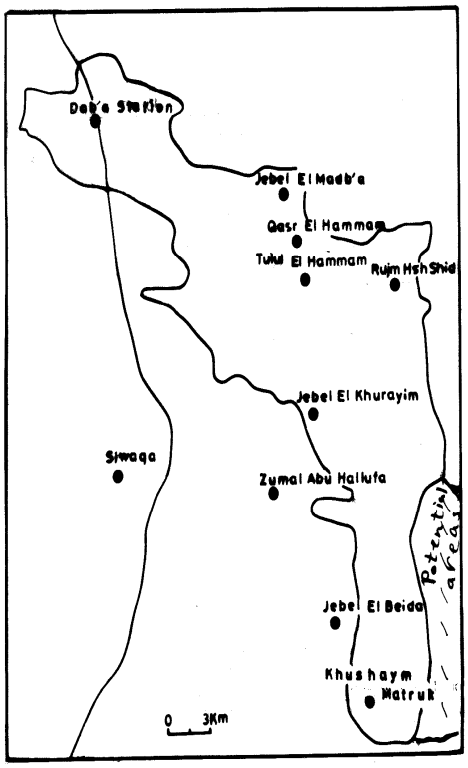

6.1.2 Topography and climate

The topography of the two areas varies in elevation from a few metres below the 660 m contour in the western part of Wadi Siwaqa to a maximum altitude of 950 m in Khushaym Matruk, in the southeastern corner of Siwaqa area. Khan Az-Zabib area is characterized by moderate relief of locally rounded peaks between 800-900 m in altitude, separated by alluvial flats and wide wadis with low-angle valley sides. The Siwaqa area is generally flat to undulating, except near the Siwaqa fault zone and the north-north-west – south-south-east trending fault blocks in the eastern part of the area. Drainage is ephemeral, wadis flow only in winter, and the stream courses are eventually directed westwards.

The weather statistics obtained from the Jordanian Meteorological Department indicates that the mean annual precipitation which occurs in winter is 110 mm. The mean summer temperature is 23^{o}C and the maximum temperature 44^{o}C. Evaporation is high and relative humidity ranges between 30-60%. The wind raises dust, especially in winter.

6.1.3 Geology and stratigraphy

The first geological map covering Jordan and Palestine was produced by Blake and Ionides (1939). Quennell (1958) published three geological maps (scale 1:250,000) for most of Jordan. Bender (1968) published five sheets (scale 1:250,000) covering the whole of Jordan. The north-south strip of 5 km width along the western edge of Siwaqa area was mapped (scale 1:25,000) by Ruef and Jeresat (1965) and the southeastern part was mapped by Sunna (1974) as part of the National Resources Authority (NRA) investigations for phosphates. The eastern part of Siwaqa area was mapped (1:50,000) by Hakki and Sassa (1978) as part of an NRA project for marble investigation in Daba (Khan Ez-Zabib) Siwaqa areas. More mapping was conducted in these two areas by Jasser (1986) and Barjous (1986).

The exposed rocks in the two areas are sedimentary and range in age from Upper Cretaceous (Turonian) to Tertiary (Eocene). Travertines and superficial deposits are Pleistocene to Recent in age. The general chronological sequence of lithological units in central Jordan is given in Table 6.1.

During the Late Cretaceous to Early Eocene (~90 - ~50 Ma ago), Daba-Siwaqa was situated in a shallow-marine, stable shelf environment of the Tethys Sea. Transgression took place during Cenomanian times, and marine sedimentation took place until the Late Eocene, despite the fluctuations in sea level. Uplift took place and gentle folding and faulting is mostly related to the continued tectonic movement along the Jordan Rift which is located ~60 km to the west of the Daba – Siwaqa area.

Table 6.1 General chronological sequence of lithological units in Central Jordan (Daba-Siwaqa aras)

Lithological Units	Age	Thickness in (m)
Alluvium and gravel	Holocene – Recent	-
Fluviatile and lacustine gravel	Pleistocene – Recent	-
Travertine	Pleistocene – Recent	-
Um Rijam Chert Limestone Formation (B4)	Eocene	30-80
Muwaqqar Chalk Marl Formation (B3)	Palaeocene – Tertiary	70-150
Al-Hisa Phosphorite Formation (B2)	Maestrichtian (Upper Cretaceous)	25-70
Amman Silicified Limestone Formation (B2a)	Campanian (Upper Cretaceous)	15-80
Wadi Umm Ghudran Formation (B1)	Campanian – Santonian	3
Wadi Es – Sir Limestone Formation (A7)	Turonian	30

6.1.4 Lithostratigraphy

Figure 6.3 shows a general lithographic column in southern Jordan and Table 6.1 and Figures 6.4 and 6.5 summarise the chronological sequence of the lithostratigraphic exposed units in the Daba–Siwaqa areas. Figure 6.6 is a detailed geological map for Khushaym Matruk. The following is a brief description of these units from base to top:

Figure 6.3 A generalised lithographic column for central Jordan

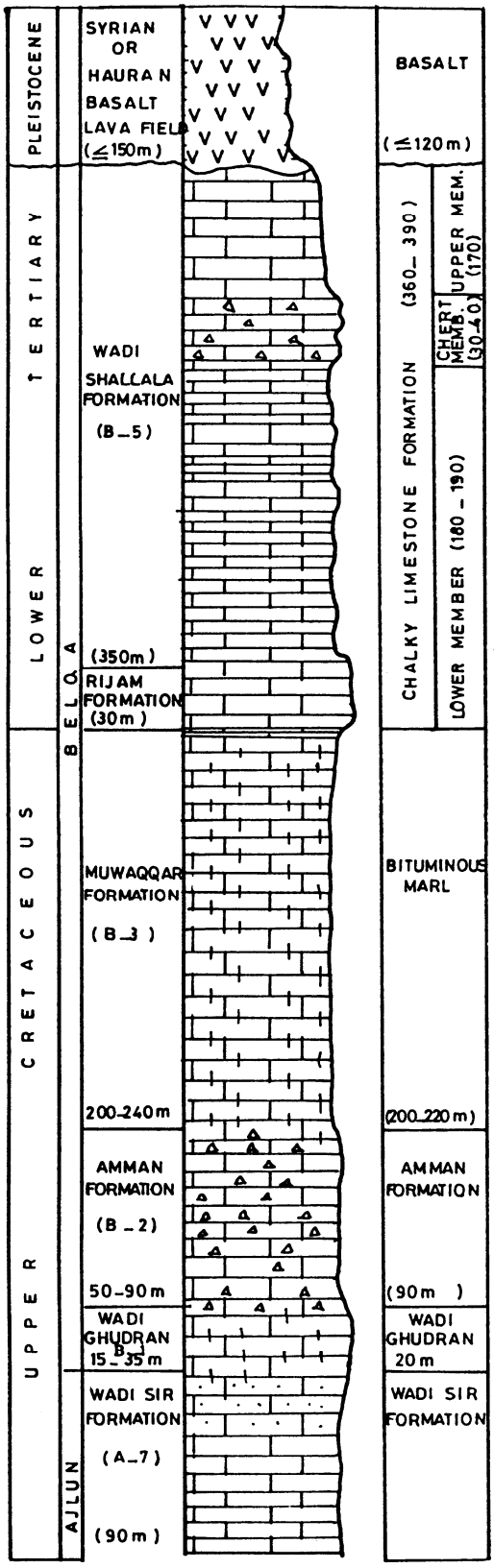

Figure 6.4 Geological map of the Daba area

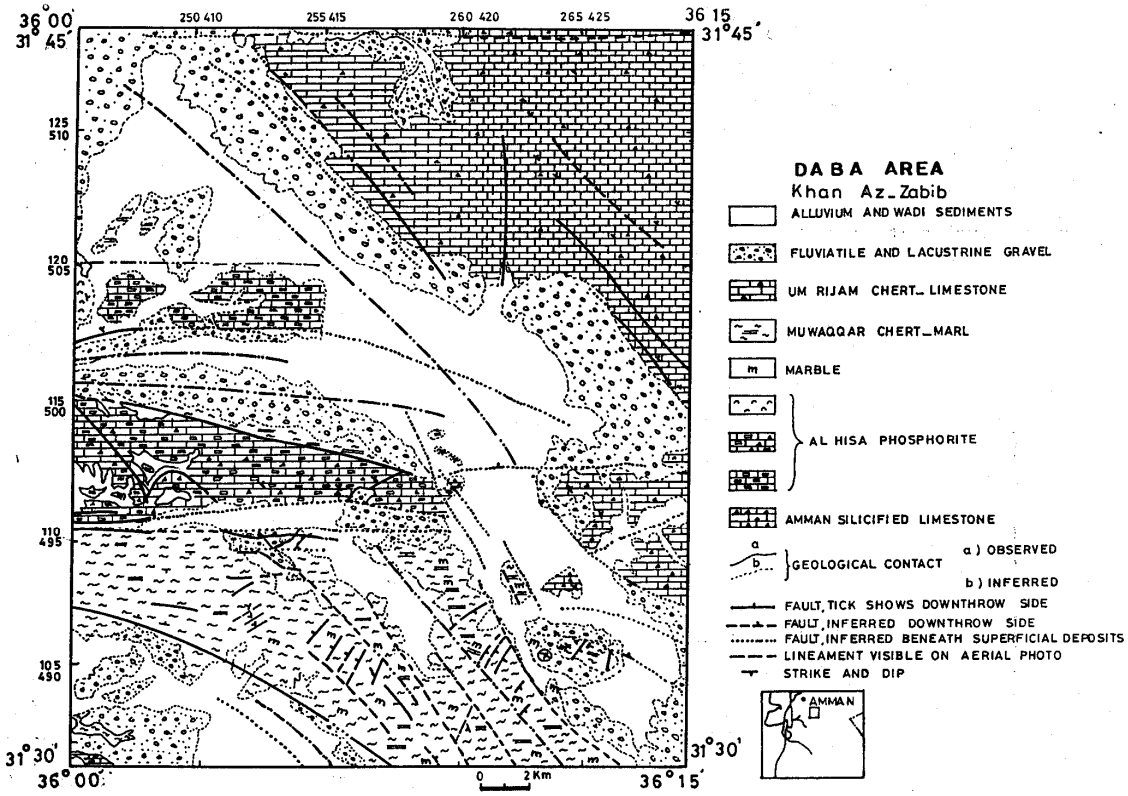

Figure 6.5 Geological map of Siwaqa area

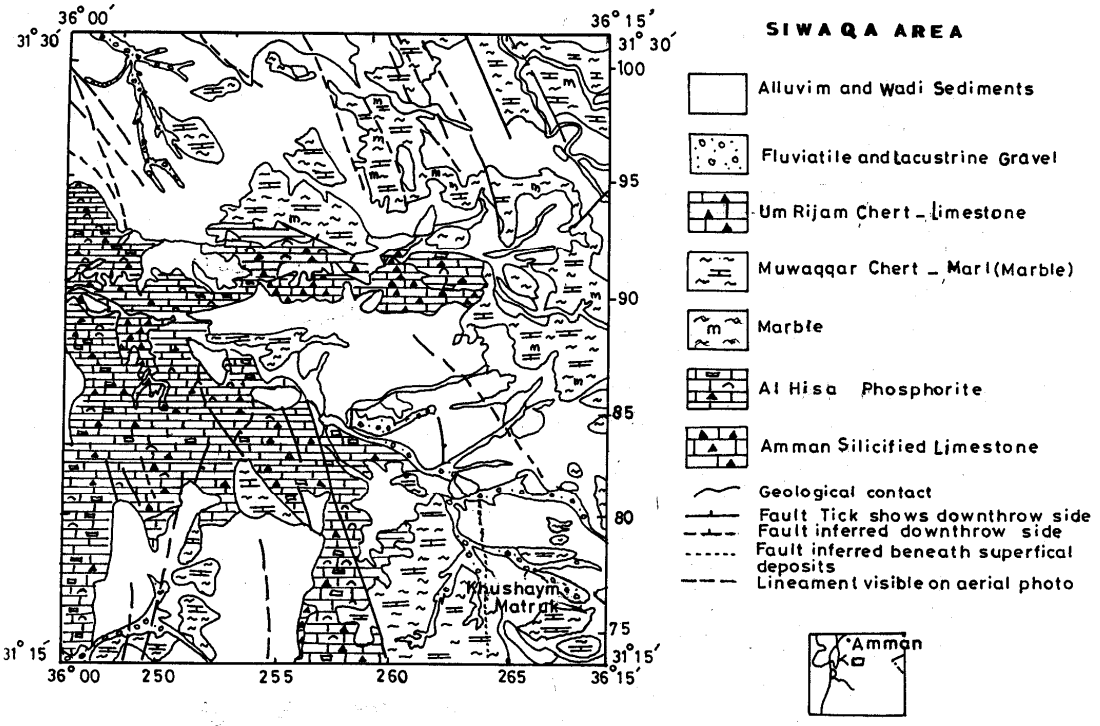

Figure 6.6 Detailed geological map of Khushaym Matruk

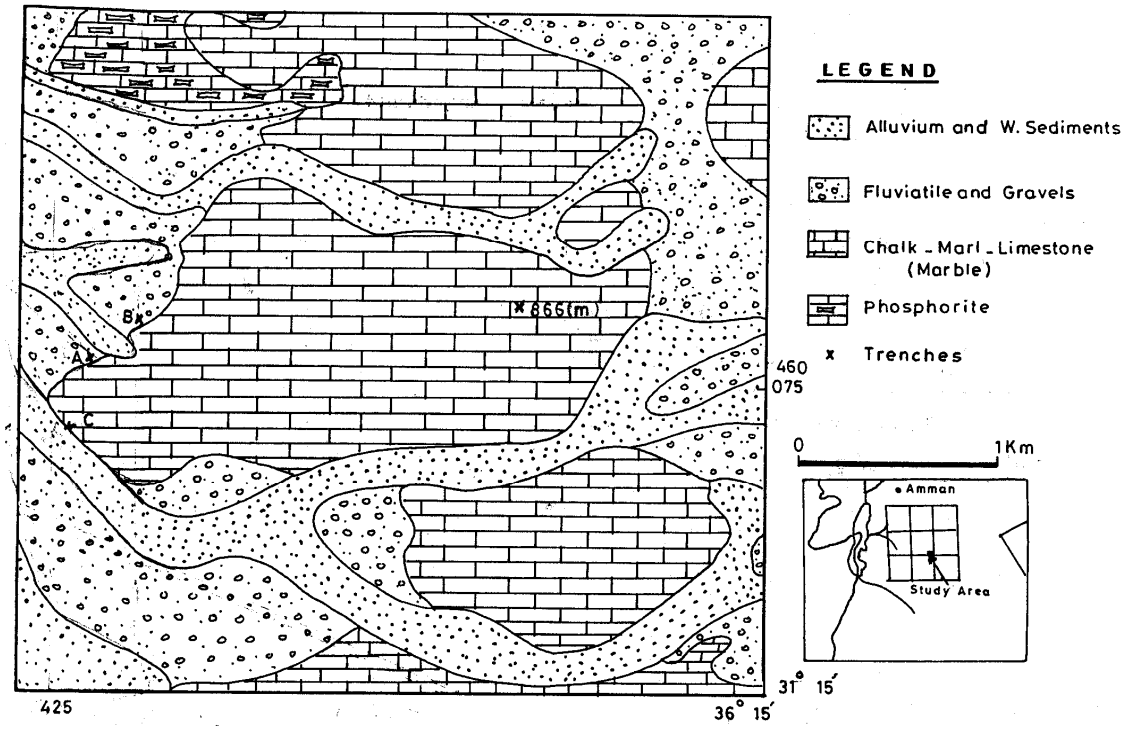

Wadi Es-Sir Limestone Formation (A7)

The formation is exposed in Jabal Siwaqa anticline (upper 30 m). It is composed of thin and thick beds of dolomitic and biomicritic limestone with chert nodules. The age is Turonian – Santonian (Bender, 1974).

Wadi Umm Ghudran Formation (B1)

The formation is exposed in the core of Jabal Siwaqa (3 m). It is composed of whitish to yellowish chalk and biomicrite and the age is believed to be Santonian.

Amman Silicified Limestone Formation (B2a)

The formation occurs in small outcrops in the mountainous areas and in the lower, steep slopes of the upthrown east-west trending faults, and in deep wadis. It is composed of alternations of chert and micritic limestone (15-80 m in thickness). The increase in proportion of granular phosphatic chert, and thin coquinal shelly limestone near the top of the formation, indicates a gradual upward-shallowing towards the overlying Al Hisa Phosphorite Formation. The age is believed to be Campanian (Bender, 1974).

Al-Hisa Phosphorite Formation (B2)

The formation consists of silicified phosphorite, phosphorite – bearing oysters, phosphatic limestone, chert, coquina and biomicrite (25 – 70 m). It ranges in age from Campanian to Danian (Bender, 1974).

Muwaqqar Chalk - Biomicrite Formation (B3)

The formation covers large areas. It consists from bottom to top of chert beds, biomicrite and biomicritic limestone with limestone concretions (70-150 m). The upper part of the formation

is organic-rich and crops out in the Khushaym Matruk area (30 m). The organic-rich beds are overlain by varicoloured marble which forms the upper part of this formation and covers an area of hundreds of square kilometres (Figure 6.2). The age of the Muwaqqar Chalk Biomicrite Formation is Maestrichtian – Lower Palaeocene.

Um Rijam Chert Limestone Formation (B4)

The formation crops out to the north-north-east part of Daba – Siwaqa areas. The formation consists of chalk biomicrite and chalky limestone with chert intercalations (30 – 80 m). The age is considered by Bender (1968) to be Upper Palaeocene – Lower Eocene.

Superficial Deposits

- **Fluvial and Lacustrine Sediments:** These sediments are composed of silt, sand and gravel and sub-angular to sub-rounded pebbles and cobbles. The most common clasts are chert, phosphatic chert and limestone and marble and are cemented by calcite cement. The age of the gravels is probably be Plio-Pleistocene.
- **Travertine:** Travertine (up to 30 m in thickness) is found in Rujm Qiyal, adjacent to the east-west fault, and on the downthrown side of Siwaqa Fault. The travertine is composed of yellow/brown/wavy vesicular, banded calcium carbonate with mineralized plant remains. The deposits are associated with the green clay mineral, volkonskoite. The age is believed to be Pleistocene.
- **Alluvium and Wadi Sediments:** The sediments are composed of sand, gravel, pebbles and boulders of chert, phosphatic chert and limestone. The sediments are poorly sorted and were deposited by ephemeral streams during the Holocene (Recent) stage.

6.1.5 Structural geology

The dominating fault trends are north-west – south-east and east - west (Figures 6.4 and 6.5). A less important trend is north-south. The main faults in the area are the Zerqa Main, Daba and Siwaqa fault systems. The fault set is an east-west group of faults and linear features. The main north-west – south-east trending faults are Wadi Al Hammam set and the Musattarat Al Falij Fault set.

The folds in central Jordan are of three types: gentle folding associated with regional compression; folding occurring adjacent to faults and directly associated with drag during faulting; and folding in interference structures caused by the interaction of east - west and north-west – south-east faulting influences. Figure 6.7 is a satellite image showing the major structures affecting the Daba – Siwaqa area (scale 1:1 000 000).

Figure 6.7 A satellite image showing the major structures affecting Daba-Siwaqa

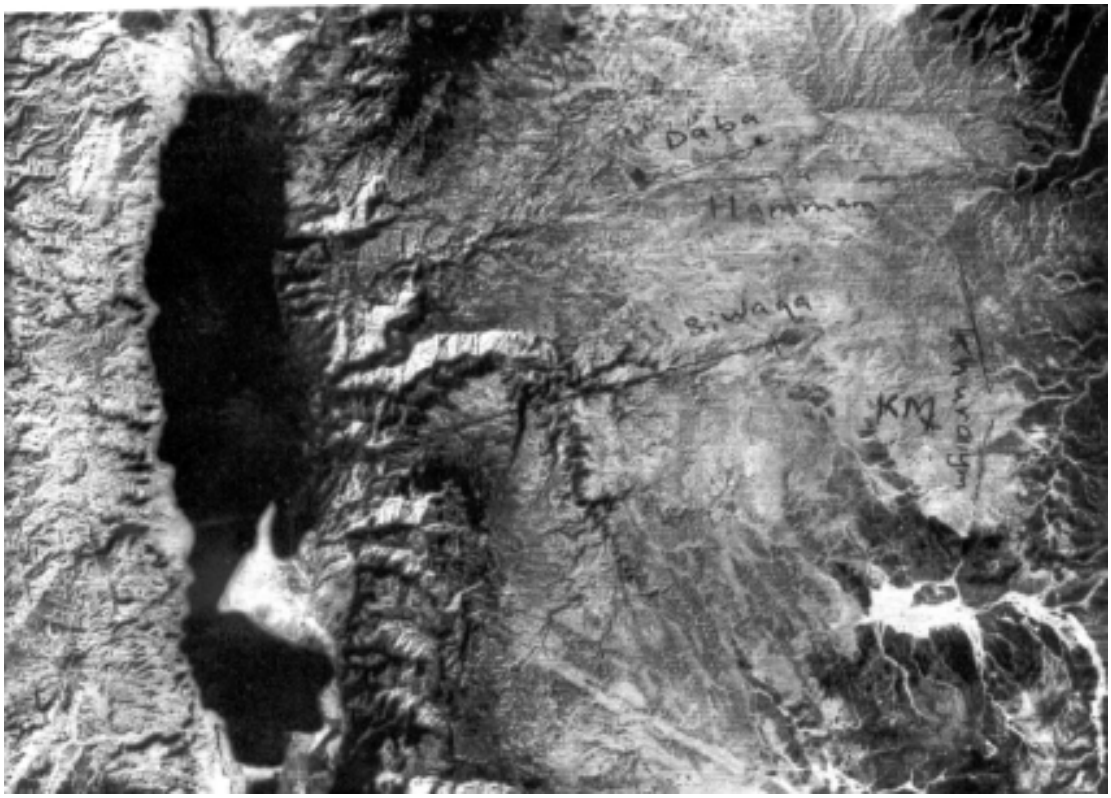

6.1.6 Hydrogeology

Two groundwater recharge zones are found in the study area and its surroundings. The first is Shihan Qatranah, which lies 20–30 km to the west-south-west of Khushaym Matruk. The other lies in the Madaba area, 30–40 km to the north-west of Khushaym Matruk. In addition, direct and indirect recharge takes place all over the area through the barren rocks or the thin soil cover or along wadi courses. The groundwater in the B_2/A_7 aquifer flows radially in all directions from both recharge zones. Both groundwater currents, coming from the north and the south, merge in the western section of the Zerka Main fault area, which strikes approximately east-west. Flow is westwards along this fault zone towards the Dead Sea. The Zerka main fault system lies 10–15 km to the north of Khushaym Matruk.

The groundwater flow system below Khushaym Matruk is directed to the north-east towards the Azraq depression, with the groundwater table lying at a depth of 150–200 m below ground level. The Siwaqa fault, south of Khushaym Matruk, forms only a weak barrier to groundwater flow, probably as a result of reduced contacts of the aquifer across the fault.

The Zerka Ma'in Fault, 10–15 km north of Khushaym Matruk, drains parts of the recharge water of both recharge zones and the direct and indirect recharge water towards the Dead Sea. It also seems to receive some deep Kurnub Sandstone groundwater leaking upwards into the B_2/A_7 along the Siwaqa fault zone. Both the recharge and the upwelling groundwaters flow westward and discharge as thermal mineralised water along the slopes overlooking the Dead Sea.

6.1.7 Hydrochemistry

The chemistry of the B_2/A_7 groundwater body differs sharply from one place to another. It does not seem to be the result of a simple dissolution process of limestone aquifer matrix. Instead, it is complicated by mixing of groundwaters from the two above-noted recharge zones, together with upwelling groundwater from below and downward infiltration of water passing through the Analogue Cement Zone (ACZ).

Two wells were chosen to illustrate the groundwater chemistry, G15 and G25 (Table 6.2 and Figure 6.8). Of particular note is the high Cr content of well G15 with 2.14 mgL^{-1} and the very high Pb, Cr and Br content of well G25, in an area devoid of any industrial activity. Pb, Cr and Br seem to originate from the ACZ overlying the B_2/A_7 groundwater body in that area.

Table 6.2 Chemical analyses of groundwater

Parameter (all mgL^{-1} unless stated)	**Borehole G 15**	**Borehole G 25**
TDS	502	1253
pH	6.9	7.2
T °C	35.5	36
Ca	39.6	134.0
Mg	62	64.4
Na	56.6	156
K	7.5	5.12
Cl	106	241.4
SO_4	74	208.5
HCO_3	285	463.5
Si	7.8	20.7
Pb	n.a*	0.41
Cr	2.140	0.160
Br.	n.a.	5.3
	Strong CO_2 and radon	H_2S smell

* n.a not analysed

Figure 6.8 The location of boreholes G15 and G25

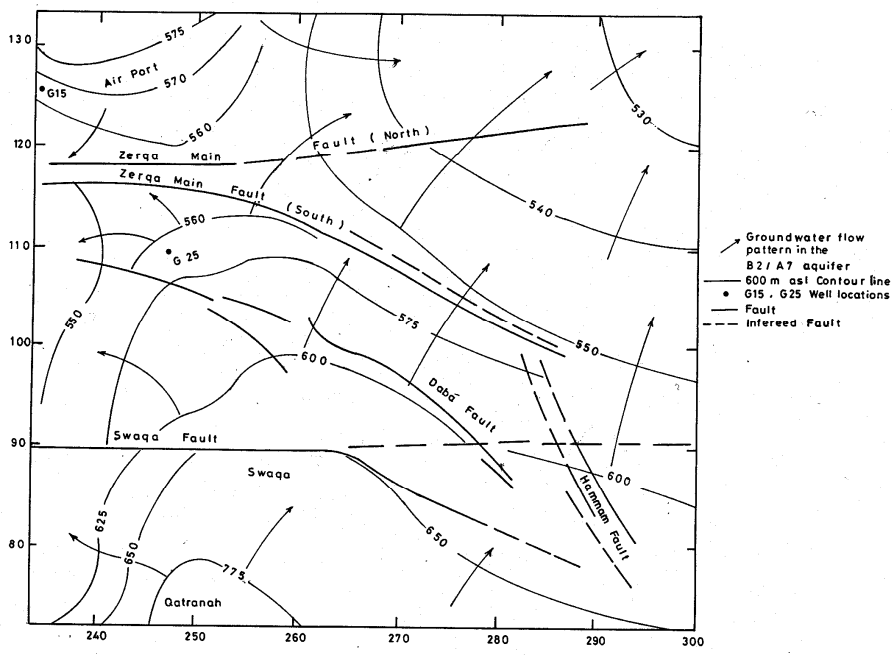

6.2. Daba (Khan Az-Zabib)-Siwaqa Marbles (Analogue Cement Zone)

6.2.1 Introduction

The Upper Cretaceous-Lower Neogene rocks of the Daba-Siwaqa area are massive, varicoloured, recrystallised and intersected by many veins and fractures (Figure 6.9 a-c). Burden (1959), Heimbach (1965), and Ruef and Jeresat (1965) reported on these rocks in central Jordan, and attributed the green colour to chromium content. Unusual minerals such as chromatite, tyuyamunite and metatyuyamunite were reported in the Chalk-Biomicrite and Phosphorite Units of Daba-Siwaqa (Heimbach, 1965; Bender, 1968). Wiesemen and Rosch (1969) reported similar rocks within the Phosphorite Unit, 5 km west-north-west of Suweileh, north of Amman. Hakki and Sassa (1978) conducted a general geological survey in the study area. Hauff (1979) identified a new mineral “Hashemite” in addition to ettringite and apatite. Heimbach and Rosch (1980) reported the presence of spurrite, pervoskite, garnet, ettringite, apatite, aragonite, vaterite, afwillite, and montmorillonite in the Daba-Siwaqa area. They proposed an origin similar to that of the Mottled Zone of Israel.

Figure 6.9 (a) marble quarry (b) varicolored marble (c) veins and voids in marble

(a)

(b)

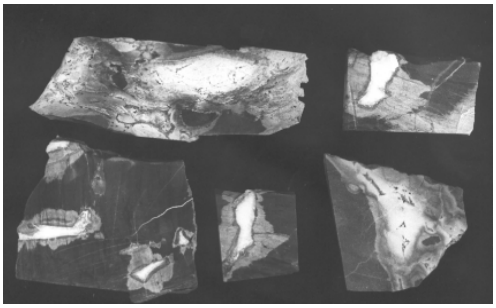

(c)

The Mottled Zone is stratigraphically and lithologically similar to Daba-Siwaqa area. High temperature minerals have been described from the Mottled Zone by Bentor et al. (1963, 1972), Gross et al. (1967), Kolodny et al. (1971), Kolodny and Gross (1974), and Gross (1977). Matthews and Kolodny (1978) and Kolodny (1979) confirmed that organic matter combustion was responsible for their formation. Gur et al. (1995) and Burg et al. (1992, 2000) indicated that combustion in the Mottled Zone was not simultaneous and they deduced two metamorphic events: one in the Miocene (~16 Ma) and the other in the Pliocene (~3 Ma). Younger ages (1.7 – 1.0 Ma) were also measured. Burg et al. (1992) indicated that the measured palaeomagnetism of the parent rock shows normal polarity and the ACZ show reverse polarity. (to compare with our preliminary data in section 6.3.3, which are not the same orientation)

Compared to the Mottled Zone, the Daba-Siwaqa area represents a more advanced stage of retrograde metamorphism and an important feature, typical to the metamorphic zone, is the presence of polygonal columnar jointing in the red and black varieties of marble (Figure 6.10).

Figure 6.10 Polygonal columnar structure in red marble

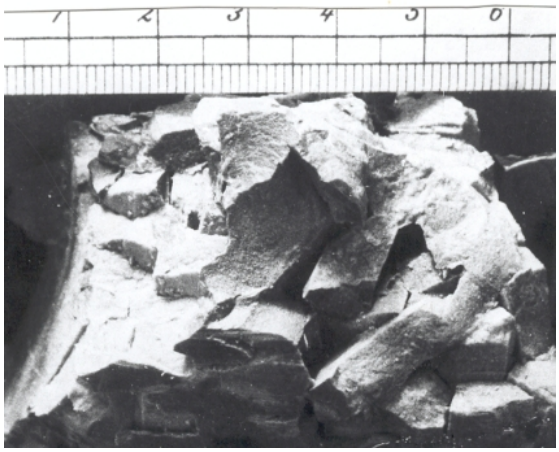

6.2.2 Mineralogy

Tables 6.3 and 6.4 summarise the minerals identified in the Daba-Siwaqa area to date, with the former representing the primary minerals in the metamorphic zone (the ACZ) and the latter representing the secondary mineral in the altered marbles (i.e. hydrated cement) and biomicrite (i.e. organic-rich biomicrite). A variety of phases present are is in Figure 6.11.

*Table 6.3 Primary metamorphic minerals in Daba metamorphic zone (decarbonation-dehydration-recrystallisation phases)**

Mineralogy	**General Formulae**
Fluorapatite	$Ca_{10}\ (PO_4)_6\ F_2$
Francolite	$Ca_{10\text{-}x\text{-}y}\ (Na,K)_x\ Mg_x\ (PO_4)_{6\text{-}z}\ (CO_3)_z\ F_{0.4z}\ F_2$
Ellestadite	$Ca_{10}\ (SiO_4)_3\ (SO_4)_3\ O_{24}\ (Cl,OH,F)_2$
Spurrite	$Ca_5\ (SiO_4)_2\ (CO_3)$
Urarovite	$Ca_3\ Cr_2\ (SiO_4)_2$
Wollastonite	$CaSiO_3$
Larnite	Ca_2SiO_4
Diopside-hedenbergite	$Ca\ (Al,Fe)\ Si_2O_6$
Anorhtite	$CaAl_2\ Si_2\ O_8$
Brownmillerite	$Ca_2\ (Al,Fe)_2\ O_5$
Pervoskite	$Ca\ Ti\ O_3$
Ferrites	Ca Fe Ba, Cr, Al, Ti, Mg, Zn, Mn-$Fe_2\ O_3$
Hematite or ferric oxide	Fe_2O_3
Ca-aluminate	Undefined
Calcite	$CaCO_3$
Graphite	C
Garnet (andradite)	$Ca_3\ (Fe^{+3},Ti)_2\ (SiO_4)_2$
Merwinite	$Ca_3\ Mg\ (SiO_4)_2$

These phases are the equivalent of an industrial cement clinker

*Table 6.4 Secondary minerals in the Daba rocks-altered marbles (analogue cement zone) and Bituminous Marl (organic-rich biomicrite)**

Mineralogy	General Formulae
Jouravskite	Ca_3 Mn (CO_3) (SO_4) $(OH)_6.12H_2O$
Hydrotalcite	Mg, Al_2 (CO_3) $(6H)_{16}.4H_2O$
Calcite	$CaCO_3$
Aragonite	$CaCO_3$
Vaterite	$CaCO_3$
Kutnahorite	$Ca_{0.75}$ (Mn, $Mg)_{0.26}$ CO_3
Ankerite	Ca (Fe Mg) $(CO_3)_2$
Strontianite	$SrCO_3$
Haematite	Fe_2O_3
Maghemite	Fe_2O_3
Gibbsite	$Al(OH)_3$
Brucite	$Mg(OH)_2$
Portlandite	$Ca(OH)_2$
Quartz	SiO_2
Opal-CT	SiO_2
Opal-A	$SiO_2.nH_2O$
Barite	$BaSO_4$
Baritocelestite	$(SrBaCa)SO_4$
Hashemite	$BaCrO_4$ to $BaSO_4$ complete solid solution
Hydrogarnet	Ca_3 Al_2 $(OH)_{12}$ – Ca_3 Al_2 $(SiO_4)_3$
Sulphur	S
Gypsum	$CaSO_4$
Bassanite	$CaCO_4.0.5H_2O$
Anhydrite	$CaSO_4$
Ettrinigte	Ca_6Al_2 $(SO_4)_3$ $(OH)_{12}.25$ H_2O
Thaumasite	Ca_6 Si_2 $(SO_4)_2$ $(CO_3)_2$ $(OH)_{12}.24H_2O$
Hydrocalumite	Ca_{16} Al_8 $(OH)_{54}$ $CO_3.2H_2O$
Hydroxyapatite	Ca_{10} $(PO_4)_6$ $(OH)_2$
Fluorapatite	Ca_{10} $(PO_4)_6$ F_2
Francolite	Ca_{10-x-y} $(Na,K)_x$ Mgx $(PO_4)_{6-z}$ $(CO_3)_z$ $F_{0.4z}$ F_2
Ellestadite	Ca_{10} $(SiO_4)_3$ $(PO_4)_3$ O_{24} (Cl, OH, $F)_2$
Afwillite	Ca_3 Si_2 O_4 $(OH)_6$
Tobermorites 14A°, 11.7A° and 9.3A°	Ca_5 Si_6 O_{16} $(OH)_2.2$-$8H_2O$
Jennite	Ca_9 H_2 Si_6 O_{18} $(OH)_8.6H_2O$
Apophyllite	KCa_4 Si_8 O_{20} (OH, F) $.8H_2O$
Birunite	Ca_{15} $(CO_3)_{5.5}$ $(SiO_3)_{8.5}$ $SO_4.15H_2O$
CSH gel	Amorphous,
CASH gel	Amorphous
Ca-Cr-Si-gel	Amorphous
Volkonskoite	Cr-smectite
Thomsonite	Na Ca_2 $[Al_2$ (AlSi) Si_2 $O_{10}]_2.6H_2O$

This material represents a mixture of hydrated cements and secondary alteration products in the biomicrite

Figure 6.11 A selection of minerals present at Daba-Siwaqa

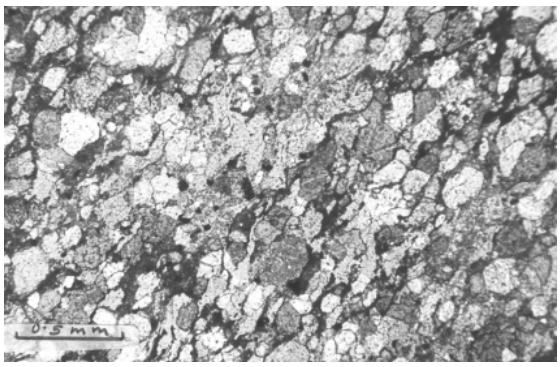

(a) Recrystalline calcite (X-nicols).

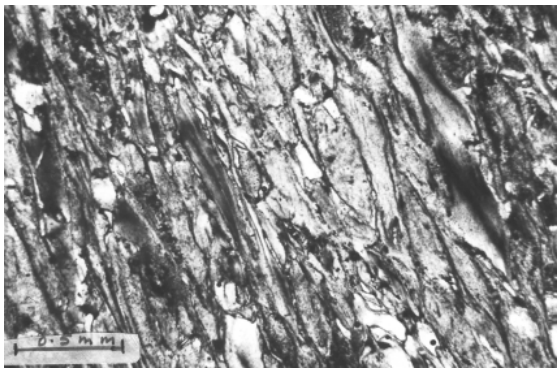

(b) Recrystalline apatite with preferred orientation (X-nicols).

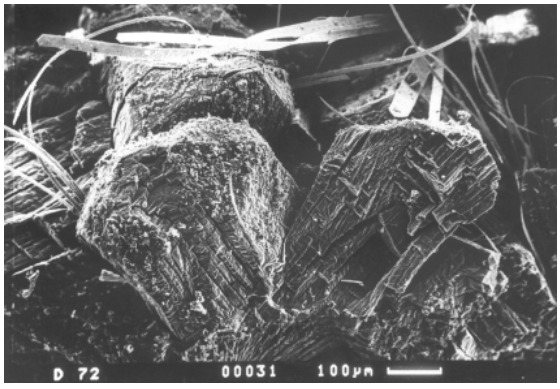

(c) SEM of bassanite, anhydrite and tobermorite crystals.

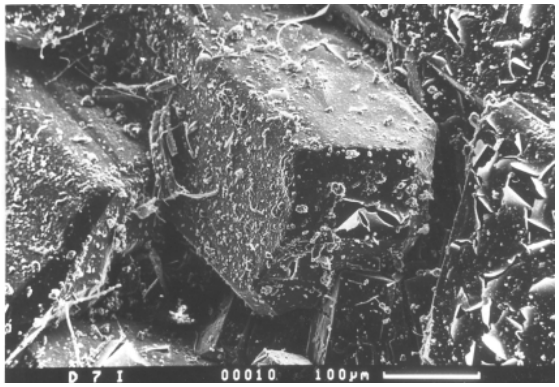

(d) SEM of secondary gypsum.

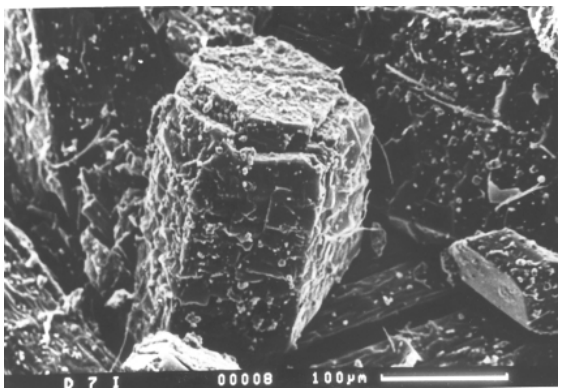

(e) SEM of apatite crystals.

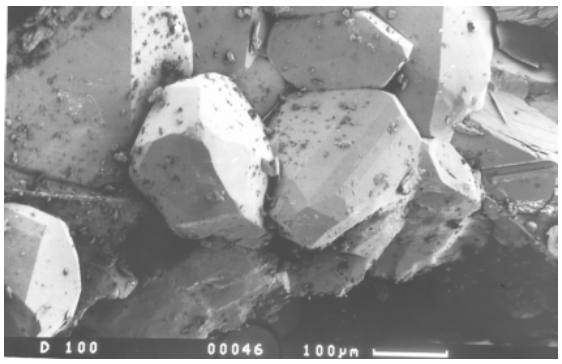

(f) SEM of apophyllite crystals.

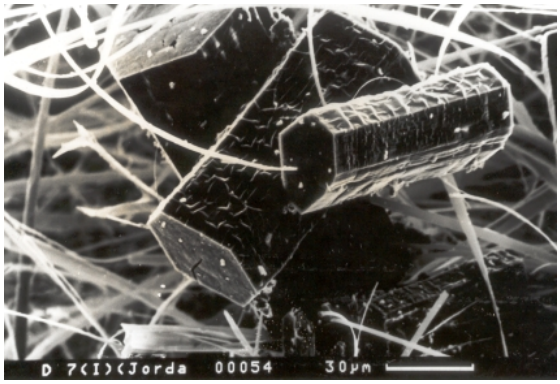

(g) SEM of tobermorite and thaumasite-ettringite crystals.

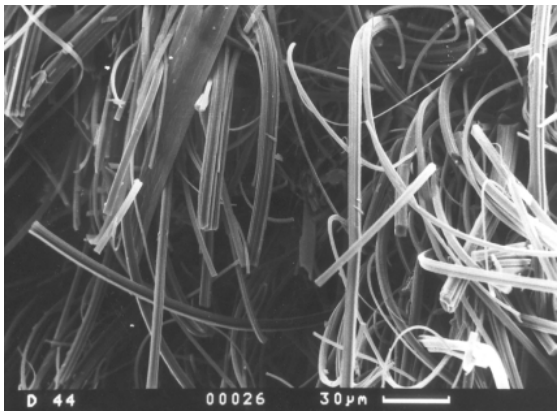

(h) SEM of tobermorite crystals

6.2.3 The varicoloured marbles

The varicolours of Daba-Siwaqa (black, white, and all shades of yellow, grey, brown, red and green) can be related to the presence of primary and secondary minerals such as iron oxides, Cr-rich minerals (such as ettringite, hashemite and volkonskoite) and apatite. Tables 6.5 and 6.6 show the major and trace elements composition of three coloured varieties. Trace elements incorporated in the structure of minerals are partially responsible for the different colours.

Table 6.5 Chemical composition of some varieties of Daba marble

Oxides%	D_1 Gray marble	D_2 Green apatite marble	D_3 Brown marble with ettringite crust
SiO_2	3.08	1.57	8.4
TiO_2	0.01	0.01	0.02
Al_2O_3	0.35	0.45	5.03
Fe_2O_3	0.27	0.17	0.26
MnO	0.68	0.01	0.00
MgO	2.18	0.28	0.2
CaO	47.75	55.12	36.66
Na_2O	0.00	0.00	0.00
K_2O	0.01	0.00	0.00
P_2O_5	0.01	22.34	1.2
SO_3	0.54	0.31	10.14
LOI	43.8	18.70	36.70
Sum.	98.68	99.00	98.61

Table 6.6 Trace element composition of some varieties of Daba marble*

Element (ppm)	D_1 Gray marble	D_2 Green apatite marble	D_3 Brown marble with ettringite crust
Ba	171	467	121
Ce	46	39	90
Co	4	1	0
Cr	17	438	4319
Cu	30	261	250
La	66	103	174
Nb	0	0	9
Ni	20	25	183
Pb	9	28	0
Rb	0	0	1
Sc	0	0	0
Sr	7262	1268	269
Th	0	4	7
V	19	150	346
Y	3	76	17
Zn	21	954	1763
Zr	159	35	4

* Analysis was carried out in BGR, Hanover.

The hydrated low-temperature minerals also contain high concentrations of trace elements which are responsible for a variety of colours. Solid-solution series are very common in the hydrated retrograde products (ettringite-thaumasite, different apatite structures with varying fluorine content, high potassium fluorine apophyllite; CrO_4^{2-} replaces SO_4^{2-}, and isomorphous substitution of CO_3^{2-}, SiO_4^{4-} and CrO_4^{2-}). Hylsop (1998) indicated that the altered wall rock in Daba marble contains slightly enhanced levels of U compared to the surrounding less-altered host rock. U is generally absent from the vein phase, but is present in a zeolite – clay mixture of vein margins.

Apatite (ellestadite and fluoroapatite) is the major cause of colouration of marble (excluding the colouration of secondary minerals filling voids, veins and fractures). A calcinations experiment was carried out on powdered sedimentary francolite. The temperature range was between 500°C and 1100°C. The gray colour was obtained at 500°C, violet at 600°C,

violet green, light-green and dark-green colours represent 700°C, 800°C and 900-1100°C, respectively. Figure 6.12 (a and b) illustrates the pyrometamorphic effect in an apatite-rich sample.

Figure 6.12a Baked phosphate (bar, top middle =50 microns)

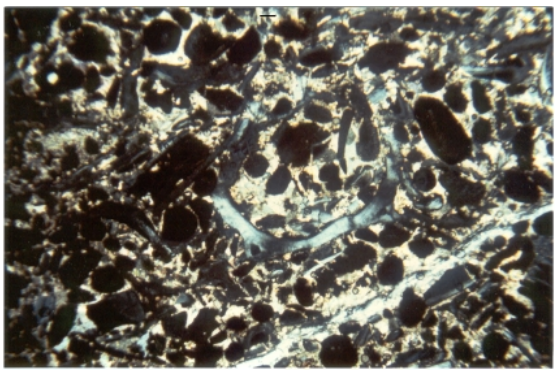

Figure 6.12b 1=apatite 2=blue luminescing calcite cement related to pyrometamorphic event

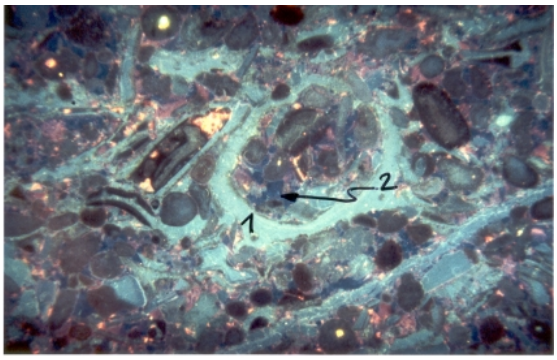

6.2.4 Origin

Field and petrological investigations of the Daba-Siwaqa area indicated the presence of a complex series of mineral assemblages, which range in abundance from essential to fairly common minerals (Nassir and Khoury, 1982). The metamorphosed rocks are the product of the metamorphism of the “Chalk-Biomicrite Unit” and its stratigraphic equivalents. The minerals in Daba-Siwaqa areas lie in two assemblages (Tables 6.3 and 6.4):

(a) Prograde metamorphic mineral assemblage (decarbonation-dehydration-recrystallisation phases, under high-temperature, low-pressure conditions). Essential minerals of this group include, among others: diopside, wollastonite, monticellite, gehlenite-akermanite, spurrite, and merwinite Such minerals are members of the decarbonation univarient progressive reaction series and are characteristic of contact-metamorphic rocks. Other important minerals are garnet, anorthite, pervoskite, magnesioferrite, fluorapatite and recrystallized calcite. The assemblage indicates an isochemical decarbonation-dehydration metamorphism of impure limestones and biomicrites. The formation of the above-mentioned mineral assemblage from such sedimentary rocks is possible. Textural and structural analyses (porphyroblastic, poikiloblastic and granulated textures, broken and fractured crystals, columnar structure), in addition to the nature of crystal growth (cavity, vein and fracture fillings

and concretionary growth) suggest a relatively rapid heating where maximum temperature was achieved. The maximum temperature was concentrated along weakness zones in the rocks where the maximum amount of oxygen was available. Spurrite is the most commonly observed rock-forming mineral in this assemblage and is present in many cases as concretionary growth with wollastonite. Such a paragenesis is an indication of prograde metamorphism. CO_2 volatiles are important products of prograde metamorphism in calcareous rocks during the formation of high-temperature minerals.

(b) Retrograde metamorphic mineral assemblage (hydration-carbonation-sulphatisation-replacement-hydrothermal alteration-weathering phases). The assemblage includes among others: calcium silicate hydrates (tobermorite, jennite, afwillite, apophyllite), sulphates (ettringite, hashemite, barite, thaumasite, gypsum), stable and metastable carbonates (calcite, vaterite, aragonite, kutnahorite), oxides and hydroxides (goethite, portlandite, hydrocalumite), and many calcium silicate hydrates. The assemblage indicates a later multi-stage retrograde metamorphism.

The occurrence of assemblages (a) and (b) is quite normal and well known from contact-metamorphosed limestones. The presence of the minerals of the (a) and (b) assemblages in Daba-Siwaqa area assumes a contact-metamorphic origin of the high-temperature mineralisation assemblage (sanidinite and pyroxene hornfels facies), as occurs in Portland cement clinkers and hydrated cement products.

A model other than igneous intrusion has to be looked for to explain the source of heat needed to form high-temperature minerals under the same conditions as contact metamorphism. The most reasonable and accepted model to explain such a phenomenon is the combustion theory. Spontaneous combustion of organic matter, especially bituminous shale, is well-known in the literature and also occurs in coal mines. Combustion depends on the availability of oxygen, the presence of organic matter and a triggering event.

The stratigraphic equivalents to the marble are rich in organic matter (up to 25% in the biomicrite – see also Chapter 2), providing a significant potential for spontaneous combustion. Miocene tectonism was possibly the event that initiated the combustion in the Daba-Siwaqa area. The studied area is crossed by several major Miocene faults. Tectonism formed fissures and fractures that acted as channels and pathways for oxygen supplies needed for combustion and for the trigger event, probably oxidation of sulphides. Secondary channels were possibly formed as a result of volume decrease following mass loss as a function of evolved volatiles and rapid cooling following combustion. Continuous heating and cooling would lead to a continuous expansion-contraction phenomenon. Secondary channels and pathways would lead to a self-generating mechanism, where spontaneous combustion of organic matter occurs.

The confinement and restriction of the metamorphosed zone in the Biomicrite Formation indicates that availability of oxygen is the controlling factor that determines where metamorphism occurs. This is proved by the occurrence of un-metamorphosed lenses of biomicrite in the lower part of the marble zone in the Daba - Siwaqa area (Khushaym Matruk). The following arguments, however, would favour the spontaneous combustion model:

(1) The metamorphic rocks in the Daba-Siwaqa and Maqarin areas, as well as in the Mottled Zone of Palestine/Israel, occur in the same stratigraphic and structural position.

(2) The predominance of ferric oxides (haematite, maghemite) at the expense of ferrous sulphides (pyrite) indicates oxidising conditions (see also Section 6.3.4).

The analysed samples of Heimbach and Rosch (1980) are essentially of recrystallised apatite, calcite varieties, with traces of spurrite, garnet, perovskite, afwillite, and quartz. From the results of isotope data, it was found that the decarbonated rocks are strongly enriched in light isotopes of oxygen and carbon. The higher the temperature of combustion, as indicated from the colours of apatite the higher the enrichment in light stable isotopes. The normal phosphatic samples average $\delta^{18}O_{PDB}$ = 6.8‰; dark grey apatitic samples average $\delta^{18}O$ = -10‰; violet apatitic samples average $\delta^{18}O_{PDB}$ = -12.4‰. Decarbonation and interaction with CO_2 derived from combustion of organic matter is a possible mechanism for the depletion of the rock of heavy isotopes. The decarbonation process involves the release of CO_2 enriched in ^{18}O whereas the CO_2 derived from the oxidation of organic matter is highly depleted in C_{13}. The higher enrichment of calcite and apatite with light carbon rather than oxygen could be attributed to interaction with groundwater during the retrograde processes.

The unmetamorphosed phosphatic rocks in Daba – Siwaqa have an isotopic compostion in the range of normal marine carbonates. The decarbonated rocks show enrichment in light isotopes, the slightly metamorphosed rocks intermediate values. Results of stable isotopes from green travertine varieties (Siwaqa) showed some enrichment in light isotopes and plotted within the range of decarbonated rocks (Clark et al., 1992a). The isotope study indicates that the ascending solutions were also responsible for the depletion of heavy isotopes from travertine.

More apatite-rich samples were collected with the help of Dr. K. Ramseyer (University of Berne) and were isotopically analysed at the University of Berne. The results are given in Table 6.7 and plotted in Figure 6.13 and confirm the previous data. The results of $\delta^{13}O$ and $\delta^{18}O$ measured in the marble are characterized by a $\delta^{13}C_{PDP}$ ranging from –5 to –11 %o and by a $\delta^{18}O_{PDB}$ ranging from –5 to 10%o. On the other hand, the marbles have generally more negative values both for $\delta^{13}C_{PDB}$ (-15 to –20%o) as well as for $\delta^{18}O_{PDB}$ (-9 to –18%o). Specifically, the large shift in the $\delta^{13}C_{PDB}$ after recrystallisation by a pyrometamorphic event clearly demonstrates the uptake of light carbon from the oxidation of organic matter.

Table 6.7 Stable isotope values of calcite in limestone and marble

Locality	Sample	Type / Color	δ^{13C}(PDB)	$\delta^{18}O$ (PDB)
Suweileh Sediment	S1	Phosphorite	-12.7	-6.8
	S2	Silicified lmst*	-10.1	-10.2
	S2-1	Silicified 1mst.	-9.1	-5.5
Suweileh marble	S3-3	dark brown	-19.5	-17.0
	S3-5	light green	-18.5	-16.3
	S3-6	grey	-18.3	-16.3
Daba-Marble Quarry	D1	Siliceous lmst.	-5.7	-7.8
	D2	ochre	-18.2	-11.8
	D2-1	ochre	-16.6	-10.5
	D2-2	green	-15.8	-11.4
	D2-3	dark brown	-15.5	-11.6
	D3-1	ochre	-19.2	-12.7
	D3-2	ochre	-18.4	-12.4
	D3-4	light green	-15.1	-10.5
	D3-5	ochre	-17.5	-12.6
	D4-2	light brown	-17.8	-11.6
	D4-2	light brown	-18.3	-12.1
	D5-1	light brown	-18.2	-12.2
Daba-Highway cut	D8-4	light red	-9.5	-6.5
	D9-1	white	-8.5	-9.7
	D9-2	ochre	-18.3	-10.7
	D9-3	ochre	-17.9	-9.9
	D9-4	ochre	-16.3	-9.2
Siwaqa-Kerak Highway outcrop	K1-2	Bituminous Marl	-11.0	-7.2

*lmst = limestone

Figure 6.13 Stable isotope data for marbles and their precursor carbonates

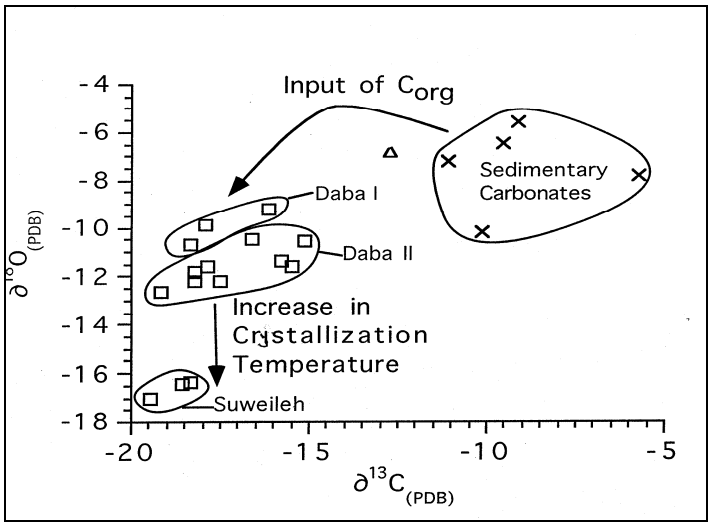

An explanation is needed, however, for the formation of some high-temperature minerals (wollastonite) at low X_{CO2}. The CO_2-rich volatiles should escape from the reaction site to derive the reaction spontaneously. Dilution of CO_2 by groundwater is likely. The evolved volatiles could produce volume change in the initially Chalky Limestone and the Bituminous

Marl (biomicrite) parent rocks, as a result of rapid increase in temperature. The evolution of volatiles could form rapidly and exceed the initial load pressure due to the low permeability of the parent rocks. Accordingly, fractures, joints and fissures would have resulted and would have acted as channels. The movement of volatiles increased the rock conductivity. Diffusion, therefore, was rapid along fissures and fractures to allow equilibrium of newly formed minerals.

The production of the low temperature phases is as at Maqarin (see Milodowski et al., 1992a, 1992b; 1998a, 1998b and Chapter 4 for details) and has been summarised by Clark et al. (1998) in Figure 6.14. Details of opaline phases and travertine from central Jordan are given in Appendix 6.

Figure 6.14 Conceptual model showing sequence of thermal metamorphic and retrograde alteration reactions with changes in temperature and humidity in the reaction zone (from Clark et al., 1998)

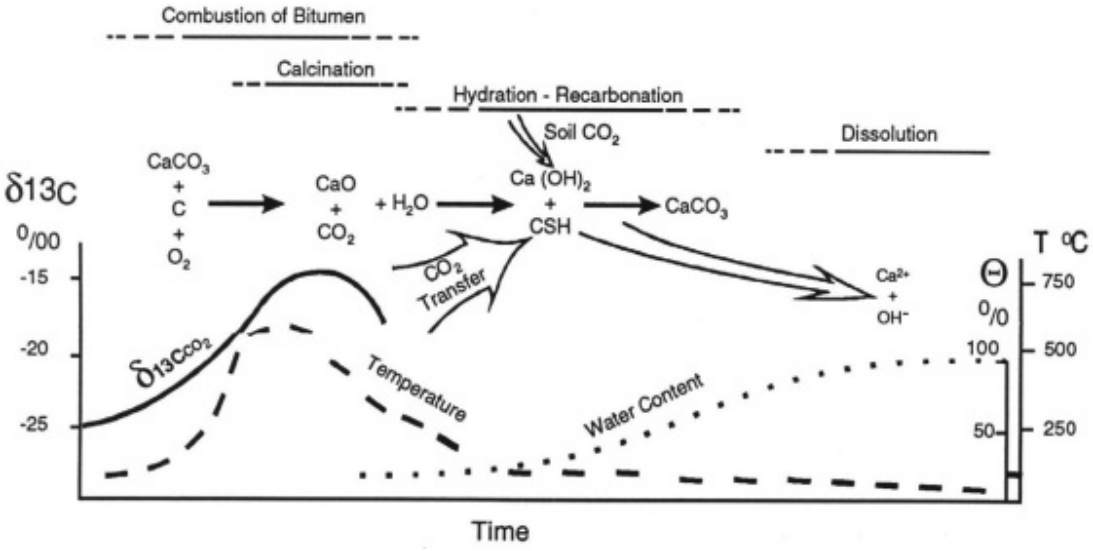

6.3 Khushaym Matruk

6.3.1 Field work and sampling

The Kushaym Matruk area (N 31°16´ 570; E 36° 14´ 775) belongs to the southern extension of the Daba Marble Zone (see Linklater, 1998). The site itself is located at the western end of a low ridge, and the contact[22] between the biomicrite and the ACZ is clearly visible in Figures 6.15 and 6.16. Biomicrite (i.e. Muwaqqar Formation) crops out at the base of the ridge, about 5 to 10 metres in vertical extent, and is obvious from the colour change to the buff cements directly above. The remainder of the ridge (about 50 m in vertical extent) is a mixture of analogue cements and travertines, with the latter standing out as more resistant

[22] It was noted in the notes on terminology for the Report (Appendix 1) that no true 'contact' can be defined. However, at Khushaym Matruk, the colour change noted above is taken to represent the contact for ease of following relative changes (in the mineralogy, porosity, and organic matter content, for example) in the rock column sampled in the trench.

zones and marking sites of former springs[23]. As noted in Section 6.2, above, the groundwater in this area is now 150-200 m below the surface.

Figure 6.15 View of the Kyushaym Matruk sampling site (from Smellie, 2000)

Figure 6.16 Khushaym Matruk site: note the grey biomicrites below the buff Analogue Cement Zone (from Smellie, 2000)

[23] Note that the ridge is capped by an ACZ.

Full details of the field work and sampling campaigns are given in Rassineux (2000) and Smellie (2000). Here, only those samples collected from a trench excavated in the biomicrite immediately below the ACZ (see Figure 6.17) are discussed. Twenty-one representative samples were collected along this profile (blue points, Figure 6.18) and twelve points were sampled for clay analyses (red arrows, Figure 6.18). A full sample catalogue is available in Appendix 6.

Figure 6.17 Sketch of the position of the sampling trench in the biomicrite

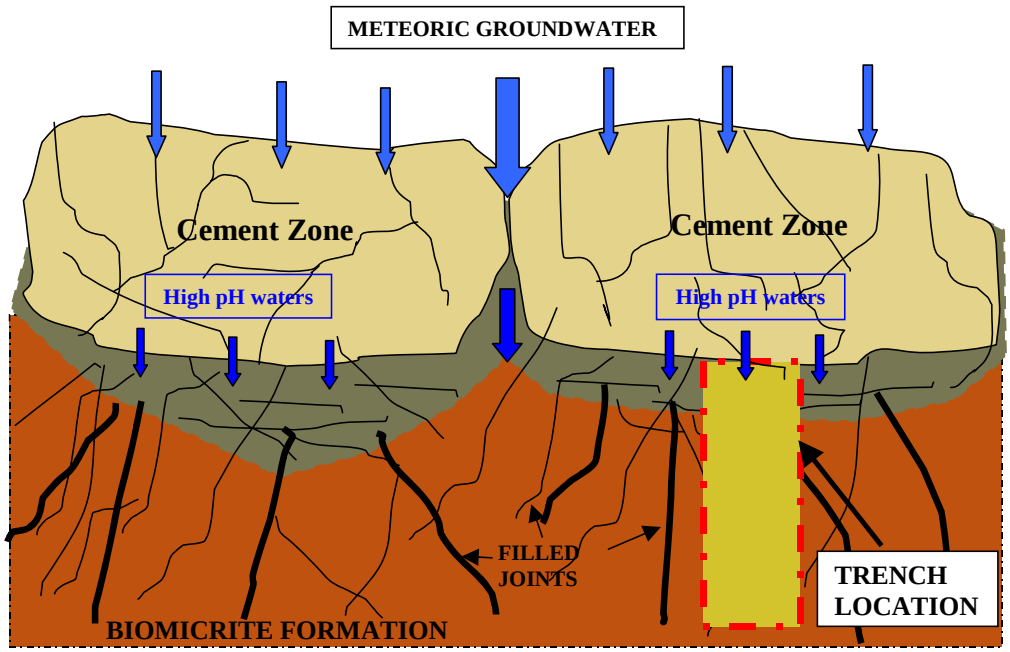

Figure 6.18 Schematic diagram of the sampling points in the trench. Red arrows indicate the sampling points for clay analyses

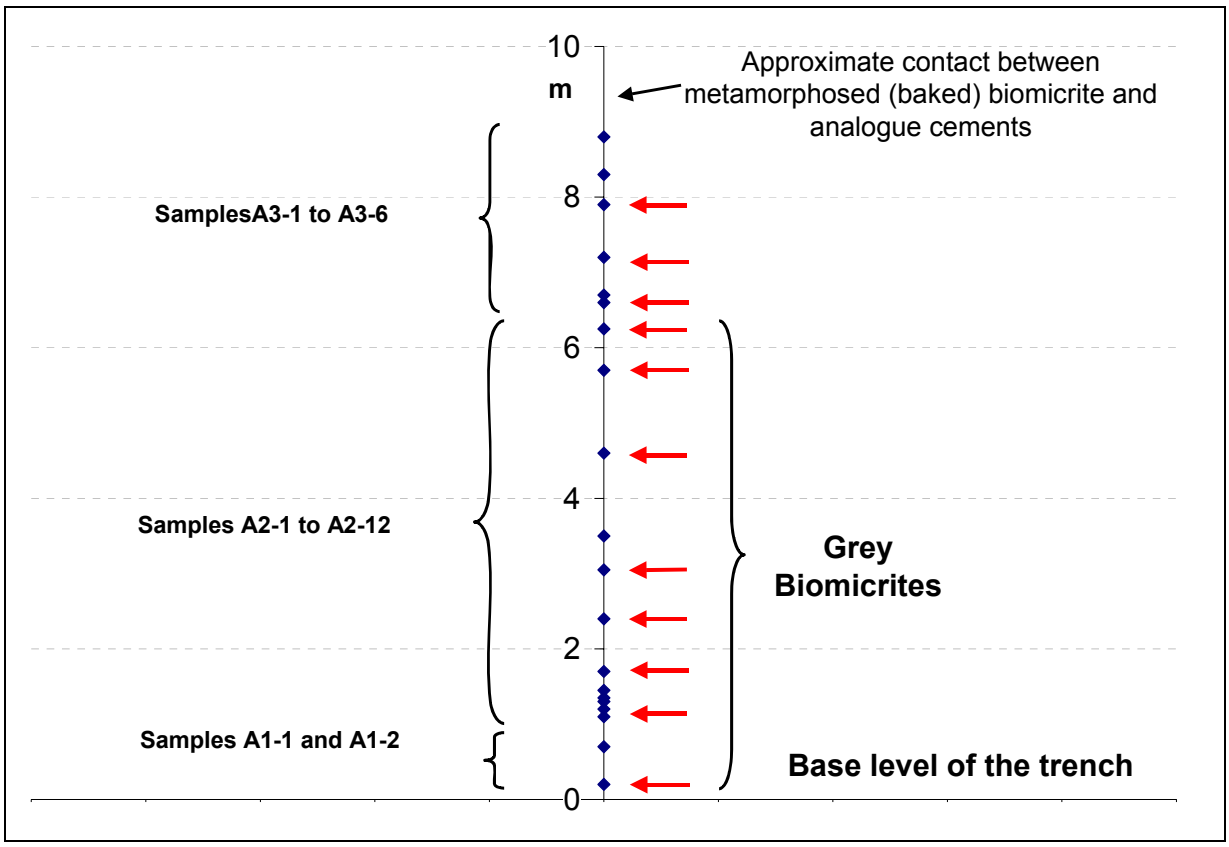

6.3.2 Clay minerals

6.3.2.1 Introduction

Initial studies at the Khushaym Matruk site revealed the presence of an alteration phenomenon in the biomicrite underlying the ACZ which resulted from three superimposed phenomena:

- transformation due to a high-temperature metamorphic event
- interaction with hyperalkaline leachates from the cement zone
- recent weathering with gypsum precipitation notable in large veins

This section synthesises the petrographical, mineralogical and chemical investigations conducted on the clay fraction from the sampled profile from the unaltered biomicrite to the ACZ to evaluate the clay-reaction products and their time and spatial evolution under the effect of natural hyperalkaline fluids.

6.3.2.2 Analytical methods

The analytical methods are detailed in Appendix 6.

6.3.2.3 Results and discussion

Initially, a large group of samples was analysed, to assess the heterogeneity of the material. The results are given in Tables 6.8 and 6.9, and indicate that the A-samples (Figure 6.18) are similar from the mineralogical and chemical point of view. The main experimental results from the detailed investigation on clay fraction of eleven representative samples, from the bottom of the biomicrite to the contact with the overlying analogue cements, are described below.

Table 6.8 XRD results of Khushaym Matruk samples

Sample No.	Calcite	Apatite	Gypsum	Smectite	Quartz
A1-1	M+	+	+	++	+
A1-2	M+	+	M	++	++
A2-1	M+	+	+	++	+
A2-2	M+	+	-	++	+
A2-3	M	+	M	++	+
A2-4	M+	+	+	++	+
A2-5	M+	+	+	++	+
A2-6	M+	+	++	++	+
A2-7	M	+	M+	++	+
A2-8	M+	+	+	++	+
A2-9	M+	+	+	++	+
A2-10	M+	+	+	++	+
A2-11	M+	+	+	++	+
A2-12	M+	+	+	++	+
A3-1a	M+	+	+	++	+
A3-1b	M+	+	+	++	-
A3-2	M+	+	++	++	-
A3-3	M+	+	+	++	-
A3-4	M+	+	+	++	+
A3-5	M+	+	+	++	-
A3-6	M+	+	++	++	-
B1	M+	+	++	+	+
B2	M+	+	++	++	+
B3	M+	+	++	++	+
B1-3	M+	+	-	-	-
C1	M+	+	-	-	+
C3	M+	+	+	+	+
C4	M+	+	-	+	-

M+ = > 50%, M = 20-40%, ++ = 10-20%, + = < 5%

Table 6.9 Chemical composition of Khushaym Matruk samples

Sample No	SiO_2	Al_2O_3	TiO_2	Fe_2O_3	CaO	MgO	MnO	Na_2O	K_2O	P_2O_5
A1-1	11.70	3.40	0.31	0.96	35.43	1.19	0.02	0.02	1.10	1.71
A1-2	12.08	3.40	0.17	1.11	35.40	0.67	0.02	0.00	1.75	1.76
A2-1	13.06	3.11	0.24	0.92	35.38	1.41	0.02	0.08	0.55	1.29
A2-2	10.42	2.76	0.22	1.15	35.04	1.24	0.02	0.09	0.75	1.20
A2-3	12.30	3.16	0.22	1.11	42.55	0.27	0.02	0.06	0.78	1.26
A2-4	14.01	3.83	0.30	1.53	34.72	1.42	0.02	0.03	1.15	1.28
A2-5	13.60	3.62	0.28	1.22	34.30	2.05	0.02	0.06	0.25	1.40
A2-6	12.32	3.87	0.24	1.41	35.45	1.33	0.03	0.06	1.17	1.30
A2-7	14.00	3.34	0.15	1.44	44.15	0.70	0.03	0.05	1.12	1.26
A2-8	10.88	3.95	0.38	1.51	34.76	1.67	0.02	0.05	1.15	1.78
A2-9	10.08	2.52	0.27	1.01	40.03	1.04	0.02	0.02	1.40	1.80
A2-10	10.07	1.58	0.52	0.75	41.29	1.03	0.03	0.08	0.98	1.86
A2-11	9.50	3.02	0.26	1.26	40.26	1.66	0.03	0.16	0.62	0.76
A2-12	10.60	2.75	0.44	0.99	38.73	1.26	0.02	0.04	0.31	0.92
A3-1a	10.39	2.18	0.21	1.01	40.80	2.48	0.03	0.22	0.53	1.22
A3-1b	9.86	2.77	0.22	1.01	40.10	3.04	0.03	0.08	0.61	0.84
A3-2	13.02	2.80	0.29	1.30	37.13	1.81	0.02	0.16	0.20	1.56
A3-3	13.17	5.05	0.32	1.86	35.60	2.27	0.02	0.04	0.85	1.17
A3-4	10.93	2.29	0.18	1.02	41.29	1.76	0.02	0.22	0.95	1.13
A3-5	9.69	2.29	0.34	1.78	41.81	2.15	0.02	0.14	0.35	0.69
A3-6	12.01	3.30	0.27	1.37	40.11	2.48	0.02	0.14	0.45	1.11
B1	12.10	3.15	0.23	0.79	35.29	1.81	0.02	0.12	0.18	1.66
B2	16.18	5.21	0.33	1.37	35.08	3.97	0.02	0.03	0.20	2.56
B3	13.73	4.12	0.28	1.39	34.39	4.88	0.02	0.05	0.65	1.90
B1-3	5.74	0.83	0.16	2.10	48.86	1.30	0.02	0.07	0.05	1.13
C1	11.45	4.6	0.30	1.28	35.71	1.83	0.02	0.04	0.10	1.77
C3	9.54	1.70	0.27	1.04	42.40	2.50	0.02	0.11	0.20	1.60
C4	7.54	1.20	0.20	1.01	44.67	2.12	0.02	0.06	0.10	0.95

Mineralogy: overview

Biomicrite

Thin sections of apparently unaltered biomicrite from Khushaym Matruk are very similar to those previously studied at the Maqarin site (e.g. Milodowski et al, 1992a, 1992b; 1998a, 1998b) and revealed that the rock was made up of silt-size bioclasts embedded in a microcrystalline matrix (Figure 6.19). The matrix was composed of a mixture of carbonates, clay minerals, calcium phosphate (collophane) and organic matter. A low content of detrital minerals such as mica, feldspars, quartz, anatase or rutile and small Fe-oxide nodules containing chromium were observed in the matrix (Figure 6.20). Analyses performed on the matrix showed slight variations due to the mineralogical heterogeneity (Table 6.10).

Bioclasts were very common, mainly as foram tests or fossil shell fragments, and mark clearly the sedimentary bedding. The foram tests had suffered some diagenetic processes such as carbonate recrystallisation and replacement by clay minerals, detrital minerals and organic matter (Figure 6.20). Hydrocarbon-rich zones were abundant and randomly disseminated in the matrix (Figures 6.19 and 6.20). Nevertheless, organic matter was mainly located on wall-rock of fractures and voids (Figure 6.21), the biggest ones (millimetres to

centimetres) being filled by gypsum crystals (> 1mm). These voids mainly lay in the plane of the sedimentary bedding.

Figure 6.19 Photomicrograph of biomicrite (x-nicols) showing general aspect of the rock: bioclasts embedded in the ochre to rust coloured microcrystalline carbonated matrix. Sample A2 – 10. Scale: 1 cm = 240 µm

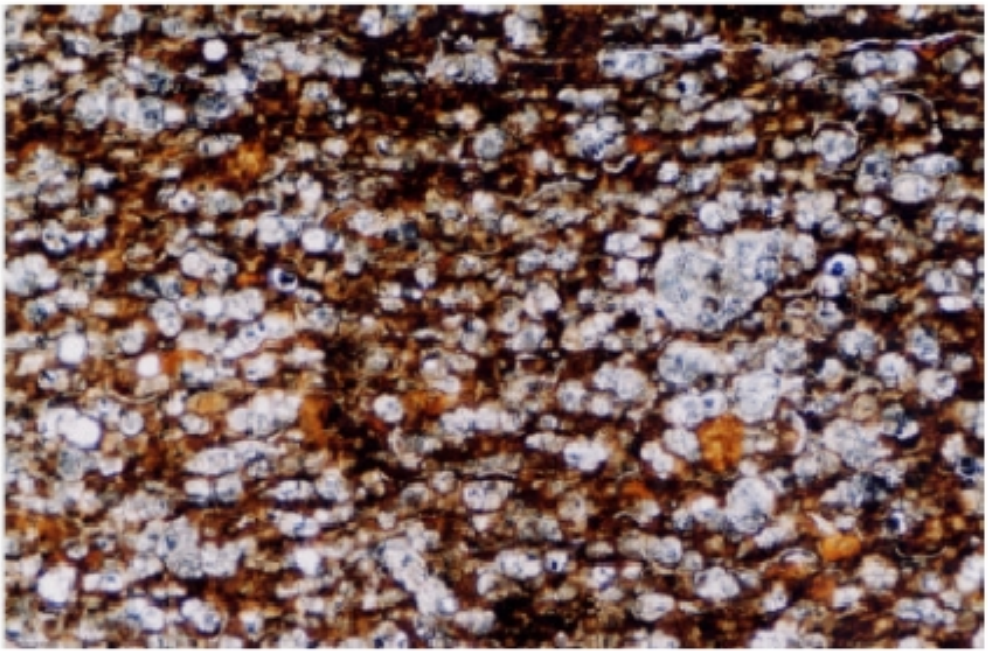

Figure 6.20 Backscattered SEM image of a thin section showing the aspect of the biomicrite matrix with many fossil fragments. Clearer zones are carbonated while darker zones are enriched in organic matter. Sample A2 – 10

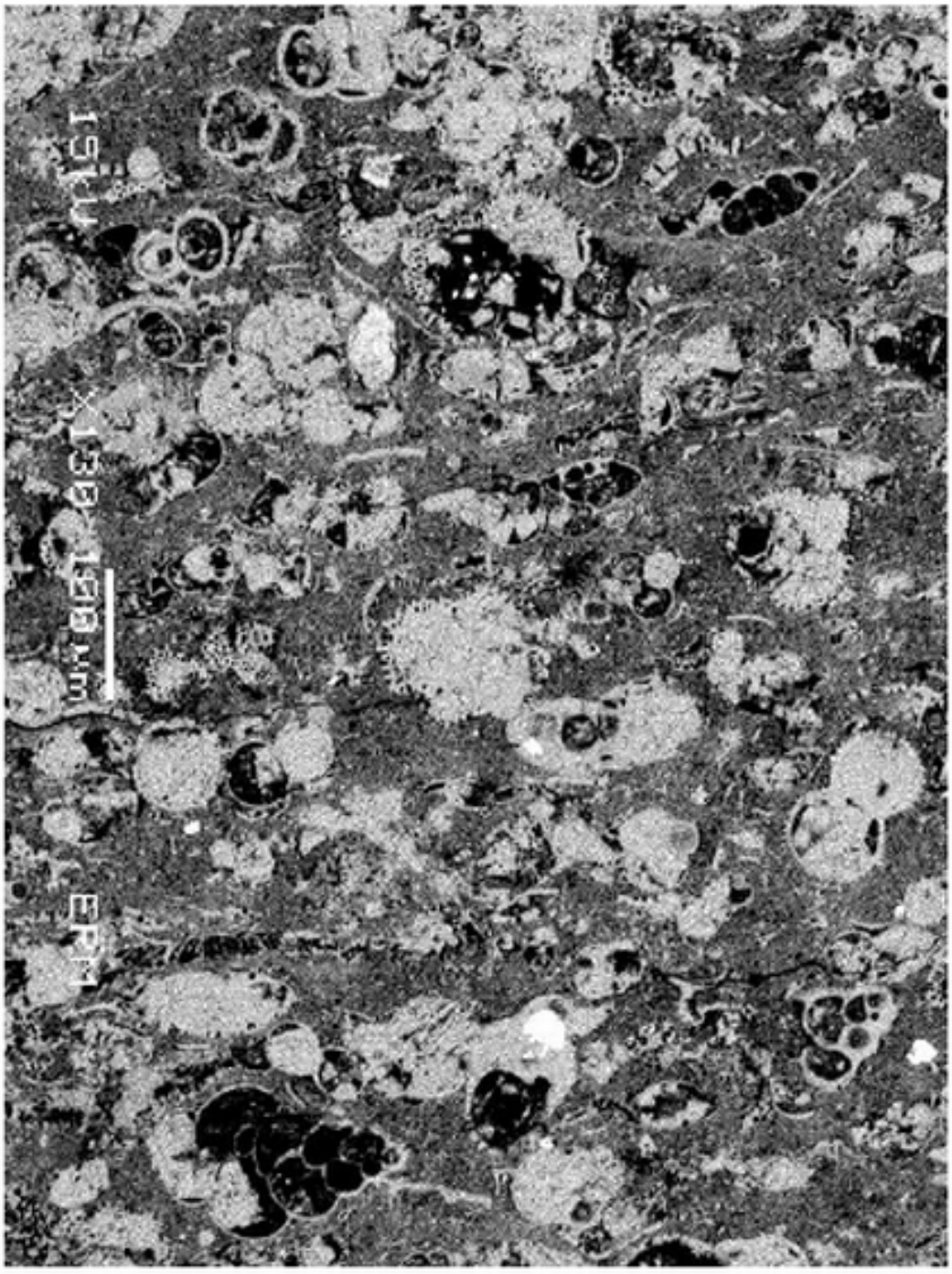

Table 6.10 Chemical composition (%)of the biomicrite obtained with X-Ray. Microfluorescence under SEM on clay carbonate matrix and other minerals. Sample A2 – 10 (cf Table 6.9)

	Na	Mg	Al	Si	P	S	Cl	K	Ca	Cr	Fe	O	Total
Iron oxides				0,63					0,79	1,42	50,99	24,08	77,91
Collophane	0,00	0,00	0,00	0,00	13,00	0,60	0,36	0,00	23,00	0,00	0,00	47,51	84,46
Clay matrix 1	0,56	0,96	4,40	9,49	0,53	0,00	0,52	0,53	17,30	0,51	0,50	47,21	82,49
Clay matrix 2	0,54	1,31	6,14	14,18	2,38	0,00	0,39	0,55	6,10	0,97	0,95	54,37	87,88
Clay matrix 3	0,35	1,29	6,48	13,78	0,88	0,00	0,42	0,75	11,66	0,73	0,83	55,33	92,51
Clay matrix 4	0,34	0,99	4,87	10,96	0,69	0,00	0,31	0,30	11,41	1,59	0,80	47,25	79,52
Clay matrix 5	0,00	1,32	5,92	14,59	1,48	0,00	0,47	0,62	6,31	2,50	2,04	56,50	91,75

Figure 6.21 Photomicrograph (x-nicols) of biomicrite showing a small fracture underlined with brown-coloured organic matter. Sample A1 – 1. Scale: 1 cm = 240 µm.

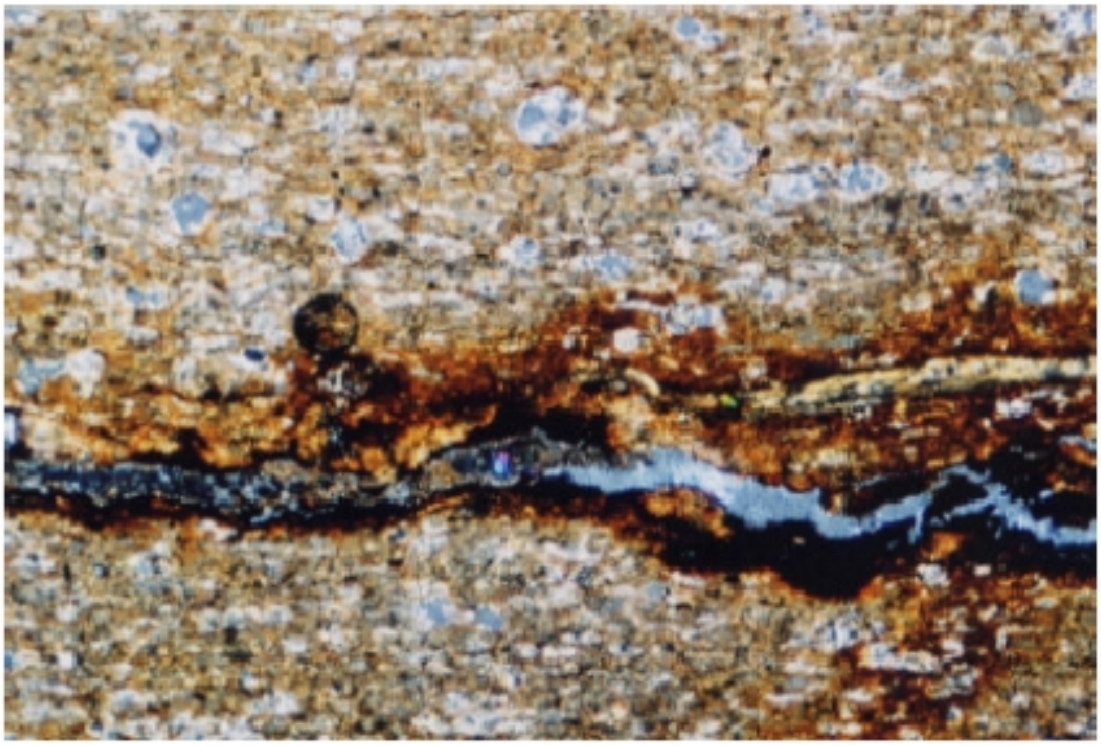

Analogue cement zone (ACZ)

The ACZ, located in the upper part of the studied profile, was characterised by a highly fractured and recrystallised carbonate matrix. Secondary minerals observed infilling fractures included carbonates, zeolites and crypto-crystalline phases with morphologies similar to calcium silicates observed in Maqarin (see Milodowski et al., 1992a, 1992b; 1998a, 1998b).

Macroscopically, the cement zone showed greater uniformity due to the significant increase in the carbonate content. Petrographical study showed that the structure of the analogue cements was similar to the biomicrite. The matrix was rich in organic matter, and the appearance and the content of the bioclast had not changed significantly. The sedimentary bedding was perfectly preserved and highlighted by the bioclasts alignment (Figure 6.22).

Evidence of the replacement of foram tests, and the presence of small calcite and Ca-Na-zeolites (thomsonite?) veins fractures cross-cutting the matrix (Figures 6.23 and 6.24), were very common. Generally, the zeolite content increased towards the top of the profile. Zeolites were also observed to replace the matrix (Figure 6.25).

The chemical composition of the analogue cement matrix, where zeolites were not present, was very similar to the biomicrite. It was characterised by the presence of Si, Ca, Al, Mg and significantly high levels of Cr and Fe (Table 6.11). Where zeolite replaced the matrix, Na and Ca increased and Cr and Fe disappeared.

Figure 6.22 Photomicrograph (x-nicols) of analogue cement. Sample A3 – 3. Scale a: 1cm = 340 µm

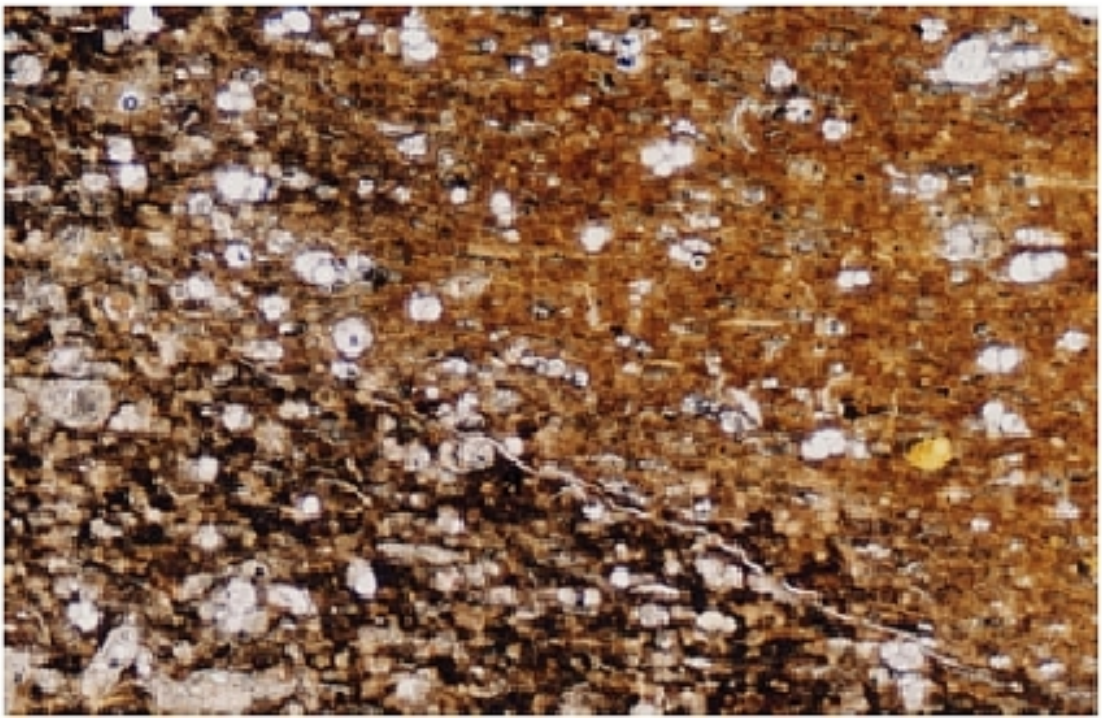

Figure 6.23 Backscattered SEM image on thin section showing the foram tests filled by calcite (light grey) and Ca-Na-zeolites (dark grey). Sample A3 – 1

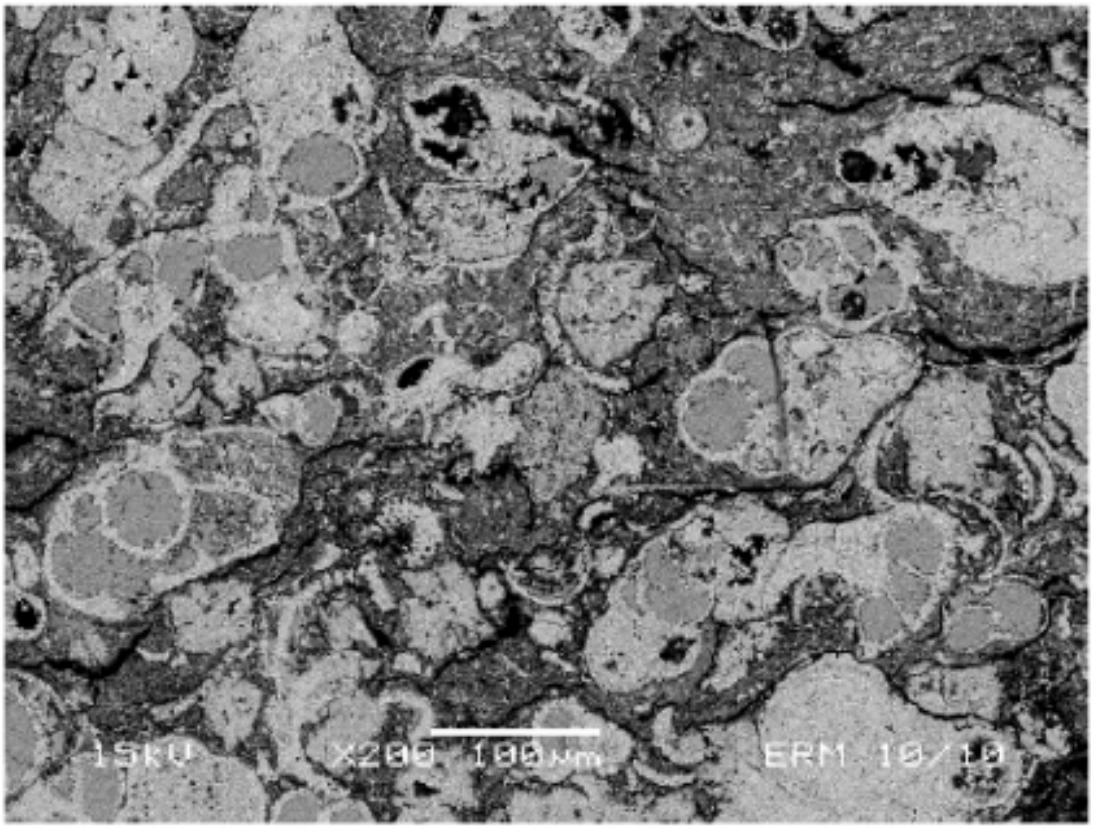

Figure 6.24 Photomicrograph (x-nicols) showing a small zeolite vein in the analogue cement. Sample A3 – 2. Scale: 1 cm = 240 µm

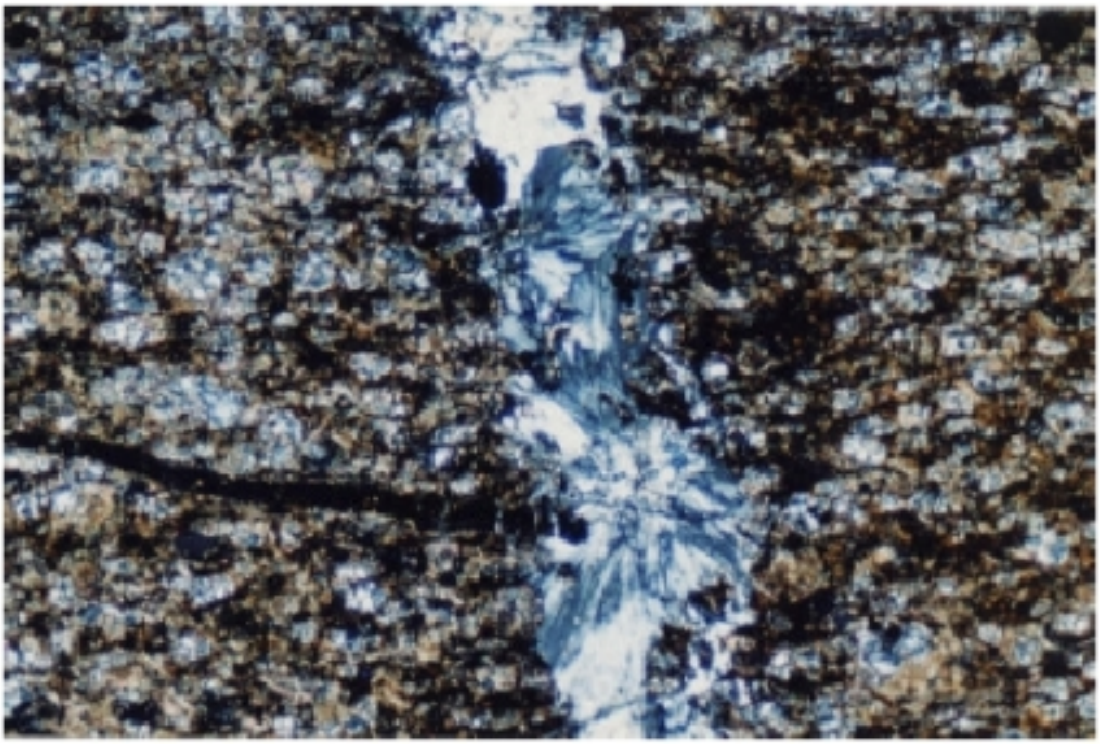

Table 6.11 Chemical composition (%) of the analogue cement matrix and separated phases (obtained with X-Ray Microfluorescence under SEM. Sample A3 - 3 (analyses done on section shown in Figure 6.25)

	Na	Mg	Al	Si	P	S	Cl	K	Ca	Cr	Fe	O	Total
Pyrite and matrix	0,57		3,85	5,02		18,65			3,14		23,52	45,25	100,00
Foraminifers full of zeolite 1	1,54		16,83	21,54					14,33			45,76	100,00
Foraminifers full of zeolite 2	1,54		16,19	21,52					15,22			45,53	100,00
Foraminifers full of zeolite 3	1,36		16,76	21,88					14,08			45,92	100,00
Zeolite matrix 1	1,32	0,16	15,90	22,24					13,28		1,35	45,74	100,00
Zeolite matrix 2	1,19		15,64	20,76					17,47			44,95	100,00
Zeolite matrix 3	1,00		16,08	22,42				0,64	13,96			45,90	100,00
Grey matrix 1		1,89	5,27	18,71	0,79		0,91	1,05	22,07	2,96	5,97	40,38	100,00
Grey matrix 2	0,15	1,86	5,99	20,40	1,33		1,32	1,33	14,53	3,57	7,32	42,20	100,00
Grey matrix 3		1,71	5,92	18,92			0,83	1,19	21,52	2,92	6,90	40,10	100,00
Grey matrix 4		1,58	4,68	17,49	2,32		0,90	1,21	19,56	2,90	9,20	40,15	100,00
Collophane			0,34		15,91	1,03	0,85		42,52			39,35	100,00

Figure 6.25 Backscattered SEM image of thin section showing (a) the matrix in an optically dark spot containing high quantities of zeolite and (b) in other part of the rock. Sample A3 – 3

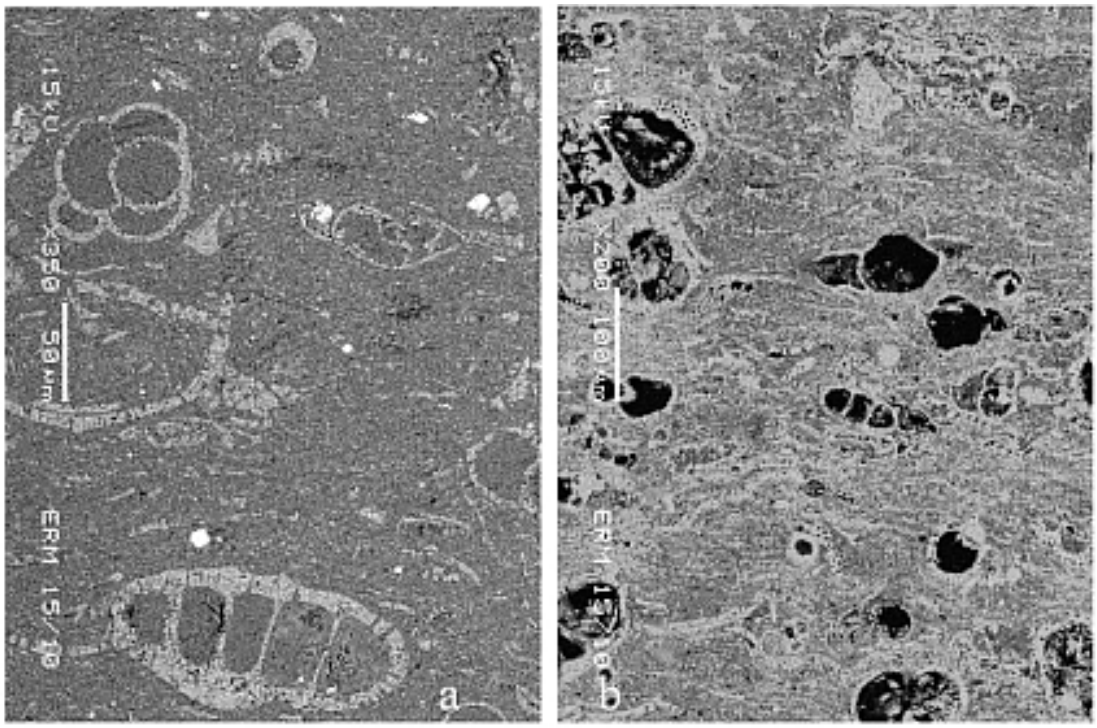

Contact between the ACZ and the biomicrite

The structure of the rock in the contact between the ACZ and the underlying biomicrites was deformed (Figure 6.26) by ubiquitous carbonate recrystallisation in the matrix and in the foram tests. Numerous microfractures were also present, oriented perpendicularly to the main fractures and filled by secondary minerals, such as gypsum, calcite and some scarce zeolites (heulandite-type, Table 6.12). Small zones containing clay minerals can be also observed (Figures 6.27 and 6.28). These clay minerals were Cr-rich (Table 6.12) and are probably volkonskoite-type (Cr-smectite; Khoury et al., 1984). The genesis of these fractures is unclear but, at the field scale, both Rassineux (2000) and Smellie (2000) reported vertical to sub-vertical fractures running perpendicularly across the sub-horizontal biomicrite/cement contact. They are observed to cross-cut the main pyrometamorphic features and so are assumed to at least post-date the combustion episode. Whether they pre- or post-date the hyperalkaline leachate/host rock interaction is less clear. The presence of gypsum, calcite and volkonskoite all suggest, in comparison with the Maqarin site, that these are late hyperalkaline leachates, more representative of the low-alkali/high silica phase of cement leachates (stage III of Berner, 1987).

Figure 6.26 Photomicrograph (x-nicols) of contact between the analogue cement zone and the biomicrite. Sample A3 – 6. Scale 1 cm = 340 µm.

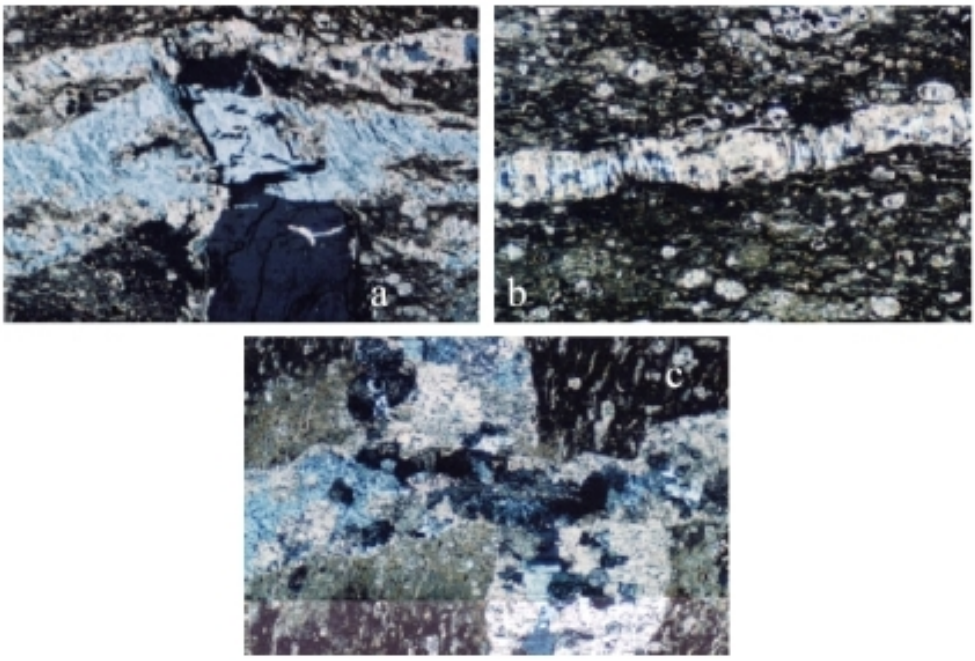

Table 6.12 Chemical composition (%) of the biomicrite matrix at the contact with the analogue cement zone (X-Ray Microfluorescence under SEM). Sample A3 - 6. See also Figure 6.27.

	Na	Mg	Al	Si	P	S	Cl	K	Ca	Cr	Fe	O	Total
Gypsum fissure (9a)			0,69	1,77		21,74			29,04			46,76	100,0
Iron oxide (9a)			0,64	1,70					1,43	1,25	71,17	23,82	100,0
Gypsum (9a)				1,40		22,19			29,73			46,68	100,0
Iron oxide (9b)		0,51	2,31	4,36					3,58	0,89	61,65	26,70	100,0
Calcium phosphates (9b)	0,28		1,68	5,55	12,72	0,57	1,20		35,80		2,11	40,09	100,0
Zeolite ± calcite (9c)	1,13		8,63	24,22			0,21	0,46	21,14			44,20	100,0
Zeolite ± calcite (9c)	0,65		8,57	26,19		0,33	0,43	0,63	17,78			45,41	100,0
Stick fissure (9c)	0,74		8,94	25,50		4,54			11,60			48,68	100,0
Needle zeolite (9c)	0,97	0,17	7,39	33,24			1,93	0,51	7,70			48,08	100,0
Zeolite matrix (9b)	1,08	0,13	6,32	36,15			1,27	0,76	4,92			49,38	100,0
Clay (9b)		3,04	13,17	29,07			1,01		4,65	0,92		48,70	100,0
Z matrix + darker (9b)		1,32	7,55	16,88	0,83		0,67		30,05	2.00		40,69	100,0
"Foraminifer zeolite" (9b)	1,14		6,79	35,31			1,45	0,47	5,77			49,06	100,0
"Foraminifer zeolite" (9b)	1,07		6,66	36,03			1,26	0,40	5,12			49,46	100,0
Chromic clay (9d)	0,09	5,26	8,02	26,72	0,45			0,89	6,74	4,91		46,92	100,0
Chromic clay (9d)		4,78	7,99	26,00	0,56			0,73	7,11	3,99		48,84	100,0
Chromic clay (9d)	0,22	4,94	7,62	25,12	0,84			1,12	6,42	5,97	1,86	45,89	100,0

Figure 6.27 Backscattered SEM image of thin section of the contact zone showing various morphologies of rock: (a) vein filled with gypsum and calcite and rare black clusters of organic matter; (b) relict foram tests; (c) small acicular zeolite crystals in carbonates; (d) zones containing Cr-rich clays between recrystallised carbonates. Sample A3-6. See also Table 6.12 for chemical analysis.

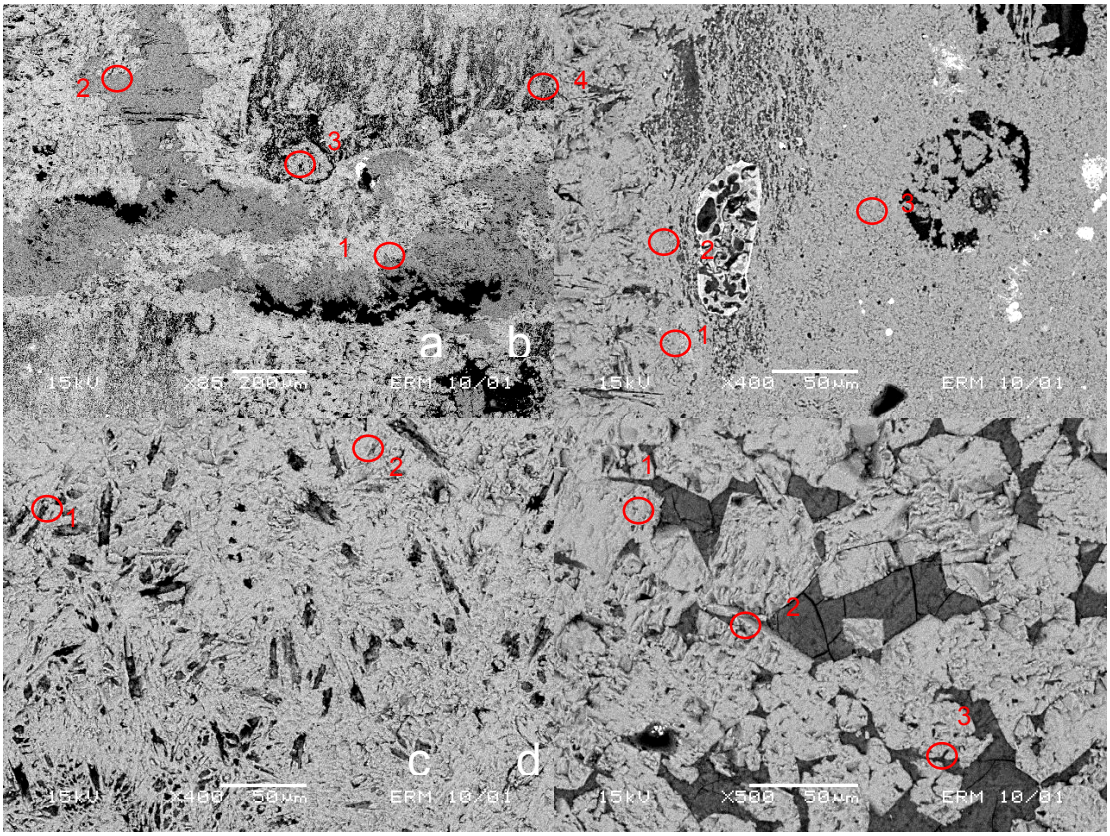

Figure 6.28 Photomicrograph (x-nicols) of the analogue cement showing vein filled with mixed secondary phases. Scale 1 cm = 240 µm

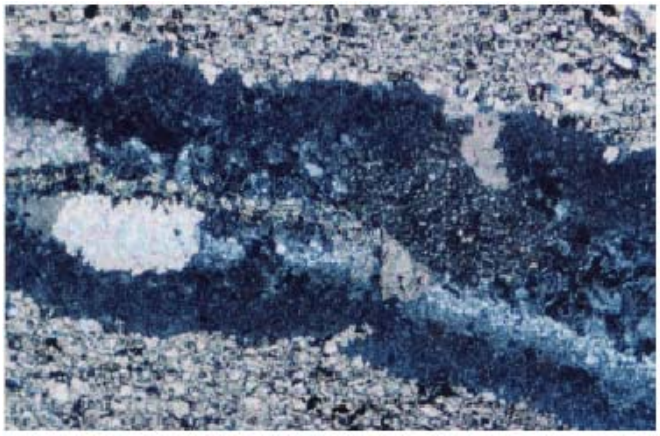

Furthermore, there is no evidence of wallrock alteration along these features, which again suggests (in comparison with observations from Maqarin,) that they have not been involved in carrying any highly reactive hyperalkaline leachates. It seems more likely that they are late joints that have dilated as a result of uplift and stress relief, or in response to regional

tectonism. The gypsum mineralisation, for example, is quite typical of evaporative 'soil moisture' precipitates (i.e. gypcrete) that are commonly found in soils in arid climates like this area. In fact, along the cuttings of the old railway line (to the west of Khushaym Matruk and the Khan-ez-zabib site), the same kind of gypsum infillings of similar types of joints can be observed in the Cretaceous micritic rocks. These have nothing to do with any nearby 'cement zone' material.

This does not argue against the zeolites (see Figure 6.27) being representative of interaction with higher pH period leachates (see also Section 6.3.6) as such multiple events are commonplace at Maqarin (e.g. Milodowski et al., 1992a, 1992b; 1998a, 1998b). Nevertheless, it does indicate that the relative order of replacement of the original matrix by these secondary phases needs to be examined in more detail. It should also be noted that heulandite is commonly found in carbonate rocks which have not undergone hyperalkaline reaction (e.g. Brown et al., 1969; Milodowski and Wilmot, 1985; Jeans, 2006) and so care has to be taken to define the precise mechanisms involved in this case.

Mineralogy: details

Along the trench profile, the carbonate content of the rocks lies between 66 and 83% (using the Bernard calcimeter), generally increasing towards the ACZ. This is in agreement with the XRD analysis in bulk samples: calcite was the main component with low content of detrital phases (quartz, K-feldspars, mica and Ti-oxides) and clay minerals. The percentage of these accessory minerals decreased towards the ACZ. Fracture fillings were mainly composed of secondary gypsum in biomicrites, while complex assemblages of calcite, gypsum and calco-sodic zeolites were present in wall-rock, and fracture fillings were observed in the ACZ.

XRD study of decarbonated clay fractions revealed a significant evolution of clay minerals with distance along the trench. XRD patterns of randomly oriented powders (Figure 6.29) showed:

- that, moving towards the cement zone, the basal reflection intensities decreased significantly while the hkl reflections showed similar intensities along the profile. This means that crystallinity of clay minerals decreased, mainly in the c direction.
- the presence of a high background in the 22-28 °2θ angular domains in the samples near the cement zone could be attributed to poorly crystallised or amorphous phases.

Figure 6.29 XRD patterns of randomly oriented powders of decarbonated clay fractions

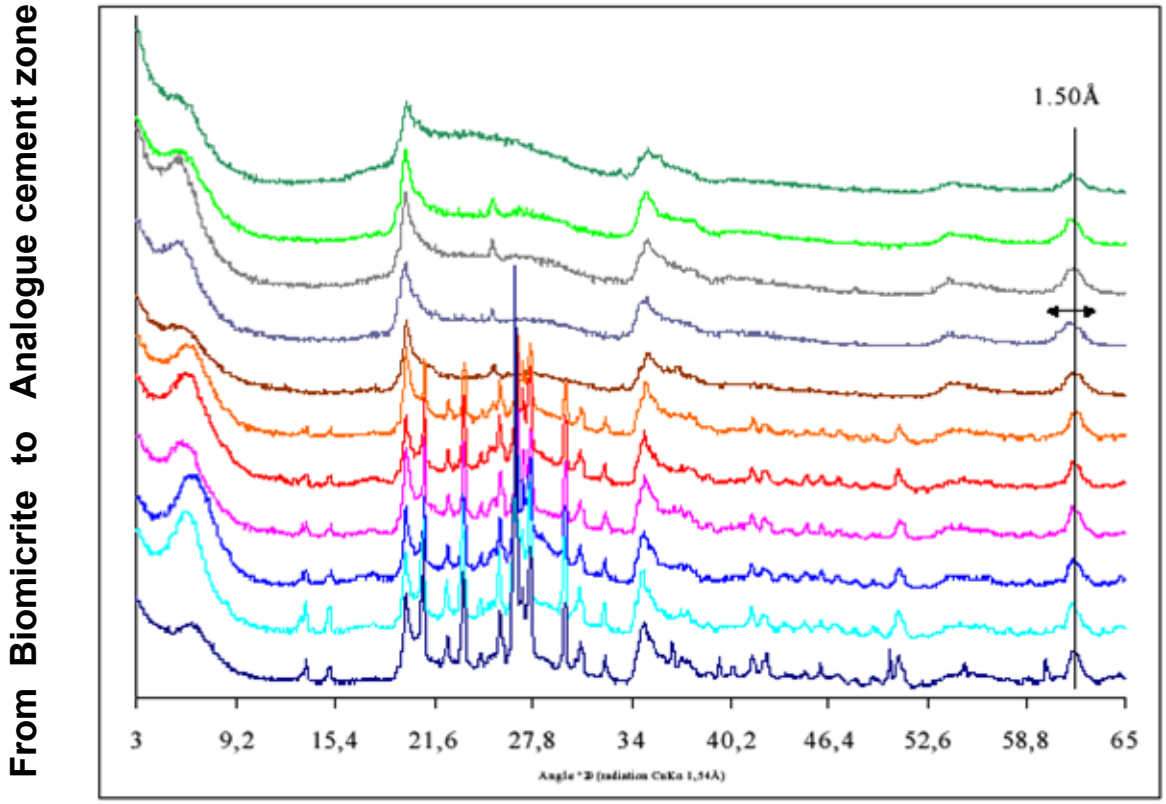

XRD patterns of natural and ethylene-glycol solvated samples are shown in Figure 6.30. The presence of expandable layers (smectite type) and the small amounts of 10 Å collapsed layers in a random mixed-layer was deduced from the position of basal reflection and from the broad 001 reflection with a high low-angle shoulder (Moore and Reynolds, 1989). The percentage of smectite layers, interstratified with illite-like layers, quantified using the procedure described by Inoue et al. (1989), decreased as a function of the distance from the cement. Expanded layers varied from 80 % for biomicrites to 60 % for the cements. Generally, mixed layer illite-smectite decreases in its expandability on moving upward from the parent rock to the ACZ.

Figure 6.30 *XRD patterns of oriented and air dried preparations (A) and of oriented and ethylene-glycol solvated (B) of decarbonated clay fractions. (Fractions extracted from samples collected in the trench, from the biomicrites to the Analogue Cement Zone).*

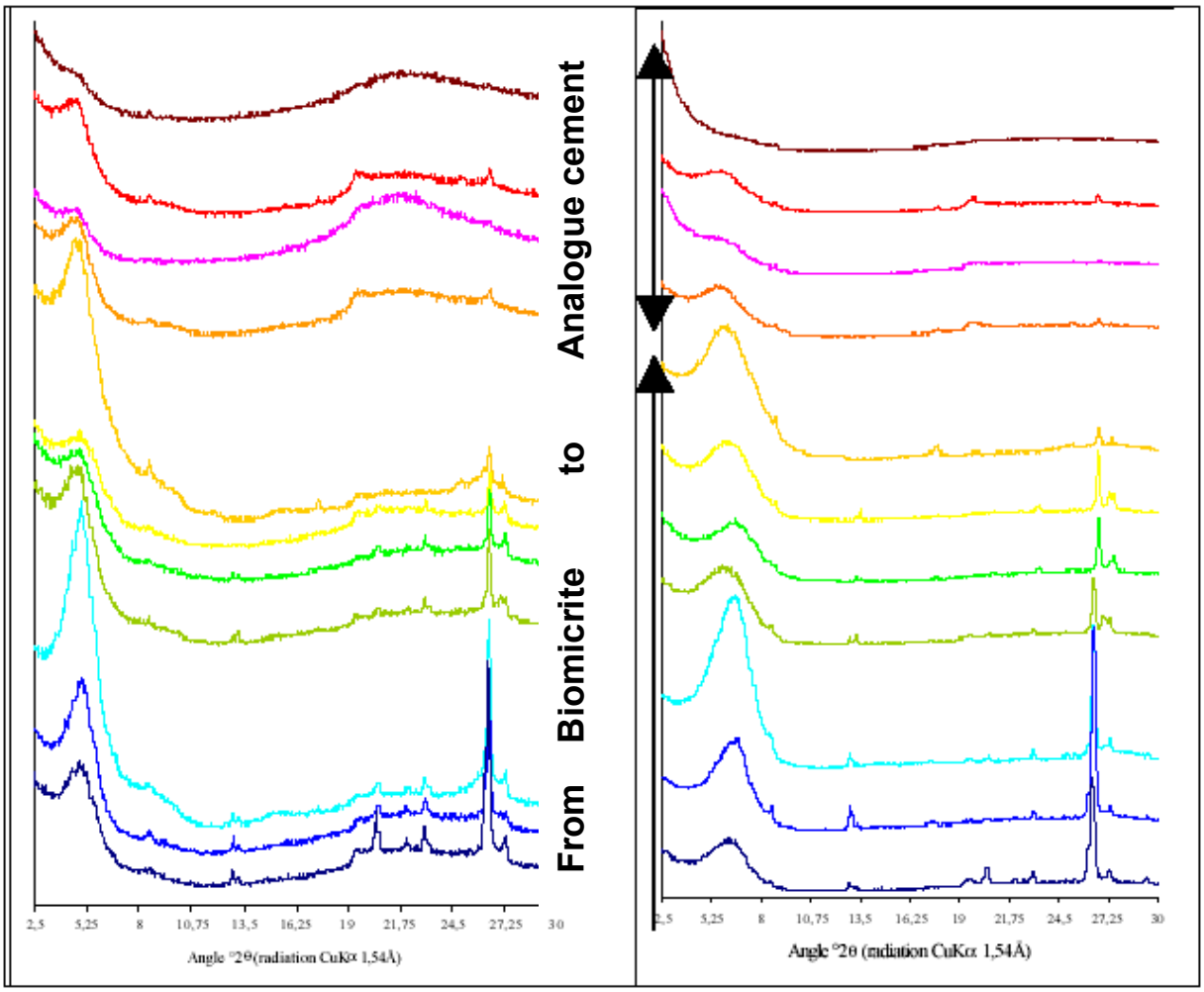

Figure 6.31 XRD patterns of decarbonated clay fractions after the Hofmann and Klemen (1950) treatment.

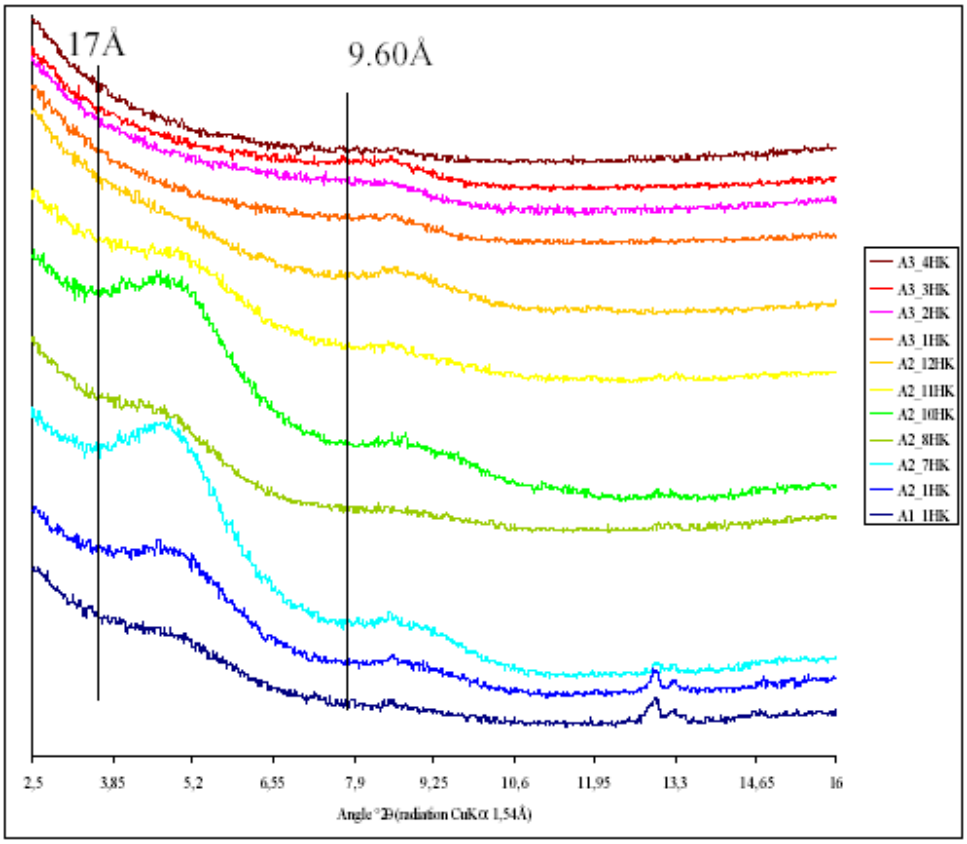

The location of the layer charge in the expandable layers of the smectite was investigated using the Hofmann and Klemen treatment (Hofmann and Klemen, 1950). At the bottom of the trench, in the biomicrite, smectite has beidellitic structure (expandable layers near 17 Å, Figure 6.32) while at the top of the trench, smectite was mainly montmorillonite (layers collapsed at about 9.60 Å, Figure 6.33).

Figure 6.32 *XRD patterns of decarbonated clay fraction after intercalation with the alkylammonium cation (nC = 12).*

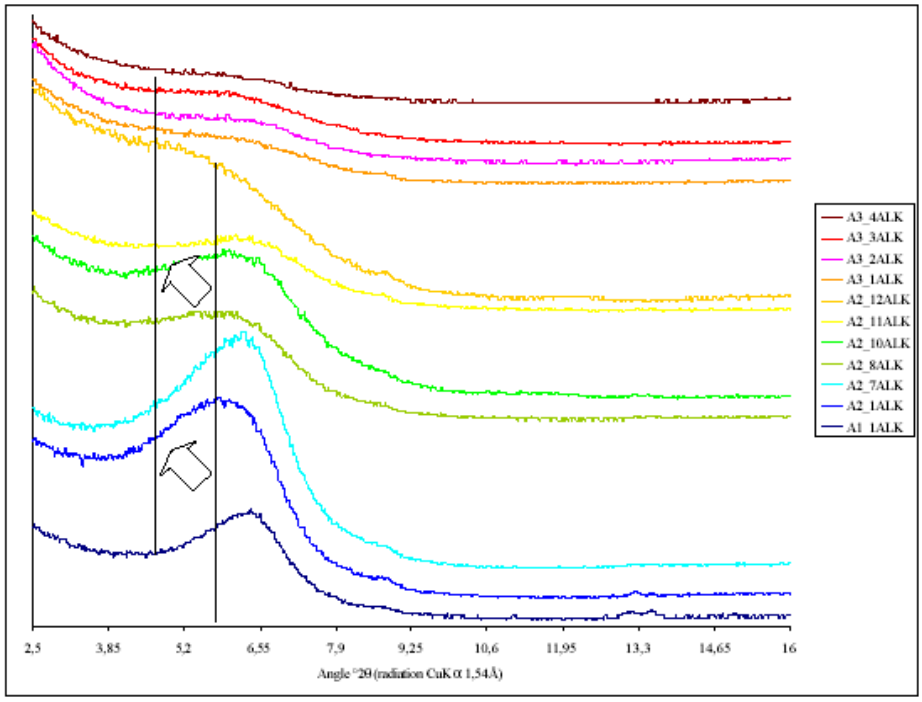

Figure 6.33 *Evolution of mean proportions of minerals calculated by a semi-quantitative approach on decarbonated clay < 2 µm fraction as a function of the distance to the Analogue Cement Zone.*

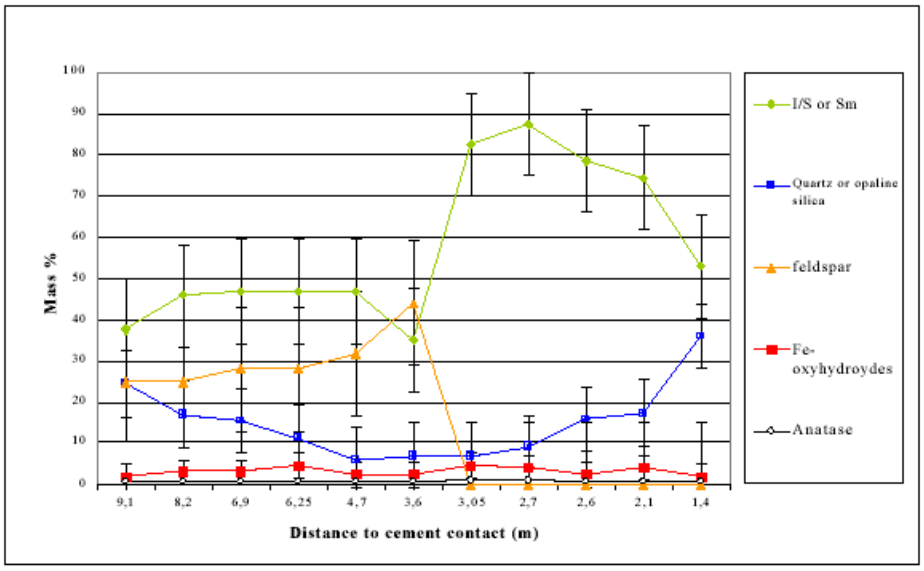

Intercalation of alkylammonium ions in the interlayer space was performed to evaluate the layer charge of smectites (Olis et al., 1990). Actually, the 001 position in the XRD patterns of samples saturated with alkylammonium ions increases with the magnitude of the layer charge. Slight variation in the position of smectite basal reflection along the profile (Figure

6.31) indicated a slight increase in layer charge in contact with alkaline rocks. Values of layer charge went from 0.56-0.60 ± 0.06/unit cell (001 reflection at 14.5 Å) in biomicrites up to 0.68-0.72 ± 0.06/unit cell in samples near the contact with the ACZ (001 reflection at about 17 Å).

A semi-quantitative mineralogical analysis was performed from the chemical composition, the mineralogical assemblage identified by XRD and the CEC values. The evolution of the mean content in different minerals of the decarbonated clay fraction (Figure 6.33) was characterised by:

- an increase of mixed layer illite-smectite minerals near the cement contact.
- a decrease of detrital accessory minerals (quartz and feldspars) associated with an increase of free silica (probably amorphous silica).

Geochemistry

Chemical analysis was performed on decarbonated clay fractions collected at between 5.5 and 6 m from the cement contact (Table 6.13). The average content of clay-sized fraction (<2μm) in the bulk sample was 12.3 ± 3.0 %. Although variable, a decrease in the content of most of the analysed elements was observed in the cement, when compared to the biomicrites with a concomitant increase in silica.

Table 6.13 Chemical composition of the decarbonated clay fractions (% oxides). Note that sample A1 is at the bottom of the trench, in the biomicrite, and A3 is in the cement

	SiO2	Al2O3	MnO	MgO	CaO	Na2O	K2O	TiO2	Fe2O3	1000°C	TOTAL
A1-1	62,93	16,52	0,00	1,49	0,18	0,00	3,92	0,74	4,07	7,99	97,84
A2-1	56,72	17,99	0,00	1,85	0,65	0,09	3,69	0,87	6,04	9,36	97,26
A2-7	57,44	18,64	0,00	1,90	0,28	0,12	3,21	0,97	6,18	8,84	97,58
A2-8	54,26	18,93	0,00	1,60	0,61	0,25	3,24	1,07	8,40	9,62	97,99
A2-10	54,75	20,79	0,00	1,86	0,84	0,12	3,22	1,02	4,60	10,41	97,62
A2-11	55,31	19,26	0,00	1,96	0,71	0,37	2,88	0,96	4,63	10,60	96,67
A2-12	52,96	18,98	0,00	2,27	1,37	0,14	1,37	0,99	8,17	11,09	97,34
A3-1	58,07	13,86	0,00	3,82	1,18	0,00	1,53	0,83	8,12	10,70	98,11
A3-2	61,07	14,28	0,00	3,21	0,76	0,04	1,02	0,92	5,34	10,62	97,27
A3-3	59,92	13,05	0,00	3,07	1,05	0,04	1,61	0,93	8,17	10,27	98,10
A3-4	67,63	10,74	0,00	2,42	0,96	0,03	0,68	0,60	4,02	11,19	98,27

Cation exchange capacity (CEC)

The CEC values of decarbonated clay fractions ranged between 35 and 65 meq/100 g and were lower at the bottom of the profile (Table 6.14). The chemical composition of the exchange complex is shown in Table 6.14. The exchange complex was saturated in calcium, which concentration went up to 45 meq/100 g, being concentrated in sodium and potassium by less than 2 meq/100 g. Two important facts were observed. On the one hand, magnesium increased signififcantly on approaching the ACZ. On the other hand, the difference between the exchangeable cations and the CEC increased in the biomicrites. This

could be attributed to the presence of non-analysed exchangeable cations like protons, aluminum, ammonium, barium, or to the influence of organic colloids coating the mineral surface.

Table 6.14 Cation exchange capacity (CEC) and exchangeable cations in decarbonated clay fractions (in cmol Kg-1 or meq/100 g). See Figure 6.18 for the sample position

Sample	Ca	Mg	Na	K	Σ exchangeable cations B.E.	CEC
A1-1	7,31	0,83	0,00	1,81	9,95	31,92
A2-1	22,99	1,58	4,59	0,74	29,90	41,54
A2-7	7,96	1,16	0,00	1,08	10,20	41,48
A2-8	23,29	1,63	0,43	1,52	26,87	42,60
A2-10	27,27	2,78	0,00	1,73	31,78	42,04
A2-11	24,32	3,47	0,00	2,04	29,83	29,92
A2-12	40,78	5,85	0,00	1,17	47,80	56,97
A3-1	44,42	14,01	0,00	1,87	60,30	63,12
A3-2	24,32	17,07	0,00	0,12	41,51	54,33
A3-3	28,69	13,12	0,00	0,99	42,80	51,63
A3-4	24,85	14,20	0,00	0,63	39,68	36,05

6.3.2.4 Conclusions

A significant evolution has been observed along the trench profile which can be characteried as:

- **Joint fillings:** In the biomicrite, which retained the original sedimentary fabric, joints were mainly filled with gypsum. In the ACZ, joints were mainly filled with calcite and thomsonite-like zeolites. Near the ACZ contact, the joint network becomes dense and well-developed. The width of joints was variable. They contained a complex mineral assemblage of calcite, gypsum and some heulandite-like zeolites.
- **Whole rocks:** A strong recrystallisation process, with a significant increase in the carbonate content, was observed when reaching the ACZ contact. Concomitantly, the dissolution was detected of primary silicates of detrital origin (quartz, felspars and micas) and probably of some diagenetic clay contained in the clayey matrix. Discrete amorphous silica could be observed in the more disturbed zones.
- **Clay minerals:** Expandable clays showed significant variation in the value and in the location of the layer charge in the upper part of the ACZ when compared to the biomicrite. Their compositions were quite similar regarding major elements (Mg, Al and Si) but they differed in the Cr concentration. In the ACZ, Cr seemed to be a part of the clay structure and the small grains of Cr oxides which were observed in the clay matrix of the biomicrite were not observed. FTIR analyses on clay should confirm this suggestion. A decrease in the content (80 % to 60 %) of smectite component of illite/smectite mixed-layer clay minerals was observed at the ACZ, when it remained unaffected by main structural transformations.

The observed transformations in the samples from the Khushaym Matruk site were mainly the secondary recrystallisation in the fractures and the mineralogical evolution in the clay-rich matrix near the contact with the ACZ. They appear to post-date the combustion processes and, consequently, they might be attributable to the circulation of hyperalkaline solutions from leaching of the overlying natural cement formation (although other processes, such as weathering, cannot yet be ruled out). This will be discussed further in Section 6.3.4.

6.3.3 Magnetic investigations

6.3.3.1 Introduction

Magnetic investigations conducted on Maqarin samples are reported in Section 4.5. and information on analytical techniques is summarised in Appendix 4. Most detailed references for magnetism are also given in Section 4.5. In Maqarin, the sampling line across the combustion front was nearly horizontally through the subvertical combustion front whereas, in Khushaym Matruk, the combustion front is horizontal and the sampling transect nearly vertical. The sampling line is relatively narrow in Khushaym Matruk (~10 m) but quite long in Maqarin (more than 100 m). The magnetic characterisations in Khushaym Matruk were also coupled to mineralogical and chemical investigations. A profile of oriented samples (see Table 6.15 for details) dedicated to magnetic studies was collected. Some magnetic measurements were also performed on unoriented samples collected for mineralogical purposes.

Table 6.15 List of samples collected in Khushaym Matruk for magnetic investigations. Full details are given in Rassineux (2000) and a full sample list is available in Appendix 6.

Sample reference	Sampling date	Distance above base level (m)	Comment
LA1-1	March 2000	0,2	Dark beige marl
LA1-2	March 2000	0,8	Dark beige marl
LA2-1	March 2000	1,25	Dark beige marl
LA2-2	March 2000	1,4	Beige brown marl
LA2-3	March 2000	1,5	Dark beige marl
LA2-4	March 2000	3,15	Grey brown marl
LA2-5	March 2000	6,3	Brown marl
LA3-1	March 2000	6,6	Grey brown marl
A3-2	March 2000	6,7	Grey marl; fissures with black fillings
LA3-2	March 2000	6,8	Grey marl
A3-3	March 2000	7,2	Dark grey marl
LA3-3	March 2000	7,5	Grey marl, baked, with black and red inclusions
A3-4	March 2000	7,9	Grey marl slightly baked
A3-5	March 2000	8,3	Beige brown pink baked marl; fissures with white fillings
LA3-4	March 2000	8,5	Grey hard marl, baked, fissures with white fillings
A3-6	March 2000	8,8	Dark grey hard baked marl; fissures with white fillings

6.3.3.2 Results and discussion

As with the Maqarin profile discussed in Section 4.5, a significant susceptibility anomaly was found within the biomicrite in Khushaym Matruk (Table 6.16 and Figure 6.34), with maximum susceptibilities of the same order of magnitude. However, the uppermost samples of the profile do not, as in Maqarin, show a return to low values of the susceptibility. It is not excluded, therefore, that the magnetic anomaly has an extension further up in the cements (note that in Maqarin, the magnetic anomaly extended for over 15 m and had two distinct maxima). The evolution of susceptibility with temperature yields Curie temperatures of 620°C (LA3-4, A3-6) and 580°C (A3-5). XRD data obtained on the magnetic extract of sample LA3-4 show the lines characteristic of haematite. The attribution of several XRD lines to maghemite or to magnetite remains, however, uncertain. These findings are consistent with observations in Maqarin and thus suggest that the production of such a magnetic anomaly is likely to be closely associated with the combustion event.

Table 6.16 Magnetic parameters for samples collected in Khushaym Matruk.

Sample Reference	Distance above base level (m)	Hc (kA/m)	Hcr (kA/m)	Mrs (mAm²/kg)	Ms (mAm²/kg)	X(m³/kg)
LA1-1	0,2	-63,24	nd	nd	0,1612	nd
LA1-2	0,8	-222,3	nd	nd	0,7966	nd
LA2-1	1,25	-161,6	nd	nd	0,05146	nd
LA2-2	1,4	80,77	nd	nd	0,1323	nd
LA2-3	1,5	nd	nd	nd	nd	nd
LA2-4	3,15	-11,2	nd	nd	0,484	nd
LA2-5	6,3	9,682	nd	nd	-0,4355	nd
LA3-1	6,6	5,817	nd	nd	0,5936	nd
A3-2	6,7	nd	nd	nd	nd	nd
LA3-2	6,8	8,367	35,75	0,3862	2,503	1,1E-07
A3-3	7,2	nd	nd	nd	nd	nd
LA3-3	7,5	8,375	nd	nd	4,205	1,1E-07
A3-4	7,9	nd	nd	nd	nd	2,9E-07
A3-5	8,3	nd	nd	nd	nd	3,1E-06
LA3-4	8,5	10,77	nd	nd	87,22	1,7E-06
A3-6	8,8	nd	nd	nd	nd	1,4E-06

Figure 6.34 Evolution of the magnetic susceptibility as a function of distance from the cement/biomicrite contact.

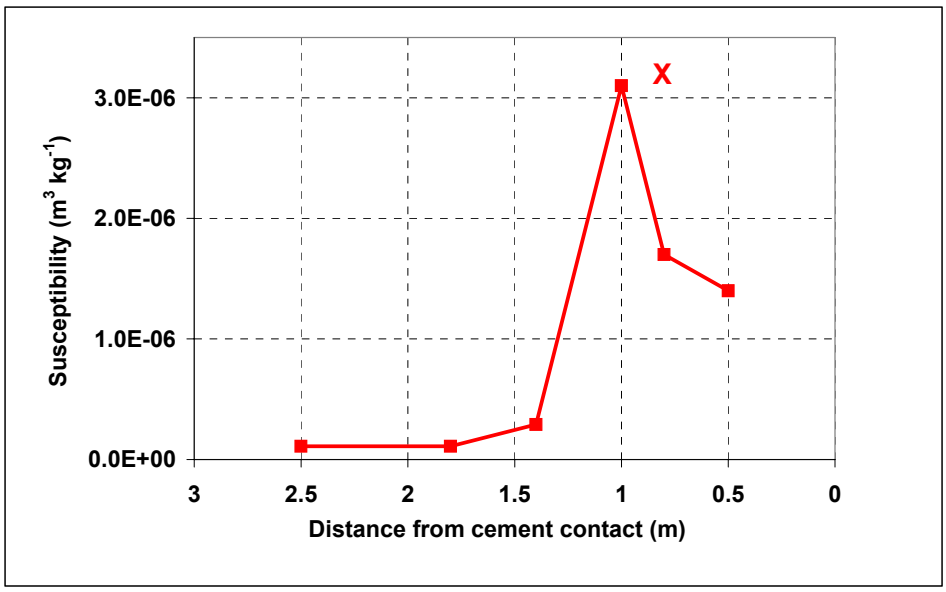

Several oriented samples of Khushaym Matruk (LA3-2, LA3-3 and LA3-4) were studied by applying two different demagnetisation protocols (see Appendix 4 for details), alternative field and thermal demagnetisation. The numerical results are given in Table 6.17 and plotted in Figure 6.35. Note that, because of the low number of studied samples and because palaeomagnetic studies are generally based on statistics on a large number of samples, the results presented here must be considered as preliminary. In particular, on several samples the signal was weak and noisy. Sample LA3-2 gave the best results, showing a magnetic component of normal direction decreasing upon heating, and a marked direction change at temperatures between 280 to 320°C. The vector representation shows then the decrease of a magnetic component of inverse direction. Sample LA3-3 behaves similarly with a direction change at about 200°C. The same inverse magnetic component as in sample LA3-2 is observed above this temperature. For sample LA3-4, the initial normal component is barely visible, and a similar inverse component is then found again. For all these samples, the room temperature susceptibility was fairly stable, which indicates no major mineralogical change during the demagnetisation procedure.

Table 6.17 Results of demagnetisation runs on selected KM samples. For each sample,demagnetisation was done following two different methods: i) by applying successive temperature stages specified in °C, ii) by applying successive alternative magnetic fields specified in mT. Xc, Yc and Zc are the three components of the magnetic momentum of the sample in the sample coordinate system. MAG is the intensity of the magnetic momentum per volume unit. Dg and Ig are the magnetic declination and inclination in the geographic coordinte system.

Sample	LA32					
T (°C)	Xc (Am2)	Yc (Am2)	Zc (Am2)	MAG(A/m)	Dg	Ig
0	6.81E-08	-4.74E-08	1.24E-07	1.36E-02	325.2	56.3
100	1.28E-08	-1.79E-08	1.39E-08	2.36E-03	305.4	32.2
150	5.86E-09	-1.83E-08	9.05E-09	1.93E-03	287.8	25.3
200	-6.37E-09	-9.94E-09	-1.20E-08	1.53E-03	237.4	-45.4
240	-1.58E-09	-7.87E-09	-5.54E-09	8.87E-04	258.6	-34.6
280	-1.04E-08	-1.32E-08	-4.72E-09	1.59E-03	231.7	-15.7
320	-9.83E-09	-1.25E-08	-3.87E-09	1.49E-03	231.9	-13.7
360	-6.40E-09	-4.76E-09	-2.12E-09	7.51E-04	216.6	-14.9
400	7.94E-09	-2.06E-08	-5.95E-08	5.77E-03	291.1	-69.7
430	3.77E-09	6.09E-10	-2.74E-09	4.27E-04	9.2	-35.6
460	-5.48E-09	-1.91E-09	-3.94E-09	6.38E-04	199.3	-34.2
490	-9.93E-10	7.02E-10	-1.97E-09	2.10E-04	144.8	-58.3

Sample	LA32AF					
AF (mT)	Xc (Am2)	Yc (Am2)	Zc (Am2)	MAG(A/m)	Dg	Ig
0	3.29E-07	-1.72E-07	2.94E-07	4.30E-02	332.4	38.4
25	5.51E-08	1.77E-08	4.86E-08	6.87E-03	17.8	40
50	5.34E-08	1.10E-08	4.59E-08	6.47E-03	11.7	40.1
75	4.58E-08	2.92E-09	3.60E-08	5.30E-03	3.6	38.1
100	3.44E-08	-2.60E-09	2.41E-08	3.83E-03	355.7	34.9
150	1.52E-08	-5.64E-09	7.82E-09	1.63E-03	339.6	25.8
200	6.92E-09	-4.92E-09	-6.42E-11	7.72E-04	324.6	-0.4
250	6.13E-10	-3.76E-09	-1.03E-09	3.59E-04	279.3	-15.1
300	-1.17E-11	-3.92E-09	-7.52E-10	3.63E-04	269.8	-10.9
350	6.91E-10	-2.59E-09	-1.73E-09	2.90E-04	285	-32.8
400	-1.45E-10	-1.91E-09	-6.41E-10	1.84E-04	265.7	-18.5
500	7.27E-11	-1.60E-09	-1.00E-09	1.71E-04	272.6	-32.1
600	1.50E-09	-1.24E-09	-2.40E-09	2.81E-04	320.3	-51
700	-1.57E-09	-1.74E-09	-8.14E-10	2.26E-04	227.9	-19.1
800	-1.30E-10	-8.35E-10	2.33E-10	7.97E-05	261.2	15.4
1000	-9.64E-11	6.09E-10	-5.50E-10	7.51E-05	99	-41.7
1500	-2.99E-08	-3.22E-09	3.40E-09	2.75E-03	186.1	6.4

Sample	LA33					
T (°C)	Xc (Am2)	Yc (Am2)	Zc (Am2)	MAG(A/m)	Dg	Ig
0	3.11E-07	7.57E-09	3.52E-07	4.27E-02	1.4	48.5
100	-6.61E-08	-7.24E-08	-1.01E-07	1.28E-02	227.6	-46
150	-1.00E-07	-6.48E-08	-1.19E-07	1.53E-02	212.9	-44.9
200	-9.23E-08	-6.93E-08	-1.49E-07	1.71E-02	216.9	-52.1
240	-4.47E-08	-2.30E-07	-8.89E-08	2.28E-02	259	-20.8
280	-3.33E-08	-9.00E-08	-7.61E-08	1.11E-02	249.7	-38.4
320	-5.13E-08	-9.31E-08	-8.07E-08	1.21E-02	241.2	-37.2
360	-4.43E-08	-3.48E-08	-5.40E-08	7.09E-03	218.1	-43.8
400	-6.59E-09	-6.96E-09	5.30E-10	8.73E-04	226.6	3.2
430	4.25E-08	6.12E-09	1.03E-08	4.01E-03	8.2	13.4
460	-1.03E-09	2.20E-10	6.85E-10	1.14E-04	168	33
490	-1.64E-08	1.64E-08	-8.67E-09	2.25E-03	135	-20.5

Sample	LA33AF					
AF (mT)	Xc (Am2)	Yc (Am2)	Zc (Am2)	MAG(A/m)	Dg	Ig
0	5.43E-08	2.09E-08	5.07E-08	7.02E-03	21	41.1
25	3.07E-07	-1.43E-07	2.83E-07	4.01E-02	335	39.9
50	2.56E-07	-1.08E-07	2.63E-07	3.48E-02	337.1	43.4
75	1.84E-07	-7.55E-08	2.05E-07	2.59E-02	337.7	45.9
100	1.11E-07	-6.24E-08	1.28E-07	1.64E-02	330.7	45
150	1.74E-08	-5.97E-08	3.01E-08	6.28E-03	286.2	25.9
200	-2.55E-08	-5.05E-08	5.67E-10	5.14E-03	243.2	0.6
250	-1.56E-08	-4.08E-08	-8.60E-09	4.05E-03	249.1	-11.1
300	3.16E-09	-2.28E-08	1.47E-08	2.48E-03	277.9	32.7
350	4.67E-09	-1.66E-08	2.07E-08	2.45E-03	285.7	50.2
400	8.76E-09	-8.95E-09	2.81E-08	2.79E-03	314.4	65.9
500	1.00E-08	7.28E-10	3.15E-08	3.00E-03	4.2	72.3
600	1.80E-07	6.51E-10	1.21E-08	1.64E-02	0.2	3.8
700	2.16E-08	2.60E-09	2.91E-08	3.30E-03	6.9	53.3
800	1.27E-08	9.64E-09	3.04E-08	3.12E-03	37.3	62.4
1000	2.52E-08	-3.90E-09	2.31E-08	3.13E-03	351.2	42.2
1500	2.33E-07	1.38E-10	-1.09E-08	2.12E-02	0	-2.7

Sample	LA34					
T (°C)	Xc (Am2)	Yc (Am2)	Zc (Am2)	MAG(A/m)	Dg	Ig
0	-3.81E-06	-7.28E-06	-5.60E-06	9.04E-01	242.4	-34.3
100	-6.20E-06	-6.84E-06	-7.91E-06	1.11E+00	227.8	-40.6
150	-7.22E-06	-5.75E-06	-8.34E-06	1.13E+00	218.6	-42.1
200	-5.96E-06	-7.05E-06	-8.68E-06	1.15E+00	229.8	-43.2
240	-4.46E-06	-7.60E-06	-7.81E-06	1.07E+00	239.6	-41.6
280	-6.86E-06	-6.50E-06	-6.91E-06	1.06E+00	223.4	-36.2
320	-5.98E-06	-5.34E-06	-6.96E-06	9.65E-01	221.7	-41
360	-5.04E-06	-5.62E-06	-6.82E-06	9.25E-01	228.1	-42.1
400	-4.02E-06	-3.19E-06	-5.71E-06	6.98E-01	218.5	-48.1
430	-3.89E-06	-3.05E-06	-3.94E-06	5.75E-01	218	-38.5
460	-1.65E-06	-1.35E-06	-1.96E-06	2.63E-01	219.4	-42.5
490	-1.25E-06	-8.14E-07	-2.60E-06	2.72E-01	213	-60.1

Sample	LA34AF					
AF (mT)	Xc (Am2)	Yc (Am2)	Zc (Am2)	MAG(A/m)	Dg	Ig
0	-4.30E-06	-6.10E-06	-7.41E-06	9.57E-01	234.8	-44.8
25	-4.15E-06	-6.27E-06	-6.95E-06	9.31E-01	236.5	-42.8
50	-3.98E-06	-6.85E-06	-6.43E-06	9.28E-01	239.8	-39.1
75	-4.39E-06	-7.25E-06	-5.96E-06	9.42E-01	238.8	-35.1
100	-5.12E-06	-7.38E-06	-5.84E-06	9.74E-01	235.3	-33
150	-6.30E-06	-6.98E-06	-5.87E-06	1.01E+00	227.9	-32
200	-5.82E-06	-5.95E-06	-5.31E-06	8.98E-01	225.6	-32.6
250	-4.92E-06	-4.46E-06	-4.85E-06	7.47E-01	222.2	-36.2
300	-3.92E-06	-3.05E-06	-3.63E-06	5.59E-01	217.9	-36.2
350	-3.03E-06	-2.08E-06	-1.98E-06	3.79E-01	214.5	-28.3
400	-1.07E-06	-1.39E-06	-1.41E-06	2.04E-01	232.4	-38.8
500	6.42E-07	-9.66E-07	-9.15E-07	1.34E-01	303.6	-38.3
600	7.31E-07	2.63E-08	-3.58E-08	6.66E-02	2.1	-2.8
700	-6.60E-07	-4.74E-07	3.28E-07	7.97E-02	215.7	22
800	1.68E-06	-7.91E-07	2.37E-07	1.70E-01	334.8	7.2
1000	3.20E-06	6.94E-07	-3.49E-07	2.99E-01	12.2	-6.1
1500	9.78E-06	1.83E-07	-9.79E-07	8.94E-01	1.1	-5.7

Figure 6.35 Zijderveld diagrams for selected samples from Khushaym Matruk.

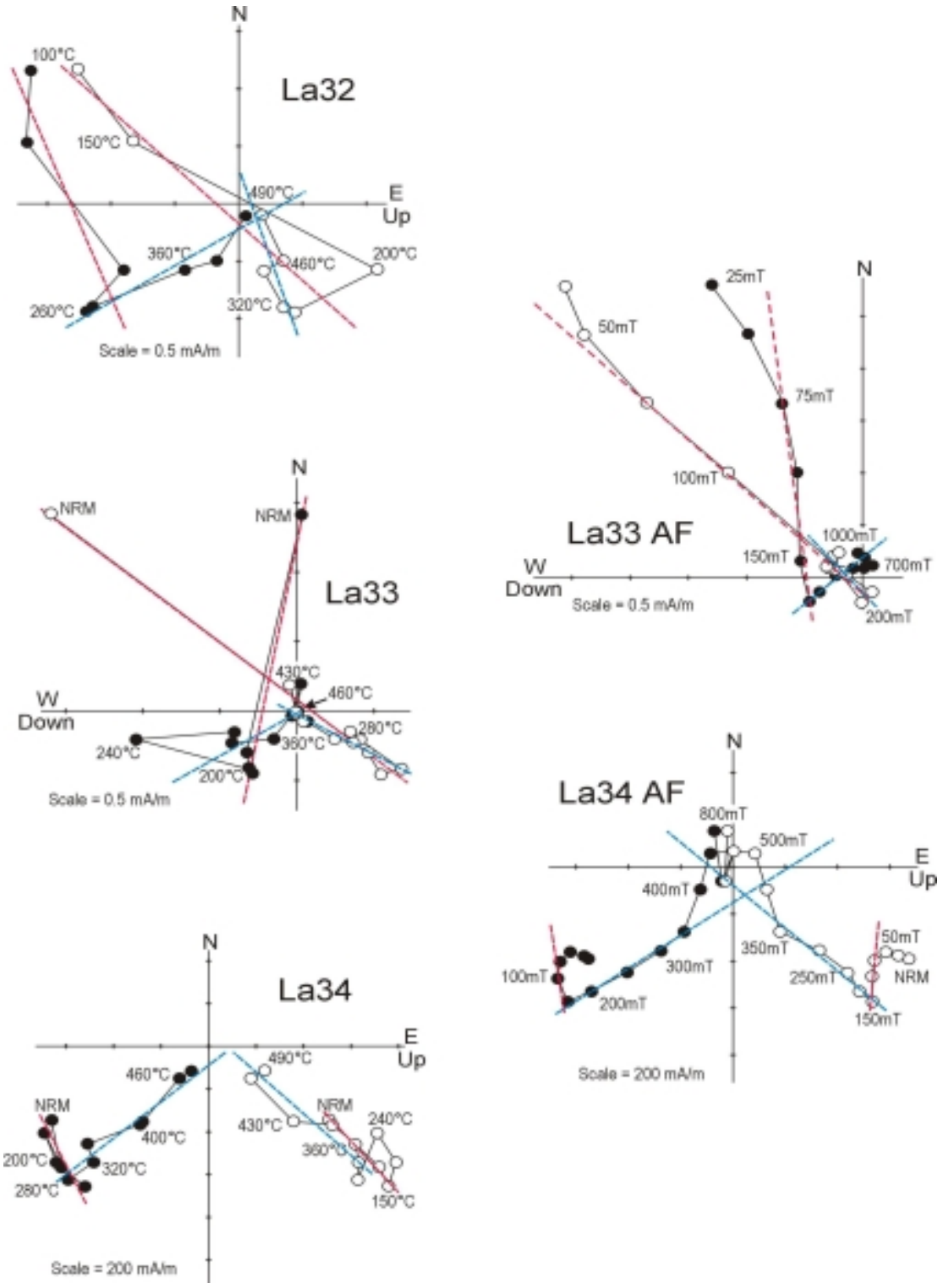

The directions of the normal and inverse field components found on the samples were estimated by statistical means (Table 6.18). The normal component is probably recent, corresponding to a normal field orientation period during the last million years (Bruhnes is not excluded). This component is best interpreted as originating from the combustion event

(heating around 200-350°C). As the samples were collected in the trench and appeared fresh, the existence of a magnetic direction linked to weathering is not probable and is discarded. The inverse component is found on all samples. It is presently interpreted as being the palaeomagnetic print of the biomicrite before combustion. However, the measured declination (234° +/- 15°) is relatively far from what is expected for a Cretaceous direction (150-170°). The difference implies a clockwise rotation of about 75° which is incompatible with the sinistrial character of the Jordan Rift Valley fault, and this unresolved point deserves further investigation.

Table 6.18 Calculated characteristics of the normal and inverse magnetic components determined in the KM samples LA32, LA33 and LA34 studied by thermal and AF demagnetisation. D: declination; I: inclination; N: sample number; K: Fischer parameter; □95: confidence angle for a probability of 95 %

Component Name	D	I	N	K	α95
Normal	350°	45°	5	50	13°
Inverse	234°	-29°	5	34	13°

Several samples of the Khushaym Matruk profile were characterised using thermal analysis (Figure 6.36). The thermal spectra display the following major heat flux events:

- ~85°C: endothermic event associated with water loss (EGA data)
- ~140°C: endothermic event
- ~440°C: strong exothermic event associated with organic matter
- ~780°C: strong endothermic event (decarbonation of calcite).

Figure 6.36 Thermal analyses and thermogravimetry for samples along the Khushaym Matruk profile

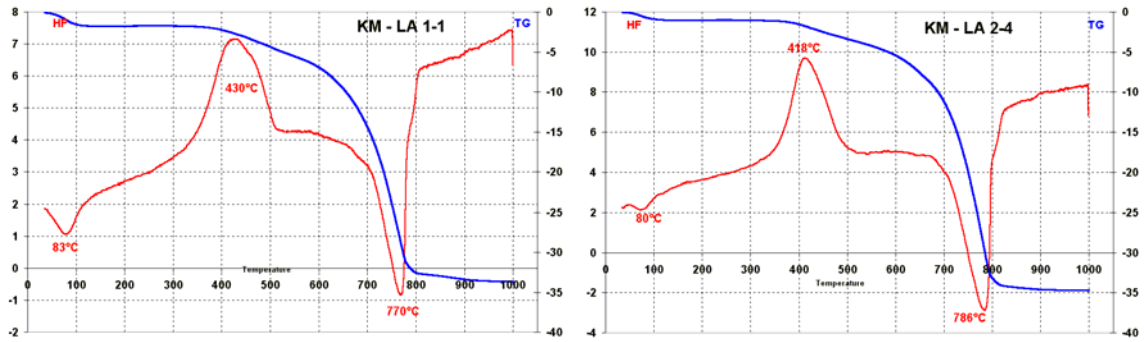

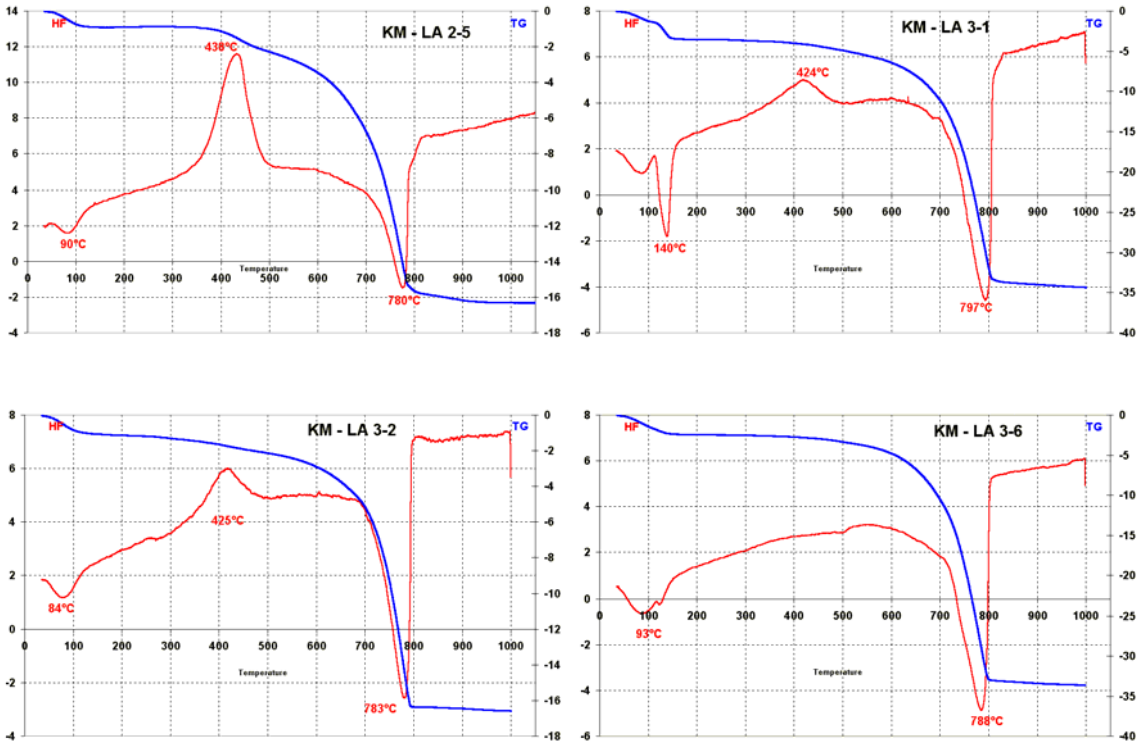

Strong fluctuations in mass loss are observed (Figure 6.37) around sample LA 3-1, i. e. at about 3 m from the cement-biomicrite contact. It is also observed that the exothermic peak associated with organic matter diminishes strongly after sample LA2-5. Figure 6.38 shows the position of the susceptibility anomaly with respect to the profile of the specific heat flux intensity, due to organic-matter decomposition during thermal analysis. The magnetic anomaly is clearly located on the side where the combustion event has destroyed or displaced the organic matter.

Figure 6.37 Evolution of relative mass loss from samples from the bottom to the top of the Khushaym Matruk profile (thermal analysis)

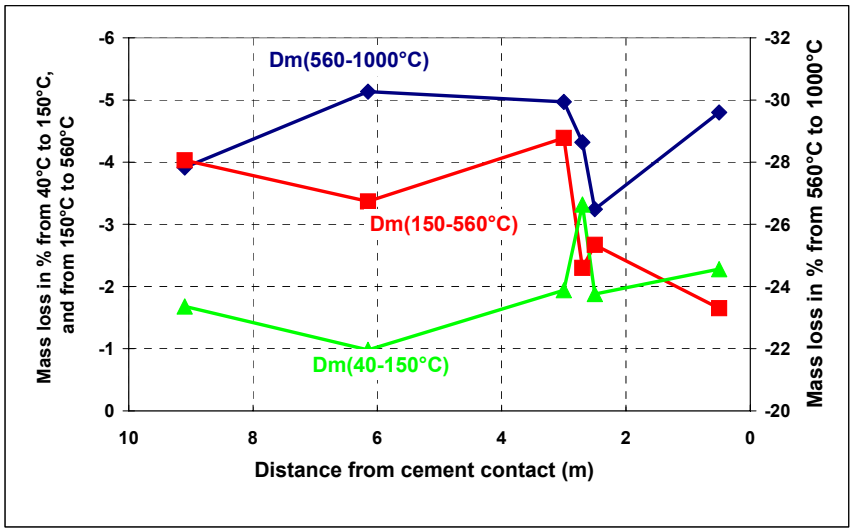

Figure 6.38 *Evolution along the Khushaym Matruk profile of the specific heat flux due to organic matter loss measured during thermal analysis (HF curve) and of the magnetic susceptibility (X curve)*

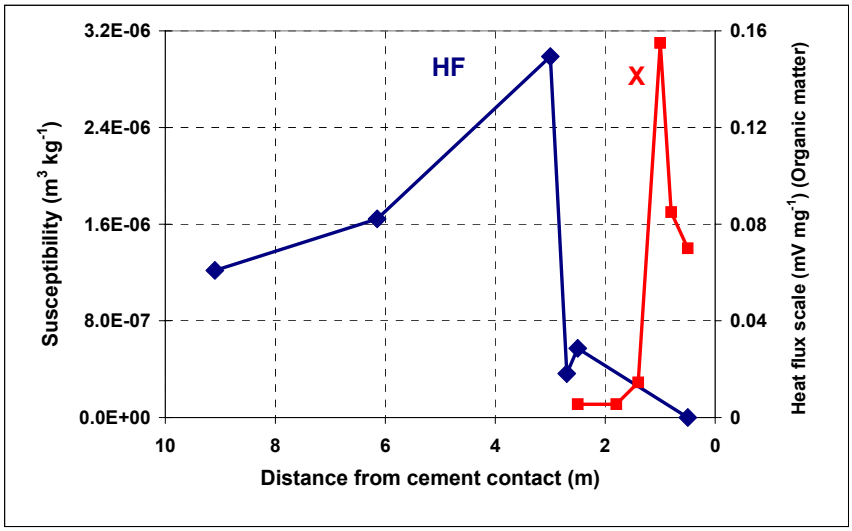

Figure 6.39 *Chemical analyses of metals (Ti, V, Cr, Fe, Ni, Cu, Zn) and Sr along the profile in Khushaym Matruk. Note also the magnetic susceptibility (X curve) in the bottom diagram*

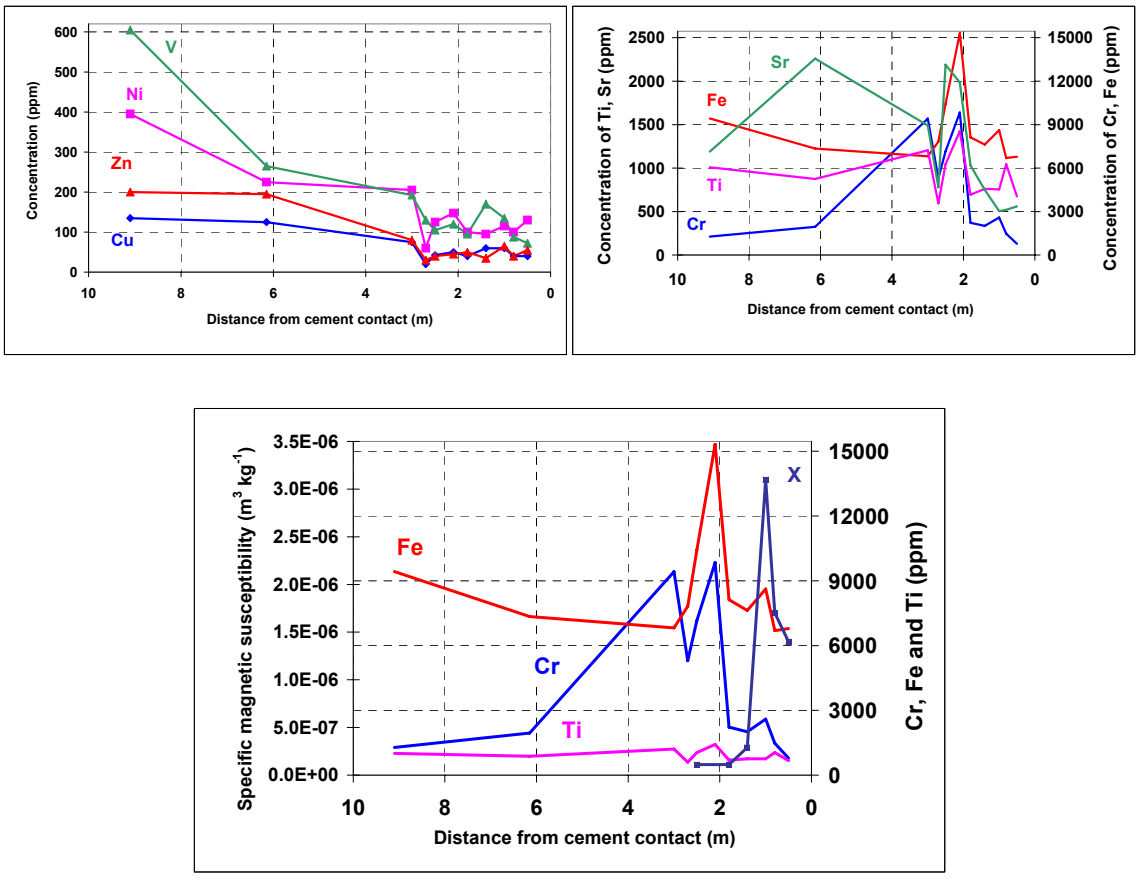

The spatial profiles for metals (Ti, V, Cr, Fe, Ni, Cu, and Zn) and Sr are plotted in Figure 6.39. V, Ni, Zn and Cu concentrations have parallel spatial evolutions, showing a regular decrease from the biomicrite to the ACZ. Fe, Ti and Cr have correlated evolutions, showing two distinct maxima at about 1 and 2 m from the cement contact. One of these maxima corresponds to the detected susceptibility anomaly. The Sr profile also displays strong fluctuations in the combustion front. Note that Cr and V concentration in Khushaym Matruk are 5 to 10 time larger than in Maqarin. This could have impacted notably on the magnetic mineralogy.

Table 6.19 Chemical analyses of Khushaym Matruk samples (whole rock)

Sample Reference	Distance above base level (m)	Ti (ppm)	V (ppm)	Cr (ppm)	Fe (ppm)	Ni (ppm)	Zn (ppm)	Cu (ppm)	Sr (ppm)
LA1-1	0,2	1010	605	1280	9430	395	200	135	1190
LA2-4	3,15	875	265	1950	7345	225	195	125	2260
LA2-5	6,3	1205	192.5	9415	6822.5	205	80	75	1490
LA3-1	6,6	595	130	5295	7820	60	30	20	780
LA3-2	6,8	1045	105	7157.5	10425	125	40	42.5	2190
A3-3	7,2	1425	120	9840	15315	147.5	45	50	1985
LA3-3	7,5	695	95	2225	8120	100	50	40	1030
A3-4	7,9	760	170	2010	7625	95	35	60	750
A3-5	8,3	755	135	2590	8620	115	65	60	505
LA3-4	8,5	1045	87.5	1475	6695	100	40	40	520
A3-6	8,8	675	72.5	780	6785	130	55	40	560

6.3.3.3 Conclusions

The magnetic investigations conducted on samples collected in the Khushaym Matruk trench transect confirm the existence of a significant magnetic anomaly between the ACZ and the biomicrite. The results are in good qualitative agreement with observations made at Maqarin. In particular, a comparable susceptibility anomaly exists at about 1 or 2 metres from the so-called “cement contact”. The order of magnitude of the susceptibility is consistent with values measured in Maqarin. Several differences are, however, noted between the two sites:

- only one susceptibility maximum was measured at Khushaym Matruk whereas the Fe profile clearly displays two distinct peaks, one of which corresponds to the χ maximum. This point has to be clarified by further measurements. It could be, for example, linked to the very high concentrations of Cr and V in Khushaym Matruk, potentially leading to a different magnetic mineralogy than that described at Maqarin.
- the organic matter in Khushaym Matruk, characterised by thermal analysis, displays a different decomposition spectrum, with only one major exothermic peak. In addition the organic matter content seems lower at Khushaym Matruk than at Maqarin.
- the spatial extension of the combustion halo seems smaller at Khushaym Matruk.

The palaeomagnetic investigation performed in Khushaym Matruk should be considered as preliminary because of the small number of samples that could be studied. Nevertheless, the results are reproducible (e.g. thermal and AF demagnetisation) and demonstrate the

feasibility of this type of measurement. They have shown that the combustion phenomenon occurred in Khushaym Matruk during a period of normal orientation of the magnetic field. The attribution of the normal component to the heating by the combustion event (characteristic temperature of 200-350°C) is plausible. The declination of the inverse component needs confirmation. In particular, measurement of samples far from the combustion front is necessary and each sample should be analysed in triplicate.

6.3.4 Isotope chemistry

6.3.4.1 Introduction

The purpose of this Section is to present a detailed isotopic characterisation of the Khushaym Matruk site in order to assess the fluid circulation processes in terms of origin, impact, extension and age. The approach consists of a systematic study of the Sr ($^{87}Sr/^{86}Sr$), C ($\delta^{13}C$) and O ($\delta^{18}O$) isotopic systems from all the lithologies cross-cut by the trench (see Section 6.3.1) i.e. biomicrites (transition zone and friable), analogue cements and travertines, and on the minerals filling the fractures which cross-cut the sediments. The list of the studied samples is given in Table 6.20. The age of the palaeo-circulation, which induced the growth of newly-formed minerals in travertines in fractures and micro-fractures, is approached using the U-Th disequilibrium method applied to vein-infilling carbonate minerals. The dates obtained are discussed on the basis of microscopic and cathodoluminescence observations. The imprint of these palaeo-circulations and their extent within the sedimentary pile underlying the ACZ are discussed on the basis of C, O and Sr isotopic data. Combining these results with a detailed study of the organic matter from the sediments also brings significant information on the thermal stress they experienced during the period which is addressed using the K-Ar method on the clay fraction (section 6.3.5).

Table 6.20 Isotopic data ($^{87}Sr/^{86}Sr$ isotopic ratios, $\delta^{13}C$ and $\delta^{18}O$ values) for the studied samples of the Khushaym Matruk site (WR: whole rock; CP: carbonate phase; OM: organic matter)

	distance*	Type	$^{87}Sr/^{86}Sr$ WR	σ .10^{-6}	$^{87}Sr/^{86}Sr$ CP	σ .10^{-6}	$\delta^{18}O$ carb	$\delta^{13}C$ carb	$\delta^{13}C$ OM
A 1-1	9.1	biomicrite	0.707875	5	0.707786	4	28.03	-2.56	-26.68
A 2-1	8.2	biomicrite	0.707833	3	0.707794	2	28.12	-3.87	
A 2-2	8.1	biomicrite					28.36	-3.63	
A 2-4	7.95	biomicrite					28.41	-4.38	-27.56
A 2-5	7.85	biomicrite			0.707804	5	28.09	-3.33	-27.69
A 2-7	6.9	biomicrite					27.71	-6.51	
A 2-8	6.25	biomicrite					27.6	-4.42	
A 2-8 ép	6.25	edge of the KHM 07 joint			0.70779	4	27.59	-4.92	
KHM 07	6,0	infilling gypsum joint	0.707856	4	0.707787	4	24.95	-4.47	
A 2-9	5.8	biomicrite			0.707792	4	27.28	-2.91	-26.61
A 2-10	4.7	biomicrite			0.707797	2	24.19	-4.69	-27,00
A 2-11	3.6	biomicrite	0.707857	3	0.707812	4	25.54	-5.06	-26.53
A 2-12	3.05	biomicrite					22.33	-6.18	-26.87
A 3-1	2.7	biomicrite			0.707785	3	21.23	-9.85	-26.4
A 3-1b	2.7	biomicrite					21.17	-11.4435	
A 3-2	2.6	biomicrite					22.29	-9.38	
A 3-2 (nodules)	2.6	black nodules					22.39	-5.986	
A 3-2 (micro-joint)	2.6	micro-joint			0.7078	8	22.51	-10.21	
KHM 13 (matrix)	2,0	biomicrite			0.707809	3	20.65	-16.88	
KHM 13 (micro-joint)	2,0	micro-joint			0.707849	2	16.40	-31.3615	
A 3-4	1.4	biomicrite	0.707844	6	0.707805	4	22.08	-12.97	
A 3-4 (micro-joint)	1.4	micro-joint					22.2	-17.45	
A 3-5f (micro-joint)	1,0	micro-joint (green minerals)			0.707802	5	21.43	-22.064	
A 3-6 a	0.5	biomicrite					20.66	-16.03 (70)	
A 3-6 b	0.5	biomicrite			0.707805	3	20.71	-18.06 (89)	
A3-6 f1	0.5	biomicrite					20.72	-16.48 (70)	
A3-6 f2	0.5	biomicrite					20.55	-15.91 (58.5)	
A3-6 f3	0.5	biomicrite					20.71	-16 (61)	
A3-6 g	0.5	biomicrite					20.95	-17.62 (69.7)	
A 3-6 V1	0.5	micro-joint parrallel to S0/S1			0.707838	3	20.21	-19.69 (100)	
A 3-6 V2	0.5	micro-joint parrallel to S0/S2					22.27	-22.33 (100)	
A 3-6 V3	0.5						22.2	-21.27	
A 3-6 V4	0.5	micro-joint secant to S0/S1					21.19	-26.28 (100)	
KHM 06 (matrix)	0.25	biomicrite			0.707793	4	22.58	-28.7	
KHM 06 (belemnite)	0.25	belemnite			0.70778	3	22.22	-28.8	
KHM 01c	0	travertine (pink)			0.70785		24.55	-20.14	
KHM17	0	travertine (pink)				6			
KHM 04	0	travertine (white-pink)			0.707869	3	23.67	-25.795	
KHM 18	-60	marble (pink)					18.68	-14.597	
KHM 19	-60	marble (pink)	0.707873	3	0.70787	2	23.68	-17.21	
KHM19 (cracks)		cracks in marble			0.7078877	2			
KHM 21	-60	marble (white)					18.37	-13.53	

6.3.4.2 Isotopic characterisation of the friable biomicrites

The grey biomicrites collected at the bottom of the trench (A1-1 to A2-5, Figures 6.16–6.18) are well-defined by their Sr, C and O compositions (Table 6.20, Figures 6.40-6.42):

- the carbonate fraction extracted from these sediments (matrix carbonates) shows C and O isotopic compositions slightly lower than the domain of C-O isotopic compositions of marine carbonates (Figure 6.40); the Sr isotopic composition of these samples matches the domain of Sr isotopic signatures attributed to Maestrichtian-Lower Paleocene sea-water (Jones et al., 1994) (Figures 6.41). As a whole, the carbonate fraction of these biomicrites could have experienced subtle alteration processes (either pre-, syn-, or post-combustion) able to affect their pristine C and O oceanic isotopic signatures, but undetectable by heavier isotopes such as those of Sr.
- the low $\delta^{13}C$ value (-26.7 to 27.7‰) for the organic matter extracted from these sediments is within range for typical organic matter.
- the whole rocks show radiogenic and heterogeneous Sr isotopic compositions ranging from 0.707833 ± 3.10^{-6} to 0.707875 ± 4.10^{-6} (Figure 6.41).

From the C and O isotopic signatures of the biomicrites located at level A1 and at the basal part of A2, it is inferred that these levels have undergone a slight disturbance which (high-pH or combustion effects?) beyond 7.85 m below the cement interface. These levels seem to have been influenced by hyperalkaline fluids (see Sections 6.3.3 and 6.3.5) that could also explained the C and O compositions. Moving upwards in the sampling profile, towards the ACZ, the isotopic values evolve significantly, with notably a decrease of δ^{13}C-values both in the matrix of baked biomicrites and in filled joints (Figure 6.40). This trend is discussed further below.

Figure 6.40 δ^{13}C vs. δ^{18}O diagram for Khushaym Matruk samples

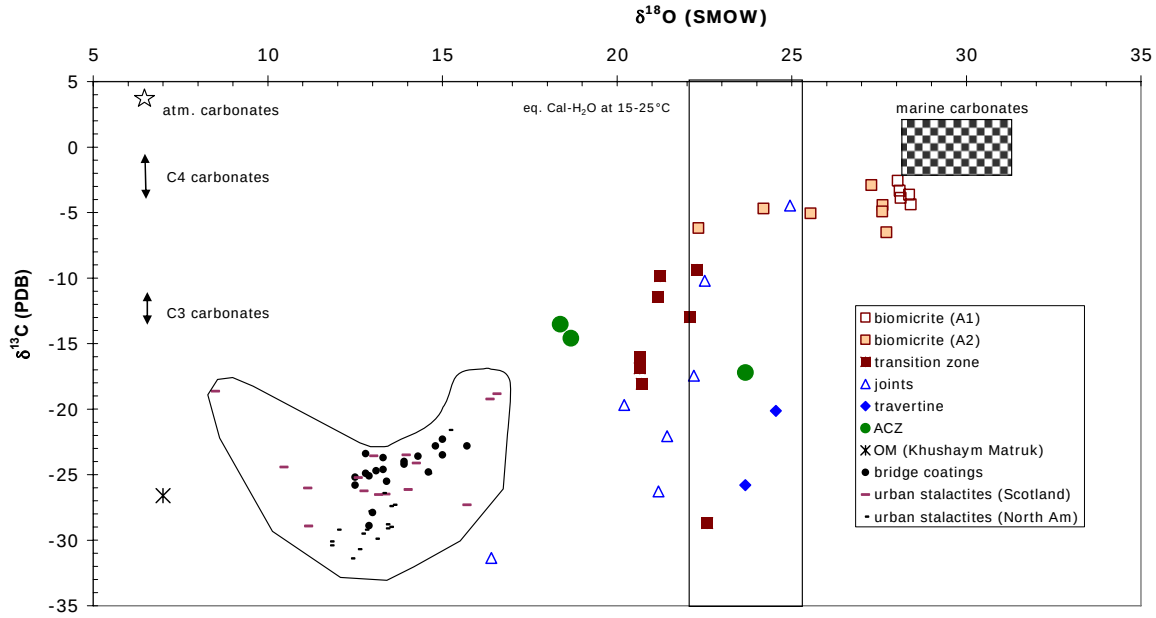

Note *Data for biomicrite (BM) and secondary carbonates from fractures/joints and travertines and from organic matter (OM). The measured isotopic compositions are compared to those of marine carbonates, carbonate concretions (coatings, stalactites) formed under/on concrete structures in North America and Scotland, and cementitious carbonates from Maqarin. The theoretical δ13C-value of a carbonate in equilibrium with atmospheric CO_2 is also reported in this diagram, together with that of an authigenic carbonate formed in a soil dominated by i) C3 plants, ii) C4 plants. See text for references*

6.3.4.3 The Analogue Cement Zone (ACZ) and the combustion event

C, O and Sr isotopic data

Samples from the ACZ display isotopic compositions quite different from those of the biomicrites located at the bottom of the trench (considered as reference):

- the carbonates fraction, extracted from two rock samples from the ACZ, shows low C isotopic compositions (δ^{13}C = -13.5 to -17.2‰) close to those reported for analogue cements from the Maqarin site. It formed, however, at the expense of a more carbonate-rich parent rock (Clark et al., 1993; Figure 6.40). The ^{87}Sr/^{86}Sr ratios of these carbonates are higher than the domain of Sr isotopic compositions attributed to Maestrichtian-Lower Palaeocene sea-water (Figure 6.41).

- one single whole-rock sample was also analysed and has a $^{87}Sr/^{86}Sr$ ratio somewhat similar to those of the carbonates (Figure 6.41).
- these whole-rock and carbonate ratios are close to, or identical with, those of some friable biomicrites (WR values) from the bottom of the profile (Table 6.20).

Figure 6.41 Sr isotopic composition (87Sr/86Sr) of the Khushaym Matruk samples along the ransect from the biomicrites to the ACZ. Comparison with Sr seawater compositions at the deposition time of the sediments (Jones et al., 1994).

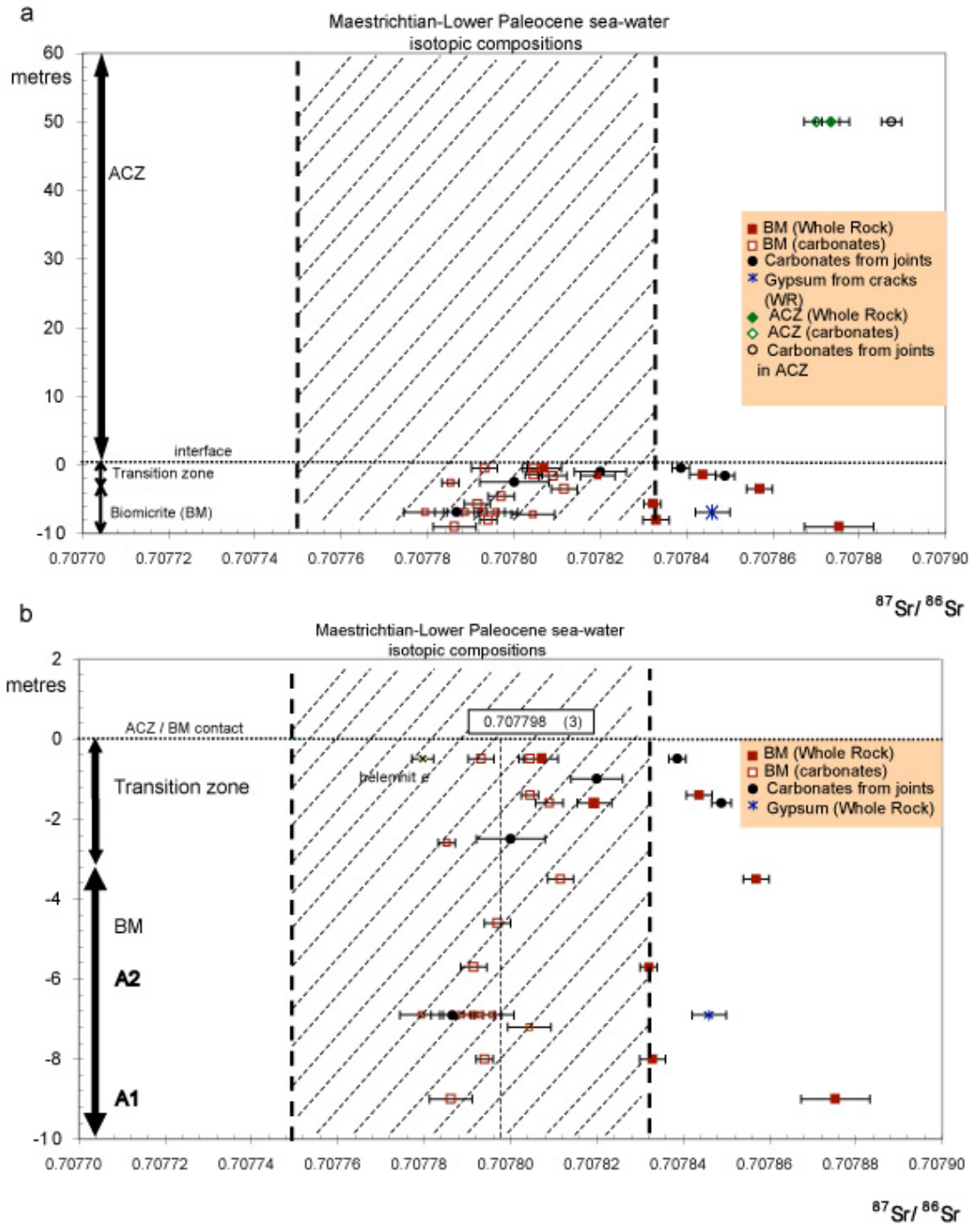

Figure 6.42 *$^{87}Sr/^{86}Sr$ vs. $\delta^{13}C$ diagram for the Khushaym Matruk samples (carbonate phase extracted from the biomicrites(BM), the secondary carbonates from fractures/joints, travertines and the ACZ). References of the distance from the cement contact are shown in this diagram. A theoretical domain of compositions for carbonates precipitated from hyperalkaline solutions in equilibrium with the ACZ is also represented.*

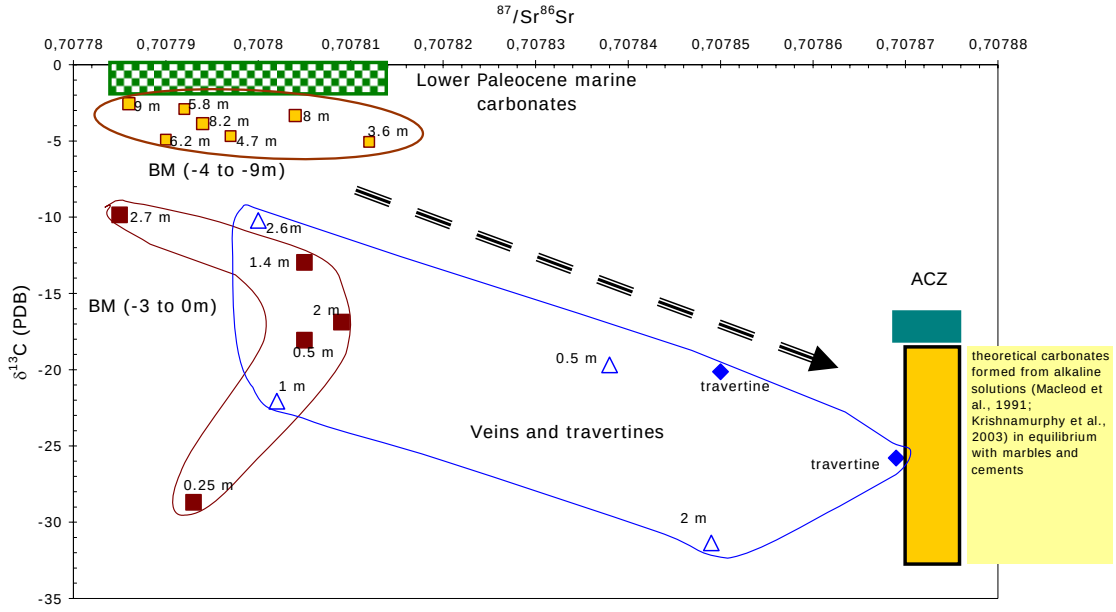

The approximate similarity of $^{87}Sr/^{86}Sr$ ratios in the whole rock and the carbonate phase in the ACZ argues for a total homogenisation of the Sr isotopic system among the different mineral phases inside the given rock volume examined here. In common metamorphic rocks, such a process, implying the diffusion of Sr element and isotopes, is known to occur for temperature conditions exceeding 500-800°C and maintained for a few millions of years (Faure and Powell, 1972; Jenkin et al., 1995). Modelling performed by Cherniak (1997) indicates that Sr diffusion is function of time and temperature. At high temperatures (>800°C), diffusion of Sr can be observed over relative short times (< 10^4 years). In the case of a system such as the ACZ, mineral species have reacted and recrystallised at temperatures exceeding 1000°C (Section 3.2 and Milodowski et al., 1992a, 1992b). A redistribution of the Sr contained in the reacting mineral species (silicates, carbonates) into contemporaneously recrystallizing phases (residual carbonate), eventually coupled with Sr diffusion, might account for this isotopic "homogenisation". This process is proposed to have occurred over a relative short period (Pitty, 1998, and see K-Ar data below).

The C and O isotopic ratios measured in the ACZ are compatible with the explanation given in Maqarin by Clark et al. (1992b) and Clark and Fritz (1998) for similar rocks and compositions, namely i) isotopic fractionation during decarbonation, ii) hydration/recarbonation involving H_2O vapour and combustion CO_2 derived from both oxidation of organic matter and decarbonation.

Age and impact of the combustion event

A preliminary attempt to evaluate the age of the combustion event by fission-track determinations of apatite from the analogue cement (Techer and Elie, 2003) was unsuccessful because of the small size of the grains (<50 µm). This precluded any reliable measurements of fission-tracks. It was thus proposed to use the K-Ar method to estimate at least the age of the pyrometamorphic event. This dating approach is based on the assumption that the K-Ar system of the clay minerals in the rock has been affected by the combustion process and was consequently more or less reset during this event. It might be mentioned here that this attempt was especially difficult for the following reasons:

- the low clay contents of the cement (less than 5%).
- the low K contents of the whole rock.
- the probably young age of the high-temperature event.

Clay-size fractions <2 µm were extracted from four selected samples of the studied profile by sedimentation of the ground rocks in distilled water (Table 6.21) and were analyzed for their K-Ar systematics. Two samples (A1-1 and A2-5) belong to the friable biomicrites. They are considered to represent the unaffected parent rock and their clay fraction yields similar results, giving a mean apparent K-Ar age of 37.0 + 0.6 Ma. This value is already younger than the stratigraphic age set at 50-70 Ma implying that, despite the unaltered appearance, the K-Ar systematics of the clay material has already been affected (as previously observed when attempting to date clay minerals e.g. Clauer and Chaudhuri, 1995). A disturbance at this level in the profile could be due either to a weak thermal effect (influence of the combustion event) or to another diagenetic phenomenon (as commonly observed in sedimentary formations). Due to a lack of data, it is currently difficult to differentiate between these processes. However, by referring to other measurements, it seems more likely that this K-Ar disturbance is due to diagenetic processes (see also Sections 6.3.3 and 6.3.5).

Table 6.21 K-Ar data obtained on biomicrites and a cement (KHM18) from the Khushaym Matruk trench.

Samples	**K_2O (%)**	**$^{40}Ar^*$ (%)**	**$^{40}Ar^*$ (10^{-6} cm^3g^{-1})**	**Age (Ma +2σ)**
A1-1	3.92	49.5	4.80	37.6 (1.1)
A2-5	3.21	42.3	3.80	36.4 (1.2)
A3-3	1.61	5.8	0.15	2.8 (0.4)
KHM18	0.06	0.2	-0.01	0 (0)

$^{40}Ar^*$ stands for radiogenic ^{40}Ar; the amounts in radiogenic ^{40}Ar are given in the STP system

The (A3-3) biomicrite from the transition zone, collected 2 m below the cement contact, contains a clay fraction providing a significantly lower value at 2.8 $\pm$ 0.4 Ma. Relative to the two previous samples, it is obvious that the clay material of this sample has been pervasively affected. Heating of the sediment can induce a $^{40}Ar_r$ loss and so a decrease of the K-Ar apparent age. The sediment could have experienced a thermal stress sufficient to disturb significantly the K-Ar system of its clay fraction. Hunziker et al. (1986) reported that the K-Ar system of illite-type clays is totally reset for temperatures higher than 250°C. In considering this result, the partial resetting of the K-Ar system of the clays from biomicrites, located 2 m below the ACZ contact, may suggest that temperature did not exceed 250°C. A the thermal pulse of short duration may have been involved too, in agreement with previous data (see Section 6.3.3). In case of a short duration process, a slightly higher temperature

could have been reached. However, values higher than 500°C cannot be reasonably considered with respect to $^{87}Sr/^{86}Sr$ data.

Alteration of clays by hyperalkaline fluids, as suggested in Section 6.3.2, could also explain the redistribution of the K and Ar elements and, currently, it is not possible to differentiate between the two processes.

The fourth sample (KHM18) is an analogue cement. The K-Ar value of its clay fraction is significantly different (Table 6.21). The K_2O content is very low at 0.05%, which provided a very small amount of radiogenic ^{40}Ar at 1.10^{-8} cm^3 g^{-1}. These very small contents required very specific analytical conditions with very accurate controls of the K and Ar determinations (measurement of blanks, standard minerals and of atmospheric Ar for precise correction). It appears that the clay fraction has no radiogenic ^{40}Ar (at the 10^{-8} level). This result implies that the thermal event which affected this cement sample occurred less than 1 Ma ago, at least.

6.3.4.4 Palaeo-circulation in the Khushaym Matruk sediments

Alteration of minerals in the analogue cement can be macroscopically ascertained by the development of numerous joints filled with secondary minerals. In the underlying formation, palaeo-fluid circulation is revealed by:

(1) the development of newly-formed minerals in joints cross-cutting the sediments at various distances from the analogue cement. Two types of joints are observed:
   - in the basal part of the ridge (see Figures 6.15 and 6.16; over the first 5-6 metres, A1 and A2 levels), wide (centimetre-sized) joints are filled mostly with gypsum and cross-cut the biomicrites. The mineralogy and structure of host biomicrites are not disturbed (see section 6.3.2). The black colour of the infillings indicates the occurrence of organic matter within the newly-formed minerals (see Figure 6.21 and Section 6.3.5).
   - a few metres below the contact with the analogue cement, numerous micrometer- to millimetre-thick joints cross-cut the indurated biomicrites (A3 level). They are mostly filled with white and green secondary minerals of carbonate type. This micro-jointing is linked with a structural disturbance of the rock matrix (Section 6.3.2).

(2) the deposition of travertines, mainly at the bottom of the ACZ, where a number of cavities have been observed, but also within this formation higher up the ridge. The presence of such travertines is common in Jordan, denoting hyperalkaline springs (see Khoury et al., 1984). These travertines are locally green in colour, due to high Cr contents (Rassineux, 2001). Red travertines are also observed.

Calcite infillings in foraminifera tests and small recrystallised calcite grains in the matrix could also be related to palaeofluid circulation (section 6.3.2). The microscopic characterisation of these phenomena, as well as their Sr, C and O isotopic compositions, will now be used to discuss the origin, nature and extent of the related fluids.

Microscopic and cathodoluminescence observations

As noted above, the centimetre-thick fractures that cross-cut the biomicrites in the basal part of the ridge (A2 level) are filled mainly with gypsum. A weak diffraction peak of calcite is also observed during XRD measurements, but this is simply due to embedding of small chips of biomicrite matrix within the sulphate material (Figure 6.43a). Observation of the gypsum

crystals in cathodoluminescence mode reveals a black-blue specific luminescence (Figure 6.43b).

Figure 6.43 *(a) SEM images of materials infilling the KHM07 centimetre-thick joint crosscutting biomicrites at 6.7 m depth: this joint is failed mainly with gypsum which embedded tiny chips of host biomicrite during its growth; (b) Same crystals observed in cathodoluminescence mode: the black-blue luminescence of gypsum is clearly different from that of matrix calcite (right side of the image).*

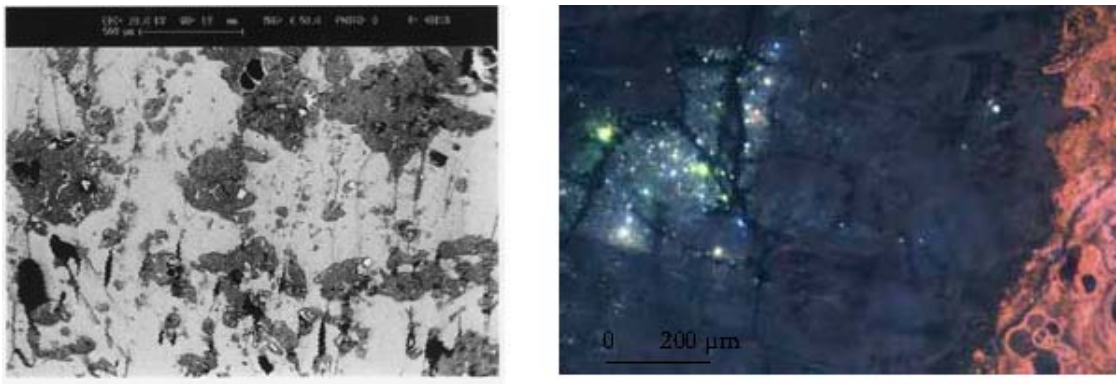

Minerals from joints cross-cutting the baked biomicrites (A3 level, 0 to 3m below the analogue cement zone) are composed of a mixture of calcite, gypsum and zeolites. They are mostly identified by microscopic observations because the weight of extracted material was not large enough to allow XRD measurements. Two types of micro-jointing exist:

(1) the first one corresponds to micro-joints sub-parallel to the stratification,
(2) the second one cross-cuts the previous micro-joints and the planar structure of the indurated biomicrites (Figure 6.44).

Figure 6.44 *(a) View of indurate biomicrite sample A3-6, with (b) a sketch showing the location of analysed matrix and vein sub-samples, and (c) a microscopic view of the polished area studied using ion-microprobe and the corresponding C isotopic compositions ($\delta^{13}C$ vs. PDB) In c, calcite appears with a white colour while the dark material in the large vein is zeolite*

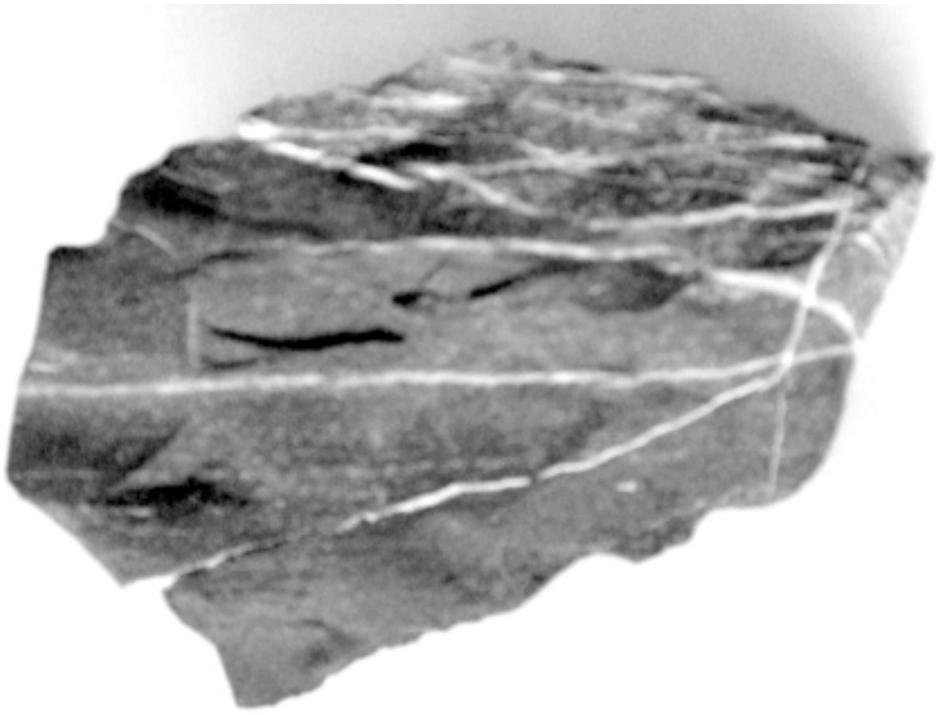

_____ 2cm

(a)

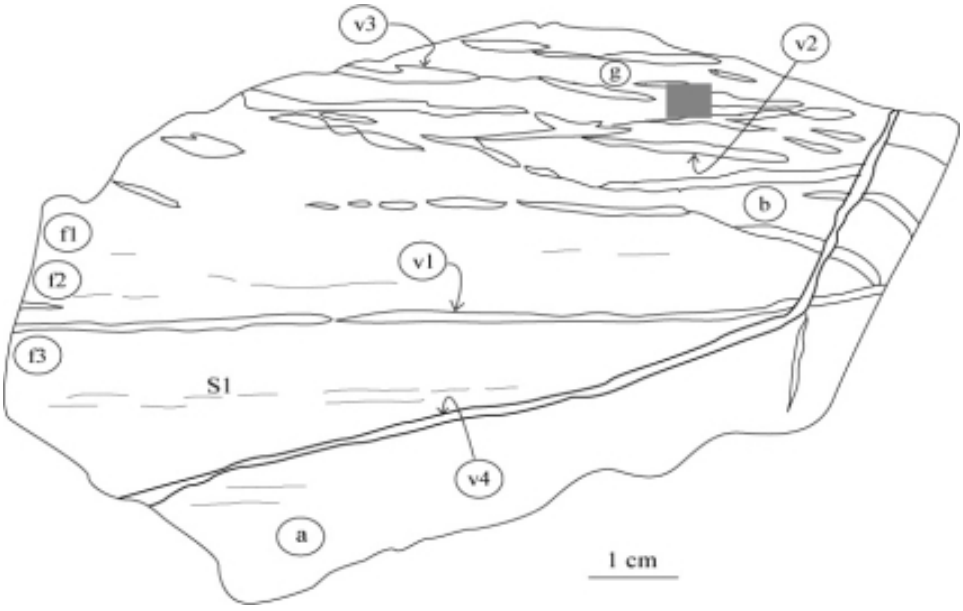

(b)

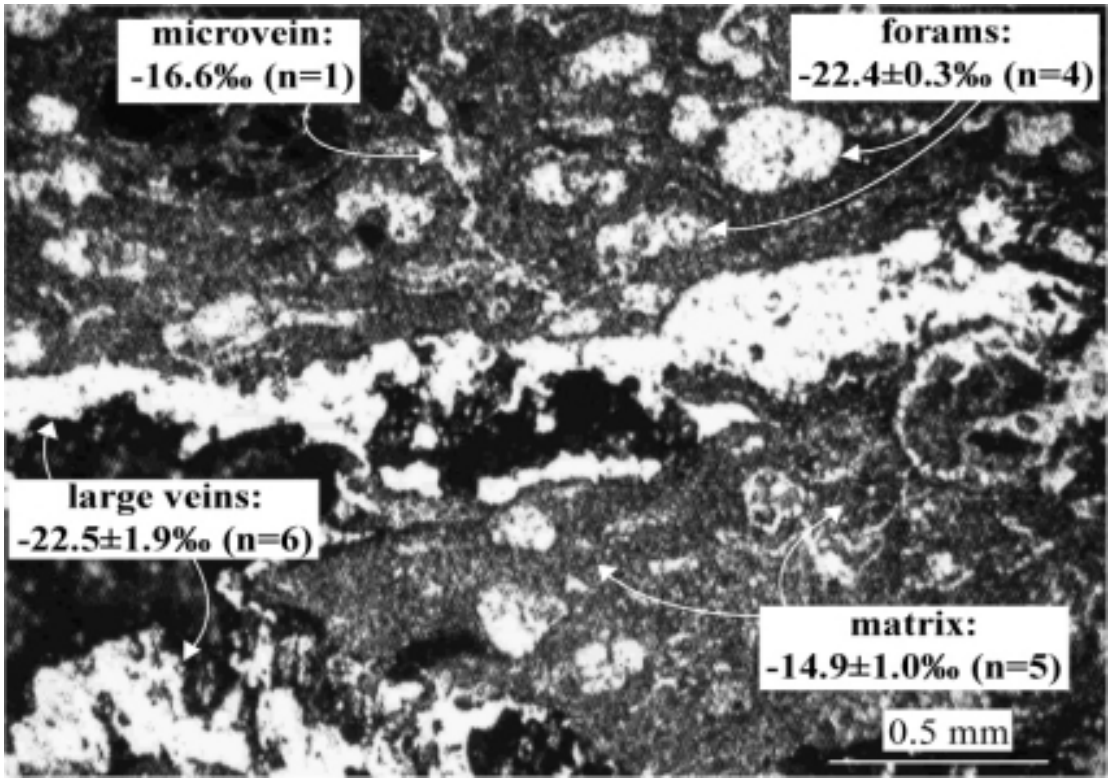

(c)

In general, micro-joints are filled with calcite crystals, the colour and shape of which[24] suggest the occurrence of different crystal generations. Cathodoluminescence observations confirm this hypothesis, as four to five luminescence hues were observed within a single joint, from the edges to the core of the structure (Figure 6.45). These luminescence hues are quite distinct from that of the pink calcite matrix. The variation of luminescence hues of secondary carbonates in the micro-joints of the biomicrites can be ascribed to different fluid chemistry or pH-T conditions (Machel and Burton, 1991; Machel, 2000) and suggests that several stages of fluid flow occurred in the structural discontinuities.

[24] Microscopic observations under x-nicols show birefringence changes as a function of the distance to the edges of the crystals.

Figure 6.45 *Optical microscope (a) and cathodoluminescence (b) imaging of a micro-joint crosscutting the KHM13 sample (scale: 1 cm = 200 µm): 4 luminescence hues from pink to blue are observed in the joint; (c) sketch of image b with 4 calcite generations; (d) In the same KHM13 sample, foram tests are partly or totally filled with calcite and zeolite, the blue luminescence hue of which can be compared to that of the minerals present in the first type of joints and is clearly distinct from that of matrix calcite (scale: 1 cm =150 µm)*

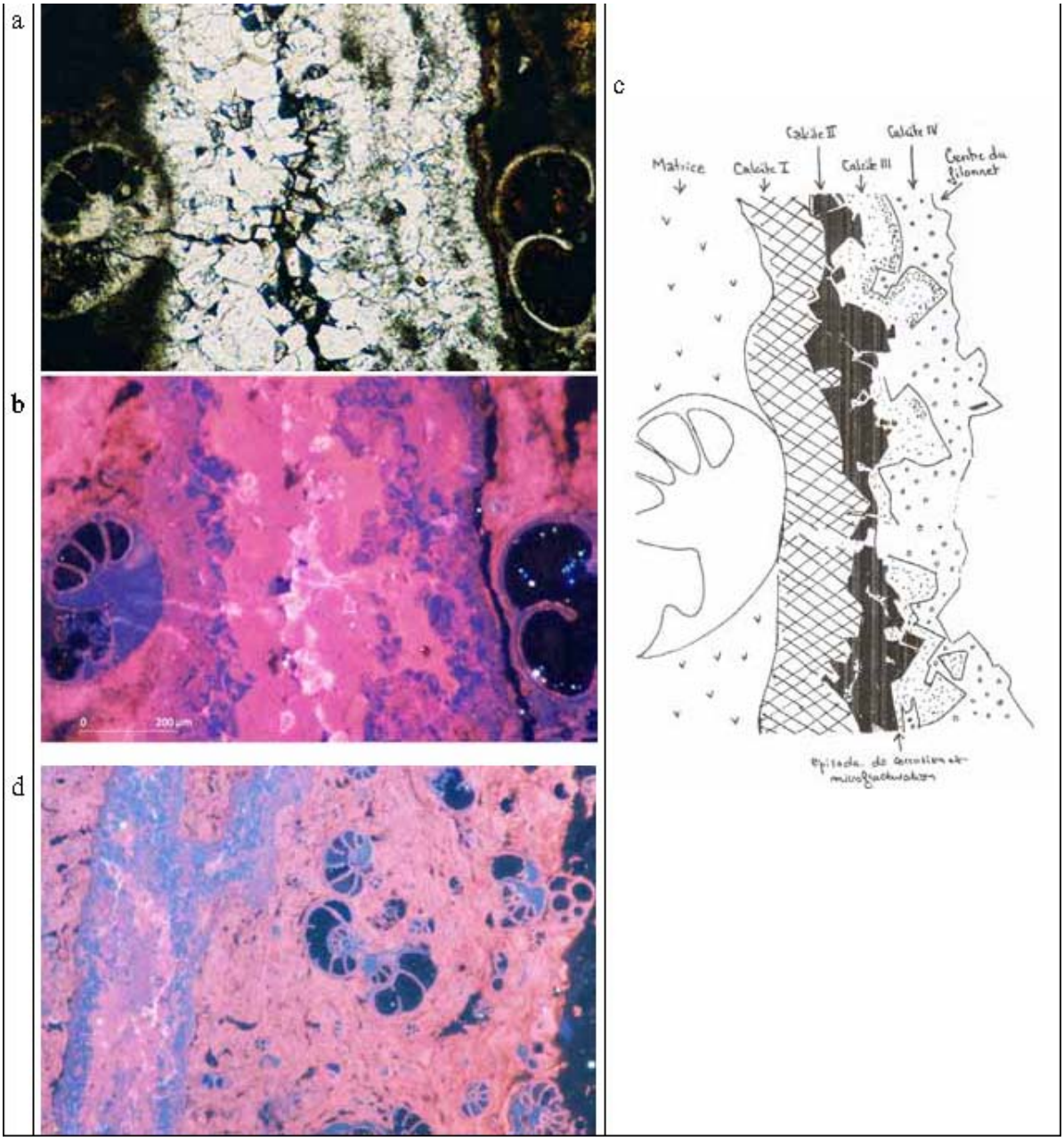

In the transition zone biomicrites, foraminifera tests are partially or totally filled with calcite and zeolite (Figure 6.45d). These secondary minerals exhibit a peculiar blue luminescence comparable to that observed in the core of the micro-joints, which suggests that the same type of fluid (same chemitry or pH-T conditions) was responsible for the carbonation in fractures and in foraminifera tests. This suggests a pervasive diffusion of fluids into the sediments, at least in the biomicrites that are close to the contact with the ACZ, but detailed

isotopic analyses are required to address this point more fully. The occurrence of zeolite suggests, as observed in other studies, circulation in a closed system at some period during evolution of the system (see Chermak, 1992, 1993; Milodowski et al., 1998a, 1998b; Ramirez et al., 2002).

Sr, C and O characterisation

All the isotopic values measured along the studied profile in the biomicrite levels, and in joints and travertines, can be discussed as a result of a thermal disturbance linked to the combustion event. Equally, they could be due to an interaction between rocks and hyperalkaline solutions and carbonation from these high pH fluids. It is also possible that both processes were involved.

(i) A closed-system isotopic equilibration between organic matter and carbonates (thermal effect) can be ruled out. Isotopic equilibration between carbonates and organic matter should be marked by a strong $\delta^{13}C$ increase of the latter, through a mass-balance effect. Considering measurements performed in this study, on a few organic matter samples extracted in the transition zone biomicrites around the transition between levels 2 and 3 (Table 6.20), no significant change of the $\delta^{13}C(OM)$ is detected relative to the most "primitive" biomicrites. Taking into quantitative account the relative amounts of C contained in organic matter and the carbonate fraction, respectively, this model cannot be accepted. At a lower temperature, in a lower part of the trench, equilibration is even less likely. Moreover, this process cannot explain other results, such as the increase of carbonate content in the whole rock upwards in the profile (Fourcade et al., 2006).

(ii) Carbonation from high pH fluids.

- The $^{87}Sr/^{86}Sr$ ratios of secondary carbonate extracted from large joints cross-cutting the baked biomicrites (A3 level) are identical to, or higher than, those measured on matrix carbonate (Figures 6.41 and 6.42). Moreover, these ratios increase towards the contact with the analogue cement, from 0.707800 ± 8.10^{-6} in sample A3-2 (2.6 m from the contact) up to 0.707838 ± 3.10^{-6} in sample A3-6 (0.5 m from the contact). At the contact with the analogue cement, carbonates from the travertines are the most Sr radiogenic with $^{87}Sr/^{86}Sr$ ratios of 0.707869 ± 5.10^{-6} and 0.707850 ± 6.10^{-6}. The Sr isotopic composition of these travertines can be considered to be identical or slightly lower than that measured in calcites from the analogue cement. The similarity of isotopic composition with those of the two reference domains (i.e., the biomicrites and the analogue cement) argues for a precipitation of secondary minerals from fluids generated in the overlying ACZ. Measurements of Sr elementary contents in these secondary carbonates would have been very useful to support this hypothesis. It is recommended that this be considered in future studies.
  The $\delta^{13}C$ signatures of the newly-formed carbonate from large joints and travertines are highly negative (Figure 6.40). They are, however, heterogeneous, with values ranging from -17.5 to -31.4‰ (Table 6.20). One sample (A3-2) shows an intermediate $\delta^{13}C$-value of -10.2‰. Sample KHM13 (2 m below the contact) exhibits the lowest δ^{13} value (-31.4‰) and the $\delta^{18}O$-value is low compared to marine values. Such ^{12}C-enriched carbonates are common in the context of hyperalkaline solutions. For example, they have been measured on carbonate coatings and stalactites developed at the surface of concrete structures, as in Scotland (Macleod et al., 1991) or in Northern America (Krishnamurthy et al.,

2003) (Figure 6.40) , and also in carbonate crusts and travertines formed in the presence of alkaline fluids (e.g., Clark et al., 1991, 1992a and references therein). Such isotopic compositions can be explained neither by the precipitation of carbonates in equilibrium with atmospheric CO_2, nor by the precipitation of carbonates from a solution where the carbon stock comes from organic matter (C3 or C4 plants-(Figure 6.40). It is suggested here that they are the signature of a neoformation at the expense of atmospheric CO_2, from a Ca^{2+}-bearing solution with a high pH. The location of most the travertines, at the bottom of the ACZ and close to numerous cavities and the laminar structure of some vein infillings, is indicative of a recurrent fracture opening. This is compatible with a process that implies access of CO_2 to open systems. During neoformation, kinetic isotopic fractionations, the nature of which is still under discussion, induce low $\delta^{13}C$ (O'Neil and Barnes, 1971; Macleod et al., 1991; Létolle et al., 1992; Clark et al., 1992b; Usdowski and Hoefs, 1986; Dietzel et al., 1992).
It can be argued that, as proposed for Maqarin (Clark *et al*., 1993), the involvement of local CO_2 released during combustion of the organic matter around the analogue cement could be responsible for the low $\delta^{13}C$-value of these secondary carbonates. In fact, the database on the concretions occurring on cementitious surfaces, with extreme $\delta^{13}C$-values (range of -28 to -31.5‰) matching those recorded in Khushaym Matruk, come essentially from urban zones (Macleod et al., 1991; Krishnamurthy et al., 2003). However, measurements of recent stalactites situated under railway bridges over rivers, in the total absence of anthropogenic contributions or of plant-respired CO_2, have obtained isotopic compositions similar to the extreme values published in urban zones[25]. This demonstrates that very low $\delta^{13}C$ values do not require any addition of combustion gas to the carbonation system. It is therefore suggested that, at Khushaym Matruk, the capture of atmospheric CO_2 by hyperalkaline solutions is the dominant factor explaining the low $\delta^{13}C$ value of secondary carbonates (travertines and large joint-fillings).

- In the transition zone (A3), the $\delta^{13}C$-values of matrix carbonates of biomicrite decrease towards the overlying analogue cement (Figure 6.46). This decrease is associated with a general increase of the carbonate content towards the ACZ (Figure 6.47) and a net carbonation indicated by cathodoluminescence observations. A newly formed carbonate, with luminescence properties similar to those of veins, fills increasing proportions of microcavities and foraminifera tests towards the contact with the ACZ. In this 3.0 m-thick zone below the contact with the ACZ, the $\delta^{18}O$-value is buffered in a tight range ($\delta^{18}O$ = +20.2 to +22.3‰, Figure 6.46). The re-crystallized carbonates display luminescence hues comparable to that of joint-filling minerals assumed to be formed through percolation of hyperalkaline solutions, as argued above (Figure 6.45). This suggests that the biomicrite matrix experienced some pervasive carbonation process, resulting from the rather pervasive infiltration of hyperalkaline solutions across the 3 m-thick zone under the ACZ.

[25] Present-day stalactites hanging from two different, well-vented bridges over the Vilaine river, Brittany: $\delta^{13}C$ = -27.7 and -28.8‰; present-day stalactites hanging from a well-vented concrete arch on the seashore, Brittany: $\delta^{13}C$ = -30.8‰;(Techer, work in progress).

Figure 6.47 Calcite contents of biomicrites reported as function of the distance to the Analogue Cement Zone

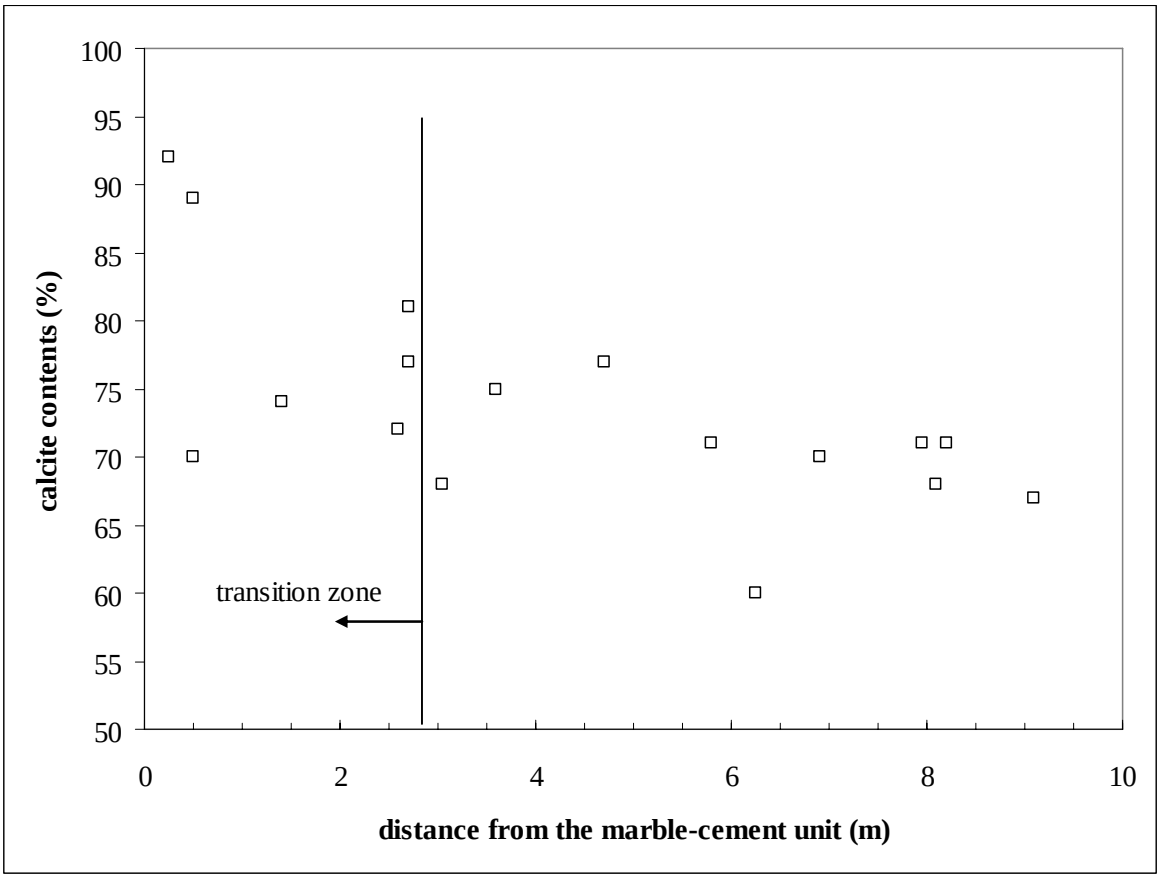

Small-scale and in-situ C isotopic measurements argue that the $\delta^{13}C$ in these biomicrites is compatible with a two-component mixture. The relevant material was collected from the A3-6 sample, from two filled joints parallel to the foliation/stratification (V1 and V2), one late filled joint strongly oblique to the foliation (V4) and six rock fragments located in more or less bleached areas of the hand specimen (a, b, f1, f2, f3, g) (Figure 6.44). The carbon isotopic compositions (Table 6.20) were plotted against the percentage of carbonate (obtained from the acid digestion technique used for isotopic measurements, Table 6.20) in Figure 6.48. The wide array observed is in reasonable agreement with a mixture model. The $\delta^{13}C$ variations of matrix carbonate are explicable in terms of addition of an isotopically lighter component that is also infilling joints parallel to the foliation. The "ancient" matrix component cannot be estimated by extrapolating the trend towards low-carbonate percentages. This is because the actual process was probably a combination of net addition of newly formed carbonate and of re-crystallisation accompanied by isotope exchange. If so, remnants of the pristine marine isotopic signatures may not exist. It is worth noting that joint fillings (or veins) V1 and V2 do not have exactly the same isotopic compositions, which indicates that they did not form from the same fluid at the same time and similar temperature conditions. By analogy to the situation at Maqarin (see Smellie, 1998), the percolation of hyperalkaline fluids and associated cementation

probably occurred in several stages as mentioned above. Late joint filling V4, with a much lighter isotopic composition, underlines this point. *In situ* C isotopic analysis of foraminifera infillings and micro-veins, using Ion Probe IMS 1270 in Nancy confirms the mixing hypothesis (Figure 6.44).

Figure 6.48 C isotopic composition of different carbonate-bearing joints and of different matrix fragments in the transition zone biomicrite A3-6. See text for discussion

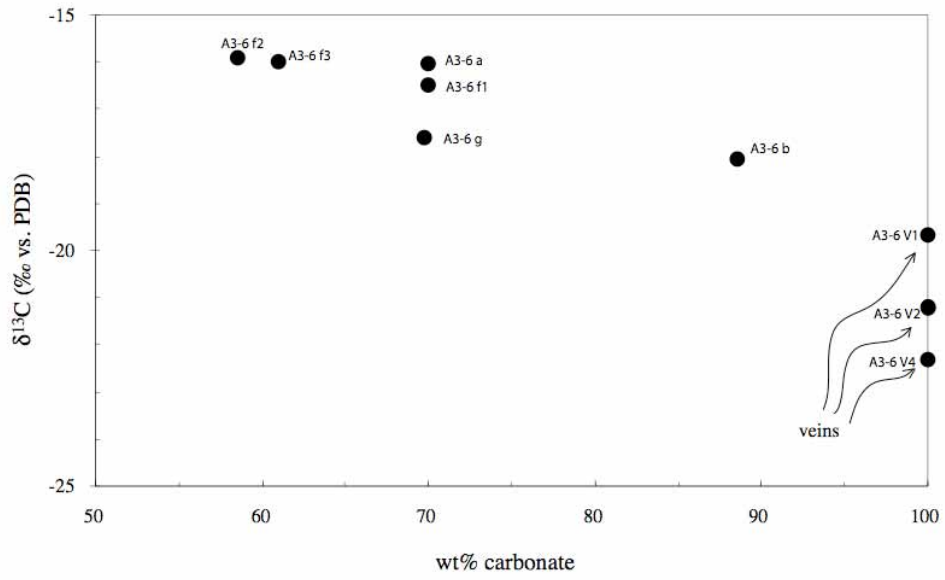

The mechanism responsible for the low $\delta^{13}C$-values found in the microporosity of the sediment is, however, under discussion. Access of atmospheric CO_2 to this microporosity might have been very limited. Moreover, the CO_2 uptake in such a situation would probably have been quantitative (Clark et al., 1992b), resulting in a lack of carbon isotopic fractionation. In these objects, the $\delta^{13}C$-value of newly formed carbonate should mimic that of the dissolved inorganic carbon in the solution, and so the involvement of "combustion CO_2" is an alternative explanation. This suggests that "combustion CO_2", introduced and stored in the sediments, reacted with the Ca^{2+}-bearing hyperalkaline solutions coming from the ACZ to produce carbonate, when rehydration of the system occurred. If so, the matrix carbonation process should have occurred rather quickly after the combustion event.

In any case, the low $\delta^{18}O$ expected for newly formed carbonate from hyperalkaline solutions is lacking (kinetic or equilibrium fractionations: see Cory-Beck et al. (2005) for a recent assessment of the effects), except in vein KHM13. Therefore, additional processes or different carbonation conditions can be discussed (Fourcade et al., 2006). Post-carbonation isotopic re-equilibration with continental hydrosphere appears feasible (Fourcade et al., 2006, and below).

- **Newly-formed minerals in structural discontinuities in the basal part of the profile (A2):** Within the friable biomicrites of level A2, the joints, although less numerous, are more developed (centimetre-size) and are essentially filled with gypsum. Calcite detected in these discontinuities texturally corresponds to biomicrite fragments trapped in the sulphate matrix. Consistently, it displays the Sr isotopic composition of reference matrix carbonates (0.707787 ± 4.10^{-6}, Figure 6.41). For the C isotopic composition, a slightly negative $\delta^{13}C$, close to the reference value of the parent rock, is measured in these wider joints ($\delta^{13}C$ = -4.47‰ for the KHM07 joint). Gypsum (whole rock composition) shows a high $^{87}Sr/^{86}Sr$ ratio (0.707856 ± 4.10^{-6}), close to the values found for secondary carbonates in micro-joints and in travertines. These data are consistent with an equilibration of fluids responsible for the gypsum veins with biomicrite (equilibrations with porewaters?) and underline a process disconnected from the input of hyperalkaline fluids. This is also consistent with the fact that such gypsum veins are observed at some distance from the ACZ. The origin of large gypsum veins in the A2 level of the studied profile appears to be the results of more recent weathering.
- **Propagation of the hyperalkaline front:** Defining a precise “limit” to the percolation of hyperalkaline fluids in the system is speculative, but it is proposed that (with the reservations due to the fact that the studied profile does not represent a true vertical, but possesses a 3D aspect) the isotopic effects of the solutions (and their alkalinity) notably diminish from the approximate point height of 3 m but subtle effects cannot be excluded beyond this distance.
- **Recent re-equilibration of newly formed carbonates:** Except for vein sample KHM13 that displays, both for C and O, the typically-low isotopic compositions of recent coatings on concrete structures, the $\delta^{18}O$ value of the transition zone biomicrites, veins and travertines is distinctly higher, between 20.7 and 25‰ ($\delta^{18}O$ mean = 22.0‰). With a $\delta^{18}O$-value of past Jordanian precipitation in the range -5 to –8‰, a range slightly enlarged with respect to the modern rainfall database of Rozansky et al. (1993) in order to take into account climatic variations, the O’Neil et al. (1969) calcite-H_2O calibration provides carbonate equilibration “temperatures” of 10 to 40°C (Figure 6.49). Such values differ considerably from the apparent unrealistic “temperatures” obtained on the recent concretions on concrete structures mentioned above. This feature likely reflects interaction between the newly formed carbonates (travertines, veins and possibly matrix) and the recent to modern continental hydrosphere. Such processes are suggested from the comparison of ancient and recent carbonates formed in the context of alkaline solutions in Oman by Clark et al. (1992b). In Khushaym Matruk, secondary equilibration with local groundwater could have buffered O isotopes but not C isotopes in the section affected by hyperalkaline fluids, on account of the availability of external C and O. Inversion of previously formed calcite polymorphs (vaterite, aragonite…) or a particular isotopic metastability of calcite formed in hyperalkaline environments is suspected.

Figure 6.49 Diagram depicting the formation temperature ('x' axis of newly-formed carbonates as a function of the isotopic composition of local meteoric waters ("y" axis) (see text).

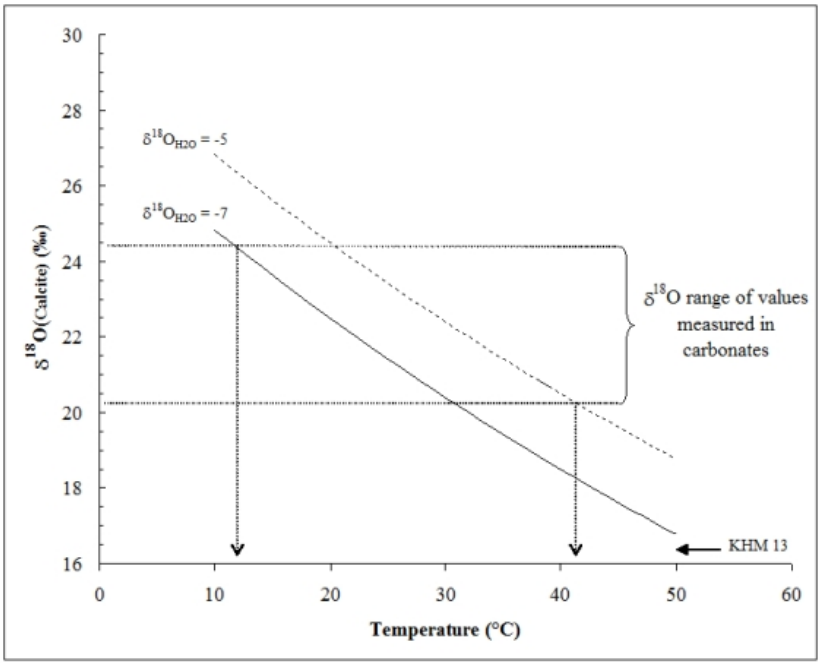

Dating with U-series disequilibria

An attempt at dating the circulation of hyperalkaline solutions was performed using the U-Th system on the joint-filling carbonates. However, this approach must be used with caution, as the behaviour of the U-Th systems of the studied samples is not well understood. U contents of calcite extracted from micro-joints in samples A3-5 and KHM13 are 0.5 and 4.4 ppm, respectively, whereas Th contents are 0.0104 and 5.10^{-6} ppm (Table 6.22). The iterative resolution of the chronometric equations (Rihs, 1998) with these values gives ages of 127 333 ± 2110 years and 111 173 ±610 years for calcites from KHM13F and A3-5F samples, respectively (Figure 6.50). However, this assumes that the system has behaved in a simple manner and that U has been introduced to the system only once. However, plotting the data on a Theil diagram (see Appendix 3.3) clearly indicates that this has not been the case. Rather, it appears that the U-Th system has been disturbed several times, in agreement with cathodoluminescence observations which indicate the occurrence of several stages of hyperalkaline solution circulation in the structural discontinuities of the rocks. As such, dating of the Khushaym Matruk system must await a more detailed, focused study.

Table 6.22 U and Th contents and isotopic compositions measured in calcites extracted in micro-joint fillings of indurated biomicrites A3-5 and KHM13. U-Th ages are determined by iterative calculations (Rihs, 1998).

Samples	(U) ppm	(Th) ppm	230Th/234U	234U/238U	"Age" (years)
Calcites	0.5	0.01 5.10^{-6}	0.7037±0.0061	1.1579±0.0033	127 333±2110
A3-5F	4.4		0.6405±0.0016	1.9309±0.0044	111 713±610
KHM13F					

Figure 6.50 Closed-system evolution of $^{230}Th/^{234}U$ and $^{234}U/^{230}U$ ratios as a function of time. Sub-horizontal curves correspond to different initial $^{234}U/^{238}U$ ratios (Schwarcz, 1979). A3-5F and KHM13F refer to calcite extracted in indurated biomicrites A3-5 and KHM13 respectively.

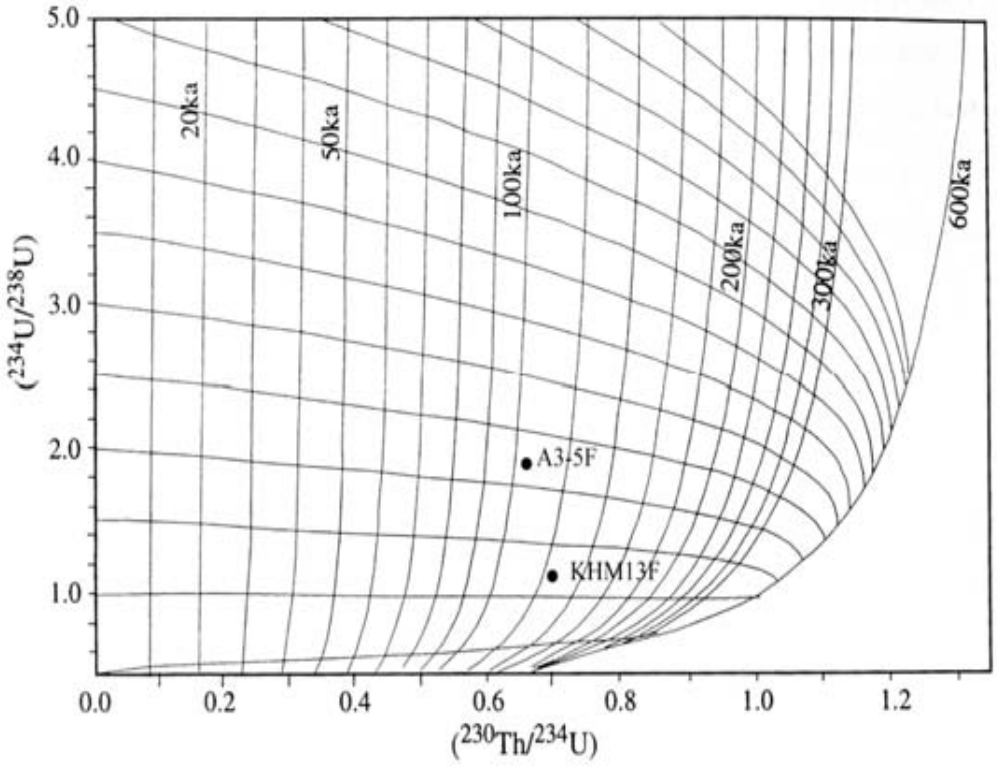

6.3.4.5 Summary

In the Khushaym Matruk sediments, the Sr, O and C isotope variations occur mostly within the upper 3 m of sediments, in the transition zone. The isotopic variations are probably expressions of the interaction between sediments and alkaline solutions, especially as a well-defined carbonation process. However, some uncertainties remain in the interpretation of isotopic characteristics (Fourcade et al., 2007; Elie et al., 2007). A most striking feature in these rocks is the lack of O isotopic disequilibrium with respect to local groundwater, such disequilibria being common during the production of carbonate from highly alkaline solutions. This suggests some post-formation re-equilibration of the carbonate fraction, which affected the O rather than the C signature. Carbon addition from a ''combustion CO_2'' and locally from the atmosphere are likely, but the temperature of the carbonation process is not constrained.

6.3.5 Organic matter characterisation

6.3.5.1 Introduction

The organic matter deposited in sediments consists primarily of the biopolymers of living organisms (carbohydrates, proteins, lipids, lignin etc). Part of this material is reworked by

bacteria, which degrade the biopolymers into simple monomers. Some biomonomers condense to form complex high-molecular-weight geopolymers that are the precursors of kerogen. In a geological environment, the organic matter undergoes a whole series of complex reactions inducing drastic changes in molecular and structural characteristics.

Under the influence of time and temperature, the thermal alteration of kerogen leads to petroleum generation in a sedimentary basin. Oil generation increases up to a maximum value with the burial depth. The different stages of oil generation are commonly called the 'oil window'. The generated oil is expelled from the source-rock, and is collected through secondary migration in reservoir rocks. With further thermal degradation, the remaining kerogen induces the formation of methane (wet-gas zone) and pyrobitumen. Bulk geochemistry and molecular parameters reveal that organic matter can also attain the oil window under the effects of a rapid heating due to igneous intrusions (Bishop and Abbott, 1995). The "thermal stress" parameters indicate that the maturity level of organic matter increases with increasing proximity to igneous intrusions.

In reservoir rocks, the oil may undergo different alteration processes. In addition to thermal effects, groundwaters induce a selective removal of hydrocarbons as a result of biodegradation and flushing. It is well known that transportation or storage are associated with oxidation processes. These are responsible for structural changes in coal affecting the coking properties, the solvent extraction yields, or the yields and nature of the pyrolysis products. The influence of weathering on organic matter has also been studied using samples collected from outcrops and oxidising groundwaters. Results show that weathering induces, in addition to the incorporation of oxygen in macromolecular structure of organic matter, transformations similar to thermal maturation.

At Khushaym Matruk, the combustion event may have induced changes in structural characteristics of the organic matter in the biomicrites underlying the ACZ. In addition to thermal stress, hyperalkaline solutions originating from the cement zone are assumed to have percolated through the biomicrites and weathering can also be assumed to occur in such a geological environment. The main problem is that these alteration processes are superimposed in nature. It is often difficult, or even impossible, to differentiate them without appropriated analytical techniques.

The purpose of this study is to examine the effects of these alteration processes, to estimate the temperature reached in the biomicrites and the extent of hyperalkaline perturbation on organic matter within the trench at the site (see Section 6.2).

6.3.5.2 Material and methods

These are detailed in Appendix 6.5.

6.3.5.3 Results

Petrographic characterisation

ACZ

The samples in this zone are completely oxidised and do not contain any type of organic matter. The observed fluorescence corresponds to the mineral fluorescence.

Transition zone

Sample KHM06 (at 0.25 m from the contact zone) presents the same characteristic as samples from the ACZ. It does not contain any type of organic matter, and the observed fluorescence corresponded to mineral fluorescence. At 1 m from the contact zone, the sample (A3-5) is oxidized and has no identifiable organic matter. The calcareous microfossils have a yellow fluorescence in their interior. Some microalgae, type lamalginite, were identified with an orange fluorescence. Thus, the fluorescence suggests an immature stage (early diagenetic generation) with an important hydrogen content for this sample (Figure 6.51).

Figure 6.51 Example of fluorescence in microalgae in sample KHM06

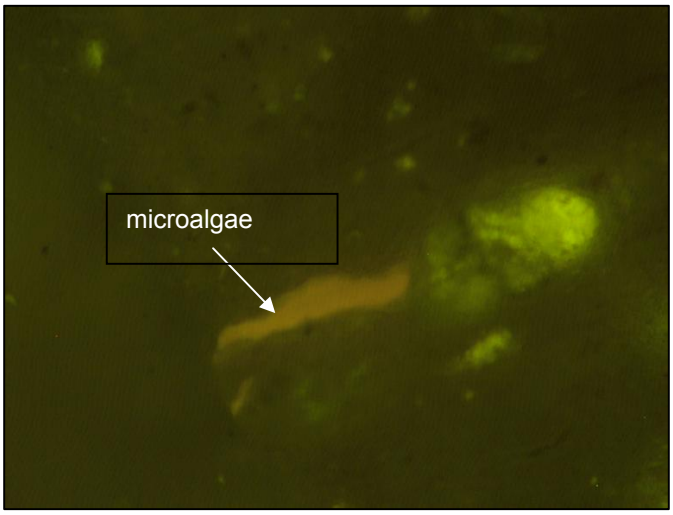

The sample KHM15 (at 2.0 m from the contact) is without organic matter visible under white light and without vitrinite particles (Figure 6.52a). Under fluorescence, some microalgae were observed with an orange coloration (Figure 6.52b-d). Mineral recrystallisation in the microfossils presented an intense yellow fluorescence. Microfossils were very abundant (Figure 6.52b-e). Thus, the fluorescence suggests an immature stage (early diagenetic generation) with an important hydrogen content for this sample, too.

Figure 6.52 Examples of fluorescence in sample KHM15

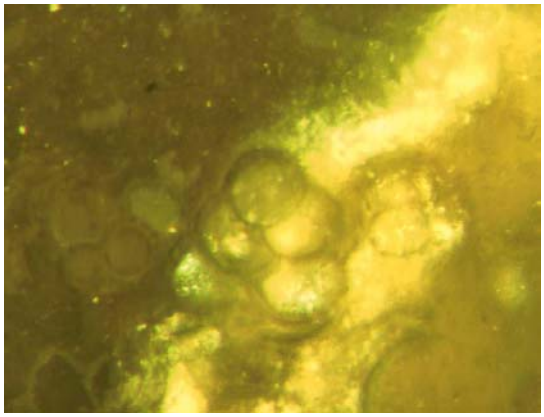

(a)

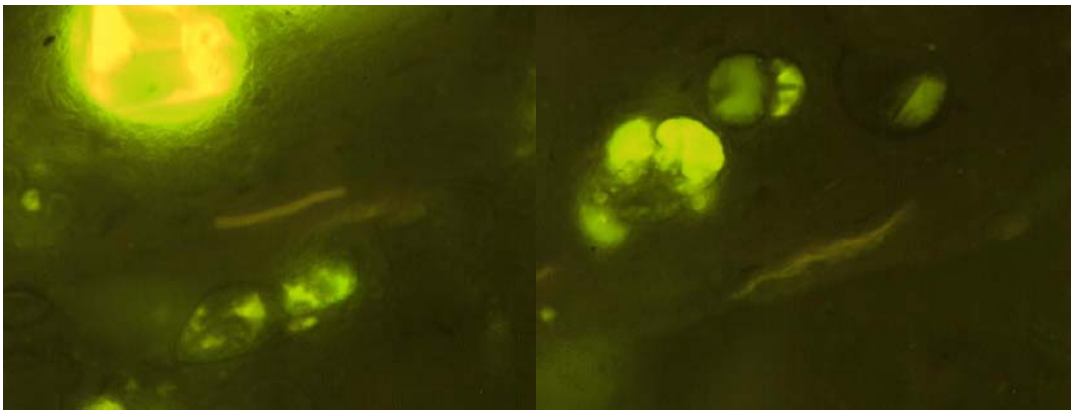

(b) (c)

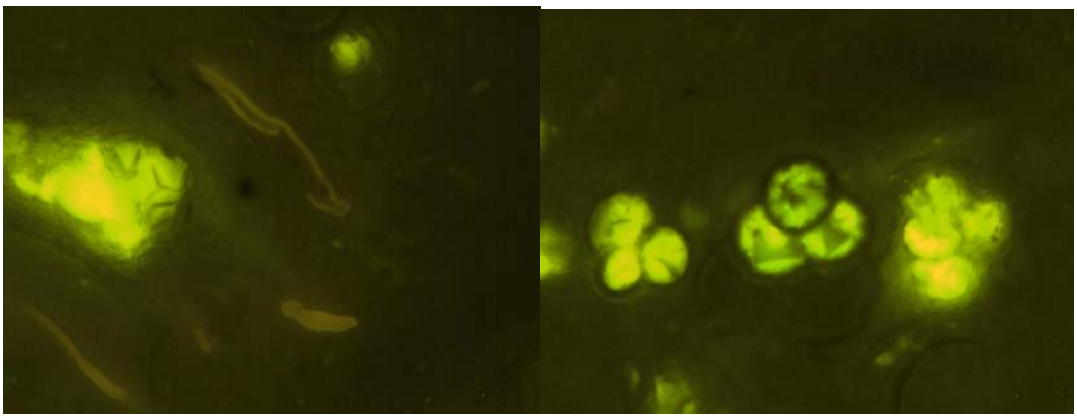

(d) (e)

The sample KHM14 (at 2.1 m from the contact zone) does not contain any identifiable organic matter under white light, and vitrinite was also not observed (Figure 6.53a-d). Under fluorescence, some microalgae with an orange coloration were found (photos Figure 6.53e, f). Calcareous microfossils with yellow fluorescence in their interior were observed (Figure 6.53g). The sample has what may be an organic mineral matrix with an orange

fluorescence. Once again, the fluorescence suggests an immature stage (early diagenetic generation) with an important hydrogen content for this sample.

Figure 6.53 Examples of fluorescence in sample KHM14

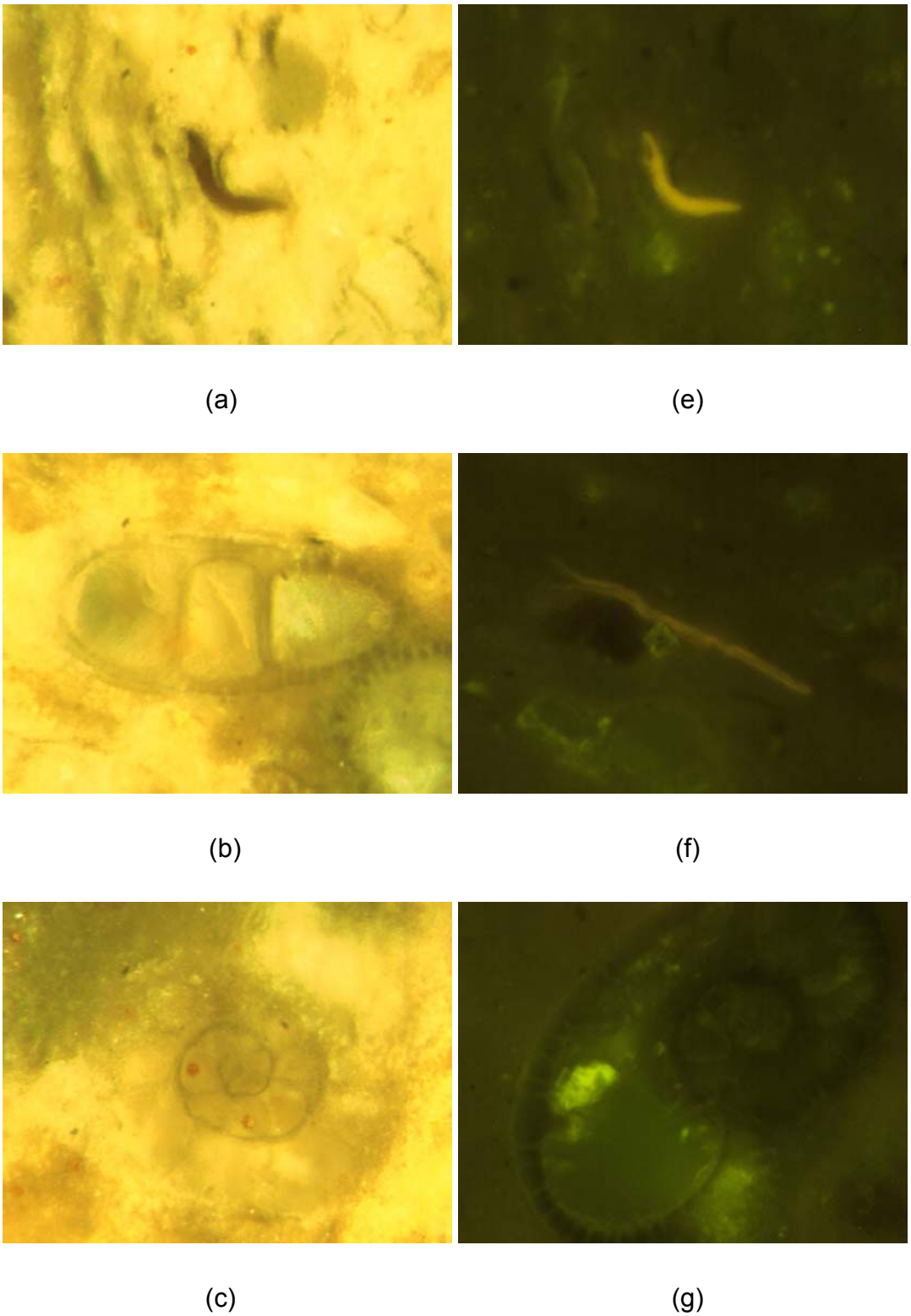

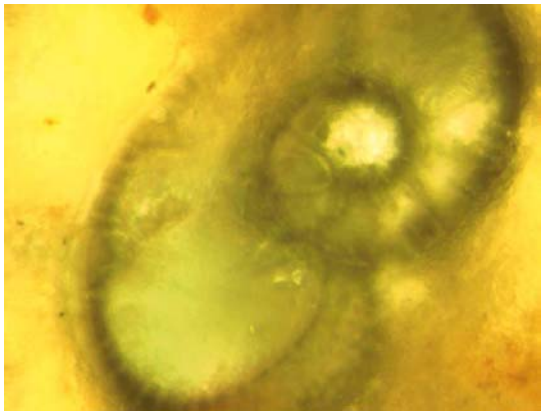

(d)

In the sample at 2.2 m from the contact (KHM 13), petrographic analysis under white light of the whole rock shows that the vitrinite is very rare, rounded and small (< 5 µm), presumably reflecting transport of the organic matter. In this case, vitrinite is oxidized and detritic (figure 6.54).

Figure 6.54 Examples of vitrinite in sample KHM13

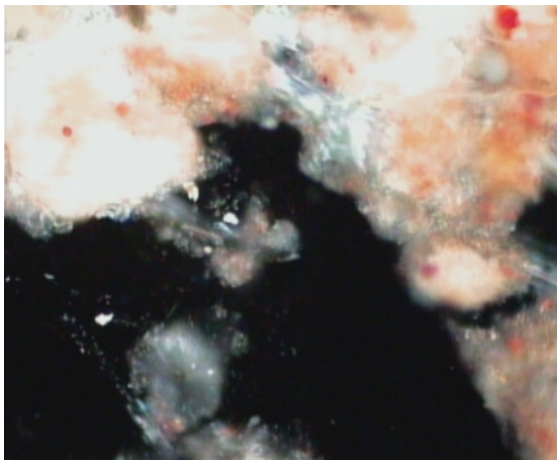

Numerous pieces of oxidised and highly reflectant lignocellulosic structures accompanied by globules or filaments were observed in the concentrated kerogen from sample A3-3 (2.1 m from the contact). These particles are present as the inertinite form and are relatively large (> 50µm, Figure 6.55a). Analysis of the whole rock shows that the vitrinite is present in gel form and/or huminite and is commonly accompanied of well-preserved lignocellulosic detritus (Figure 6.55b), suggesting the low maturity level of the particles.

Figure 6.55 Examples of lignocellulosic material in sample A3-3

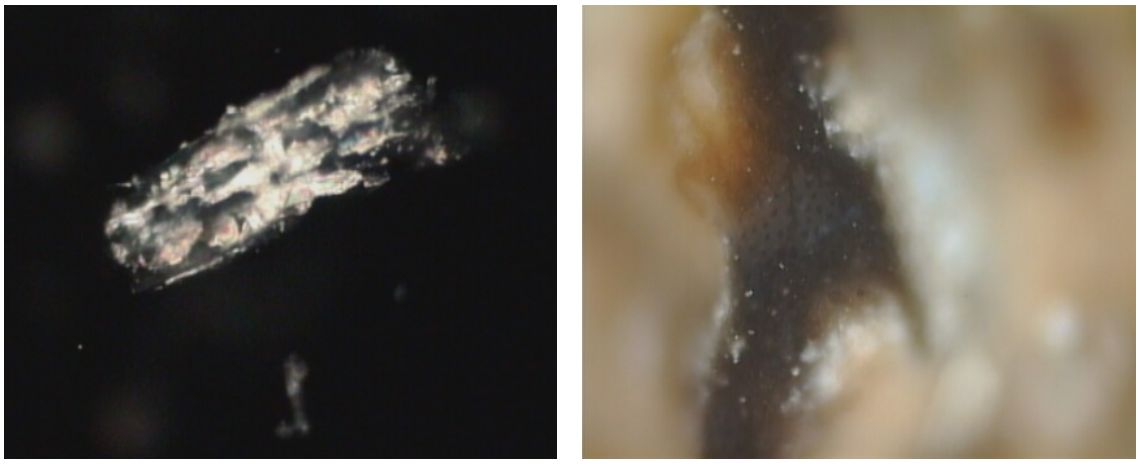

(a) (b)

Petrographic analysis under white light of whole rock A3-2 (2.6 m from the contact) shows that the vitrinite is present in gel form and/or huminite (Figure 6.56a) and is commonly accompanied by a lignocellulosic porosity, with characteristic cellular structure (Figure 6.56b) again, showing the immature character of the particles.

Figure 6.56 Gel-like vitrinite (a), accompanied by a (b) lignocellulosic porosity, with characteristic cellular structure (sample A3-2)

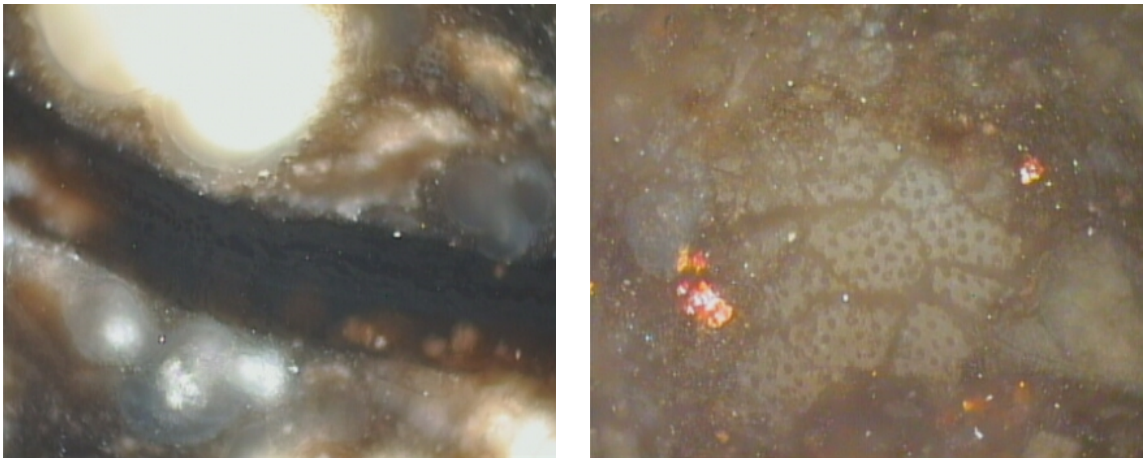

(a) (b)

Sample A2-12 (at 3.1 m from the contact zone) has a low organic matter content. There are zooclast tests with a mean reflectance of 0.7%, with a dark colouration and orange fluorescence (Figure 6.57a, b). Vitrinite was observed in six particles, with a mean reflectance of 0.24%, although this may actually relate to the background mineralogy due to the small size of the particles. Under fluorescence, some microalgae with an orange colouration were found (Figure 6.57c). This sample exhibits many calcareous microfossils with a intense yellow-green fluorescence in their interior (Figure 6.57d). The other part of the sample did not show the fluorescence. Thus, the fluorescence and the vitrinite reflectance

suggest an immature stage (early diagenetic generation) with an important hydrogen content.

Figure 6.57 Sample A2-12. Lower organic matter content sample. (a, b) zooclasts. (c, d) possible vitrinite

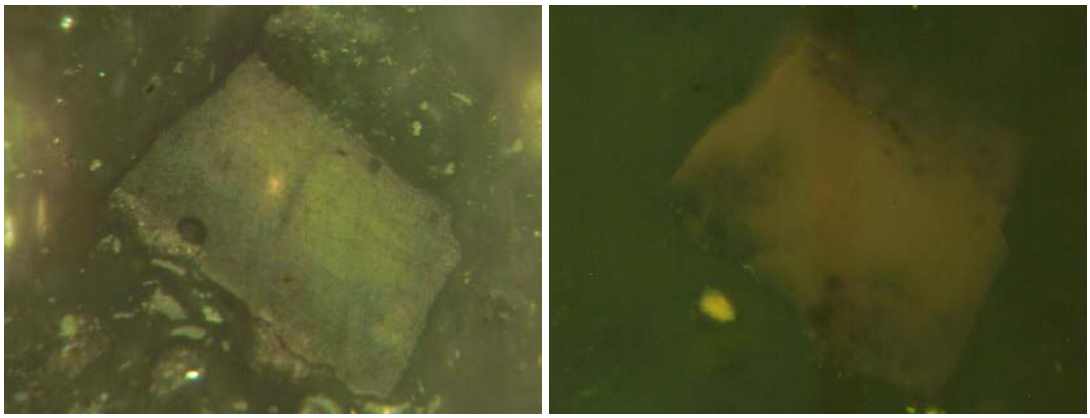

(a) (b)

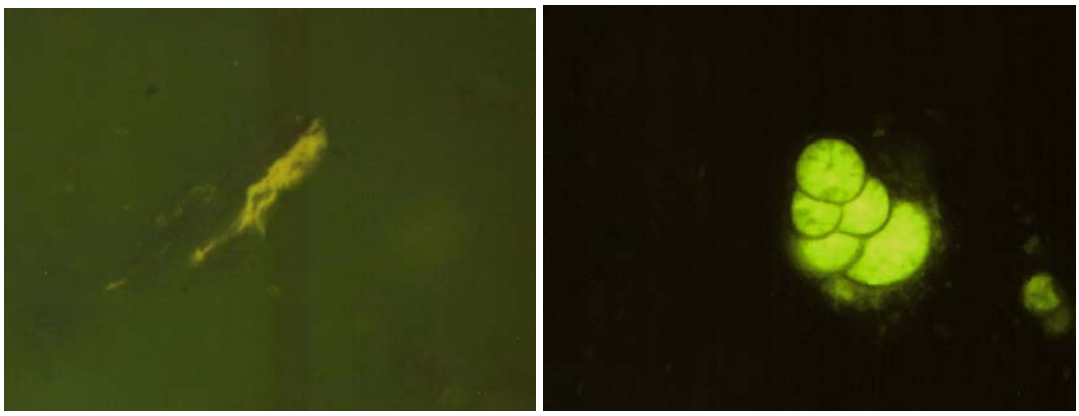

(c) (d)

Clay biomicrite

Sample KHM08A shows a low organic matter content (6 m, 0-7 cm). Only the zooclasts (Figure 6.58a,b) were identified as having similar characteristics to sample A2-12 (at 3.1 m from the contact). Mean reflectance was 0.09% and fluorescence was orange-red in colour. Vitrinite particles were not found in this sample. Under fluorescence, the microalgae fragments were observed to have an orange colouration (Figure 6.58c). This sample also exhibits many calcareous microfossils with a intense yellow-green fluorescence in their interior (Figure 6.58d). The other part of the sample did not show any fluorescence. Thus, the fluorescence and the vitrinite reflectance suggest an immature stage (early diagenetic generation) with an important hydrogen content for this sample.

Figure 6.58 Sample KHM08a. Lower organic matter content sample. (a, b) zooclasts. (c) microalgae fluorescence. (d) calcareous microfossil fluorescence

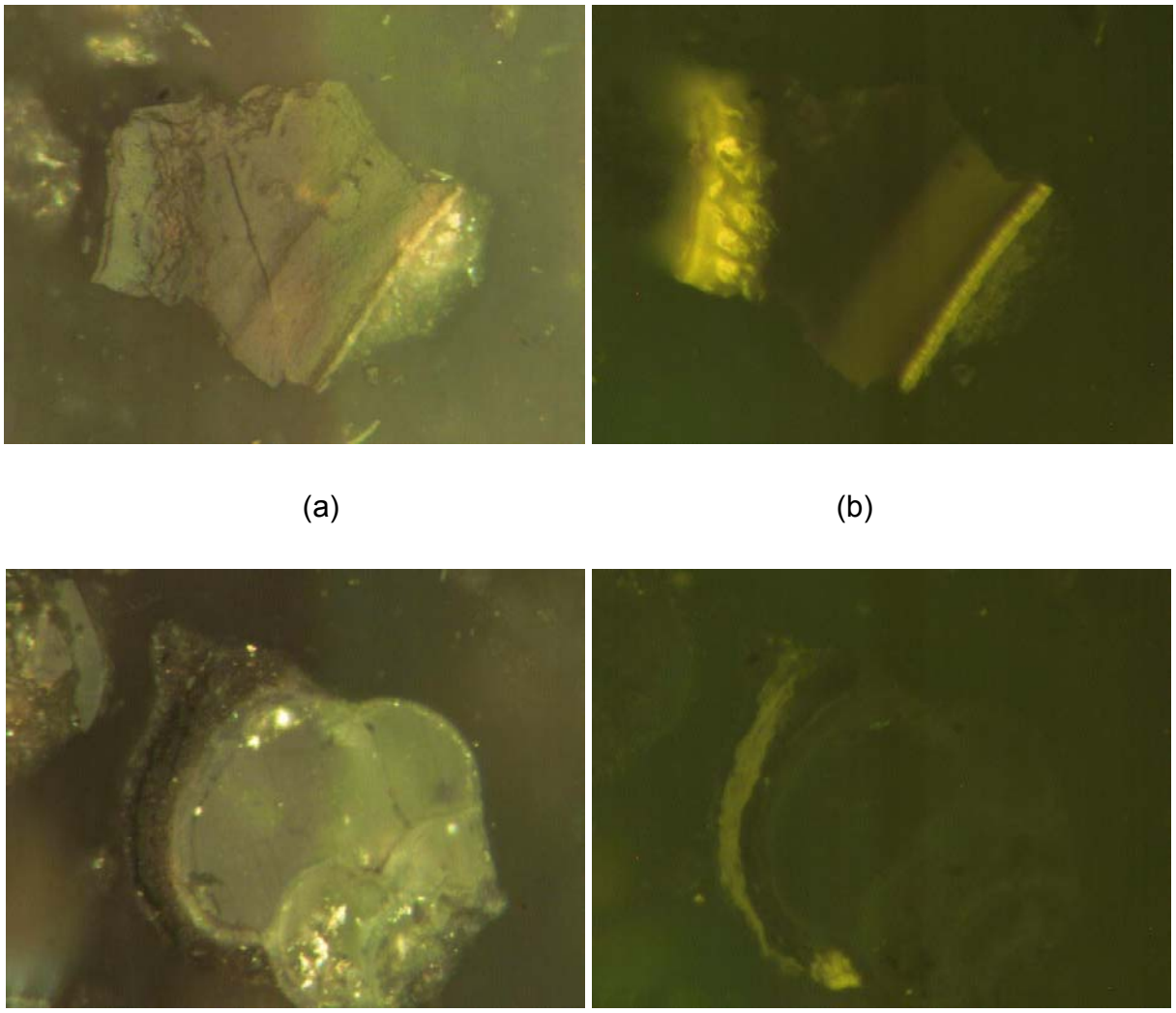

(a) (b)

(c) (d)

Sample A2-4 (7.9 m from the contact) has a low organic content. Generally, the fragments are of dark tests of zooplankton (zooclasts) with a low reflectance (0.08%). Only two vitrinite-like particles were observed, with a reflectance of 0.20% and 0.24% (but, as in sample A2-12, these values may be from the background mineralogy). Others particles of vitrinite do not appear to exist. Microalgae (lamalginite) with a yellow-orange fluorescence were identified. This sample contains many calcareous microfossils with a yellow-green fluorescence in their interior. Thus, the fluorescence and the vitrinite reflectance suggest an immature stage (early diagenetic generation) with an important hydrogen content for this sample.

Numerous pieces of oxidised and highly reflectant lignocellulosic structures accompanied by globules or filaments were observed in sample A2-1 (8.2 m from the contact) under white light. These particles are present in the semifusinite form and are relatively large (> 50µm, Figure 6.59a). These particles are frequent and represent about 50 % of the observed

organic matter present (Figure 6.59b). Iron oxide gels (probably goethite) with a red core and reflecting gel contour were also observed (Figure 6.59c).

Figure 6.59 Sample A2-1. (a,b) oxidised organic matter in semifusinite form (c) iron-oxide gels

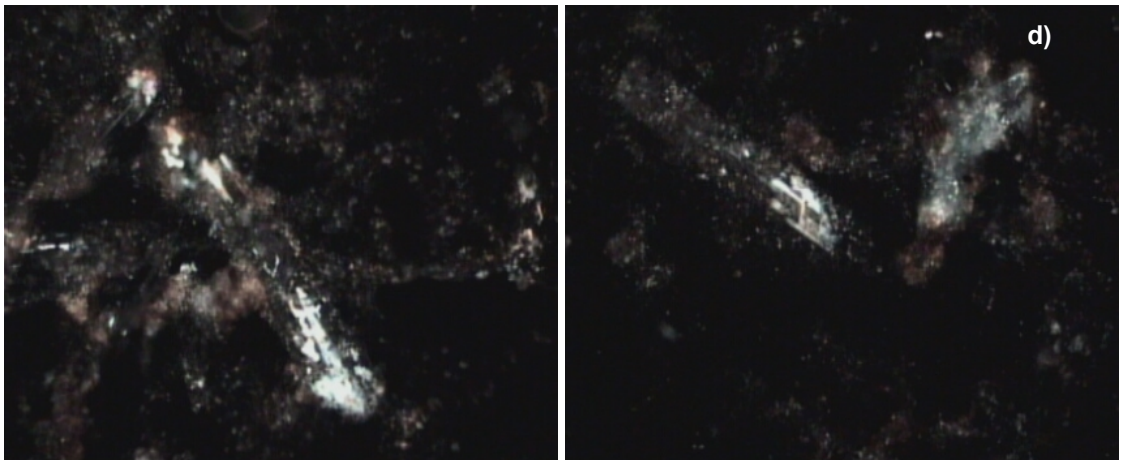

(a) (b)

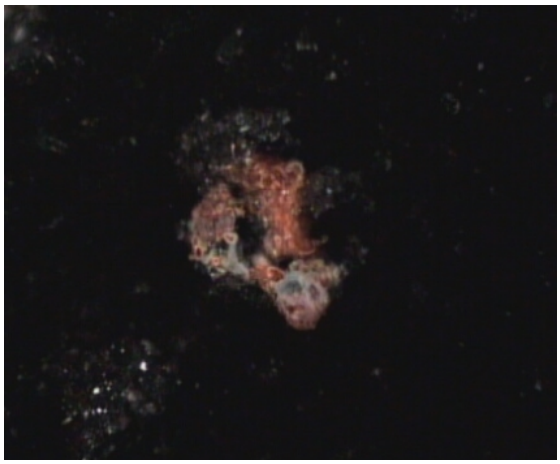

(c)

Rock-Eval analysis

The TOC profiles of whole-rock samples and isolated kerogens from Khushaym Matruk site are shown in Figure 6.60a. No significance change in the TOC content for whole rock samples has been found along the profile. TOC values higher than 30% were obtained for concentrated kerogens from the biomicrites and a slight decrease may be suspected toward the transition zone. This zone is the interval of drastic decrease in the TOC content, indicating a significant carbon loss in the samples nearest to the ACZ. The TOC content of kerogen is lower than 1% in the ACZ.

Figure 6.60a Variations in TOC Rock-Eval for whole rock samples (wt% of rock) and isolated kerogens (wt% of kerogen) from the Khushaym Matruk site with the distance from the contact zone based on Rock-Eval 6 pyrolysis.

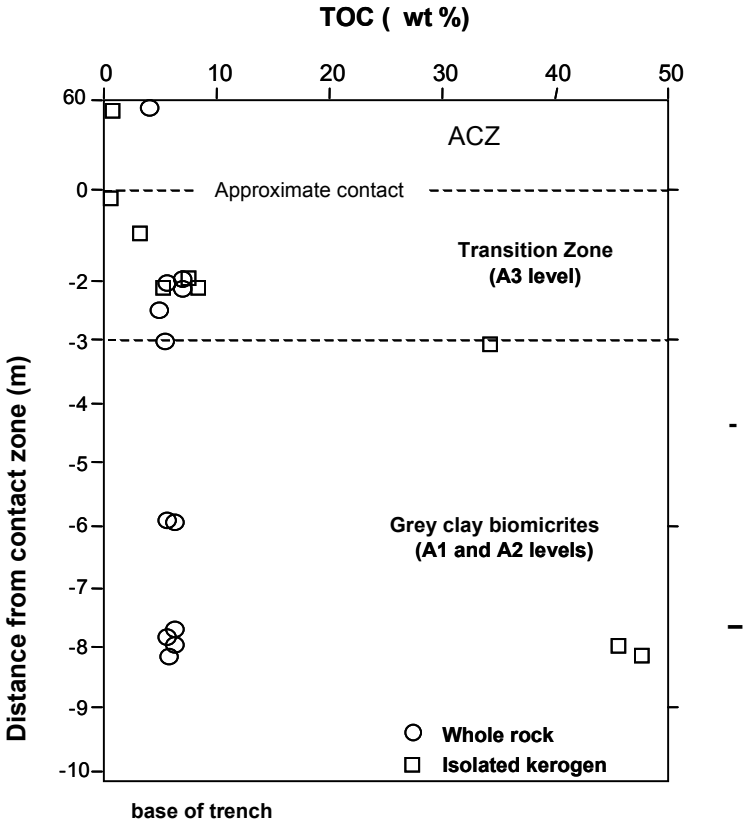

Figure 6.60b shows that the T_{max} values are higher than 480°C in the whole rock and isolated kerogens. With the exception of two samples, nearly constant T_{max} values were observed in the whole rock within the studied profile. On the other hand, kerogens from the biomicrites have 485 to 512°C Tmax, whereas those from biomicrite and the ACZ have 484 to 551°C T_{max}. Most rocks enter the oil window at about 435°C, and the beginning of the gas wet zone is observed at 465°C Rock-Eval T_{max} values. The high T_{max} values suggests overmature stage. However, some natural alteration processes such as weathering, bacterially mediated or not, or mild-oxidation under controlled laboratory conditions can induce an increase in the Rock-Eval T_{max} values (Landais et al., 1984; Copard et al., 2000, 2002, 2004).

Figure 6.60b Variation in Rock-Eval T_{max} (°C) in whole rock samples and isolated kerogens with the distance from the Analogue Contact Zone.

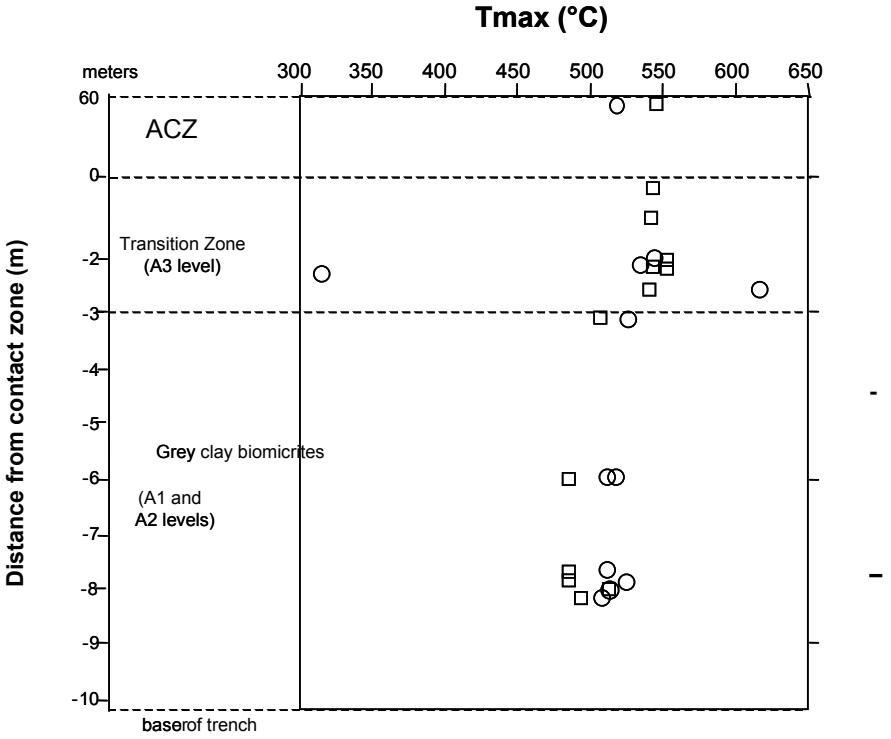

Tissot's classification of the whole-rock samples and isolated kerogens from Khushaym Matruk is given in Figure 6.60c. Type I and II kerogens are dominated by liptinite macerals whereas vitrinite macerals are predominant in type III kerogens. Type IV kerogen is "dead carbon" that has relatively high oxygen content and does not generate significant hydrocarbons. It is dominated by inertinite macerals, which have the highest reflectance of all the macerals in low and medium-rank organic matter (ICCP, 2001). Reviewing the data in Figure 6.60c, it is apparent that kerogens from the Khushaym Matruk site point to a large contribution of strongly oxidised inert organic matter and identified as inertinite. This maceral is known to derive from either wildfires (Falcon and Snyman, 1986; Guo and Bustin, 1998; Bustin and Guo, 1999; Glasspool, 2000) or reworked woody materials (Beeston, 1983; Falcon and Snyman, 1986; Taylor et al., 1989; Diessel and Smyth, 1995; Moore et al., 1996).

Figure 6.60c Classification of type I, II, III and IV kerogens in an hydrogen index versus oxygen index (Rock-Eval pyrolysis of kerogen) diagram. Types I and II generate oil, type III gas and type IV little or no hydrocarbons.

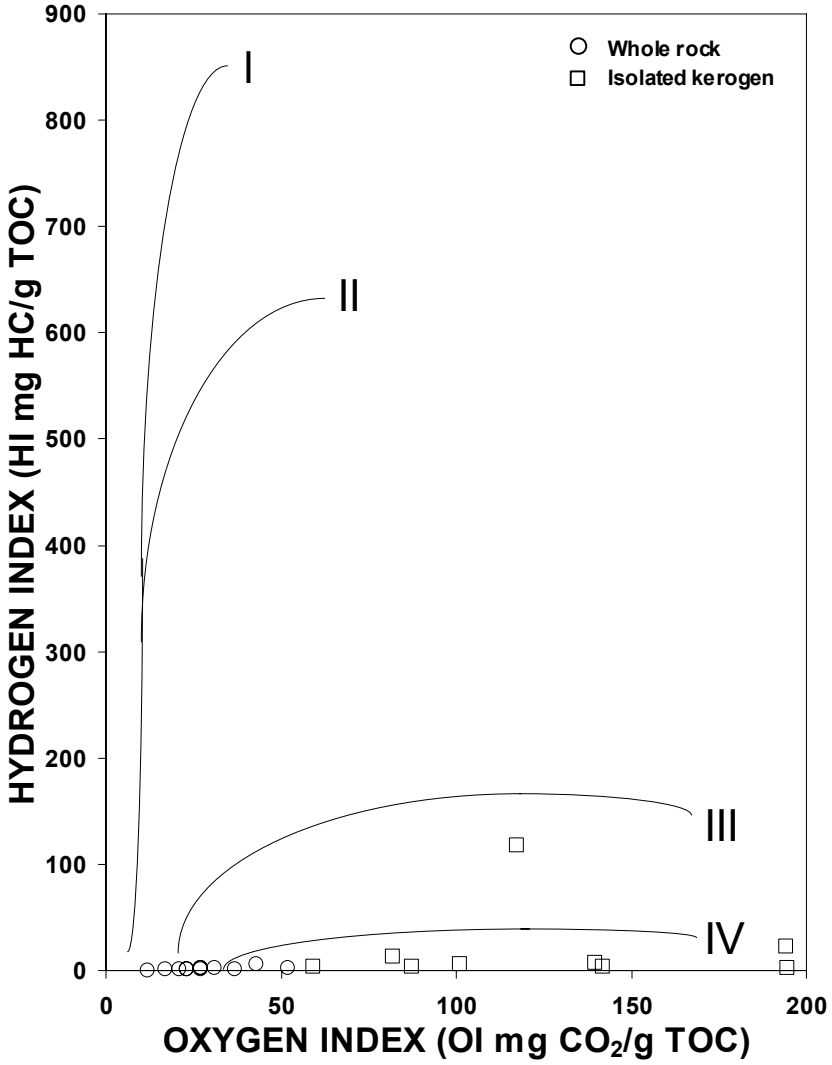

Micro-infrared spectroscopy

FTIR spectra of isolated kerogens from Khushaym Matruk samples are presented in Figures 6.61a and b. The i.r. spectra in Figure 6.61a were recorded in the organic matrix whereas those in Figure 6.61b were recorded in the lignocellulosic debris.

All the FT-i.r. spectra in Figure 6.61a show high concentrations of oxygen functionalities in the macromolecular kerogen structure as found in highly oxidised organic matter (Rhoads et al., 1983; Iglesias et al., 1998). The broad absorption band in the 3700-2200 cm^{-1} region indicates a high OH functionality of the organic matrix due to phenol, hydroxyl and carboxyl groups (Starsinic et al., 1984). The absorption at circa 1712 cm^{-1} is commonly attributed to the C=O stretch in carboxylic acids. All samples show an absorption band centred at approximately 1450 cm^{-1} that can be assigned at in-plane C-O-H bending of carboxylic acids. The increase in the broad band, centred at c.1250 cm^{-1} and its broadening into the

950 cm^{-1} region, also suggests the presence of carboxylic acids. The occurrence of ethers must be included since this contributes to the increase in the broad band at c.1250 cm^{-1} (Cookes et al., 1986). The assignment of the band at c.1620 cm^{-1} is more uncertain because it can be caused by aromatic C=C bonding and by oxygen-containing structures such as carboxylates, phenolic groups and highly conjugated carbonyl groups such as diaryl ketones or quinines (Painter et al., 1980, 1981; Low and Glass, 1989). The absence of ester bands, as in Ar-O-COR (1780-1760 cm^{-1}), R-O-CO-R (1755-1740 cm^{-1}) and Ar-O-CO-Ar (1740-1720 cm^{-1}) (Painter et al, 1980; Calemma et al., 1988), should also be noted.

Figure 6.61a FT-i.r. spectra of the organic matrix from the Khushaym Matruk site.

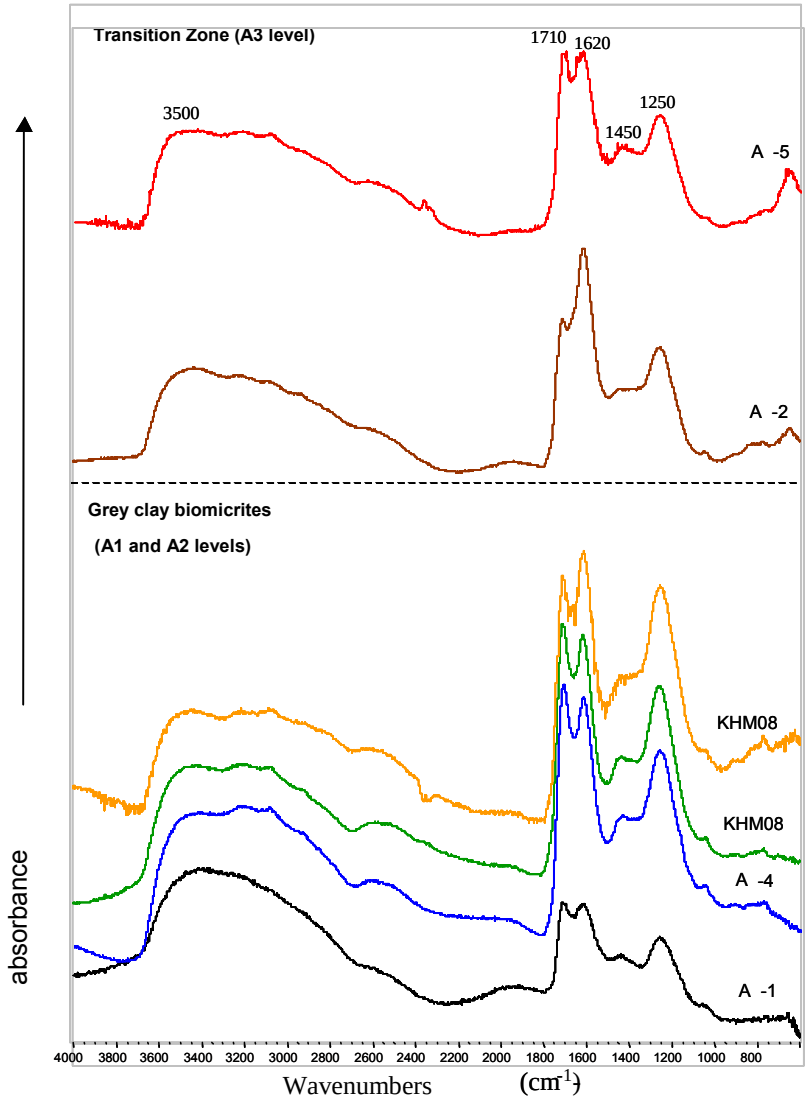

Figure 6.61b FT-i.r. spectra of lignocellulosic detritus from the Khushaym Matruk site.

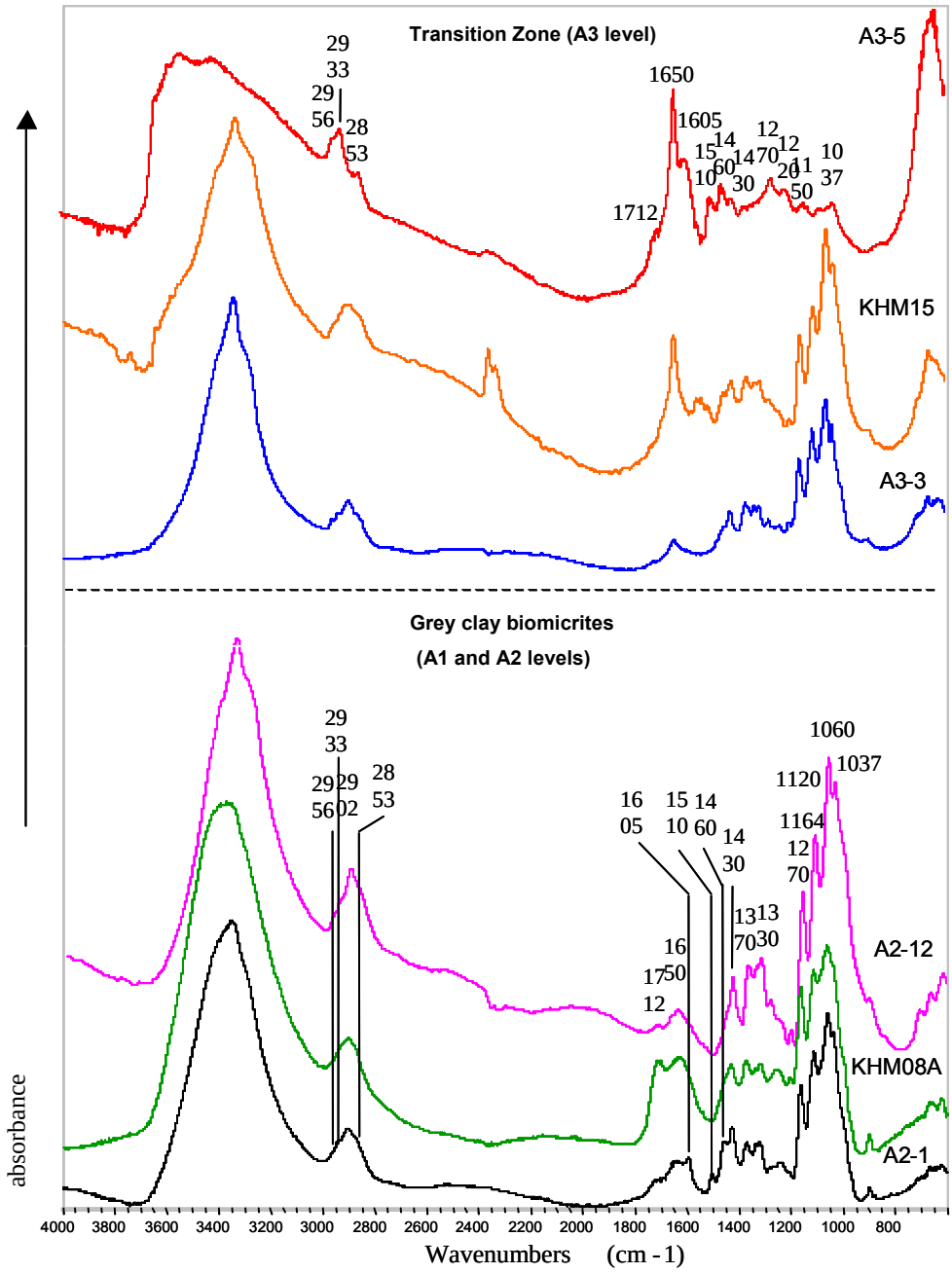

The weakness or absence of the bands between 2970 and 2840 cm^{-1}, assigned to symmetric and asymmetric stretching of CH_3 and CH_2 groups, leads to the conclusion that the aliphatic content in the organic matrix is small or nil. The aromatic hydrogen concentration must be negligible because no absorption bands was observed at c.3040 cm^{-1} and in the 900-700 cm^{-1} region arising from aromatic CH stretching and out-of-plane bending, respectively (see also the comments in Geyer et al., 1998).

FT-i.r. spectra recorded in lignocellulosic debris show major differences within the profile (Figure 6.61b). In the grey biomicrites, the broad band centred at 3350 cm^{-1} can be identified as corresponding to OH functionality in phenolic, alcoholic and carboxyl groups. The

absorption band observed at 3000-2800 cm^{-1} is caused by methyl and methylene group stretching vibrations. The low discrimination of methyl and methylene groups could result from a highly cross-linked structure. The spectral feature in the 2000-800 cm^{-1} region of the lignocellulosic debris from grey biomicrites closely resemble those in the spectra of unaltered lignocelluloses (Given et al., 1984). In the carboxyl/carbonyl region, samples display a shoulder at 1712 cm^{-1}, originating from stretching of C=O unconjugated to aromatic rings, and an absorption band at 1650 cm^{-1} that can be assigned to conjugated carbonyl/carboxyl stretching. The absence of ester bands as in Ar-O-COR (1780-1760 cm^{-1}), R-O-CO-R (1755-1740 cm^{-1}) and Ar-O-CO-Ar (1740-1720 cm^{-1}) (Painter et al, 1980; Calemma et al., 1988) should again be noted. Aromatic skeleton vibrations are assigned at the adsorption bands 1605, 1510 and 1430 cm^{-1}. Absorption at 1460 cm^{-1} is indicative of aliphatic C–H deformations and aromatic ring vibrations. The band at 1370 cm^{-1} could result from both OH in-plane bending and symmetric bending of aliphatic C-H. Lignocellulosic debris also exhibit intense bands in the 1200-950 cm^{-1} region. A band at 1164 cm^{-1} is assigned to C-O-C vibrations in aliphatic ethers (Landais et al., 1993). The absorption at 1060-1030 cm^{-1} can be attributed to C-O stretching in methoxyl, phenols and primary alcohols.

In the transition zone, the adsorption band attributed to the hydrogen vibrations of alcoholic OH, phenol or carboxyl is broadened. The aliphatic band in the 3000-2800 cm^{-1} is better resolved, suggesting that the alkyl chains are less cross-linked. The lignocellulosic detritus from transition zone appears strongly depleted in C-O and C-O-C bonds in the sample collected 1 m under the cement zone (Figure 6.61b). On the other hand, the absorption bands assigned to aromatic skeleton vibrations 1605, 1510 and 1460 cm^{-1} and conjugated carboxyl/carbonyl stretching increase.

6.3.5.4 Discussion

The extractable organic matter profile at the Khushaym Matruk site (in $\mu g\ g^{-1}$ of rock) is very similar to those observed during the thermal stress of hydrocarbon source-rocks, maximising within the transition zone at 2.6 m from the ACZ (Figure 4 in Techer et al., 2004). Thermal effects may also be suspected regarding the hydrocarbon content, which showed a maximum value at 2.1 m under the ACZ (Figure 4 in Techer et al., 2004).

Molecular analyses revealed that the shorter *n*-alkanes are prominent in all the chromatograms of aliphatic hydrocarbons (Figure 5 in Techer et al., 2004). A slight odd-to-even preference was also observed in the C_{23} to C_{33} range. A mixed origin (marine + land-derived) of organic matter may explain these results. The Pr/Ph ratio, deduced from the *n*-alkanes distribution, progressively increases when the cement zone is approached, suggesting a thermal effect due to the combustion process (Figure 7 in Techer and Elie, 2003). Hopanes (*m/z* 191) have been detected in low abundance and their distribution is dominated by the stable thermodynamically 17α(H),21β(H)-isomers (Figure 6 in Techer et al., 2004). The calculated R/S isomerisation ratios for the C_{32} hopanes are ranged between 0.50 and 054 along the profile, close to values found in the main phase of oil generation. Hopanes distribution (*m/z* 191) and high isomerisation ratio values may be regarded as the result of the thermal influence due to combustion phenomena.

Concerning the insoluble organic matter, some data seem to indicate that the samples have experienced high heating. Figure 1 in Techer and Elie (2003) shows that the production index (PI), deduced from Rock-Eval runs of rocks, increases from values lower than 0.1 in

the grey biomicrites to around 0.5 in the transition zone, thus passing through the oil window (0.1-0.4) defined by Peters (1986). The high Rock-Eval T_{max} values for both isolated kerogens and whole rocks suggest that organic matter from Khushaym Matruk site has reached the wet-gas zone (Figure 6.60b). The low Rock-Eval hydrogen index (HI) may reflect a severe thermal maturation (Figure 1 in Techer et al., 2004). The slight enrichment in heavy ^{13}C isotope in the transition zone when the contact zone is approached suggests the splitting of C-C bond in kerogen upon the thermal stress.

Petrographic analyses of the whole rock show that the vitrinite is present under the gel form and/or huminite, and is commonly accompanied of well-preserved lignocellulosic structures, which are typical of immature particles (Figure 6.61). Vitrinite reflectance values, varying from 0.2-0.24% in the grey biomicrites up to 0.6% in the transition zone, indicate that organic matter in the transition zone has only reached the onset of oil generation. The fluorescence observation allows identification of some micro-algae (lamalginite) with a yellow-orange colouration. Lamalginite has been regarded as derived from both *Cyanophyceae* and *Chlorophyceae,* and their presence suggests a freshwater lacustrine depositional setting. The high hydrogen content of these microalgae is indicative of an immature stage of organic matter (early diagenesis). The Rock-Eval TOC of the whole rocks does not show any significant trend within the profile, and ranged from 4 to 7%. TOC content of isolated kerogens progressively decrease as the ACZ is approached, probably due to an extensive formation of ralsonite-like fluorides (Na, Mg, Al, (F, OH), H_2O) as a result of kerogen isolation treatment. The Methylphenanthrene Index values (MPI), deduced from GC-MS analyses of aromatic hydrocarbons and based on the relative abundances of phenanthrene (*m/z* 178) and its methyl homologs (*m/z* 192), coincide with the immature zone.

The uncertainty regarding the influence of the combustion event on the underlying biomicrites is because alteration processes, such as thermal stress, weathering, and hyperalkaline disturbance, are superimposed at the Khushaym Matruk site.

Tissot's classification (Figure 6.60c) of isolated kerogens points to a large contribution of strongly oxidized organic matter, and identified as Type IV kerogen which is typically dominated by inertinite macerals. Evidence is growing that the predominant oxidising process is wildfire, and that most inertinites equate to charcoal (Bustin and Guo, 1999). However, this view is not uniformly held. Type IV kerogens are common in siltstones and sandstones accessible to oxygenated groundwaters. The proposed methods of formation of inertinite, other than wildfire, include the decomposition of woody material in aerobic or subaerobic conditions (Beeston, 1983; Falcon and Snyman, 1986; Diessel and Smyth, 1995), degradation by fungal activity and rotting (Moore et al., 1996), and exposure and dehydration of gelified material in a cold-climate setting (Taylor et al., 1989). The very low Hydrogen Index (HI) values of the samples do not result simply from inertinite content. Type IV kerogen can be derived from other kerogen types that have been reworked and oxidised. Oxidation tends to remove hydrogen and add oxygen to the kerogen explaining the low HI and the high Oxygen Index (OI) observed in Figure 6. 3.45c. The influence of oxidising percolating fluids is also evidenced by µ-FT-i.r. spectra, which revealed high concentrations of oxygen functionalities and very low aromatic and aliphatic hydrogen contents in the macromolecular organic matter structure (Figure 6.61a). Copard et al. (2002) show that weathering induces a drastic increase in the Rock-Eval T_{max}. Formation of etheric cross-linking is believed to be an important reaction that increases the thermostability of organic material under oxidising conditions. Molecular fingerprint of organic matter is also modified under oxidising conditions. Elie et al. (2000) experimentally demonstrated that, similar to

what is observed during thermal maturation, the *n*-alkanes distribution is shifted towards low molecular weight compounds and a 'mature' biomarkers distribution occurred with oxidation. Thus, great caution must be taken when using Rock-Eval, FT-ir and molecular parameters for estimating the thermal influence of combustion event on the underlying biomicrites.

Studies of samples from outcrops revealed that weathering produces several petrographic changes such as the appearance of microfractures, micropores and weathering rims (Ingram and Rimstidt, 1984; Ganz et al., 1990; Kruszewska and Du Cann, 1996). The weathering effects on vitrinite reflectance have been examined both naturally and under controlled laboratory conditions. No overall consensus exists concerning the influence of weathering on petrographic characteristics of organic matter, and the mechanisms involved remain to be elucidated. Study of naturally weathered seam coal clearly showed a decrease in vitrinite reflectance when the surface is approached (Ganz et al., 1990). On the other hand, it has been experimentally demonstrated that vitrinite reflectance was unaffected by low-temperature oxidation (Chandra, 1958; Copard et al., 2004). Ingram and Rimstidt (1984) claimed that natural weathering effects did not significantly alter the reflectivity of coal particles, and concluded that vitrinite reflectance may be a reliable indicator of maturity in geological environment disturbed by oxidising groundwaters. The presence of well-preserved lignocellulosic structures and the vitrinite reflectance values of samples from Khushaym Matruk make major increase in temperature due to the combustion event rather unlikely.

Optical microscopy shows the presence of well-preserved lignocellulosic detritus derived from vascular plants, and frequently found in wetland ecosystems (Hodson et al., 1983). Lignocellulose is mainly formed of three components closely associated, hemicellulose, cellulose and lignin. Basically, cellulose forms a skeleton which is surrounded by hemicellulose and lignin. Covalent cross-linkages have been suggested to occur between lignin and carbohydrates (cellulose, hemicellulose) in the form of ester and ether functionalities. Delignification reactions include saponification of intermolecular ester bonds and de-etherification. The extent to which lignocellulosic materials are altered depends on its original chemical and structural composition and, in no small part, surrounding factors such as alkaline pH, temperature, reaction time, redox conditions (Draude et al., 2001). Intensive chemical treatments are required to separate cellulose, hemicellulose and lignin. Alkaline-extraction at temperatures in the range 130-180°C is one chemical treatment used in the paper industry for opening up the closed structure of lignocellulosic materials (Kraft process). A pre-heat at temperatures lower than 240°C for 3 s to 20 min, during a steam-explosion experiment, also promotes the separation of the main components of lignocellulose by diluted aqueous NaOH solution (2%) at room temperature (Fernández-Bolaños et al., 1999). Figure 6. 3.46b shows that spectral features in the 2000-800 cm^{-1} region of lignocellulosic detritus from the grey biomicrites closely resemble those of unaltered lignocelluloses, explaining the low vitrinite reflectance values (0.2-0.24%). This result suggests that thermal effect due to the combustion event is negligible in the biomicrites and/or pH of percolating fluids did not enable the degradation of lignocellulose. On the other hand, the relative abundance of the band in the 2000-800 cm^{-1} region progressively decreases when the cement zone is approached. Two possible scenarios can be proposed: either hyperalkaline leachates have percolated through the transition zone or the combustion event has partially altered lignocellulose, making it more soluble in hyperalkaline solution. The second scenario seems more realistic on account of the occurrence of oil migration and petrographic evidence revealing that organic matter from the transition zone has only reached the onset of oil generation. FT-ir spectra of lignocellulosic

materials reveal that the influence of the hyperalkaline perturbation at Khushaym Matruk is at a maximum at 0 to 1 m under the cement zone, and evidence of progressive pH buffering of the hyperalkaline leachates by mineralogical assemblages along the profile. The extent of hyperalkaline perturbation at the Khushaym Matruk site deduced from this study of organic matter is comparable to values estimated by modelling diffusion of of a hyperalkaline plume in a clay barrier (Gaucher et al., 2004).

6.3.5.5 Conclusions

Study of organic matter from Khushaym Matruk reveals that the thermal aureole due to the combustion event is limited to a few metres (0-3 m) in the clay biomicrite (cf. section 6.3.3). Weathering induces an 'overmaturation' of organic matter at Khushaym Matruk and geochemical parameters deduced from biomarker studies or Rock-Eval pyrolyses cannot be used to infer the temperatures experienced in the underlying biomicrites. However, organic petrography analysis, GC-MS analysis of aromatic hydrocarbons and μ-IRTF clearly indicate that organic matter has only reached the onset of oil generation in the transition zone. The effect of hyperalkaline reaction is at a maximum at between 0 and 1 m under the cement zone, and a progressive pH buffering by mineral matrices can be suspected to occur with the downwards propagation of the leachates.

However, study of the Khushaym Matruk site does not allow observation of all the products generated during natural alteration of the organic matter because generally the most mobile fractions are depleted. Without this information, it is impossible to draw quantitative conclusions on the leaching of organics by hyperalkaline leachates and the toxicity of the alteration products. Moreover, it does not enable clearly to discriminate the effects of thermal stress, weathering and hyperalkaline leachate perturbation on organic matter whereas laboratory experiments remain a means to do so. The understanding of the processes involved at the Khushaym Matruk site - thermal effects induced by the combustion event, influence of hyperalkaline reaction and pH buffering by the mineral matrix - need to be checked against the observed transformations in the laboratory. Comparisons of data deduced from natural analogue studies and laboratory experiments would facilitate (i) the validation of the experimental simulation conditions, (ii) a better estimation of temperature reached in the transition zone (iii) a better understanding of the mechanisms involved and (iv) the estimation of rate and extent of hyperalkaline alteration. Such an approach would provide an alternative pathway using organic matter for the geochemical modelling of the potential effects of a hyperalkaline plume in radioactive waste repositories.

6.3.6 Mineralogy: study of a hydrated cement sample from the Khushaym Matruk site

6.3.6.1 Introduction

As noted in Chapters 1, 2, 4 and 6, the ACZ represents a mixed system of essentially cement slag through to fully hydrated cement. Here, a brief description is given of a modelling study which attempted to reproduce the mineralogical changes as a cement slag is hydrated. Several samples were collected from the ACZ at the Khushaym Matruk site and one of these (BL2b, see Appendix 6 for the full list), from about 20 m below the top of the site (see Figure 6.15), presents interesting reaction features in the vicinity of joints in the rock. A mineralogical and chemical study of this sample was undertaken; eventually, modelling attempts were carried out to reproduce the observed zonations from the joint,

through layers of hydrated cement and into the cement slag, deeper in the metamorphosed core of the rock.

6.3.6.2 Analytical methods

These are presented in Appendix 6.6.

6.3.6.3 Modelling

Modelling of the cement alteration was carried out using the reactive transport code Hytec 3.2.6 run on a 12 nodes Linux cluster (Pentium IV, Redhat 7.3) (Van der Lee et al., 2002).

6.3.6.4 Binocular microscope study of the sample

An image of the polished sample is shown in Figure 6.62. The examination of the sample under the binocular revealed following major features:

- major joints (~100 µm width) filled with white, grey or yellowish products
- thin (~10 µm width) and white joint
- dark-reddish lineaments with the same orientation as the thin white joints
- red-black nodules (diameters from 50 µm to 300 µm) probably containing iron oxides (haematite colour)
- a red-brown matrix corresponding to the cement far from the large joints. Large (~100 µm) translucent calcite crystals are visible in this matrix.
- a salmon–to-beige matrix corresponding to the cement adjacent to the large joints. A sharp front showing some colour texture separates this hydrated matrix from the intact material. The width of this zone seems to be roughly proportional to the width of the internal joint.

Details of several of these features are presented in Figures 6.63 to 6.65.

Figure 6.62 Polished slab of sample BL2b observed with a binocular microscope (mosaic of several individual pictures). The yellow line indicates the position of a profile studied by SEM

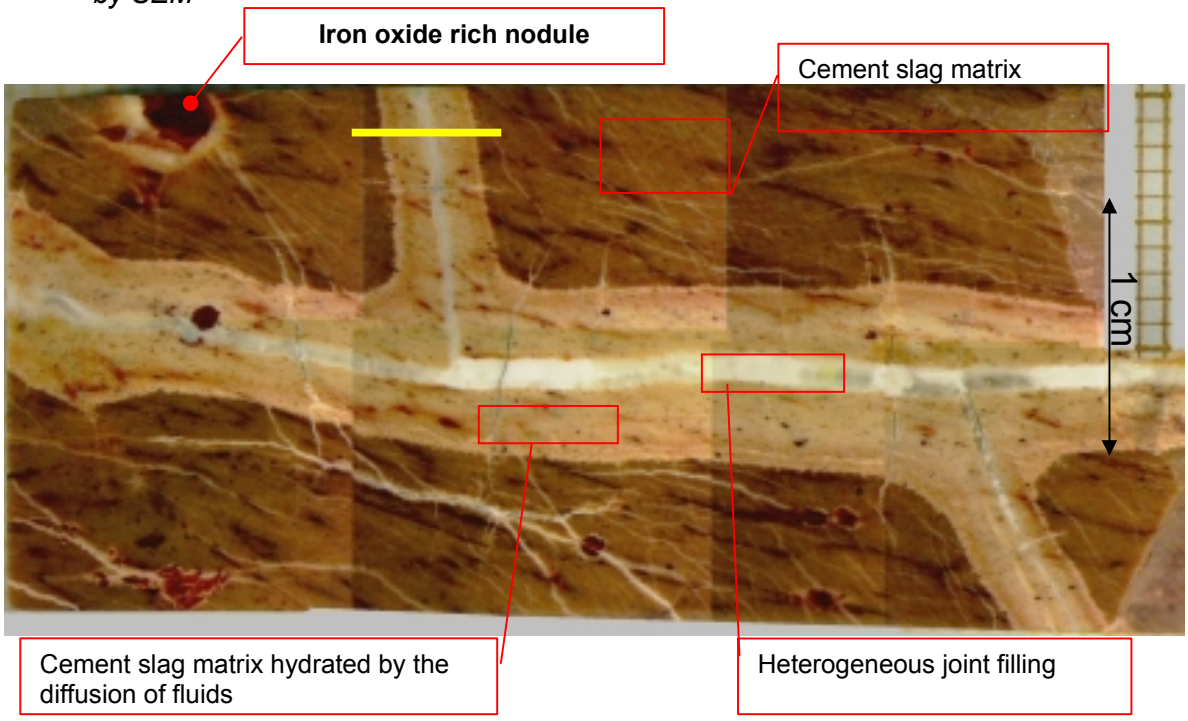

Figure 6.63 KM-BL2b Details of the joints seen under the binocular microscope

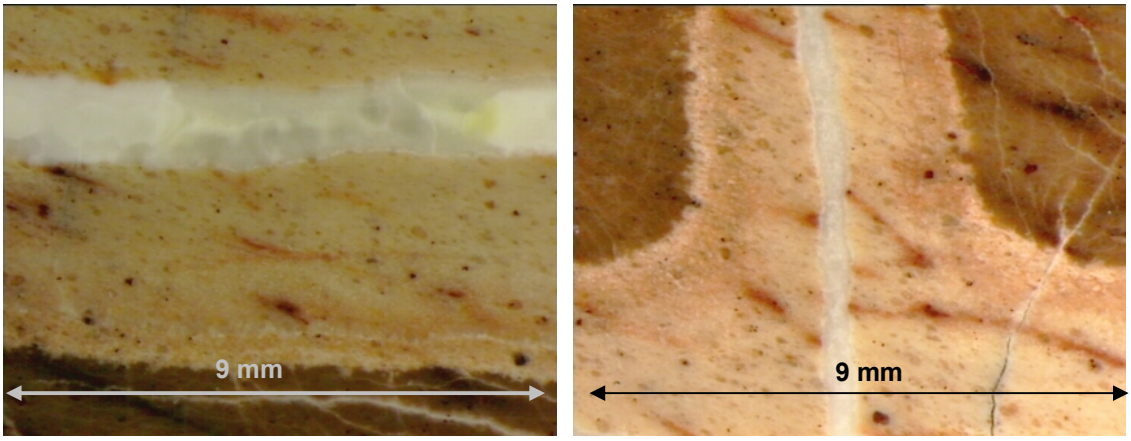

Figure 6.64 KM-BL2b – Details of a large iron oxide-rich nodule seen under the binocular microscope

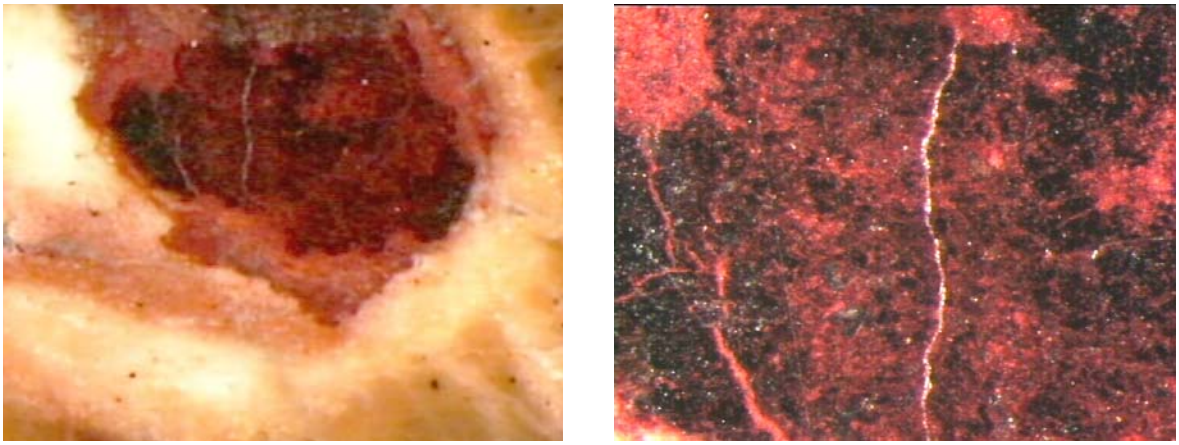

Figure 6.65 KM-BL2b Aspect of the unaltered cement matrix as seen under the binocular microscope

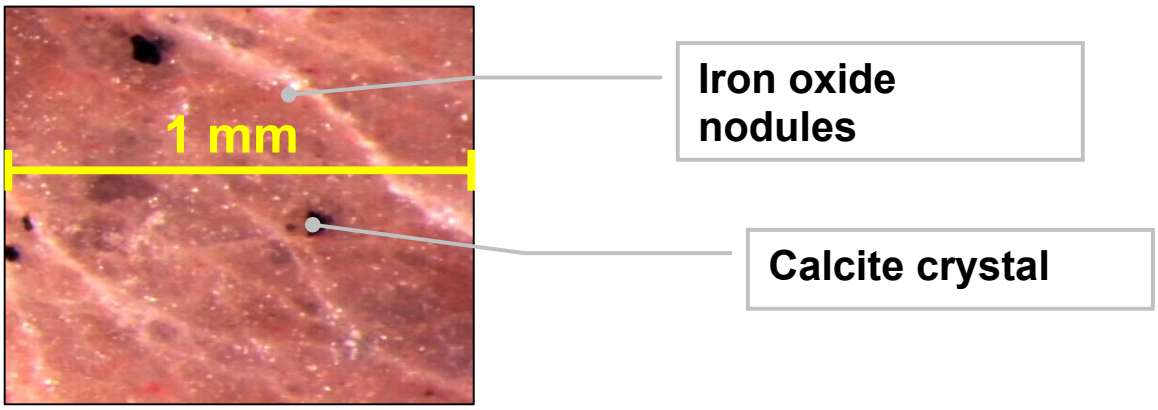

6.3.6.5 XRD Spectra

Unhydrated matrix

The XRD spectrum of the powdered material representing the unhydrated matrix (i.e.the cement slag) in sample BL2b shows its strongest lines for calcite (05-0586) spurrite (75-0620) and thaumasite (46-1360). As these three phases have a lot of diffraction lines, it is difficult to attribute weak residual lines that frequently overlap or edged by strong calcite or spurrite peaks. In agreement with SEM observations, the attribution of several lines to brucite (44-1482) and iron oxide chloride (72-0619) could be proposed.

Hydrated matrix mixed with white fillings

The XRD spectrum of the altered matrix differs mainly from the preceding by the absence of the lines of spurrite. Lines of afwillite (weak) and jennite (medium) are identified.

White filling in large joint

The XRD spectrum of powdered material collected from the inner joint filling revealed the presence of mainly calcite and jennite (Ca9H2Si6O18-6H20) and, to a lesser extent, thaumasite and ettringite.

6.3.6.6 SEM/EDX observations of the sample

Unhydrated matrix

A section of the unhydrated matrix is presented in Figure 6.66 (SEM BSE image). Several mineral phases are distinguished on this section. Calcite crystals range from 5 µm to more than 50 µm in diameter and sometimes occurs as rounded grains inside another undetermined phase labelled ‘mineral X’. Spurrite is also clearly identified and occurs in crystals ranging from 5 to 15 µm in diameter. Calcite and spurrite clearly represent the two dominating minerals of this matrix. The phase labelled mineral X appears in BSE as very bright rectangular patches around 50 µm long and 20 µm wide. Detailed inspection (Figures 6.67 and 6.68) shows that this phase also contains minute inclusions (shown to be BaSO4 by EDX analyses). The Mineral X clearly displays a preferential cleavage, ressembling that of a micaceous phase (Figure 6.67). Several other minor phases could be identified:

- a phosphate-rich phase that could be identified as ellestadite (see EDX data below).
- Brownmillerite.
- brucite, visible as very dark intergrain zones in Figure 6.66.
- an undetermined Ca-aluminate occuring as grey fillings in Figure 6.66.

Figure 6.66 *KM-BL2b. Observation of the unhydrated cement (slag) matrix with the SEM (BSE, 20 kV, carbon coated sample). Samples of the main mineral phases are shown by the tags.*

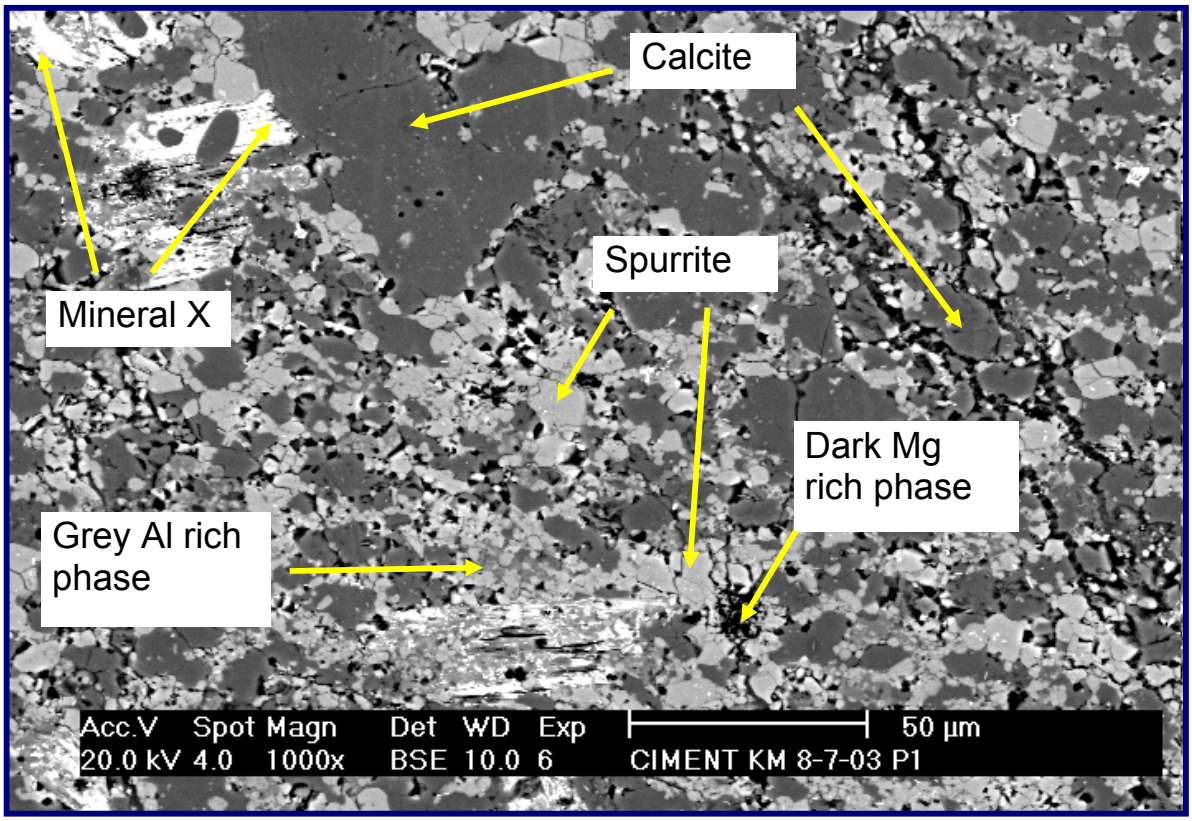

Figure 6.67 *Top: detailed view of mineral X showing the well-developed cleavage and small Ba-rich inclusions. Bottom: grain contact between spurrite (S), calcite (C) and mineral X (X).*

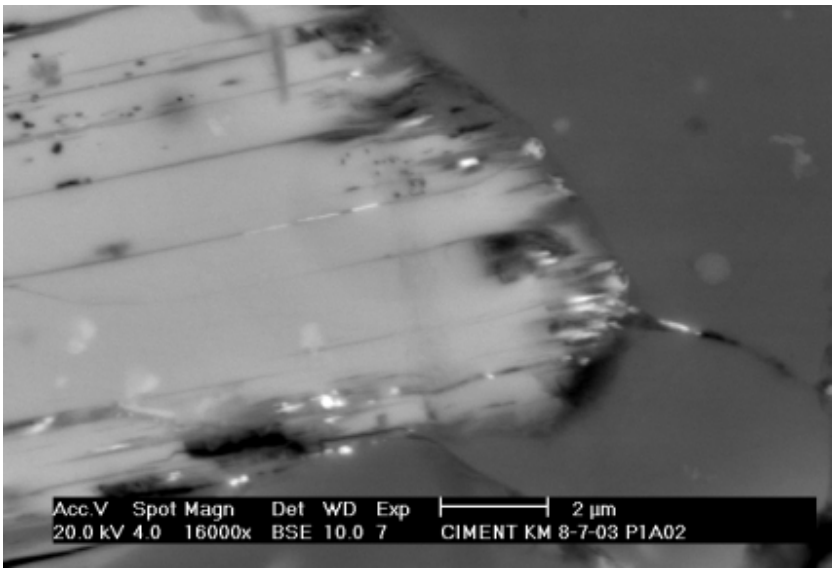

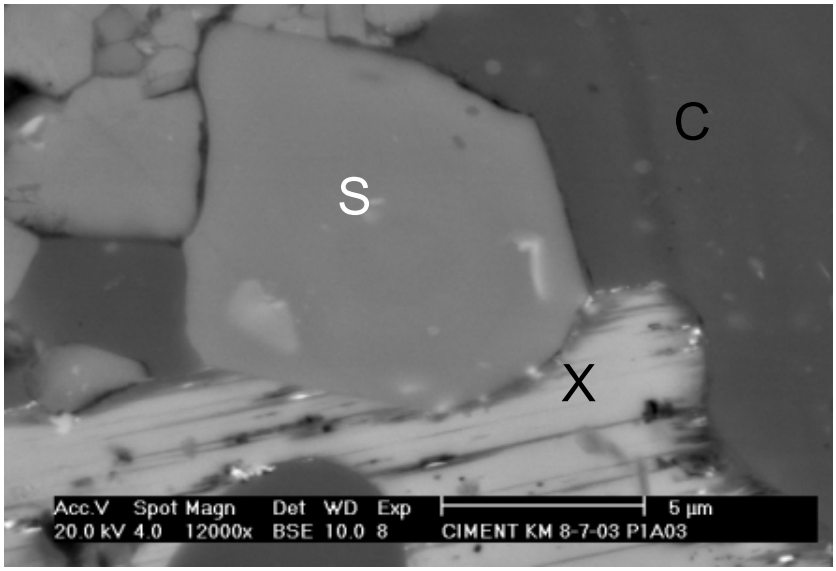

Figure 6.68 Detail of mineral X showing dark regions rich in Mg and bright grains of $BaSO_4$

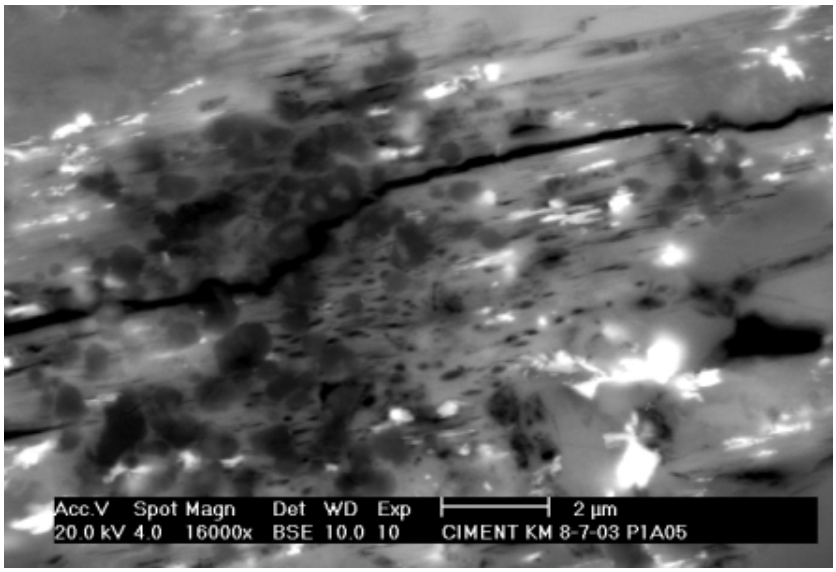

Table 6.23 summarises chemical compositions deduced from EDX analyses performed on these different phases. It appears that mineral X contains potassium and exhibits some similarities with a potassium-bearing phase identified in Maqarin (see Chapter 4). Mineral X has also some similarities in chemical composition with thaumasite. However, the exact carbonate content of the phase could not be established. Figure 6.69 shows selected EDX spectra of the minerals.

Table 6.23 Summary of minerals observed and analysed under the SEM/EDX. Figures derived from the treatment of the spectra give the relative proportion of cations in individual phases.

Observed under the SEM in BSE	Ca	Si	Al	Fe	S	P	K	Mg	Interpretation
Bright rich in Fe	2		0.5	1.5					Brownmillerite $Ca_2(Al,Fe)_2O_5$
Major medium grey phase	1								Calcite $CaCO_3$
Pale grey Ca Si phase	5	2							Spurrite $Ca_5(SiO_4)_2CO_3$
Pale grey play displaying cleavage and bright $BaSO_4$ inclusions	6	2	0.3		1		0.4		Undetermined calc-silicate-sulfate with K (Mineral X)
Al rich medium grey phase	1	0.2	0.7						Undetermined Ca-aluminate
Mg rich dark grey	5	2	tr		tr			6	Mixture of brucite $Mg(OH)_2$ and spurrite
Pale grey phase rich in P	10	3			1.5	2.5			Ellestadite

Figure 6.69 Sample KM BL2b - EDX spectra obtained on ellestadite, larnite and the undetermined mineral X.

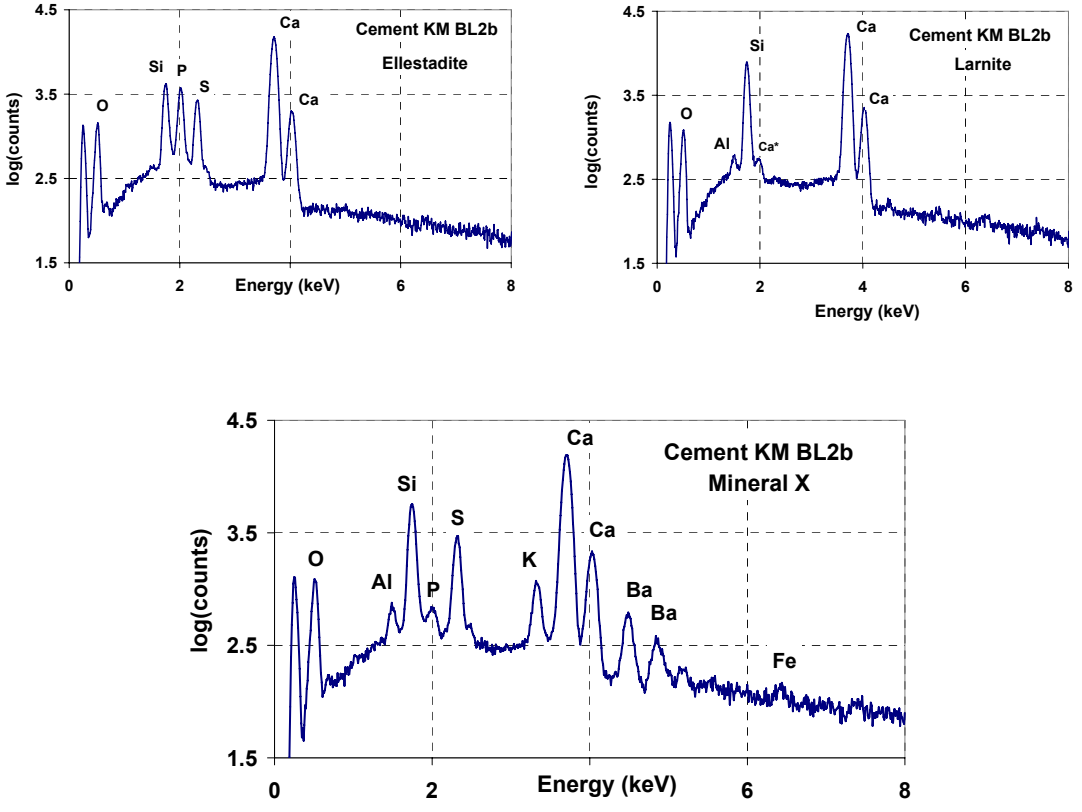

Front between the unhydrated matrix and the hydrated matrix

A sharp front is found between the unhydrated and hydrated matrix (Figure 6.70). This front corresponds to the dissolution front of spurrite. In the hydrated matrix where no spurrite is

present, CSH gels are found instead, between the calcite crystals (EDX spectrum shown in Figure 6.71).

Figure 6.70 *Sample BL2b – Khushaym Matruk – Reaction front between the unhydrated matrix (left) and the hydrated matrix (right of the dotted line). C: calcite, S: spurrite, G: CSH gels having replaced spurrite. On the right, a residual grain of spurrite enclosed in calcite is visible*

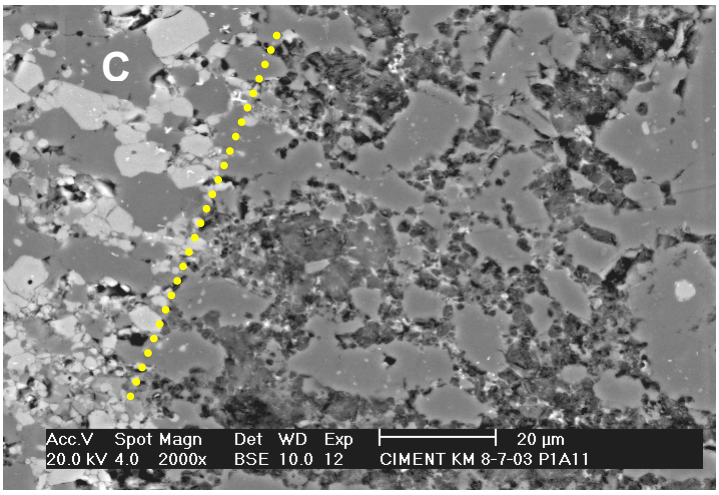

Figure 6.71 *Sample KM-BL2b – EDX spectrum of CSH gels that have replaced spurrite. The gels also contain Al, S and Cl*

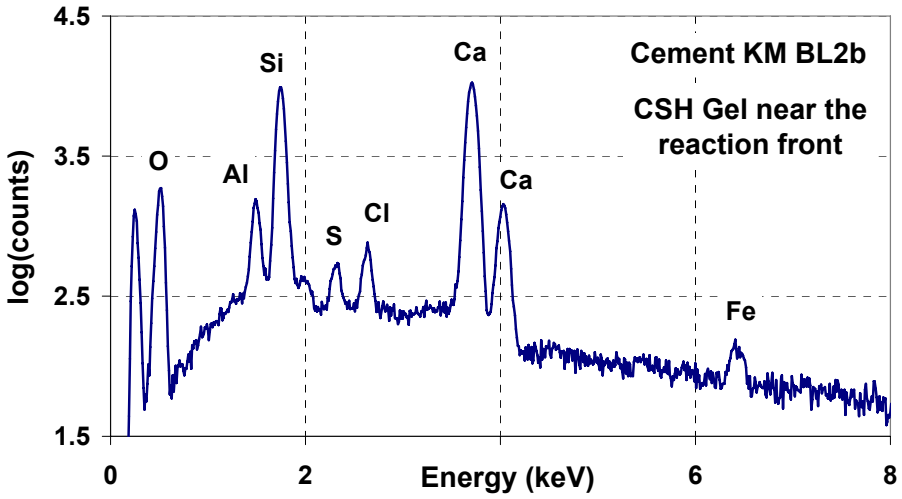

EDX elemental maps have been carried out on a zone containing this reaction front (Figure 6.72). On the BSE image of the mapped zone, the unhydrated cement is clearly visible as a bright region on the left whereas the hydrated matrix is grey. The Al map shows, on the left side, bright spots corresponding to the intact calcium aluminates. The Al appears to be

disseminated in the CSH gels in the altered region. The Ba map shows ghosts of mineral X appearing in the hydrated region, but the $BaSO_4$ inclusions are not affected by the hydration. The Ca map shows that the hydration front leads to an important loss in Ca. In contrast, Si is enriched relative to Ca in the hydrated regions where residual gels form. The potassium map shows that only the mineral X grain that is far from the alteration zone has retained some K. This element is thus removed and diluted in the gels very quickly. The P map shows bright ellestadite grains and faint ghosts of the mineral X grains. The S map shows the progressive loss of S by mineral X and its dilution in the gels.

Figure 6.72 Sample KM-BL2b. Elemental EDX map across the reaction front between the unhydrated and hydrated cement matrix

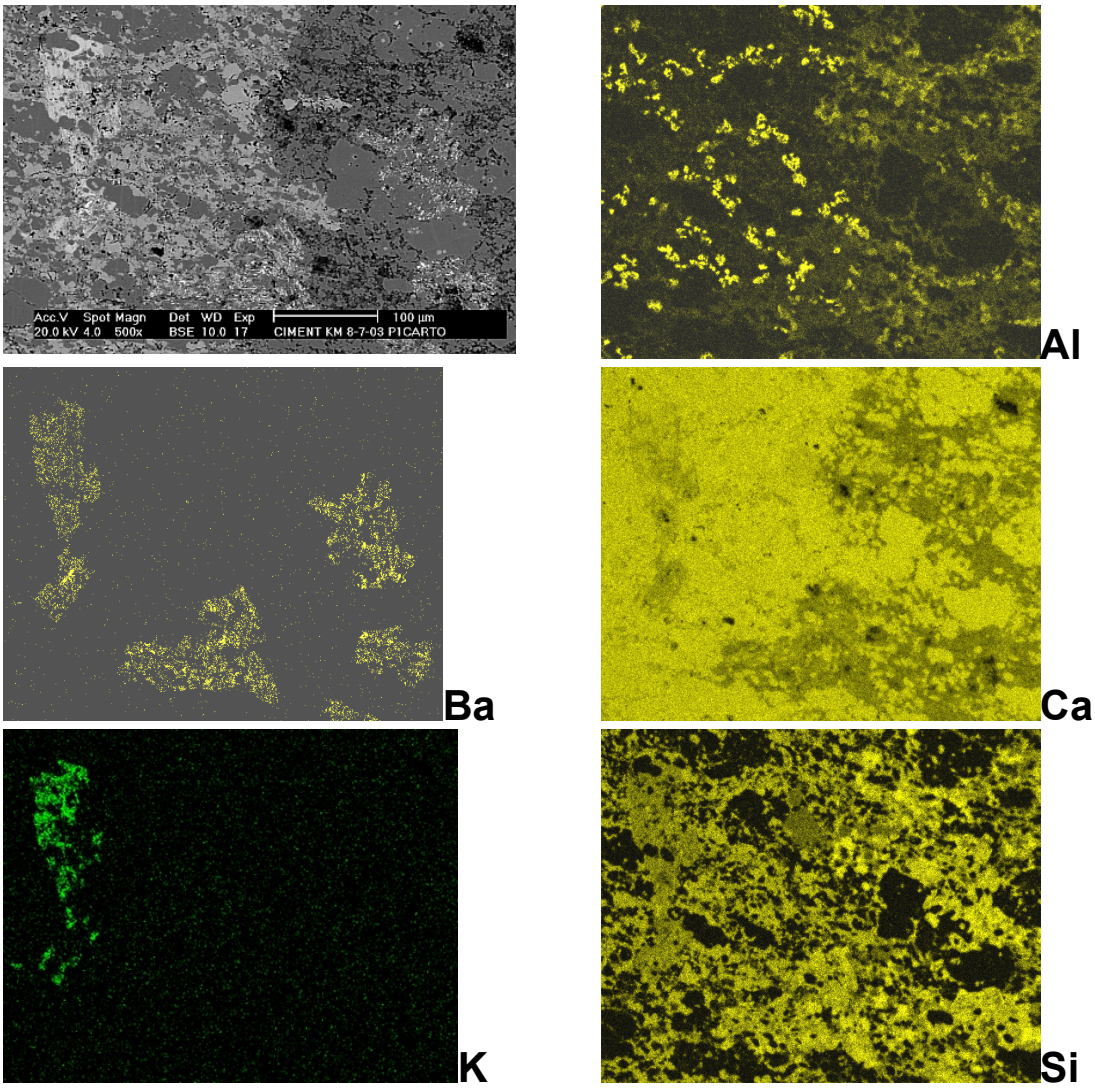

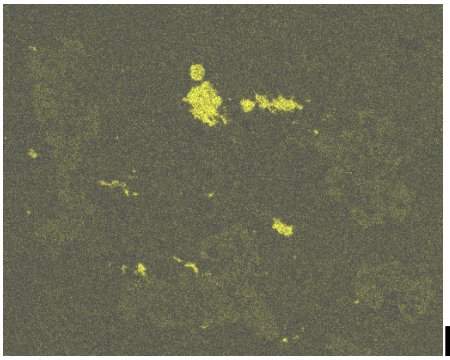

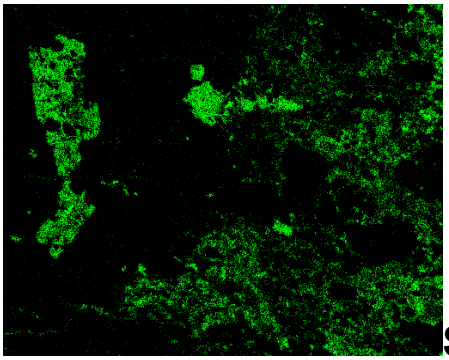

Evolution across a major joint

When going from the hydrated front to the joint infill, CSH gels are found to evolve both in composition and texture. The Ca/Si ratio increases from about 1 to 1.5-1.8 and the Al content of gels increases. At about 300 µm from the hydration front, the gels are found to evolve towards a crystalline phase (Figure 6.73). EDX analyses of this phase are compatible with a composition close to that of afwillite $Ca_3Si_2O_4(OH)$.

Figure 6.73 *Sample KM-BL2b – BSE SEM micrograph of the median part of the hydrated matrix. Afwillite type precipitates (Af) replace progressively the gels (G). The image also shows calcite (Ca) and ellestadite (El)*

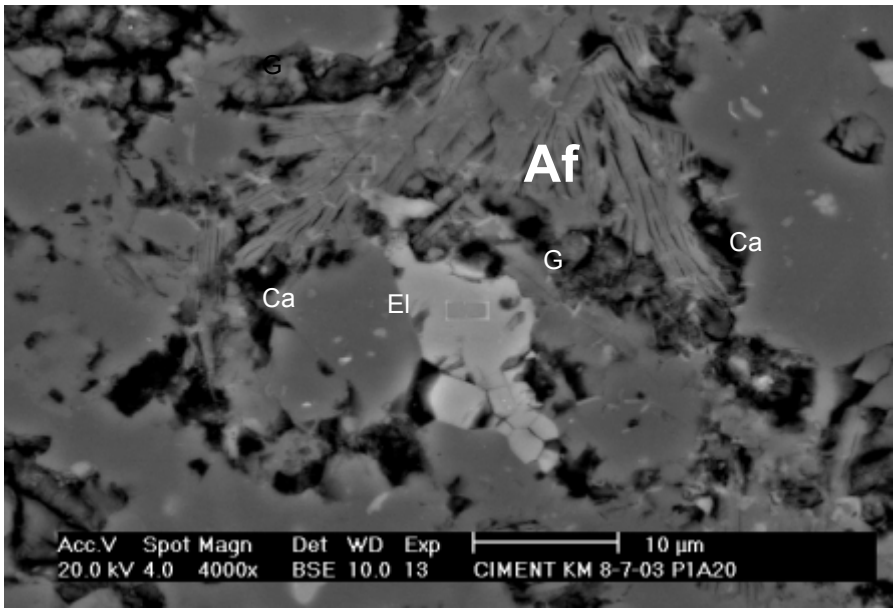

A profile (along the line drawn in yellow in Figure 6.62) was studied by EDX (Figure 6.74). Global spectra were acquired on a 250 x 200 µm window which was moved by steps of 150 µm along the transect. The size of this window is a compromise to average data on a representative area, and to avoid problems encountered when maps or analyses are done on too large an area. The intensity of peaks for several elements in the EDX spectra (Figure 6.75) were reported as a function of distance along the profile. Increases of S, Mg and Al in the hydrated cement matrix are observed. In contrast, a massive loss in Ca is noted with, in parallel, a massive increase of oxygen. The minimum of Ca corresponds to the limit where afwillite-type phases begin to form in the hydrated matrix. The enrichment in Si, noted in the

central fracture, is linked with the presence of the very compact jennite precipitate (Figure 6.76).

Figure 6.74 *KM BL2b – SEM BSE composite image showing the transect studied by EDX analyses. The window shown in yellow (250 x 200 µm) was shifted by 150 µm increments*

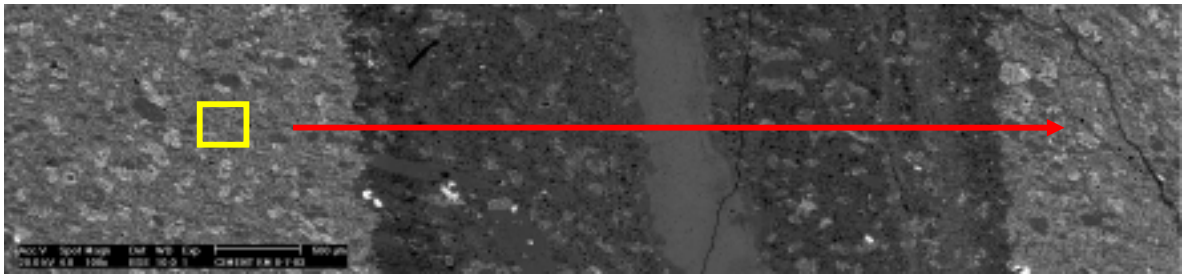

Figure 6.75 *Peak intensity (SEM/EDX spectra) for major elements along the transect crossing the joint filling (see Figure 6.74). The colour bar represents different zones: i) in brown, the unhydrated cement, ii) in yellow, the hydrated cement matrix containing only CSH, iii) in orange, the hydrated matrix containing both CSH and afwillite, iv) in grey, the central joint filling composed of jennite and calcite (cf. Figure 6.76)*

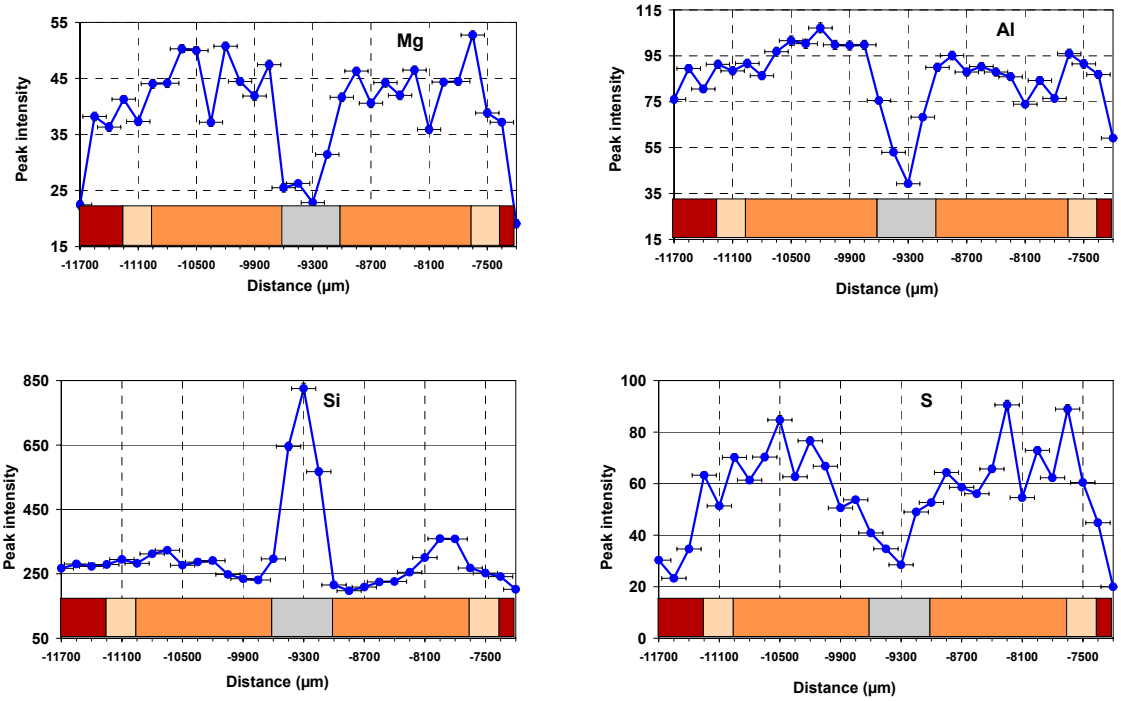

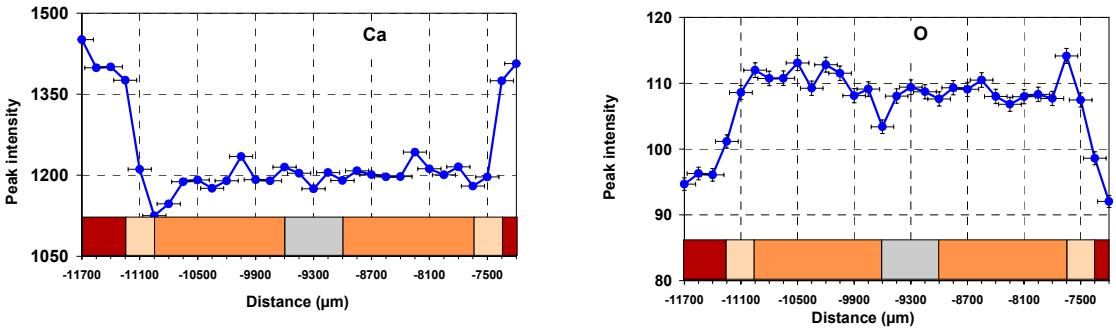

Figure 6.76 KM-BL2b – Aspect of the jennite filling in the central fracture

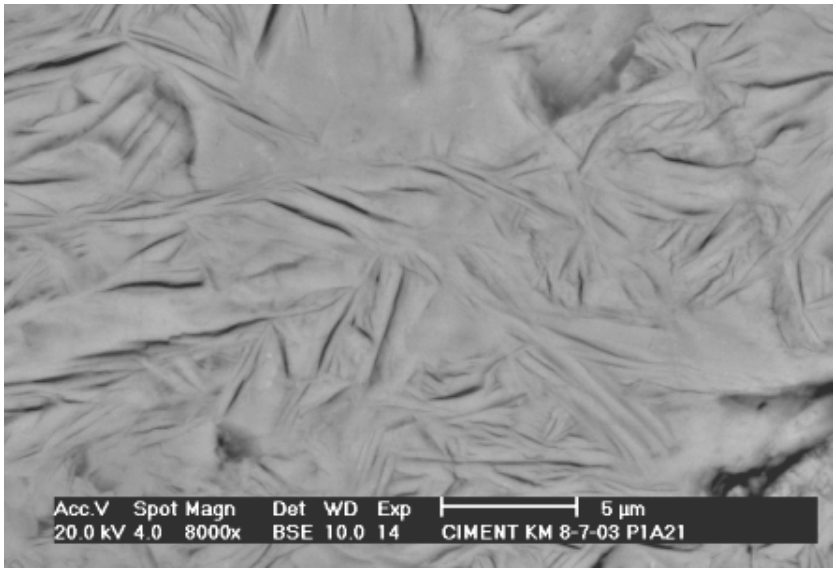

A scheme is proposed in Figure 6.77 to summarise the main observations from the hydrated cement matrix. In the vicinity of the dissolution of spurrite, the formed CSH gels have a low Ca/Si ratio (close to CSH 1.1 = 1.1(CaO).SiO_2.3 H_2O). The Ca/Si ratio of the precipitated CSH gels is then found to increase up to about 1.5 to 1.8 over a distance of 300 µm from the spurrite dissolution front (close to CSH 1.65 = 1.65(CaO); SiO_2; 4.95 H_2O). At this location, fibrous phases with the composition of afwillite ($Ca_3Si_2O_4(OH)_6$) are progressively replacing the CSH gels (the CSH gels actually contain some Al).

Figure 6.77 Sketch of the evolution of Ca-Si phases across the altered matrix

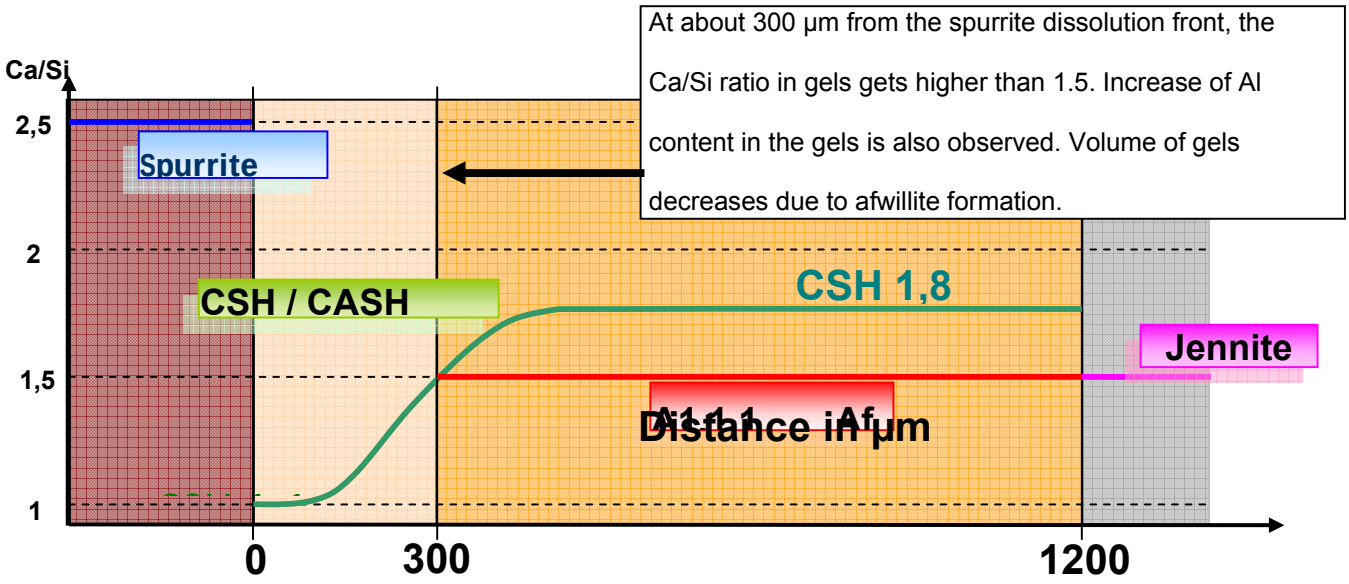

Observation of an iron rich aggregate

The iron-rich aggregate shown in Figure 6.74 was observed in greater detail using the SEM (Figure 6.78). This type of oxide aggregate is believed to represent remnants of the internal cavity of fossil tests in which sulphides were concentrated in the original biomicrite (see sections on the magnetism in Chapter 4, Section 6.3.3 and Milodowski et al., 1992a, 1992b). The aggregate studied is found to be composed of several types of phases: Ca-ferrites, haematite and also a phase containing high concentrations of Cl. The possible attribution of certain XRD peaks to FeOCl suggests that this type of mineral is present in the aggregates. An EDX spectrum of the Cl-rich fibrous mineral shown in Figure 6.79) is given in Figure 6.80. This spectrum suggests that also other Fe-Ca-Cl minerals are trapped inside the iron-rich aggregate.

Figure 6.78 KM-BL2b: Iron rich aggregate (cf Figure 6.64). In the pores of this aggregate are iron oxides (haematite), Ca-ferrites and other phases, a fibrous mineral is found (right). This is a Cl rich phase (see EDX spectrum in Figure 6.79).

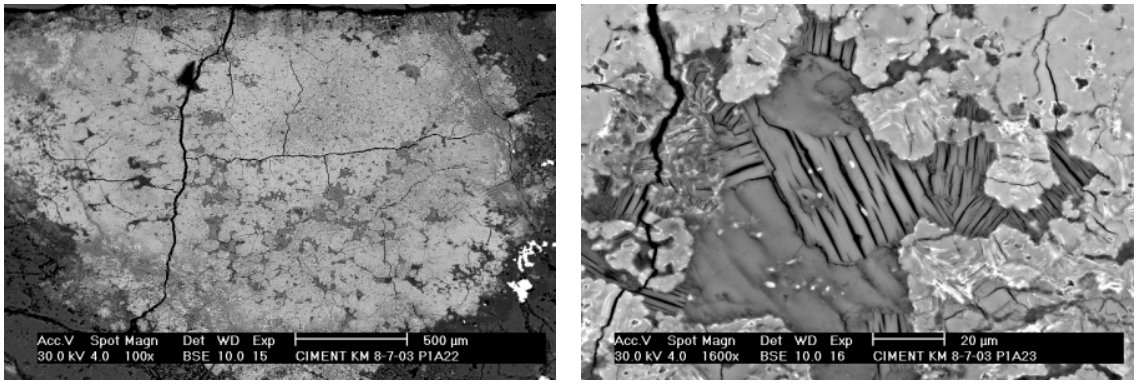

Figure 6.79 *KM-BL2b: EDX spectrum of the fibrous phase found inside the pores of the iron-rich aggregate. Due to the high Cl and Ca content, secondary peaks labelled Ca* and Cl* are found for Ca and Cl at the Kα nominal energy minus the Si Kα energy (detector).*

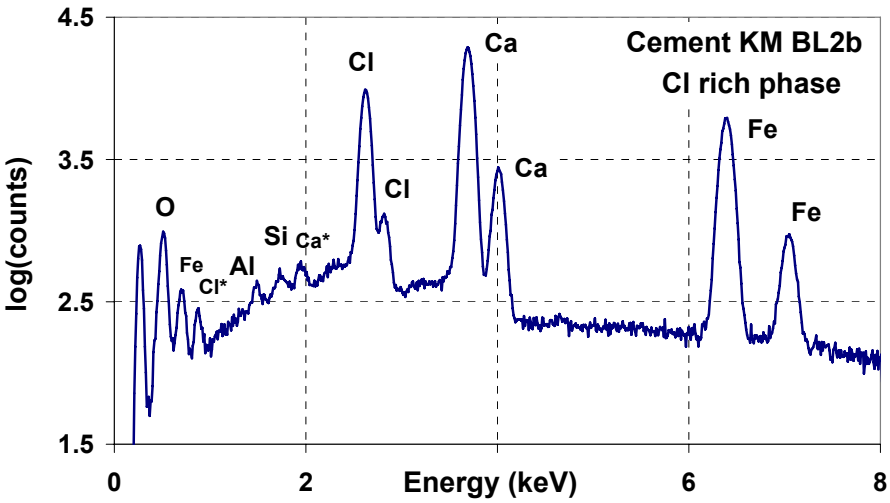

Figure 6.80 *KM-BL2b: EDX spectrum of the fibrous phase found inside the pores of the iron-rich aggregate. Due to the high Cl and Ca content, secondary peaks labelled Ca* and Cl* are found for Ca and Cl at the Kα nominal energy minus the Si Kα energy (detector).*

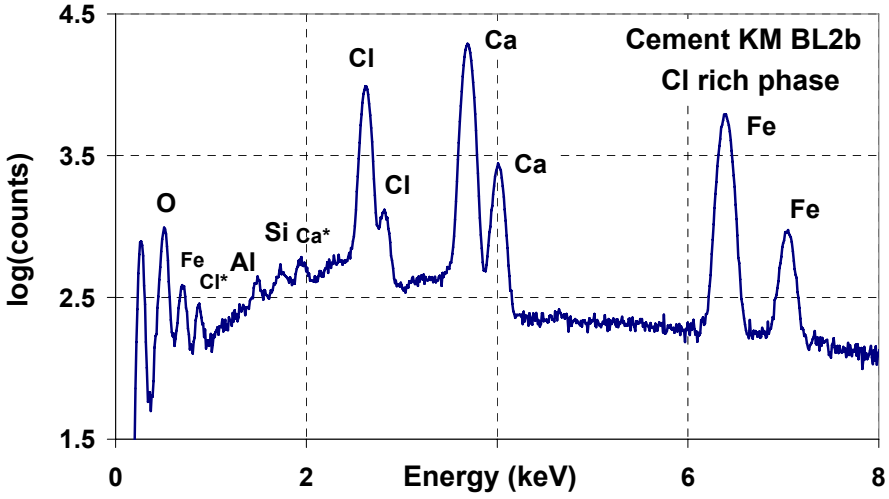

6.3.6.7 Preliminary simulation of the hydration profile using a reactive transport code

A qualitative 1-D simulation of the hydration of the KM-BL2b cement was attempted by considering that the initial material is a porous medium composed of calcite (40 mol L^{-1}) and

spurrite (7 mol L^{-1}) in equilibrium with a hypothetical interstitial aqueous solution. The initial porosity of the material was set at 5% and the initial effective diffusion coefficient of solutes set at 10^{-11} m^2 s^{-1}. The power for the Archie Law of diffusion coefficient was given a value of 1.8. Secondary phases considered in this modelling exercice were discrete CSH (Ca/Si = 1.1, 1.65, afwillite, jennite). The initial pH of the hypothetical solution present in the cement matrix is computed to be 11. The solution circulating in the joint is considered to be in equilibrium with calcite, jennite and CSH 1.65, the ion balance is by Cl^-. The 1-D model extended to 1 cm with a regular finite volume discretisation (200 finite volumes of 50 µm length). Precipitation of secondary phases was assumed to occur at equilibrium. It was found that this model could not reproduce properly the zonation observed in the sample (in particular, the fact that low Ca/Si CSH precipitate close to the reaction front). In addition, the time scale for the development of the observed alteration profile could not be evaluated with confidence (clearly irrelevant values ranging from 10 to 100 days were found).Several hypotheses can explain this difficulty to simulate properly the alteration profile:

- the dissolution of spurrite and precipitation of secondary CSH phases is limited by kinetics (see for example the leaching experiment and related modeling presented in sections 4.6 and 4.7). In particular, the spurrite dissolution process may cause low Ca/Si CSH phases to form preferentially first :

  $Ca_5(SiO_4)_2CO_3 + 7.8\ H_2O \rightarrow CaCO_3 + 2(1.1\ CaO.SiO_2.3\ H_2O) + 1.8\ Ca^{2+} + 3.6\ OH^-$

  The excess calcium then migrates, first along the joint when the hydration rim is not developed, later in the hydrated zone where low Ca/Si CSH are already present. These low Ca/Si CSH then evolve towards crystalline Ca/Si phases (afwillite, jennite) with higher Ca/Si.
- the unaltered matrix is in reality an initially desaturated medium and the reaction front is primarily a hydration front. The code used assumes that the cement matrix is initially saturated with some aqueous solution, which is probably not the case. Actually, the spurrite dissolution front is partly driven by a water diffusion/reaction front (i.e. as the zone containing the cement slag resaturates and the slag hydrates after the combustion event) and this is not described properly in the simulation tool. The observed zonation could be simply related to the fact that low Ca/Si CSH precipitate first at the reaction front because of the influence of the water activity from the joint to the cement matrix.

6.3.6.8 Summary

The observation and analyses performed on a sample of cement (BL2b) collected on the ridge above the main sampling site at Khushaym Matruk revealed several interesting features:

- the unhydrated cement slag is mainly composed of calcite, spurrite, calcium aluminate and a K-bearing Ca-Si-S phase. Other minor phases include brownmillerite, ellestadite and Mg containing minerals (cf. Milodowski et al., 1992a, 1992b).
- the interface between hydrated and unhydrated cement is marked by a sharp front, corresponding to the dissolution of spurrite. The zonation between the spurrite dissolution front and the joint displays CSH phases with increasing Ca/Si ratio with distance from the reaction front. The gels transform into afwillite, far from the reaction front, and jennite is found inside the joint filling.
- attempts at modelling the hydration zonation lead to the conclusion that the CSH

precipitation may be driven both by kinetics and the water diffusion/reaction front. The reactive transport codes used for this type of modelling usually consider saturated porous media, which is probably not the case for the unhydrated cement slag matrix.

- the dissolution of the unidentified K-bearing Ca-Si-S phase (mineral X) is the source of an important sulphate release towards the fracture. Massive gypsum fillings are indeed found in the fractures under the cement bodies (see other parts of this Chapter), but this should not be over-interpreted as such fillings are a regional feature, even when the ACZ is absent.

6.4 Summary and Conclusions

6.4.1 Introduction

The Kushaym Matruk area belongs to the southern extension of the Daba Marble Zone in central Jordan. At this site, the contact between the biomicrite (Muwaqqar Formation, as at Maqarin) and the overlying ACZ is nearly horizontal and exposed at the bottom of a ridge formed by partly eroded analogue cements (see Figures 1.8 and 1.9). Preliminary investigations by the University of Jordan showed that the clay content of the biomicrite in this location was higher than in Maqarin (> 10 % instead of < 5 %), indicating that the site was worthy of further study on hyperalkaline leachate/clay host rock and hyperalkaline leachate/bentonite interactions. Although the site has been visited several times, the data reported here are primarily on samples taken from a 10m long trench, dug from the base of the ACZ down into the clay biomicrite.

The clay biomicrite parent rock at Kushaym Matruk has undergone a long and complex history. Sedimentation at the end of the Cretaceous era was followed by diagenesis, uplift, erosion and faulting in connection with regional and large scale tectonic events. Subsequently, local pyrometamorphism and contact metamorphism occurred, adjacent to the combustion zones. Then hyperalkaline fluid interaction followed cement hydration and weathering under a range of climatic conditions. The main aim of the work conducted at Khushaym Matruk was to define the combustion event at the site and to examine the parent rock for evidence of hyperalkaline interaction, following hydration of the cement slag. In particular, the higher clay content of the parent rock at Khushaym Matruk might afford closer examination of hyperalkaline leachate/aluminosilicate interaction than has been the case at Maqarin. However, the combustion event probably left an alteration ‘fingerprint’ on the clay biomicrite in the immediate vicinity of the ACZ. It was appreciated that this, along with weathering reactions, would complicate interpretations.

6.4.2 Combustion event

The combustion event at Kushaym Matruk appears as a major regional feature, due to the thickness and spatial extent of the ACZ. Only a few cement samples were examined during the project and they show materials of the spurrite-calcite-brownmillerite type, compatible with the combustion of clay-rich biomicrites (see also Chapter 4). Typical temperatures for this paragenesis are in the range of 1000 to 1100°C. Investigations conducted during the project, in order constrain the age of the pyrometamorphism, have given qualitative indications that:

- the K-Ar method applied to an analogue cement sample suggests an age of less than 1 Ma for the combustion event.
- if the magnetic investigations of a limited number of samples and showing an inverse polarity for the thermally altered biomicrites are confirmed, the most probable time window would thus correspond to the end of the Matuyama period (between 700 000 and 1 Ma BP).
- geomorphological arguments, based on the elevation on the Kushaym Matruk ridge above the surrounding plateau and on typical differential erosion rates, are compatible with an age in the range of 600 ky to 800 ky (A.F.Pitty, *pers. comm*., 2004).

6.4.3 Hyperalkaline leachate interaction with the protolith

Based on the assumption that the hyperalkaline leachates from the ACZ have been transported down into the parent rock, a wide range of indicators have been used to examine the nature of the changes along the studied profile.

- **Joint fillings:** In the clay biomicrite, which retained the original sedimentary fabric, joints were mainly filled with gypsum. In the ACZ, joints were mainly filled with calcite and thomsonite-like zeolites. Near the ACZ/parent rock contact, the joint network becomes dense and well-developed. The width of the joints is variable and they contain a complex mineral assemblage of calcite, gypsum and some heulandite-like zeolites.
- **Whole rocks:** A strong recrystallisation process with a significant increase in the carbonate content was observed when moving from the parent rock into the ACZ. Concomitantly, the dissolution of primary silicates of detrital origin (quartz, felspars and micas), and probably part of diagenetic clays contained in the clayey matrix, was detected. Discrete amorphous silica could be observed in the more affected zones. This recrystallisation is mirrored in the C, O and Sr isotopic signatures, both in the whole rock and in the joint-fillings. The specific isotopic signatures, especially when taken in combination, strongly imply that the whole sampled profile has been exposed to hyperalkaline fluids.
- **Clay minerals:** Expandable clays showed significant variation in the value and in the location of the layer charge in the upper part of the ACZ when compared to the biomicrite. Their compositions were quite similar regarding major elements (Mg, Al and Si) but they differed in the Cr concentration. A decrease in the content (80 % to 60 %) of smectite component of illite/smectite mixed layer clay minerals was observed at the ACZ, when it remained unaffected by main structural transformations.

The observed transformations in the samples from the Khushaym Matruk site were mainly secondary recrystallisation in joints and the mineralogical evolution in the clay-rich matrix near the contact with the ACZ. They appear to post-date the combustion processes and, consequently, they might be attributable to the circulation of hyperalkaline solutions from leaching of the overlying ACZ (although other processes, such as weathering, cannot yet be ruled out). Zeolites have been found in the joint fillings and in foram tests in the matrix. The weight of evidence suggests that these phases have been produced by interaction with hyperalkaline fluids. However, it is not yet possible to discount the matrix zeolites as a primary diagenetic feature of the sediments, without further isotopic analyses.

It is apparent that the entire sampled profile at Khushaym Matruk has experienced some interaction with hyperalkaline leachates, but with the most pronounced impact occuring in the top 0-3 m of the contact. Admittedly, the palaeotemperature reconstruction (obtained by

combining information from the cement mineralogy, organic matter degradation, Sr, C and O isotopes and magnetic mineralogy), also shows a clear thermal imprint of pyrometamorphism on the zone of the sampled profile.

- **ACZ:** T ~ 1100 °C (presence of spurrite, sections 6.3.2 and 6.3.6)
- **ACZ:** T>500-800°C (homogenisation of Sr isotope signal, section 6.3.4)
- **0 m (contact):** T ~780°C (decarbonation of calcite, section 6.3.3)
- **~2m:** T~435°C (organic matter reaching oil window, section 6.3.5)
- **~2m:** T probably <250°C and certainly <500°C (resetting the K-Ar clock and Sr isotope signal, respectively, section 6.3.4)
- **0.8-2.5m:** T~200-350°C (sample LA3-5 to LA3-3, 6.3.3)
- **2.5m:** T<250°C (sample LA3-5, section 6.3.4).

Organic matter studies did not shed any additional light on the temperature regime, as weathering processes apparently caused ‘over-maturation’ of the material This induced high apparent temperature signatures. In addition, for both the palaeomagnetics study in Section 6.3.3, and for the isotope chemistry study in Section 6.3.4, the number of samples analysed was too few (see Section 6.3.3.3). From such a pilot study, therefore, it is not yet possible to confirm that the secondary zeolites, observed in the clay biomicrite, are present due to hyperalkaline leachate/host rock/clay interaction. Equally, they could be the product of contact metamorphism, due to the ACZ directly above. or even due to weathering which apparently affected the entire profile that was sampled.

Despite these reservations, this pilot study has demonstrated the potential of the Khushaym Matruk site as a natural analogue of hyperalkaline leachate/clay interaction. Its direct relevance to repository SA is made clear, as is the need to fund a wider-ranging scientific study of the site.

Chapter 7

Conclusions and SA Implications

W.R.Alexander

7.1 Introduction

Here, the main findings of Phase IV of the Maqarin Natural Analogue Study will be briefly listed on a thematic basis to provide an overview of the most important conclusions of the work. Additionally, the main SA relevant points of all four phases of the project will be presented with the aim of producing an immediately accessible list of salient areas of this extended study.

The natural cements and associated hyperalkaline groundwaters (cement leachates) of the Maqarin and Khushaym Matruk areas of Jordan are excellent natural analogues of cement-dominated repositories[26] and provide the best sites currently known for examining the processes associated with their long-term behaviour. The Maqarin site now provides a consistent picture explaining the origin of the hyperalkaline leachates, the persistence of some of the hyperalkaline springs/seepages and the sequence of alterations occurring when such leachates react with various rock types and provide quantitative support for shorter-term laboratory (eg Mäder et al., 2006) and modelling work (eg Soler et al., 2006). Additionally, the studies have produced good quality measurements of the concentration (and general speciation) of several safety relevant elements in hyperalkaline leachates along with microbial and colloidal populations which have be utilised to put short-term laboratory experiments in an appropriate perspective (eg West et al., 1995; Alexander and Möri, 2003).

Khushaym Matruk, as a 'fossil' site (ie no active groundwater system is currently present in the ACZ or immediate protolith) is nevertheless of significance in that it probably represents a diffusion-controlled host rock and is therefore a contrast to the advective system at Maqarin. As such, it is of direct relevance to the behaviour of cementitious repositories in the 'tight' repository host rocks such as the numerous clays, salts and unfractured igneous rocks currently under examination around the world (see Alexander and McKinley, 2007, for details). In addition, the higher clay content of the protolith at Khushaym Matruk is of direct relevance to the assessment of the long-term containment efficiency of the various argillaceous formations currently under study in, for example, Belgium, France and Switzerland and can be used to support the results of short-term laboratory experiments on clay host rock alteration (eg Mäder and Adler, 2004).

[26] Including repositories for VLLW, LLW, L/ILW and ILW (or TRU).

7.2 Phase IV Conclusions

The Phase IV project, initiated in 2000 and continued to 2006, was focussed on several topics of PA concern which included:

- detailed characterisation of the source term (ie the ACZ mineralogy) to strengthen the analogy with industrial cements: further data were required to constrain the paragenesis of the hydration products and to fully understand the duration of hydration, alteration and evolution of CSH minerals and to quantify dissolution fluxes
- rigorous evaluation of the site-scale hydrostructural character at Maqarin to help determine solute flux rates through the bedrock and to establish the spatial and age relationships to further develop the scenario of episodic fracture formation, sealing and reactivation which characterises the site
- further quantify microbial activity and assess its implications in hyperalkaline environments of relevance to cementitious repositories
- detailed study of clay mineral stability in the presence of hyperalkaline fluids as an analogy of a clay-based repository host rocks and to the use of bentonite, either as a backfilling material in cementitious repositories or for HLW/SF designs which may require significant amounts of concrete (e.g. for construction purposes)

Seven main objectives were identified, several essentially reflected the open questions remaining from Phases I-III:

(A) definition of path lengths and description of flow pathways
(B) dating the system (including the near-field cement hydration and the longevity of C-S-H phases)
(C) rock matrix diffusion
(D) source term definition and cement alteration characteristics
(E) clay-leachate interaction
(F) coupled code modelling and data organisation
(G) microbial studies.

The results of the work on these seven objectives may be briefly summerised as:

Definition of path lengths and description of flow pathways

This work has covered several areas, including fracture characterisation, hydrogeology and tectonics.

- *fracture characterisation:* previous work at Maqarin (e.g. Milodowski et al.1998a,b) has clearly shown that small aperture fractures are efficiently sealed by the reacting hyperalkaline leachates, but it has always been open whether this would be the case for larger aperture fractures. In Phase IV, a study of fractures from a wider area of the Yarmouk Valley in the vicinity of the Eastern Springs (Figure 2.6) was undertaken to address this and the results indicate that:
  - only those fractures which are in close vicinity to Adit A-6[27] show secondary leachate interaction phases such as ettringite, CSH etc and these are predominantly small (millimetre width, see Figure 1.10) aperture fractures
  - moving away from Adit A-6, to the valley bottom, around the Wadi Shalala area,

[27] Generally associated with the anticline to which the adit runs parallel and erosion-induced gravitational tectonics.

for example, the fractures (associated with the regional tectonic stress fields) are of larger aperture (1-2 cm), but are generally filled with multi-generation, crack-seal fracture calcite

- higher up the valley walls, younger fractures (associated with the erosion-induced gravitational tectonics) are either infill-free or occasionally contain gypsum

It is therefore not possible to assess, on the evidence collected so far, whether or not larger aperture fractures will seal as effectively as those found around Adit A-6. Although this site has now been destroyed by the new Friendship Dam (see Figure 1.7), both the Wadi Sijin and Western Springs sites (Figures 2.2 and 2.6) are still accessible, with the former site possibly offering the better chance of success due to greater exposure of the bedrock. Interestingly, an ongoing study of a natural analogue of low alkali cements (also known as low pH cements) in the Philippines (e.g. Yamakawa et al., 2008) indicates that larger aperture fractures can be sealed by the secondary cement phases.

- *hydrogeology:* evidence from laboratory tests (eg Bateman et al., 1995; 1998; Adler et al., 2001) and one URL experiment (the HPF experiment at the Grimsel Test Site; see Mäder et al., 2008, for details) indicate that sealing of fractures 'disrupts' the pre-existing flow conditions. In the HPF experiment, formation of secondary phases in the experimental shear zone induced a decrease in fracture transmissivity and a focussing of flow in the remaining open porosity. However, the data from HPF must be treated with caution as the pressure in the groundwater injection system was constantly increased to maintain constant flow conditions. In the case of a repository, the hydrogeologic system will probably be largely dominated by the relative elevations of the recharge and discharge regions, and these elevations can be assumed to remain largely constant over the timescales of interest[28]. This situation is best represented by constant-gradient conditions, which means that when permeability decreases (at constant gradient), flux will also decrease. In the case of the HPF supporting laboratory studies on a fractured rock core (see Mäder et al., 2004, 2008), a constant gradient was applied during infiltration of hyperalkaline leachates and the production of secondary phases led to a decrease in hydraulic conductivity of 20-fold (over a 9 month period).

  However, at the repository scale (unlike in the confined rock core in the laboratory), flow can obviously be displaced around 'blocked' zones, something of concern for PA modellers as most assessments to date have simply ignored this effect[29]. It was hoped that this could be addressed at Maqarin by detailed hydrological tests at the site scale but, as noted in chapter 2, it proved too difficult and time consuming to obtain this information. Nevertheless, the results of the hydrochemical modelling in chapter 3 indicate that there are two flow systems present at Maqarin: one, 'slow' system which appears to move through the ACZ and then passes the hyperalkaline leachates into the protolith and a second, 'fast' system which, at periods of high groundwater inflow, bypasses the ACZ and mixes with the 'slow' flow downstream. This may be taken to be analogous to the likely processes which will occur in a sealing host rock: as the host rock downstream from the repository begins to seal, the groundwater will, like the 'fast' system at Maqarin, probably bypass the repository and affected host rock – a

[28] Obviously, this will not be the case in an area of significant uplift or erosion or at coastal sites (see McKinley and Alexander, 2008, for discussion)

[29] The exceptions to date are Posiva, who have carried out an initial assessment for their ONKALO facility (see comments in Alexander and Neall, 2007) and Nagra (see Mäder, 2004) for the proposed Opalinus Clay host rock.

potentially positive side effect of host rock sealing. Clearly, however, this needs to be studied further under relevant conditions (e.g. in the LCS project at the Grimsel Test Site – see www.grimsel.com for details) before such a scenario can be considered in detail in a repository PA.

- *tectonics:* although it is known from Maqarin that the sealed fractures may be tectonically re-activated (Milodowski et al., 1998a,b), the full consequences of such reaction in a tectonically active host rock remain unclear. The potential impact of fracture re-activation (and repository disruption via fracturing) on the performance of a cementitious repository in a tectonically active zone should be further studied as the results will be of use in guiding site characterisation, repository design and PAs. To date, Maqarin offers the only possibility to study such processes at site scale.

Dating the system

- To set some constraints on the longevity of the hyperalkaline plume flow, it is not only necessary to understand the site hydrogeology and flow path evolution, but also to have some grasp of the timescales of (natural) cement production and the longevity of the secondary cement phases (produced following interaction of the leachates with the host rock). This will also allow some assessment of differing plume environments due to variations in the host rock transport properties, so allowing greater transferability of the data to other (repository) sites. Attempts to date the cements and the secondary mineral phases were made in previous phases and here in Phase IV and indicate:
- from geomorphological considerations (Pitty, 1998), a probable date of ignition has been set to around 600 ka, and certainly not later than 150 ka for the Eastern Springs cement. More hypothetically, a second, later phase of triggered landslides might also be considered to explain the geomorphological features observed in the Western Springs area. Speculatively, such an event might have occurred in the last 100 ka (Late Quaternary), or even as recently as the last 10 ka (Holocene).
- Some vein minerals (and associated fracture wallrock) from sealed fractures in Adit A-6 have been analysed for natural decay series radionuclides and dates have been very tentatively assigned to the hyperalkaline groundwater alteration (Milodowski et al., 1998a). A diagenetic calcite vein was dated by the ^{230}Th ingrowth method at between 500ka and 2Ma, providing a maximum age for the metamorphism which produced the cement zone mineral assemblage. Analyses of samples of tobermorite vein filling and jennite-ettringite vein filling produced ages of 90ka and 80ka respectively. A reported ^{14}C age of less than 650a (Clark et al., 1994) for recarbonated cement zone material from Adit A-6 does not necessarily contradict the ^{230}Th ingrowth ages, rather it confirms the scenario of repeated re-activation of fractures (due to gravitational tectonics) with consequent mutli-phase fracture infill. However, all these dates must be treated with caution as most of the vein samples are so thin that it is almost impossible to guarantee samples which contain no pieces of the underlying host rock (A.E.Milodowski, *pers comm*., 1998). In addition, two studies in Phase IV (see appendix 3.3 and chapter 6) have highlighted the complexity of these multi-phase systems and the attendant difficulty of obtaining meaningful dates on the material.
- The use of rock magnetism as a dating tool was attempted in Khushaym Matruk. Due to the small number of samples studied, only preliminary results are available, suggesting that the combustion phenomenon occurred in Kushaym Matruk during a period of inverse orientation of the magnetic field.

Rock Matrix Diffusion

has long been recognised as a potentially significant mechanism for the retardation of contaminants in the geosphere (eg Neretnieks, 1980) and the importance of the mechanism is two-fold: sorbing radionuclides (e.g. ^{137}Cs) are able to access a much greater volume of rock, so providing greatly increased retardation potential, and non-sorbing radionuclides (e.g. ^{129}I) which would otherwise be transported at the advection rate of the groundwater, are also delayed and diluted within the matrix porosity. Within the hyperalkaline plume downstream from a cementitious repository, it is possible that the interaction of the host rock with the hyperalkaline leachates may initially seal the fracture face, so reducing radionuclide retardation during the period of slow fracture sealing.

Indeed, initial data from Maqarin tended to suggest that this would indeed be the case, with several samples from open fractures which were undergoing interaction displaying apparently sealed fracture faces (Milodowski, 1994). However, the presence of similar, apparently sealed[30], fracture faces in flow paths at the Wellenberg potential repository site (Alexander and Mazurek, 1996) which still showed clear, geochemical, signatures of matrix diffusion suggested that assuming no matrix diffusion within a plume would be over-conservative. This prompted a re-examination of matrix diffusion at Maqarin within Phase IV.

Here, a profile was taken across a filled joint and into the biomicrite matrix and the distribution of the natural decay series in the samples was studied. The results clearly indicate that the porosity of the biomicrite matrix was open at some point. Unfortunately, it is difficult to place any firm dates on the sequence of events (i.e. does the observed U leaching in the matrix pre-date the closing of the joint, what is the connection between the removal of U from the matrix and deposition of U in the vein?) due to the complex, multi-phase nature of the U reaction and a lack of data on additional U-series daughters such as ^{226}Ra. To say much more about matrix diffusion in the biomicrites which have reacted with hyperalkaline leachates, it is necessary to collect additional data, such as:

- looking deeper into the matrix to assess just how much is accessible to contaminants because this depth is the single most important parameter for the retardation calculations (cf. Ota et al., 2003).
- the porosity distribution and mineralogy of the core, which would allow a clear focus on the areas of most importance (e.g. in and around those areas of reduced porosity).
- ^{226}Ra ($t_{1/2}$ = 1.608 ka) to assess very young perturbations to the obviously complex system at Maqarin.
- separates from the matrix samples to allow better dating of the leaching event(s).

Finally, with this additional data, attention could once more be turned to the vein: a profile of analyses across the vein to assess age(s) of vein closure (very useful at Maqarin due the already noted re-activation of the fractures and joints at the site) to compare these with the data from the matrix. Only then will it be possible to give a definitive answer to whether the Maqarin matrix porosity remains open during and after reaction of the matrix with the hyperalkaline groundwaters at the site – and, by analogy, whether a repository host rock matrix would remain open during and after interaction with cementitious leachates from the repository.

[30] In both these studies, evidence for fracture face sealing was obtained from the study of thin sections.

Source term definition and cement alteration characteristics

Several PA relevant processes may be better understood by examining the Maqarin ACZ in detail.

- *cement leaching*: long-term alteration of the physical structure of concrete due to leaching and precipitation effects is extremely difficult to study. Attempts have been made with archaeological samples with varied results (see Miller et al., 2000 for discussion) and this is generally problematic in that the structures are usually not in an appropriate physico-chemical environment (shallow, oxiding). Many are now also protected against further study (eg Hadrian's Wall, the Roman ruin in northern England, is now an UNESCO World Heritage Site and so no longer available for sampling). Although any data collected on the natural cements of Jordan will only be qualitative as the original structure of the natural cement is dissimilar to that of anthropogenic cement and concrete, it could nevertheless provide indications of the likely mechanisms of long-term alteration. For example, in standard laboratory accelerated leach tests, amorphous cement phases (e.g. CSH) are often observed to dissolve rapidly, but seemingly very long-lived amorphous phases have been found at Maqarin (e.g. Milodowski et al., 1998a,b). Does this indicate that the laboratory test procedures are of little relevance to the repository environment?
  It should be noted, however, that detailed examination of the Maqarin site makes it clear that the ACZ of the Eastern Springs is not being leached as one, homogeneous body, rather as small, fracture-isolated pods of the main body[31] (see figure 1.10, for example). While this tends to make the site hydrochemisty difficult to model (as the current hydrochemistry will be typical of the group of pods currently being leached), this should not distract from the fact that examination of individual cement pods will still provide an insight into long-term leaching processes.
  The identification of a new Ca-Si-SO_4 phase among major constituents of the unhydrated ACZ places constraints on the ACZ alteration and CSH genesis at Maqarin. This very reactive phase (much more than larnite) will indeed contribute to a massive initial sulfate release, to the early precipitation of CSH phases and therefore drives the initial steps of ACZ alteration and potentially further events such as thaumasite/ettringite precipitation.
  In addition to direct petrological observations on samples from Maqarin, a limited number of column experiments were carried out to provide a better understanding of the evolution of the Maqarin natural cements. Such laboratory experiments, necessarily short term, give some emphasis to rate limited processes. In particular, they show that the acquisition of high pH values (> 12) by groundwaters via interaction with the Maqarin natural cements is a slow process. This finding may constrain residence times of groundwaters at the site. The experiments also suggest several key parameters need to be taken into account in the modelling of such systems, for example:
  - the rate limited precipitation of CSH phases
  - the pH dependence of ettringite dissolution (and probably precipitation)

  Further experiments and modelling of this type is needed to understand how (and how fast) the Maqarin cements react and are altered by groundwater leaching. Such information will be useful to better bracket the extent of precipitation of secondary CSH phases in the near field of a repository by allowing a better direct comparison between

[31] This has also been observed at most of the sites examined, including Daba, Khushaym Matruk and Sweileh.

the natural cements from Maqarin and the industrial cements used in radwaste disposal.
Geochemical and magnetic investigations conducted in Maqarin along Adit 6 provided new insight on the physico-chemical zonation extending through the combustion front, from the totally metamorphosed ACZ to unperturbed biomicrite. Similar investigations were also conducted in Khushaym-Matruk. The obtained results constrained temperature points in the rock mass surrounding the ACZ and also pinpoint how redox sensitive transition elements (Re, Cr, Fe, Se, Mo, Cu) have been mobilised by fluids or possibly trapped by organic matter. Detailed solid state data acquired on several of these elements has been discussed in relation to redox conditions potentially prevailing inside the ACZ or in the biomicrite.

- *carbonation*: carbonation is likely to protect repository cements against leaching by groundwaters (by sealing the near-surface porosity of the cement) and so the current generation of cement leaching models are probably over-conservative in their assumptions of relatively rapid leaching of the cement (see above). Although it is likely to be difficult to quantify the extent of carbonation (see Alexander, 1992, for example) and therefore to take credit for positive effects on repository performance, better understanding of the influence of carbonation on, for example, water flow paths through the cement and subsequent degradation should mean that some benefit could be taken if necessary. In addition, a better understanding of carbonation will be useful in demonstrating that long-term cement leaching does not necessarily result in catastrophic failure of the structure or containment. Unfortunately, although originally an area of focus in Phase IV, a change in project priorities meant that little effort was invested in this area.
  Finally, ^{14}C retardation due to carbonation has been studied only briefly at Maqarin (Clark et al., 1994) with ambiguous results due to the complexity of isotopic signals produced by the multi-phase groundwater flow systematics. In hindsight, the much simpler Khuysham Matruk site would be a more appropriate area to study this retardation process in the future.

Clay-leachate interaction

Previous studies of clay-hyperalkaline leachate interaction at Maqarin produced only ambiguous data due to the paucity of clay at the site[32]. It was felt that the significantly higher clay content of the protolith at Khushaym Matruk would allow a better chance to examine hyperalkaline leachate/aluminosilicate interaction than has been the case at Maqarin. However, it was also recognised that the combustion event would have left an alteration 'fingerprint' on the clay biomicrite in the immediate vicinity of the ACZ and that this (along with weathering reactions) would complicate the interpretation.

The observed transformations in the samples from the Khushaym Matruk site were mainly secondary recrystallisation in joints and mineralogical evolution in the clay-rich matrix near the contact with the ACZ. They appear to post-date the combustion processes and, consequently, they might be attributable to the circulation of hyperalkaline solutions from leaching of the overlying ACZ (although other processes, such as weathering, cannot yet be ruled out). Zeolites have been found in the joint fillings and in foram tests in the matrix and the weight of evidence suggests that these phases have been produced by interaction with

[32] Although it is of note that a kaolinite-rich zone was identified in Adit A-6 in the Eastern Springs and samples have been collected and preserved for future clay/leachate interaction analysis.

hyperalkaline fluids. However, it is not yet possible to rule out if the matrix zeolites are a primary diagenetic feature of the sediments without further isotopic analysis.

Alteration mineralogy inside fracture of the ACZ at Khushaym Matruk suggests that the pH of past leachates (the system is at present dry) was possibly lower than in Maqarin (Fourcade et al., 2007), probably <pH12 at 25°C. This feature could also explain the absence of CSH phases outside the ACZ in Khushaym Matruk.

It is clear from the above conclusions that it seems likely that the entire sampled profile at Khushaym Matruk has experienced some interaction with hyperalkaline leachates, but with the most pronounced impact occuring in the top 0-3m of the contact. Unfortunately, this is the zone of the sampled profile which has experienced a thermal imprint from the pyrometamorphism. In addition, all analyses of the site suffer from the paucity of samples and so lack statistical significance. Consequently, it is not yet possible to definetly state that the secondary zeolites observed in the clay biomicrite are present due to hyperalkaline leachate/host rock/clay interaction or are an artefact of the contact metamorphism (due to the presence of the ACZ directly above) or the weathering which appears to have affected the entire sampled profile or are possibly even a primary diagenetic feature.

Nevertheless, this should not detract from the fact that this study of an extremely limited number of samples has clearly shown the potential of this site as a natural analogue of hyperalkaline leachate/clay interaction and emphasises the need to examine the site with enough resources to allow a wide-ranging scientific study of direct relevance to repository PA.

Coupled code **modelling**

Although originally an area of focus in Phase IV, a change in project priorities meant that little effort was invested in this area. However, the simulation of column experiments with the use of reactive transport codes has emphasised the role of kinetics on several key parameters of groundwaters in the altered ACZ. The same conceptual model was found to be valid for describing the leaching of industrial cement pastes and Maqarin cements but:

- the heterogeneous nature of the natural sample (ettringite veins) makes the leaching regime more complicated.
- the influence of phosphate minerals complicates the system (precipitation outside the sample, several logK data not available).

Preliminary investigation of a fracture subsystem in ACZ material from Khushaym Matruk suggets that temperature gradients between the fluid and the cement matrix are responsible for the observed mineralogical features (cf Fourcade et al., 2007).

Microbiology

In Maqarin, it is plausible that the micro-organisms in the groundwater have adapted over a long time period to the hyperalkaline conditions. However, the absence of deeply branching 16S rRNA species tends to suggest that the populations in Maqarin have adapted to the hyperalkaline environment in a relatively short time. If this is true, it is difficult to exclude the possibility of similar adaptations in cementitious radwaste repositories.

In previous phases of work at Maqarin, it was not possible to state if the microbes present in the system were metabolically active and so influencing the site environment. Here it was

clearly shown that the microbes could be cultured at low, but significant, numbers and that some were most certainly metabolically active, even if the growth and activity found were not dramatic. Rather, slow growth to low numbers and a generally low metabolic *in situ* activity was found. Although this could be taken to imply that microbial activity will be low during the hyperalkaline phase of a repository, this does not take into account the differences in the nutrient sources in both systems. Previous work (West et al., 1995) indicated that, although the environment at Maqarin was not nutrient limited in theory, it was certainly possible that the form of the nutrients (e.g. the presence of phosphate in apatite grains) was a potential constraint on microbial growth. This is in agreement with the findings here where assimilation investigations strongly suggested that part or all of the microbes in the studied Maqarin springs were viable and responded to introduced carbon sources[33], even under hyperalkaline conditions. This suggests that the activity of microbes in the nutrient-rich, nutrient-available environment of a L/ILW repository, for example, could well be significant (see also the discussion in McKinley et al., 1997).

7.3 PA Relevant Conclusions from Phases 1-IV

The Maqarin and Khushaym Matruk natural analogue sites are therefore unique locations to examine the mechanisms and processes associated with cementitious repositories, particularly when cement pore fluids will be dominated by the dissolution of portlandite and calcium silicate hydrate gel phases. The evidence from these sites, relating to the evolution of a generic cementitious repository for radioactive waste, has been evaluated with respect to the form of input (quantitative or qualitative) to a repository PA.

7.3.1 Quantitative conclusions

- the conceptual model for the evolution of a hyperalkaline plume in a generic host rock is largely consistent with observations at the site.
- hyperakaline pore fluid conditions generated by minerals directly analogous to those in OPC are long-lived (in excess of tens of thousands of years) under the Maqarin flow conditions.
- the effects of the site hydrology (and tectonic/erosional processes) upon fracture sealing need to be considered on a repository site-specific basis. To date, only two sites have been evaluated at a preliminary level, but it is expected that this will change as more national programmes move to actual site characterisation.
- reactions between hyperalkaline waters and the host rock mostly have positive reaction volumes and thus fractures are sealed by the precipitation of secondary phases.
- interaction between hyperalkaline waters and the host rock occur extensively and (small aperature) fracture sealing occurs within short timescales (years to hundreds of years).
- the altered rock matrix appears to be accessible to diffusion of aqueous species to a depth of at least several centimetres.
- sequences of minerals predicted by coupled codes are very close to those observed in the hyperalkaline alteration zones at Maqarin, even if the specific phases cannot be represented due to a paucity of relevant thermodynamic and kinetic data.

[33] For reasons unknown, attached cells seemed to be more active that the unattached.

- thermodynamic databases of elements of interest to radioactive waste disposal provide conservative (*ie* solubilities are overestimated) estimates of solubility, despite the fact that the representation of the solubility controlling solid phases is too simplistic.
- the amounts of colloidal material generated at the cement zone/host rock interface appears to be low, although any future analogue and laboratory work would benefit from a common approach to minimise method inherent differences.
- microbes are present in the hyperalkaline groundwaters, although their precise activity is currently difficult to define.

7.3.2 Qualitative conclusions

- the cement zone at Maqarin may be considered a good analogy to an industrial cement.
- to date, all fractures examined within the plume at Maqarin (other than those currently water conducting) are sealed. However, as the aperatures of the fractures examined to date are generally small (mm to cm), it is currently possible to state only that thin fractures will be probably self-healing.
- as a consequence of the fast rate of interaction between hyperalkaline waters and the wallrocks, it seems likely that radionuclides released from a cementitious repository will migrate through rock that has already been altered by the high-pH plume (although it must be emphasised that the radionuclide release scenarios for most repositories are still somewhat unclear here). This alteration affects both the geochemical (mineralogy) as well as the physical (porosity, connectivity) properties of the rocks.
- once a fracture is sealed, no further alteration can take place unless new pore-space is created by fracture reactivation. In this case, the fracture may then ”see” a pulse of hyperalkaline leachate with a composition no longer in equilibrium with the existing fracture infill (*ie* secondary minerals) and this will initiate further interaction with both the host rock and the fracture infill, possibly releasing any radionuclides associated with the original secondary mineralogy. The numerous phases of fracture precipitation (and dissolution) identified at Maqarin bear witness to recurrent events of alteration/precipitation, sealing and reactivation as does the range of ages so far reported for infill mineralogy.
- in a highly porous rock (or flow system), it is possible that reaction will not rapidly seal the flow porosity. In this case, the distal part of the plume may be over-run by the middle part which may, in turn, be over-run by the proximal part of the plume. Partial to complete replacement of previous secondary phases is to be expected, with the potential implications this has for radionuclide retardation. Such flow systems are probably of little relevance to deep repository host rocks.
- where very wide fractures are present, the same processes described immediately above may also occur and this could be of more significance to a repository.
- due to the high permeability in this surficial environment, the length of the plumes downstream of the cement zones appear to be on the order of hundreds of metres. In the lower advection rate systems of relevance to deep repository host rocks, plume lengths will probably be much smaller.
- in those parts of the flow system which may be defined as 'open' (in the geochemical sense), or groundwater dominated, C-S-H phases are seen to dominate the secondary mineral assemblage whereas 'closed' , or rock dominated, parts are zeolite dominated. By comparison with Maqarin, deep repository host rocks with low groundwater fluxes

might be expected to be zeolite dominated.

- despite major differences between the rock types at the Eastern and Western Springs, the mineralogical composition of the secondary minerals at both sites is very similar, implying that similar reactions could be expected to occur at a repository host rock, *ie* the mineralogical information from Maqarin appears to be directly transferable to repository conditions.

7.3.3 Demonstration and validation

One of the most important tasks in a repository site characterisation is to develop a full understanding of the site hydrogeology and hydrogeochemistry as these are of critical importance to the repository performance. Such features indicate whether the site can reasonably be expected to protect the repository engineered barriers (via suitable groundwater chemistry and groundwater fluxes) and whether the host rock can act as an additional barrier to radionuclide release (via radionuclide retardation due to suitable groundwater chemistry, host rock mineralogy and water flow systems). In the case of a repository which includes significant amounts of cementitious material, confidence can be increased in the site if it can be shown that potential perturbations to the site will not significantly alter the overall repository performance in a negative manner by changing the original characteristics of the host rock.

The advantages of investigating the Maqarin site is that the perturbations of the original retardation qualities of the Bituminous Marl Formation can be studied directly at repository scales under relevant *in situ* conditions, demonstrating that the appropriate tools exist to carry out the work at a repository site. In addition, coupling the site investigations closely with ongoing laboratory and *in situ* studies (in rock laboratories) can demonstrate the relevance of laboratory data to the repository site and provides confidence in the transferability of the so-produced data. Finally, tests of the limits of applicability of performance assessment models to the hyperalkaline system under study not only increases confidence in the use of the codes in the repository site performance, but also provides a form of code validation.

Of importance to the overall use of the data provided by study of the Maqarin site is the closer coupling of the various laboratory, field (both rock laboratory and analogue) and modelling programmes currently ongoing or planned: only then can the strengths of the Maqarin site aid the weaknesses of the other programmes and *vice versa*.

7.4 Recommendations

The study of the natural cement analogue sites in Jordan started over a decade and a half ago, but there remain additional areas to study. This is partly because the security situation at the sites, Maqarin in particular, made access a difficult and time-consuming matter which ate into project time and resources. In addition, as national programmes have matured over the duration of the project, the type and nature of questions addressed at the sites has changed and so new considerations have arisen as the original questions have been answered. Consequently, further effort could usefully be expended on:

- the effects of the site hydrology upon the degree and form of fracture sealing: this remains open due to the difficulties of studying the sites, but perhaps too much

emphasis was placed on the Eastern Springs at Maqarin at the expense of the Western Springs (and even Wadi Sijin). In addition, full integration of the data from the HPF experiment at Grimsel has not yet been possible and this would certainly aid the extrapolation of both data sets to potential repository sites.

- do larger aperture fractures seal? The data from Maqarin do not help here but this process has not been addressed at the sites at Daba and Sweilah. In addition, provisional data from the new low alkali cement natural analogues in the Philippines and Cyprus suggest that wider fractures and joints can seal. If possible, this should be addressed in detail at these sites and should include an estimation of likely rates of sealing.
- matrix diffusion appears to continue in the matrix behind fractures as they seal, but the results are not statistically valid and this needs to be repeated before such an important mechanism can be included in repository Pas.
- testing of thermodynamic databases and their associated codes: changes in both the databases and the codes mean that it would be worth updating these tests.
- colloids: additional work at the Western Springs would be useful as the current data represent no more than a single snapshot. Future assessments should strive, where possible, to develop a common approach to minimise method inherent differences between NA and laboratory studies and try to access the distal part of the hyperalkaline plume where it is likely that most colloid formation will occur.
- nitrate reduction: for those national programmes with a large waste nitrate inventory (e.g. Japan, UK), further examination of the nitrogen chain in the Western Springs would be of interest. This could include examination of denitrifying and/or ammonium reducing microbes – for example, are the populations significantly higher than other microbes? An assessment of the ammonium data would be of use to examine if the exchange of high levels of ammonium onto minerals in both the ACZ and the clay biomicrite reduces radionuclide retardation. Apophyllite crystals from Maqarin show a significant deficiency in K+ site occupancy (up to 25 %) compared to ideal apophyllite stoichiometry, indicating probable major lattice substitution of K^+ by NH_4^+.
- Assessment of Thaumasite Sulphate Attack (TSA) may affect concrete in waste disposal systems. Until recently, it was thought that TSA could only occur at low temperatures (less than 10°C). Recent observations and published thermodynamic data suggest that TSA also occurs at temperatures around 25°C or even higher. Maqarin is a site in which thaumasite and thaumasite-ettringite solid solution precipitation occur at ~25°C and therefore constitutes a unique place to test predictions of thermodynamic models of TSA.
- deep repository host rocks with low groundwater fluxes might be expected to be zeolite dominated and the implications of this on radionuclide retardation could be examined at Khushaym Matruk, even if the zeolites are not necessarily a product of the hyperalklaine plume interaction.
- Khushaym Matruk appears to be an excellent analogy for a diffusively controlled host rock and should be the focus of additional studies to improve the statistical relevance of the results presented here.
- a full integration of the results of Phases I-IV with the now extensive body of laboratory data and (much fewer) URL experiments and modelling studies remains to be carried out. This would appear to be the most cost-effective manner to advance understanding of the likely long-term performance of the numerous existing and planned cementitious repositories.

Chapter 8

References

Adenot, F. (1992) Durabilité du béton: caractérisation et modélisation des processus physiques et chimiques de dégradation du ciment. PhD Thesis, University of Orléans, France.

Adler, M., Mäder, U.K. and Waber, H.N. (2001). Core infiltration experiments investigating high pH alteration of low permeability argillaceous rock at 30°C. pp1299-1302 *in* R.Cidu (*ed*) Proc. WRI-10, Balkema, Amsterdam, The Netherlands.

Akagawa, F., Yoshida, H., Yogo, S. and Yamomoto, K. (2006) Redox front formation in fractured crystalline rock: a natural analogue of matrix diffusion in an oxidizing front along a water conducting fracture. Geochemistry: Exploration, Environment, Analysis, 6, 249–56.

Alexander, W.R. (editor) (1992) A natural analogue study of cement buffered, hyperalkaline groundwaters and their interaction with a repository host rock. I: definition of source terms. Nagra Technical Report, NTB 91-10, Nagra, Wettingen, Switzerland.

Alexander, W.R. (editor) (1992) A natural analogue study of cement-buffered, hyperalkaline groundwaters and their interaction with a sedimentary host rock. I: definition of source terms. Nagra Technical Report, NTB 91-10, Nagra, Wettingen, Switzerland.

Alexander, W.R. and Mazurek, M. (1996). The Maqarin natural analogue: possible implications for the performance of a cementitious repository at Wellenberg. Nagra Unpublished Internal Report, Nagra, Wettingen, Switzerland.

Alexander, W.R. and McKinley, I.G. (1999) The chemical basis of the Swiss high-level radioactive waste disposal concept (near-field). *In* R.Metcalfe and C.A.Rochelle (editors) Chemical Containment of Wastes in the Geosphere.. Geological Society of London, Special Publication, 157, 47-69.

Alexander, W.R. and McKinley, L.E. (*eds*) (2007). Deep geological disposal of radioactive wastes. Elsevier, Amsterdam, The Netherlands.

Alexander, W.R. and Möri, A. (2003). Cementitious colloids: integration of laboratory, natural analogue and *in situ* field data. Goldschmidt Conference Abstracts, Geochim. Cosmochim. Acta, 18(S1): A11, 159-160.

Alexander, W.R. and Neall, F.B. (2007). Assessment of potential perturbations to Posiva's SF repository at Olkiluoto caused by construction and operation of the ONKALO facility. Posiva Working Report 2007-35, Posiva, Olkiluoto, Finland.

Alexander, W.R. and Smellie, J.A.T. (1998) Maqarin natural analogue project. ANDRA, CEA, Nagra, Nirex and SKB synthesis report on Phases I, II and III. Nagra Unpublished Project Report, NTB 98-08, Nagra, Wettingen, Switzerland.

Alexander, W.R., Arcilla, C.A., McKinley, I.G., Kawamura, H., Takahashi, Y., Aoki, K. and Miyoshi, S. (2008) A new natural analogue study of the interaction of low-alkali cement leachates and the bentonite buffer. Scientific Basis for Nuclear Waste Managment, XXX, 493-500.

Alexander, W.R., Gautschi, A. and Zuidema, P. (1998) Thorough testing of performance assessment models: the necessary integration of in situ experiments, natural analogues and laboratory work. Extended abstract *in* Scientific Basis for Nuclear Waste Management, XXI, 1013-1014.

Alexander, W.R., McKinley, I.G., Frick, U. and Ota, K. (1997) The Grimsel field tracer migration experiment - what have we achieved after a decade of intensive work? OECD Proceedings: Workshop on Field Tracer Experiments (Role in the Prediction of Radionuclide Migration), Cologne, Germany, 28-30 August, 1996, NEA/OECD, Paris, France.

Alexander, W.R., McKinley, I.G., MacKenzie, A.B. and Scott, R.D. (1990) Verification of matrix diffusion in granite by means of natural decay series disequilibria. Scientific Basis for Nuclear Waste Management, XIII, 567-576.

Alexander, W.R., Scott, R.D., MacKenzie, A.B. and McKinley, I.G. (1988) A natural analogue study of radionuclide migration in a water conducting fracture in crystalline rock. Radiochimica Acta 44/45, 283-298.

Alexander, W.R., Smith, P.A. and McKinley, I.G. (2003) Modelling radionuclide transport in the geological environment: a case study from the field of radioactive waste disposal. Chapter 5 *in* E.M. Scott (editor) Modelling Radioactivity in the Environment. Elsevier, Amsterdam, The Netherlands.

Atkinson, A. (1985) The time-dependence of pH within a repository for radioactive waste disposal. UKAEA Technical Report, AERE-R11777, Harwell, U.K.

Bajjali, W., Clark, I.D. and Fritz, P. (1997) The artesian thermal groundwaters of northern Jordan: insights to their recharge history and age. Journal of Hydrology, 192, 355-382.

Balashova, V.V. and Zavarsin, G.A. (1980) Anaerobic reduction of ferric iron by hydrogen bacteria. Microbiology, 48, 635-639.

Barenblatt, G.I., Zheltov, I.V. and Kochina, I.N. (1960) Basic concepts in the theory of seepage of homogenous liquids in fissured rock. Journal of Applied Mechanics, 24, 1286.

Barjous M. (1986) The geology of Siwaqa. Bulletin 4, Natural Resources Authority, Amman, Jordan.

Barnes, I., O'Neil, J.R. and Trescares, J.J. (1978) Present day serpentinization in New Caledonia, Oman and Yugoslavia. Geochimica et Cosmochimica Acta, 42, 144-145.

Barnes, I., Presser, T.S., Saines, M., Dickson, P. and Van Goos, A.F.K. (1982) Geochemistry of highly basic calcium hydroxide groundwaters in Jordan. Chemical Geology, 35, 147-154.

Barnett, S.J., Macphee, D.E., Lachowski, E.E. and Crammond, N.J. (2002) XRD, EDX and IR analysis of solid solutions between thaumasite and ettringite. Cement and Concrete Research, 32, 719-730.

Bateman, K., Coombs, P., Noy, D.J., Pearce, J.M. and Wetton, P. (1995) Nagra/Nirex/SKB column experiments. I: results of experiments and modelling. Nagra Unpublished Internal Report, Nagra, Wettingen, Switzerland.

Bateman, K., Coombs, P., Noy, D.J., Pearce, J.M. and Wetton, P. (1998) Nagra/Nirex/SKB column experiments. II: fluid/rock interactions in the disturbed zone. Nagra Unpublished Internal Report, Nagra, Wettingen, Switzerland.

Bath, A.H., Christofi, N., Neal, C., Philp, J.C., Cave, M.R., McKinley, I.G. and Berner, U. (1987) Trace elements and microbiological studies of alkaline groundwaters in Oman, Arabian Gulf: A natural analogue for cement pore water. Fluid Processes Research Group Report FLPU 87-2, British Geological Survey, Keyworth, U.K.

Bath, A.H., Berner, U., Cave, M., McKinley, I.G. and Neal, C. (1987b). Testing geochemical models in a hyperalkaline environment. *In* Come, B. and Chapman, N.A. (editors), Natural Analogues in Radioactive Waste Disposal. Proceedings of 1st NAWG Symposium, Brussels, 28-30 April 1987, CEC Report EUR11037, Brussels, Belgium.

Bath, A.H., Christofi, N., Neal, C., Philp, J.C., Cave, M.R., McKinley, I.G. and Berner, U. (1988), Trace Element and Microbiological Studies of Alkaline Groundwaters in Oman, Arabian Gulf: A Natural Analogue for Cement Pore Waters. Nagra Technical Report, NTB 87-16, Nagra, Wettingen, Switzerland.

Bath, A.H., Christofi, N., Neal, C., Philp, J.C., Cave, M.R., McKinley, I.G. and Berner, U. (1987a) Trace element and microbiological studies of alkaline groundwaters in Oman: a natural analogue for cement pore-waters. Nagra Technical Report, NTB 87-16, Nagra, Wettingen, Switzerland.

Beeston, J.W. (1983) The application of coal petrology to source rock studies in the Denison Trough, Queensland. *In* Permian Geology of Queensland. Geological Society of Australia, Queensland Division, 53–56.

Bénard A. (2004) Le plomb et le chrome dans les ciments: spéciation et modélisation du transfert au cours de la lixiviation. PhD Thesis, University of Aix-Marseille III, France.

Bender, F. (1968) Geologie von Jordanian. Beitrage zur Regionalen Geologie der Erde, Band 7. Borntraeger, Berlin 230 pp.

Bender, F. (1974) Geology of Jordan – Contributions to the Regional Geology of the Earth. V.7. Bornträger, Berlin, 196 pp.

Bentor, Y.K., Gross, S. and Heller, I. (1963a) Some unusual minerals from the 'Mottled Zone Complex', Israel. American Mineralogist, 48, 924-930.

Bentor, Y.K., Gross, S. and Heller, I. (1963b) High temperature minerals in non-metamorphosed sediments. Nature, 199, 478.

Bentor, Y.K., Gross, S. and Kolodny, Y. (1972) New evidence on the origin of the high temperature assemblage of the 'Mottled Zone' Israel. Proceedings of the 24th International Congress, Section 2, 265-275.

Bentor, Y.K., Gross, S., and Heller, L. (1963) Some unusual minerals from "Mottled Zone". Complex, Israel. Amererican Mineralogist, 48, 924-930.

Bentor, Y.K., Gross, S., and Kolodny, Y. (1972) New evidence on the origin of high temperature assemblage of the "Mottled Zone",,Israel. Proceedings of the 24th International Geological Congress, Section 2, 265-275.

Berner, U. (1987) Modelling porewater chemistry in hydrated cement. Materials Research Society Symposium Proceedings, 84, 319.

Berner, U. (1990) A thermodynamic description of the evolution of pore water chemistry and uranium speciation during degradation of cement. PSI Report 62, Paul Scherrer Institute, Villigen, Switzerland.

Beydoun, Z.R. (1999) Evolution and development of the Levant (Dead Sea Rift) Transform System; A historical-chronological review of a structural controversy. In: MacNiocaill, C. and Ryan, P.D. (editors) Continental Tectonics. Geological Society of London, Special Publication, 164, 239-255.

Birck, J.L. and Allègre, C.J. (1978) Chronology and chemical history of the parent body of basaltic achondrites studied by the ^{87}Rb–^{87}Sr method. Earth and Planetary Science Letters. 39, 37–51.

Bishop, A.N. and Abbott, D.G. (1995) Vitrinite reflectance and molecular geochemistry of Jurassic sediments: the influence of heating by Tertiary dykes (northwest Scotland). Organic Geochemistry, 22, 165-177.

Blake, G. and Ionides, M. (1939). Report on the water resources of Transjodan and their development. Crown Agents for Colonies. London, 372 pp.

Blander, M. (1971) The constrained equilibrium theory: sulphide phases in meteorites. Geochimica et Cosmochimica Acta, 35, 61-76.

Bouchet, A. (1992) Mise au point d'un programme de determination automatique des minéraux argileux. Collection de Rayons X Siemens, 2, 51-61. Comptes Rendus, Paris, France.

Bouwer, H. and Rice, R.C. (1976) A slug test for determining hydraulic conductivity of unconfined aquifers with complete or partially penetrating wells. Water Resources Research, 12, 423-428.

Bradbury, M.H. and Green, A. (1986a) Retardation of radionuclide transport by fracture flow in granite and argillaceous rocks. Nuclear Science and Technology Report EUR 10619, Commission of the European Communities, Brussels, Belgium.

Bradbury, M.H. and Green, A. (1986b) Investigations into the factors influencing long range matrix diffusion rates and pore space accessibility at depth in granite. Journal of Hydrology, 89, 123-139.

Bradbury, M.H. and Stephen, I.G. (1986). Diffusion and permeability based sorption measurements in intact rock samples. Scientific Basis for Nuclear Waste Management, IX, 81-90.

Bredehoeft, J.D. and Papadopulos, S.S. (1980) A method for determining the hydraulic properties of tight formations. Water Resources Research, 16, 233-238.

Brookins, D.G. (1986) Rhenium as analog for fissiogenic technetium: Eh-pH diagram (25°C, 1 bar) constraints. Applied Geochememistry, 1, 513-517.

Brown, G., Catt, J.A., and Weir, A.H. (1969) Zeolites of the clinoptilolite-heulandite type in sediments of south-east England. *Mineralogical Magazine*, **37**, 480-488.

Bulter, B.C.M. (1977) Al-rich pyroxene and melilite in a blast-furnace slag and a comparison with the Allende meteorite. Mineralogical Magazine, 41, pp.493-499.

Burdon, D. (1959) Handbook of the geology of Jordan. Benham, Colchester, U.K. 82 pp.

Burg, A., Kolodny, Y., and Lyakhovskg, V. (2000) Hatrurim-2000. The Mottled Zone revisited forty years later. Israel Journal of Earth Science, 48, 209 – 223.

Burg, A., Starinsky, A., Bartov, Y. and Kolodny, Y. (1992) Geology of the Hatrurim Formation. Israel Journal of Earth Science, 40, 107-124.

Bustin, R.M. and Guo, Y. (1999) Abrupt changes (jumps) in reflectance values and chemical compositions of artificial charcoals and inertinite in coals. International Journal of Coal Geology, 38, 237–260.

Butler, J.J. (1997) Theoretical analysis of impact of incomplete recovery on slug tests. Kansas Geological Survey Open-File Report, 97-59.

Calemma, V., Rausa, R., Margarit, R. and Girardi, E. (1988) FT – i.r. study of coal oxidation at low temperature. Fuel, 67, 764-770.

Cave, M.R. and Green, K.A. (1989) Feasibility study of the determination of iodide, tin, arsenic, selenium, and hydrogen carbonate in groundwaters by inductively coupled plasma atomic emission spectroscopy using a membrane gas-liquid separator. Journal of Analytical Spectroscopy, 4, 223-225.

Chambers, A.V. and Haworth, A. (1998) Coupled modelling for the Jordan natural analogue project. Chapter 13 *in* C.M.Linklater (editor) A natural analogue study of cement buffered, hyperalkaline groundwaters and their interaction with a repository host rock: Phase II. Nirex Science Report, S-98-003, UK Nirex, Harwell, UK.

Chandra, D. (1958) Reflectance of oxidized coals. Economic Geology, 53, 102-108.

Chenery, S. and Cook, J.M. (1993) Determination of Rare Earth Elements in single mineral grains by laser ablation microprobe-inductively coupled plasma mass spectrometry. Journal of Analytical Atomic Spectroscopy, 8, 299-303.

Chermak, J.A. (1992) Low temperature experimental investigation of the effect of high pH NaOH solutions on the Opalinus Shale, Switzerland. Clays and Clay Minerals,40, 650-658.

Chermak, J.A. (1993) Low temperature experimental investigation of the effect of high pH KOH solutions on the Opalinus Shale, Switzerland. Clays and Clay Minerals, 41, 365-372.

Cherniak D.J. (1997) An experimental study of strontium and lead diffusion in calcite, and implications for carbonate diagenesis and metamorphism. Geochimica et Cosmochimica Acta, 61, 4173-4179.

Cisowski, S.M. and Fuller, M. (1987) The generation of magnetic anomalies by combustion metamorphism of sedimentary rock, and its significance to hydrocarbon exploration. Geological Society of America Bulletin, 99, 21-29.

Clark I.D., Fontes J.C., and Fritz P. (1992b) Stable isotope disequilibria in travertine from high pH waters: laboratory investigations and field observations from Oman. Geochimica et Cosmochimica Acta, 56, 2041-2050.

Clark, I.D. and Fritz, P. (1998) Isotope hydrogeology of the Maqarin hyperalkaline groundwaters. Chapter 10 *in* C.M.Linklater (editor) A natural analogue study of cement buffered, hyperalkaline groundwaters and their interaction with a repository host rock. II. Nirex Science Report, S-98-003, UK Nirex, Harwell, U.K.

Clark, I.D., Fritz, P., Milodowski, A.E. and Khoury, H.N. (1992) Sampling and analytical methods *in* W.R.Alexander (editor) A natural analogue study of cement buffered hyperalkaline groundwaters and their interaction with a repository host rock. Nagra Technical Report, NTB 91-10, Wettingen, Switzerland.

Clark, I., Firtz, P. Seidlitz, H., Khoury, H., Trimborn, P., Milodowski, A.E., and Pearce, J. (1993) Recarbonation of metamorphosed marls, Jordan. Applied Geochemistry, 8, 473-481.

Clark, I., Khoury, H., Salameh, E., Fritz, P., Goksu, Y., Wieser A., Causse, C., and Fontes, J. (1992a) Travertines in central Jordan. IAEA – SM – 319/6, 551-565.

Clark, I.D. and Fritz, P. (1997). Environmental Isotopes in Hydrogeology, Lewis Publishers, Boca Raton, U.S.A..

Clark, I.D. and Fritz, P. (1998) Isotope hydrogeology of the Maqarin hyperalkaline groundwaters. Chapter 10 *in* J.A.T.Smellie (editor) Maqarin natural analogue study: Phase III. SKB Technical Report, TR-98-04, Volumes I and II, SKB, Stockholm, Sweden.

Clark, I.D., Dayal, R. and Khoury, H.N. (1994). The Maqarin (Jordan) natural analogue for 14-C attenuation in cementitious barriers. Waste Manag. 14, 467-477.

Clauer, N. and Chaudhuri, S. (1995) Clays in crustal environments, isotope dating and tracing. Springer-Verlag, Germany, 359 pp.

Colodner, D., Sachs, J., Ravizza, G., Turekian, K., Edmond, J. and Boyle, E. (1993) The geochemical cycle of rhenium: a reconnaissance. Earth and Planetary Science Letters, 117, 205-221.

Cook, A. and Sherwood, N.R. (1991) Classification of oil shales, coals and other organic-rich rocks. Organic Geochemistry, 17, 211-222.

Cookes, N.E., Fuller, O.M. and Gaikwad, R.P. (1986) FT-i.r. spectroscopic analysis of coals and coal extracts. Fuel, 65, 1254-1260.

Coombs, P., Gardner, S.J., Rochelle, C.A. and West, J.M. (1994) Microbiological processes under hyperalkaline conditions - Results from Phase III of the Maqarin natural analogue study. Unpublished Nagra Internal Report, Nagra, Wettingen, Switzerland.

Coombs, P., Gardner, S.J., Rochelle, C.A. and West, J.M. (1998) Natural analogue for geochemistry and microbiology of cement pore waters and cement pore water/host rock/near-field interactions. Chapter 11 *in* Linklater, C.M. (editor) A natural analogue study of cement buffered, hyperalkaline groundwaters and their interaction with a repository host rock. II. Nirex Science Report, S-98-009, UK Nirex, Harwell, U.K.

Cooper, H.H. and Jacob, C.E. (1946) A generalized graphic method for evaluating formation constants and summarizing well-field history. Transactions of American Geophysical Union, 27, 526-534.

Cooper, H.H., Bredehoeft, J.D. and Papadodulos, I.S. (1967) Response of a finite diameter well to an instantaneous charge of water. Water Resources Research, 3, 263-269.

Copard, Y., Disnar, J.R. and Becq-Giraudon, J.F. (2002) Erroneous maturity assessment given by Tmax and HI Rock-Eval parameters on highly mature weathered coals. International Journal of Coal Geology, 49, 57–65.

Copard, Y., Disnar, J.R., Becq-Giraudon, J.F. and Boussafir, M. (2000) Evidence and effects of fluid circulation on organic matter in intramontane coalfields (Massif Central, France). International Journal of Coal Geology, 44, 49–68.

Copard, Y., Disnar, J.R., Becq-Giraudon, J.F. and Laggoun-Defarge, F. (2004) Erroneous coal maturity assessment caused by low temperature oxidation. International Journal of Coal Geology, 58, 171–180.

Crusius, J. and Thomson, J. (2000) Comparative behavior of authigenic Re, U and Mo during reoxidation and subsequent long-term burial in marine sediments. Geochimica et Cosmochimica Acta, 13, 2233-2242.

Crusius, J., Calvert, S., Pedersen, T. and Sage, D. (1996) Rhenium and molybdenum enrichments in sediments as indicators of oxic, suboxic and sulfidic conditions of deposition. Earth and Planetary Science Letters, 145, 65-78.

Day, R., Fuller, M.D. and Schmidt, V.A. (1977). Hysteresis properties of titanomagnetites: grain size and composition dependence. Physics of the Earth and Planetary Intereriors, 13, 260-267.

Dercourt, J., Zonenshain, L.P., Ricou, L.-E. and 16 others (1986) Geological evolution of the Tethys belt from the Atlantic to the Pamirs since the Lias. Tectonophysics, 123, 241-315.

Desjardin, V., Bayard, R., Huck, N., Manceau, A. and Gourdon, R. (2002) Effect of microbial activity on the mobility of chromium in soils. Waste Management, 22, 195-200.
Diessel, C.F.K. and Smyth, M. (1995) Petrographic constituents of Australian coals. *In* C.R.Ward, H.J. Harrington, C.W. Mallett and J.W.Beeston (editors) Geology of Australian Coal Basins. Geological Society of Australia Incorporated Coal Geology Group, Special Publication, 1, 63–81.
Dietzel, M., Usdowski, E. and Hoefs, J. (1992) Chemical and $^{13}C/^{12}C$- and $^{18}O/^{16}O$- isotope evolution of alkaline drainage waters and the precipitation of calcite. Applied Geochemistry, 7, 177.
Draude, K.M., Kurniawan, C.B. and Duff, S.J.B. (2001) Effect of oxygen delignification on the rate and extent of enzymatic hydrolysis of lignocellulosic material. Bioresource Technology, 79, 113-120.
Duckworth, A.W., Grant, W.D., Jones, B.E. and Van Steenbergen, R. (1996) Phylogenetic diversity of soda lake alkaliphiles. FEMS Microbiology Ecology, 19, 181-191.
Dynamic Graphics (1997). see http://www.dgi.com/earthvision/index.shtml
Eary, L.E. and Rai, D. (1987) Kinetics of Chromium(III) oxidation to chromium(VI) by reaction with manganese dioxode. Environmental Science & Technolology, 21, 1187-1193.
Ekendahl, S. and Pedersen, K. (1994) Carbon transformations by attached bacterial populations in granitic ground water from deep crystalline bed-rock of the Stripa research mine. Microbiology, 140, 1565-1573.
Elie, M., Faure, P., Michels, R., Landais, P. and Griffault, L. (2000) Natural and laboratory oxidation of low-organic-carbon-content sediments: comparison of chemical changes in hydrocarbons. Energy & Fuels, 14, 854-861.
Elie, M., Techer, I., Trotignon, L., Khoury, H., Salameh, E., Vandamme, D., Boulvais, P. and Fourcade, S. (2007) Cementation of kerogen-rich marls by alkaline fluids released during weathering of thermally metamorphosed marly sediments. Part II: Organic matter evolution, magnetic susceptibility and metals (Ti, Cr, Fe) at the Khushaym Matruk natural analogue (Central Jordan). Applied Geochemistry, doi:10.1016/j.apgeochem.2007.02.013.
Falcon, R.M.S. and Snyman, C.P. (1986) An introduction to coal petrography: atlas of petrographic constituents in the bituminous coals of Southern Africa. Geology Society of South Africa, Review Paper, 2, 27.
Faure, G. and Powell, J.L. (1972) Strontium Isotope Geology. Springer-Verlag, Berlin, Germany.
Felsenstein, J. (1985) Confidence limits on phylogenies: An approach using bootstrap. Evolution, 39, 783-791.
Felsenstein, J. (1989) PHYLIP - phylogeny inference package. Cladistics, 5, 164-166.
Fendorf, S.E. and Zasoski, R.J. (1992) Chromium(III) oxidation by □-MnO_2. 1. Characterisation. Environmental Science & Technolology, 26, 79-85.
Fernández-Bolaños, J., Felizón, B., Heredia, A., Guillén, R. and Jiménez, A. (1999) Characterization of the lignin obtained by alkaline delignification and of the cellulose residue from steam-exploded olive stones. Bioresource Technology, 68, 121-132.
Fincham, C.J.B. and Richardson, F.D. (1954) The behaviour of sulphur in silicate and aluminate melts. Proceedings of the Royal Society of London, Series A, 223, 40-62.
Fourcade S., Trotignon L., Boulvais P., Techer I, Elie M., Vandamme D. Salameh E., Khoury H. (2007) Cementation of kerogen-rich marls by alkaline fluids released during weathering of thermally metamorphosed marly sediments. Part I: isotopic (C,O) study of the Khushaym Matruk natural analogue (Central Jordan). Applied Geochemistry, 22, 1293-1310.
Fourcade, S., Trotignon, L., Boulvais, P., Techer, I., Elie, M., Vandamme, D., Salameh, E. and Khoury, H. (2007) Cementation of kerogen-rich marls by alkaline fluids released during weathering of thermally metamorphosed marly sediments. Part I: Isotopic (C,O) study of the Khushaym Matruk natural analogue (central Jordan). Applied Geochemistry, doi:10.1016/j.apgeochem.2007.02.012.
Francis, C.A. and Tebo, B.M. (2002) Enzymatic manganese(II) oxidation by metabolically dormant spores of diverse Bacillus species. Applied and Environmental Microbiology, 68, 874-880.
Fredrickson, J.K. and Fletcher, M. (2001) Subsurface microbiology and biogeochemistry. Wiley-Liss, New York, 341 pp.
Ganz, H.H., Kalkreuth, W., Ganz, S.N., Öner, F., Pearson, M.J. and Wehner, H. (1990) Infrared analysis – State of art. Berliner Geowissschaft Abhandlung, A, 1011-1026.
Garrels, R.M., Dreyer, R.M. and Howland, A.L. (1949) Diffusion of ions through intergranular spaces in water saturated rocks. Bulletin of the Geological Society of America, 60, 1809-1924.
Gascoyne, M. (1992) Geochemistry of the actinides and their daughters. *In* M Ivanovich and R.S.Harmon (editors) Uranium-series disequilibrium: applications to earth, marine and environmental sciences. Clarendon Press, Oxford, U.K., 34-61.
Gascoyne, M. and Cramer, J.J. (1987) History of actinide and major element mobility in an Archean granitic batholith in Manitoba, Canada. Applied Geochemistry, 2, 37-54.

Gaucher, E.C., Blanc, P., Matray, J-M. and Michau, N. (2004) Modeling diffusion of an alkaline plume in a clay barrier. Applied Geochemistry, 19, 1505–1515.

Geyer, S., Pörschmann, J., Hanschman, G., Geyer, W., Kopinke, F.-D., Boehlmann, W. and Fritez, P. (1998) Organic chemistry of the bituminous marls. Chapter 9 *in* J.A.T. Smellie, (editor) Maqarin natural analogue study: Phase III. SKB Technical Report, TR-98-04, SKB, Stockholm, Sweden.

Geyer, S., Pörschmann, J., Hanschman, G., Geyer, W., Kopinke, F-D., Boehlmann D. and Fritz, P. (1998) Organic chemistry of the Bituminous Marls. Chapter 9 *in* Smellie, J.A.T. (editor) Maqarin natural analogue study: Phase III. SKB Technical Report, TR 98-04, Volumes I and II, SKB, Stockholm.

Given, P.H., Spackman, W., Painter, P.C., Rhoads, C.A. and Ryan, N.J. (1984) The fate of cellulose and lignin in peats: an exploratory study of the input to coalification. Organic Geochemistry, 6, 399-407.

Glasspool, I. (2000) A major fire event recorded in the mesofossils and petrology of the Late Permian, Lower Whybrow coal seam, Sydney Basin, Australia. Palaeogeography Palaeoclimatology Palaeoecology, 164, 357–380.

Goldstein, J.I., Newbury, D.E., Echlin, P., Joy, D.C., Fiori, C. and Lifshin, E. (1981) Scanning Electron Microscopy and X-Ray Microanalysis. Plenum Press, New York.

Graham, A.L., Easton, A.J. and Hutchison, R. (1977) The Mayo Belwa meteorite: a new enstatite achondrite fall. Mineralogical Magazine, 41, 487-492.

Grant, W.D., Mwatha, W.E. and Jones, B.E. (1990) Alkaliphiles, ecology, diversity and applications. FEMS Microbiology Reviews, 75, 255-270.

Griffiths, H.M., Clark, R.A., Thorp, K.M. and Spencer, S. (2000) Strain accommodation at the lateral margin of an active transpressive zone: geological and seismological evidence from the Lebanese restraining bend. Journal of the Geological Society of London, 157, 289-302.

Grisak, G.E. and Pickens, J.F. (1980) Solute transport through fractured media. Part I: the effect of matrix diffusion. Water Resources Research, 16, 719-730.

Gross, S. (1977) The mineralogy of Hatrurim Formation, Israel. Geological Survey of Israel Bulletin, 70, 80 pp.

Gross, S. (1977) The mineralogy of the Hatrurim Formation, Israel. Bulletin of the Geological Survey of Israel, 70, 21-23.

Gross, S., Mazor, E., Saas, S. and Zak, I. (1967) The 'Mottled Zone' Complex of Nahal Aylon (central Israel). Israel Journal of Earth Science, 16, 84-96.

Gross, S., Mazor, E., Sass, S., and Zak, I. (1967) The "Mottled Zone" complex of Nahal Ayalon (Central Israel). Israel Journal of Earth Science, 16, 84-96.

Guo, Y. and Bustin, R.M. (1998) FTIR spectroscopy and reflectance of modern charcoals and fungal decayed woods: implications for studies of inertinite in coals. International Journal of Coal Geology, 37, 29-53.

Gur, D., Steinitz, G., Kolodny, Y., Starinsky, A. and McWilliams, M. (1995) Ar^{40}/Ar^{39} dating of combustion metamorphism. Chemical Geology, 122, 171-184.

Hadermann, J. and Rösel, F. (1985) Radionuclide chain transport in homogeneous crystalline rocks: limited matrix diffusion and effective surface sorption. Nagra Technical Report, NTB 85-40, Nagra, Wettingen, Switzerland.

Hakki, W. and Sassa, A. (1978) Daba marble project. Unpublished Report, National Resources Authority, Amman, Jordan, 40 pp.

Hallbeck, L. and Pedersen, K. (1990) Culture parameters regulating stalk formation and growth rate of *Gallionella ferruginea*. Journal of General Microbiology, 136, 1675-1680.

Harza (1978) Hydrological investigations at the Maqarin damsite, Harza Engineering Company. Unpublished Internal Report, November, 1978. Archives of the Jordan Valley Authority, Amman, Jordan.

Harza (1980) Jordan Valley Irrigation Project, Maqarin Dam, Vol. XD - Geotechnical data (Harza Overseas Engineering Company). Hashemite Kingdom of Jordan, Jordan Valley Authority.

Hauf, P. (1979) Hashemite from Daba, Jordan. Unpublished Internal Report, United States Geological Survey, Renton, U.S.A.

Haveman, S.H., Pedersen, K. and Routsalainen, P. (1999) Distribution and metabolic diversity of microorganisms in deep igneous rock aquifers of Finland. Geomicrobiology Journal, 16, 277-294.

Haworth, A., Sharland, S.M., Tasker, P.W. and Tweed, C.J. (1987) Evolution of the groundwater chemistry around a nuclear waste repository. Scientific Basis for Nuclear Waste Management, XI, 645-651.

Heihmbach, W. and Rosch, H. (1980) Die mottled zone in Zentral-Jordanien. Geologisches Jahrbuch, 40, 3-17.

Heimbach, W. (1965) The geological and hydrogeological survey in the area between the Hedjaz Railway, Qatrana-El Hasa, and eastern border of Jordan. Unpublished Report, German Geologic Mission, 2-20.

Heimbach, W. and Rosch, H. (1980) Die Mottled Zone in Zentral Jordanian. Geologische Jahrbuch. 40, 3-17.

Hellmuth, K.-H., Siitari-Kauppi, M. and Lingberg, A. (1992) Applications of the ^{14}C Polymethylmethacrylate (PMMA) impregnation method in studies on porosity and matrix diffusion. Materials Research Society Symposium Proceedings, 257, 649-656.

Helz, G.R. and Wyllie, P.J. (1979) Liquidous relationships in the system CaCO3-Ca(OH)2-CaS and the solubility of sulphur in carbonatite magmas. Geochimica et Cosmochimica Acta, 43, 259-265.
Hewlett, P.C. (editor) (1998) Lea's Chemistry of Cement and Concrete (4th Edition). Arnold, London, 1053 pp.
Hodgkinson, D.P. and Robinson, P.C. (1987) Nirex near-surface repository project. Preliminary radiological assessment: Summary. Nirex Safety Studies Report, NSS/RA100, UK Nirex, Harwell, U.K.
Hodson, R.E., Benner, R. and Maccubin, A.E. (1983) Transformations and fate of cellulosic detritus in marine environments. *In* T.A. Oxley and S. Barry (editors), Biodeterioration, 5, Wiley, New York, 185-195.
Hofmann, B.A. (1990) Reduction spheres in haematitic rocks from northern Switzerland: implications for the mobility of some rare elements. Nagra Technical Report, NTB 89-17, Nagra, Wettingen, Switzerland.
Hofmann, U. and Klemen, E. (1950) Verlust der Austauschkapazität von Lithiumionen an Bentonit durch Erhitzung. Zeitscrift für Anorgische Chemie, 262, 95-99.
Horowitz, A. (1987) Palynological evidence for the age and state of sedimentation along the Dead Sea rift, and structural implications. Tectonophysics, 141, 107-116.
Hvorslev, M.J. (1951) Time lag and soil permeability in groundwater observations. U.S. Army Corps of Engineers, Waterways Experimental Station Bulletin, 36. Vicksburg, U.S.A.
Hyslop, E. (1998).Uranium distribution and whole rock geochemistry. *In* C.M.Linklater (editor) A natural analogue study of cement buffered, hyperalkaline groundwaters and their interaction with a repository host rock. Phase II. Nirex Science Report, S-98-003, UK Nirex, Harwell, U.K.
Hyslop, E.K. (1998) Uranium distribution and whole rock geochemistry. Chapter 7 *in* C.M. Linklater (editor) A natural analogue study of cement buffered, hyperalkaline groundwaters and their interaction with a repository host rock: Phase II. Nirex Science Report, S-98-003, UK Nirex, Harwell, U.K.
Ibrahim, K.M., Tarawneh, K. and Rabba, I. (2002) Phases of activity and geochemistry of basaltic dyke systems in northeast Jordan parallel to the Red Sea. Journal of Asian Earth Sciences, 21, 467-472.
ICCP (2001) International Committee for Coal and Organic Petrology (ICCP). The new inertinite classification (ICCP System 1994). Fuel, 80, 459–471.
Iglesias, M.J., de la Puente, G., Fuente, E. and Pis, J.J. (1998) Compositional and structural changes during aerial oxidation of coal and their relations with technological properties. Vibrational Spectroscopy, 17, 41–52.
Ingram, G.R. and Rimstidt, J.D. (1984) Natural weathering of coal. Fuel, 63, 292-296.
Inoue, A., Bouchet, A., Velde, B. and Meunier, A. (1989) A convenient technique for estimating smectite layer percentage in randomly interstratified illite/smectite minerals. Clays and Clay Minerals, 37, 227-234.
Ivanovich, M., Latham, A.G. and Ku, T.L. (1992) Uranium-series disequilibrium applications in geochronology. *In* M.Ivanovich and R.S.Harmon (editors) Uranium-series disequilibrium: applications to earth, marine and environmental sciences. Clarendon Press, Oxford, U.K., 62-94.
Jackson, M.L. (1964) Soil chemical analyses. Prentice Hall, New Jersey, U.S.A., 3rd edition.
Jaser, D. (1986). The geology of Khan Ez Zabib. Bulletin 3, Natural Resources Authority, Amman, Jordan.
Jeans, C.V. (2006). Clay mineralogy of the Cretaceous strata of the British Isles. Clay Minerals, 41, 47-100.
Jenkin, G.R.T., Rogers, G., Fallick, A.E. and Farrow, C.M. (1995) Rb-Sr closure temperatures in bi-mineralic rocks: a mode effect and test for different diffusion models. Chemical Geology, 122, 227-240.
Jenkins, P.M. (1936) Reports of the Percy Sloden expedition to some rift valley lakes in Kenya in 1929. VII: summary of the ecological results, with special reference to the alkaline lakes. Annual Magazine of. Natural History, 18, 133-181.
Jones, B.E., Grant, W.D., Duckworth, A.W. and Qwenson, G.G. (1998) Microbial diversity of soda lakes. Extremophiles, 2, 191-200.
Jones, C.E., Jenkyns, H.C., Coe, A.L. and Hesselbo, S.P. (1994) Strontium isotopic variations in Jurassic and Cretaceous seawater. Geochimica et Cosmochimica Acta, 58, 3061-3074.
Jordan River Authority (1980) Maqarin Project. Site Geology Map. Harza Overseas Engineering Company, for the Hashemite Kingdom of Jordan, Jordan River Authority, Jordan Valley Irrigation Project – Stage II.
Kamei, G., Alexander, W.R. and Smellie, J.A.T. (2005) Overview of the Maqarin Natural Analogue Project: results from Phase I-III. JNC Technical Report, JNC TN8400 2005-005 (*in Japanese with English abstract*), JNC, Tokai, Japan.
Keil, K. (1968) Mineralogical and chemical relationships among enstatite chondrites. Journal of Geophysical Research, 73, 6945-6976.
Keith-Roach, M.J. and Livens, F.R. (2002) Interactions of microorganisms with radionuclides. Elsevier, Amsterdam, 400 pp.
Keller, C.K. and Van der Kamp, G. (1992) Slug tests with storage due to trapped air. Ground Water, 30, 2.
Khoury, H. and Milodowski, A. (1992) High temperature metamorphism and low temperature retrograde alteration of spontaneously combusted marls. The Maqarin cement analogue. *In* Y.K.Kharaka and A.S.Maest (editors), Water-rock interaction, Rotterdam. 1515-1518.

Khoury, H. and Nassir, S. (1982a) A discussion on the origin of Daba – Siwaqa marble. Dirasat, 9, 55-56.
Khoury, H.N. (1989) Mineralogy and petrology of the opaline phases from Jordan. Neues Jahrbuch für Mineralogie - Abhandlungen, 10, 433-440.
Khoury, H.N. and Abu-Jayyab, A. (1995) Research note to the mineral volkonskoite; four new localites in central Jordan. Dirasat, 22, 189-198.
Khoury, H.N. and Nassir, S. (1982b). High temperature mineralization in Maqarin area, Jordan. Neues Jahrbuch für.Mineralogie - Abhandlungen,144, 187-213.
Khoury, H.N. Salameh, E., Clark, I., Fritz, P., Bajjali, W., Milodowski, A., Cave, M. and Alexander, W.R. (1992) A natural analogue of high pH cement pore waters from the Maqarin area of northern Jordan 1:Introduction to the site. Journal of.Geochemical Exploration, 46, 117-132.
Khoury, H., Mackenzie, R., Russell, J. and Tait, J. (1984) An iron free volkonskoite. Clay Minerals, 19, 43-57.
Khoury, H.N. and Salameh, E. (1986) The origin of high temperature minerals from Sweileh area, Jordan. Dirasat, 13, 261-269.
Khoury, H.N., Salameh, E., Mazurek, M. and Alexander, W.R. (1998) Geology and hydrogeology of the Maqarin area. Chapter 2 *in* Smellie, J.A.T. (editor) Maqarin natural analogue study: Phase III. SKB Technical Report, TR-98-04, Volumes I and II, SKB, Stockholm, Sweden.
Kim, E. and Boulègue, J. (2003) Chemistry of rhenium as an analogue of technetium: experimental studies of the dissolution of rhenium oxides in aqueous solutions. Radiochimica Acta, 91, 211-216.
Kimura, M. (1980) A simple method for estimating evolutionary rates of base substitutions through comparative studies of nucleotide sequences. Journal of Molecular Evolution, 16, 111-120.
Klinke, H.B., Ahring, B.K., Schmidt, A.S. and Thomsen, A.B. (2002) Characterization of degradation products from alkaline wet oxidation of wheat straw. Bioresource Technology, 82, 15-26.
Klinkenberg, L.J. (1951) Analogy between diffusion and electrical conductivity in porous rocks. Bulletin of the Geological Society of America, 62, 559-660.
Kolodny, Y. (1979) Natural cement factory: A geological story. *In* J.Skalny (editor) Cement production and use. Engineering Foundation Conference, 203-215..
Kolodny, Y. and Gross, S. (1974) Thermal metamorphism by combustion of organic matter: isotopic and petrological evidence. Journal of Geology, 82, 489-506.
Kolodny, Y., Barr, N. and Saas, E. (1971) Fission track age of the 'Mottled Zone Event' in Israel. Earth and Planetary Science Letters, 11, 269-272.
Kolodny, Y., Schulman, N. and Gross, S. (1973) Hazeva formation sediments affected by the "Mottled Zone Event". Israel Journal of Earth Science, 22, 185-193.
Kostka, J. and Nealson, K.H. (1998) Isolation, cultivation and characterization of iron- and manganese reducers. *In* Burlage, R.S., Atlas, R., Stahl, D., Geesey, G. and Sayler G. (editors) Techniques in microbial ecology. Oxford University Press, New York, 58-78.
Krishnamurthy, R.V., Schmitt, D., Atekwana, E.A. and Baskaran, M. (2003) Isotopic investigations of carbonate growth on concrete structures. Applied Geochemistry, 16, 435-444.
Kruszewska, K.J. and Du Cann, V.M. (1996) Detection of the incipient oxidation of coal by petrographic techniques. Fuel, 75, 769– 774.
Laaksoharju, M., Skarman, E. and Skarman, C. (2000) Multivariate mixing and mass balance calculations (M3) – A new concept and computer program for decoding hydrochemical information. SKB Technical Report, TR-00-01, SKB, Stockholm, Sweden.
Landais, P., Monthioux, M. and Meunier, J.D. (1984) Importance of the oxidation/maturation pair in the evolution of humic coals. Organic Geochemistry, 7, 249-260.
Landais, P., Rochdi, A., Largeau, C. and Derenne, S. (1993) Chemical characterization by transmission micro-FTIR spectroscopy: Origin and extent of compositional heterogeneities. Geochimica et Cosmochimica Acta, 57, 2529-2539.
Larimer, J.W. (1968) An experimental investigation of oldhamite, CaS, and the petrologic significance of oldhamite in meteorites. Geochimica et Cosmochimica Acta, 32, 965-982.
Lea, F.M. (1970) The Chemistry of Cement and Concrete. Edward Arnold (3rd edition).
Létolle R., Gegout P., Rafia N. and Revertegat, E. (1992) Stable isotopes of carbon and oxygen for the study of carbonation/decarbonation in concrete. Cement and Concrete Research, 22, 235-240.
Lindberg, R.D. and Runnels, D.D. (1984) Ground water redox reactions: an analysis of equilibrium state applied to Eh measurements and geochemical modelling. Science, 225, 425-427.
Linklater C.M. (editor) (1998) A natural analogue study of analogue cement buffered, hyperalkaline groundwaters and their interaction with a repository host rock: Phase II. Nirex Science Report, S-98-003, UK Nirex, Harwell, U.K.

Linklater, C.M. (editor) (1998) A natural analogue study of cement buffered, hyperalkaline groundwaters and their interaction with a repository host rock: Phase II. Nirex Science Report, S-98-003, UK Nirex, Harwell, U.K.

Linklater, C.M., Albinsson, Y., Alexander, W.R., Casas, I., McKinley, I.G. and Sellin, P. (1996) A natural analogue of high pH cement pore waters from the Maqarin area of northern Jordan: comparison of predicted and observed trace element chemistry of uranium and selenium. Journal of Contaminant Hydrology, 21, 59-69.

Llani, S., Harlavan, Y., Tarawneh, K., Rabba, I., Weinberger, R., Ibrahim, K., Peltz, S. and Steinitz, G. (2001). New K-Ar ages of basalts from the Harrat Ash Shaam volcanic field in Jordan: implications for the span and duration of the upper-mantle upwelling beneath the western Arabian plate. Geology, 29, 171-174.

Loop, J. and Hall, G. (1992) Results of the source term digestions by UO and GSC. Appendix B. *In* W.R.Alexander (editor) A natural analogue study of cement buffered, hyperalkaline groundwaters and their interaction with a repository host rock. I: definition of source terms. Nagra Technical Report, NTB 91-10, Wettingen, Switzerland.

Lovley, D.R. (1993) Dissimilatory metal reduction. Annual Review of Microbioliology, 47, 263-290.

Low, M.J.D. and Glass, A.S. (1989) The assignment of the 1600 cm-1 mystery band of carbons. Spectroscopy Letters, 22, 417-429.

MacLeod, G., Fallick, A.E. and Hall, A.J. (1991) The mechanism of carbonate growth on concrete structures, as elucidated by carbon and oxygen isotope analyses. Chemical Geology (Isotope Geosciences Section), 86, 335-343.

Mäder, U., Fierz, Th., Frieg, B., Eikenberg, J., Rüthi, M., Albinsson, Y., Möri, A., Ekberg, St. and Stille, P. (2006) Interaction of hyperalkaline fluid with fractured rock: Field and laboratory experiments of the HPF project (Grimsel Test Site, Switzerland). Journal of.Geochemical Exploration, 90, 68-94.

Mäder, U.K. (2004). Mass balance estimate of cement clay stone interaction with application to a HLW repository in Opalinus Clay. In: N. Micheau (ed), ECOCLAY-II: Effects of Cement on Clay Barrier Performance Phase II (Eurpean Union Project FIKW-CT-2000-00028), Final Report, External Document C.RP.ASCM.04.009, ANDRA, Agence Nationale pour la gestion des déchets radioactifs, France, 186-190.

Mäder, U.K. and Adler, M. (2004). A long-term in-situ experiment for interaction of Opalinus Clay with hyperalkaline fluid at the Mont Terri URL (Switzerland). In: N. Micheau (ed), ECOCLAY-II: Effects of Cement on Clay Barrier Performance Phase II (Eurpean Union Project FIKW-CT-2000-00028), Final Report, External Document C.RP.ASCM.04.009, ANDRA, Agence Nationale pour la gestion des déchets radioactifs, France, 190-195.

Mäder, U.K. and Traber, D. (2004) Reactive transport model of cement clay stone interaction with application to a HLW repository in Opalinus Clay. *In* N.Micheau (editor), ECOCLAY-II: Effects of Cement on Clay Barrier Performance Phase II (European Union Project FIKW-CT-2000-00028), Final Report, External Document C.RP.ASCM.04.009, ANDRA, Paris, France, 283-289.

Mäder, U.K., Fierz, T. et al. (2006). Interaction of hyperalkaline fluid with fractured rock: field and laboratory experiments of the HPF project (Grimsel Test Site, Switzerland). J.Geochem. Explor. 90, 68-94.

Mäder, U.K., Fierz, T. et al. (2007). HPF final report. Nagra Technical Report NTB 05-01, Nagra, Wettingen, Switzerland (*in press*).

Mäder, U.K., Frieg, B., Puigdomenesch, I., Decombarieu, M. and Yui, M. (2004) Hyperalkaline cement leachate-rock interaction and radionuclide transport in a fractured host rock (HPF Project). Mat. Res. Soc. Symp. 807, 861-866.

Manceau, A. and Charlet, L. (1990) In-situ X-ray absorption study of the mechanism of Cr(III) oxidation at the Mn oxide/water interface. Geochemistry of the Earth's Surface and of Mineral Formation, 2nd International Symposium, 275-278.

Manceau, A. and Charlet, L. (1992) X-ray absorption spectroscopic study of the sorption of Cr(III) at the oxide/water interface. I. Molecular mechanism of Cr(III) oxidation on manganese oxides. Journal of Colloid and Interface Science, 148, 425-442.

Marriner, G.F., Tarney, J. and Langford, J.I. (1991) Apophyllite group:effects of chemical substitutions on dehydration behaviour, recystallisation products and cell parameters. Mineralogical Magazine, 54, 567-577.

Marshall, J.D. (1987) Cathodoluminescence of Geological Materials. Unwin Hyman, London, U.K.

Marshall, K.C. (1984) Microbial adhesion and aggregation. Springer Verlag, Berlin, 423 pp.

Mathews, A.. and Kolodny, Y. (1978) Oxygen isotope fraction in decarbonation metamorphism. The Mottled Zone Event. Earth and Planetary Science Letters, 39, 179-192.

Mazurek, M., Alexander, W.R. and MacKenzie, A.B. (1996) Contaminant retardation in fractured shales: matrix diffusion and redox front entrapment. Journal of Contaminant Hydrology, 21, 71-84.

Mazurek, M., Gimmi, T., Waber, H.N. and Gautschi, A. (2004) Geochemical stability of clay-rich rock formations: Evidence based on natural tracer profiles. *In* Stability and buffering capacity of the geosphere for long term isolation of radioactive waste: Application to argillaceous media. Proceedings of the NEA workshop, OECD/NEA, Paris, France, 139-146.

McClusky, S., Balassanian, S., et al. (2000). Global Positioning System constraints on plate kinematics and dynamics in the eastern Mediterranean and Caucasus. Journal of Geophysical Research, 105 (B3), 5695-5719.

McConnell, J.D.C (1960) Vaterite from Ballycraigy, Larne, Northern Ireland. Mineralogical Magazine, 32, 535-545.

McCrea, J.M. (1950) On the isotope chemistry of carbonates and a paleotemperature scale. Journal of Chemical Physics, 18, 849-857.

McKinley, I.G. and Alexander, W.R. (2008). Coastal repositories *in* Volcanism, Tectonism and the Siting of Nuclear Facilities (*eds* C.Conner, L.Conner and N.A.Chapman), Cambridge University Press, Cambridge, UK. (*in press*).

McKinley, I.G., Alexander, W.R. and Blaser, P.C. (2007) Development of geological disposal concepts. Chapter 3 *in* W.R.Alexander and L.E.McKinley (*editors*) (2007) Deep geological disposal of radioactive wastes. Elsevier, Amsterdam, The Netherlands.

McKinley, I.G., Bath, A.H., Berner, U., Cave, M. and Neal, C. (1988). Results of the Oman analogue study. Radiochimica Acta, 44/45, 311-316.

McKinley, I.G., Berner, U. and Wanner, H. (1987). Predictions of radionuclide chemistry in a highly alkaline environment. PTB-SE-14, 77-89.

McKinley, I.G., Hagenlocher, I., Alexander, W.R. and Schwyn, B. (1997). Microbiology in nuclear waste disposal: interfaces and reaction fronts. FEMS Microbiol.Rev. 20, 545-556.

Miller, W.M., Alexander, W.R., Chapman, N.A., McKinley, I.G. and Smellie, J.A.T. (2000) Geological disposal of radioactive wastes and natural analogues. Waste management series, vol. 2, Pergamon, Amsterdam, The Netherlands.

Milodowski A.E., Pearce J.M., Hughes C.R. and Khoury H.N. (1992b) A preliminary mineralogical investigation of a natural analogue of a cement-buffered hyperalkaline groundwater interaction with marl, Maqarin, northern Jordan – Nagra Unpublished Internal Report. Nagra, Wettingen, Switzerland.

Milodowski, A E., Hyslop, E.K., Pearce, J.M., Wetton, P.D., Kemp, S.J., Longworth, G., Hodginson, E. and Hughes, C.R. (1998b) Mineralogy and geochemistry of the Maqarin and Daba areas. Chapter 5 *in* J.A.T. Smellie (editor) Maqarin natural analogue study: Phase III. SKB Technical Report, TR-98-04, Volumes I and II, SKB, Stockholm, Sweden.

Milodowski, A E., Pearce, J.M., Hyslop, E.K., Hughes, C.R., Inglethorpe, S.D.J., Strong, G.E., Wheal, N., McKenzie, A.B., Karnland, O. and Khoury, H.N (1998a) Mineralogy and petrology. Chapter 6*, in* C.M. Linklater (editor.) A natural analogue study of analogue cement buffered, hyperalkaline groundwaters and their interaction with a repository host rock: Phase II. Nirex Science Report, S-98-003, UK Nirex, Harwell, U.K.

Milodowski, A E., Pearce, J.M., Hyslop, E.K., Hughes, C.R., Inglethorpe, S.D.J., Strong, G.E., Wheal, N., McKenzie, A.B., Karnland, O. and Khoury, H.N (1998a) Ch. 6 *in* Linklater, C.M. (Ed.), 1998. A natural analogue study of cement buffered, hyperalkaline groundwaters and their interaction with a repository host rock II. Nirex Science Report, S-98-003, UK Nirex, Harwell, Oxon., GB.

Milodowski, A.E. (1996) A natural analogue study of the Maqarin hyperalkaline groundwaters: A draft report on hyperalkaline groundwater/rock interaction. Unpublished Nagra Internal Report, Nagra, Wettingen, Switzerland.

Milodowski, A.E., Khoury, H.N., Pearce, J.M. and Hyslop, E.K. (1992a) Discussion of the mineralogy, petrography and geochemistry of the Maqarin source-term rocks and their secondary alteration products. Chapter 3 *in* W.R.Alexander (editor) A natural analogue study of cement-buffered, hyperalkaline groundwaters and their interaction with a repository host rock. I: definition of source terms. Nagra Technical Report, NTB 91-10, Wettingen, Switzerland.

Milodowski, A.E. and Wilmot, R.D. (1985) Mineralogical and petrographic studies of Jurassic and Cretaceous sediments from southern England and their relevance to radioactive waste disposal. Mineralogical Magazine, 49, 255-263.

Milodowski, A.E., Constantinou, C.A., Alexander, W.R., Rigas, M., Tweed, C., Sellin P. and Korkeakoski, Pchee(2009) Reaction of bentonite in low-alkali cement leachates: preliminary results from the Cyprus Natural Analogue Project. Proc. ICEM'09 Conference, October, 2009, Liverpool, UK, ASME, USA.

Milodowski, A.E., Hyslop, E.K., Khoury, H.N., Hughes, C.R., Mäder, U.K., Griffault, L.Y. and Trotignon, L. (2001) Mineralogical alteration by hyperalkaline groundwater in northern Jordan. Proceedings of the 10th

International Water Rock Interaction Symposium, Villasimius, Italy (June 10-15, 2001). Balkema, Amsterdam, The Netherlands.

Milodowski, A.E., Hyslop, E.K., Pearce, J.M., Wetton, P.D., Kemp, S.J., Longworth, G., Hodginson, E. and Hughes, C.R. (1998b). Mineralogy and geochemistry of the Maqarin and Daba areas. Chapter 5 *in* Smellie, J.A.T. (editor) (1998) Maqarin natural analogue study: Phase III. SKB Technical Report, TR-98-04, Volumes I and II, SKB, Stockholm, Sweden. Milodowski, A.E., Khoury, H.N., Pearce, J.M. and Hyslop, E.K. (1992a). Discussion of the mineralogy, petrography and geochemistry of the Maqarin source-term rocks and their secondary alteration products. Chapter 3 *in* Alexander, W.R. (editor) (1992) A natural analogue study of the Maqarin hyperalkaline groundwaters. I definition of source terms. Nagra Technical Report, NTB 91-10, Nagra, Wettingen, Switzerland.

Milodowski, A.E., Khoury, H.N., Pearce, J.M. and Hyslop, E.K. (1992a) Discussion of the mineralogy, petrography and geochemistry of the Maqarin source-term rocks and their secondary alteration products. Chapter 3 in W.R. Alexander (editor) A natural analogue study of the Maqarin hyperalkaline groundwaters. I: definition of source terms. Nagra Technical Report, NTB 91-10, Nagra, Wettingen, Switzerland.

Milodowski, A.E., Pearce J.M., Hugues C.R. and Khoury H.N. (1992b) A preliminary mineralogical investigation of a natural analogue of a cement-buffered hyperalkaline groundwater interaction with marl, Maqarin, northern Jordan. Nagra Unpublished Internal Report, Nagra, Wettingen, Switzerland.

Milodowski, A.E., Pearce, J.M., Hyslop, E.K., Hughes, C.R., Inglethorpe, S.D.J., Strong, G.E., Wheal, N., McKenzie, A.B., Karnland, O. and Khoury, H.N. (1998a). Chapter 6 *in* Linklater, C.M. (editor) (1998) A natural analogue study of analogue cement buffered, hyperalkaline groundwaters and their interaction with a repository host rock. II. Nirex Science Report, S-98-003, UK Nirex, Harwell, UK.

Moeri, A., Mazurek, M., Adler, M., Schild, M., Siegesmund, S., Vollbrecht, A., Ota, K., Ando, T., Alexander, W.R., Smith, P.A., Haag, P. and Bühler, Ch. (2003) The Nagra-JNC in situ study of safety relevant radionuclide retardation in fractured crystalline rock: IV. The in situ study of matrix porosity in the vicinity of a water-conducting fracture. Nagra Technical Report, NTB 00-08, Nagra, Wettingen, Switzerland.

Moore, D.M. and Reynolds, R.C. (editors) (1989) X-ray diffraction and identification and analysis of clay minerals. Oxford University Press, New York.

Moore, T.A., Shearer, J.C. and Miller, S.L. (1996) Fungal origin of oxidised plant material in the Palangkaraya peat deposit, Kalimantan Tengah, Indonesia: implications for 'inertinite' formation in coal. International Journal of Coal Geology, 30, 1–23.

Nassir, S. and Khoury, H. (1982). Mineralogy, petrology, and origin of Daba-Siwaqa marble, Jordan. Dirasat, 9, 107-130.

Nassir, S.G. and Khoury, H.N. (1982) Geology, mineralogy and petrology of Daba Marble, Jordan. Dirasat, 9, 107-130.

Neretnieks, I. (1980) Diffusion in the rock matrix: an important factor in radionuclide migration? Journal of Geophysical Research, 85, 4379-4397.

NGB (1985) Nukleare Entsorgung Schweiz: Konzept und übersicht über das Projekt Gewähr. Nagra Gewähr Reports, NGB 85-09 (English summary), Nagra, Wettingen, Switzerland.

O'Neil, J.R. and Barnes, I. (1971) 13C and ^{18}O compositions in some fresh water carbonates associated with ultramafic rocks and serpentinites, Western United States. Geochimica et Cosmochimica Acta, 35, 687-697.

Olis, A.C., Malla, P.B. and Douglas, L.A. (1990) The rapid estimation of the layer charges of 2:1 expanding clays from a single alkylammonium ion expansion. Clay Minerals, 25, 39-50.

Osmond, J.K and Cowart, J.B. (1992) Groundwater. *In* M.Ivanovich and R.S. Harmon (editors) Uranium-series disequilibrium: applications to earth, marine and environmental sciences. Clarendon Press, Oxford, U.K., 291-333.

Ota, K., Moeri, A., Alexander W.R., Frieg, B. and Schild, M. (2003) Influence of the mode of matrix porosity determination on matrix diffusion calculations. Journal of Contaminant Hydrology, 61, 131 – 145.

Painter, P.C., Snyder, R.W., Pearson, D.E. and Kwong, J. (1980). Fourier transform infrared study of the variation in the oxidation of a coking coal. Fuel, 59, 282-285.

Painter, P.C., Snyder, R.W., Starsinic, M., Coleman, M.M., Kuehn, D.W. and Davis, A. (1981) Concerning the application of FT-IR to the study of coal: A critical assessment of band assignments an the application of spectra analysis program. Applied Spectroscopy, 35, 475-485.

Pandit, N.S. and Miner, R.F. (1986). Interpretation of slug test data. Ground Water, 24, 743.

Papadopulos, S.S., Bredehoeft, J.D. and Cooper, H.H. (1973). On the analysis of 'slug test' data. Water Resources Research, 9, 1087-1089.

Pedersen, K. (2001) Diversity and activity of microorganisms in deep igneous rock aquifers of the Fennoscandian Shield. *In* Fredrickson, J.K. and Fletcher, M. (editors) Subsurface microbiology and biogeochemistry. Wiley-Liss, New York, 97-139.

Pedersen, K. and Ekendahl, S. (1992a) Incorporation of CO_2 and introduced organic compounds by bacterial populations in groundwater from the deep crystalline bedrock of the Stripa mine. Journal of General Microbiology, 138, 369-376.

Pedersen, K. and Ekendahl, S. (1992b) Assimilation of CO_2 and introduced organic compounds by bacterial communities in ground water from Southeastern Sweden deep crystalline bedrock. Microbial Ecology, 23, 1-14.

Pedersen, K., and Ekendahl, S. (1990) Distribution and activity of bacteria in deep granitic groundwaters of southeastern Sweden. Microbial Ecology, 20, 37-52.

Pedersen, K., Arlinger, J., Erlandson, A-C. and Hallbeck, L. (1997) Culturability and 16S rRNA gene diversity of microorganisms in the hyperalkaline groundwater of Maqarin, Jordan. *In* Pedersen, K. (editor) Investigations of subterranean microorganisms and their importance for performance assessment of radioactive waste disposal. Results and conclusions achieved during the period 1995 to 1997. SKB Technical Report, TR 97-22, SKB, Stockholm, Sweden, 239-262.

Pedersen, K., Arlinger, J., Hallbeck, L. and Pettersson, C. (1996) Diversity and distribution of subterranean bacteria in ground water at Oklo in Gabon, Africa, as determined by 16S-rRNA gene sequencing technique. Molecular Ecology, 5, 427-436.

Pedersen, K., Holmström, C., Olsson, A-K. and Pedersen, A. (1986) Statistic evaluation of the influence of species variation, culture conditions, surface wettability and fluid shear on attachment and biofilm development of marine bacteria. Archives of Microbiology, 145, 1-8.

Pedersen, K., Nilsson, E., Arliner, J., Hallbeck, L. and O'Neill, A. (2004) Distribution, diversity and activity of microorganisms in the hyper-alkaline springs waters of Maqarin in Jordan. Extremophiles, 8, 151-164.

Peters, K.E. (1986) Guidelines for evaluating source rock using programmed pyrolysis. American Association of Petroleum Geologists Bulletin, 70, 318-329.

Peucker-Ehrenbrink B. and Hannigan R.E. (2000) Effects of black shale weathering on the mobility of rhenium and platinum group elements. Geology, 28, 475-478.

Pitty, A.F. (1998). Geomorphology of the Maqarin area. Ch. 3 *in* J.A.T.Smellie (editor). Maqarin Natural Analogue Study: Phase III. SKB Technical Report 98-04, SKB, Stockholm, Sweden.

Pitty, A.F. (1998). Geomorphology of the Maqarin area. Chapter 3 in J.A.T.Smellie (editor) (1998) Maqarin natural analogue study: Phase III. SKB Technical Report, TR-98-04, Volumes I and II, SKB, Stockholm, Sweden.

Pitty, A.F. (2000) Notes and data on some ground-surface features with geomorphological interpretations. *In* Smellie, J.A.T. (editor). Maqarin natural analogue project; Phase IV. Reconnaissance mission report (April 28th to May 7th, 1999). SKB Report, R-00-34, 17-28.

Planel, D. (2002) Les effets couplés de la précipitation d'espèces secondaires sur le comportement mécanique et la dégradation chimique des bétons. PhD Thesis, University of Marne la Valéée, France.

Price, M.W. (1972) Calcium sulphosilicate in lime-kiln wall coating. Mineralogical Magazine, 38, 968-971.

Quennell, A. (1958) The structural and geomorphic evolution of the Dead Sea rift. Quarterly Journal of the Geological Society of London, 114, 1-24.

Quennell,A. (1958). The structural and geomorphic evaluation of the Dead Sea Rift. Quarterly Journal of the Geolological Society of London, 64, 1-24.

Rai, D., Eary, L.E. and Zachara, J.M. (1989) Environmental chemistry of chromium. Science of the Total Environment, 86, 15-23.

Rai, D., Sass, B.M. and Moore, D.A. (1987) Chromium(III) hydrolysis constants and solubility of chromium(III) hydroxide. Inorganic Chemistry, 26, 345-349.

Ramirez, S., Cuevas, J., Vigil, R., and Lequey, S. (2002) Hydrothermal alteration of 'La Serrata' bentonite (Almeria, Spain) by alkaline solutions. Applied Clay Science, 21, 257-269.

Rasmuson, A. and Neretnieks, I. (1981) Migration of radionuclides in fissured rock: the influence of micropore diffusion and longditudinal dispersion. Journal of Geophysical Research, 86, 3749.

Rassineux, F. (2000) Maqarin Project: sampling report – Khushaym Matruk site. Report ERM 00 108 FR 196 – ANDRA – D RP 0.ERM 00-012, Unpublished ANDRA Internal Report, ANDRA, Paris, France.

Rassineux, F., Parneix, J., Griffault, L., Trotignon, L., Raynal, J., Khoury, H., Mercier, F. and Smellie, J.A.T. (2001) Mineralogical evolution of clay-bearing rock during alkaline alteration (Khushaym Matruk,central Jordan). *In* R.Cidu (editor) Water-Rock Interaction 2001. Swets and Zeitlinger, Lisse.

Reasoner, D.J. and Geldreich, E.E. (1985) A new medium for the enumeration and subculture of bacteria from portable water. Applied Environmental Microbiology, 49, 1-7.

Rhoads, C.A., Senftle, J.T., Coleman, M.M., Davis, A. and Painter, P.C. (1983) Further studies of coal oxidation. Fuel, 62, 1387-1392.

Richard, F.C. and Bourg, A.C.M. (1991) Aqueous geochemistry of chromium: a review. Water Resources Research, 25, 807-816.

Rihs, S. (1998) Nucléides radioactifs naturels dans quelques systèmes hydrothermaux carbogazeux du Massif Central. Application à la datation des dépôts anciens et à l'étude de la mobilité des radioéléments. PhD Thesis, University Blaise Pascal.

Robertson, A.H.F. and Dixon, J.E. (1984) Aspects of the geological evolution of the Eastern Mediterranean. *In* Robertson, A.H.F. and Dixon, J.E. (editors). The geological evolution of the Eastern Mediterranean. Geological Society of London, Special Publication, 17, 1-74.

Robertson, A.H.F., Clift, P.D., Degnan, P.J. and Jones, G. (1991) Palaeogeographic and palaeotectonic evolution of the Eastern Mediterranean Neotethys. Palaeogeography Palaeoclimatology and Palaeoecology, 87, 289-343.

Rollion-Bard, C., Chaussidon, M. and France-Lanord, C. (2003) pH control on oxygen isotopic composition of symbiotic corals. Earth and Planetary Science Letters, 215, 275-288.

Ron, H. and Kolodny, Y. (1992) Paleomagnetic and rock magnetic study of combustion metamorphic rocks in Israël. Journal of. Geophysical Research, 97, B5, 6927-6939.

Rose, J., Bénard, A., Susini, J., Borschneck, D., Hazemann, J-L, Cheylan, P., Vichot and Bottero, J-Y. (2003) First insights of Cr speciation in leached Portland analogue cement using X-ray spectromicroscopy. Environmental Science and Technolology, 37, 4864 – 4870.

Rozanski, K., Araguas-Araguas, L. and Gonfiantini, R. (1993) Isotopic patterns in modern global precipitation. *In* Climate change in continental records, Geophysical Monographs, American Geophysical Union, 78, 1-36.

Ruef, M. and Jeresat, K. (1965) Geology of Jiza-Qatrana, central Jordan. Unpublished Report, German Geologic Mission, 5-35.

Russell, J.D. and Fraser, A.R. (1992) Infrared methods. *In* M.J.Wilson (editor) Clay mineralogy: spectroscopic and chemical determinative methods. Chapman Hall, London, U.K., 11-67.

Schroeder, D.C. and Lee, G.F. (1975) Potential transformations of chromium in natural waters. Water Air and Soil Pollution, 4, 355-365.

Scott, P.W., Critchley, S.R. and Wilkinson, F.C.F. (1986) The chemistry and mineralogy of some granulated and palletised blastfurnace slags. Mineralogical Magazine, 50, 141-147.

Scott, R.D., MacKenzie, A.B. and Alexander, W.R. (1992) The interpretation of 238U-234U-230Th-226Ra disequilibria produced by rock-water interaction. Journal of Geochemical Exploration, 46, 323-343.

Skagius, K. and Neretnieks, I. (1982) Diffusion in crystalline rocks of some sorbing and non-sorbing species. SKBF/KBS Technical Report, TR-82-12, SKB, Stockholm, Sweden.

Skagius, K. and Neretnieks, I. (1986) Diffusivity measurements and electrical resistivity measurements in rock samples under mechanical stress. Water Resources Research, 22, 570-580.

Skinner, I.J. and Luce, F.D. (1971) Solid solutions of the type (Ca, Mg, Mn, Fe)S and their use as geothermometers for the enstatite chondrites. American Mineralogist, 56, 1269-1296.

Smellie J.A.T. (editor) (2000) Maqarin natural analogue project: Reconnaissance mission report (April 28th to May 7th, 1999). SKB Report, R-00-34, SKB, Stockholm, Sweden.

Smellie, J.A.T. (editor) (1998) Maqarin natural analogue study: Phase III, SKB Technical Report, TR-98-04, Volumes I and II, SKB, Stockholm, Sweden.

Smellie, J.A.T. (editor) (2000) Maqarin natural analogue project: Phase IV. Reconnaissance mission report (April 28th to May 7th, 1999). SKB Report, R-00-34, SKB, Stockholm, Sweden.

Smellie, J.A.T. and Stuckless, J.S. (1985) Element mobility studies of two drillcores from the Götemar granite (Krakemala test site), SE Sweden. Chemical Geology, 51, 55-78.

Smellie, J.A.T., Karlsson, F. and Alexander, W.R. (1997) Natural analogue studies: present status and performance assessment implications. Journal of.Contaminant Hydrology, 26, 3-17.

Smith P.A. (2003) Illustrating the effects of the magnitude and extent of connected matrix porosity on radionuclide transport in a fractured geological medium. Chapter 9 *in* Moeri, A., Mazurek, M., Adler, M., Schild, M., Siegesmund, S., Vollbrecht, A., Ota, K., Ando, T., Alexander, W.R., Smith, P.A., Haag, P. and Bühler, Ch. The Nagra-JNC in situ study of safety relevant radionuclide retardation in fractured crystalline rock IV: The *in situ* study of matrix porosity in the vicinity of a water-conducting fracture. Nagra Technical Report, NTB 00-08, Nagra, Wettingen, Switzerland.

Smith, P.A., Alexander, W.R., Kickmaier, W., Ota, K., Frieg, B. and McKinley, I.G. (2001) Development and testing of radionuclide transport models for fractured rock: examples from the Nagra/JNC Radionuclide Migration Programme in the Grimsel Test Site, Switzerland. Journal of Contaminant Hydrology, 47, 335-348.

Soler, J.M., Pfingsten, W. et al. (2006). HPF modelling report. Nagra Technical Report NTB 05-01, Nagra, Wettingen, Switzerland.

Starsinic, M., Otake, Y., Walker, P.L. and Painter, P.C. (1984) Application of FT-i.r. spectroscopy to the determination of COOH groups in coal. Fuel, 63, 1002-1007.

Steefel, C.I. and Lichtner, P.C. (1994) Diffusion and reaction in rock matrix bordering a hyperalkaline fluid-filled fracture. Geochimica et Cosmochimica Acta, 58, 3595-3612.

Stone, N.S. (1998) Mass transfer properties of rock samples containing alkaline fractures taken from the Maqarin site. Chapter 9 *in* C.M.Linklater (editor) A natural analogue study of cement buffered, hyperalkaline groundwaters and their interaction with a repository host rock: Phase II. Nirex Science Report, S-98-003, UK Nirex, Harwell, U.K.

Strunk, O., Gross, O., Reichel, B., May, S., Hermann, S., Struckmann, B., Nonhoff, M., Lenke, M., Vilbig, A., Ludwig, T., Bode, A., Schleifer, K.H. and Ludwig, W. (1998) ARB: a software environment for sequence data. Department of Microbiology, Technische Universität München, Munich, Germany.

Stumpf, T, Tits, J., Walther, C., Wieland, E. and Fanghänel, T. (2004) Uptake of trivalent actinides (Cm-III) by hardened cement paste: a time-resolved laser fluorescence spectroscopy study. Journal of.Colloid and Interface Science, 276, 118-124.

Sunna, B. (1974) Phosphate exploration and beneficiation studies, Vol. 1. National Resources Authority, Unpublished Report, UNDP/NRA 70/521, Amman. Jordan.

Szulczewski, M.D., Helmke, P.A., Bleam, W.F. (1997) Comparison of XANES analyses and extractions to determine chromium speciation in contaminated soils. Environmental Science and Technology, 31, 2954-2959.

Tajima, T., Ogata, H., Kuro, H. and Mihara, M. (2006) Influence of cement leachate on bentonite impermeability. Clay Science, 12, 137-142.

Tarawneh, K., Ilani, S., Rabba, I., Harlavan, Y., Peltz, S., Ibrahim, K., Weinberger, R. and Steinitz, G. (2000) Dating of the Harrat Ash Shaam basalts, northeast Jordan (Phase 1). Geological Survey of Israel and the Natural Resources Authority of Jordan, Report GSI/2/2000.

Taylor, G.H., Liu, S.Y. and Diessel, C.F.K. (1989) The cold-climate origin of inertinite-rich Gondwana coals. International Journal of Coal Geology, 11, 1–22.

Techer, I. and Elie, M. (2003) Natural analogue contribution to the understanding of the long-term behaviour of argillaceous formations towards a high-alkaline fluid circulation: Study of the Khushaym Matruk site (Central Jordan) - Isotope Chemistry and Dating, and Organic Matter Characterisation. FORPRO Report 2003/09 Re, GdR FORPRO (CNRS-ANDRA), Nîmes, France.

Techer, I., Fourcade, S., Elie, M., Martinez, L., Boulvais, P., Claude, C., Clauer, N., Pagel, M., Hamelin, B. and Lancelot, J. (2004) Contribution des analogues naturels à la compréhension du comportement à long terme des milieux argileux vis-à-vis de la circulation de fluides hyper-alcalins: Etude du site de Khushaym Matruk en Jordanie Centrale-Géochimie Isotopique du Sr, C, O, datation U-Th et K-Ar et Caractérisation de la Matière Organique. FORPRO Report 2004/01 Rf, GdR FORPRO (CNRS-ANDRA), Nîmes, France.

Theil, K., Vorwerk, R., Saager, R. and Stupp, H.D. (1983) ^{235}U fission tracks and ^{238}U-series disequilibria as a means to study recent mobilisation of U in Archaean pyritic conglomerates. Earth and Planetary Science Letters, 65, 249-262.

Torstenfelt, B., Ittner, T., Allard, B., Andersson, K. and Olofsson, U. (1982) Mobilities of radionuclides in fresh and fractures crystalline rock. SKB Technical Report, TR-82-26, SKB, Stockholm, Sweden.

Treiman, A.H. and Essene, E.J. (1983) Phase equilibria in the system CaO-SiO2-CO2. American Journal of Science, 283A, 97-120.

Trotignon, L., Rose J., Khoury H., Milodowski, A., Bienvenu P., Provitina O., Mercier F. and Susini, J. (2006) Rhenium migration at the Maqarin natural analogue site (Jordan). Radiochimica Acta, 94, 755-761.

Tweed, C.J., Linklater, C.M., Eikenberg, J., Alexander, W.R., Dayal, R. and Eagleson, K. (1992) Geochemical modelling of high pH analogue cement pore waters from the Maqarin area of northern Jordan. Chapter 5 *in* W.R.Alexander (editor) A natural analogue study of cement-buffered hyperalkaline groundwaters and their interaction with a repository host rock. I. definition of source terms. Nagra Technical Report, NTB 91-10, Nagra, Wettingen, Switzerland.

Upstill-Goddard, R.C., Alexander, W.R., Elderfield, H. and Whitfield, M. (1989). Chemical diagenesis in the Tamar estuary. Contributions to Sedimentology, 16, I-49.

Usdowski, E. and Hoefs, J. (1986) $^{13}C/^{12}C$ partitioning and kinetics of CO_2 absorption by hydroxide buffer solutions. Earth and Planetary Science Letters, 80, 130-134.

Valkiainen M. (1992): Diffusion in the rock matrix-A review of laboratory tests and field studies. YJT Report, 92-04, Helsinki, Finland.

Van der Lee J., de Windt L., Lagneau V. and Goblet P. (2002) Presentation and application of the reactive transport code HYTEC. Computer Methods in Water Resources, 1, 599-606.
Van der Lee, J. (1998) Thermodynamic and mathematical concepts of CHESS. Technical Report LHM/RD/98/39, Centre d'Informatique Geologique,, Ėcole des Mines de Paris, Fontainebleau, France.
Van der Lee, J. and De Windt, L. (2000) CHESS Tutorial and Cookbook. User's Manual. Technical Report LHM/RD/00/13, Centre d' Informatique Geologique, Ėcole des Mines de Paris, Fontainebleau, France.
Van der Lee, J., de Windt, L., Lagneau, V. and Goblet P. (2002) Presentation and application of the reactive transport code HYTEC. Computer Methods in Water Resources, 1, 599-606.
Van der Marel, H.W. and Beutelspacher, H. (1976) Atlas of infrared spectroscopy of clay minerals and their admixtures. Elsevier, Amsterdam.
van Eijk, R.J. (2001) Hydration of cement mixtures containing contaminants: Design and application of the solidified product. PhD. Thesis, University of Twente, The Netherlands.
Vandamme, D.L., Fontanini, L., Trotignon, L., Raynal, J., Khoury, H., Milodowski, A., Rassineux, F., Mäder, U., Bienvenu, P. (2003) Investigations on the combustion metamorphism halo of bituminous micrites (Maqarin site - Northern Jordan). Proceedings of the EUG 2003 Conference, 6-11th April 2003, Nice, France.
Weaver, R.M. and Hochella, M.F. (2003) The reactivity of seven Mn-oxides with Cr^{3+}aq: a comparative analysis of a complex, environmentally important redox reaction. American Mineralogist, 88, 2016-2027.
West, J.M., Degueldre, C., Allen, M., Brüetsch, R., Gardner, S., Ince, S. and Milodowski, A.E. (1992) Microbial and colloidal populations in the Maqarin groundwaters. *In* Alexander W.R. (editor) A natural analogue study of cement-buffered, hyperalkaline groundwaters and their interaction with a sedimentary host rock. I: definition of source terms. Nagra Technical Report, NTB 91-10, Wettingen, Switzerland.
West, J.M., Coombs, P., Gardner, S.J. and Rochelle, C.A. (1995) The microbiology of the Maqarin site, Jordan. A natural analogue for cementitious radioactive waste repositories. Scientific Basis for Nuclear Waste Management, XVIII, 181-189.
Wharton, M.J., Atkins, B., Charnock, J.M., Livens, F.R., Pattrick, R.A.D. and Collison, D. (2000) An X-ray absorption spectroscopy study of the coprecipitation of Tc and Re with mackinawite (FeS). Applied Geochemistry, 15, 347-354.
White, W.B. (1974) The carbonate minerals. *In* V.C.Farmer (editor) The infrared spectra of minerals. Mineralogical Society, London, 227-284.
Wieland, E., Tits, J. and Bradbury, M.H. (2004) The potential effect of cementitious colloids on radionuclide mobilisation in a repository for radioactive waste. Applied Geochemistry, 19, 119–135.
Wieseman, G. and Rosch, H. (1969) Das Apatite-vorkomen von Suweilih bei Amman (Nord Jordanien). Geologische Jahrbuch Beitrage, 81, 177-214.
Winkler, H.G.F. (1976) Petrogenesis of Metamorphic Rocks. Springer-Verlag, Berlin, Germany.
Wolin, E.A., Wolin, M.J. and Wolfe, R.S. (1963) Formation of methane by bacterial extracts. Biological Chemistry, 238, 2882-2886.
Xiong, Y. and Wood, S.A. (2001) Hydrothermal transport and deposition of rhenium under subcritical conditions (up to 200°C) in light of experimental studies. Economic Geology, 96, 1429-1444.
Xiong, Y. and Wood, S.A. (2002) Experimental determination of the hydrothermal solubility of ReS2 and the Re-ReO2 buffer assemblage and transport of rhenium under supercritical conditions. Geochemical Transactions, 3, 1-10.
Xiong, Y. and Wood., S.A. (1999) Experimental determination of the solubility of ReO2 and the dominant oxidation state of rhenium in hydrothermal solution. Chemical Geology, 158, 245-256.
Yamakawa, M., Alexander, W.R., McKinley, I.G., Arcilla, C.K., Takahashi, Y and Namiki, K. (2008). The potential in the Philippines for studying natural analogues of the interaction of low-alkali cement leachates and bentonite barriers in a radioactive waste repository. Radioactive Waste Disposal 2008: Perspective of Science and Engineering, 4th Japan-Korea Joint Workshop, Hakone, Japan.

Ackowledgements

The authors would like to acknowledge all their colleagues in the Maqarin Natural Analogue Study Group for their work in Phases I-III which provided the basis of the work carried out in Phase IV reported here. ANDRA (France), CEA (France), JNC (now JAEA, Japan), Nagra (Switzerland), Nirex (now the NDA-RWMD, UK) and SKB (Sweden) are gratefully acknowledged for funding these Phase IV studies. Thanks also to Gento Kamei (JAEA), for reviewing this Report. Finally, thanks to Les Knight (formerly Nirex) and Cherry Tweed (NDA-

RWMD) for supporting publication of this Report.

List of Contributors

F. Adam, CEA, Direction de l'Energie Nucléaire, CE Cadarache, France
W.R. Alexander, Bedrock Geosciences, Auenstein, Switzerland (formerly Nagra)
N. Arnal, CEA, Direction de l'Energie Nucléaire, CE Cadarache, France
N. Barré, Laboratoire Pierre Süe, CE Saclay, France
P. Bienvenu, CEA, Direction de l'Energie Nucléaire, CE Cadarache, France
P. Boulvais, 'University of Rennes 1, Rennes Géosciences, France
C. Bulle, , CEREGE, CNRS-Université Paul Cézanne, France
S.R. Chenery, BGS, Keyworth, UK
I.D. Clark, University of Ottawa, Ottawa, Canada
J. Cook, BGS, Keyworth, UK
N. Crouzet, CEREGE, CNRS-Université Paul Cézanne, France
P.J. Degnan, IAEA, Vienna, Austria (formerly Nirex)
A. Didot, , CEA, Direction de l'Energie Nucléaire, CE Cadarache, France
M. Elie, Shell Malaysia Exploration & Production, Sarawak, Malaysia (formerly G2R, Nancy-Universite, Vandoeuvre-les-Nancy, France)
I. Félines, CEA, Direction de l'Energie Nucléaire, CE Cadarache, France
L. Fontanini, CEREGE, CNRS-Université Paul Cézanne, France
S. Fourcade, 'University of Rennes 1, Rennes Géosciences, France
E.S. Hodgkinson, BGS, Keyworth, UK (formerly University of Manchester)
H. Khoury, University of Jordan, Amman, Jordan
J.Kramers, University of Berne, Berne, Switzerland
J. McKervey, BGS, Keyworth, UK
U.K.Mader, University of Berne, Berne, Switzerland
L.Martinez, G2R, Nancy-Universite, Vandoeuvre-les-Nancy, France
F. Mercier, Laboratoire Pierre Süe, CE Saclay, France
V. Michaud, CEA, Direction de l'Energie Nucléaire, CE Cadarache, France
A.E. Milodowski, BGS, Keyworth, UK
J.-C. Parneix, ERM Poitiers, France
K. Pedersen, University of Gothenburg, Gothenburg, Sweden
H. Peycelon, CEA, Direction de l'Energie Nucléaire, CE Saclay, France
A.F. Pitty, Pitty Consulting, Norwich, UK
S. Pontremoli, CEA, Direction de l'Energie Nucléaire, CE Cadarache, France
O. Provitina, CEA, Direction de l'Energie Nucléaire, CE Cadarache, France
L. Raimbault, Ecole Nationale Supérieure des Mines, Centre de Géosciences, Fontainebleau, France
F. Rassineux, ERM Poitiers, France
J. Raynal, CEA, Direction de l'Energie Nucléaire, CE Cadarache, France
J. Rose, CEREGE, CNRS-Université Paul Cézanne, France
E.Salameh, University of Jordan, Amman, Jordan
J.A.T. Smellie, Conterra, Stockholm, Sweden
J. Susini, ESRF, Grenoble, France
I.Techer, University of Nîmes, Nîmes, France
P. Trocellier, CEA, Direction de l'Energie Nucléaire, France
L. Trotignon, CEA, Direction de l'Energie Nucléaire, CE Cadarache, France
D. Vandamme, CEREGE, CNRS-Université Paul Cézanne, France
I.Villa, University of Berne, Berne, Switzerland
M.J. White, Galson Sciences, Rutland, UK

Maqarin Phase IV Report: Appendices

Pitty, A and Alexander, R (editors).

A joint-funded international project report between NDA RWMD, Andra, CEA, SKB, Nagra and JNC

Table of Contents

Appendix 1

A Short Guide to the Terminology Used in this Report

A.E. Milodowski

Introduction

Various parent materials make up the different components of the cementitious natural analogue sites studied throughout Jordan. In consequence, these rock masses have been described rather inconsistently in previous publications and reports. For example, differing terminology and abbreviations have been used, depending on whether the rock mass has been described in terms of its geological definition, or its analogue relationship to the various components of a hypothetical cementitious radioactive waste repository. To minimise any further inconsistency, the terminology used in this Report is defined below.

Metamorphic Zone

The region or volume of rock mass, within which the mineralogy and chemistry of the rock have been altered by the **thermal effects** of the combustion event(s). The *Marble Zone*, the *Combustion Zone*, the *Baked Marl* and the *Transition Zone* are all part of the Metamorphic Zone. Although predominantly within the Bituminous Marl Formation, this Zone may also include part of the overlying Chalky Limestone Formation.

Marble Zone

The region or volume of rock mass within the *Metamorphic Zone* that comprises recrystallised carbonate-dominated rock, and which contains a mineral assemblage characteristic of high-temperature/low-pressure thermal metamorphism (i.e. petrologically defined as *marble)*. This term may be used in this Report in the geological sense, but may be used interchangeably with Analogue Cement Zone (ACZ), where the mineralogy is appropriate, and where the emphasis of the context of the account is on the natural analogue characteristics (see also Analogue Cement Zone).

Combustion Zone

The region or volume of rock mass within which the organic matter (OM), originally present in the parent sedimentary rock (organic-rich limestone or organic-rich clay biomicrite), has been burnt and lost as a result of *in situ* spontaneous combustion. It may, or may not, include volumes of the rock mass affected by hyperalkaline groundwater leaching of OM. This may extend beyond the region of the Marble Zone rock, within which rock mass recrystallisation has occurred. The Combustion Zone does not include sedimentary host rocks where the OM has been lost by interaction with hyperalkaline groundwater.

Cement Zone or Near Field Cement Zone or Analogue Cement Zone

The region or volume of rock, within the *Metamorphic Zone*, that contains minerals, or an assemblage of minerals, analogous to those found in hydrated (or hydrating) Ordinary Portland Cement (OPC) paste and clinker. Essentially, this is equivalent to the parts of

the *Marble Zone* that contain lime and high-temperature, low-pressure aluminosilicate minerals (and their retrograde hydration alteration products).

The terms 'Cement Zone' or 'Near Field Cement Zone (NFCZ)' have been used variously in earlier accounts. However, for consistency and simplicity, the term **Analogue Cement Zone** (abbreviated to **ACZ**) is adopted in this Report.

Rock-water interaction within the NFCZ is regarded as the source-term for the hyperalkaline groundwaters at the cementitious natural analogue sites studied throughout Jordan. Therefore, intervals of pure calcite or dolomite marble would not provide a mineral assemblage that could be designated as Cement Zone or Near-Field Cement Zone, in the context of a natural analogue for a cementitious radioactive waste repository.

Contact Zone, Metamorphic Contact and Contact Boundary

The *Contact Zone* has been variously described in earlier reports as *Contact Zone, Contact Boundary* and *Metamorphic Contact*, often interchangeably and occasionally mistakenly.. The inconsistent use of these terms originates from the definition of the contact metamorphic aureole in the host rock around an igneous body, and the boundary between an igneous body and the country rock. This implies that there is a discrete interface or surface between the metamorphic rocks and the country rock, or between the heat source causing metamorphism (e.g. an igneous body) and the metamorphic aureole. In the sites studied to date in Jordan, there is no discrete intrusive or structural interface between the Marble Zone and the unmetamorphosed rocks. Instead, there is a *transitional* region between the two, where the metamorphic rocks (marbles) grade into the unmetamorphosed *Country Rock or Parent Rock*. For example, this transitional region may vary from <0.5 m wide to around 10 m wide in different parts of the Maqarin site.

The terms Contact Zone, Contact Boundary and Metamorphic Contact are misnomers in the context of the sites reported here. It is recommended that their use, to describe features of the metamorphic geology here, is discontinued. The term *Transition Zone* is more appropriate, in defining the region between the Marble Zone (or ACZ) and the unmetamorphosed country rocks.

Transition Zone

The region where the rock mass grades between the high-temperature metamorphic rocks and the unmetamorphosed *Host Rock*, *Country Rock or Parent Rock*. This transitional region is where the rock mass has been partially altered, or affected to some extent by, thermal metamorphism and combustion. Here, the rock fabric and mineralogy varies between: (i) that of the low-temperature sedimentary and diagenetic assemblage and fabric of the original parent rock – distal to the heat source; and (ii) the high-temperature mineral assemblage and recrystallised fabric of the metamorphic marbles.

The Transition Zone includes the *Baked Marl*. The synonymous use of the terms Baked Marl and Transition Zone, however, may result in some inconsistency. The term *Transition Zone* is preferable in defining the general region of transition between the unmetamorphosed parent rocks and the high-temperature Marble Zone.

Baked Marl

The distal sub-region of the *Transition Zone,* where the thermal affects of metamorphism are evident (e.g. magnetic properties, loss of OM) but where there is no evidence of recrystallisation and major mineralogical change. However, the original fabric of the

parent sedimentary rocks is still preserved. In general, *Baked* Marl should not be used as a technical term (see above).

'Indurated biomicrite' and 'non-indurated biomicrite'

At Khushaym Matruk, the biomicrite immediately below the ACZ (i.e. in the transition zone) has been described as *'indurated'*, to set it apart from the rest of the biomicrite, which is friable (and has been described as *'non-indurated'*). Neither of these terms is appropriate as the 'indurated' biomicrite is in the *transition zone* and the metamorphism has presumably protected it against the weathering which has made the 'non-indurated' biomicrite so friable. Consequently, in this case, the terms '*transition zone biomicrite*' and '*friable biomicrite*' are preferred.

Alteration Zone, Altered Zone

The terms '*Alteration Zone' and 'Altered Zone'* have been variously and inconsistently used in previous accounts. They refer to the *Transition Zone* (described above) and to the volume(s) of hydrated metamorphic rocks in the *Metamorphic Zone.* Parts of the adjacent unmetamorphosed sedimentary rocks, that have been affected by interaction with hyperalkaline groundwater, discharging from the metamorphic zone, may also be included. Due of such ambiguities, these terms should only be used when qualifying exactly what is being altered; e.g. the *alteration zone* adjacent to fractures in biomicrite; *hydration altered zones* in marble; *altered cement samples*.

Host Rock, Country Rock

The original unmetamorphosed Tertiary and Upper Cretaceous sedimentary strata at the sites studied, comprising the organic-rich limestones and clay biomicrites that enclose the combustion-metamorphic bodies of marble. The terms *Host Rock* and *Country Rock* have been used interchangeably in previous accounts of the Maqarin site, in particular. This usage may make the relationship between the metamorphosed rocks and the original sedimentary strata unclear.

Parent Rock, Protolith

The terms *Parent Rock* or *Protolith* are specifically used to define the *original* sedimentary parent rock type that was metamorphosed to produce the marbles in the Metamorphic Zone. These rocks may, or may not, be identical to the Country Rock or Host Rock (which is dependant on the heterogeneity of the original rock mass) and which may influence those parts of the rock mass underwent combustion. The term *Parent Rock* may be preferable to *Protolith*, for the benefit of non-specialist readers.

Hyperalkaline Disturbed Zone

The region of *Host Rock* or *Country Rock,* enclosing the *Marble Zone,* that has been by altered physically, mineralogically or geochemically by interaction with hyperalkaline (pH>10) groundwater discharging from the Analogue Cement Zone (ACZ). The term 'alkaline disturbed zone' has been much used in previous Nirex reports but the technically more correct *Hyperalkaline Disturbed Zone* (HDZ) is preferred for this Report.

Bituminous Marl Formation

This term refers to the *stratigraphic* name of the unit of that part of the Tertiary and Cretaceous sequence of chalks and micritic limestones which contains a very high OM component. Locally, this unit combusted *in situ* to produce the pyrometamorphic rocks that are found in Maqarin and central Jordan. The term 'Bituminous' is not indicative of the type of OM present (see *bituminous, kerogen, organic-rich* below).

Bituminous, kerogeneous, kerogen, organic-rich

The *parent rock* or *country rock* to the pyrometamorphic bodies at Maqarin and in central Jordan have been various described, in previous reports and published literature, as *'bituminous', 'organic-rich'* or *'kerogenous'.* The use of the term *'bituminous'* is misleading because 'bitumen' is a residual hydrocarbon produced after the natural or artificial cracking of OM. The term *'kerogen'* is specific to a particular type of natural OM It should only be used when referring to material which has been characterised and identified appropriately. If information on the specific characteristics of the OM present in these rocks is lacking, the term *'organic-rich'* is used to qualify the name of these rock types described in this Report. The term *'Bituminous'* is used only when referring to the Formation name, without implications about the nature of the OM present.

Appendix 2

Tectonic Setting, Geology and Hydrogeology of Maqarin: Analytical Methods

A2.1 Fracture Data from Outcrop Mapping & Adit A-6

Maqarin Railway Cutting

Dominant fracture set		010/90								
Fracture Number	**Strike**	**Dip**	**Dip azimuth**	**Half-length (m)**	**Intersection character**	**Vein-fill**	**Distance from start (m)**	**Separation**	**Comments**	**Formation**
1	18	80	108							B3
2	340	83	250			calcite	15		multi-generation crack seal	
3	342	88	252				10		multi-generation crack seal	
4	342	90	252				14		multi-generation crack seal	
5	10	86	100							
6	264	74	354						3 cm downthrow north	
7	290	30	20						listric shear surface	
8	270	70	360							
9	12	90	102			gypsum				
10	12	46	102							
11	4	90	94	1.5	bedding	gypsum	0	3.2	Beginning of scan line	
12	296	46	26	T-G			3.2	2		
13	12	86	102	0.6		gypsum	5.2	2.1		
14	12	90	102	T-G			7.3	4.3		
15	10	90	100	T-G			11.6	6.1	Down east (?) drag-fold	
16	6	90	96	2	fracture	gypsum	17.7	0.5		
17	8	90	98	2	fracture	gypsum	18.2	2		
18	9	90	99				20.2	1.9		
19	8	84	98				22.1	1.3		
20	12	90	102				23.4	3.8		

Dominant fracture set		010/90								
Fracture Number	**Strike**	**Dip**	**Dip azimuth**	**Half-length (m)**	**Intersection character**	**Vein-fill**	**Distance from start (m)**	**Separation**	**Comments**	**Formation**
21	10	54	100			gypsum	27.2	9		
22	4	90	94			gypsum	36.2	0.08		
23	10	90	100			gypsum	36.28	0.92		
24	12	90	102	1	bedding		37.2	2		
25	12	90	102	T-G			39.2	2.2		
26	14	90	104				41.4	0.1		
27	14	90	104				41.5	0.1		
28	14	90	104				41.6	2.6		
29	290	60	200	1	fracture		44.2	0.4		
30	8	84	98			gypsum	44.6	2.6		
31	10	88	100				47.2	5		
32	12	90	102				52.2	1.55	10 cm-wide fracture zone (2 cm space)	
33	348	62	78				53.75	5.15		
34	12	90	102				58.9	0.6		
35	10	60	100			calcite	59.5	0.05		
36	10	90	100			calcite	59.55	0.45		
37	10	90	100			gypsum	60	2		
38	10	90	100			gypsum	62	6		
39	10	62	100				68	4.6		
40	10	90	100				72.6	1.3		
41	10	90	100				73.9	7.5		
42	12	90	102				81.4	4.8		
43	8	90	98				86.2	3.95		
44	10	90	100				90.15	8.2		
45	16	90	106				98.35	0.2		
46	8	90	98				98.55	8.95		
47	10	90	100				107.5	5		
48	10	90	100				112.5		End scanline	
49	354	90	84						en-echelon	

Dominant fracture set	010/90

Fracture Number	Strike	Dip	Dip azimuth	Half-length (m)	Intersection character	Vein-fill	Distance from start (m)	Separation	Comments	Formation

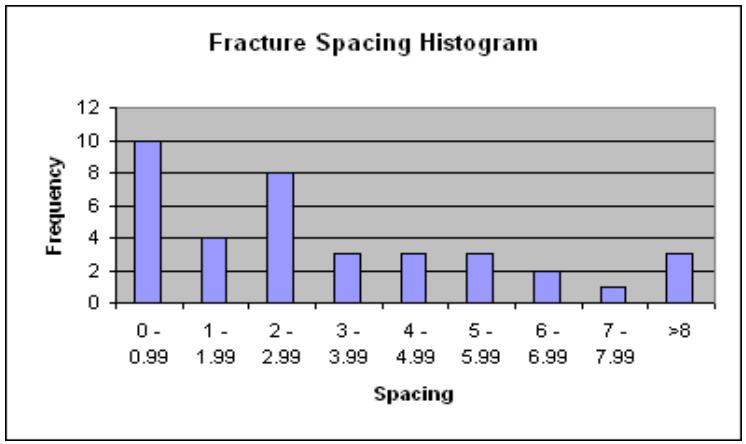

Bin	*Frequency*
0 - 0.99	10
1 -1.99	4
2 -2.99	8
3 - 3.99	3
4 -4.99	3
5 - 5.99	3
6 - 6.99	2
7 - 7.99	1
>8	3
Total	37

Summary Statistics (Fracture spacing)	
Mean	3.04054054
Standard Error	0.42912631
Median	2.1
Mode	2
Standard Deviation	2.61027345
Sample Variance	6.81352748
Kurtosis	-0.148791
Skewness	0.84419972
Range	8.95
Minimum	0.05
Maximum	9
Sum	112.5
Count	37

Sentry Post Cutting (Maqarin Bridge)

Dominant fracture set	320/74								
Fracture Number	**Strike**	**Dip**	**Dip azimuth**	**Half-length (m)**	**Intersection character**	**Vein-fill**	**Distance from start (m)**	**Separation**	**Comments**	**Formation**
1	82	72	172				0	0	Start of scan line: Fracture zone	B3
2	314	74	44	1.5	fracture		0.1	0.10		B3
3	310	74	40	1.5	fracture		0.46	0.36		B3
4	318	70	48	2.4	fracture	calcite	0.91	0.45		B3
5	235	70	325	2.2	intact		1.69	0.78		B3
6	30	70	300				2.33	0.64		B3
7	350	82	80	0.22	fracture		2.39	0.06		B3
8	176	73	266	0.15	fracture	calcite	3.59	1.20		B3
9	353	74	263	1.5	fracture	calcite	3.71	0.12		B3
10	220	70	310	2.3	fracture		4.13	0.42		B3
11	308	68	38			calcite	4.23	0.10		B3
12	310	70	40			calcite	4.29	0.06		B3
13	308	72	38			calcite	4.33	0.04		B3
14	312	70	42			calcite	4.43	0.10		B3
15	0	88	270	1.2	fracture	calcite	4.51	0.08		B3
16	320	82	50	0.2	fracture		4.6	0.09		B3
17	320	82	50	0.05	fracture		4.65	0.05		B3
18	320	82	50	0.08	fracture		4.78	0.13		B3
19	24	84	114	1.2	fracture	calcite	5.41	0.63		B3
20	312	76	222				5.88	0.47		B3
21	304	58	54	2	fracture	calcite	6.9	1.02		B3
22	290	60	20				7.4	0.50	End Scan line. Major shear	B3
23	149	68	239			calcite			crack-seal multi-generation	B3
24	346	72	76		fracture				this is cut by latter calcite vein (#23)	B3
25	340	90	70			calcite			crack-seal multi-generation	B3
26	300	72	30			calcite			crack-seal multi-generation	B3
27	320	62	50			calcite			crack-seal multi-generation	B3
28	326	78	56			calcite				B3

Dominant fracture set		320/74								
Fracture Number	**Strike**	**Dip**	**Dip azimuth**	**Half-length (m)**	**Intersection character**	**Vein-fill**	**Distance from start (m)**	**Separation**	**Comments**	**Formation**
29	334	72	64			calcite				B3
30	310	78	40			calcite				B3
31	294	82	200			calcite				B3
32	114	60	204			calcite				B3
33	146	62	236			calcite				B3
34	284	90	14			calcite			slickenfibres indicate dextral	B3
35	330	84	244			calcite			slickenfibres indicate dextral	B3
36	330	82	240			calcite				B3
37	300	80	30			calcite				B3
38	320	78	230			calcite				B3
39	332	78	62			calcite				B3
40	22	60	322			calcite				B3
41	332	80	62			calcite				B3
42	330	82	240			calcite				B3
43	328	82	238							B3
44	328	80	238							B3
45	332	80	242			calcite				B3
46	330	80	240			calcite				B3
47	326	82	236			calcite				B3
48	330	78	240			calcite				B3
49	334	80	244			calcite				B3
50	324	88	234			calcite				B3
51	328	78	238			calcite				B3
52	330	84	240							B3
53	328	78	238			calcite				B3
54	326	82	236			calcite				B3
55	332	82	242			calcite				B3
56	332	82	242			calcite				B3

Dominant fracture set	320/74

Fracture Number	Strike	Dip	Dip azimuth	Half-length (m)	Intersection character	Vein-fill	Distance from start (m)	Separation	Comments	Formation

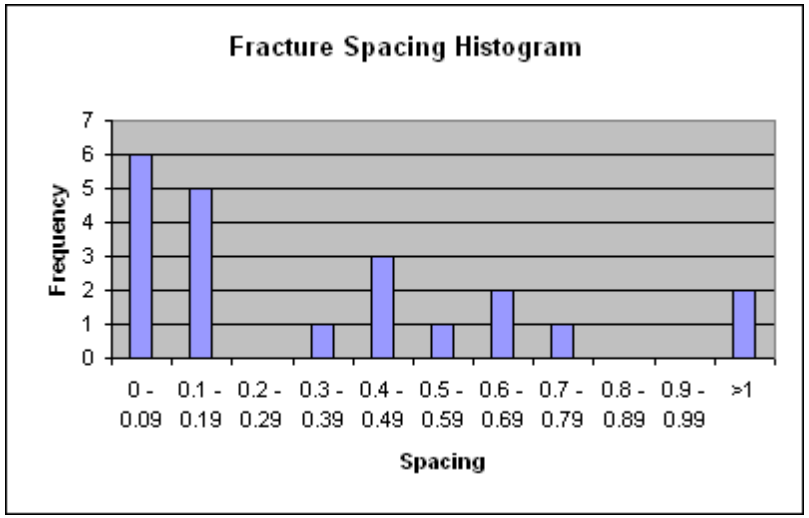

Bin	*Frequency*
0 - 0.09	6
0.1 -0.19	5
0.2 - 0.29	0
0.3 - 0.39	1
0.4 - 0.49	3
0.5 - 0.59	1
0.6 - 0.69	2
0.7 - 0.79	1
0.8 - 0.89	0
0.9 - 0.99	0
>1	2
Total	21

Summary Statistics (Fracture spacing)	
Mean	0.35
Standard Error	0.07
Median	0.13
Mode	0.10
Standard Deviation	0.34
Sample Variance	0.12
Kurtosis	0.50
Skewness	1.12
Range	1.16
Minimum	0.04
Maximum	1.20
Sum	7.40
Count	21.00

Wadi Shallala

Horizontal distance [m]	Strike	Dip Azimuth	Dip	Trace length [m]	Intersection or termination characteristics	Deformation	Displacement [m]	Mineral fill	Comments
0	354	264	88	>8	T	NONE	NONE	U	
0.1	348	258	85	>8	T	NONE	NONE	U	
0.4	350	80	90	>8	T	NONE	NONE	U	
1	2	92	88	>8	T	NONE	NONE	U	
1.3	348	258	90	>8	T	NONE	NONE	U	
1.55	348	258	90	>8	T	NONE	NONE	U	
1.8	348	78	88	>8	T	NONE	NONE	U	
2.6	348	78	88	>8	T	NONE	NONE	U	
4.6	348	258	90	>8	T	NONE	NONE	U	
4.8	356	86	90	>8	T	NONE	NONE	S	micritic sediment fill
6.5	353	83	88	>8	T	NONE	NONE	S	micritic sediment fill
6.8	349	259	90	>8	T	NONE	NONE	S	micritic sediment fill
9	348	78	87	>8	T	NONE	NONE	S	micritic sediment fill
9.1	356	86	87	2	I	NONE	NONE	C	
9.3	354	84	88	4	I	NONE	NONE	C	
10.7	358	268	88	>8	T	NONE	NONE	U	
11	358	268	88	4	I	SLICKEN	0.001	G	1 mm normal slip, polished and slickensided surface pre-dates powdery gypsum fill
11.2	349	259	88	>8	T	NONE	NONE	G/S	white powdery gypsum fill developed on top, and along dilated margins of micritic sediment fill
11.4	358	88	90	0.5	I	NONE	NONE	G	
11.42	358	88	90	0.5	I	NONE	NONE	G	
11.48	354	84	90	>1	R	NONE	NONE	U	
11.58	356	86	88	>8	T	NONE	NONE	G	
13.5	346	256	86	0.5	I	NONE	NONE	G	
14.4	344	254	84	1.2	I	NONE	NONE	G	
14.42	348	78	89	0.2	I/R	NONE	NONE	U	
14.45	345	255	84	0.9	I	NONE	NONE	U	

Horizontal distance [m]	Strike	Dip Azimuth	Dip	Trace length [m]	Intersection or termination characteristics	Deformation	Displacement [m]	Mineral fill	Comments
15.2	354	84	90	>8	T	NONE	NONE	G/S	white powdery gypsum fill developed on top, and along dilated margins of micritic sediment fill
15.27	354	84	90	>0.5	I	NONE	NONE	S/C	sediment fill resting on early calcite coating
15.43	352	262	88	>4	I/O	NONE	NONE	G	
16	352	262	88	>8	T	NONE	NONE	G	
16.5	352	262	88	>8	T	NONE	NONE	C	
17	356	266	88	>8	T	SLICKEN	U/K	G/S	polished and slickensided calcite coating indicating normal down thrown movement to the east, associated with a 10-15 cm wide fracture zone with euhedral nailhead calcite coatings
17.9	356	86	88	>8	T	NONE	NONE	G/C	
17.9	70	340	88	>0.5	R/O	SLICKEN	U/K	G/S	polished and slickensided calcite surface indicating reversed movement, down throwing to north. Two generations of calcite: (a) early calcite fill deformed by slicken development; (b) later euhedral nailhead calcite lining voids between asperities. 3 mm aperture
18.95	354	84	90	>8	T	NONE	NONE	G/C	
18.97	354	84	90	0.4	R	NONE	NONE	G/C	
19.1	352	82	90	1.6	R/I	NONE	NONE	G/C	
19.25	352	82	88	>8	T	NONE	NONE	G	curvilinear
19.3	352	82	90	>0.5	O/R	NONE	NONE	S/G	
22.5	0	270	88	>8	T	BRECCIA	NONE	G/S	fracture zone with 15-20 cm wide jigsaw breccia containing <1 to 6 cm decalcified marl blocks, with micritic gypsum and infiltrated sediment matrix fill
20.8	0	270	88	>8	T	NONE	NONE	U	
22.8	2	92	90	0.2	R	NONE	NONE	U	
23.3	2	92	90	>8	T	NONE	NONE	U	
23.9	352	82	90	>8	T	NONE	NONE	U	
24.6	354	84	90	>8	T	NONE	NONE	G/S	
24.7	350	260	88	1.2	I	NONE	NONE	U	

Horizontal distance [m]	Strike	Dip Azimuth	Dip	Trace length [m]	Intersection or termination characteristics	Deformation	Displacement [m]	Mineral fill	Comments
24.9	344	74	90	0.3	I	NONE	NONE	U	
25.3	38	128	23	>2	B	NONE	NONE	U	dilated bedding plane
25.3	353	83	90	>8	T	NONE	NONE	C/G/S	
26.5	350	260	74	N/D	N/D	NONE	NONE	U	
26.6	350	260	74	N/D	N/D	NONE	NONE	U	
28.7	352	262	82	>8	T	SLICKEN	U/K	C	late euhedral nailhead calcite coating rests on earlier slickensided calcite surface
29.6	348	258	80	>8	T	SLICKEN	U/K	C	late euhedral nailhead calcite coating rests on earlier slickensided calcite surface
30.4	324	234	70	0.5	R	NONE	NONE	U	curvilinear
30.4	38	128	48	2	I/R	NONE	NONE	G	sub-parallel to bedding
33.1	346	256	86	>2	R/T	NONE	NONE	C	
33.3	354	84	90	>8	T	NONE	NONE	G/C	
34.1	354	264	88	0.2	R	NONE	NONE	FE/	Iron-stained surfaces
34.6	348	258	82	>8	T	NONE	NONE	FE/G	white powdery gypsum fill developed on top, and post-dates Fe oxide film
35.1	344	254	82	>8	T	NONE	NONE	FE/G	white powdery gypsum fill developed on top, and post-dates Fe oxide film. Fe oxide staining of wallrock to depth of 4 mm
35.5	342	252	82	>8	T	NONE	NONE	C/FE/G	calcite pre-dates iron oxide, which in turn is post-dated by white powdery gypsum
35.6	344	254	82	>8	T	NONE	NONE	C/FE	
35.75	340	250	84	>8	T	NONE	NONE	C/FE	
35.76	345	255	90	0.2	I	NONE	NONE	C/FE	
35.79	348	258	90	0.8	I	NONE	NONE	G	
37.15	348	258	90	0.15	I	NONE	NONE	G	
37.2	348	258	90	>8	T	FAULT	0.4	G	fault showing 40 cm displacement, illustrated by displacement of concretion. Downthrows to west
37.45	354	254	90	1.6	I	NONE	NONE	U	
37.88	349	259	82	>8	T	NONE	NONE	G	
38.1	349	259	84	0.7	I	NONE	NONE	U	
39	64	154	68	>2	O/R	NONE	NONE	S/G	

Declination 3 degrees 30 minutes east (2001)

Miscellaneous measurements

Location	Strike	Dip Azimuth	Dip	Trace length [m]	Intersection or termination characteristics	Deformation	Displacement [m]	Mineral fill	Comments
Railway cut	90	0	90	>10	O		Dextral	Calcite	
Valley Bottom near WS	173	263	88	>10	T				
Valley Bottom near WS	356	86	88	>10	T				
Valley Bottom near WS	34	124	34	>10				Calcite	
Valley Bottom near WS	356	86	90	>10				Calcite	
Valley Bottom near WS	358	88	88	>10				Calcite	
Valley Bottom near WS	0	90	88	>10	T				
Valley Bottom near WS	30	120	20	>10	I				
Valley Bottom near WS	356	86	90	>10	T				
Valley Bottom near WS	356	86	88	>10	O				
Valley Bottom near WS	170	260	88	>10	T				
Valley Bottom near WS	358	88	90	>10					
Valley Bottom near WS	356	86	90	>10					
Valley Bottom near WS	32	122	26	>10					
Valley Bottom near WS	174	264	88	>10	T			Calcite	
Valley Bottom near WS	358	88	90	>10	T				
Valley Bottom near WS	30	120	20	>10					
Valley Bottom near WS	0	90	90	>10					
Valley Bottom near WS	358	88	86	>10					
Valley Bottom near WS	176	266	88	>10					
Valley Bottom near WS	2	92	90	>10					
Valley Bottom near WS	356	86	88	>10					
Valley Bottom near WS	354	84	88	>10	T				
Valley Bottom near WS	176	266	88	>10	T				
Valley Bottom near WS	356	86	88	>10	T				
Valley Bottom near WS	356	86	86	>10	T				
Valley Bottom near WS	0	90	88	>10	T				
Valley Bottom near WS	358	88	90	>10	O				
Valley Bottom near WS	172	262	88	>10	T				
Valley Bottom near WS	356	86	90	>10				Calcite	
Valley Bottom near WS	356	86	90	>10				Calcite	
Valley Bottom near WS	30	120	30	>10					

Location	Strike	Dip Azimuth	Dip	Trace length [m]	Intersection or termination characteristics	Deformation	Displacement [m]	Mineral fill	Comments
Valley Bottom near WS	32	122	28	>10	T				
Valley Bottom near WS	352	82	88	>10	T			Calcite	
Valley Bottom near WS	358	88	88	>10	T				
Valley Bottom near WS	356	86	88	>10	T				
1km east of bridge	10	100	90						
1km east of bridge	6	96	90						
1km east of bridge	10	100	90						
1km east of bridge	6	96	90						
1km east of bridge	6	96	90		I				
1km east of bridge	8	98	90						
1km east of bridge	8	98	88						
1km east of bridge	12	102	90		T				
1km east of bridge	6	96	90		T				
1km east of bridge	10	100	90		T				
1km east of bridge	10	100	88						
1km east of bridge	12	102	88						
1km east of bridge	8	98	90						
1km east of bridge	8	98	90						
1km east of bridge	8	98	90						
1km east of bridge	8	98	90						
1km east of bridge	10	100	88						
1km east of bridge	6	96	90						
1km east of bridge	18	108	80						
1km east of bridge	18	108	88						
1km east of bridge	340	70	83					Calcite	
1km east of bridge	342	72	86		I				
1km east of bridge	10	100	86						
1km east of bridge	92	2	2						
1km east of bridge	264	354	74			Fault	Normal (down north)		
1km east of bridge	12	102	90		O			Gypsum	
1km east of bridge	12	102	46						
1km east of bridge	46	136	90						
1km east of bridge	314	224	70						
1km east of bridge	320	230	68		I				

Location	Strike	Dip Azimuth	Dip	Trace length [m]	Intersection or termination characteristics	Deformation	Displacement [m]	Mineral fill	Comments
River base near bridge	20	110	90						
River base near bridge	316	226	88		I				
River base near bridge	318	228	90		O				
River base near bridge	316	226	90		T				
River base near bridge	312	222	90		T				
River base near bridge	22	112	90		T				
River base near bridge	316	226	70						
River base near bridge	316	226	82						
River base near bridge	316	226	70						
River base near bridge	318	228	72						
River base near bridge	312	222	72						
River base near bridge	316	226	74						
4km west of A6	290	10	82						
4km west of A6	294	14	84						
4km west of A6	290	10	80						
4km west of A6	290	10	80						
4km west of A6	290	10	82		O				
4km west of A6	292	12	82		O				
4km west of A6	290	10	82		O				
4km west of A6	296	16	84		O				
4km west of A6	208	298	86		T				
4km west of A6	210	300	88						
4km west of A6	206	296	86						
4km west of A6	208	298	82						
4km west of A6	208	298	86						
4km west of A6	332	62	82						
4km west of A6	228	138	82						
4km west of A6	270	0	30		T				
4km west of A6	148	248	68						
4km west of A6	346	76	72		T		crack seal	Calcite	
4km west of A6	340	70	90				Crack seal	Calcite	
4km west of A6	300	30	72		I				
4km west of A6	320	50	62						320 strike cuts 300 strike
4km west of A6	326	56	78						

Location	Strike	Dip Azimuth	Dip	Trace length [m]	Intersection or termination characteristics	Deformation	Displacement [m]	Mineral fill	Comments
4km west of A6	334	64	72						
4km west of A6	304	34	68					Calcite	
4km west of A6	310	40	78					Calcite	
4km west of A6	294	24	82						
4km west of A6	114	204	88						
4km west of A6	114	204	60						
4km west of A6	284	14	90						
4km west of A6	330	60	84						
4km west of A6	334	64	84			Fault	Dextral	Calcite	
4km west of A6	330	60	82						
4km west of A6	300	30	80						
4km west of A6	320	50	78						
4km west of A6	332	62	78						
4km west of A6	324	54	88						
4km west of A6	22	112	60						
Above Eastern Springs	316	46	88						
Above Eastern Springs	316	46	88		T				
Above Eastern Springs	32	122	86		T				
Above Eastern Springs	314	44	88		O				
Above Eastern Springs	316	46	88		T				
Above Eastern Springs	42	132	52						
Above Eastern Springs	50	140	58						
Above Eastern Springs	319	229	90						
Above Eastern Springs	318	228	90						
Above Eastern Springs	350	80	90						
Above Eastern Springs	352	82	90		T				
Above Eastern Springs	356	86	90		T				
Above Eastern Springs	354	84	90						
Above Eastern Springs	354	84	76						
Above Eastern Springs	168	78	70		O				
Above Eastern Springs	162	72	78						
Above Eastern Springs	4	94	90						
Road-cut above Adit	286	16	60			Fault (listric)	Down north		
Road-cut above Adit	102	12	86		I				Cut by listric fault

Location	Strike	Dip Azimuth	Dip	Trace length [m]	Intersection or termination characteristics	Deformation	Displacement [m]	Mineral fill	Comments
Road-cut above Adit	140	230	64			Fault	Sinistral (10 to 314)		
Road-cut above Adit	2	92	90						
Road-cut above Adit	2	92	88						
Road-cut above Adit	358	88	88						
Road-cut above Adit	356	86	90		O				
Road-cut above Adit	4	94	86						
Road-cut above Adit	76	166	82						
Road-cut above Adit	84	174	88		O				
Road-cut above Adit	78	168	82						
Road-cut above Adit	0	90	90						
Wadi Sijin	150	60	40						
Wadi Sijin	156	66	44						
Wadi Sijin	172	82	36			Fault (listric)	Down west		
Wadi Sijin	20	110	60						
Wadi Sijin	358	88	90		I				Cut by listric fault
Wadi Sijin	176	86	78			Fault (listric)	Normal (30 to 340)		
Wadi Sijin	226	136	50						
Wadi Sijin	2	92	78						
Wadi Sijin	10	100	80						
Wadi Sijin	6	96	80						
Wadi Sijin	10	100	82						
Wadi Sijin	2	92	78						
Wadi Sijin	2	92	80						
Wadi Sijin	40	130	60						
Wadi Sijin	42	132	60						
Wadi Sijin	40	130	68						
Wadi Sijin	50	140	66						
Wadi Sijin	48	139	60						
Wadi Sijin	270	0	60						
Wadi Sijin	272	2	58		T				
Wadi Sijin	104	194	70		T				
Wadi Sijin	6	96	90						
Wadi Sijin	6	96	88						
Wadi Sijin	2	92	90		T				

Location	Strike	Dip Azimuth	Dip	Trace length [m]	Intersection or termination characteristics	Deformation	Displacement [m]	Mineral fill	Comments
Valley side (1-3km east)	24	114	60					Calcite	
Valley side (1-3km east)	24	114	60		T			Calcite	
Valley side (1-3km east)	18	108	64		T			Green ?	
Valley side (1-3km east)	120	30	74		T				
Valley side (1-3km east)	140	50	90		T				
Valley side (1-3km east)	124	34	88						
Valley side (1-3km east)	126	36	90		T				
Valley side (1-3km east)	122	32	90						
Valley side (1-3km east)	124	34	90						
Valley side (1-3km east)	138	48	90		O				
Valley side (1-3km east)	130	40	90						
Valley side (1-3km east)	134	44	86						
Valley side (1-3km east)	130	40	88						
Valley side (1-3km east)	140	230	30						
Valley side (1-3km east)	310	40	40		I				
Valley side (1-3km east)	310	40	90						Cuts 310/40 set
Valley side (1-3km east)	310	40	72			Fault	?		
Valley side (1-3km east)	312	42	84						
Valley side (1-3km east)	314	44	86						
Valley side (1-3km east)	312	42	88						
Valley side (1-3km east)	312	42	84						
Valley side (1-3km east)	314	44	86						
Valley side (1-3km east)	320	50	72		I				
Valley side (1-3km east)	126	216	80			Fault			Cuts 320/72
Valley side (1-3km east)	260	350	70			Fault	Sinistral		
Valley side (1-3km east)	284	14	34						
Valley side (1-3km east)	292	22	36						
Valley side (1-3km east)	216	306	56						
Valley side (1-3km east)	350	80	68						
Valley side (1-3km east)	2	92	78						
Valley side (1-3km east)	100	190	70						
Valley side (1-3km east)	160	250	74					Gypsum	
Valley side (1-3km east)	320	50	80		I				
Valley side (1-3km east)	230	320	16						Cuts 320/80

Location	Strike	Dip Azimuth	Dip	Trace length [m]	Intersection or termination characteristics	Deformation	Displacement [m]	Mineral fill	Comments
Valley side (1-3km east)	320	50	90						
Valley side (1-3km east)	134	44	86			Fault	Sinistral	Calcite	
Valley side (1-3km east)	356	86	90						
Valley side (1-3km east)	356	86	90						
Valley side (1-3km east)	354	84	90						
Valley side (1-3km east)	320	50	90						
Valley side (1-3km east)	298	38	90						
Valley side (1-3km east)	2	92	90						
Valley side (1-3km east)	0	90	90						
Valley side (1-3km east)	358	88	88						
Valley side (1-3km east)	354	84	96						

River Bridge Terrace

Dominant fracture set	315/90

Fracture Number	Strike	Dip	Dip azimuth	Half-length (m)	Intersection character	Vein-fill	Distance from start (m)	Separation	Comments	Formation
1	314	70	224					ca. 10cm		B3
2	320	68	230					ca. 10cm		B3
3	318	74	228					ca. 10cm		B3
4	306	78	216					ca. 10cm		B3
5	316	78	226					ca. 10cm		B3
6	308	78	218					ca. 10cm		B3
7	308	78	218					ca. 10cm		B3
8	14	88	284					ca. 10cm		B3
9	332	86	62					ca. 10cm		B3
10	310	90	40					ca. 10cm		B3
11	28	90	118					ca. 10cm		B3
12	20	90	110					ca. 10cm		Alluvium
13	22	90	112					ca. 10cm		Alluvium
14	20	90	110					ca. 10cm		Alluvium

A2.2 Adit 6 Fracture Logs

The images presented below represent a record of the fracture traces measured in Adit A-6 with the distance from the adit entrance noted down the left-hand axis of the profiles. The fracture numbers on the log relate to the fracture numbers in the Adit A-6 spreadsheet of Appendix 2.1

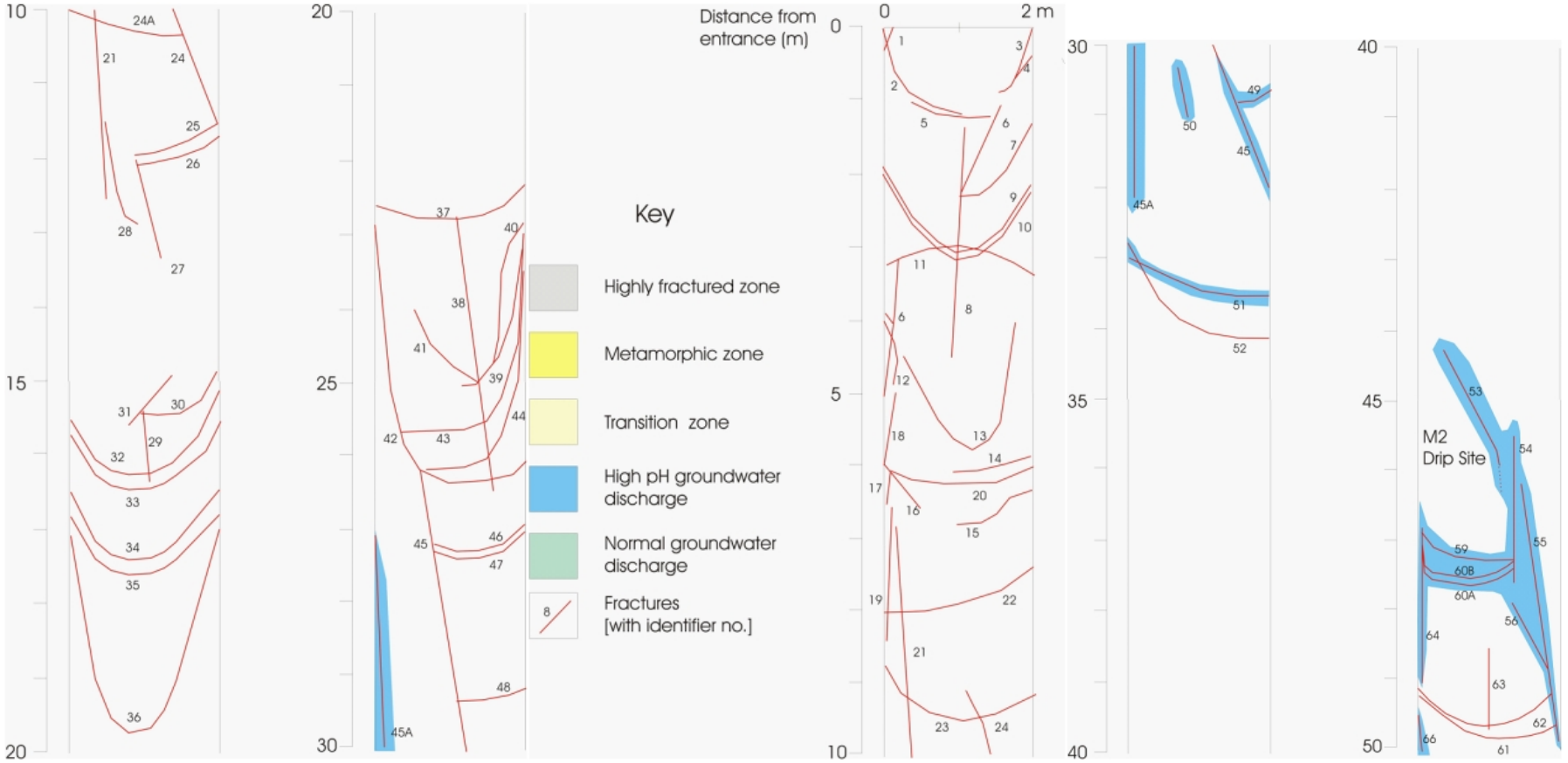

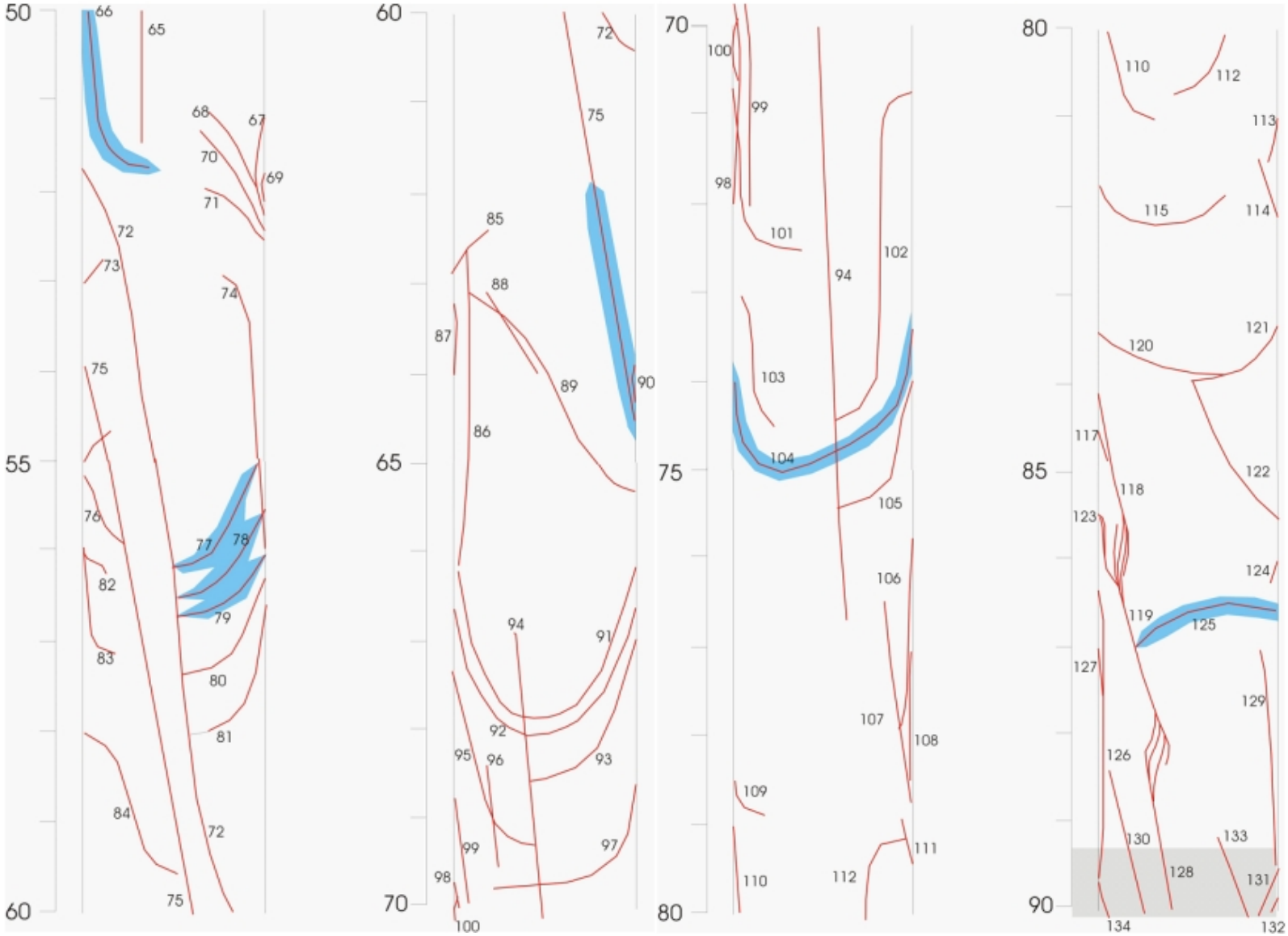
50
55
60
60
65
70
70
75
80
80
85
90

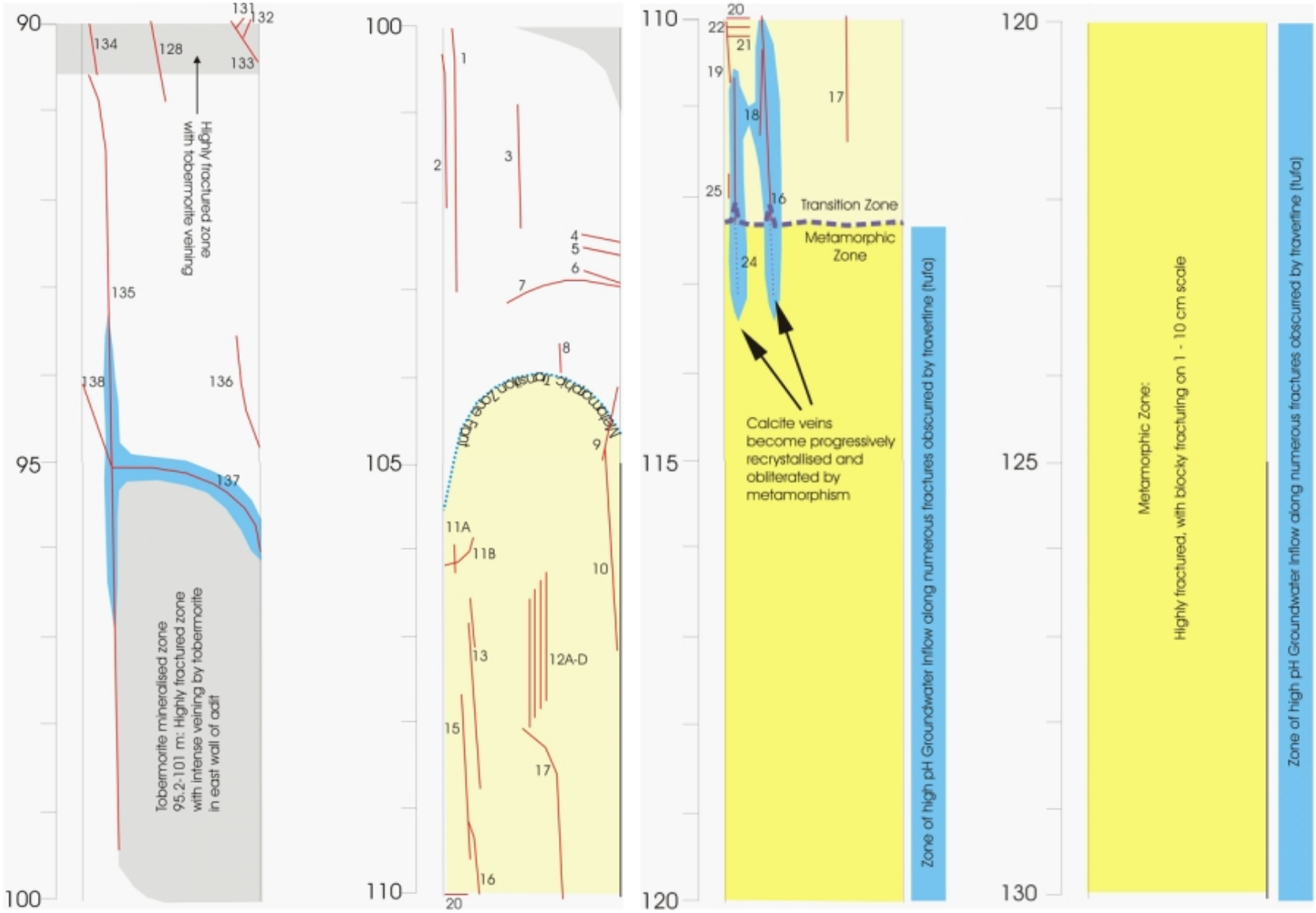
90
95
100
105
110
115
120
125
130
131
132
134
128
133
Highly fractured zone with tobermorite veining
135
138
136
137
Tobermorite mineralised zone 95.2-101 m: Highly fractured zone with intense veining by tobermorite in east wall of adit
1
2
3
4
5
6
7
8
9
10
11A
11B
12A-D
13
15
16
17
20
Metamorphic fracture zone front
20
22
21
19
18
17
25
16
24
Transition Zone
Metamorphic Zone
Calcite veins become progressively recrystallised and obliterated by metamorphism
Zone of high pH Groundwater Inflow along numerous fractures obscured by travertine (tufa)
Metamorphic Zone:
Highly fractured, with blocky fracturing on 1 - 10 cm scale
Zone of high pH Groundwater Inflow along numerous fractures obscured by travertine (tufa)

A2.3 Hydrogeological Methodology and Data Interpretation

All drilling and testing at the Adit A-6 locality was performed within the Bituminous Marl Formation and the ACZ. The parent rock is massive and bedding is usually not discernible. Abundant visible zones of minor flow or seepage are invariably hyperalkaline waters (see Chapter 3). Thus, flow is confined to structural elements such as mineralised fractures, small shear zones, joints and brecciated zones. The parent rock is dry in further back along Adit A-6, beyond the ACZ.

It seems that fracture-controlled groundwater flow penetrating the ACZ is fed from the aquifer immediately above (Chalky Limestone), and conducted within the Bituminous Marl Formation only along fracture-controlled and mineralised flow paths. A detailed description of the hydrogeology and rock properties is included in the Phase III report (Smellie, 1998), and some new structural details are included above in Section 2.2.

The Bituminous Marl Formation is a relatively tight hydrogeological unit, with low intrinsic permeability. Consequently, the conventional approach for testing the performance and analysis of slug and pump tests in aquifers is of rather limited use. Therefore, monitoring equipment was installed in the probe holes and slug and constant rate injection tests were carried out as shut-in test between defined intervals using single and double packer systems.

The parent rock was tested by boreholes D1, D3, D6 and the ACZ was tested by borehole D2. Some boreholes penetrate active and inactive (conductive or sealed), mineralised fractures, calcite-filled older fractures and joints. The test interval length ranged from 0.75 to 1.47 m in D1, D2, and D6. The pressure pulse test in D3 was not evaluated due to undefined initial conditions. Shut-in slug and pump tests were performed not only to keep the test duration at reasonable time length, but also because of almost horizontal borehole orientation with a dip of approximately 15 degrees towards the open tunnel.

Slug test

The slug test (or pressure-pulse test) was chosen as the basis for analysis. It is a frequently used field technique because of its logistical and economic advantages over alternative approaches. In open borehole slug tests, the change in head in the screened interval is a function of water level changes in the open casing due to flow from/to the well (Cooper et al, 1967).

$$\pi r_c^2 \frac{dH}{dt} = 2\pi r_s T \frac{\partial h}{\partial r}$$

where,

h = deviation of hydraulic head in the formation from static conditions, [L];
H = deviation of head in well from static conditions, [L];
T = radial component of transmissivity, [L^2/T];
r_s = effective radius of well screen, [L];
r_c = effective radius of well casing, [L];
r = radial direction, [L];
t = time, [T].

The mathematical model from Cooper et al.(1967) is derived for confined formations and based on several assumptions about the slug-induced flow system.

- homogeneous formation
- Darcy flow perpendicular to the test interval
- instantaneous initial displacement
- no hydrologic boundaries in the vicinity
- the elastic storage mechanisms represented by the specific storage parameter affect test responses

In a shut-in slug test (pressure-pulse test), the packed-off interval is isolated from the open casing. Subsequently, head changes are a function of the compressibility of water and the test equipment (packer and associated tubing). The relationship between the head change (H) at any time (t) after pressurisation in the system and the hydraulic response of the tested interval can be expressed after Bredehoeft and Papadopulos (1980) as

$$V_w C_w \rho_w g \frac{dH}{dt} = 2\pi r_s T \frac{\partial h}{\partial r}(r_s, t)$$

where,

V_w = volume of water within the pressurized section of the system, [L^3];

C_w = compressibility of water, [LT^2/M];

ρ_w = density of water, [M/L^3];

g = gravitational acceleration, [L/T^2].

Notice that the compressibility of the test equipment is not included in the formulation by Bredehoeft and Papadopulos (1980). Calculating an effective casing radius for the shut-in test (r_c') allows the comparison with the conventional test:

$$r_c' = \left(\frac{V_w C_w \rho_w g}{\pi} \right)^{0.5}$$

Slug tests can be preformed in almost any type of borehole, and are simple to carry out, low cost and perceived to be straightforward in analysis. The main advantage of slug tests performed in closed intervals is the relative short test duration. This method is therefore ideal for estimating hydraulic parameters in low-conductivity formations. Nevertheless, in addition to the consideration of equipment compressibility, there are several other issues to consider when evaluating data from shut-in slug tests. The most important is the extreme sensitivity to near-well disturbances often induced by drilling and products of biochemical action. As the effective casing radius decreases, the amount of flow required to produce a unit change in head decreases. Thus, only a very small volume of water moves into/out of the test interval in response to the slug-induced head change. Subsequently, the volume of the formation affected by the test decreases as well. Note that the hydraulic parameters evaluated by shut-in slug tests are associated with a very small volume of the formation surrounding the test interval. Another issue is that of test initiation prior to obtaining equilibrium conditions. Head disturbances might have been caused by setting the packer system in place and by subsequent re-filling of the test intervals with water. Also remaining air pockets in the test interval will affect the test data due to their compressibility. An issue of practical importance is that of type curve matching. As the shape of type curves can become quite similar (for very low storage parameter, as well as for alternate boundary conditions) it is difficult to

distinguish on the shape alone. Which set of type curves is used for analysis depends on the test design and the hydrogeologic setting of the test well.

When performing a series of slug tests, it is important to consider (1) the equipment used, (2) the methods involved in initiating the pressure pulse, and (3) the degree of head recovery prior to test repetition in a tested interval. For measuring head changes in the test interval a pressure transducer was used in Adit A-6. The sensor measures the pressure and converts the physical quantity into an electrical signal. The main advantages of using a pressure transducer at Maqarin was that a high frequency of measurements could be taken and, combined with a built-in data-acquisition device, allowed unattended data collection. This procedure resulted in recovery data sets from shut-in slug tests of 200 to 3000 readings, depending on the duration of the test.

Initial pressurisation of the test interval was carried out with a hand pump. Three main disadvantages are associated with this procedure. (1) Test initiation cannot be considered instantaneous in all cases. Filling the test interval with water and pressurisation took from a few seconds (D1-3) up to several minutes (D6-2-20A). (2) It was also not possible to pre-set the magnitude of the initial displacement, which hindered the conductance of a series of repeated slug tests with identical initial displacement. (3) The amount of water pumped into the test interval is unknown, and therefore no reasonable estimate of the expected initial displacement can be made. A comparison between expected (H_0*) and measured (H_0) displacement is most valuable. The presence of trapped air can be recognized (Keller and Van der Kamp, 1992), the time of test initiation can be estimated in the case of non-instantaneous slug introduction, and the effective casing radius can be evaluated independently.

The effect of incomplete recovery is a function of *S*, the dimensionless storage parameter (Hvorslev, 1951; Bouwer and Rice, 1976).

$$\alpha = \frac{r_s^2 S}{r_c^2}$$

For moderate to small values of *S*, hydraulic parameters from repeat slug test agree within 10% when the recovery is within 20% of H_0. For large *S* values, the residual deviation from static should be less than 5% of H_0. For the degree of head recovery on repeating tests in the same interval, the recovery is evaluated relative to the initial displacement H_0 of the following test. For repeated slug tests the recommended degree of head recovery was not established after D1-3 and D6-2-20A. This can also be seen in the non-linear logarithm of normalized head ($H(t)/H_0$) versus time (Butler, 1997).

Pre-analysis processing

The transducer response data were transformed into the normalised deviation from static. This is of importance as the data were collected with a pressure transducer and errors in the calibration parameters can result in false absolute head values for the recovery data. An appropriate calibration of the pressure transducer in the laboratory or in the field to convert transducer output into pressure head was not conducted. This emphasises even more that only normalized response data could be taken for analysis. All transducers were new and factory calibrated at 0-10 bar to 0.02% full scale and 0.05% full scale for 20 bar units and 40 bar units, respectively. Zero-bar displacements are <0.002 bar for 20 bar units and <0.01 bar for 40 bar units.

In a first step, the transducer data are converted into pressure heads. After examination of the data set and determination of the static conditions, the deviation of the pressure head from static conditions is calculated. This is equal to the deviation of the total head

from static conditions. In order to normalize the data an estimate of the initial displacement from static (H_0) must be obtained. As a result of early oscillations in the data record, produced by the method of initial pressurization with a hand pump, the estimate of H_0 and t_0 (the time of test initiation) can be rather difficult. In cases of non-instantaneous slug introduction the translation method was used to estimate H_0 and t_0 (Pandit and Miner, 1986). In this approach the early time portion in the data record is ignored and test initiation starts after oscillation has ceased.

In cases where the response data set exceeded a few hundred readings and an automated analysis approach with a log time scale was carried out, the data are screened and the number of data points reduced. As data collection was set to a defined time interval (1 to 4 seconds), such data reduction is important so that the middle and late portion of the recovery data are not over-weighted.

Data analysis

The recovery data from six shut-in slug tests were evaluated after pre-analysis processing. The data were analysed with automatic and manual-type, curve-matching procedures after Cooper et al.(1967) and Bredehoeft and Papadopulos (1980). Automatic data analysis was performed with the software package PUMPTEST by Phil Hall and Joe Chen. The hydraulic parameters derived with the conventional slug test method after Cooper et al (1967) with PUMPTEST are transformed into parameters comparable with Bredehoeft and Papadopulos (1980) using the ratio between conventional and shut-in test effective casing radius. The type curves for manual matching are taken from Cooper et al.(1967), Papadopulos et al.(1973) and Bredehoeft and Papadopulos (1980).

Pump yest

Pressure build-up tests are frequently used in the petroleum industry to characterise reservoirs and in hydrogeology to estimate hydraulic parameters in low-permeability formations. An injection test is analogous to a drawdown (production) test, where the pumping rate used in equations is negative for injection and positive for drawdown tests.

Analysis: Cooper-Jacob Method

For an ideal injection test, the rate of injection stays constant. The pressure in the test interval increases during injection. The pressure buildup is rapid at first and then decreases and asymptotically approaches zero pressure buildup. Cooper and Jacob (1946) derived a graphical method to analyse time-pressure response data by using an abbreviated Theis equation for non steady-state flow. A plot of the pressure response data vs. the logarithm of injection time should have a straight-line segment, where the slope is proportional to the pumping rate (Q), and inversely proportional to the transmissivity (T). Hydraulic parameters are calculated from semi-log plots by measuring the pressure head buildup over one log cycle and determine the elapsed time (Cooper and Jacob, 1946).

$$T = \frac{0.183Q}{\Delta s}$$

where,

T: transmissivity [m^2/d]

Q: pumping rate [m^3/d]

□s: pressure head buildup over one log cycle [m].

This graphical method was developed for confined aquifers. The storage coefficient is calculated from the transmissivity and the zero pressure buildup intercept of the response data from an observation well.

$$S = \frac{2.25Tt_0}{r^2}$$

where,

S: storage coefficient (or storativity)

t_0: zero intercept [d]

r: distance from the observation to the pumping well.

The extent of the cone of depression, which is the radius to which extent pumping affects the hydraulic heads in the surrounding formation, is directly proportional to the elapsed time (t), and the transmissivity (T). The extent is inversely proportional to the storage coefficient (S). The radius of the cone of depression (r_0) can be estimated from the hydraulic parameters with

$$r_0[m] = \sqrt{\frac{2.25T[m^2/d]\,t[d]}{S}}$$

Before evaluating the test data obtained at Maqarin, a few general comments are made on test design of transient pump tests.

Pump test design

Major issues in the design of pump tests are (1) well spacing, (2) selection of pump equipment and pumping rate, (3) well orientation, and (4) time constraints on pump tests. It is advisable to space wells on a log scale, and to estimate the extent of the cone of depression during the test. The distance between pumped well and observation well should be less than those between the pumped well and known boundaries. The pump must be able to run consistently for the duration of the test. It is important to check the head vs. capacity curves of the pump to assure that the pumping rate can be maintained during the test as the pressure builds up. The orientation of wells depends mainly on the presence of boundaries, and structures that may control the hydraulic parameters. The duration of a pump test should be long enough to (i) overcome wellbore storage effects, (ii) evaluate aquifer parameters beyond the zone of disturbance, and (iii) to analyse boundary effects when encountered. As part of the preliminary design also a prediction of the test outcome should be carried out.

Data analysis

A single, constant rate injection test was conducted in the packed-off test interval in borehole D1. The injection rate (Q) was 7.6 ml/min (10% of the pump capacity), and the time length of the injection period extended over 265 minutes after which the test had to be broken off due to the constrained working hours. No response data from adjacent boreholes are recorded.

A2.4 Earthvision: Instructions on Viewing the Refined Geological Model and Background to its Development

A2.4.1 Instructions on use

The Refined Geological Model is presented with this Report and may be viewed using the EarthVision 3D Encrypted Viewer (also provided on the CD-ROM). The encrypted viewer is a free product from Dynamic Graphics, the vendors of EarthVision, with the functionality to interactively view geological models in 3D. The encrypted viewer is installed by simply copying the executable and files onto a PC. The software is then run by double-clicking on the executable icon.

A series of files have been prepared for presenting the encrypted model. These include five encrypted models (which have the extension .enc.faces) and also visualisation files (which have the extension .vue). To select the encrypted models use Menu 5 (simply press key 5 on the keyboard) and edit the selected files list (shortcut available is to press *b*). To select the visualisation file press e and select one of the files from the list. It is suggested that the files are visualised in the following order:

1. Visualisation of the large-scale model:
    - Select the encrypted model ***watertable.enc.faces***. Then load the following views one-by-one:
        - ***Pres1.vue:*** This file views the Refined Geological Model from the south east.
        - ***Pres2.vue:*** This file views the Refined Geological Model from the north west.
        - ***Pres3.vue:*** In this visualisation the water table interpretation is shown in red.
        - ***Pres4.vue:*** In this visualisation the Refined Geological Model is sectioned at easting 231899 which corresponds to the orientation of Adit A-6.
        - ***Pres5.vue:*** In this visualisation the Refined Geological Model is sectioned in an east-west direction.
        - ***Pres6.vue:*** In this visualisation the Refined Geological Model is sectioned at an elevation of 78.5 which corresponds to the elevation of Adit A-6.
        - ***Pres7.vue:*** In this visualisation a 3D block is removed from the Refined Geological Model and all of the adits depicted on the geological map are shown.
        - ***Pres8.vue:*** In this visualisation the wells are shown alongside the geological structure.
2. Visualisation of the Adit 6 fractures:
    - Select the encrypted model ***Adit6Fractures.enc.faces***. Then load the following views one-by-one:
        - ***Adit6CSH.vue***: This file presents the visualisation of the CSH fractures integrated with the Adit 6 geological model.
        - ***Adit6EarlyCalcite.vue***: This file presents the visualisation of the Early Calcite fractures integrated with the Adit 6 geological model.
        - ***Adit6Ettringite.vue***: This file presents the visualisation of the Ettringite/Thaumasite fractures integrated with the Adit 6 geological model.
        - ***Adit6Gypsum.vue***: This file presents the visualisation of the Gypsum fractures integrated with the Adit 6 geological model.

- ***Adit6Jennite.vue***: This file presents the visualisation of the Jennite fractures integrated with the Adit 6 geological model.
- ***Adit6LateCalcite.vue***: This file presents the visualisation of the Late Calcite fractures integrated with the Adit 6 geological model.
- ***Adit6Tobermorite.vue***: This file presents the visualisation of the Tobermorite fractures integrated with the Adit 6 geological model.
- ***Adit6Unmin.vue***: This file presents the visualisation of the unmineralised fractures integrated with the Adit 6 geological model.

3. Visualisation of the Adit 6 investigations:
   - Select the encrypted model Adit6.enc.faces. Then load the following views one-by-one:
     - ***Adit6Bores.vue***: This file presents the visualisation of the boreholes drilled from Adit 6.
     - ***Palaeomag.vue***: This file presents the visualisation of the palaeomagnetic sampling locations. The sample numbers may be revealed by clicking with the right mouse button on the blue spheres.
4. Visualisation of the Adit 6 and S15 geology:
   - Select the encrypted model Adit6andS15.enc.faces. The visualisation of the lithology in Adit 6 and S15 will be automatically loaded
5. Visualisation of the Adit 6 groundwater chemistry data:
   - Select the encrypted model Adit6geochem.enc.faces. Then select the analysis by pressing Ctrl-b, choosing either GWchemDEC2000.pdat or GWchemMAY2000.pdat and finally selecting the chemical component that should be visualised. The analytical results can be revealed by clicking on the cubes with the right mouse button.

All of the visualisations may be rotated or sliced. To rotate the models, hold the shift key and left mouse button simultaneously. To slice the model use the function keys F1 to F6 or Menu 2[1] on the EarthVision interface.

A2.4.2 Background to the development of the model

The Initial Geological Model

During the early course of Phase IV, an Initial Geological Model was constructed (Figure A2.1). This Initial Geological Model was built using a subset of the available well logs and the general geological map of the Maqarin area (Figure 2-2 of Smellie, 1998). Only seventy vertical wells were initially used in the interpretation. In addition, contour data were digitised from available topographic maps and from this a Digital Terrain Model (DTM) was constructed for import into the EarthVision modelling environment. However, ground levels in the well logs did not match the elevations in the DTM. The discrepancies were not systematic, as may be expected by the well logs recording depths from an artificial datum such as Kelly Bushing or Derrick Floor. Initially it was assumed that the discrepancies were caused by errors in the well logs. Therefore, new ground levels were calculated from the gridded DTM data.

The Initial Geological Model includes the following units:

- Alluvium (in the Yarmouk River channel)
- Soil (on the hill tops)
- Basalt
- Chalky Limestone Formation
- Bituminous Marl Formation
- Amman Formation

[1] To navigate to menus in the EarthVision 3D Viewer interface, simply type the number required.

The dimensions of the initial model are 3000 x 2000 x 600 m and are defined by the local coordinates:

- X minimum: 230000.
- X maximum: 233000.
- Y minimum: 236000.
- Y maximum: 238000.
- Z minimum: -200 metres above sea-level (masl).
- Z maximum: 400 masl

The alluvium, soil and basalts were modelled as isopachs, defined using a combination of outcrop information and well data. Eighteen wells were available for defining the alluvium surface, eleven for the soil surface and fifteen for the basalt. Additional data were interpreted to guide extrapolation of the isopach maps. Following the construction of isopach grids, the base of each unit was calculated by subtracting its thickness from the DTM surface.

The interpretation of the base Chalky Limestone Formation was based on outcrop and Twenty-two well logs that were combined in a file and gridded directly. The base of the Bituminous Marl Formation is present in only a few vertical boreholes. Therefore, a shape transfer method was applied to the base Chalky Limestone Formation surface to generate an interpretation of the base Bituminous Marl Formation surface that had the same general shape as the base of the Chalky Limestone Formation, but was 200-220 metres deeper.

Figure A2.1 The Initial Geological Model of the Maqarin area, viewed from the north west

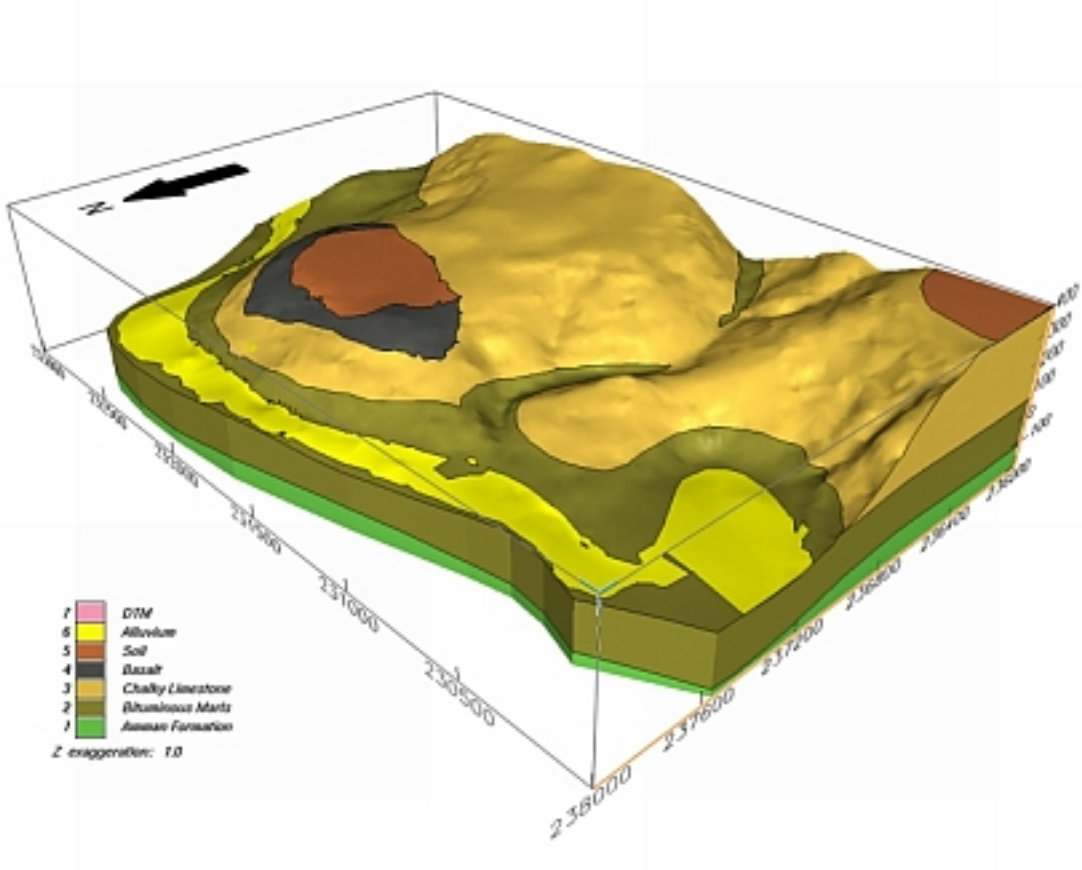

In the Initial Geological Model, the water table was modelled directly from well measurements. Sixteen wells were used. The data were gridded directly in order to

generate the water-table surface. Two gridding algorithms were used, first, a minimum tension algorithm and second, a second-order trend surface corrected to the water-table depths measured in the wells.

Three geological models were initially constructed: the first model, named *simple.faces*, did not include the water table (Figure A2.1). The second and third models, *water.faces* (Figure A2.2) and *water_t2s.faces*, (not shown) incorporated the models of the water table constructed using the minimum tension and trend gridding algorithms respectively.

The Refined Geological Model

Due to limitations of the Initial Geological Model, a second phase of modelling was subsequently undertaken. The dimensions of this later model, termed the Refined Geological Model (Figures A2.3 and A2.4), were extended to 3000 x 2500 x 800 m and are defined by the local coordinates:

- X minimum: 230000.
- X maximum: 233000.
- Y minimum: 236000.
- Y maximum: 238500.
- Z minimum: -400 masl.
- Z maximum: 400 masl.

Figure A2.2 The Initial Geological Model of the Maqarin area including an interpretation of the water table surface, illustrated by the red line, constructed using a minimum tension algorithm. A 3D block has been removed from the model to allow for 3D visualisation of the geological structure.

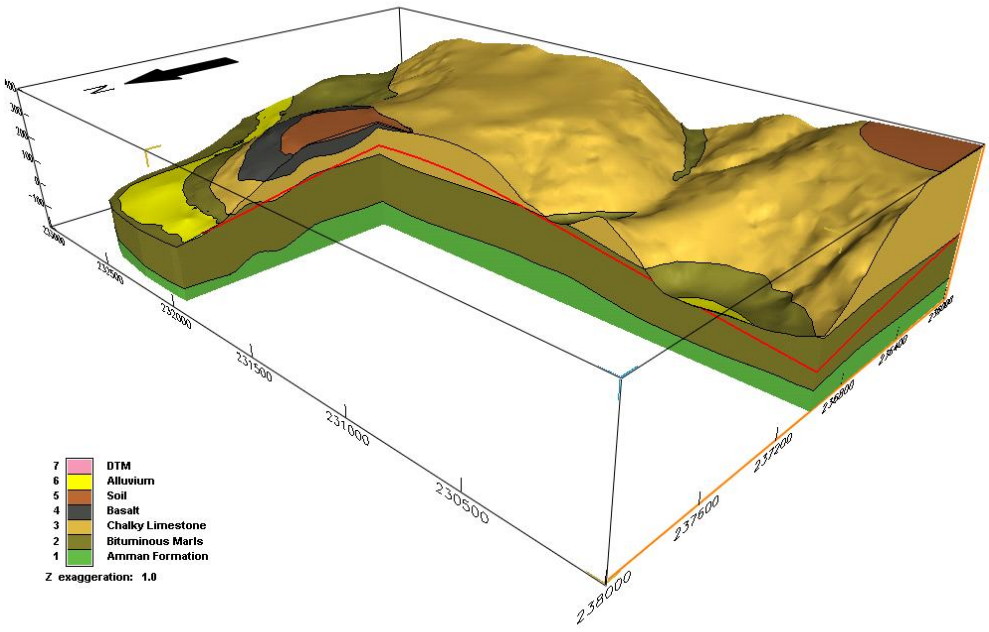

In order to extend the model to the north of the Yarmouk River valley, photocopies of a previously published Maqarin geological map were used. The geological map was prepared by Harza during site investigations related to Stage III of the Jordan Valley Irrigation Project (Jordan River Authority, 1980). The contours on the map were poorly reproduced during the photocopying and in a number of areas the form of the contours had to be interpreted and hand-drawn. Errors of the order of a few tens of metres are possible in the interpretation.

Several sets of data were available to refine the interpretation of the Bituminous Marl Formation, compared to that produced in the Initial Geological Model. These included:

- The geological map produced by the Jordan River Authority (1980). In particular, this provided the crop line of the top of the Bituminous Marl Formation on the northern side of the Yarmouk River Valley. On the southern side of the Yarmouk River Valley the crop line of the top of the Bituminous Marl Formation is covered by Quaternary deposits except in a few locations.
- Well logs (Smellie, 1998). In order to extend the well database available for modelling the top Bituminous Marl Formation, the x and y locations of the base of the wells were digitised and used to calculate the trajectory of the inclined wells. In total, sixty-one wells were identified as having an inclined trajectory. Of these, the base of eleven wells could not be identified on the geological map (Jordan River Authority, 1980). In addition, some wells could not be located on the map or their inclination could not be determined.
- The general geological map of the Maqarin area was also used (Figure 2-2 of Smellie, 1998). This map includes the crop line used to construct the interpretation of the top of the Bituminous Marl Formation in the Initial Geological Model.
- A structure contour map of the top of the Bituminous Marl Formation (Figure A-2 of Smellie, 1998). This map includes three sets of information. First, contours illustrating an interpretation of the anticline and its extrapolation. Second, an interpretation of the detailed structure of the top of the Bituminous Marl Formation in the location of the mine adits. Third, the crop pattern of the top of the Bituminous Marl Formation.

Figure A2.3 The Refined Geological Model of Maqarin, viewed from the north west

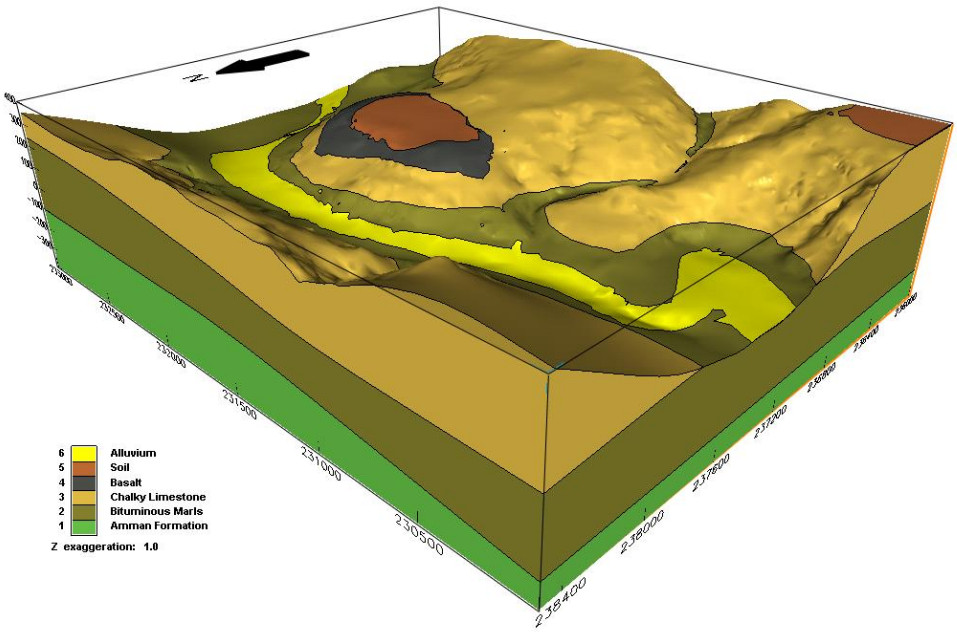

The different datasets are not consistent with each other. Indeed, even the three sets of information in the structure contour map of the top Bituminous Marl Formation (Figure A-2 of Smellie, 1998) are inconsistent. Therefore, a number of alternative models were constructed and evaluated. The final interpretation of the top Bituminous Marl Formation was based on a combination of different sets of data, as follows:

- To the south of the Yarmouk River Valley, the crop line indicated on the general

geological map of the Maqarin area (Figure 2-2 of Smellie 1998) was used. The crop line drawn on the structure contour map of the top of the Bituminous Marl Formation (Figure A-2 of Smellie 1998) did not correlate with the shape of the topography. Small lengths of crop line were indicated on the geological map (Jordan River Authority, 1980) but, compared with the crop line used, these data did not correlate well with the shape of the topography.

Figure A2.4 The Refined Geological Model of Maqarin, viewed from the south east

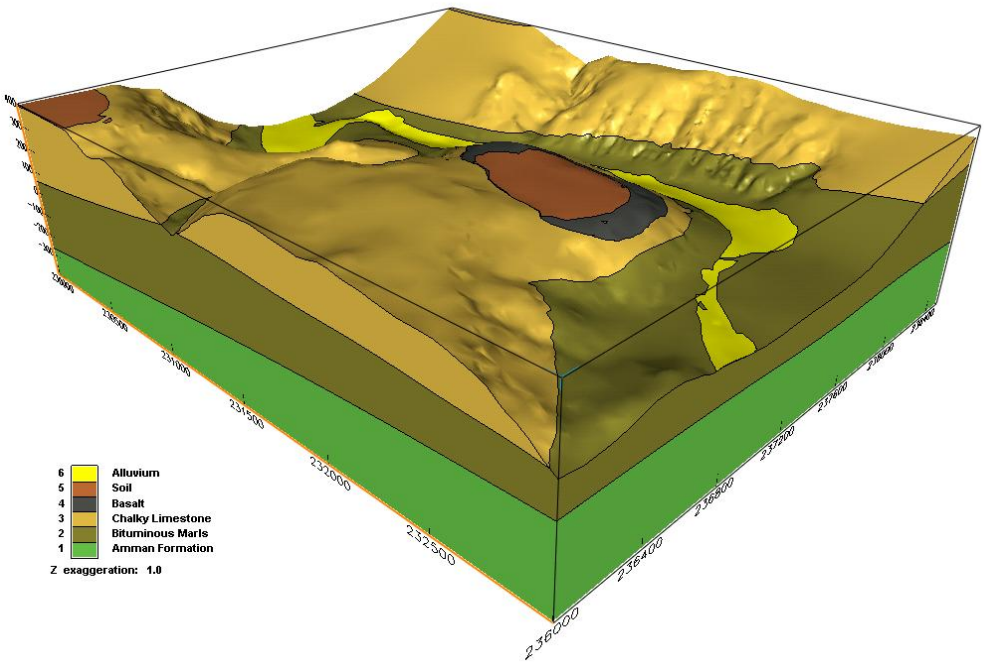

- To the north of the Yarmouk River Valley, the crop line indicated on the geological map (Jordan River Authority, 1980) was used. It was considered that this is appropriate as the lithostratigraphic contact can be observed in the field. An alternative dataset was available from the structure contour map of the top of the Bituminous Marl Formation (Figure A-2 of Smellie, 1998). However this dataset was poorly located in comparison with the data from the geological map.
- The elevations of the top of the Bituminous Marl Formation in the well logs were used. However, to the north of the Yarmouk River Valley the elevations recorded in the wells did not correlate with the elevations indicated by the crop line. Therefore, the data from the wells on the north side of the Yarmouk River Valley were not used.

Following the construction of the top of the Bituminous Marl Formation, the other surfaces were added in order to build up the stratigraphic sequence in the geological model. First, the Alluvium, Soil and Basalt were incorporated by directly transferring the interpretation in the Initial Geological Model into the Refined Geological Model. Second, a new interpretation of the top Amman Formation was constructed. The data available for this surface included the structure contour map of the top of the Amman Formation (Figure A-1 of Smellie, 1998) and the elevation of the top Amman Formation in ten wells. The new interpretation was constructed by gridding all of the available data.

As described above, in the Initial Geological Model the water table had been interpreted by two different algorithms, both of which are distance-weighted methods. This means that, outside the areas in which there is data control, the interpretation is constructed by extrapolation. However, in reality the water table is likely to be closely related to the

topography and in the Maqarin area the topography is quite variable (compare the smooth form of the water table and the relatively irregular form of the topography in Figure A2.2). In particular, the Yarmouk River Valley is a large geomorphological feature and there are also large valleys cut into both the north and south slopes. These include Wadi Sijin in the west and Wadi Shallala in the east.

In the further phase of work, in order to construct a more realistic interpretation of the water table, the data used to develop the Initial Geological Model were re-evaluated and augmented. First, the water-table elevations were plotted against the topography for all sixteen wells used initially. Regression of the data was used to determine the relationship between the elevations of the water table and the surface (Figure A2.5). Second, the wells used in the analysis were reviewed. In particular, it was suggested that there might be perched water tables in the Maqarin area that formed above relatively impermeable clay-rich Bituminous Marl horizons. Therefore, the water-table elevations were plotted in EarthVision and wells with anomalous values were deleted from the dataset. Four wells were removed from the dataset and the remaining data plotted as before (Figure A2.6).

Regression analysis indicated the following relationship between the water table elevation and the topography:

$$y = 0.53x + 14.43 \quad \text{[Equation 1]}$$

where y is the water table elevation and x is the topographic elevation.

Figure A2.5 Analysis of the relationship between the water table and the topography, based on all sixteen wells used in the development of the Initial Geological Model

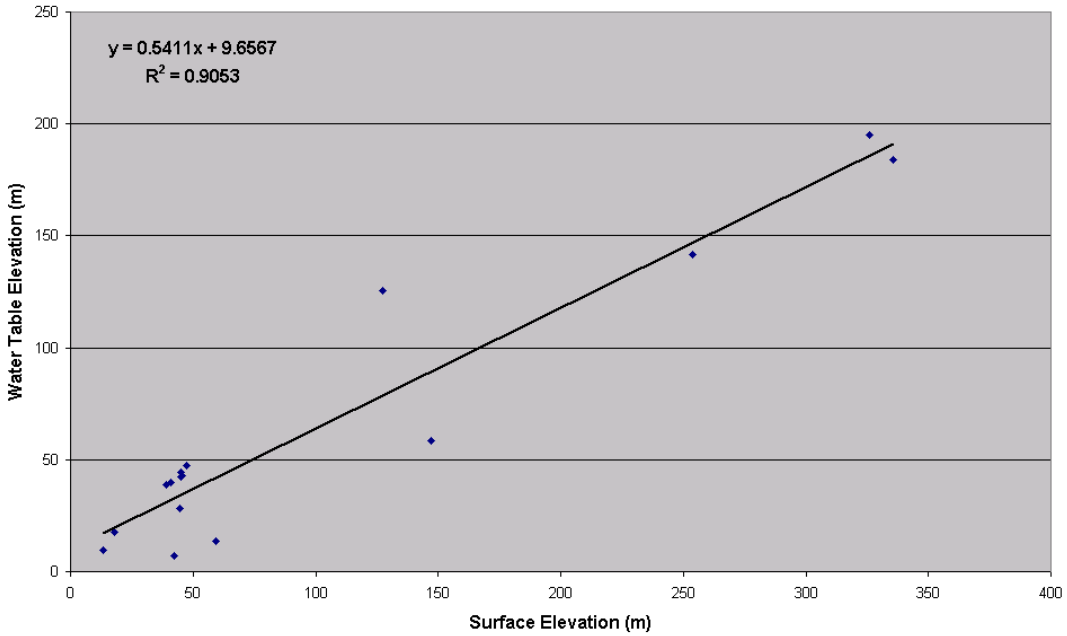

Figure A2.6 Analysis of the relationship between the water table and the topography, based on twelve wells used in the development of the Initial Geological Model

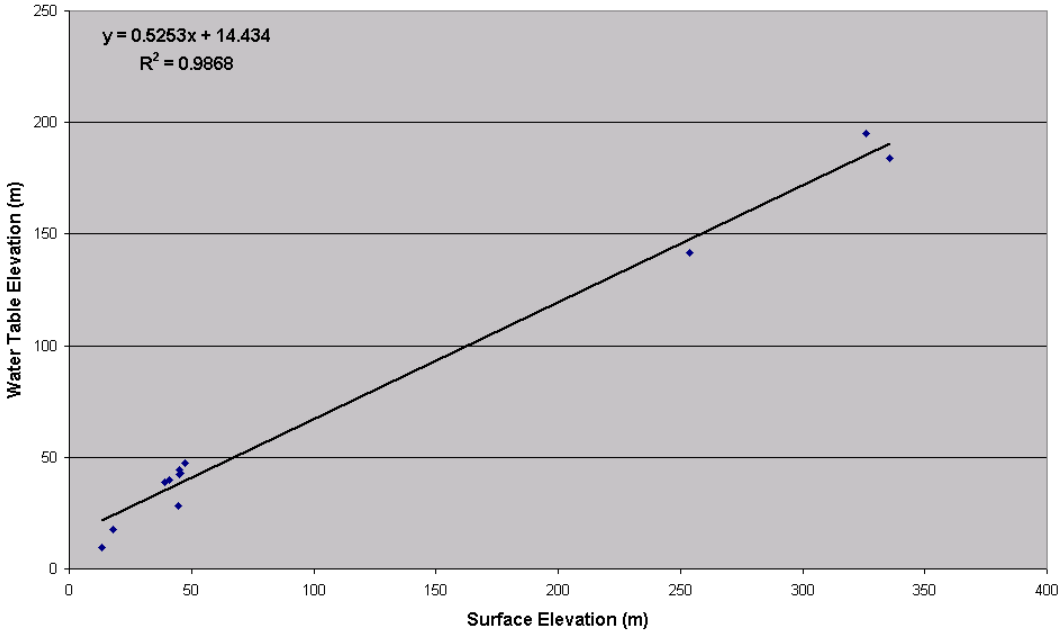

Following the data analysis, a water-table surface was constructed, derived from the topography using the regression equation [1]. The water-table surface was then incorporated into the geological model as illustrated in Figure A2.7. This interpretation is considered more appropriate than the initial interpretation since the water-table surface intersects the topography in the river valleys across the model.

The interpretation of the water table initially made use of the measurement of the water-table elevation in sixteen wells. However, data on the water-table elevation were available for a total of fifty-nine wells. Therefore, as a further refinement the water-table interpretation was re-evaluated and based on the more extensive dataset.

Of the fifty-nine wells for which water table data existed, thirty-five measurements were from inclined wells and nineteen from vertical wells. The remaining five wells were from outside the area of the geological map (Jordan River Authority, 1980) and therefore it could not be determined whether they were vertical or inclined wells. For the purposes of the analysis it was assumed that they were vertical. Since these wells were located away from the Yarmouk River, this approximation was supported by observations that the inclined wells were drilled close to the Yarmouk River, which is in the centre of the map.

The water-table data on the well logs were poorly documented. The logs indicated that the measurements were water levels with units of ft MSL, which is assumed to be feet above mean sea-level. However, the data are compatible with all other measurements which are in metres. Modelling for the Initial Geological Model assumed that the measurements were elevations in metres, rather than depths. Also, the measurements are consistent with the ground-surface elevations indicated on the well logs which support the assumption of the units being metres above sea level.

Figure A2.7 The Initial Geological Model of the Maqarin area including an interpretation of the water table surface, illustrated by the red line, constructed using the equation derived from the analysis shown in Figure A2.6

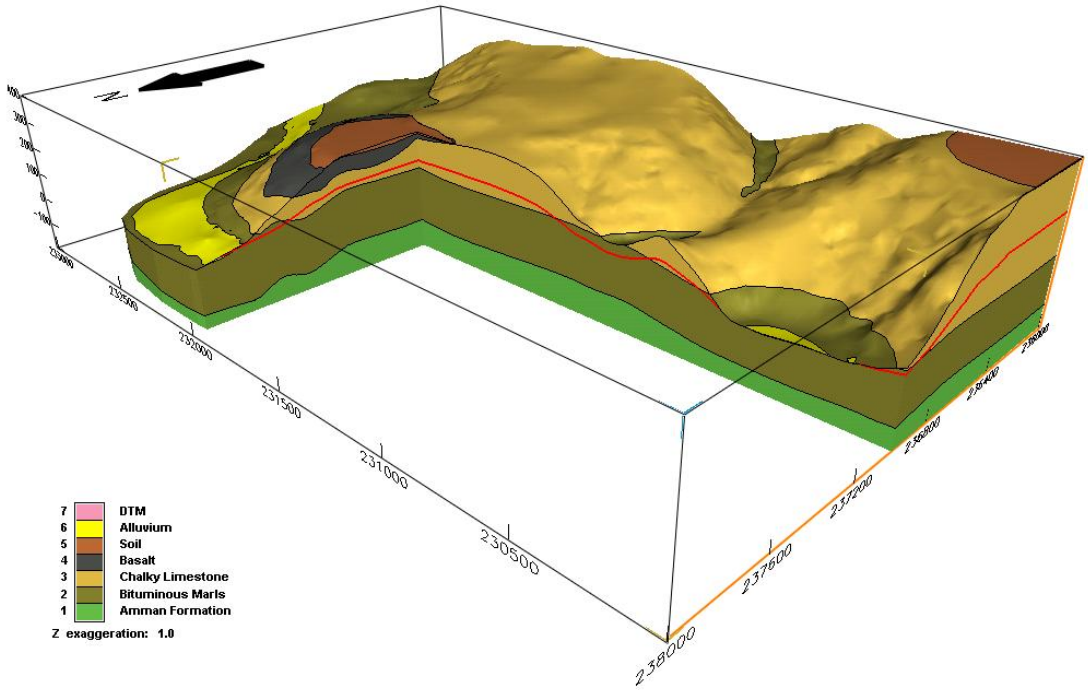

The data recorded for the inclined wells is also specified with units of ft MSL. For the purposes of analysing the data, it was assumed that the data were derived in a similar fashion. That is, the data were elevations, in metres, calculated by subtracting the depth of the water table measured in the well, from the measured ground elevation. Although there is no independent evidence to support this assumption, the subsequent analysis of the derived data indicated a good correlation between the inclined and vertical wells and, therefore, that the assumption could be a sensible one.

In order to convert the water-table data recorded in the logs to elevations, a three-step procedure was followed. First, the recorded data were modified to give depths in the well using the elevation given in the well log. Second, the angle of the well was calculated using the x and y coordinates of the top and base of the well, and the total depth (i.e. length) of the well. Third, a new elevation for the water table was derived using the angle of the borehole and the calculated depth.

Once the well data had been collated, the water-table elevations were plotted against the topographic elevations, as for the analysis during the development of the Initial Geological Model. The plot for all of the wells is illustrated in Figure A2.8. A revised interpretation, with potentially anomalous well data removed was developed and is illustrated in Figure A2.9. The following revised relationship between the water table elevation and the topography was calculated:

$$y = 0.52x + 11.96 \quad \text{[Equation 2]}$$

where y is the water table elevation and x is the topographic elevation.

The basis for removing certain well data from the analysis was subjective. However, the general uncertainty regarding the input data and the close correlation achieved with the

final dataset supports this approach. In addition, the relationship calculated between the water table and surface elevations is consistent with that developed for the smaller dataset used for the interpretation of the water table in the Initial Geological Model (Equation 1).

A further revision to the water-table interpretation was to incorporate observations of the saturation state of rocks observed from within Adit A-6. In particular, during mapping of the Adit, it was observed that the rocks became saturated between 25 and 40 m from the front of the Adit entrance, and that the rocks were unsaturated beyond 320 to 350 m along the tunnel. The higher elevations of the water table at the front of the Adit are considered to be the result of the development of a recharge mound due to increased infiltration. The increase in infiltration above the front of the Adit is possibly due to its karstification and to the development of dilational structures associated with gravitational movements. Elsewhere in the area, the presence of dolines support a karstic interpretation for enhanced groundwater flow. In addition, along the road-cut from the plateau to the base of the river valley angular breccia and weathered gravel infills collapsed karstic structures in the Chalky Limestone Formation. It is noteworthy that the deeper parts of the Adit lie underneath the basalt and a palaeosol (see resistivity survey in section 2.3.5), both of which are of relatively low permeability and hence reduce infiltration potential.

Figure A2.8 Analysis of the relationship between the water table and the topography, based on fifty-nine wells used in the development of the Refined Geological Model

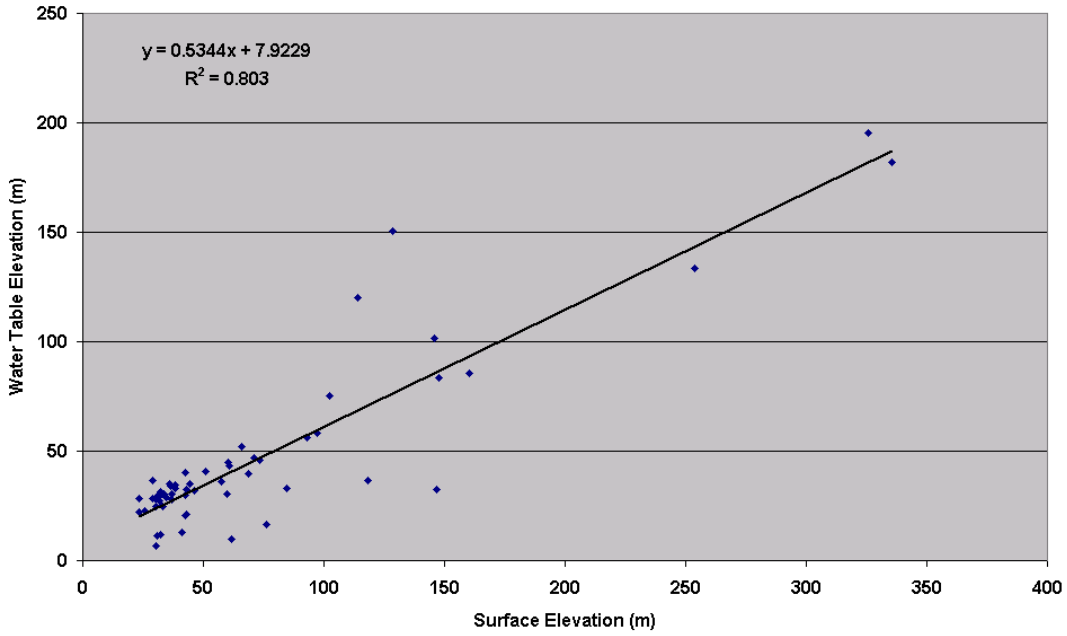

Figure A2.9 Analysis of the relationship between the water table and the topography, based on forty-five wells used in the final development of the Refined Geological Model

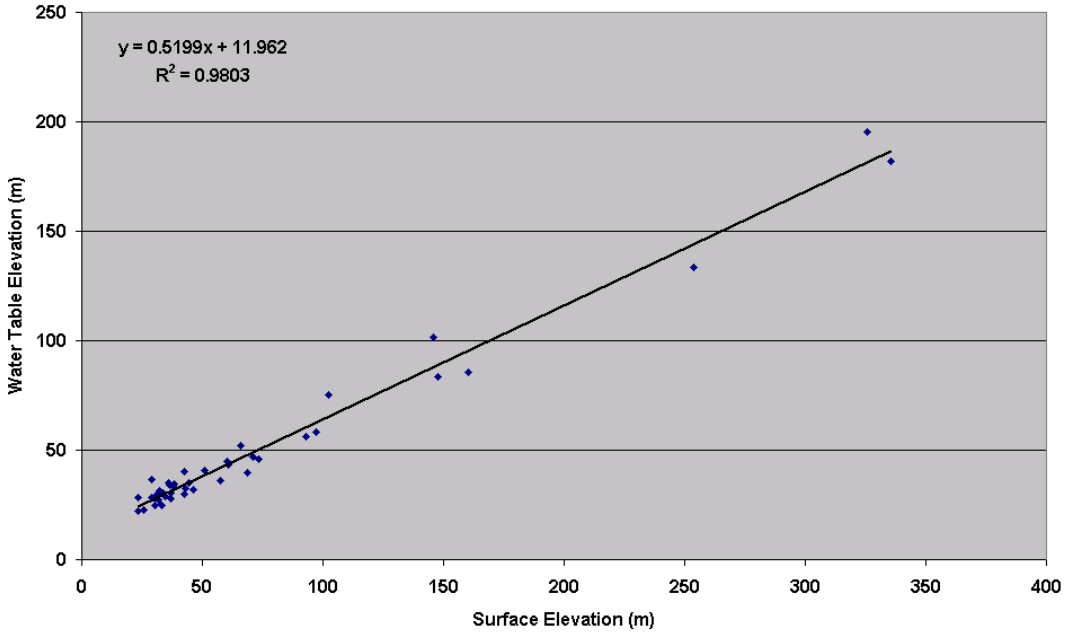

The water-table interpretation based on the relationship to the topography was modified to accommodate the above observations in Adit A-6. This was done by exporting the calculated grid to a data file, deleting the data in the vicinity of Adit A-6 and adding interpreted data that incorporated the observations made in Adit A-6. The final version of the water-table interpretation is illustrated in Figure A2.10.

Two electronic files have been prepared which allow the 3D geometry of the wells and the mine adits to be visualised alongside the geological models and the resulting images are illustrated in Figures A2.11 and A2.12. In Figure A2.11 the geometry of the wells is illustrated. To create this visualisation the top and bottom coordinate of each well was digitised from the geological map (Jordan River Authority, 1980), the elevation of the top of the well was calculated from the DTM, and the bottom elevation was calculated from the depth given in the well logs (Smellie, 1998).

The geometries of the adits (Figure A2.12) were determined in a similar fashion. All adits were assumed to be horizontal and therefore the elevation of their access point was determined from the DTM. In addition, the geometry of the side adit to Adit A6 was used.

The intersection of the side adit with the main adit was measured as 256 m from the access point during field mapping and this measurement was used in the visualisations.

In order to communicate the results of the fracture logging specifically undertaken in Adit A-6 (see Section 2.3) and to illustrate the spatial variability of different fracture infills, the Adit A-6 fracture log data have been visualised using EarthVision in a small-scale structural model of Adit A-6 (the *Adit A-6 Model,* see Figures A2.13 to A2.28). The model is nested within the larger-scale model illustrated above. It contains the same interpretation of the geology and the local water table as presented. The dimensions of the Adit A-6 Model are 40 x 160 x 100 m and are defined by the coordinates:

- X minimum: 231880.
- X maximum: 231920.
- Y minimum: 237590.
- Y maximum: 237750.

- Z minimum: 50 masl.
- Z maximum: 150 masl.

Two figures based on the EarthVision modelling are presented for each fracture fill. In the first figure, the strike and dip of the logged fractures are illustrated as disks along the trace of the Adit. In the second figure, the strike and dip of the logged fractures are illustrated as planar surfaces along the trace of the Adit. These surfaces have been extrapolated 10 m in each direction from the centre of the Adit. In most cases this may well overestimate the size of the fractures. However, this is intended to help in the visualisation of the orientation of the features, particularly when viewed interactively and rotated in EarthVision.

Figure A2.10 The completed Refined Geological Model of the Maqarin area, viewed from the north-west. The model includes an interpretation of the water table surface, illustrated by the red line, constructed using the equation derived from the analysis shown in Figure 2.46 and incorporating the observations made in Adit A-6 regarding the presence of a recharge mound, as described in the text. Adit A-6 is illustrated by the thick yellow line along the north-south section

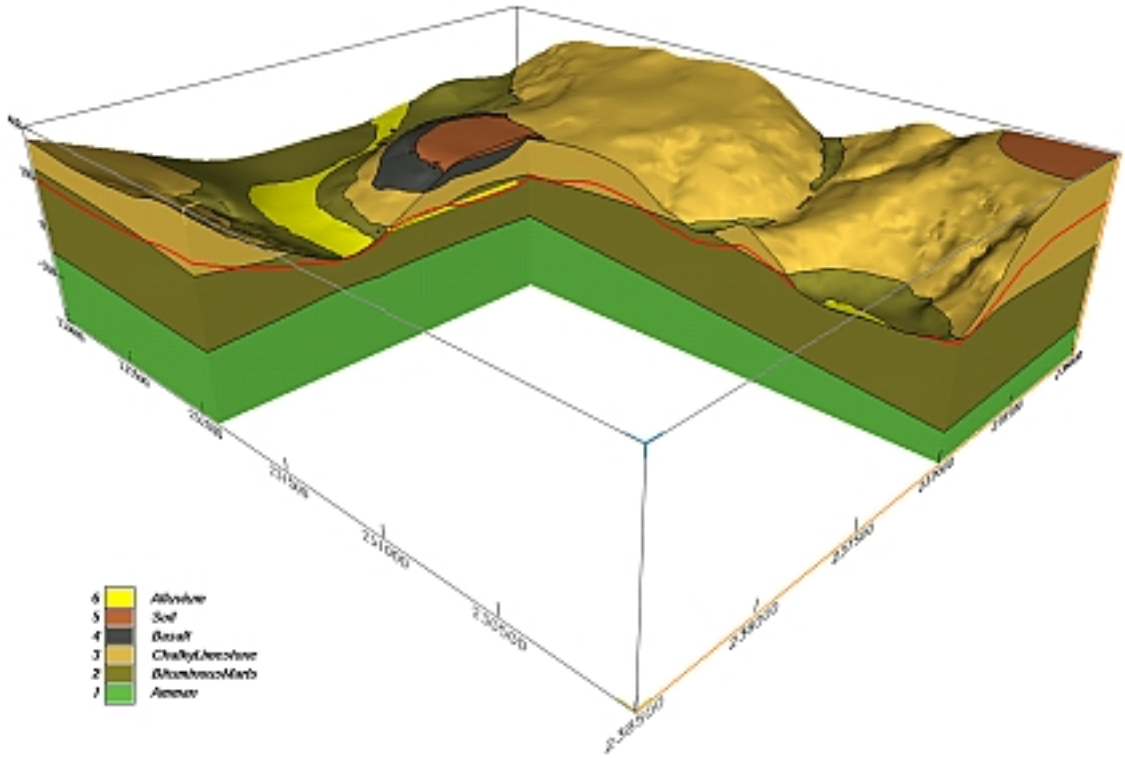

Figure A2.11 Visualisation of the wells drilled at the Maqarin natural analogue site

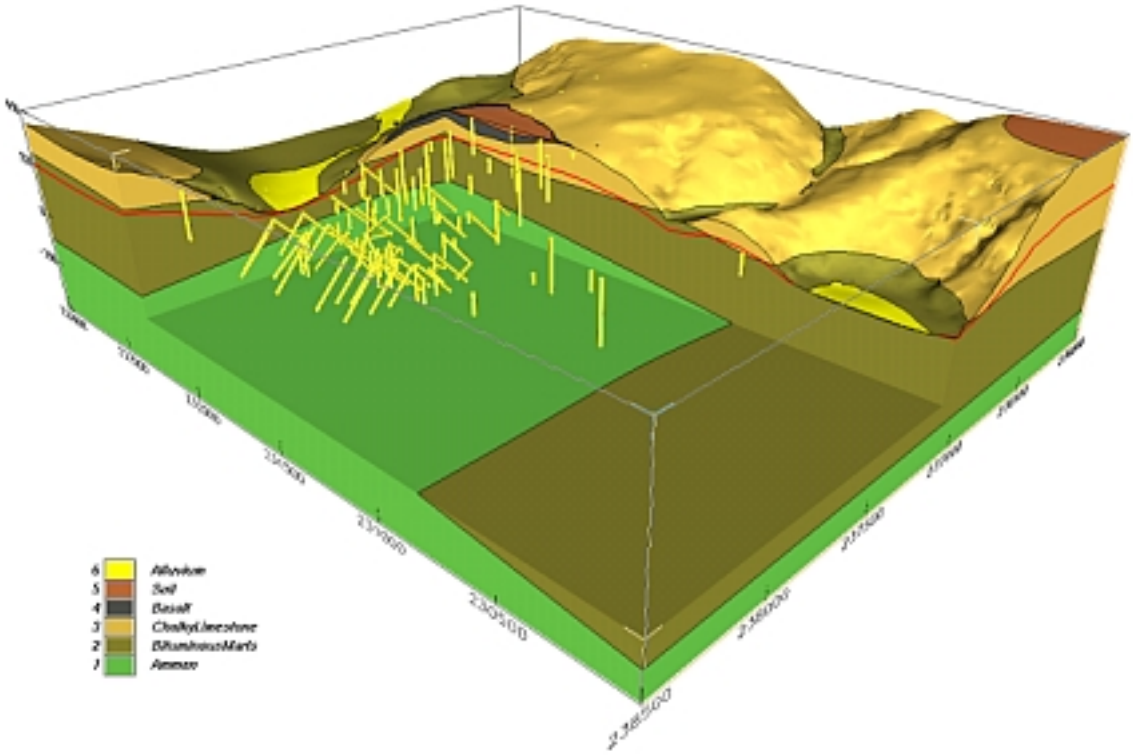

Figure A2.12 Visualisation of the adits at the Maqarin natural analogue site. The adits are numbered in the visualisation data files and may be identified by clicking on the data points in the viewer

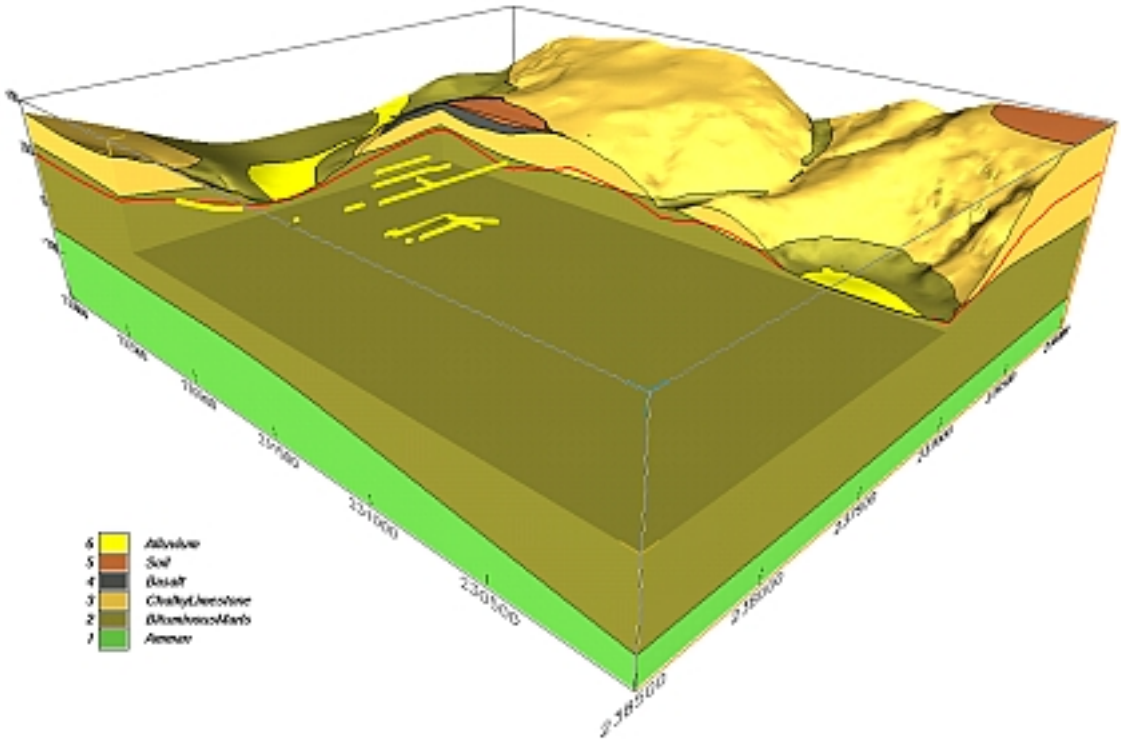

Figure A2.13 Visualisation of the CSH fractures logged in the first 130 m of Adit A-6. The fractures are visualised as yellow discs. The red line indicates the estimated water table

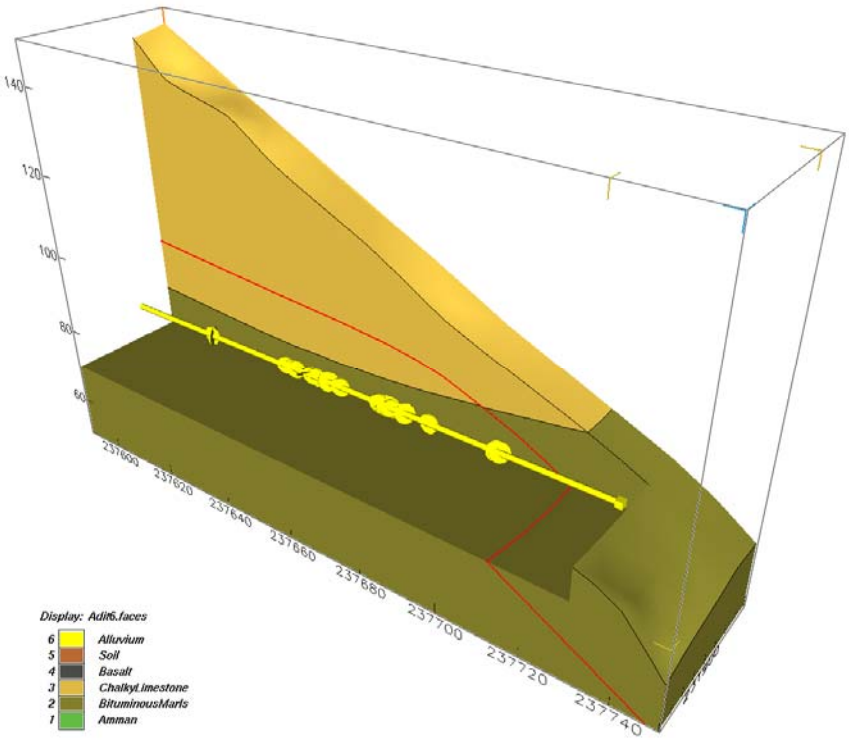

Figure A2.14 Visualisation of the CSH fractures logged in the first 130 m of Adit A-6. The fractures are visualised as red planes. The red line indicates the estimated water table

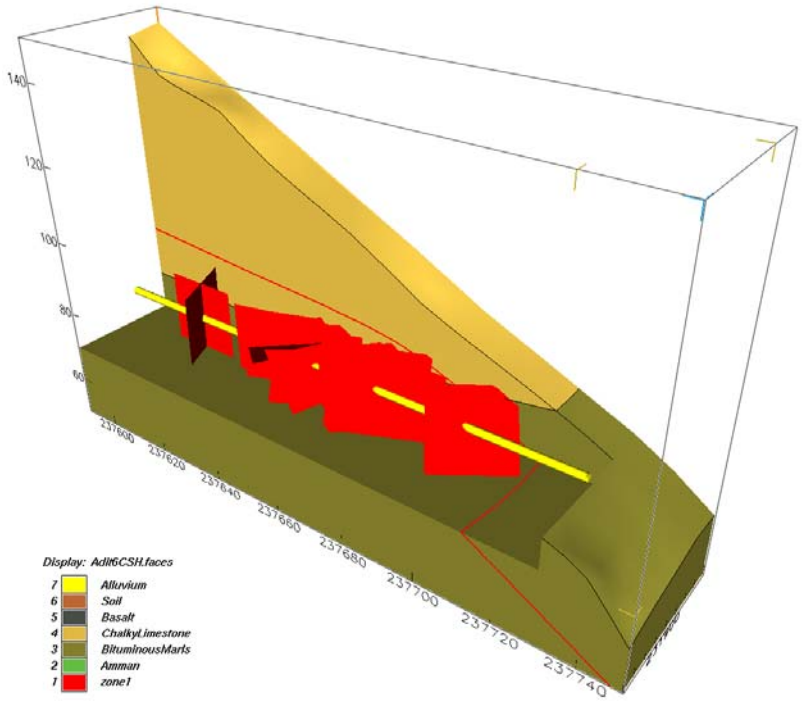

Figure A2.15 Visualisation of the Early Calcite fractures logged in the first 130 m of Adit A-6. The fractures are visualised as yellow discs. The red line indicates the estimated water table

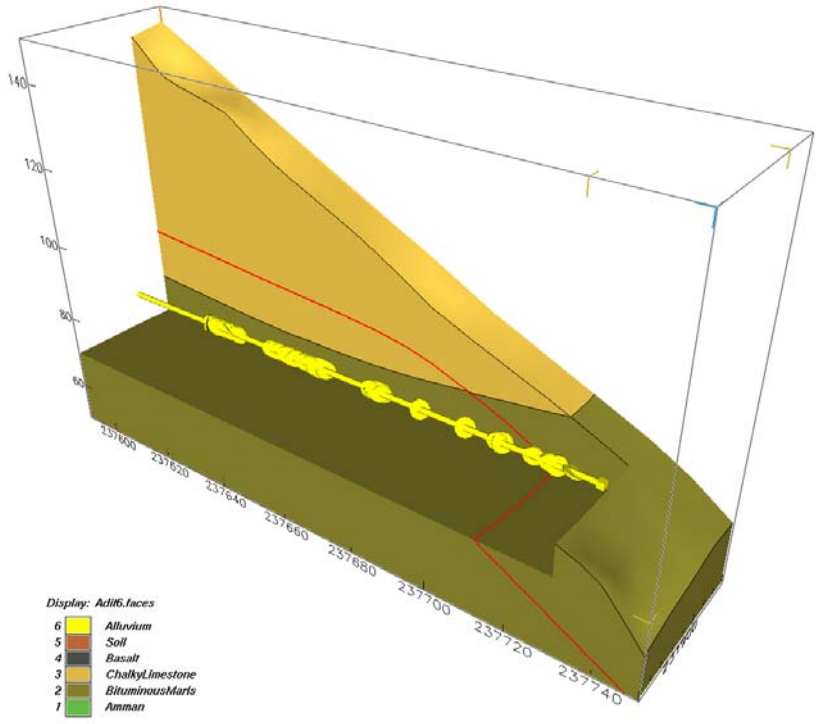

Figure A2.16 Visualisation of the Early Calcite fractures logged in the first 130 m of Adit A-6. The fractures are visualised as red planes. The red line indicates the estimated water table

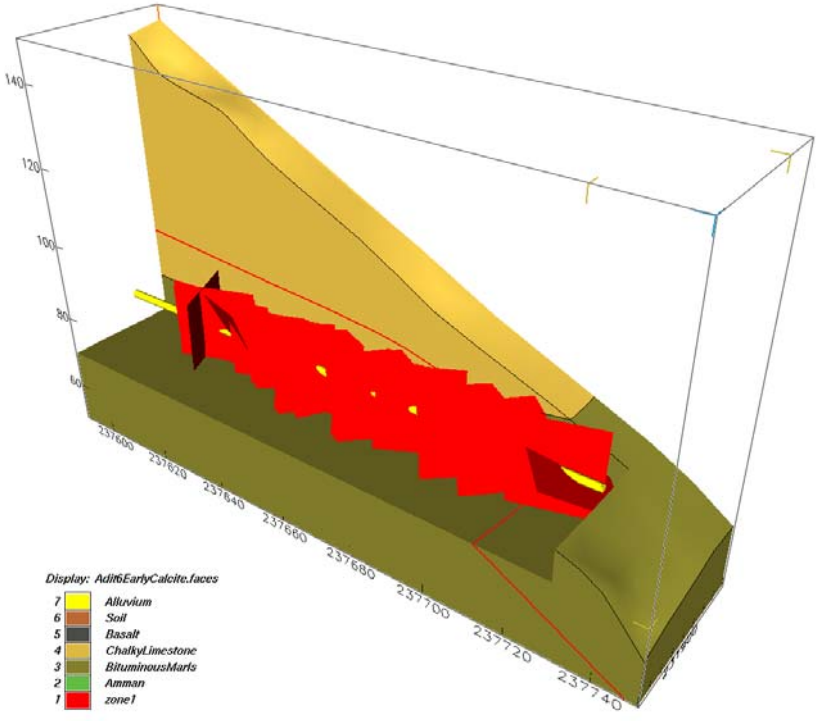

Figure A2.17 Visualisation of the Ettringite/Thaumasite fractures logged in the first 130 m of Adit

A-6. The fractures are visualised as yellow discs. The red line indicates the estimated water table.

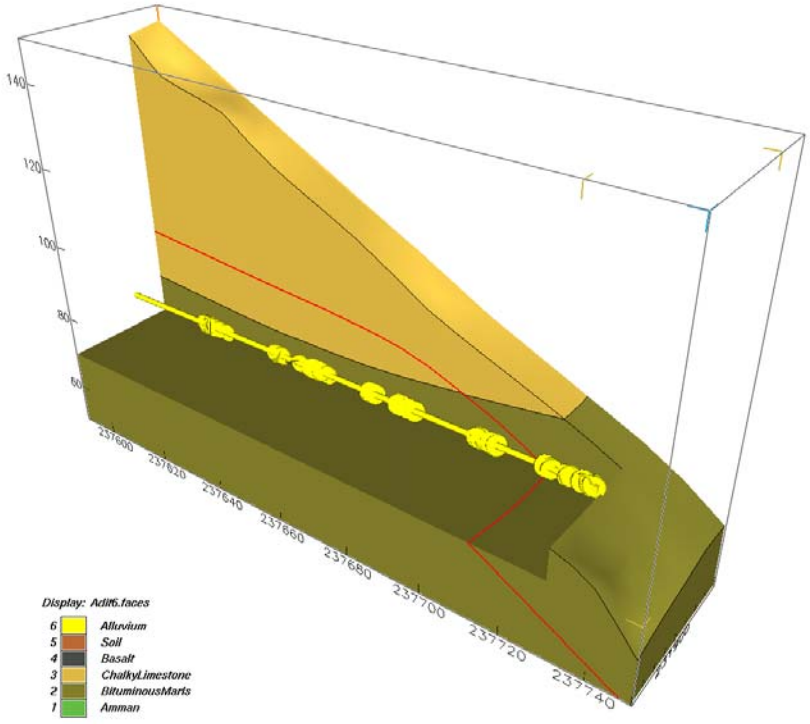

Figure A2.18 Visualisation of the Ettringite/Thaumasite fractures logged in the first 130 m of Adit A-6. The fractures are visualised as red planes. The red line indicates the estimated water table.

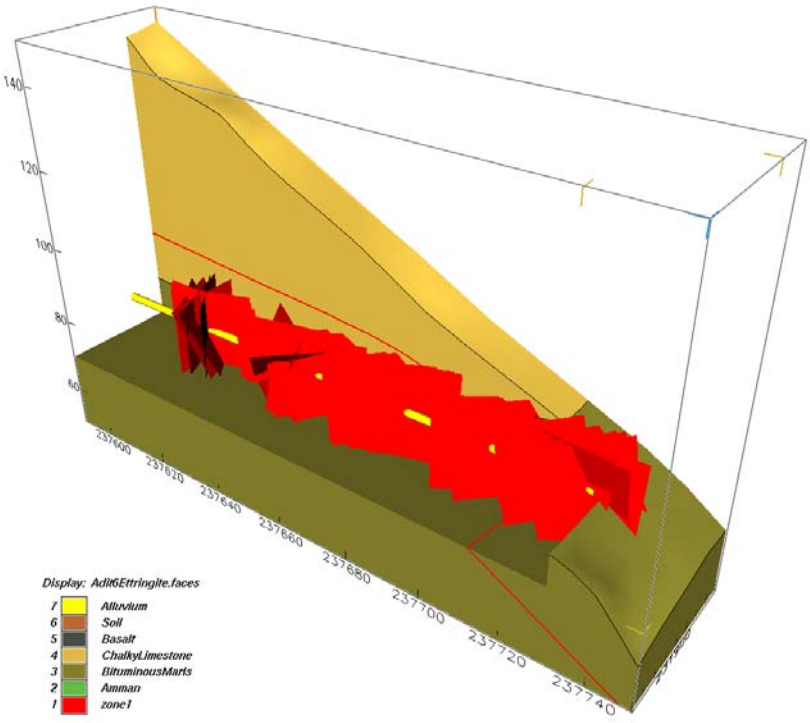

Figure A2.19 Visualisation of the Jennite fractures logged in the first 130 m of Adit A-6. The fractures are visualised as yellow discs. The red line indicates the estimated water table

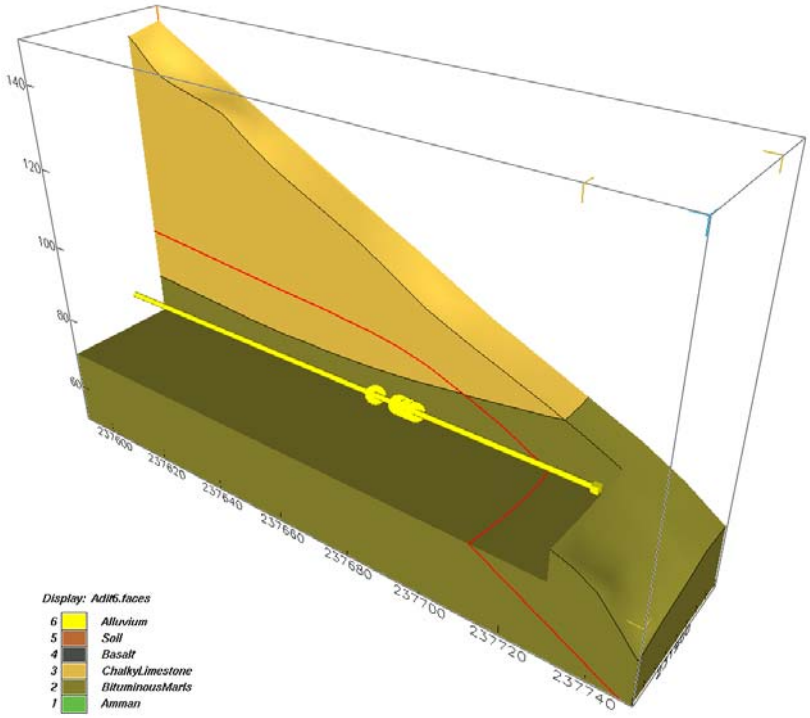

Figure A2.20 Visualisation of the Jennite fractures logged in the first 130 m of Adit A-6. The fractures are visualised as red planes. The red line indicates the estimated water table.

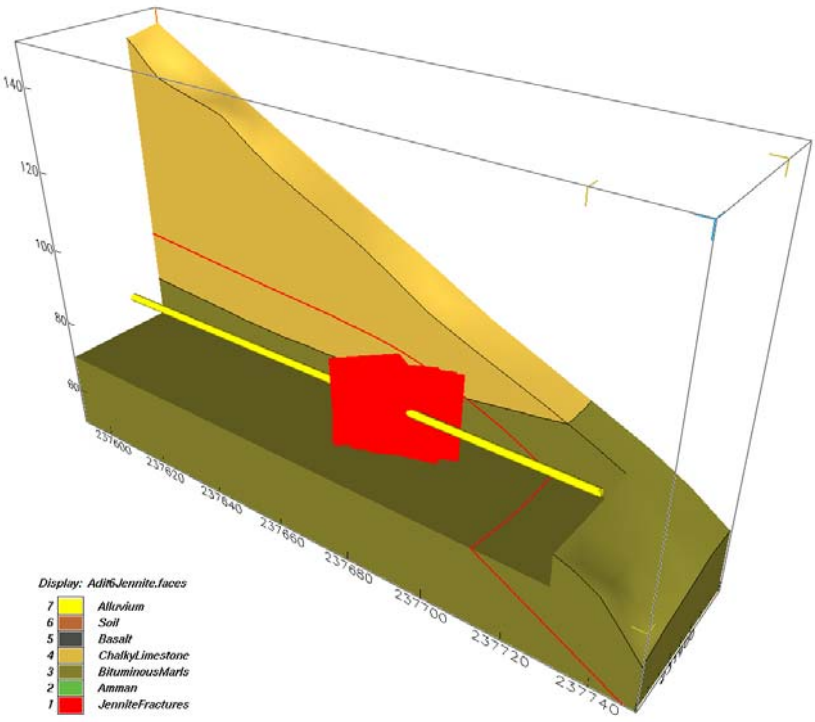

Figure A2.21 Visualisation of the Gypsum fractures logged in the first 130 m of Adit A-6. The fractures are visualised as yellow discs. The red line indicates the estimated water table.

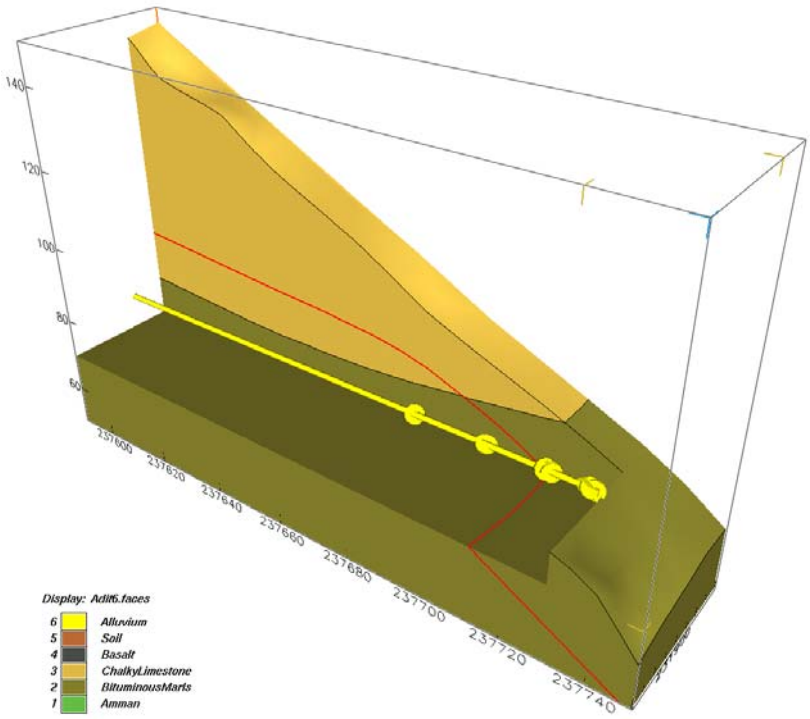

Figure A2.22 Visualisation of the Gypsum fractures logged in the first 130 m of Adit A-6. The fractures are visualised as red planes. The red line indicates the estimated water table

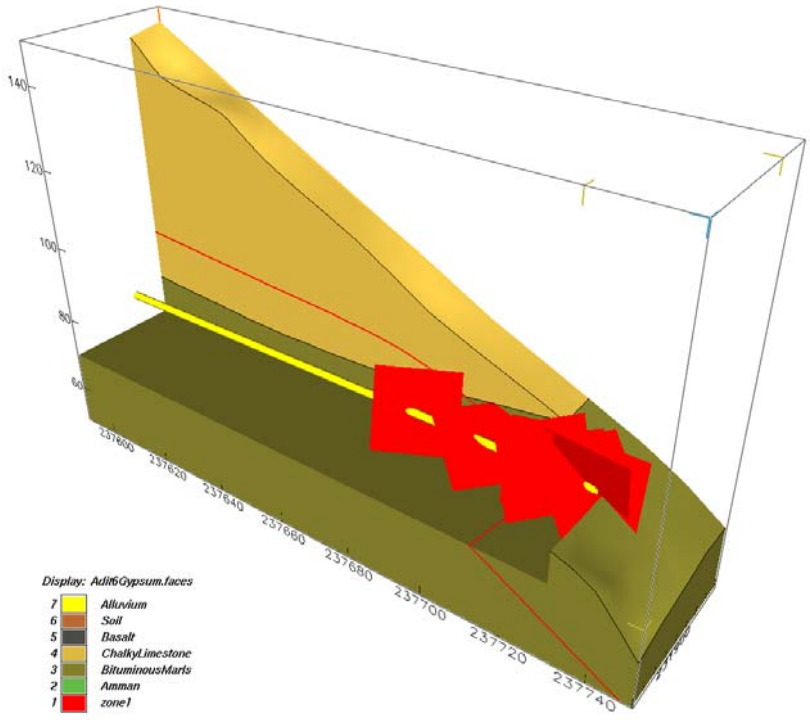

Figure A2.23 Visualisation of the Late Calcite fractures logged in the first 130 m of Adit A-6. The fractures are visualised as yellow discs. The red line indicates the estimated water table.

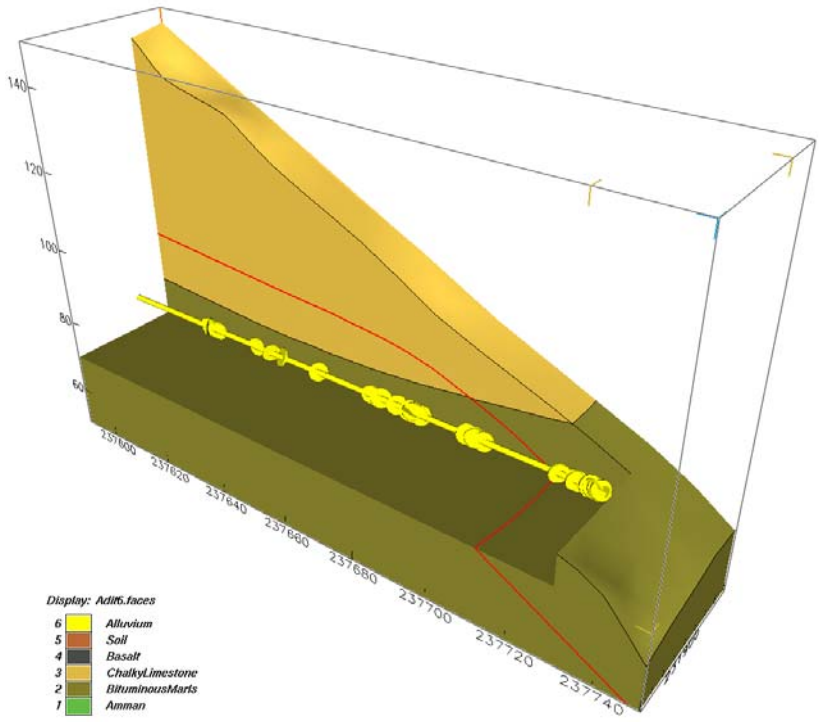

Figure A2.24 Visualisation of the Late Calcite fractures logged in the first 130 m of Adit A-6. The fractures are visualised as red planes. The red line indicates the estimated water table.

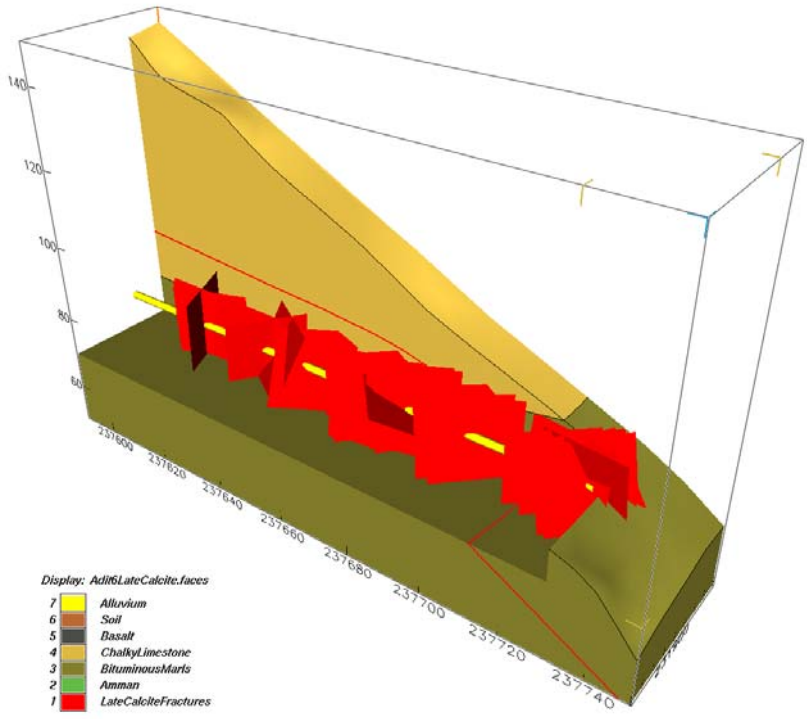

Figure A2.25 Visualisation of the Tobermorite fractures logged in the first 130 m of Adit A-6. The fractures are visualised as yellow discs. The red line indicates the estimated water table.

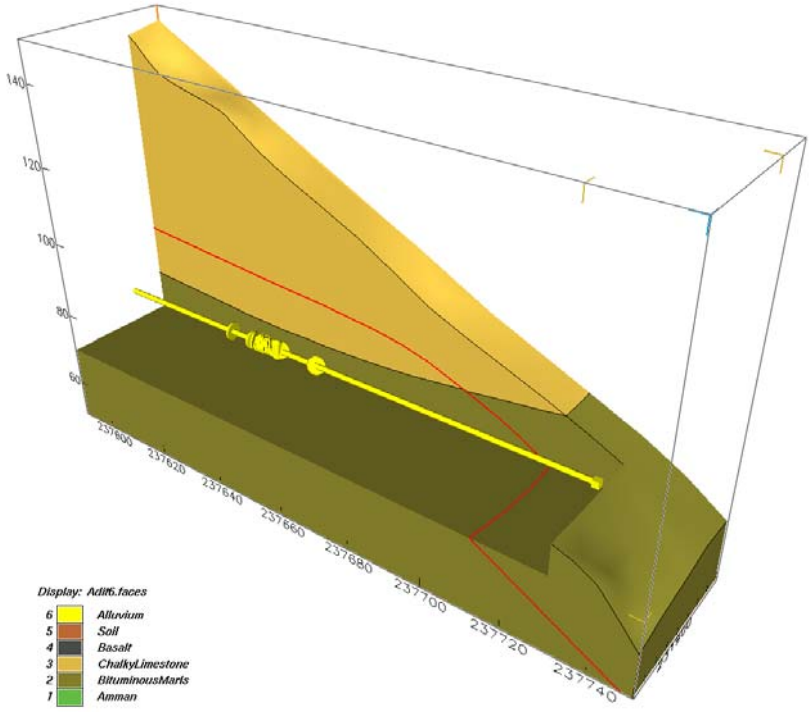

Figure A2.26 Visualisation of the Tobermorite fractures logged in the first 130 m of Adit A-6. The fractures are visualised as red planes. The red line indicates the estimated water table.

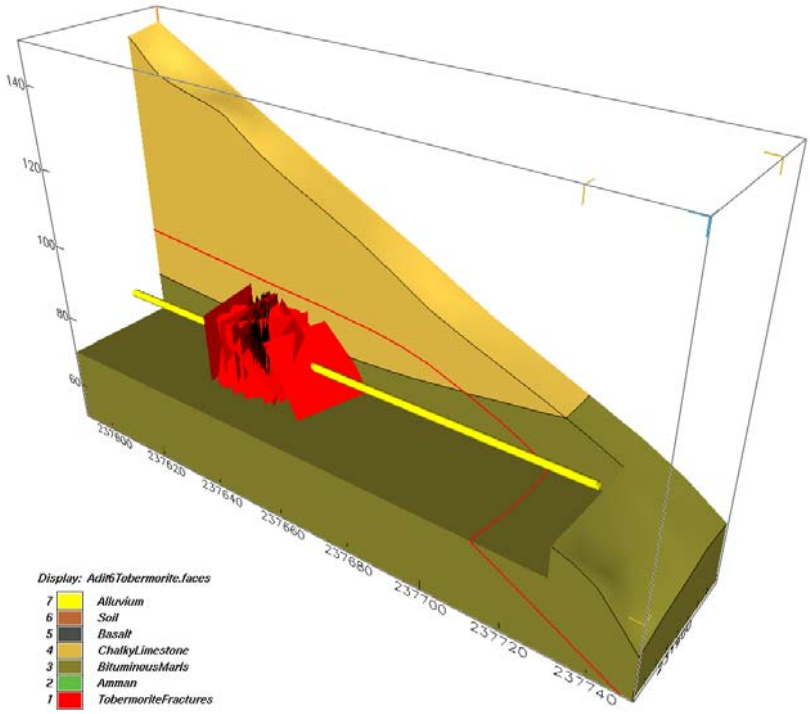

Figure A2.27 Visualisation of the unmineralised fractures logged in the first 130 m of Adit A-6. The fractures are visualised as yellow discs. The red line indicates the estimated water table

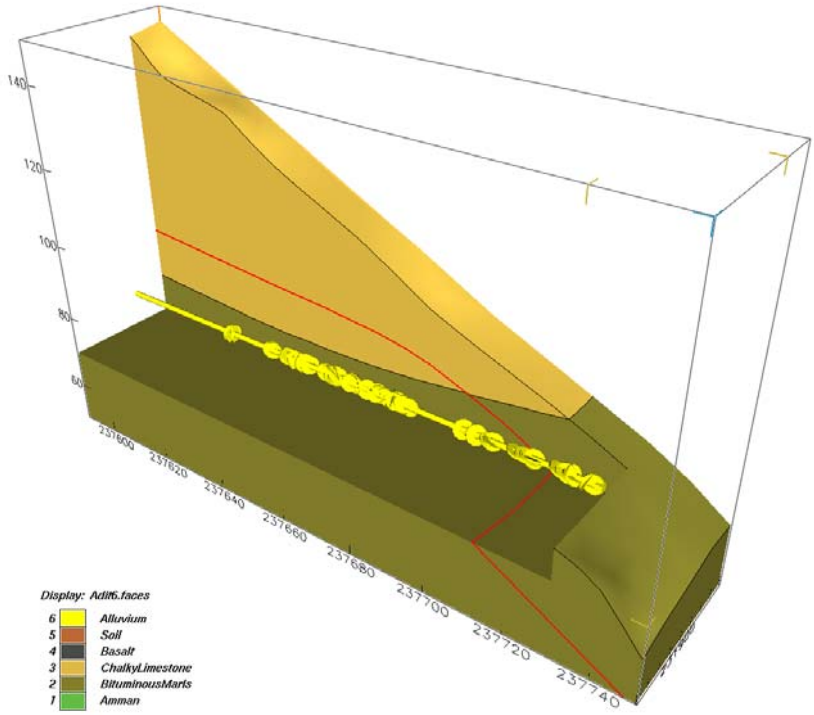

Figure A2.28 Visualisation of the unmineralised fractures logged in the first 130 m of Adit A-6. The fractures are visualised as red planes. The red line indicates the estimated water table.

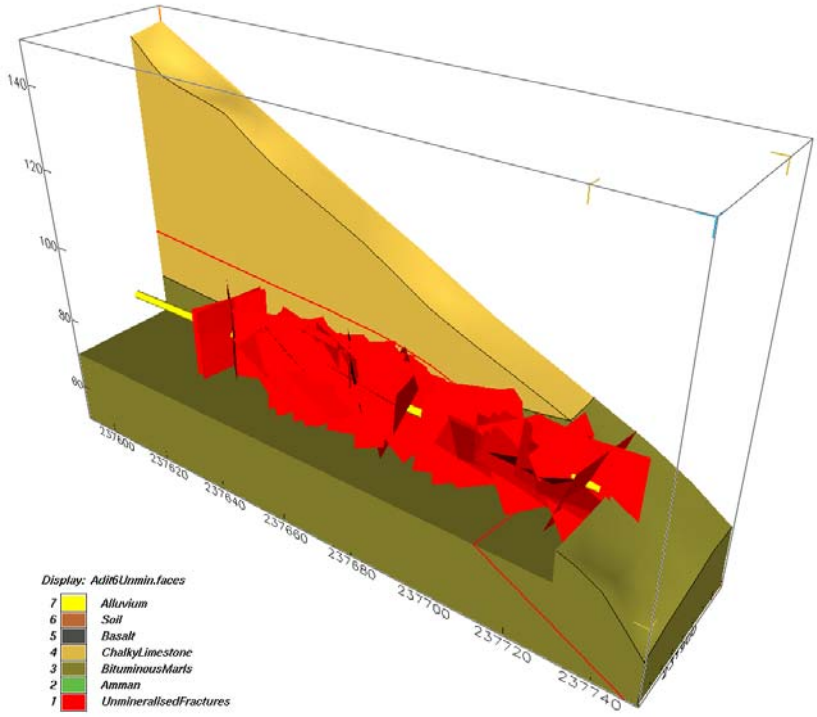

Figure A2.29 Visualisation of the location of samples collected in Adit A-6 for magnetic investigations. The locations are illustrated as blue spheres. The first sampling point has been highlighted in white, and the data for this point, including the sample reference number, is provided in the white box. The spheres may be rescaled interactively within EarthVision.

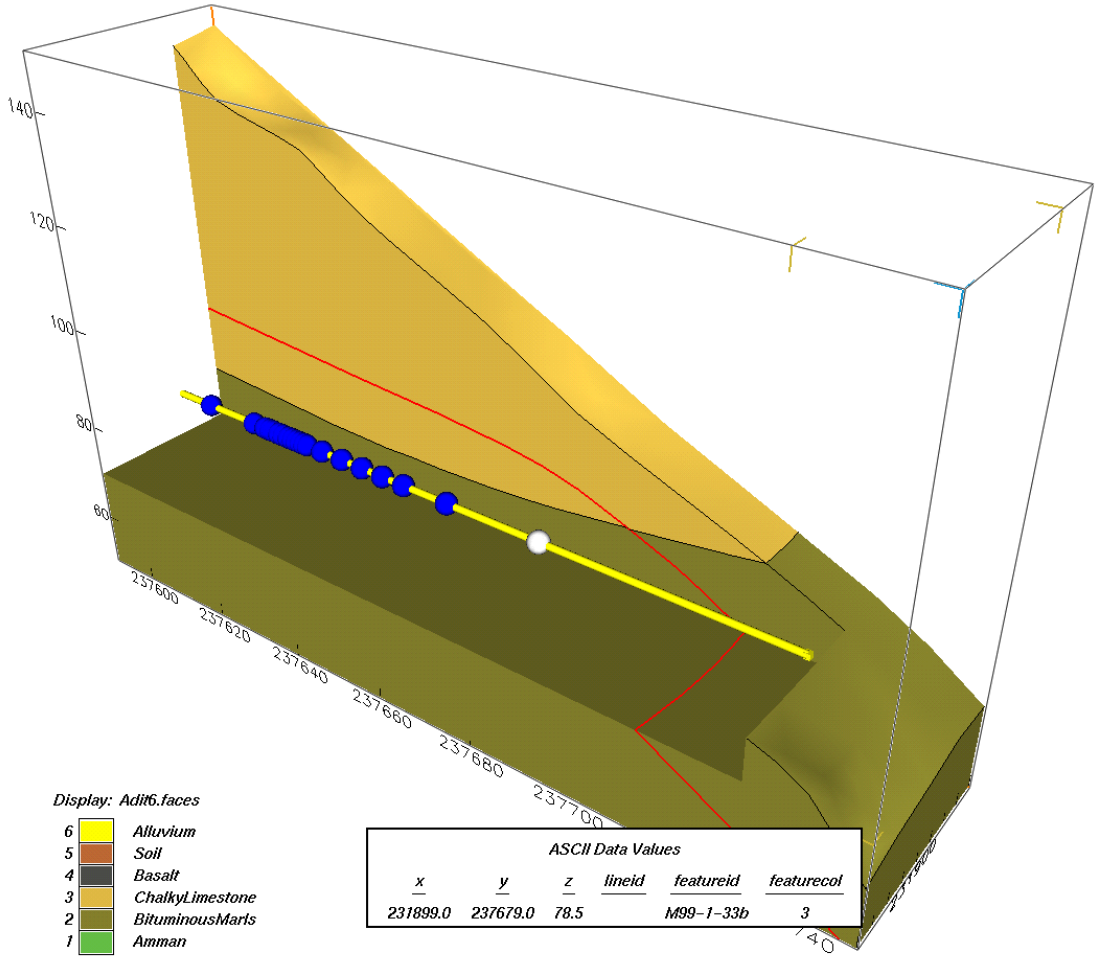

In addition, the locations of samples collected in Adit A-6 for magnetic investigations (unoriented samples from the west wall) were visualised (Figure A2.29, see Chapter 4 for detail). The visualisations represent the sample locations as spheres. The sample reference is included in the visualisation.

The lithology of Adit A-6 and that of core recovered from a previously sunk borehole adjacent to the Adit, number S14 (see Smellie, 1998), was logged during 1999 and 2000. Figure A2.30 presents a visualisation of the logging data. In the figure the lithologies mapped in the core and the Adit are represented by specific colours:

- Green represents the Bituminised Marl Formation.
- Dark Blue/Purple represents the marble.
- Light Blue represents the transition zone between the Bituminised Marl Formation and the marble.

Figure A2.30 Visualisation of the lithology in Adit A-6 and Borehole S14.

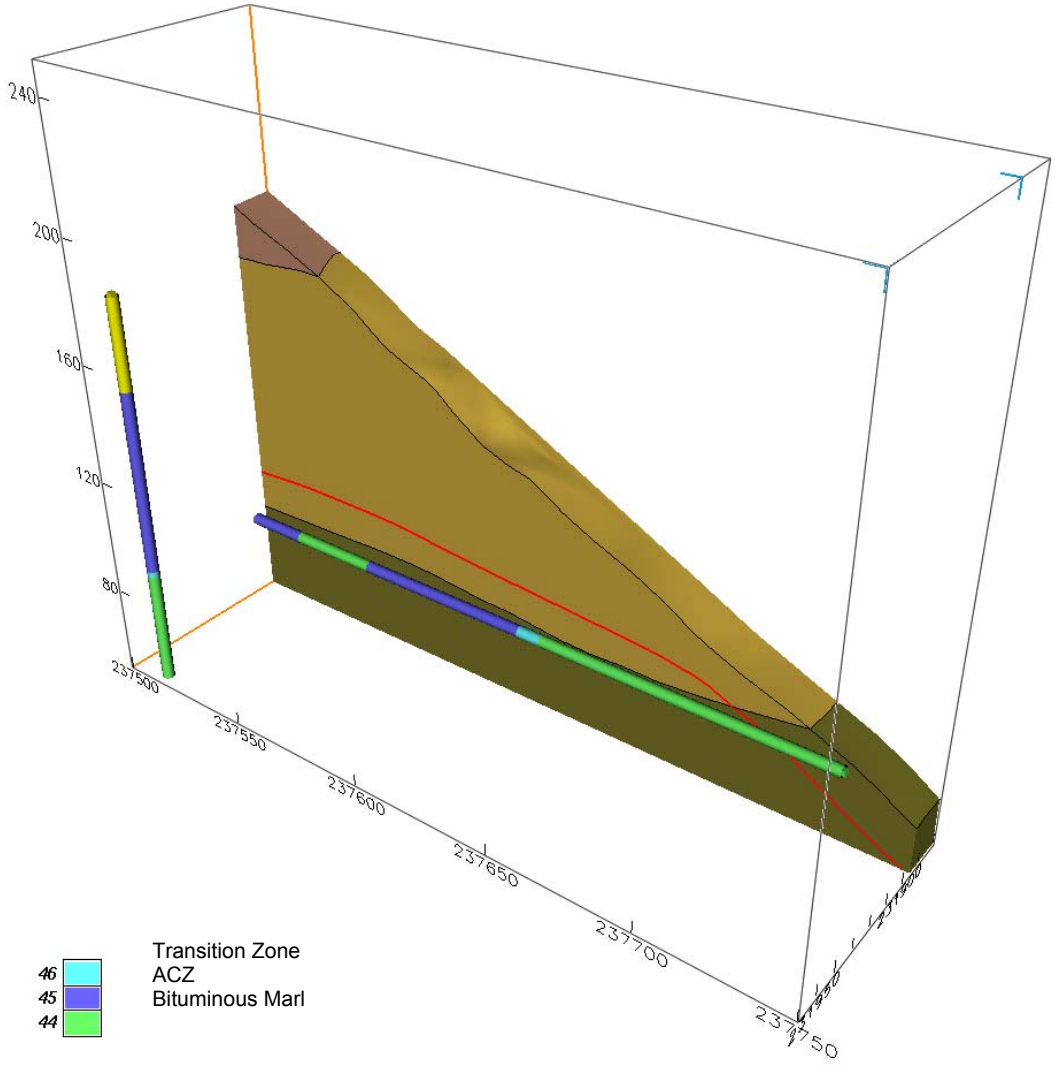

Note that the parent rock re-appears for a short distance, presumably as a 'pod' within the ACZ, between approximately 168 and 207 m along the Adit. There is a clearly defined southern metamorphic contact to this pod at 207 m along the Adit between the parent rock (to the north of the contact) and the ACZ (to the south of the contact). However, the northern contact lies somewhere between 168-183 m but is obscured by roof fall and extensive travertine deposition.

Chemical analyses of groundwater samples collected during two sampling campaigns, in May 2000 and December 2000, were collected from the boreholes and mineral seepage sites along Adit A-6. In addition, groundwater analyses from previous phases of work were available from the Western Springs, Eastern Springs and Wadi Sijin surface seeps. The groundwater data contain analyses of all of the principal chemical components (56 different components)[2]. This information is reported in full in Chapter 3, but to support understanding, visualisation files have been produced that allow the user to interactively select and visualise the different chemical components. A separate data file is available for groundwater data from May 2000 and December 2000 in Adit A-6 and four files for the data from the surface seeps, for groundwater data from June 1990, May 1992, November

[2] For the Eastern Springs data points the location was moved 61 m to the west so that the data points lay on the edge of the 3D model.

1994 and March 1995. An example of the visualisation of geochemical data in Adit A-6 is illustrated in Figure A2.31 and an example of the surface seeps is illustrated in Figure A2.32.

The satellite images derived from the combined multispectral SPOT and Landsat Thematic Mapper data presented in section 2.3 were incorporated as an overlay on top of the EarthVision model. In order to overlay the imagery, the files were converted to Silicon Graphics RGB format and registered by defining the coordinates of three points. The resulting visualisation is illustrated in Figure A2.33.

Figure A2.31 Illustration of the visualisation of groundwater chemistry in Adit A-6. The figure shows pH values measured in May 2000

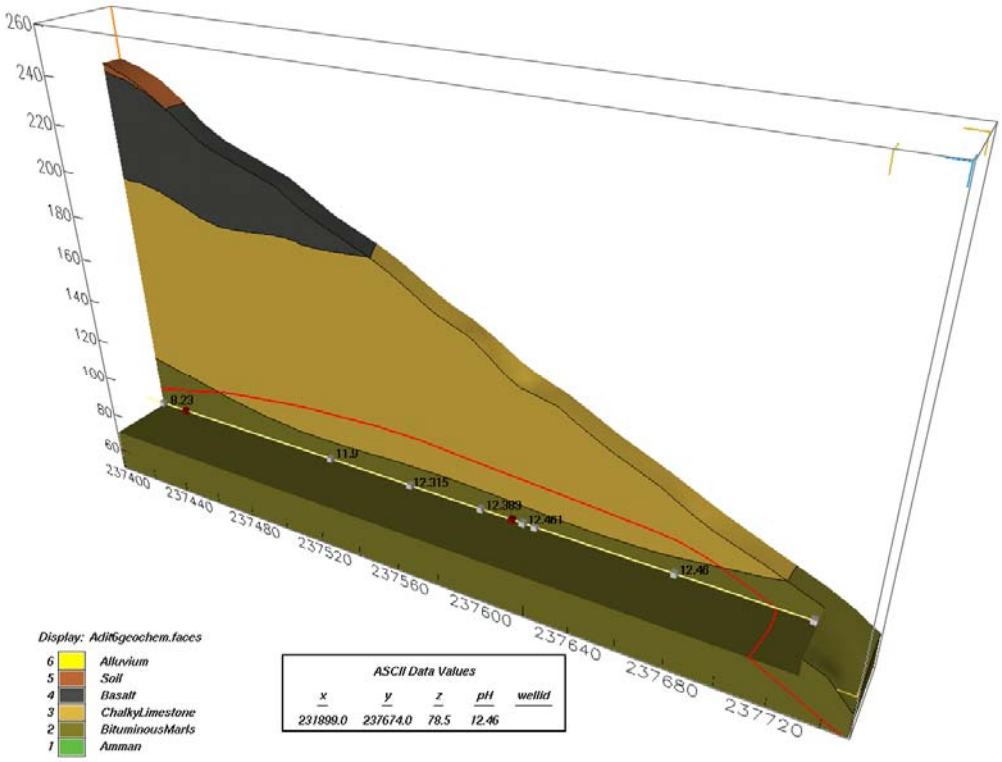

Figure A2.32 Illustration of the visualisation of groundwater chemistry in surface seeps. The figure shows temperature values measured in March 1995

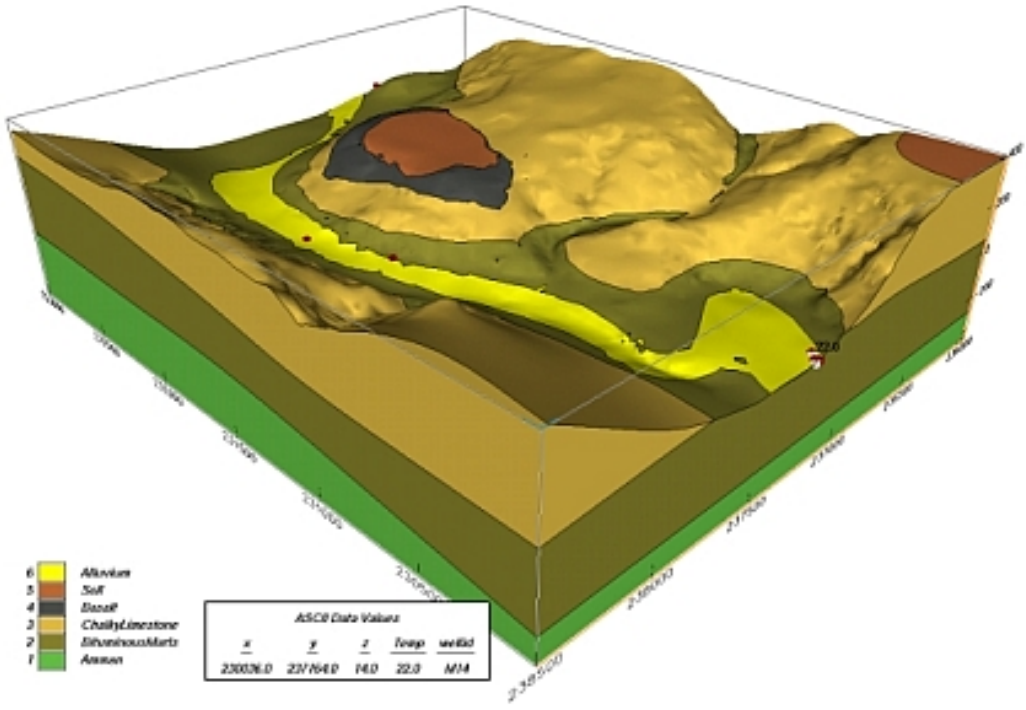

Figure A2.33 Geological model of Maqarin with satellite image overlay. The key relates to the subsurface lithologies only, while the colours on the surface topography are false and simply indicate spectral contrasts.

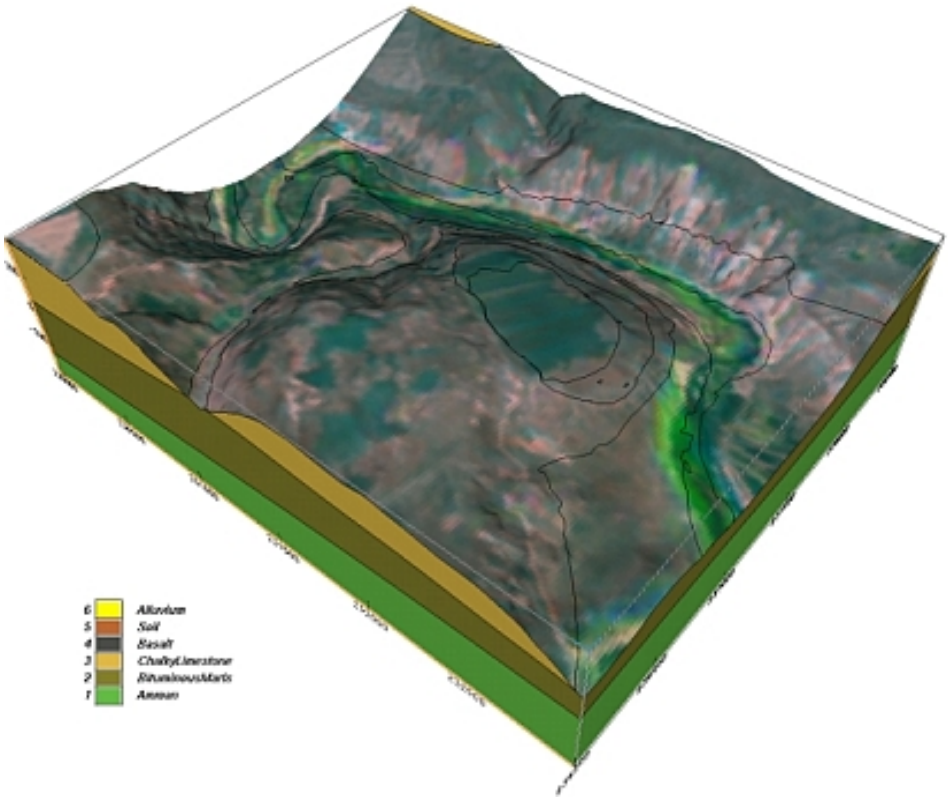

A2.5 Earthvision Model and Images (CD)

Appendix 3.1

Groundwater Sampling, Analytical Methodology and Analysis

A3.1 Field Sampling and Analysis

Sampling and analysis of groundwaters from the Maqarin site for the Phase IV programme was undertaken by the British Geological Survey (BGS) and the University of Jordan. BGS undertook all of the field sampling, field measurement and laboratory analysis of groundwaters during the sampling campaign in May 2000. A subsequent sampling campaign and field measurements in December 2000 was carried out by the University of Jordan, following protocols and instructions provided by BGS. The samples collected were then shipped to BGS for detailed laboratory analysis.

Additional groundwater sampling at all other times during the Phase IV programme was undertaken independently by the University of Jordan using the BGS protocols. Analysis of these additional samples was carried out by the University of Jordan, the University of Ottawa and the University of Waterloo.

A3.1.1 British Geological Survey (BGS)

A3.1.1.1 Groundwater sampling protocol

Groundwater samples were sampled and preserved on-site directly at the sampling points. Where possible, samples were collected so as to minimise atmospheric contact as far as possible. This limited potential interaction with atmospheric CO_2 in particular (which may impact on the determination of OH^-, pH and alkalinity of the hyperalkaline groundwaters). For seepage samples from the Western Springs and Wadi Sijin, this was achieved by pushing a short length of plastic tubing beneath the surface of the pooled water and into the fissures in the Quaternary sediments through which the groundwater discharged. The waters were then sampled using a plastic syringe connected to the plastic tubing.

In Adit A-6, waters collected from the M1 and M2 discharge sites were sampled using Teflon sampling cups that had been installed during the Phase III programme (Smellie, 1998). At the M1 site, the Teflon cup had been embedded into the thick travertine coating on the Adit wall at the location of a major hyperalkaline groundwater discharge point within the ACZ. At the M2 site, the Teflon cup had been placed across a discharging fracture in the Bituminous Marl Formation parent rock and sealed on to the roof of the Adit using silicone sealant. Both of the Teflon cups had become encased and sealed in travertine by the time of the Phase IV sampling campaign. A length of plastic tubing filled with water was connected to the Teflon cups, and formed into a U tube to form an air-lock to prevent back-streaming of air. The air uptake was further minimised by maintaining a continuous flow of groundwater through the tubing. Water was collected in l L Nalgene bottles, with the tubing placed in the bottom of the bottle, allowing the bottle to overflow. Sub-samples were then taken from these bottles by plastic syringe.

Sampling sites M19, M20 and M22 (Adit A-6) and the M3 (Maqarin Railway Station Cutting) were all sites where hyperalkaline groundwater discharged as slow seeps

through fractures to produce slowly dripping stalactites. Dripping water was collected by fixing a polythene bag around the major dripping point or around a cluster of several dripping stalactites. This was drained into a 1 L Nalgene bottle along a plastic tube fixed to the bottom of the bag. Flow rates at these sites were very slow (typically 5-10 drips per minute). Sampling took between 1.5 to 17 hours to collect sufficient water for analysis, clearly meaning that it was impossible to exclude contact with the atmosphere during sampling. Consequently, the potential for interaction with atmospheric CO_2 must be considered when interpreting the water chemistry from these sites. However, no difference in pH was noted between the start and completion of sample collection, suggesting that the water chemistry was able to buffer the small amounts of CO_2 involved.

Water was also sampled from the new short boreholes drilled in Adit A-6 (boreholes D2, D5, D6 and D7). In each borehole, the water was collected from a packed-off interval isolating a conductive fracture or group of fractures. The boreholes had been drilled into the Adit walls with a slight upwards inclination to allow drainage to the borehole outlet. Prior to sampling, the boreholes were opened and allowed to drain, before being closed to allow water to fill the packed intervals afresh. This was repeated three times to flush the borehole before sampling. Water flow was very slow and it took several hours to collect sufficient water for analysis from all of these boreholes. Therefore, the potential for changes in water chemistry through diffusion of air, or other alteration during long storage time within the packed interval, must be considered.

Water samples were sub-sampled and preserved directly on-site as follows:

Major and trace cations

30 mL samples were collected for the analysis of major cations (Ca, Mg, Na and K), total S and Si. These were sampled by using a plastic syringe to minimise atmospheric contact, and filtered 'on-line' through 0.45 µm pore diameter Acrodisc® disposable nylon filter cartridges directly into Nalgene bottles. The samples were preserved by acidification to 1 % with respect to AristaR® nitric acid. The bottles were completely filled to allow no headspace. A blank reference sample was prepared on-site using double-distilled water (provided by BGS) and processed using the same protocol.

Separate 125 mL samples were collected and preserved in the same manner for determination of trace cations.

Major and trace anions, total organic carbon and total inorganic carbon

30 mL samples were collected for the analysis of major anions (Cl, SO_4, NO_3, NO_2), Total Organic Carbon (TOC) and Total Inorganic Carbon (TIC). These were sampled by using a plastic syringe to minimise atmospheric contact, and filtered 'on-line' through 0.45 µm pore diameter Acrodisc® disposable nylon filter cartridges directly into Nalgene bottles. The samples were preserved unacidified and the bottles completely filled to allow no headspace. A blank reference sample was prepared on-site using double-distilled water (provided by the BGS) and processed using the same protocol.

Separate 125 mL samples were collected and preserved in the same manner for determination of trace anions.

Reduced sulphur

30 mL samples for determination of reduced sulphur were taken by plastic syringe directly at the sampling points. The samples were not filtered but were preserved to 1 % with respect to sodium hydroxide, by the addition of a pellet of sodium hydroxide. The

bottles completely filled to allow no headspace. A blank reference sample was prepared on-site using double-distilled water (provided by the BGS) and processed using the same protocol.

Selenium and arsenic

30 mL samples for the analysis of Se and As were sampled and filtered as for major and trace cations but were preserved by acidification to 1 % with respect to AristaR hydrochloric acid. The bottles completely filled to allow no headspace. A blank reference sample was prepared on-site using double-distilled water (provided by the BGS) and processed using the same protocol.

Ammonium

30 mL samples for the analysis of ammonium were sampled and filtered as for major and trace cations but were preserved by acidification to 1 % with respect to AristaR sulphuric acid. A blank reference sample was prepared on-site using double-distilled water (provided by the BGS) and processed using the same protocol.

Ferrous iron

15 mL samples were collected and preserved for the determination of ferrous iron using a plastic syringe. These were then filtered through a 0.45 µm pore diameter Acrodisc® disposable nylon filter cartridges directly into Sterylin® polycarbonate tubes, to which 1 mL of 1 % 2,2-dipyridyl solution (hydrochloric acid acidified) had previously been added. The volume was made up to 10 mL. The 2,2-dipyridyl forms a stable red complex with ferrous iron in solution. A blank reference sample was prepared on-site using double-distilled water (provided by BGS) and processed using the same protocol.

Stable isotopes

125 mL samples of water were collected for stable isotope ($\delta^{18}O$ and δD) analysis. The samples were unfiltered and stored in Nalgene bottles, which were filled to leave no headspace. Samples for stable isotope analysis by BGS were only taken during the April-May 2000 field campaign.

A3.1.1.2 Field measurements

A number of hydrochemical measurements were recorded in the field at each sampling point. These include temperature, pH, Eh, electrical conductivity and dissolved oxygen.

Temperature, pH and Eh were recorded by specific ion electrodes using two Orion portable meters (Orion Research Model SA250). Where possible, the Eh and pH were measured at the Western Springs, Wadi Sijin, Adit A-6 sites M1 and M2 with the electrode in the flowing discharging groundwater. However, in all other cases the Eh was measured in static water collected in a glass beaker. pH (±0.01 pH unit) and temperature (±0.1 °C) were determined using a Ross combination glass electrode. BGS had found that this type of electrode had previously proved very reliable for use in the study of high pH groundwaters at Maqarin and in experimental laboratory studies of high pH pore fluid-rock interaction (Linklater, 1998; Smellie, 1998). The pH electrodes were calibrated with standard buffer solutions at pH 4, 7, 10 and 13 depending on the pH range of the sample being analysed. Eh was measured with a standard Pt-Ag/AgCl electrode verified with Zobell's solution (standard solution Eh = 200-250 mV) and corrected for temperature (corrected Eh = uncorrected Eh + (244-T), where T is the temperature in degrees Celsius).

Conductivity was measured using a hand-held conductivity probe (Bibby SMC-1). This was calibrated using a KCl conductivity standard solution.

The University of Jordan did not make field measurements of the pH, Eh, temperature or conductivity during the December 2000 sampling campaign. Data for these parameters are only available from the subsequent BGS laboratory measurements.

A3.1.1.3. Laboratory analysis

Groundwater samples were flown to the U.K. for analysis by BGS, and on receipt were stored at 4°C in a temperature-controlled cold-store prior to analysis. The analytical methods used are similar to those described previously in the Phase II (Linklater, 1998) and Phase III (Smellie, 1998) programmes and are summarised in Table A3.1.

Table A3.1 Summary of groundwater chemical analytical methods used by BGS

Parameter	Analytical Method	Notes
Major and trace elements: Al, As, Ba, Ca, Cd, Co, Cr, total Fe, Mg, Mn, Na, Ni, total P, total S, Se, Si, Sr and V	ICP-AES	A
K	ICP-AES	N
Li, Cu, Zn, Mo, W, Re, Pb, Th and U	ICP-MS	N
Cl, SO_4, NO_3, NO_2, Br and F	Ion chromatography	A
pH and OH^-, HCO_3^- and CO_3^{2-}	Potentiometric titration	A
TOC, TIC	TOC analyser	A
Reduced iron	Colourimetric analysis	N
Ammonium	Colourimetric analysis	S
Reduced sulphur	Hydride generation ICP-AES	N
Stable O and H isotopes	Gas source mass spectrometry	N

Notes: Tests marked A in the above table are included in the UKAS Accreditation Schedule for the BGS laboratories. Tests marked N in the above table are not included in the UKAS Accreditation Schedule for the BGS laboratory. Tests marked S in the above table were subcontracted to the analytical laboratory of the Environment Agency in Nottingham, who hold UKAS accreditation for the method concerned.

pH, bicarbonate, carbonate and alkalinity

Laboratory determination of pH, alkalinity, bicarbonate and carbonate was carried out by potentiometric titration as soon as possible after receipt of the samples by the BGS laboratory. Effort was made to ensure that there was minimal opportunity for contact and reaction with the atmosphere in order to minimise any sample alteration.

Theoretically, total alkalinity is a measure of the hydroxide, carbonate (x2) and bicarbonate ion content, as well as any contributions from other anions that take part in hydrolysis (e.g. organic bases, silicates, borates, sulphides and phosphates). The following assumptions form the basis of the identification of titrimetric end points:

- For samples with pH >12, bicarbonate is assumed to be negligible (<5 mgL^{-1} HCO_3^-), and alkalinity has been characterised in terms of hydroxide and carbonate concentration for the purposes of this calculation;
- For samples with pH <9, the alkalinity is assumed to be predominantly due to carbonate and bicarbonate species, and the concentration of hydroxide is assumed to be negligible (<22 mgL^{-1} OH^-).

Major and minor cations, trace cations, total iron, and total sulphur

Major cations (Ca, Mg, Na, K), Al, Ba, Ca, Cd, Co, Cr, total Fe, Mn, Ni, total P, total S, Si, Sr and V were analysed by inductively-coupled plasma – atomic emission spectroscopy (ICP-AES). Trace elements (Li, Cu, Zn, Mo, W, Re, Pb, Th and U) were determined by

inductively coupled plasma – mass spectrometry (ICP-MS) technique. These analyses were undertaken on the filtered and nitric acid preserved water samples.

Anions

Major and trace anions, including Cl, SO_4, NO_3, NO_2, Br and F, were analysed by ion chromatography. These analyses were undertaken on the filtered but unacidified water samples.

Most of these anions are stable in solution for an appreciable length of time. Nitrate and nitrite may, however, be affected by microbial activity. Therefore, analyses for all anions were carried out as soon as possible after receipt of the samples, to minimise any post-sampling chemical alteration.

Ammonium

Ammonium was determined on the filtered and sulphuric acid preserved water samples by colourimetric analysis.

Ammonium is strongly affected by the sampling method and the amount of free ammonia present varies with pH. Above pH 12, the ammonium/ammonia equilibrium in solution is such that over 90% exists as free ammonia. Therefore, it is likely that some ammonia will potentially have been lost from the high pH groundwaters during sample collection and filtering in the field. It is impossible to quantify such losses, so the ammonium values should probably be regarded as minimum values and this should be taken into consideration when interpreting the data.

Reduced iron (Fe^{2+})

Ferrous iron was determined by colourimetric analysis on filtered and acidified water samples preserved with the chromogenic reagent 2,2-dipyridyl which forms a stable ferrous iron complex in solution. The deterioration of this complex is considered to be negligible over the timescale between sample collection and analysis. The validity of the data can also be checked by comparing the results for the colorimetric determination of ferrous iron with the determination of total iron by ICP-AES. The value for reduced iron should not exceed that of the total iron (within analytical error).

Oxidised iron (Fe^{3+})

Ferric iron is assumed to be the difference between the measured total iron and the measured total ferrous iron. In the case of the Maqarin groundwater samples, determined ferrous iron contents were all less than the limit of quantification. Therefore, it may be assumed that, within analytical error, all of the iron present is in the ferric form.

Reduced sulphur

Reduced sulphur was determined on the unfiltered water samples that had been preserved with sodium hydroxide.

Although sulphide is stabilised in solution under alkaline conditions it may possible that some loss of reduced sulphur may occur over time. For this reason the samples were analysed as soon as possible after sample receipt. Because the analysis is made on unfiltered water samples (to avoid degassing of H_2S) there is a possibility that particulate sulphide may contribute to the analysis. It is unlikely that this will be a significant problem in water samples collected from the ACZ (where sulphides have largely been oxidised by combustion metamorphism). However, the potential for contribution from particulate sulphide should be considered when evaluating data from waters percolating through the

Bituminous Marl Formation parent rock, since these rocks contain significant fine-grained diagenetic pyrite and other minor sulphides (see Chapter 3).

Arsenic and selenium

Arsenic and selenium were determined by ICP-AES after hydride generation, following the method published by Cave and Green (1989). Analyses were carried out on filtered water samples preserved by acidification with hydrochloric acid.

Total organic carbon and total inorganic carbon

TOC and TIC were determined on filtered unpreserved water samples, using a non-dispersive infrared total organic carbon analyser. Inorganic carbon content essentially represents the sum of the carbonate and bicarbonate. Before determination of TOC and TIC, the high pH samples were neutralised by addition of a known volume of 0.5M sulphuric acid.

The inorganic carbon values determined for the hyperalkaline groundwaters should be regarded as maximum values. It is likely that small amounts of atmospheric carbon have probably been adsorbed during the sample collection procedures, particularly for those sampling sites where collection required several hours in order to collect sufficient water for analysis.

Stable isotopes

$\delta^{18}O$ and deuterium analyses were carried out using a VG-Optima gas-source mass spectrometer, after preparation by CO_2 equilibration for $\delta^{18}O$, and Zn reduction for δD. Analyses of $\delta^{18}O$ and δD are reported with a 2 sigma error of 0.1‰ and 1‰ respectively

A3.1.1.4 Data quality

As shown in Table A3.1, most analyses were carried out under UKAS Accreditation. Those analyses which are not included within the UKAS Accreditation Schedule for the BGS Laboratory were undertaken in compliance with ISO9001, which is consistent with the standard required for UKAS accreditation.

Limited sample volume available for analyses meant that only one analysis per sample could be undertaken. Detection limits quoted are based on 3σ data for blanks run as part of validation of the analytical method. No blank correction has been applied. Data from the BGS data validation indicate that analytical uncertainty for all methods used in this study is typically better than 5%. The unusual nature of these samples may result in slightly greater uncertainty, which unfortunately cannot be tested because of the limited sample volume. Nevertheless, experience with similar samples indicates that the analytical uncertainties are likely to be better than 10% for these waters.

The ionic charge balance provides an additional check on data quality. The ionic charge balances are poorer than normally expected for groundwaters, but are mostly within 10%. This is considered acceptable given the unusual sample matrices of these hyperalkaline groundwaters. In all cases where the ionic charge balance is >5%, the analyses have a deficit of anionic charge, suggesting that a major anionic component has been underestimated. This can most probably be accounted for by errors in the analysis for OH^-, which is particularly difficult to estimate accurately but is a major component of these high-pH waters. A significant potential problem with analysing these high-pH water samples is probably contamination by adsorption of atmospheric CO_2 during sample handling and storage. Although efforts were made to minimise this effect by ensuring that sample bottles were filled to the brim to avoid any head space, and by analysing the samples as soon as possible after collection, there is still a possibility that some

adsorption of CO_2 will have occurred e.g. by diffusion-in of CO_2 gas through the walls of the sample bottles. Therefore, the values for OH^- and pH should be regarded as minimum values.

A3.1.2 University of Jordan

Following the sampling campaign described above, the University of Jordan continued to sample groundwaters from the same localities on nine occasions from January 13th, 2001 to May 26th, 2002 to monitor seasonal variations. Not all localities were sampled on each occasion. M19 was a priority, together with D5, D7, D8, M20, M21 and M22. In addition, samples were collected for analysis in November 2000 from the four municipal water-supply springs at Aqraba, Ein Turab, Khreiba and Quelba.

At all localities the groundwaters were sampled and preserved according to the BGS protocol. The pH electrodes used for field measurements were calibrated with a standard buffer solution of pH 10. Analysis of major ions Ca, Mg, Na, K, OH, CO_3, HCO_3, Cl, SO_4 and NO_3 were analysed at the Universty of Jordan using the methods given in Table A3.2. Analytical errors (indicated also in Table A3.1.1) are up to 3% for Ca, Mg, Na, K, Cl and HCO_3, and up to 5% for NO_3 and SO_4.

Table A3.2: Summary of groundwater chemical analytical methods used by the University of Jordan

Parameter	Analytical method
pH	Field pH electrode (WTW Co.)
Electrical Conductivity (EC)	Field EC probe (WTW Co.)
Temperature	Field temperature probe (WTW Co.)
Ca^{2+}	1. Titration with 0.02 N EDTA (ethylenediaminetetraactic acid) 2. Reagents: • Buffer as sodium hydroxide (NaOH), 1 N • Indicator as murexide
Magnesium (TH-Ca^{2+})	1. For TH Titration with 0.02 N EDTA 2. Reagents: • Buffer as (NH_4OH/NH_4Cl) • Indicator as eriochrome black T
Cl^-	1. Titration with =.01 N silver nitrate ($AgNO_3$) 2. Indicator as potassium chromate (K_2CrO_4)
HCO_3^-	1. Titration with 0.02 N H_2SO_4 2. Indicator as bromocrysol
CO_3^{2-}	1. Titration with 0.02 N H_2SO_4 2. Indicator as phph (phenol phthalein)
Na^+	Flame photometer
K^+	Flame photometer
SO_4^{2-}	Specrometer using wavelength of 492 nm
NO_3^-	Specrometer using wavelength of 206 nm

A3.1.3 University of Ottawa

Analyses were mostly confined to $\delta^{18}O$ and deuterium:

$\delta^{18}O$ *analysis* was carried out by CO_2 calibration using a VG SIRA-12 dual inlet gas-source mass spectrometer with a 2 sigma error of 0.15‰ (for high pH samples, a drop of orthophosphoric acid is added).

Deuterium analysis was carried out using the method of water reduction on zinc metal under vacuum at high temperature, followed by measurement using the the VG SIRA-12 dual inlet gas-source spectrometer with a 2 sigma error of 1‰.

Tritium analysis was done by electrolytic enrichment; errors are listed in the dataset.

A3.1.4 University of Waterloo

$\delta^{37}Cl$ analysis was carried out using a VG SIRA-9 mass spectrometer with a 1 sigma error of 0.15‰.

Appendix 3.3

Matrix Diffusion

J. Kramers, I. Villa, U.K. Mäder and W.R. Alexander

A3.3.1 Introduction to matrix diffusion

The term 'matrix diffusion' is applied to the process by which solute, advectively transported in distinct flow paths,[3] penetrates the surrounding rock matrix by diffusional transport. Diffusion into this matrix occurs in a connected system of pores or microfractures - diffusion through the solid phase is insignificant by comparison (see the review of Valkiainen, 1992, for example). The importance of matrix diffusion, in the context of a radioactive or chemotoxic waste repository, is that it provides mechanisms for greatly enlarging the area of rock surface in contact with advecting contaminants. These include flow-path surfaces, fracture-infill materials and the much larger portion of the bulk rock (Neretnieks, 1980; Grisak and Pickens, 1980; Rasmuson and Neretnieks, 1981; Haderman and Rösel, 1985).

The matrix-diffusion theory proposes that dissolved contaminants will diffuse from a water-filled fracture (for example), through any fracture coating layer, into the rock matrix. If they are reactive, they will sorb on to the inner surface of the pores, or else remain dissolved within the immobile porewater. This process can be envisaged as an extreme case of a dual porosity medium, in which advective flow occurs entirely within the fracture system, or primary porosity, whilst all solute transport in the bulk rock, the secondary porosity, takes place by diffusion (see, for example, Barenblatt et al., 1960; Grisak and Pickens, 1980). The porosity of the rock matrix can be very small in many hard rocks (0.1 to 1% in many granites; see, for example, Möri et al., 2003) and diffusion into the matrix is likely to be slow. The impact of matrix diffusion will, as a consequence, not be significant along short or rapid flow paths. However, for the longer and slower paths, likely in a repository host rock, the maximum concentration of contaminants in the groundwater entering the biosphere may be significantly reduced In the case of radioactive waste disposal, this process is particularly important if the resulting transport time to the biosphere is greater than the half-life of any given radionuclide. This reduces the total release by several orders of magnitude (see for example, Neretnieks, 1980 and Smith, 2003, for discussion). In addition, pulse releases can be spread over longer time periods, thereby decreasing release concentrations by a process of temporal dilution (NGB, 1985). For non-sorbed contaminants, this process also represents an important retardation mechanism, since these contaminants would otherwise be transported at the advection rate of the groundwater.

Although the theoretical basis for matrix-diffusion has been fairly well-established for several decades (see, for example, Garrels et al., 1949; Klinkenberg, 1951), the matrix-diffusion concept required experimental verification. Work has since been carried out on various sedimentary rocks (e.g. Bradbury and Green, 1986a; Bradbury and Stephen, 1986; Hofmann, 1990 ; Mazurek et al., 1996, 2004) and crystalline rocks (e.g. Skagius and Neretnieks, 1982, 1986; Torstenfelt et al., 1982; Smellie and Stuckless, 1985; Bradbury and Green, 1986b; Bradbury and Stephen, 1986; Alexander et al., 1988, 1990;

[3] In fractured rocks, these will be water-conducting fractures or other linear features (such as joints, dykes or sills). In unfractured rocks, these will be areas of enhanced porosity (e.g. lenses or horizons of silt and sand in an otherwise clay-dominated rock) and linear features, such as dykes.

Hellmuth, et al., 1992 ; Ota et al., 2003; Akagawa et al., 2006). These several contributions have shown that matrix diffusion clearly occurs and can result in significant retardation of migrating contaminants, although care must be taken when conducting laboratory based experiments (for example, see Möri et al., 2003, for discussion).

However, the above work generally relates to systems which are relatively simple. There is some concern, therefore, that 'altered' host rocks, with some physico-chemical changes to the near-fracture rock matrix, such as the deposition of secondary coatings on the fracture surfaces, may display only very limited matrix diffusion due to reductions in matrix porosity. For example, Steefel and Lichtner (1994) modelled the effects of a hyperalkaline cementitious leachate on a 'simplified' marl host rock and considered diffusion of the leachates into the matrix. Here, diffusion of porewater HCO_3^- towards the fracture, from the matrix, was seen to induce calcite precipitation on interacting with the leachates. This completely closed the matrix porosity and blocked off matrix diffusion. Further modelling (e.g. Chambers and Haworth, 1998; Mäder and Traber, 2004) seems to support these results. It is a concern, therefore, that the retardation of non-sorbing contaminants will be greatly reduced (when compared with pristine host rocks[4]) in host rocks which have undergone reaction with hyperalkaline leachates.

Consequently, a matrix-diffusion study in clay biomicrite at the Maqarin site, which had been altered by reaction with hyperalkaline groundwaters, (Milodowski et al., (1998) utilised natural decay series equilibrium studies and examined the matrix porosity. The results were complicated by the presence of secondary cement phase-filled microfractures up to 4 cm behind the fracture wall. Nonetheless, deviations from unity in the $^{226}Ra/^{230}Th$ isotopic ratios indicated accessible porosity up to 3-7 cm behind the fracture wall. However, such is the importance of matrix sealing on the retardation of non-sorbing contaminants, that it was decided to add to these data with a new study of biomicrite matrix samples. Although significant improvements in analytical techniques were used, it proved impossible to analyse a profile as long as that examined by Milodowski et al. (1998a). Therefore, attention was focused on the zone where the model calculations indicated sealing, namely in the near-fracture zone of the matrix.

A3.3.2 Use of ^{238}U-^{234}U-^{230}Th systematics: isotope systematics and geochemical behaviour

The isotope ^{234}U (half life ($t_{1/2}$) of 245.5 ka) is the first relatively long lived intermediary species in the ^{238}U ($t_{1/2}$ 4.470 Ma) decay chain. It decays to ^{230}Th ($t_{1/2}$ 75.7 ka). This, in turn, decays to ^{226}Ra ($t_{1/2}$ 1.608 ka). The further intermediate products in the chain, ultimately leading to stable ^{206}Pb, all have much shorter half lives and are not relevant to this Project.

In a closed system which has existed for >> 1 Ma, all the intermediate decay products of the ^{238}U chain are present in constant abundances, which self-regulate. As a result, their decay rate equals that of production. The ratios of activity (number of decays per unit time) of all nuclide pairs then equals unity. Their actual abundance ratios of the species are then proportional to $1/ t_{1/2}$, a situation referred to as secular equilibrium. Interesting situations arise when systems are not closed and the relative abundances of the nuclides ^{238}U, ^{234}U and ^{230}Th are fractionated. These facilitate the study, and possibly place time constraints on, geological processes in the time scale of about 100 a to 1 Ma. In rock-water interaction and weathering, a fractionation of U from Th isotopes is expected as Th occurs only in the tetravalent state and is effectively insoluble in water (see Gascoyne,

[4] Note that a geochemical study of secondary-calcite coated, water-conducting fractures in the marl of the Palfris Formation (Swiss Alps), found no evidence of blocking of the matrix, despite the coating appearing optically (i.e. in thin section) relatively tight (W.R.Alexander and M.Mazurek, unpubl. data).

1992, for a review). In addition, in oxidising environments, U is hexavalent and forms highly soluble complexes, e.g. UO_2^{2+} and $UO_2(CO_3)_2^{2-}$. More subtly, preferential leaching of ^{234}U over ^{238}U is also expected, due to α-recoil effects: ^{238}U first decays by α-decay to short-lived ^{234}Th. This then decays to ^{234}U by two β decays. The first α-decay causes recoil of the ^{234}Th (displacement in a mineral of about 100 nm) which can thus be "shot" out of a grain. ^{234}U has, therefore, a greater probability of being outside mineral grains than ^{238}U. Further, even when inside a grain, it resides in a damaged-lattice portion (α-recoil track) from where it can be comparatively easily leached.

While the α-recoil hypothesis is probably valid, there are observations which highlight that this preferential leaching has an additional cause. While ^{238}U and ^{235}U occur in silicate minerals in the tetravalent state, ^{234}U is probably hexavalent from the moment it is generated. This is because ^{234}Th, which is the first daughter product of the ^{238}U decay, is tetravalent (note that this is the only valency of Th under most geological conditions). In the double β-decay, leading to ^{234}U, the positive charge of the nucleus is increased by 2. In contrast, in an insulating environment, no electrons can be added to compensate for this (the β-particles are generally projected far enough as to be unavailable for local-charge neutralisation). There are a number of observations which strongly support this working hypothesis:

1. in groundwaters, very low overall U contents generally correlate with large ^{234}U excesses (e.g. Osmond and Cowart, 1992). Generally, this is to be expected in reducing fluids and groundwaters, as only hexavalent U forms soluble complexes
2. significant ^{234}U deficiencies are seen in deep, reducing, coarse-grained granitic rocks of extremely low porosity, where α-recoil "liberation" is unlikely to be highly significant (e.g. Gascoyne and Cramer, 1987)
3. ^{234}U deficiencies are less marked in surface samples where weathering occurs under oxidising conditions, so that ^{238}U and ^{234}U are both hexavalent.

A3.3.3 Sampling and analytical methods

In a drillcore from Adit A-6 at Maqarin, a biomicrite sample was taken which displayed evidence of hyperalkaline leachate reaction (cf. Figure 1.10) and a 1 mm thick carbonate vein (joint filling) was encountered. This vein was sampled for U-Th analysis. In addition, the wall rock, immediately adjacent to the vein, was sampled at different distances from the vein. Thin slices were sawn parallel to the vein, providing samples at 1, 2, 3 an 4 mm distance from it (samples A1-A4) and, in parallel, slabs at 2 and at 7 mm, using a coarser saw. Samples were spiked with a $^{236}U/^{229}Th$ mixed spike (to assess recovery efficiency) and dissolved using 7 N HNO_3. U and Th were separated from the matrix, and from each other, using Dowex 1x8 anionic resin column and 7N HNO_3 as an eluent. Isotope ratios were measured on a Nu Instruments® multicollector ICP mass spectrometer. This was equipped with three ion- counting electron multipliers, one of which has a retardation-abundance sensitivity filter in front of it.

Table A3.3 Results from the natural decay series analysis

		Concentrations				Activity ratios											
Sample	**Distance from vein (mm)**	**ppb U**	**2SE**	**ppb Th**	**2SE**	**(234U/ 238U)**	**2SE**	**(238U/ 232Th)**	**2SE**	**(234U/ 232Th)**	**2SE**	**(230Th/ 232Th)**	**2SE**	**(230Th/ 238U)**	**2SE**	**(230Th/ 234U)**	**2SE**
Maqarin vein	0	214.4	2.1	8.7	0.1	1.8026	0.0146	74.0	1.1	133.3	2.3	85.6	1.3	1.217	0.017	0.675	0.011
Maqarin A1	1	18103	48	925.4	7.4	0.8571	0.0007	59.1	0.5	50.6	0.4	57.0	0.7	0.965	0.009	1.126	0.011
Maqarin 2mm	2	18279	56	905.6	8.1	0.9247	0.0012	60.9	0.6	56.4	0.5	61.2	0.8	1.004	0.010	1.086	0.011
Maqarin A2	2	18695	48	962.1	8.7	0.8860	0.0010	58.7	0.5	52.0	0.5	57.5	0.8	0.980	0.012	1.106	0.013
Maqarin A3	3	18454	50	931.2	7.8	0.9161	0.0011	59.8	0.5	54.8	0.5	59.1	0.8	0.989	0.010	1.079	0.011
Maqarin A4	4	17937	48	894.6	7.4	0.9094	0.0011	60.5	0.5	55.1	0.5	59.6	0.7	0.984	0.008	1.082	0.009
Maqarin 7 mm	7	20317	62	988.6	10.2	0.9036	0.0019	62.0	0.7	56.1	0.6	61.2	0.9	0.986	0.010	1.091	0.012

A3.3.4 Results and discussion

The results are listed in Table A.3.3. They show an unusual behaviour in the "leaching" context, in that there is no significant fractionation of ^{238}U from ^{232}Th associated with the vein formation. Although the contents of both are much lower in the vein than in the wall rock, $^{238}U/^{232}Th$ ratios are similar. Meanwhile, however, a marked fractionation of ^{234}U from ^{238}U in the vein forming event is suggested. A marked relative enrichment of ^{234}U complements a depletion in the wall rock, particularly very close to the vein. The pronounced disequilibrium between ^{230}Th and ^{234}U, in both wall rock and vein, and comparatively uniform $^{230}Th/^{232}Th$ ratios (Table A3.3), indicate that ^{230}Th behaved similarly to ^{232}Th during leaching, in spite of α-recoil. This unusual behaviour of the systematics can be explained in the context of transport under reducing conditions, using the hypothesis outlined in 1, above, i.e. that ^{234}U was already hexavalent, whereas the oxidation potential of the leachate was insufficient to oxidise ^{238}U.

Regardless of the precise mechanisms of interaction, Figure A3.1 shows that there has been clear removal of ^{234}U from the biomicrite matrix, with all matrix values displaying $^{234}U/^{238}U$ ratios of less than unity (and note that the data plots include a 2 σ uncertainty). Although there has been significant uptake of ^{234}U in the vein, this may not relate to the U lost from the matrix. It is significant that the matrix immediately in the vicinity of the joint has been accessible at some time to circulating fluids. Plotting the data on a Theil diagram (Figure A3.2a,b) shows clearly that the matrix samples have undergone a relatively simple leaching event. It is not possible, however, to state if the U removal has been one sudden event or a continuous process over some time. Similarly with the vein datum point, it is impossible to state whether the U deposition event was sudden or continuous (see also Scott et al., 1992, for the implications of these limits on further modelling of the data).

Figure A3.1 Variation in the 234U/238U isotopic ratio with distance from the vein. Note that the 2σ uncertainty values are included within the symbol (average of circa 1% or less, see Table A3.3)

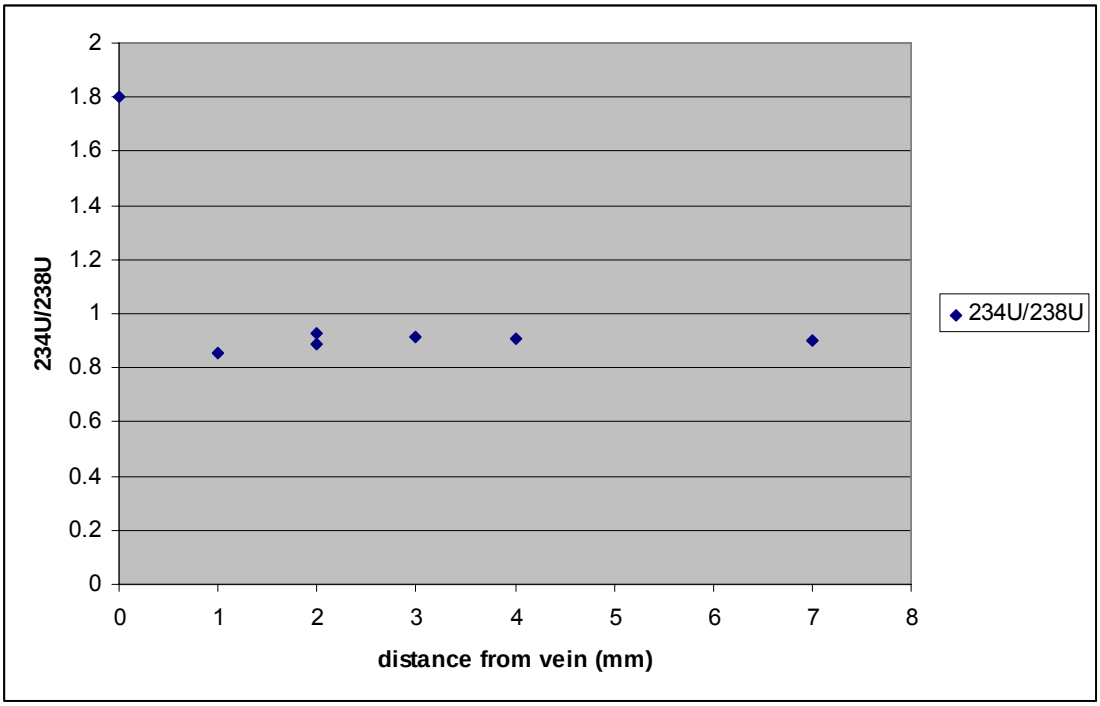

A3.3.5 Conclusion

Although only a small number of samples was analysed here, the results demonstrate that the porosity of the biomicrite matrix was open at some stage. Unfortunately, it is difficult to place any firm dates on the sequence of events, as some questions arise. Does the U leaching in the matrix pre-date the closing of the joint? What is the connection between the removal of U from the matrix and deposition of U in the vein? The latter query is due to the complex nature of the U reaction, and to a lack of data on additional U-series daughters, such as ^{226}Ra.

Nonetheless, the age of the event can be calculated by iteration using the equation:

$$\left(\frac{^{230}Th}{^{234}U}\right)=\left(\frac{^{230}Th_{init}}{^{234}U}\right)e^{-\lambda_{230}t}+\frac{1-e^{-\lambda_{230}t}}{\left(^{234}U/^{238}U\right)}+\left(1-\frac{1}{\left(^{234}U/^{238}U\right)}\right)\frac{\lambda_{230}}{\lambda_{230}-\lambda_{234}}\left(1-e^{-(\lambda_{230}-\lambda_{234})t}\right)$$

equation A3.1

(Ivanovich et al., 1992). While the ^{230}Th/^{234}U and ^{234}U/^{238}U ratios are directly measured, an assumed initial ^{230}Th/^{234}U is required and unity is usually taken for simplicity. In many systems where it can be convincingly shown that the system being measured has been stable for significant periods, this is a sound assumption. However, as it is already known that the flow system at Maqarin has had a complex history, and has been subject to repeated re-activation (see discussions in Smellie, 1998), this would be a fruitless exercise here. In addition, Figure A3.2 clearly shows that the U leaching process was probably not a simple, single event, making the use of equation A3.1 questionable.

Figure A3.2a Uranium deposition and removal sectors in a plot of rock ^{234}U/^{238}U activity ratio against ^{230}Th/^{238}U activity ratio (after Theil et al., 1983).

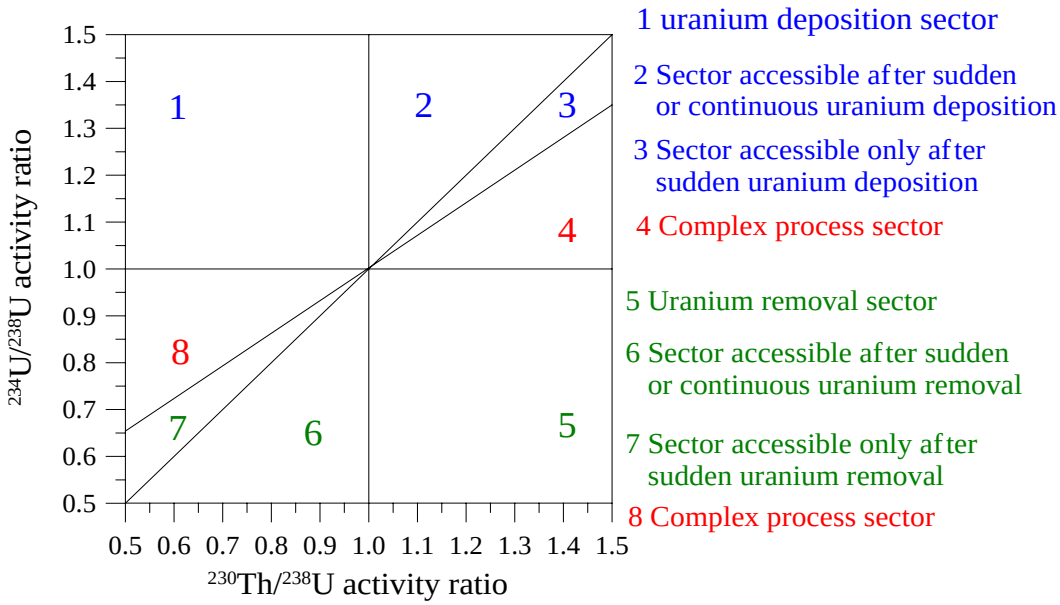

Figure A3.2b Theil diagram of the $^{2304}Th/^{234}U$ versus $^{234}U/^{238}U$ ratios for the biomicrite and vein samples. In comparison with Figure A3.2a, it can be seen that the biomicrite samples are within the sector which is accessible after sudden or continuous U removal. The vein is in the sector which is accessible after sudden or continuous U deposition. See Scott et al. (1992) for a detailed discussion of the implications of these restrictions.

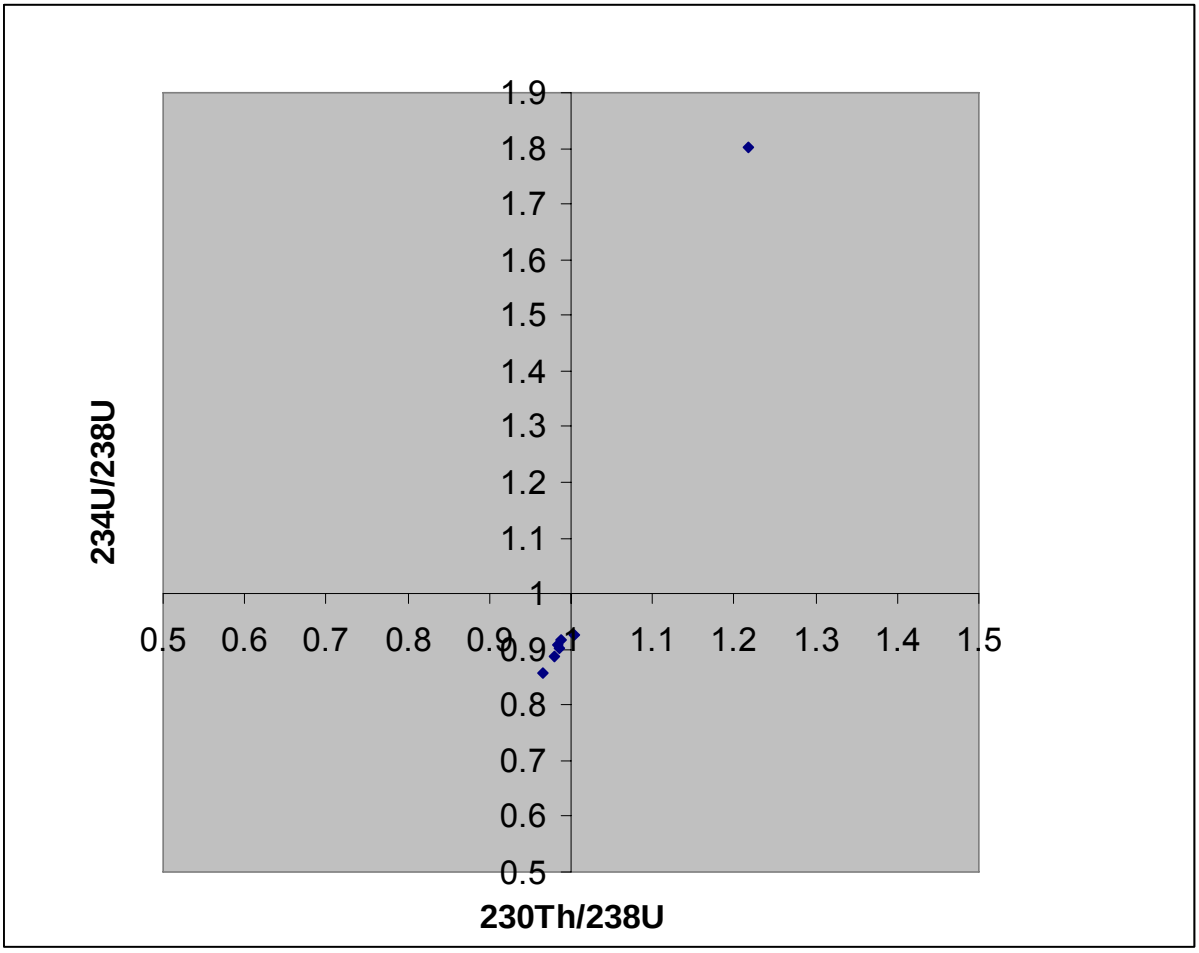

An age of the event can also be calculated by the Th ingrowth method (cf. Chapter 6). Briefly, it is assumed that the sample begins with no Th, so any present has been produced by decay from ^{234}U. Thus, as the decay constant is well-known, the period for ingrowth of any given amount of Th can be back-calculated (see Ivanovich et al., 1992, for details). While this might be valid for the vein material, it is invalid for the matrix data as these are bulk rock samples and so will include detrital Th of an unknown (and unknowable) amount, so making the material appear older.

To say much more about matrix diffusion in the biomicrites which have reacted with hyperalkaline leachates, it is necessary to collect additional data (cf. Milodowski et al., 1998a). It would be of use to analyse:

- additional samples from this core, looking deeper into the matrix to assess just how much is accessible to contaminants (because, as noted in NGB, 1985, this depth is the single most important parameter for the retardation calculations)
- the porosity distribution and mineralogy of the core, which would allow a clear focus on the areas of most importance (e.g. in and around those areas of reduced porosity)

- ^{226}Ra ($t_{1/2}$ 1.608 ka) to assess very young perturbations to the demonstrably complex system at Maqarin
- separates from the matrix samples to allow better dating of the leaching event(s)

Finally, with this additional data, attention could be re-focused on the vein. This would be most appropriate at Maqarin, because of the demonstrable re-activation of the fractures and joints at the site). A profile of analyses across the vein could then be compared with the data from the matrix, to assess age(s) of vein closure. Only then would it be possible to give a definitive answer to whether the Maqarin matrix porosity remains open during and after reaction of the with the hyperalkaline groundwaters at the site – and, by analogy, whether a repository host rock matrix would remain open during and after interaction with cementitious leachates from the repository.

Appendix 4

Analogue Cement Zone

(A.E. Milodowski, L. Trotignon, F. Adam, N. Arnal, N. Barré, P. Bienvenu, C. Bulle, S.R. Chenery, J. Cook N. Crouzet, L. Fontanini, E.S. Hodgkinson, H. Khoury, J. McKervey, U. Mäder, F. Mercier, V. Michaud, H. Peycelon, S. Pontremol, O. Provitina, L. Raimbault, F. Rassineux, J. Raynal, J. Rose, E. Salameh, J. Susini, P. Trocellier and D. Vandamme)

A4.1 Analytical Methods

A4.1.1 BGS methods

A4.1.1.1 Petrographical analyses

Detailed petrographical analysis was carried out by the British Geological Survey (BGS) on representative samples of the primary and altered metamorphic zone rocks from Maqarin. 30 um-thick polished thin sections were prepared, following vacuum impregnation with blue-dyed epoxy resin. The polished thin sections were initially examined in transmitted light by Zeiss AXIOPLAN 2 optical microscope. High-resolution petrographical observations were subsequently made by backscattered scanning electron microscopy (BSEM). Before examination by BSEM, the polished thin sections were coated with a thin (20-30 nm) film of carbon. BSEM observations were made using a LEO 435VP variable-pressure digital scanning electron microscope (SEM), fitted with a solid-state 4-element (diode) backscattered electron detector. It was equipped with an Oxford Instruments ISIS 300 energy-dispersive X-ray microanalysis (EDXA) system with a Si-Li X-ray detector. The LEO 435VP instrument was operated in high-vacuum mode ($<1 \times 10^{-4}$ torr chamber vacuum). The SEM instrument was operated using a 20 kV electron beam and BSEM images were recorded digitally as standard TIF images. Image brightness in BSEM images is related to the average atomic number of the phases observed (Goldstein et al., 1981), allowing differentiation of the different minerals present. Mineral/phase identification was aided by microchemical information obtained from EDXA spectra recorded simultaneously during BSEM analysis.

A4.1.1.2 Electron probe microanalysis (EMPA)

EPMA was carried out by the BGS to determine the microchemical composition of individual mineral species. It was also used to generate images of the distribution of key elements (microchemical maps) in thin sections of selected samples of the primary and retrograde hydrated and altered rocks from the metamorphic zone at Maqarin.

Microchemical analysis

Quantitative wavelength-dispersive (WD) EPMA was undertaken, using a computer-controlled Cameca SX50 electron microprobe fitted with three wavelength-dispersive spectrometers. An electron beam accelerating voltage of 15 kV and 30 mA beam current was used for the analyses.

Microchemical mapping

Microchemical X-ray (WD) maps of polished thin sections were recorded using the Cameca SX50 electron microprobe. The maps were recorded on a grid of 1024 x1024 pixels, and were generated using a beam accelerating voltage of 15 kV and a beam current of 100 nA. Typically, the spot size was 2 µm diameter, with a pixel dwell-time of 90 milliseconds (analytical run time of approximately 7 hours per map). Maps were recorded to examine the distributions for Ca, Na, K, S, Se and P, in particular. The results are presented as colour maps with a rainbow scale, where magenta shows low concentrations and red high concentrations. The scale is relative, to suit the range of counts in each map, and absolute concentrations vary from map to map.

A4.1.1.3 Laser-ablation mass spectrometry (LAMP-ICP-MS)

LAMP-ICP-MS analysis was undertaken by BGS, using a purpose-built laser ablation microprobe system designed and built for the BGS by the Department of Chemistry, Birkbeck College, University of London. The system comprises a Spectron Nd YAG ultraviolet laser linked to a high-quality Leitz optical microscope. The laser-microscope system utilises a BGS custom-designed laser ablation chamber, with an optical quartz window, which is flushed by an argon carrier gas stream. The argon stream transfers ablated material to the plasma source in a VG Plasmaquad 2+ spectrometer ICP-MS instrument, using a modified dual-flow sample introduction system. The LAMP-ICP-MS system has been described in detail by Chenery and Cook (1993).

The LAMP-ICP-MS system provides data in terms of relative element (ion mass) ratios. This is converted to absolute concentrations by internal normalisation of the data to an element of known concentration in the mineral, analysed simultaneously during the LAMP-ICP-MS analysis. Where appropriate, LAMP-ICP-MS analyses are cross-referenced to equivalent EPMA analyses, to compare the data derived by each technique. This approach has been applied very successfully by the BGS to study the distribution of uranium, and other trace elements in single mineral grains, for previous natural analogue studies (e.g. Linklater, 1998).

A4.1.1.4 X-ray diffractometry (XRD)

Material was selectively removed from the hand specimen (using a diamond micro-drill where necessary) and ground up under acetone. The resulting suspension was placed on a silicon wafer and the acetone evaporated off to leave an oriented mount. XRD was performed using a Philips PW1700 series diffractometer with Co-Kα radiation, operating at 45kV and 40mA. The samples were scanned over the range 1.5-$^{\circ}2\theta$, at a scanning speed of 0.5$^{\circ}2\theta$/minute. Diffraction data were analysed using Philips X'Pert software, coupled to a International Centre for Diffraction Data (ICDD) database.

A4.1.2 CEA methods

A4.1.2.1 Protocols for the bulk analysis of rock samples

UT2A (Bordeaux University): after grinding, the samples were dissolved in different acid baths (see Table A4.1) with microwave stimulation.

The liquid volume is then adjusted to 50 mL with high purity DI water. A frontal filtration (0.45 µm) is done before measurement. Two measurements were made for each sample using high resolution ICP-MS. Quantification is done by a technique of spike additions at 5, 10 and 15 ppb. Based on the mineralization of 0.5 g of solid sample, the quantification limit, taken as ten times the detection limit of blanks, was 0.1 µg g^{-1} for Mo, 0.05 µg g^{-1} for W and 0.01 µg g^{-1} for Re. Concentration evaluations were done using the following isotopes: ^{95}Mo, ^{182}W, ^{185}Re. The uncertainty of the results depends on the concentration range. For Mo, the uncertainty is about 5 %; for W and Re, uncertainty ranges between 5 % and 30 %, depending on the concentration level. For sample M00-1-23, undissolved black residues were found after mineralization.

Table A4.1 Mineralisation protocol used by UT2A

Stage	Reactant	Volume (mL)	Power (W)	Time (minutes)
1	HNO_3	6	20	5
2	HCl	5	40	5
3	HF	15	40	10
4	-	-	170	20
5	HCl	3	30	10
6	H_2O	40	70	10

BGS: The ICP-MS used in this work was a VG Plasmaquad 2+ in conjunction with a Gilson 222 autosampler. The system is controlled by a Dell Optiplex 433/MX computer through dedicated ICP-MS software. The ICP RF forward power used is 1350 W. Coolant, auxiliary and injector gas-flow rates were set at 13, 1.0 and 0.93 l min^{-1}, respectively. Data were acquired in peak jumping mode using 3 x 30 s acquisitions.

On receipt, the samples were registered and then dried at 40°C. The sample weights were recorded, before and after drying, and the loss of mass calculated. The samples were disaggregated and, where necessary, milled in agate.

The samples were then subjected to a mixed-acid attack by weighing 0.2 g into a PTFE dish, adding a few drops of deionised water and 5 mL of concentrated nitric acid and leaving for two hours. The samples were then heated at 100°C to dryness before adding 5 mL of hydrofluoric acid and leaving overnight. The following day, 4 mL of nitric acid and 2 mL of perchloric acid were added and the samples heated at 100°C for four hours, and then at 140°C until near dryness. Another 4 mL of nitric acid and 2 mL of perchloric acid were added and the samples heated at 190°C until near dryness. When cool, 1 mL of nitric acid and 4 mL of deionised water were added and the solutions warmed for 10 minutes. The solutions were then decanted into HDPE bottles with 15 mL of deionised water, which was used to rinse the PTFE dishes. Two blanks and reference material AGV-1 were processed in an identical manner to the samples.

An element menu, containing isotopes of the elements of interest, was compiled. To ensure that the elements were free from polyatomic interferences, a number of isotopes of each element were selected: ^{95}Mo, ^{98}Mo, ^{182}W, ^{183}W, ^{184}W, ^{185}Re and ^{187}Re. The sample solutions were diluted by a factor of ten, by the addition of 1% nitric acid and 10 µgL^{-1} In and Bi internal standards, before aspiration into the ICP. Calibration standards containing the elements of interest were prepared by serial dilution from 10 mg L^{-1} Spex ICP-MS multi-element standards. A 10 µg L^{-1} check solution was included at regular intervals throughout the analysis run and used to correct for instrumental drift.

Raw data were transferred to an Excel spreadsheet and corrected for instrumental drift, matrix suppression, dilution and reagent blanks. All calculations were independently checked.

Independent QC solutions were also included in the analytical runs, and were within normal 2σ control limits of ±10%. Data for duplicate dissolutions were also within ±10% of each other where the concentrations were not close to the detection limit. Values obtained for AGV-1 were 90% for Mo and 112% for W of the quoted concentration. No suitable reference materials could be found for Re (which is why it is often used as an internal standard). All the isotopes for each element recorded the same value within experimental error, indicating there were no spectral interferences on these samples.

LARC (Cadarache) : (from analytical report 2000/1008 of December 13th, 2000): after drying at 105°C during 24 h, mass loss was recorded. Samples were kept in a dessicator and stability of samples mass checked.

Semiquantitative panoramic analysis :

Alkaline fusion at 1100°C in a Li metaborate - Li – tetraborate mixture (0,2 g of sample + 1 g de fusing mixture). ICP-MS analysis in semi-quantitative mode. This first stage produced qualitative to semi-quantitative data (depending of the element) on a large panel of elements. Re was, however, lost during this preliminary exploration, due to the heating.

Quantitative analyses of Mo, W, Re, Cr, Mn and Fe

Three different procedures were used for the mineralization of the rock samples :

- alkaline fusion and dissolution in nitric acid (one measurement, 0.2 g per sample)
- mineralization under microwave in an open reactor under reflux in two stages (HCl + HNO_3 then HNO_3 + HF) for the cement and basalt samples (two measurements, 0.2 to 0.5 g per sample).
- mineralization under microwave in a closed reactor in three stages (HNO_3 + H_2O_2 then addition of $HClO_4$ then HNO_3 + HF) for micrite samples (two measurements, 0.2 to 0.5 g per sample).

Blanks were done for each procedure and taken into account for the quantification. Analyses were done by ICP-MS in quantitative mode with internal and external standards. For the quantification of iron, ICP-AES was also used due to the weak proportion of the ^{57}Fe isotope (isotope ^{56}Fe is strongly interfered by ArO). Figure A4.1 shows an example of mass spectrum for the Re and W isotopes.

In all cases the mineralisation of the sample was complete (clear solutions without residues). Homogeneous values were found for each technique. The alkaline fusion technique leads to losses of Mo and Re. Only values obtained by the microwave mineralization were kept. Quantification limits were considered to be 0.2 and 0.1 µg/g for W and Mo. However, detection limits are much lower, and a semi-quantitative estimation of Re was possible down to 0.03 µg/g. Typical mass spectra are presented in Figure A4.1.

Figure A4.1 Spectrum on the 180-190 mass interval (LARC) Top: blank, middle: cement M99-1-43a, bottom: cement M00-1-4

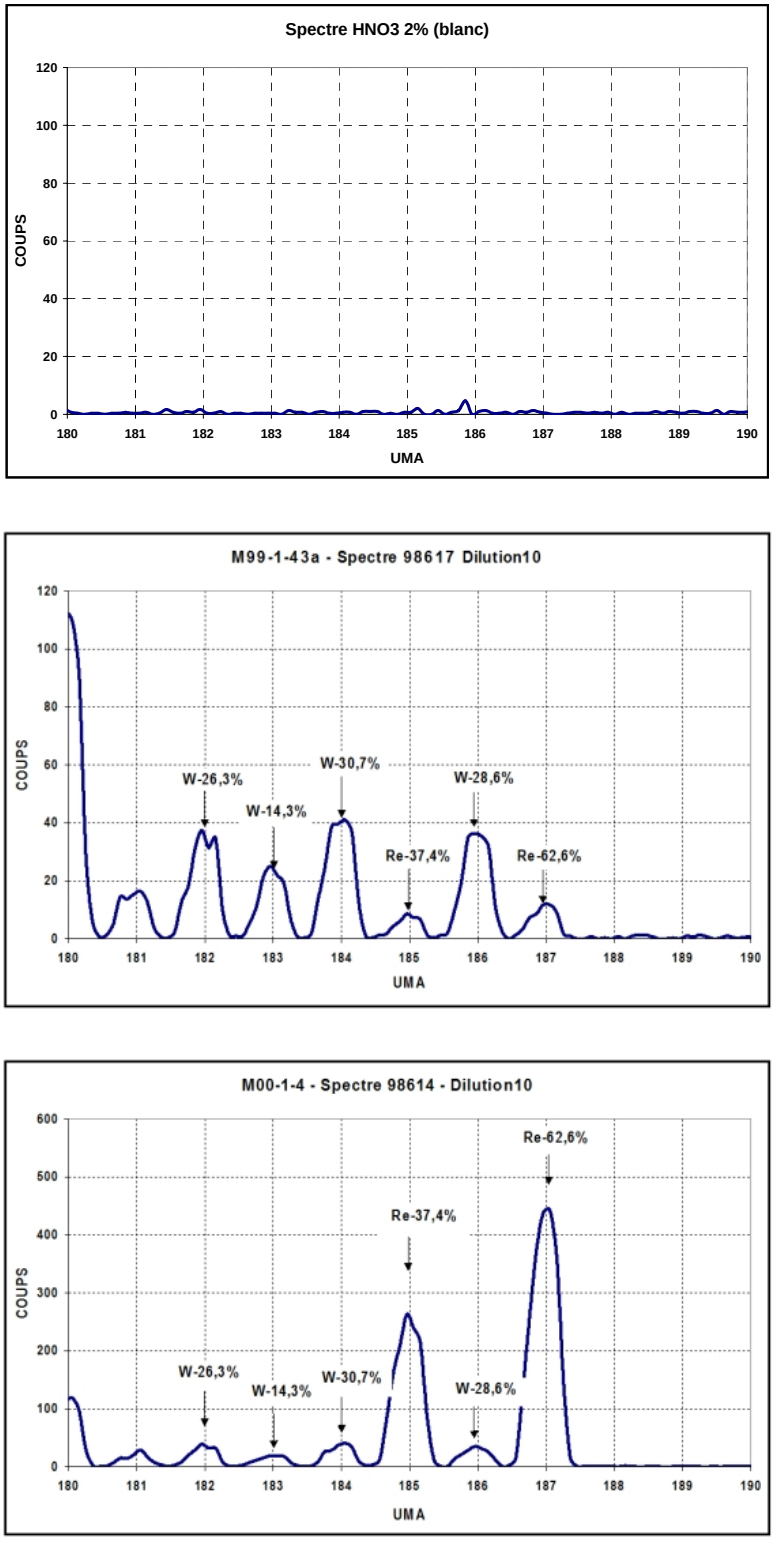

A4.1.2.2 Protocol for SEM observations

The samples were sawn and polished using ethanol and avoiding any contact with water. The same samples were used for SEM, µXANES, SIMS, nuclear microprobe and ICP-MS LA analyses. Therefore, SEM reconnaissance work could be used for all techniques in which observation capabilities were limited by low-quality sample lighting or binocular observation. It was also possible to combine on the same spot or profile different

analytical techniques. A carbon coating was evaporated under vacuum on the surface of the samples.

A Philips XL30 SEM was used, combined with an Oxford Link EDX analyser. The SEM was usually operated at 20 kV, 25kV or 30 kV and the working distance was 10 mm. Acquisition time for EDX analyses ranged from 20 to 100 sec. Spot size and other analytical settings were checked, to ensure ~20 % electronic dead time.

A4.1.2.3 Protocol for XANES and µXANES investigations

X-ray absorption Near Edge Structure Spectroscopy (XANES) can provide information about the oxidation state of an atom and the symmetry and bonding of its local environment. The pre-edge region of the Cr XANES changes drastically between the Cr(VI) and Cr(III) oxidation states. A strong pre-edge, due to a 3d-4p atomic orbital mixing in the four-coordinate Cr(VI), appears in the K-edge XANES. The height and/or the area of this pre-edge in a chromium spectrum is proportional of the amount of Cr(VI) in the sample.

Bulk Cr K-edge XANES spectra were scanned on the BM 30-b beam line (FAME) at the European Synchrotron Radiation Facility (ESRF, Grenoble, France) with Si (111) monochromator crystals. Spectra were scanned using the fluorescence mode, due to the very low Cr concentration. The storage ring was operated at 6 GeV with a current of 200 mA. The size of the X-ray source was 0.4x0.2 mm, to allow determination of the mean Cr(VI)/Cr(tot) ratio in the samples. Energy of XANES spectra was scanned from 40 eV below the pre-edge to 100 eV above. Samples were crushed before analysis to obtain homogeneous samples.

Samples were examined using the ID21 X-ray microscopy beam-line, at the ESRF (Grenoble, France). The beam spot was focused down to 1x1 μm^2 using a 69.7 µm diameter Fresnel Zone Plate lens (FZP). FZP focal length and depth of focus were 67.9 mm and 64 µm, respectively, at 5.989 KeV. The white beam was monochromatized with a double Si(111) monochromator. The energy calibrations were performed using pure Na_2CrO_4 and Cr_2O_3, for Cr(VI) and Cr(III) respectively.

The evolution of Cr in the material was assessed by moving the sample through the X-ray microprobe. Transverse scans and fluorescence 2D maps were performed at three energies: E_1=5.980, E_2=5.993 and E_3=6.017ev characteristic of the background, the presence of Cr(VI)(pre-edge)) and total Cr, respectively. The ratio $[(E_2-E_1)/(E_3-E_1)]$ of the spectra lines and the 2D Cr speciation images depicts the Cr(VI) distribution. This procedure generates 2D chemical maps at the micron scale. Ca Kα fluorescent maps and lines were simultaneously acquired with an energy dispersive spectrometer associated to a Ge multi-channel analyzer. Micro-XANES spectra were collected at different points of interests (POIs). Since, for a Fresnel zone plate, the focal length varyies with the incident X-ray energy, the size of the microprobe is kept constant during the XANES scan by changing automatically the distance between the X-ray lens and the sample.

A4.1.2.4 Protocol for nuclear microprobe (PIXE)

The nuclear microprobe analyses were conducted at the Laboratoire Pierre Süe (CEA/CNRS) in Saclay. The proton beam (3 MeV, 300 to 400 pA) was aimed perpendicular to the sample surface. The diameter of the beam was about 2 µm. The emitted X rays were detected by a cylindrical SiLi detector, covered by a 52 µm thick Al foil, in order to select the high-energy part of the spectrum (> 3 keV). Energy calibration was achieved using quartz, glass and metal standards. Deposited charge for analyses ranged from 0.2 to 6 µC, the latter corresponding to about 6 hours of acquisition time for 2D map.

A4.1.2.5 Protocol for ICP-MS laser ablation

The polished sample was placed in a cylindrical ablation chamber, flushed by pure Ar (1.1 l/min). The laser used for ablation was a Microprobe2 Nd YAG pulsed laser (λ = 266 nm, maximum energy 5 mJ). The diameter of the laser spot on the sample was set at 10 µm and the sample movement under the beam was controled by a programmable stage (20 µm/s for individual transects, transects separated by 30 µm). The laser was used at 70 % of its maximum energy and the laser shots were done with a 5 Hz frequency. The laser and stage-steering softwares (Merchantek E0) were coupled to analysis software of the VG Elemental PQ Excell ICP-MS. This is used for isotope ionisation and detection (Ar plasma, quadrupole separation). The dwell-time was set at 20 ms.

A4.1.2.6 Magnetic measurements

Magnetic characterisations were conducted on whole rocks or separated fractions. On oriented samples, plugs were cored and sawn using diamond-drilling machines and saws. The saturation remnant magnetisation **Mrs** (mA m^2 kg^{-1}), saturation magnetisation **Ms** (mA m^2 kg^{-1}), coercitive field **Hc** (kA m^{-1}) and remnant coercitive field **Hcr** (kA m^{-1}) were evaluated. This was achieved by applying a magnetic field and studying the resulting hysteresis cycles on 60 mg aliquots, using a VSM Micromag. The determinations are done in triplicate in order to evaluate the reproducibility of the measurements. Figure A4.2 shows where these quantities are determined on a hysteretic cycle.

The specific magnetic susceptibility χ (m^3 kg^{-1}) was measured using a Kappabridge KLY2 – CS2 susceptometer. The powdered sample is placed into a quartz tube. The measurements may be performed from –196°C to 700°C.

For some samples, the magnetic minerals were separated and concentrated, using a chemical treatment (diluted acetic acid attack during 6 to 10 hours. The clay fraction was then dispersed, using sodium hexametaphosphate) combined with a magnetic separation (REE magnet in a clean plastic tube).

For the palaeomagnetic investigations, thermal and HF demagnetisation protocols were applied to oriented plugs cored in selected samples of Khushaym Matruk (LA32, LA33, LA34). Trials were also conducted on two unoriented samples from Maqarin. A Pyrox amagnetic annular furnace was used to apply progressive temperature steps on the samples from 50°C to 450°C. Between each temperature step (45 minutes duration), the samples were cooled down and the intensity (I), declination (d) and inclination (i) of the remnant magnetisation were measured using a 2G cryogenic magnetometer. The magnetic susceptibility at room temperature was also monitored between each temperature step, in order to detect possible changes in magnetic mineralogy during the process. Another demagnetisation protocol was applied to duplicates of the same samples by successive steps, during which an appropriate alternative magnetic field is applied to the cores (AF demagnetisation). Results of these investigations were plotted in orthogonal vector plots (Zijdervelt diagrams).

Figure A4.2 Schematic hysteretic cycle showing measured magnetic quantities for a hypothetical ferromagnetic phase (H: magnetic field; M: magnetisation; Hc: coercitive field; Ms: saturation magnetisation; Mr: remnant magnetisation)

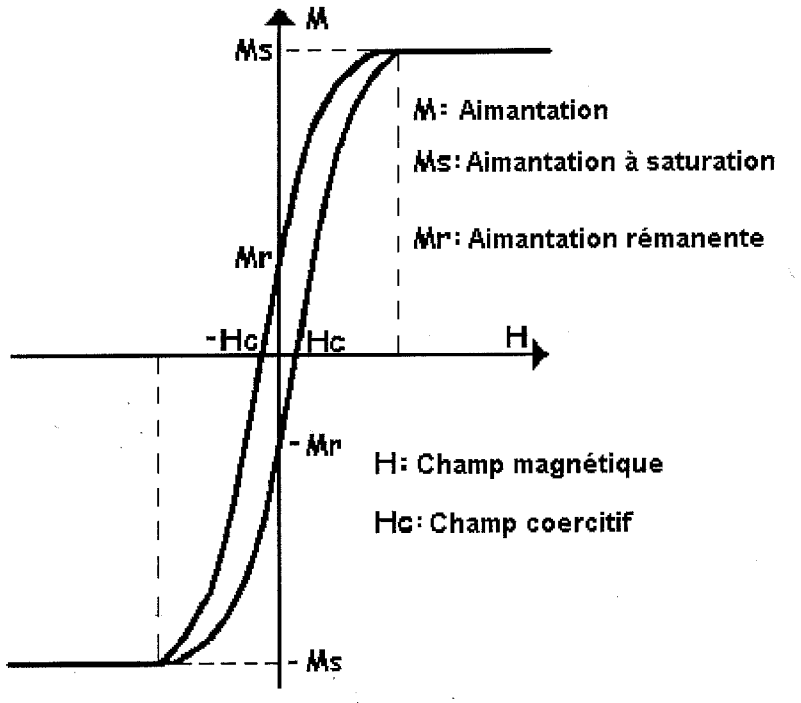

A4.1.2.7 XRD and SEM

XRD spectra were collected on separated fractions or ground whole rock with a Philips 1729 (Co anticathode) and a Brüker (Cu anticathode) diffractometers.

Separated magnetic fractions or whole rock polished sections were observed with a JSM-6320F using a field emission gun or a Philips XL30 SEM coupled to an Oxford EDX analyser. The samples were coated with an evaporated carbon layer. The acceleration tension was usually set at 15 kV or 20 kV and the working distance set at 10 mm.

A4.1.2.8 Thermal analyses

DTA-TG measurements were done on a Setaram TGA 92 thermogravimeter. The samples were ground in an agate mortar, dried in air at 50°C overnight. The measurements were done under a N_2 atmosphere. However, trace O_2 was probably present in the gas phase, as shown by the occurrence of oxidation reactions of organic matter. From 20 to 70 mg of ground sample was put in a Pt crucible and heated at a heating rate of 4 K min^{-1} from 40°C to 1000°C.

Evolved-gases analysis was performed on selected samples using a Netsch STA409 thermobalance coupled to a Balzers Thermostar 300 mass spectrometer. The analyses were done under air atmosphere. The sample preparation is identical as above for DTA-TG.

A4.1.2.9 Infrared spectrometry

Absorption IR spectra were collected on a Nicolet Nexus Fourier transform IR spectrometer (KBr separator, DTGS KBr detector). Prior to measurements, the samples were ground in an agate mortar and dried for several hours at 50°C or 105°C under air atmosphere. The samples were diluted and pressed into 200 mg KBr pellets at dilutions between 0.5 % and 1.2 %. The spectra were obtained in the spectral range 400-4000 cm^{-1} after 64 scans and with a 2 cm^{-1} resolution. Several duplicate or triplicate spectra were

obtained, to evaluate the representativity of measurements (about 1 mg at each samples, against about 50 mg for thermal analyses). The altered biomicrite is a complex mixture containing, for example, calcite, kaolinite, apatites, organic matter, aragonite, calcium sulphates and ettringite. Therefore, it was necessary to identify all spectral lines and to find absorption bands with minimum cross-interferences. In order to process the data, the spectra were set on an absorbance scale and individual peak baselines were estimated. The absorbance was normalised to a dilution of 0.5 %. Table A4.2 provides information on the main absorption bands observed on the spectra, together with their identification. The spectral line 2927 cm^{-1} was chosen to compare bitumen concentrations. The underlying background, due to calcite lines at 2874 and 2982 cm^{-1}, was taken into account. The 875 cm-1 absorption band was used for comparing calcite concentrations because this line is generally interference-free and well-defined. The 603 cm^{-1} band was used for apatite when no gypsum was present in the sample. Otherwise, the 569 cm-1 band was taken to evaluate the intensity of the interfered 603 cm^{-1} band. For kaolinite, the sharp 3692 cm^{-1} band was used. Peak base lines were carefully drawn to compute absorbances.

Table A4.2 Identification of IR absorption bands

Absorption Wavenumber (cm-1)	**Mineral phases**	**Comment**
3692	Kaolinite	Sharp ; used to normalise kaolinite
3648	Kaolinite	Sharp
3619	Kaolinite	Sharp
3610	$CaSO_4$ $0.5H_2O$	Weak
3565-3570	Apatite	Weak
3550	$CaSO_4$ $0.5H_2O$	Weak
3540	Gypsum	Weak
2982	Calcite	Weak
2925	Bitumen	Used to normalise bitumen
2873-2875	Calcite	Weak
2852	Bitumen	Weak
2512	Calcite	Weak
2590	Calcite	Weak
1797	Calcite	Sharp ; weak
1638	Structural water in thaumasite-ettringite	Weak
1618	$CaSO_4$ $0.5H_2O$	Weak
1484	Thaumasite, Vaterite	Strong
1475	Aragonite	Strong
1452	Ankerite ?	Strong
1422-1426	Calcite, Vaterite	Strong ; broad
1149-1152	$CaSO_4$ $0.5H_2O$	Strong ; broad
1113	$CaSO_4$ $0.5H_2O$	Strong
1110	Kaolinite	Strong
1109	Ettringite, Thaumasite	Strong ; broad
1093-1095	Apatite, $CaSO_4$ $0.5H_2O$	Strong ; broad
1082	Aragonite	Sharp ; weak
1033	Kaolinite	Strong ; broad
1038-1040	Apatite	Broad ; strong
1010	Kaolinite	Medium ; broad
962	Ettringite, Thaumasite	Weak to medium ; broad
938	Kaolinite	Weak
911-913	Kaolinite	Sharp ; weak
875	Calcite (+ Thaumasite)	Sharp ; strong; used to normalise calcite
870	Vaterite	Sharp
855	Aragonite	Sharp

848	Calcite	Weak ; sharp
795	Kaolinite	Weak
755	Kaolinite	Weak
712	Calcite	Sharp ; strong
701	Aragonite	Sharp ; weak
660-667	$CaSO_4$ $0.5H_2O$	Medium ; sharp
606	$CaSO_4$ $0.5H_2O$	Weak
603-605	Apatite	Sharp ; weak ; used to normalise apatite
569	Apatite	Weak
540	Kaolinite	Medium
470	Kaolinite, Apatite	Sharp ; medium
429	Kaolinite	Weak

A4.1.2.10 Leaching test at constant pH in a dilute solution

The selected leaching test has been developed to test the leaching of industrial cements (Adenot, 1992).

Characterisation of the cement samples

The cement samples used for this experiment were taken from the D2 core (Figure A4.3). The D2 borehole, drilled in May 1999 is located in the metamorphosed zone at about 141 m from Adit 6 entrance (Smellie, 2000). The core has a total length of 2.4 m. Two subsamples were allotted to the leaching experiment:

- DD-M-99-2/1: core section from 124 to 135 cm. This section is strongly altered at one end. The other end displays a state of much lower alteration but an important fracture. The cement matrix is crossed overall by fine veins filled with white/translucent minerals.
- DD-M-99-2/2: core section from 99 to 106 cm. This core section shows moderate to low alteration on inspection. The drill core material is composed of cylindrical coupons of about 1 cm thickness. The red stain of the two samples indicate the probable presence of iron(III) oxides.

Figure A4.3 Visual aspect of the D2 core in the field (left). The fragmentation of the core is due to the mechanical stresses during drilling. On the right: subsample DD-M-99-2/1 (124-135 cm).

A XRD characterisation of these two subsamples was done on their less-altered part. The results (Table A4.3) show differences in the mineralogy of the two core sections. Except for mono carbo aluminate, all detected minerals were previously identified in Maqarin metamorphosed rocks. In both cases, calcite is an important constituent. Larnite is found only in subsample DD-M-99-2/1. This subsample was therefore selected to conduct the leaching experiment, by reference to industrial cements containing C3S and

C2S phases. Several coupons of this material were prepared in the less altered part, in order to conduct the leaching test as well as further characterisations.

Table A4.3 XRD characterisation of the two cement samples selected for the test

DD-M-99-2/1	DD-M-99-2/2	Chemical formula	Ref.
Calcite	Calcite	$CaCO_3$	05-0586
Fluorellestadite	Fluorellestadite	$Ca_{10}(SiO_4)_3(SO_4)_3F_2$	45-0009
Brownmillerite	Brownmillerite	$Ca_2(Al,Fe)_2O_5$	30-0226
Ettringite	Ettringite	$Ca_6Al_2(SO_4)_3(OH)_{12}26H_2O$	41-1451
Mono carbo aluminate	Mono carbo aluminate	$Ca_4Al_2(OH)_{12}(CO_3)5H_2O$	87-0493
Larnite (weak)		Ca_2SiO_4	33-0302
Portlandite (?)	Portlandite (?)	$Ca(OH)_2$	44-1481

A thermogravimetric analysis of the ground cement was conducted from ambient temperature to 1000°C under an N_2-O_2 atmosphere. The sample was placed in a Pt crucible and heated at 5 K min-1. Two major endothermic events are recorded at 120°C and 770°C, respectively, and attributed to ettringite (water loss) and calcite (decarbonatation). These two events are accompanied by mass losses of –12.5 % (40-215°C) and –10.8 % (630-850°C), respectively. A continuous mass loss of –5.64 % is also noted between 215 and 630°C and was not clearly attributed (CSH phases?). Wet chemical analyses have been also performed on the cement and reported in Table A4.4. A polished section was examined using the SEM, in order to characterise the fracture fillings and the matrix mineralogy. Qualitative and quantitative EDX analyses confirm that the fracture filling is composed of ettringite. This phase displays a typical lamellar section (Figure A4.4).

Figure A4.4 SEM – SE image of ettringite fracture fillings. Scale bar is 20 µm on the left and 5 µm on the right.

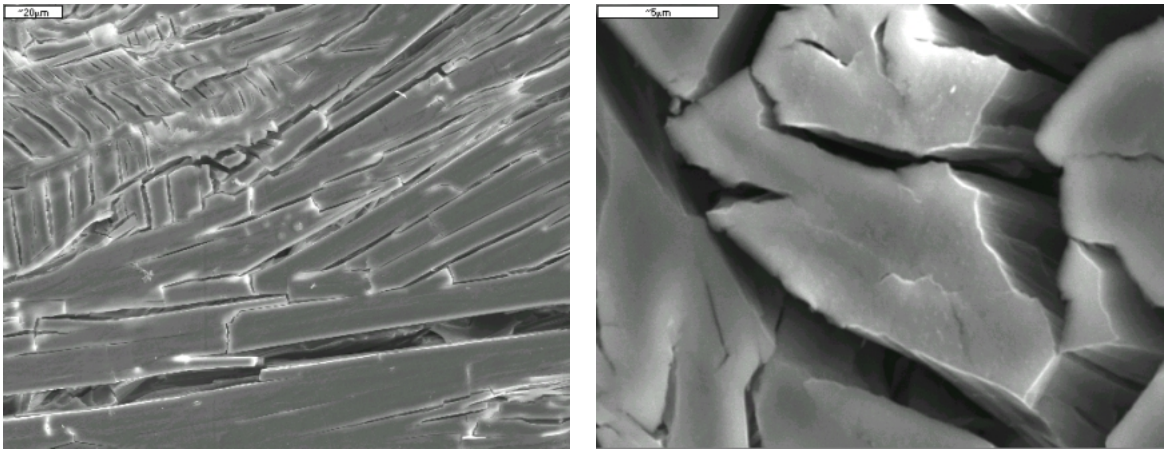

Figure A4.5 presents the aspect of a zone of the cement that is free of fractures. The cement matrix is clearly composed of several distinct mineral phases, with typical crystal sizes comprised between about 1 µm to more than 40 µm. Quantitative and qualitative EDX analyses conducted on this zone help to locate several of the phases identified by XRD: mono-carbo-aluminate, larnite, calcite. Spots containing Ca, P, Si and S were located but could not be interpreted in terms of a pure mineral phase. They probably correspond to a Si-Al-P containing ellestadite and perhaps apatite (although apatite was not detected using XRD).

Figure A4.5 Sample DD M99 2/1 – SEM/BSE image of a polished section of the cement matrix (20 kV ; bar scale = 20 µm on the top image, 5 µm on the bottom images). This image reveals the texture of this material made of different grains ranging from less than 5 to more than 50 µm. Several important phases are identified (ellestadite with Ca-Si-S-P, larnite, monocarboaluminate).

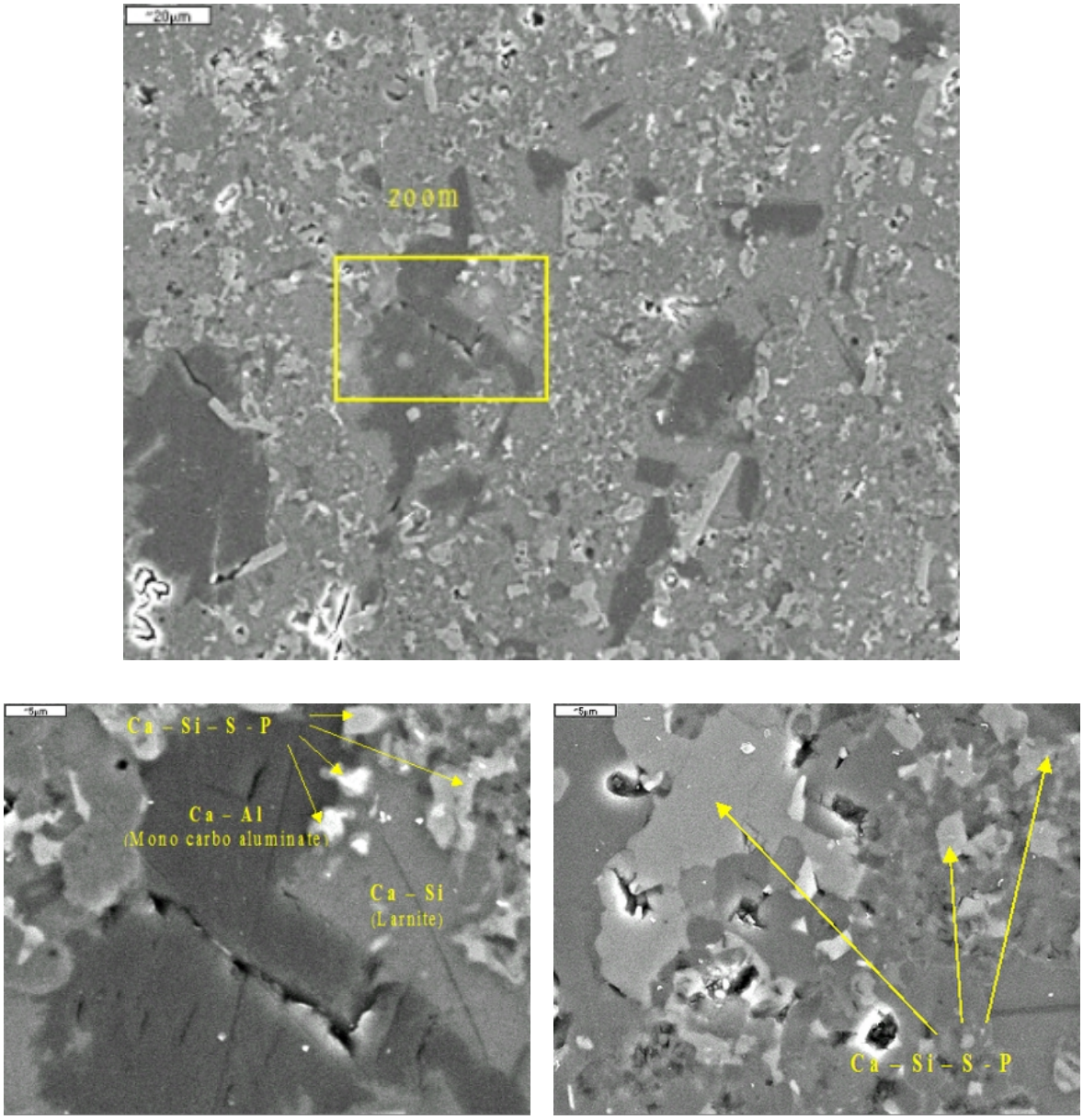

Figure A4.6 shows the qualitative spatial repartition of Al, Si, P, S and Ca on the section presented in Figure A4.5, showing the heterogeneous nature of this material.

The presence of portlandite was checked by putting 0.75 g of powdered cement in 10 mL of DI water and following the pH evolution. The pH instantaneously raises to 11 and then stabilises around 11.9 after 1-day interaction. This suggests that portlandite is initially not present in significant quantities in the cement (on the contrary, pH should have been raised to about 12.4). However, the hydration of C2S could produce, as a secondary product, a mixture of portlandite and CSH phases. A better compatibility between Ca, Si and water contents has suggested a cement model based on CSH1.1 rather than on pure larnite. A global mineralogical composition for the cement (Table 4.6.1) was computed, with the hypothesis that the ellestadite had an equimolar P/Si/S composition

and that brownmillerite had a Al/Fe ratio of 1. These assumptions are consistent with EDX spectra.

Figure A4.6 Sample DD M99 2/1 – SEM/EDX maps showing the distribution of Al, Si, P, S and Ca among the different minerals of the cement matrix.

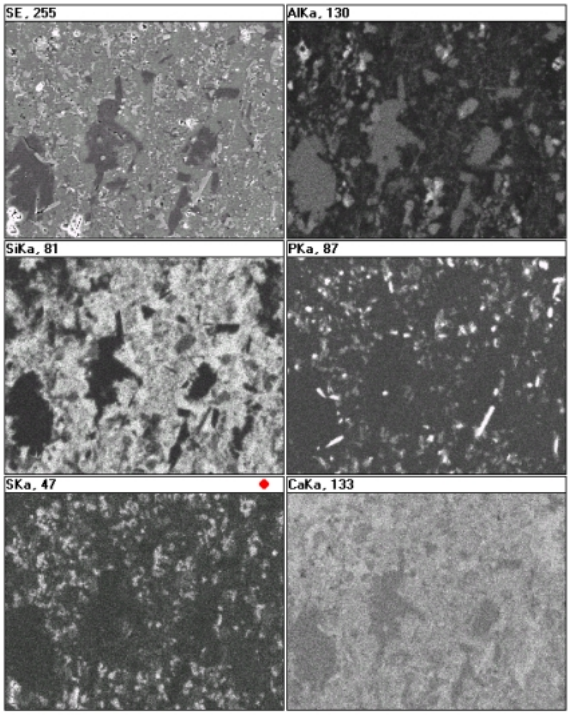

Experimental set up and protocol

The slab initially selected for the alteration experiment had to be changed because of a failure of the pH regulator. A new run was then started, using another cement monolith displaying a stronger initial alteration. The sample has a cylindrical shape (47.05 mm diameter, 7.4 mm thickness; Figure A4.7). The sample surface was polished prior to the alteration run.

Figure A4.7 Sample DD M 99 2/1 – Photograph sketch of the cement slabs used in the experiment (diameter 47 mm).

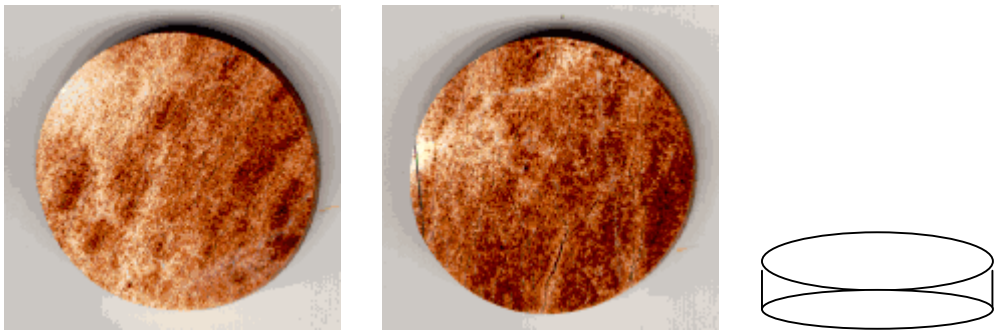

Table A4.4 Bulk chemical analyses of sample DD-M-99-2. The second column corresponds to the computation of oxide weight fractions from the model composition given in Table 4.6.1.

Compound (wt %)	**DD-M-99-2 (Adit 6 – 141 m) Analysis**	**Model cement (CSH based) Recomputation**
SiO_2	9.29	9.39
TiO_2	0.01	0
Al_2O_3	4.28	4.28
Fe_2O_3	1.52	1.52
MgO	0.04	0
CaO	43.84	42.76
Na_2O	0.04	0
K_2O	0.03	0
P_2O_5	2.21	2.26
CO_2 (*)	10.8	10.85
H_2O (**)	12.5	13.3
H_2O (***)	5.6	4.64
SO_4	not determined.	11.25
Total (****)	92.48	100.25

The sample is suspended in a reactor containing 1 litre of deionised water (Figure A4.8). The solution pH is maintained at 7 using an electronic burette delivering 0.25 M nitric acid. The leachate is completely renewed when 10 mL of nitric acid have been added. As a result, the solution volume is nearly constant and the ion concentrations remain low in the reactor, by comparison to pore-volume concentrations. The solution temperature is regulated at 20°C and homogenised by a magnetic stirrer. A CO_2 free nitrogen atmosphere is maintained in the reactor in order to prevent carbonation of the sample surface.

Figure A4.8 Sketch of the experimental set-up for constant pH leaching without contact with air.

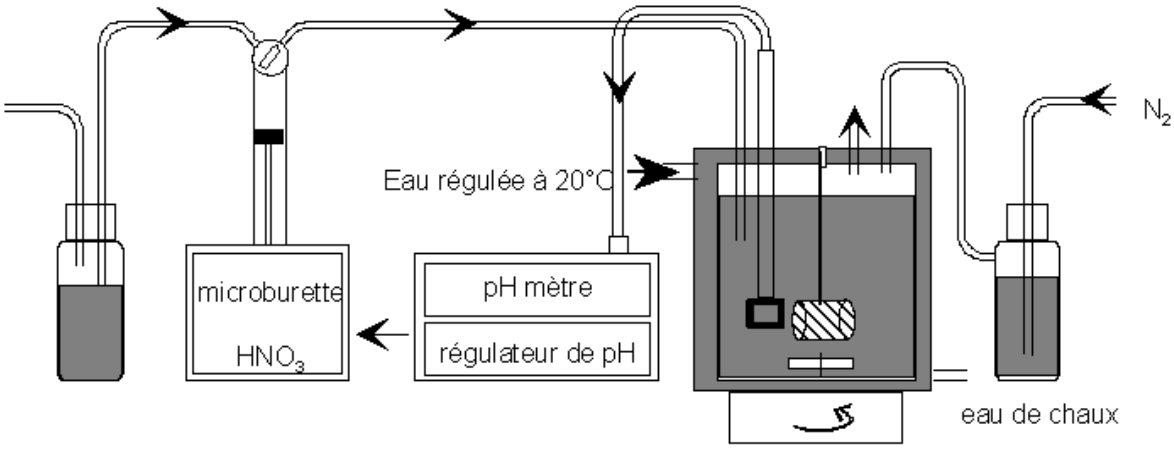

A4.1.2.11 Column leaching experiments

The experimental set-up is shown in Figure 4.75. A chromatography PEEK column filled with powdered material is placed in a thermostated cabinet (T = 25°C) and connected to a HPLC pump (JASCO PV 980) with 1/16" PEEK tubing. The internal volume of the columns is ~4.5 mL (10 cm length with 0.75 cm diameter) and the mean porosity of the filled columns was ~0.3 (pore volume ~1.5 mL). A pH electrode in a low-volume, flow-through cell is placed after the column and connected to a Consort C835 pH-meter. Measurements of pH, pressure drop and temperature are collected on a computer using the Hyperterminal software (Microsoft). Fluid samples are collected in PE tubes. Contact between the sample and the atmosphere was limited, but could not be totally avoided. No specific filtration process was applied to samples that were collected from the column through a PEEK frit with 5 µm cutting diameter. Two types of experiment were conducted (Table 4.7.4) :

- alteration of cement samples M99-1-41 and M00-1-4 by deionised water in equilibrium with the atmosphere
- alteration of the biomicrite M00-1-23 by deionised water equilibrated with portlandite. In this case, the deionised water in contact with atmosphere was pumped through a prequilibration column containing $Ca(OH)_2$ before injection in the marl column.

The flow rate was fixed at 0.01 mL/mn. In some experiments the flow rate was varied at definite stages in order to evaluate the effect of flow on the leached elements. The rock samples were first broken with a hammer wrapped in Al foil and then ground in an agate mortar. The 40-160 µm was selected for the leaching experiments. In order to avoid segregation between mineral phases, grinding was done in several stages with short grinding runs (30 s) and recovery of the coarser fraction (> 200 µm) for further grinding until no coarse fraction was left. A control by XRD was done on the calibrated powders. The powders were also characterised using binocular observation, BET surface area measurement (Table 4.7.5) and laser granulometry. The binocular observation of the powdered samples confirmed the existence of small particles adherent to large grains, as is suggested by grain-size distributions, especially for samples M00-1-4 and M00-1-23 (Figure 4.76).

XRD diffraction spectra of the heads of altered columns were also acquired in order to evaluate the dissolution of specific mineral phases.

A4.2 List of Samples Studied for Phase IV

Sample no.	Location	Description	XRD	Probe	Light micro-scopy	SEM	LAB ICP-MS
DD-M-99-2 core	140-150 cm	Partially altered marble				Yes	
M-99-1-29	Adit 6, 112 m	Recrystallised calcite vein			Yes		
M-99-1-28	Adit 6, 113 m east wall	Calcite vein overprinted by metamorphism			Yes		
M-99-1-16	E of bridge sentry post	Calcite vein			Yes		
M-00-1-42	Harza S14 core, 89.7 m	Marble with white veins	Yes	Yes		Yes	Yes
M-00-1-44	Harza S14 core 92.95 m	Altered to white + cobweb mesh of veins				Yes	
M-00-1-47	Harza S14 core 123.25 m	Fresh marble + alteration along fractures	yes	Yes			
M-00-1-50	Harza S14 core 127.7 m	Altered with veins, brecciation, yellow patches		Yes		Yes	
M-00-1-12 (*ex-M15 of phase I*)	Harza M15 core	Unaltered marble + red oxidised fractures		Yes		Yes	
M-00-1-16	Adit 6, 256 m	Green & purple veins in black marble	Yes	Yes	Yes	Yes	Yes
M-00-1-5 (*ex-M00-1-4*)	Adit 6, 256 m	Thick green & purple vein + marble	Yes			Yes	Yes
M99-1-31	Adit 6, 99 m	Tobermorite veins in BMF	Yes	Yes	Yes	Yes	Yes
M-00-1-34	Adit 6, 100 m	Small tobermorite vein.				Yes	x
M99-1-30	Adit 6, 100 m	Yellow and white vein fills in BMF			Yes	Yes	Yes
M-00-1-11	Harza S14 core 90.5 m	Core with ett/th/CSH in shear fractures			Yes		
M-00-1-17	Adit 6, 280 m	Ett/th/CSH veins in black marble	Yes		Yes		Yes
M-00-1-37	Adit 6, 318 m	White, hard vein fill in BMF. *Fracture source of M19 seep*.	Yes		Yes	Yes	Yes
M-00-1-21	Adit 6, 220 m	Cream vein fill in BMF	Yes				Yes

A4.3 XRD Traces from Maqarin Phase IV

Figure A4.9 XRD trace for sample M00-1-42.

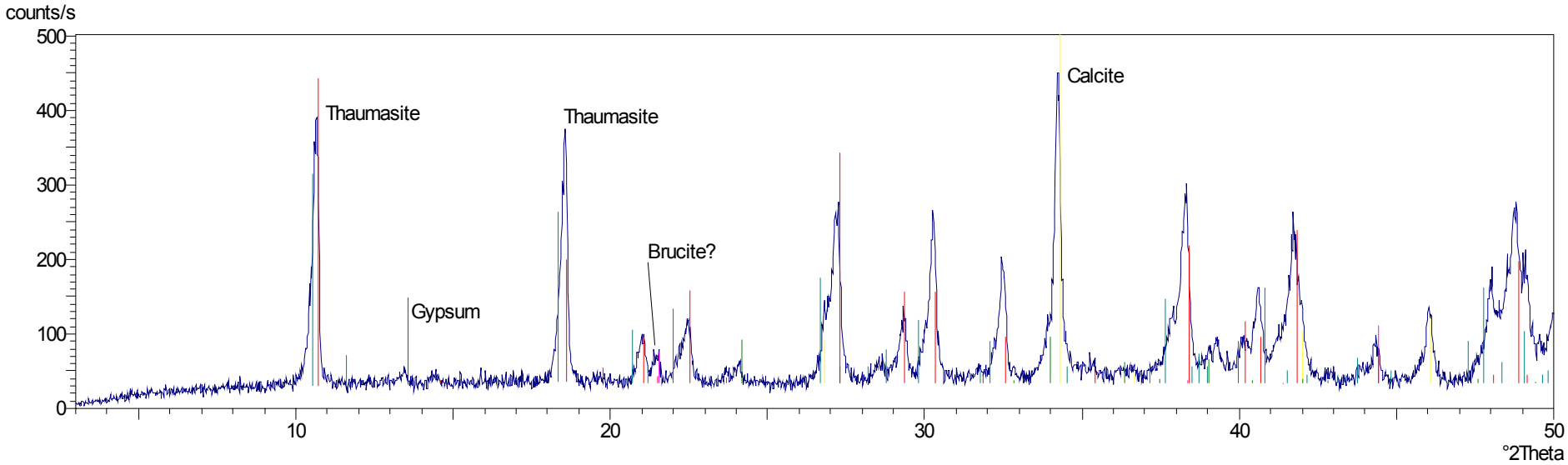

Figure A4.10 XRD trace for sample M00-1-47

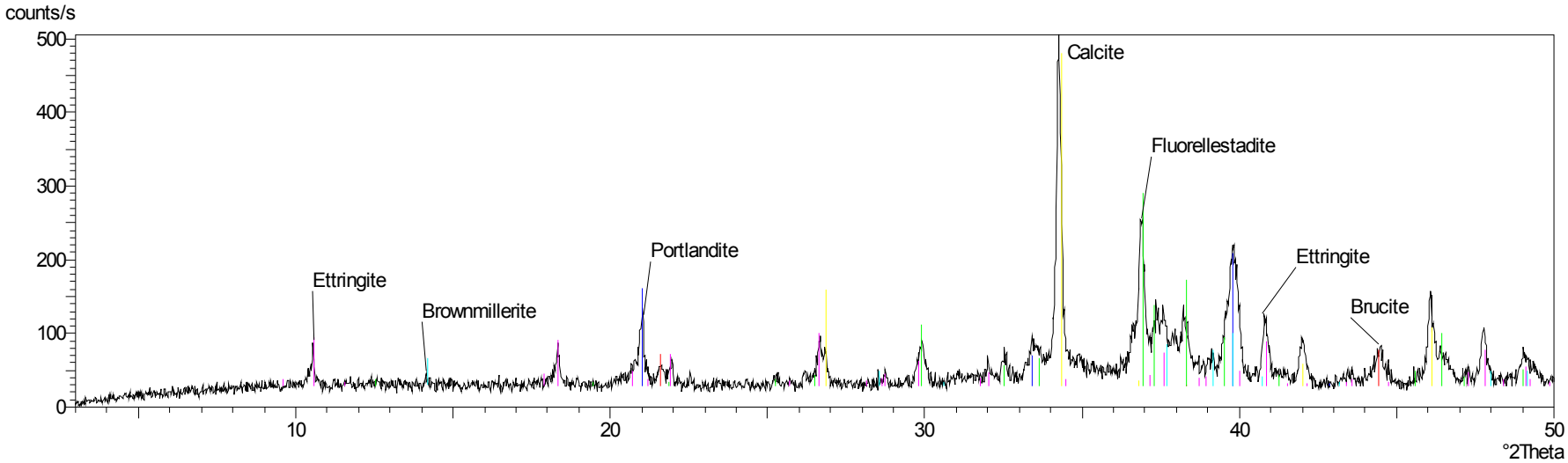

Figure A4.11 XRD trace for sample M00-1-16 (alteration products).

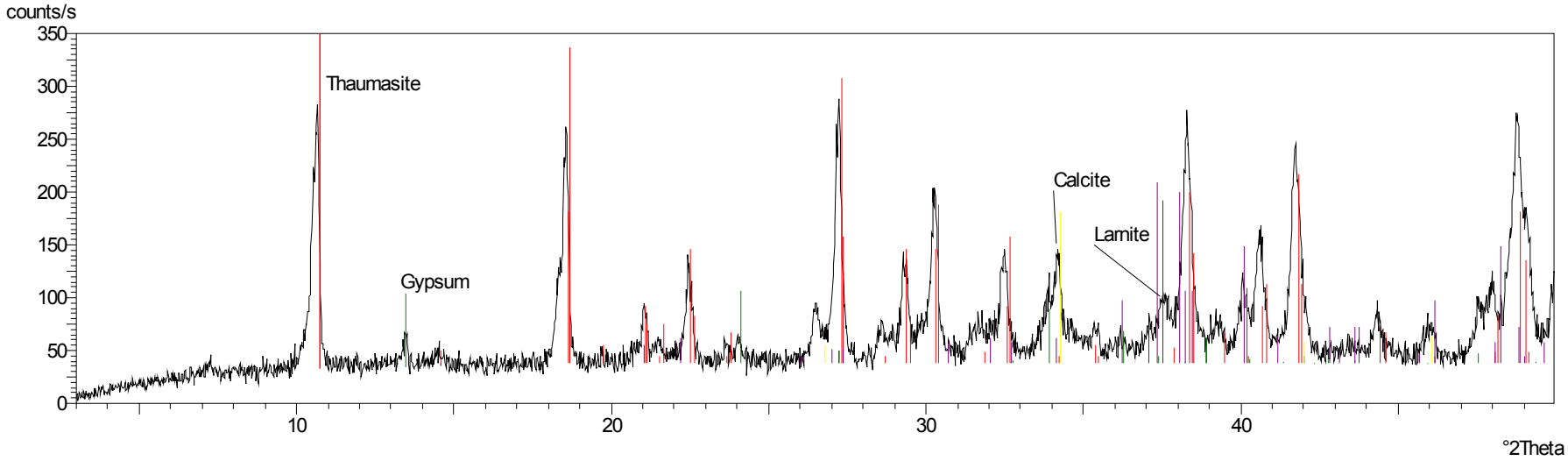

Figure A4.12 XRD trace for sample M00-1-16 (marble matrix)

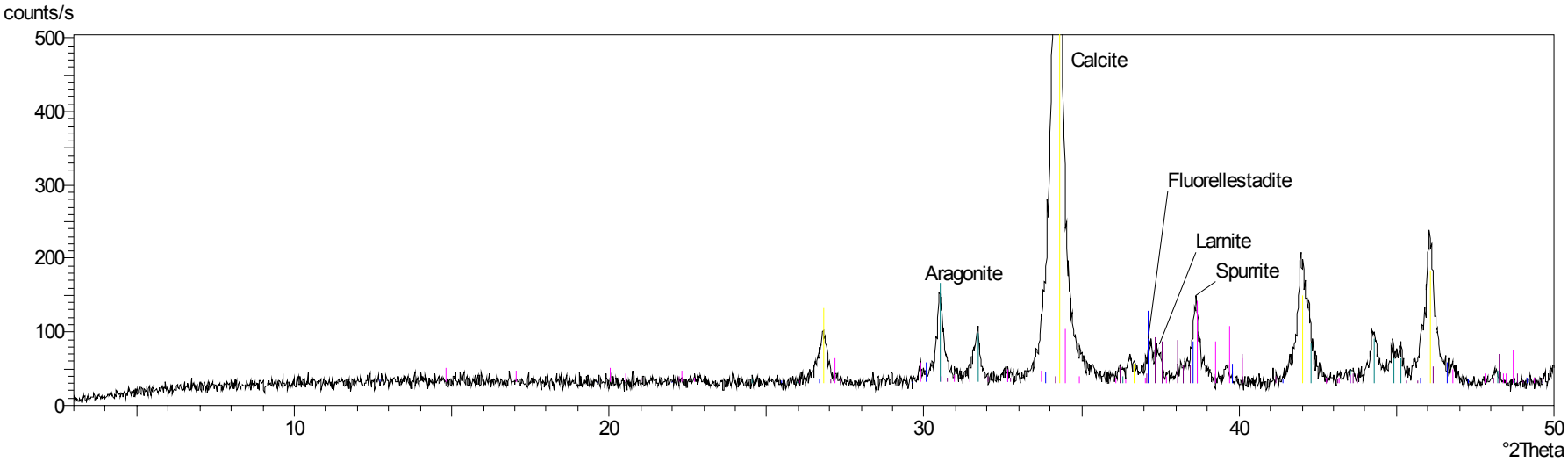

Figure A4.13 XRD trace for sample M00-1-5

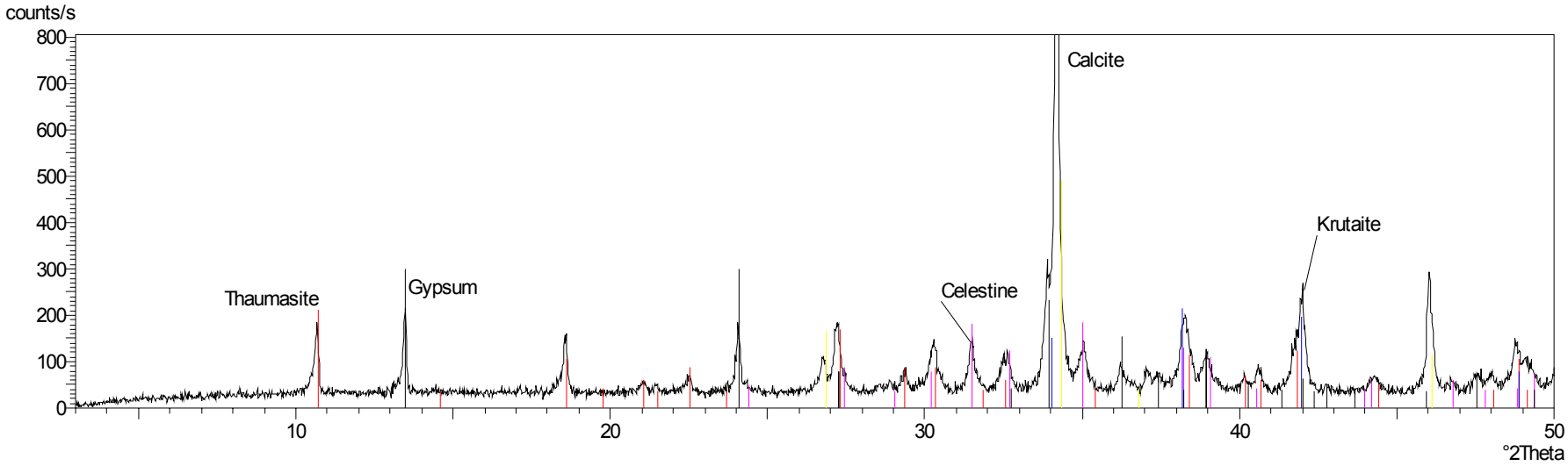

Figure A4.14 XRD trace for sample M99-1-31

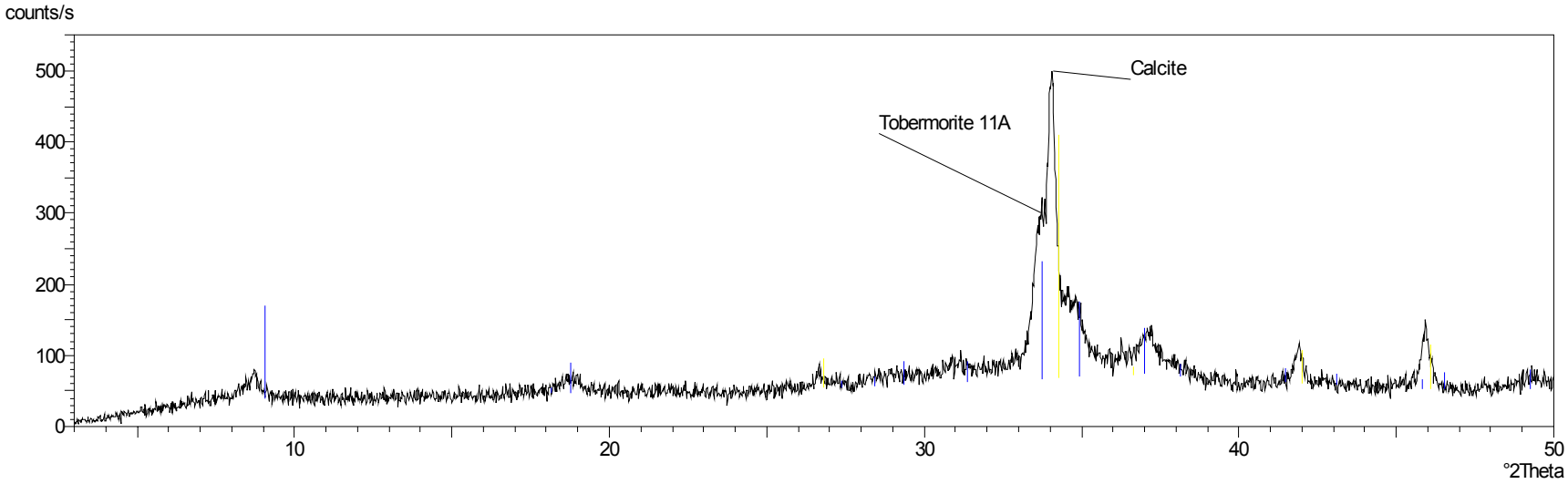

Figure A4.15 XRD trace for sample M00-1-17

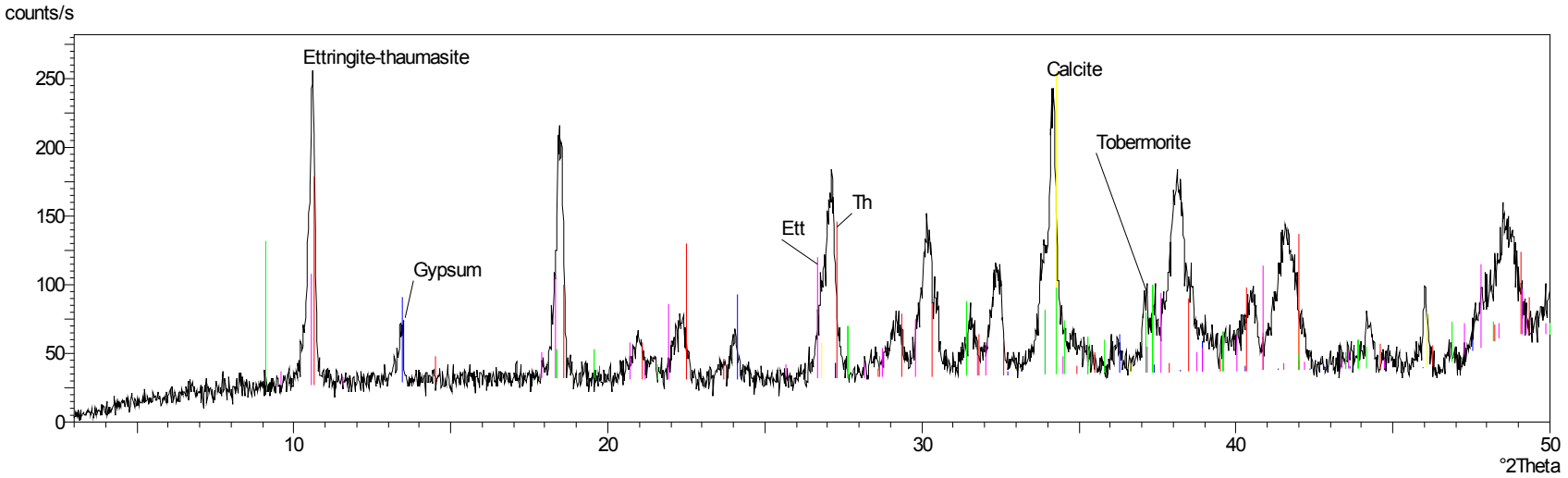

Figure A4.16 XRD trace for sample M00-1-21

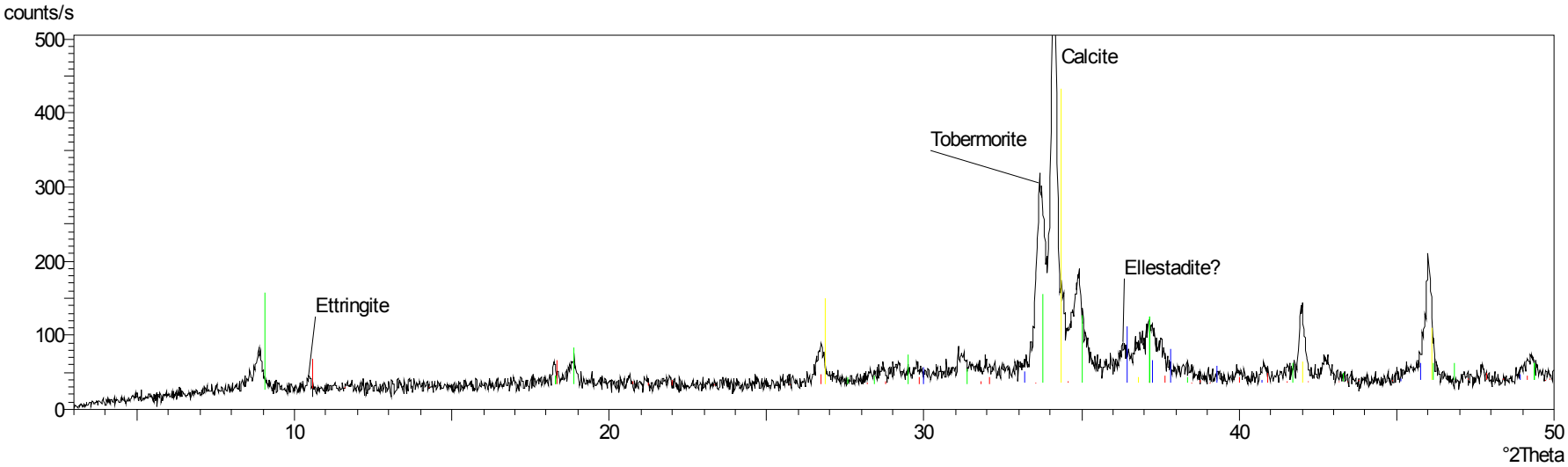

Figure A4.17 XRD trace for sample M00-1-37

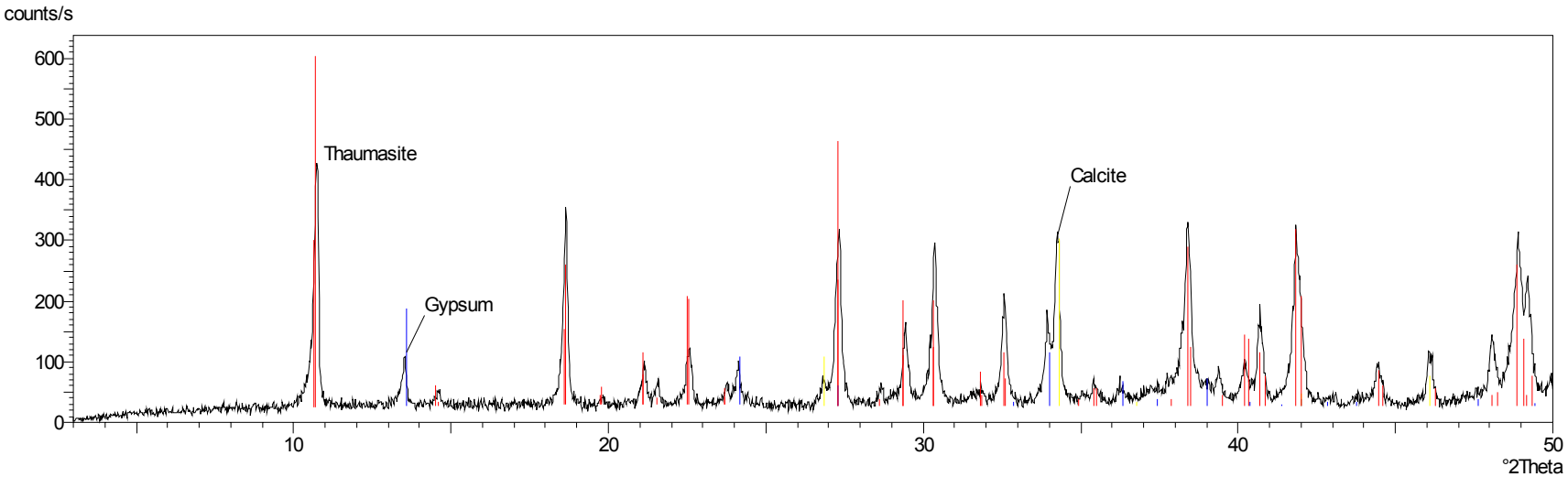

Figure A4.18 XRD trace for sample M00-1-47 showing reference-stick pattern for XRD lines corresponding to $Ca_5(SiO_4)_2SO_4$

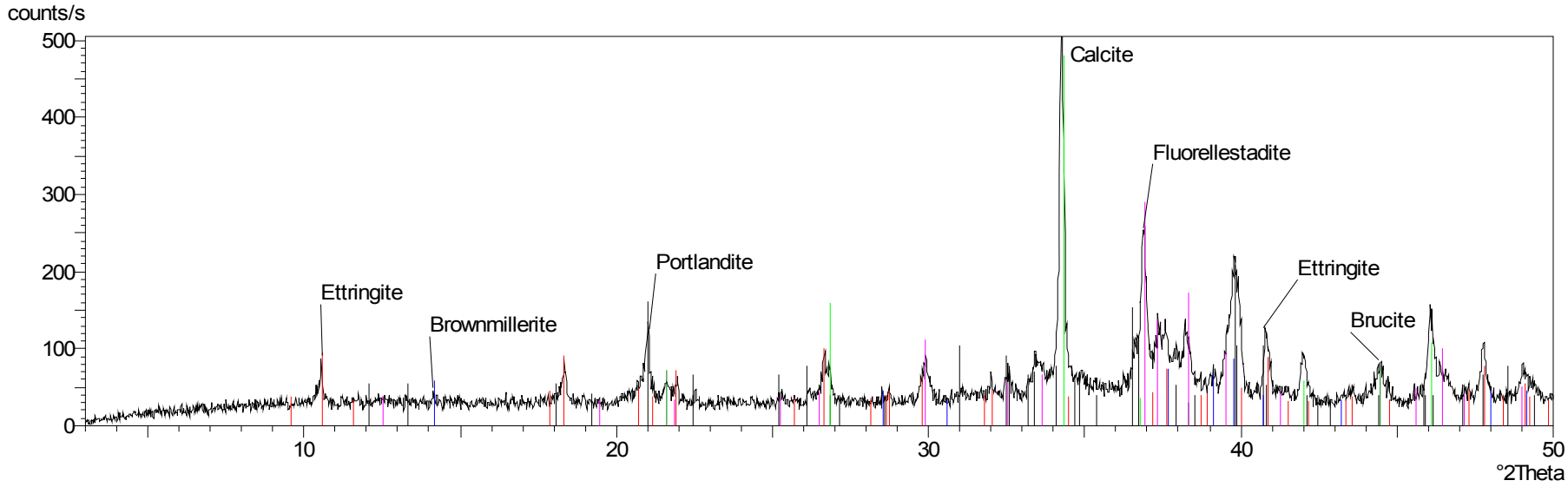

Key: *Ettringite = red; Portlandite = cyan; Brownmillerite = Blue; Brucite = Dark green; Fluorellestadite = Magenta; Calcite - green; $Ca_5(SiO_4)_2SO_4$= black.*

A4.4 Summary of XRD Results

Sample no	Larnite	Spurrite	(Fluor)-ellestadite	Brownmillerite	Krutaite ($CuSe_2$)	Portlandite	Tobermorite 11 A	Brucite	Thaumasite	Ettringite	Celestine ($SrSO_4$)	Gypsum	Calcite	Aragonite
M00-1-42								?TR	MAJ	MIN			MAJ	
M00-1-47			?MAJ	?TR		MIN		MIN		MIN			MAJ	
M00-1-16 alteration	MIN								MAJ			TR	MIN	
M00-1-16 matrix	TR	MIN	MIN										MAJ	MIN
M00-1-5					MIN				MIN		MIN	MIN	MAJ	
M99-1-31							MIN						MAJ	
M00-1-17							MIN		MAJ			TR	MAJ	
M00-1-21			?TR				MAJ			TR			MAJ	
M00-1-37									MAJ			MIN	MAJ	

Key to table

? = presence uncertain

MAJ = major: peak height >200 cps

MIN = minor: peak height 50 to 200 cps

TR = trace: peak height <50 cps.

The above assignations are arbitrarily defined, in order to give a rough estimate of relative amounts. Note that more poorly crystalline phases (namely tobermorite) will produce a broader, lower peak. Therefore, the above assignation probably underestimates its abundance.

Ettringite-thaumasite: it can be seen from the traces that ettringite and thaumasite peaks actually tend to lie between these two end-members of the (incomplete) solid solution. Mostly, they tend to be identifiably closer to either the thaumasite or ettringite end-member. In one case (M00-1-42), there may actually be a doublet resolved at high angles, with a major, more thaumasitic phase accompanied by minor ettringite. For this reason, the two have been identified as separate components.

A4.5 Electron Probe Microanalysis Data

Table A4.5 Chemical data obtained by electron probe microanalysis (ionic ratio)

Marble phases	**Brownmillerit-e**	**Brownmillerite**	**$Ca_5(SiO_4)_2SO_4$**	**?Spurrite**	**Spurrite**	**?Rankinite**	**Ellestadite**		**Oldhamite****
Sample no.	**M-00-1-47**	**M-00-1-12**	**M-00-1-47**	**M-00-1-47**	**M-00-1-47**	**M-00-1-50**	**M-00-1-12**		**M-00-1-12**
Description			**K-bearing**	**K-free**	**Alteration**	**Zn-rich**			**Inclusion**
Formula (balanced to oxygen equivalents)					**of K-phase**				**in carbonate**
Na	0.00	0.01	0.03	0.00	0.04	0.08	0.06	Fe	0.00
Mg	0.05	0.11	0.01	0.01	0.02	0.02	0.05	Mn	0.00
Al	0.81	0.49	0.02	0.03	0.04	0.00	0.01	Mg	0.00
Si	0.04	0.03	1.65	1.93	2.07	2.00	0.93	Ca	1.06
P	0.00	0.04	0.09	0.10	0.12	0.01	1.43	**S**	**1.00**
S	0.02	0.01	0.73	0.73	0.41	0.00	0.40	V	0.00
K	0.02	0.00	0.33	0.00	0.02	0.00	0.00	Cr	0.00
Ca	2.00	2.02	5.04	4.61	5.15	1.99	5.74	Co	0.00
Ti	0.04	0.05	0.01	0.01	0.01	0.00	0.00	Ni	0.00
Mn	0.00	0.00	0.00	0.00	0.00	0.00	0.00	Cu	0.00
Fe	0.95	1.15	0.01	0.01	0.02	0.01	0.02	Zn	0.00
Cr	0.03	0.06	0.00	0.00	0.01	0.00	0.00	As	0.00
O	**5.00**	**5.00**	**11.00**	**11.00**	**11.00**	**7.00**	**12.50**	Se	0.00
Cl	0.00	0.00	0.00	0.00	0.00	0.00	0.00	Pb	0.00
F	0.00	0.02	0.00	0.00	0.00	0.00	0.45	** Balanced to S = 1	
V	0.00	0.00	0.00	0.00	0.00	0.00	0.00		
Co	0.00	0.00	0.00	0.00	0.00	0.00	0.00		
Cu	0.00	0.00	0.00	0.00	0.00	0.00	0.00		
Zn	0.00	0.00	0.00	0.00	0.00	0.90	0.00		
As	0.00	0.00	0.00	0.00	0.00	0.00	0.00		
Se	0.00	0.00	0.00	0.00	0.00	0.00	0.00		
Mo	0.00	0.00	0.00	0.00	0.00	0.00	0.00		
W	0.00	0.00	0.00	0.00	0.00	0.00	0.00		
Pb	0.00	0.00	0.00	0.00	0.00	0.00	0.00		

Table A4.5 Chemical data obtained by electron probe microanalysis (ionic ratio) (cont)

Alteration products	**Ettringite**	**Ettringite**	**Thaumasite**	**Thaumasite**	**Tobermorite***	**Tobermorite***	**CSH***	**Afwillite***
Sample no.	**M-00-1-50**	**M-00-1-42**	**M-00-1-16**	**M-00-1-42**	**M99-1-31**	**M99-1-31**	**M-00-1-50**	**M-00-1-42**
Description		**Vein-fill**	**Traverse**	**Vein-fill**	**Vein-fill,**	**Vein-fill,**	**Near**	**Vein-fill**
Formula (balanced to oxygen equivalents)			**across vein**		**BSEM 'grey'**	**BSEM 'white'**	**Zn-phases**	
Na	0.00	0.00	0.01	0.00	0.01	0.00	0.00	0.00
Mg	0.00	0.00	0.00	0.00	0.00	0.00	0.00	0.00
Al	1.64	1.46	0.20	0.04	0.19	0.18	0.00	0.03
Si	0.17	0.36	1.76	1.93	**1.00**	**1.00**	**1.00**	**1.00**
P	0.00	0.00	0.00	0.00	0.00	0.00	0.00	0.00
S	2.41	2.28	1.84	1.80	0.01	0.00	0.03	0.09
K	0.01	0.00	0.00	0.00	0.02	0.02	0.07	0.00
Ca	4.92	5.23	5.63	5.67	0.52	0.73	1.06	1.61
Ti	0.00	0.00	0.00	0.00	0.00	0.00	0.00	0.00
Mn	0.00	0.00	0.00	0.00	0.00	0.00	0.00	0.00
Fe	0.02	0.00	0.01	0.00	0.00	0.00	0.00	0.00
Cr	0.00	0.00	0.01	0.00	0.00	0.00	0.00	0.00
O	**15.00**	**15.00**	**15.00**	**15.00**				
Cl	0.00	0.01	0.02	0.01	0.00	0.00	0.00	0.00
F	0.00	0.00	0.00	0.00	0.00	0.00	0.00	0.00
V	0.00	0.00	0.00	0.00	0.00	0.00	0.00	0.00
Co	0.00	0.00	0.00	0.00	0.00	0.00	0.00	0.00
Cu	0.00	0.00	0.00	0.00	0.00	0.00	0.00	0.00
Zn	0.01	0.00	0.00	0.00	0.00	0.00	0.00	0.00
As	0.00	0.00	0.00	0.00	0.00	0.00	0.00	0.00
Se	0.00	0.00	0.00	0.00	0.00	0.00	0.00	0.00
Mo	0.00	0.00	0.00	0.00	0.00	0.00	0.00	0.00
W	0.00	0.00	0.00	0.00	0.00	0.00	0.00	0.00
Pb	0.00	0.00	0.00	0.00	0.00	0.00	0.00	0.00
					* Balanced to Si = 1			

Table A4.6 Chemical data obtained by electron probe microanalysis (weight % oxide)

Marble phases	**Brownmillerite**		**Brownmillerite**		**$Ca_5(SiO_4)_2SO_4$**		**?Spurrite**		**Spurrite alteration**		**?Rankinite**		**Ellestadite**			**Oldhamite**	
No. of analyses	**n = 7**		**n = 2**		**n = 9**		**n = 5**		**n = 5**		**n = 4**		**n = 10**			**n = 10**	
Wt% oxide	**Mean**	**SD**	**Mean**	**SD**	**Mean**	**SD**	**Mean**	**SD**	**Mean**	**SD**	**Mean**	**SD**	**Mean**	**SD**	***Wt% element***	**Mean**	**SD**
SiO2	1.10	0.86	0.76	0.05	21.16	0.56	26.02	1.29	22.63	2.60	37.86	0.26	9.99	2.80	Fe	0.10	0.05
TiO2	1.47	0.39	1.55	0.21	0.10	0.02	0.13	0.05	0.12	0.03	0.02	0.02	0.04	0.03	Mn	0.03	0.04
Al2O3	16.82	1.92	9.57	1.13	0.19	0.06	0.33	0.19	0.34	0.42	0.05	0.04	0.12	0.07	Mg	0.00	0.00
Fe2O3	30.98	2.18	35.26	4.74	0.13	0.06	0.12	0.05	0.26	0.17	0.16	0.07	0.22	0.27	Ca	54.16	0.27
MnO	0.06	0.03	0.04	0.02	0.01	0.01	0.01	0.01	0.01	0.02	0.00	0.00	0.02	0.02	S	41.00	0.98
MgO	0.78	0.17	1.67	1.92	0.06	0.03	0.06	0.11	0.12	0.10	0.22	0.05	0.34	0.49	V	0.01	0.01
CaO	45.75	0.64	43.45	0.79	60.48	1.08	57.90	1.08	52.34	1.80	35.20	0.35	57.78	1.64	Cr	0.01	0.02
Na2O	0.04	0.05	0.15	0.03	0.17	0.04	0.01	0.01	0.20	0.12	0.79	0.11	0.34	0.06	Co	0.01	0.01
K2O	0.47	0.67	0.02	0.01	3.32	0.49	0.04	0.03	0.13	0.05	0.04	0.02	0.03	0.01	Ni	0.03	0.03
P2O5	0.08	0.09	1.23	0.51	1.37	0.45	1.55	0.43	1.58	0.55	0.19	0.15	18.21	5.34	Cu	0.37	0.17
SO3	0.69	0.71	0.43	0.18	12.52	0.51	13.05	0.80	5.91	1.34	0.04	0.06	5.72	4.04	Zn	0.03	0.03
V2O3	0.01	0.01	n.a.	n.a.	0.03	-	0.02	0.01	0.02	0.02	n.a.	n.a.	0.07	0.02	As	0.00	0.01
Cr2O3	1.02	0.56	1.80	0.77	0.04	0.03	0.07	0.05	0.10	0.03	0.01	0.01	0.03	0.03	Se	0.05	0.05
CoO	n.a	n.a	n.a.	n.a.	0.01	-	0.01	0.02	0.02	0.03	n.a.	n.a.	n.a.	n.a.	Pb	0.18	0.08
CuO	0.03	0.04	n.a.	n.a.	0.00	-	0.03	0.02	0.01	0.02	n.a.	n.a.	0.02	0.02	Total	95.98	1.20
ZnO	0.27	0.10	n.a.	n.a.	0.00	-	0.03	0.05	0.04	0.04	23.10	0.28	0.02	0.04			
As2O3	0.00	0.00	n.a.	n.a.	0.00	-	0.00	0.00	0.00	0.00	n.a.	n.a.	0.00	0.00			
SeO2	0.00	0.00	n.a.	n.a.	0.01	-	0.01	0.01	0.01	0.01	0.01	0.01	0.01	0.01			
MoO3	0.00	0.01	n.a.	n.a.	n.a.	n.a.	0.00	0.00	0.00	0.00	n.a.	n.a.	0.10	0.08			
WO3	0.09	0.13	n.a.	n.a.	n.a.	n.a.	0.11	0.13	0.15	0.07	n.a.	n.a.	0.00	0.00			
PbO	0.01	0.01	n.a.	n.a.	0.04	-	0.01	0.03	0.02	0.03	n.a.	n.a.	0.00	0.01			
Cl	n.a.	n.a.	0.01	0.00	n.a.	n.a.	n.a.	n.a.	n.a.	n.a.	0.01	0.01	0.01	0.00			
F	n.a.	n.a.	0.12	0.03	n.a.	n.a.	n.a.	n.a.	n.a.	n.a.	n.a.	n.a.	1.91	0.29			
Total	99.37	0.50	96.07	0.79	99.55	0.93	99.45	0.76	83.91	2.74	97.70	0.30	94.45	2.27			

Table A4.7 Chemical data obtained by electron probe microanalysis (weight % oxide)

Alteration products	**Ettringite n = 3**		**Ettringite n = 6**		**Thaumasite n = 12**		**Thaumasite n = 11**		**Tobermorite* n = 3**		**Tobermorite* n = 11**		**CSH n = 15**		**Afwillite* n = 2**	
Wt% oxide	**Mean**	**SD**	**Mean**	**SD**	**Mean**	**SD**	**Mean**	**SD**	**Mean**	**SD**	**Mean**	**SD**	**Mean**	**SD**	**Mean**	**SD**
SiO2	1.41	0.72	2.84	1.20	16.83	0.91	13.43	1.26	25.54	1.08	44.17	0.90	38.54	2.59	30.79	1.00
TiO2	0.01	0.01	0.01	0.00	0.01	0.01	0.01	0.01	0.00	0.01	0.00	0.01	0.02	0.02	0.00	0.00
Al2O3	11.21	0.49	9.77	1.05	0.29	0.28	1.28	0.76	4.07	0.25	6.61	0.25	0.12	0.05	0.87	0.21
Fe2O3	0.18	0.04	0.02	0.02	0.02	0.02	0.07	0.06	0.04	0.03	0.03	0.03	0.13	0.09	0.04	0.03
MnO	0.00	0.01	0.00	0.01	0.01	0.01	0.00	0.01	0.01	0.01	0.01	0.02	0.01	0.01	0.00	0.00
MgO	0.00	0.00	0.03	0.04	0.00	0.00	0.02	0.05	0.00	0.01	0.01	0.01	0.04	0.02	0.00	0.00
CaO	37.09	0.28	38.51	0.71	46.15	1.32	40.13	1.17	12.36	1.78	30.08	0.99	38.23	1.97	46.26	0.41
Na2O	0.02	0.02	0.01	0.01	0.02	0.02	0.03	0.04	0.16	0.03	0.10	0.06	0.06	0.04	0.00	0.00
K2O	0.04	0.02	0.00	0.00	0.01	0.01	0.00	0.01	0.42	0.03	0.67	0.17	2.11	0.68	0.00	0.00
P2O5	0.03	0.03	0.03	0.03	0.02	0.02	0.03	0.03	0.02	0.04	0.03	0.02	0.03	0.03	0.00	0.01
SO3	25.95	0.26	23.99	0.41	20.92	0.63	18.75	0.72	0.26	0.10	0.17	0.03	1.58	0.60	3.54	1.62
V2O3	n.a.	n.a.	n.a.	n.a.	n.a.	n.a.	n.a.	n.a.	n.a.	n.a.	n.a.	n.a.	n.a.	n.a.	n.a.	n.a.
Cr2O3	0.00	0.00	0.01	0.01	0.00	0.01	0.05	0.06	0.01	0.01	0.01	0.01	0.01	0.01	0.02	0.00
CoO	n.a.	n.a.	n.a.	n.a.	n.a.	n.a.	n.a.	n.a.	n.a.	n.a.	n.a.	n.a.	n.a.	n.a.	n.a.	n.a.
CuO	n.a.	n.a.	n.a.	n.a.	n.a.	n.a.	n.a.	n.a.	n.a.	n.a.	n.a.	n.a.	n.a.	n.a.	n.a.	n.a.
ZnO	0.06	0.06	0.02	0.03	0.02	0.03	0.02	0.02	0.29	0.07	0.13	0.10	1.71	1.45	0.01	0.00
As2O3	n.a.	n.a.	n.a.	n.a.	n.a.	n.a.	n.a.	n.a.	n.a.	n.a.	n.a.	n.a.	n.a.	n.a.	n.a.	n.a.
SeO2	0.01	0.01	0.01	0.01	0.00	0.00	0.00	0.01	0.01	0.01	0.01	0.01	0.01	0.01	0.02	0.01
MoO3	n.a.	n.a.	n.a.	n.a.	n.a.	n.a.	n.a.	n.a.	n.a.	n.a.	n.a.	n.a.	n.a.	n.a.	n.a.	n.a.
WO3	n.a.	n.a.	n.a.	n.a.	n.a.	n.a.	n.a.	n.a.	n.a.	n.a.	n.a.	n.a.	n.a.	n.a.	n.a.	n.a.
PbO	n.a.	n.a.	n.a.	n.a.	n.a.	n.a.	n.a.	n.a.	n.a.	n.a.	n.a.	n.a.	n.a.	n.a.	n.a.	n.a.
Cl	0.02	0.02	0.02	0.02	0.03	0.02	0.10	0.05	0.28	0.04	0.03	0.01	0.06	0.03	0.04	0.02
F	n.a.	n.a.	n.a.	n.a.	n.a.	n.a.	n.a.	n.a.	n.a.	n.a.	n.a.	n.a.	n.a.	n.a.	n.a.	n.a.
Total	76.03	0.76	75.26	1.10	84.33	2.28	73.93	1.89	43.47	2.78	82.05	1.56	82.66	0.85	81.60	0.45

A4.6 Ternary Plots of Mineral Phase Chemistry

Figure A4.19 Ternary Ca-Al-Si mol% element plot

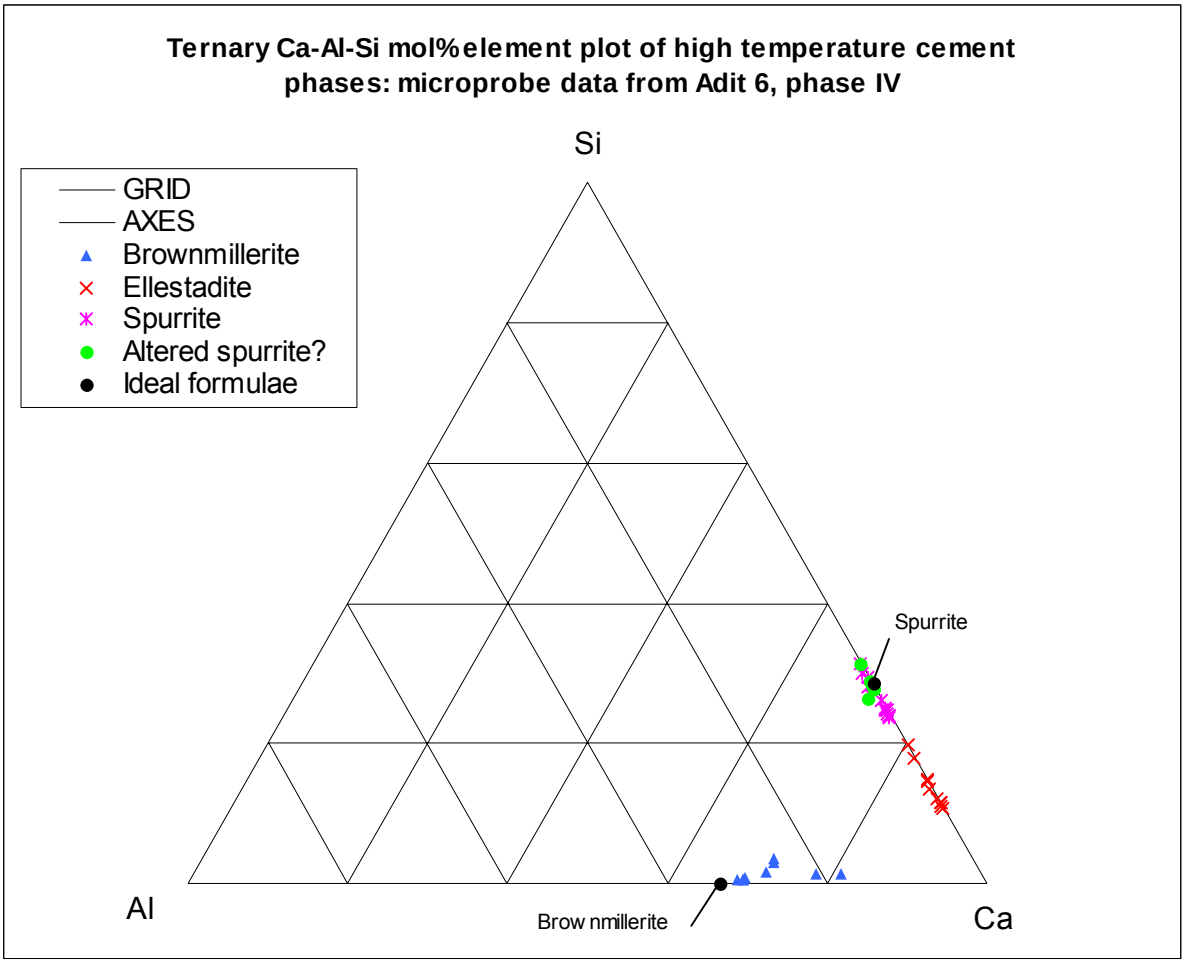

Figure A4.20 Ternary Ca-Al-Si mol% element plot

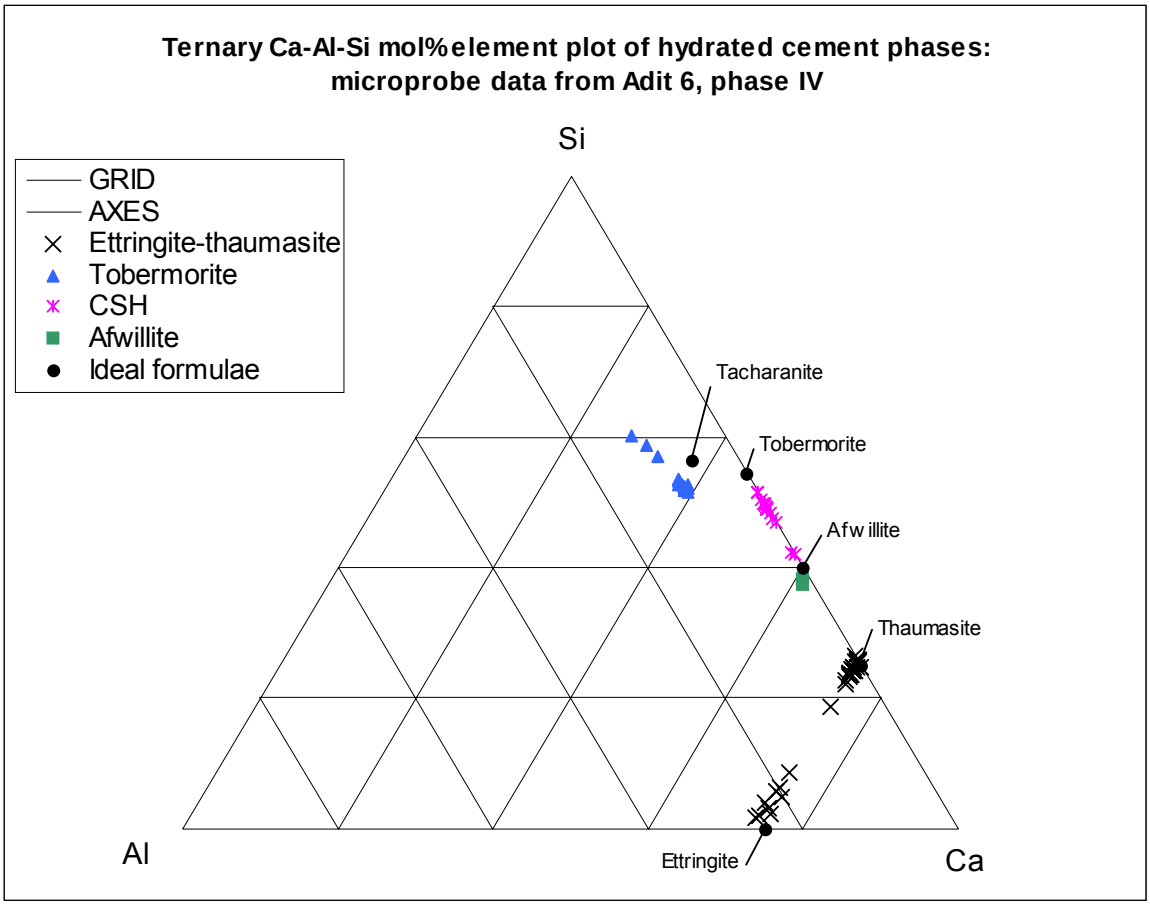

Figure A4.21 Ternary Ca-Al-S mol% element plot

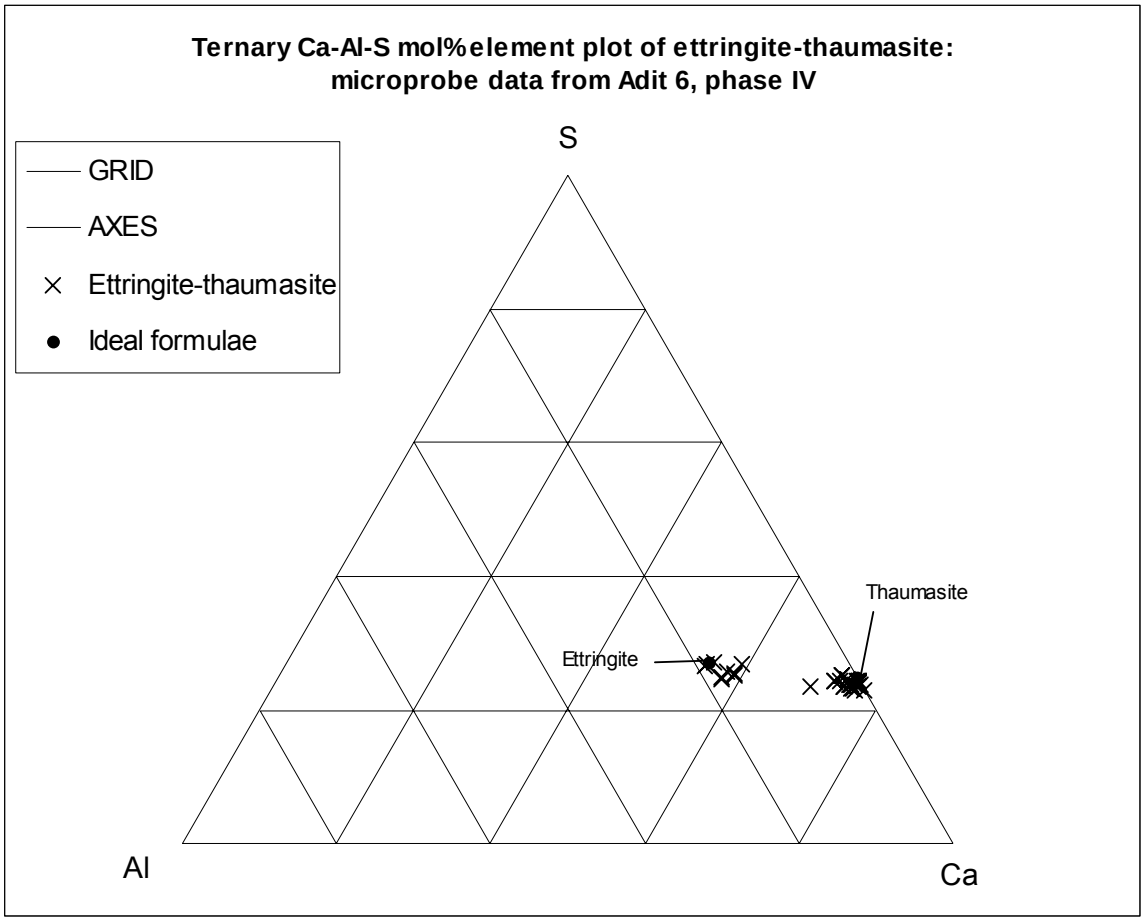

Figure A4.22 Ternary Ca- Si-S mol% element plot

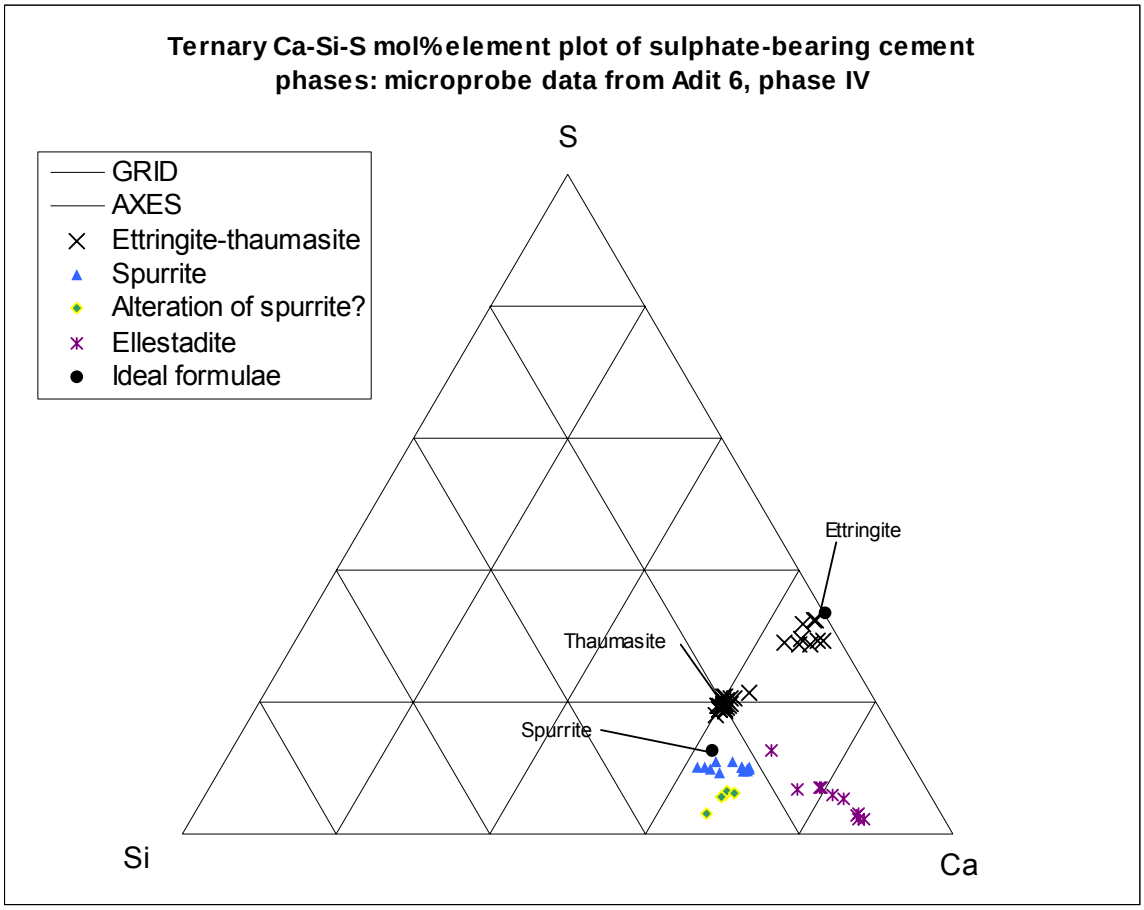

Figure A4.23 Ternary Ca-P-Si mol% element plot

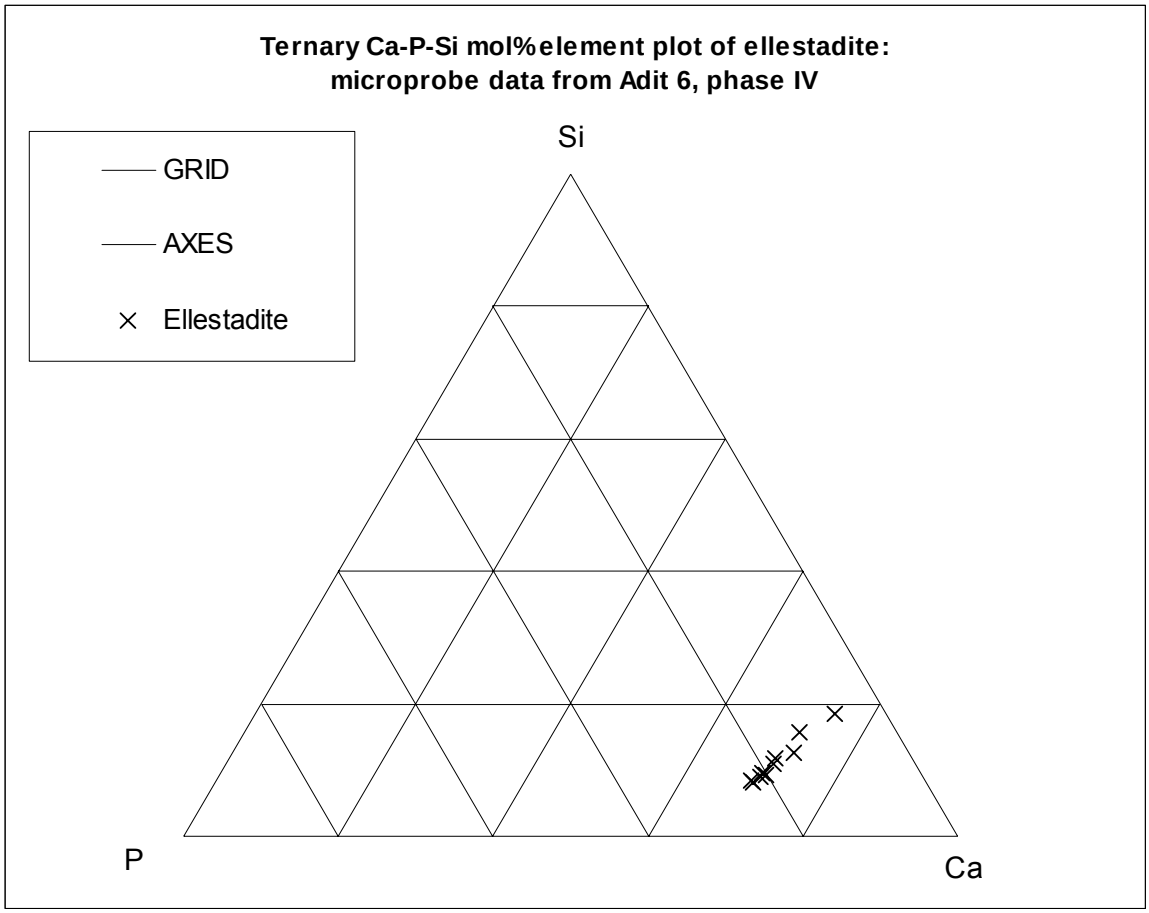

Figure A4.24 Ternary (Ca+Zn)-Al-Si mol% element plot

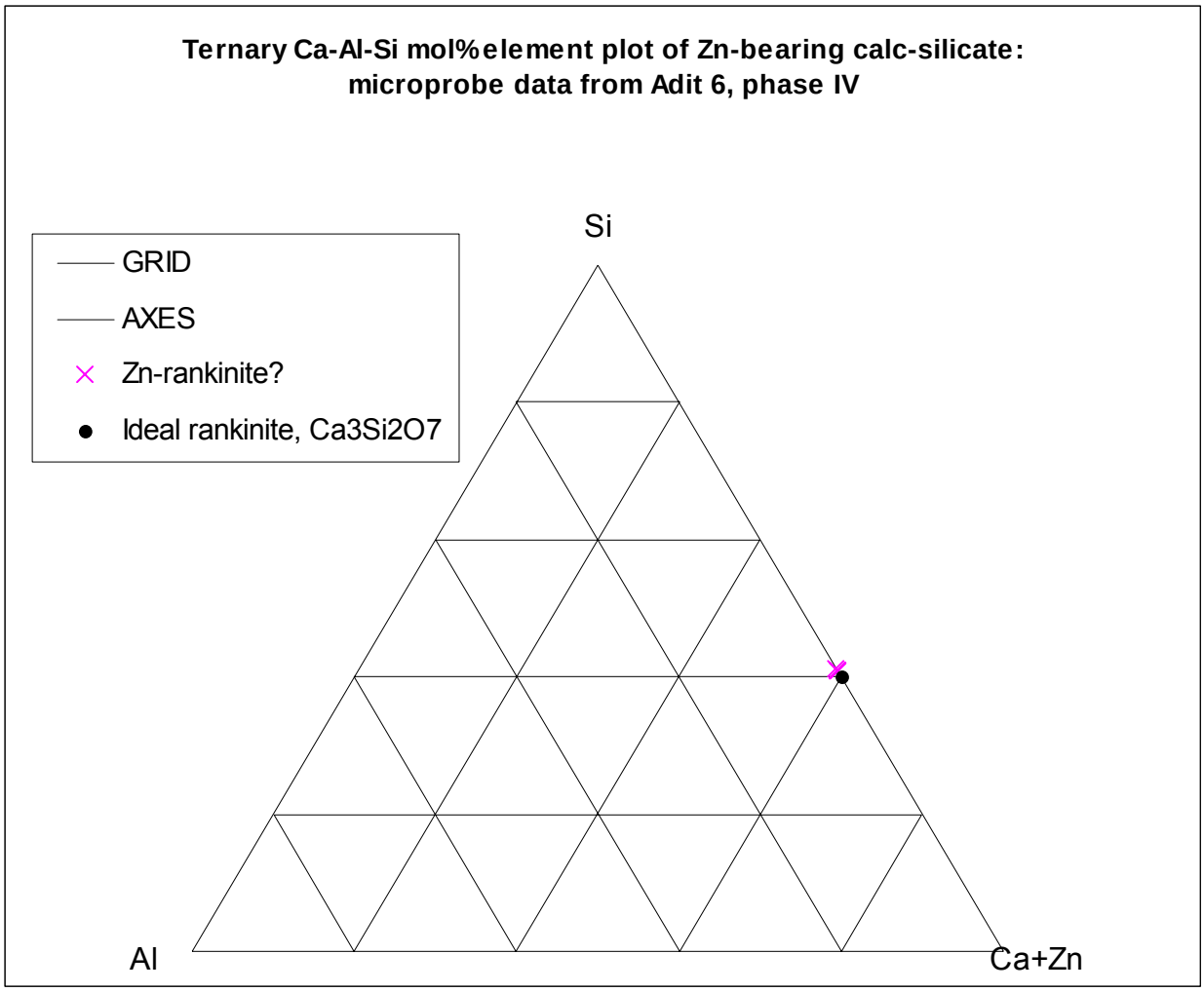

A4.7 LAMP-ICP-MS Data

All concentrations in ppm or $mgkg^{-1}$. NB Concentrations in italic are 'less than' figures.

Sample	Mineral	Mg 24 ppm	Al 27 ppm	Si 29 ppm	Ca 44 ppm	Cr 52 ppm	Sr 88 ppm	Y 89 ppm	Ba 138 ppm	La 139 ppm	Pb 208 ppm	Th 232 ppm	U 238 ppm
M99-1-31	Tobermorite	3521	67647	241912	215000	*269*	6310	1.7	913	*2.2*	*35*	*2.8*	9.4
	Tobermorite	3361	64386	242275	215000	*244*	5164	2.5	779	*2.0*	*32*	*2.5*	13
	Tobermorite	1617	66715	*297580*	215000	*386*	6066	*1.9*	781	*3.2*	*50*	*4.0*	7.0
	Tobermorite	156	58390	133527	215000	144	4718	*0.2*	950	*0.3*	*5*	*0.4*	15
	Tobermorite	121	54320	130439	215000	79	4315	*0.2*	876	*0.3*	*5*	*0.4*	16
	Tobermorite	150	56589	125287	215000	*68*	4777	*0.2*	796	*0.4*	*6*	*0.5*	11
	Tobermorite	230	44875	122727	215000	28	3653	*0.1*	1257	*0.1*	*2*	*0.2*	9.2
	Tobermorite	175	51441	136487	215000	53	4103	*0.1*	1127	*0.2*	*3*	*0.2*	3.7
M00-1-21	Tobermorite	69	21904	72668	215000	*15*	3184	0.2	650	*0.1*	3	*0.1*	0.8
	Tobermorite	88	25345	75861	215000	19	3434	0.7	629	*0.1*	*2*	*0.1*	1.9
	Tobermorite	77	25223	54154	215000	*38*	3092	0.6	366	*0.3*	33	*0.3*	1.7
	Tobermorite	132	25283	76524	215000	21	3358	0.3	583	0.2	2	*0.1*	1.1
	Tobermorite	69	24089	64371	215000	20	3158	0.2	499	0.1	4	*0.1*	1.8
M99-1-30	CSH - porous	58	21300	52526	89000	*16*	1547	*0.1*	823	0.2	*2*	*0.2*	2.7
	CSH - porous	61	24441	59610	89000	*24*	1732	0.2	969	*0.2*	*3*	*0.2*	4.2
	CSH - porous	88	25084	45465	89000	*21*	1488	*0.1*	867	*0.2*	*3*	*0.2*	3.3
	CSH - porous	51	20562	43753	89000	*19*	1519	0.3	810	*0.2*	*2*	*0.2*	4.0
	CSH - porous	61	23104	56195	89000	*20*	1774	*0.1*	898	*0.2*	*2*	*0.2*	4.5
M99-1-30	CSH - ordered	26	10522	30018	89000	*15*	2130	0.1	548	*0.1*	*2*	*0.1*	4.4
	CSH - ordered	53	11588	36809	89000	*14*	1763	*0.1*	797	*0.1*	*2*	*0.1*	3.2
	CSH - ordered	49	15859	37388	89000	*15*	1369	0.1	616	*0.1*	*2*	*0.1*	1.4
	CSH - ordered	41	9483	26057	89000	*13*	1689	0.1	374	*0.1*	*2*	*0.1*	3.1
M00-1-37	Thaumasite	*233*	709	*117552*	307000	*154*	135	*0.7*	*11*	*1.3*	*20*	*1.6*	*0.5*
	Thaumasite	*128*	349	*64634*	307000	*84*	83	0.5	*6*	1.1	*11*	*0.9*	*0.3*
	Thaumasite	46	240	57282	307000	*7*	133	*0.03*	*0.5*	*0.06*	*1*	*0.1*	*0.02*
	Thaumasite	*18*	267	41433	307000	*12*	113	*0.1*	*1*	*0.1*	*2*	*0.1*	*0.04*

Sample	Mineral	Mg 24 ppm	Al 27 ppm	Si 29 ppm	Ca 44 ppm	Cr 52 ppm	Sr 88 ppm	Y 89 ppm	Ba 138 ppm	La 139 ppm	Pb 208 ppm	Th 232 ppm	U 238 ppm
M00-1-37	Thaumasite	81	18483	81726	307000	*44*	386	0.6	6	*0.4*	*6*	*0.4*	*0.1*
	Thaumasite	205	63177	158216	307000	*127*	1062	3.2	16	2.9	*16*	*1.3*	0.5
M00-1-42	Thaumasite	*95*	7132	66970	330000	*63*	64	0.6	*4*	0.7	*8*	*0.6*	*0.2*
	Thaumasite	*106*	3054	*53305*	330000	*70*	84	0.8	*5*	*0.6*	*9*	*0.7*	*0.2*
	Thaumasite	*78*	5802	*38976*	330000	*51*	63	*0.2*	*4*	*0.4*	*6*	*0.5*	*0.2*
	Thaumasite	*71*	4338	*35388*	330000	*47*	101	0.3	9	0.5	*6*	0.7	0.3
	Thaumasite	65	5107	38901	330000	*38*	59	0.7	*3*	0.4	*5*	*0.4*	*0.1*
	Thaumasite	113	5576	*46699*	330000	*62*	105	1.2	*4*	0.6	*8*	*0.6*	*0.2*
M00-1-16	Thaumasite	*81*	5933	42281	287000	*57*	130	*0.3*	*4*	*0.4*	*7*	*0.5*	0.3
	Thaumasite	57	6424	42575	287000	59	125	*0.2*	*2*	*0.3*	*4*	*0.4*	0.4
	Thaumasite	65	11548	55773	287000	149	181	*0.2*	*2*	0.3	*4*	*0.3*	0.4
	Thaumasite	*43*	7321	46092	287000	96	132	*0.1*	*2*	*0.2*	*4*	*0.3*	0.3
	Thaumasite	*40*	6108	40872	287000	63	119	*0.1*	*2*	0.3	*3*	*0.3*	0.3
	Thaumasite	44	7131	43755	287000	63	116	*0.1*	*1*	*0.2*	*3*	*0.2*	0.2
M00-1-17	Thaumasite	*220*	585	*109060*	307000	*146*	51	*0.7*	*10*	*1.2*	*18*	*1.4*	*0.5*
	Thaumasite	*170*	2165	*84207*	307000	*113*	61	*0.5*	*8*	*0.9*	*14*	*1.1*	*0.3*
	Thaumasite	*98*	3077	*48793*	307000	*65*	128	*0.3*	*4*	*0.5*	*8*	*0.6*	*0.2*
	Thaumasite	73	2812	41139	307000	*27*	60	*0.1*	*2*	*0.2*	*3*	*0.3*	*0.1*
	Thaumasite	241	*2779*	*112016*	307000	*150*	77	*0.7*	*10*	*1.2*	*18*	*1.5*	*0.5*
	Thaumasite	*52*	3348	26242	307000	*34*	79	*0.2*	*2*	*0.3*	*4*	*0.3*	*0.1*
M00-1-42	Ettringite	87	28957	*34991*	275000	*61*	237	1.7	*3*	*0.4*	*6*	*0.5*	*0.1*
	Ettringite	*63*	26075	*31431*	275000	*42*	298	0.4	*3*	*0.3*	*5*	*0.4*	*0.1*
	Ettringite	*81*	*25475*	*40294*	275000	*53*	276	*0.3*	*4*	*0.4*	*7*	*0.5*	*0.2*
	Ettringite	*92*	31794	*46108*	275000	*61*	346	*0.3*	*6*	*0.5*	*8*	*0.6*	*0.2*
	Ettringite	*89*	26987	*44399*	275000	*59*	245	0.6	*4*	*0.5*	*7*	*0.6*	*0.2*
M00-1-37	Gypsum	*189*	*320*	*95209*	235000	*125*	1185	*0.6*	*9*	1.9	*16*	*1.3*	*0.4*
	Gypsum	*707*	*1198*	*355752*	235000	*467*	416	3.0	*32*	*3.8*	*59*	*4.7*	*1.5*
	Gypsum	*261*	*442*	*131118*	235000	*172*	810	*0.8*	*12*	*1.4*	*22*	*1.7*	*0.6*
M00-1-5	Gypsum	*59*	359	*29882*	235000	*39*	602	*0.2*	*3*	*0.3*	*5*	*0.4*	*0.1*
	Gypsum	*33*	94	*16360*	235000	*22*	798	*0.1*	*1*	*0.2*	*3*	*0.2*	*0.1*
	Gypsum	*20*	312	*9889*	235000	*13*	827	0.1	*1*	0.1	*2*	*0.1*	*0.04*

Sample	Mineral	Mg 24 ppm	Al 27 ppm	Si 29 ppm	Ca 44 ppm	Cr 52 ppm	Sr 88 ppm	Y 89 ppm	Ba 138 ppm	La 139 ppm	Pb 208 ppm	Th 232 ppm	U 238 ppm
	Gypsum	*16*	335	*8064*	235000	*11*	776	0.1	*1*	*0.1*	*1*	*0.1*	*0.03*
	Gypsum	*17*	636	*8626*	235000	*11*	401	*0.1*	*1*	0.1	*1*	*0.1*	*0.04*
	Gypsum	*18*	610	*9044*	235000	*12*	367	*0.1*	*1*	*0.1*	*2*	*0.1*	*0.04*

Appendix 5

Microbiology Analytical Methods

A5.1 Sampled sites

Sampling was performed at the three major sites at Maqarin, namely the Eastern Springs, Adit A-6 and the Western Springs. Table A5.1 gives further details about the sampled sites.

Table A5.1 Site and sampling information for six subsequent campaigns to Maqarin. Two sampling campaigns were undertaken during the year 2000.

Sampling site[5]	pH condition	Site description	Sampling performed				
			Phase III			Phase IV	
			1994	1995	1996	1999	2000
Eastern springs							
M3	hyperalkaline	Seeps from unmetamorphosed clay biomicrites exposed by a road cut. The rock face displays numerous fractures from which the water flows and drips. As a result of the water flow travertine precipitates have developed on the rock face.		x	x	x	x
M8	hyperalkaline	Similar to M3.	x		x		
M18	neutral	A borehole drilled in December 1993 in the road next to the M3 and M8 sites. It represents a mixture of mostly rainwater and also some hyper-alkaline groundwater.	x		x		
Adit A-6 (tunnel)							
M1	hyperalkaline	A seep site in the metamorphic/cement zone situated approximately 125 m from the Adit entrance.		x	x	x	x
D3	hyperalkaline	A borehole drilled in 1999 in the unaltered clay biomicrites downstream from the metamorphic zone. The borehole is situated approximately 51 m from the Adit.				x	x

[5] See Chapters 2 and 3 and Smellie (1998) for details of the sampling sites.

A5.2 Groundwater chemistry

Groundwater from seeps and boreholes (Table A5.1) was collected in 1 L polyethylene bottles for analysis. Swedish standard analytical protocols were used, as indicated in the results section (Section 5.4). The groundwater was sampled simultaneously with groundwater used for microbiology analysis and experiments.

A5.3 pH measurements

Field measurements of pH (±0.01) were made using a portable pH meter (ORION RESEARCH Model SA250) with a Ross combination glass electrode. The flow from the hyperalkaline seeps was commonly too low to enable sealed flow-through cell measurements and pH was therefore measured by immersing the electrode directly in the discharging water or in standing pools of water, from which samples were taken. In addition, water samples for groundwater chemistry was analysed for pH in the laboratory using a Swedish Standard method (SS028122-2 mod/PH-25 – see www.sis.se). The field and laboratory pH values differed at most by a few tenths of a pH unit. Measurement of pH in cultivation vessels was made using colour-fixed indicator sticks (Macherey Nagel, Germany). Sub-samples were withdrawn to a small container and analysed. pH was registered in 0.5 increments, as indicated by the pH interpreter on the stick box.

A5.4 Sampling for total numbers of unattached and attached cells

All samples of unattached cells were obtained concomitantly with sampling of groundwater used for inoculation of cultures and the assimilations studies (see below). The samples were collected in 50 mL, sterile, screw-capped polypropylene tubes (Sarstedt, Landskrona, Sweden). Immediately after sampling, 2.6 mL of acid-free 37% (v/v) formaldehyde was added to each tube to kill the microorganisms and preserve the samples until the microscopic counts were carried out. The final concentration of formaldehyde was 1.8% v/v. Sampling dates are given in Tables A5.2 and A5.3.

Table A5.2 The number of samples and the sampling dates for total number of unattached microorganisms at the sampled sites.

Sampled Site	1999		2000	
	No of Samples	Date	No of Samples	Date
M1	2	01 December	2	02 May
M3	2	28 November	1	03 May
M5	2	26 November	2	02 May
D3	2	01 December	-	-
D6	1	05 December	2	30 April
D6	1	07 December	-	-

Table A5.3 The type of sampler, the number of samples and the sampling dates for total number of unattached cells collected in November 1999 and May 2000.

Sampled Site	Sampler	No of Samples	Date	Days in flow
M1	FTB	8	07 December 1999	8
D6	FTC	4	29 April 2000	54
M1	FTC	4	01 May 2000	56
M1	FTC	2	06 May 2000	5

Flow-through systems with solid surfaces for attachment of microorganisms were prepared. Flow-through boxes (FTBs) (Pedersen et al., 1986) were used during the November 1999 campaign (Figure A5.1). With the exception of the aluminium lid, all

components were made of polycarbonate. The test pile contained twelve layers of two adjacent glass slides (60 × 24 × 1.0 mm), with a 1 × 20 mm flow channel between each slide layer. Hydrophilic surfaces were obtained by heating the glass slides for 4 hours at 450°C in a muffle furnace (VRB4-1200-017, Phoenix Furnaces Limited, Sheffield, U.K.) before installation. The FTB was connected with the glass surfaces standing in a vertical position, to avoid sedimentation on the surfaces. Connection to the sampled boreholes was made via plastic tubing. Unfortunately, the high pH made the polycarbonate brittle and all FTBs cracked soon after installation. Only one FTB could finally be sampled. After these problems with the FTBs, flow-through cylinders (FTCs) were developed and employed. The polycarbonate flow through box (Figure A5.1) was replaced with a flow through cylinder made of polyethylene. It was connected to the sampled boreholes in the same manner as was previously done with the FTB.

Figure A5.1: FTB at M1 November 1999 (left) FTC at M1 May 2000 (right)

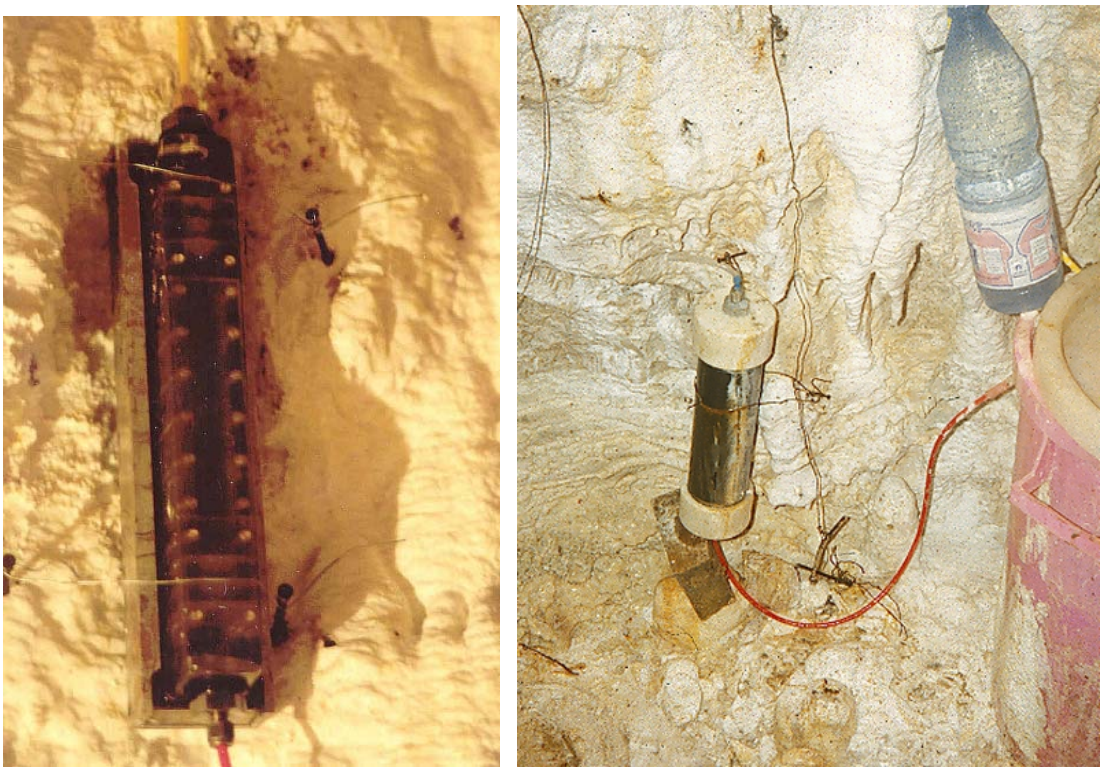

The FTB was connected to seepage locality M1, in the Adit A-6 tunnel, on 29 November 1999 and sampled on 7 December 1999. Two FTCs were connected to M1 and borehole D6 on 6 March 2000. The FTC connected to D6 was removed and initially sampled on 29 April 2000, while the one connected to M1 was sampled for the first time on 1 May. The M1 test pile was thereafter replaced with a new set and the FTC was reconnected. This flow cell was sampled a second time on 6 May and was thereafter finally removed. The glass slides were removed from the FTB/FTC with a pair of heat-sterilised tweezers and rinsed with 5 mL of 0.2 µm filtered groundwater. The slides were stored in sterile 50 mL polypropylene, screw-capped tubes containing a sterile preservation mixture consisting of 18 mL 0.2 µm filtered groundwater from the respective sites and 2 mL acid-free formaldehyde (37 % v/v).

A5.5 Enumeration of unattached and attached cells (G1)

The total numbers of cells in the groundwater samples and the total number of cells attached to the glass slides were counted using blue-stain 4’6-diamino-2-phenylindole

(DAPI). Acridine orange (AO) could not be used because of its high interference with calcite crystals, which created too high a background fluorescence. A standard protocol for fluorescent staining was used (Pedersen and Ekendahl, 1990). Salt crystals from the groundwater on the filters (diameter 13 mm) were dissolved by rinsing twice with 5 mL of 0.2 µm filtered, double-distilled water heated to 40°C prior to staining. The filters were stained with 0.15 mL DAPI (10 µg mL^{-1}) for 10 minutes and counted under an Olympus BH-2 microscope (Olympus, Göteborg, Sweden) with ultraviolet (UV) filters for DAPI. For each filter 30 microscopic fields were counted, with each field measuring 80 µm × 80 µm = 0.0064 mm^2. The results were calculated as an average of two filters, with a standard deviation (SD) as the error. The glass slides with attached microbes were rinsed with 5 mL of 0.2 µm filtered, double-distilled water to remove possible unattached cells. The slides were then air-dried, stained with DAPI and counted as described above.

A.5.6 Re-evaluation of phase III 16S-ribosomal deoxyribonucleic acid diversity

Groundwater for DNA analysis was sampled from locations M5, M8, M17 and M18 in November 1994, and from the locations M1, M3 and M5 in April 1995. The groundwater was collected directly from the boreholes or seeps in sterile 50 mL polypropylene, screw-capped tubes and was immediately deep-frozen with CO_2 ice and transported frozen to the laboratory in Göteborg, where 10 mL samples were filtered on to sterilised 0.2 µm pore-sized Nuclepore filters. Thereafter, DNA extraction, polymerase chain reaction (PCR) amplification, cloning and sequencing followed using a procedure published elsewhere (Pedersen et al. 1996). A Pfu DNA polymerase (Stratagene) was used, which has a proof-reading ability that minimises the chance of chimera formation.

PCR amplification of 16S rDNA was performed using a 27f/1492r primer set encompassing all bacteria. Partial sequences were imported and taxa selected for analysis with the ARB software environment for sequence data (Strunk et al., 1998). After masking of unambiguously alignable segments, phylogenetic trees were constructed including 258 nucleotides for analysis with PHYLIP (Felsenstein, 1989). The reliability of branching points was determined by performing 1000 bootstrap replications of the data using both evolutionary distance with the Kimura-2-Parameter (Kimura, 1980) correction, and maximum parsimony methods (Felsenstein 1985, 1989).

A.5.7 Cultivation (G2)

Media for cultivation were prepared with groundwater from the sampled sites. Growth factors such as carbon sources, electron acceptors, vitamins, trace elements and, in the case of anaerobic cultures, reducing agents were added to the groundwater. This provided appropriate hyperalkaline pH media for growth of different physiological groups of microbes. Since groundwater from Maqarin could not be obtained in advance, additions of growth factors to empty bottles were made initially in the laboratory. The different types of Maqarin groundwater were then added at the sampling sites, serving both as *in situ* pH buffers and as inoculum. Bottles used for the cultures were 300 mL, hard plastic, screw-capped Erlenmeyer flasks (Nalgene) (November 1996) and 100 mL (November 1999) and 50 mL (May 2000) serum-type glass bottles (Bellco Biotechnology, Bie & Berntsen, Malmö, Sweden). For sub-cultures prepared from the enrichment cultures, 300 mL Erlenmeyer flasks (Nalgene) were used in 1996 and 50 mL serum bottles were used in 1999 and 2000. All culture vessels were acid-washed with 10% v/v HCl and sterilised by autoclaving prior to use.

During the Phase III 1996 campaign, a total of 100 mL of spring and seepage water was collected directly from each hyperalkaline spring/seepage in two separate 300 mL sterile Erlenmeyer flasks (with a screw lid) supplied with different carbon sources and stored at room temperature. Extra water was collected in sterile, empty flasks for use during sub-culturing. Two different media were prepared and inoculated with alkaline water from the sampled localities: Medium 1 contained (g per litre) peptone (Difco), 1; yeast extract (Difco), 1; and glucose, 5. Medium 2 contained (g per litre) peptone (Difco), 1; yeast extract (Difco), 1; and lactate, dissolved in 5 mL distilled, sterile H_2O, 5. When they arrived in Göteborg, 3 days after sampling, the enrichments were put in a shaker for 27 days at room temperature. Subsequently, the total number of cells in the cultures was assayed using an AO direct count technique (Pedersen and Ekendahl, 1990). Enrichments with growing cells were sub-cultured in fresh media.

During the Phase IV 1999 and 2000 campaigns, all water was collected in one container and distributed to the separate experiments. Briefly, the groundwater was sampled in sterile 3 L hospital intravenous (IV) bags (Pharmacia & Upjohn, Letterkenny Ltd., Donegal, Ireland). The IV bag was connected through one of its three inlets to the sampled seepage (M1) or groundwater (D3 and D6) source via a plastic tube (Figure A5.2). After sampling, the used inlet was closed and permanently sealed. This procedure enabled sampling without exposure to air during the prolonged sampling times required owing to the low flow rates of the boreholes, springs and seepages. It was not possible to sample M3 with an IV bag. Instead, dripping groundwater at this location was collected in sterile plastic bottles. To the cultivation bottles were allocated 60 and 20 mL of sampled groundwater, in 1999 and 2000 respectively, from the IV bags using 60 and 20 mL sterile plastic syringes.

Figure A5.2: Collection of groundwater at the M1 site in Adit A-6

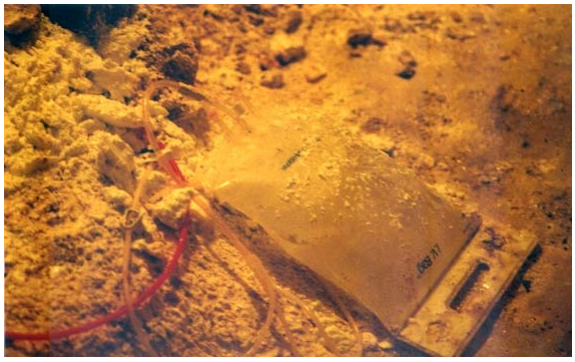

Aerobic media were prepared in acid-washed, sterile bottles sealed with blue silicon septa aluminium clamps (Chromacol Ltd., Trumbull, CT, U.S.A.) that allowed diffusion of gases, including oxygen. All media components were added from sterile, aerobic stock solutions. With the exception of R2A, to all culture vessels 1 mL trace element solution (Haveman et al., 1999) and 1 mL vitamin solution (Wolin et al., 1963) were added. The final concentrations of added growth factors were as follows: standard aerobic media contained (mgL^{-1}) glucose, lactate, acetate or formate, 8 (1999) or 50 (2000). The CH_4 oxidation medium contained (per culture vessel) 5 mL methane (1 atm), which was added after inoculation, while the R2A medium (Reasoner and Geldreich 1985) contained (mgL^{-1}) peptone (Difco), 30/90; casmino acid (Difco), 30/90; yeast extract (Difco), 30/90; glucose, 30/90; soluble starch, 30/90; and sodium-pyruvate, 20/60 (1999/2000). Enrichment cultures were sub-cultured in the respective fresh media, with 20 mL of 0.2 µm sterile-filtered groundwater from the respective sampled site added.

Anaerobic media were prepared in acid-washed bottles placed in an anaerobic chamber (Coy Laboratory Products Inc., MI, U.S.A.) with an atmosphere of approximately 4% H_2, 5% CO_2 and balance N_2 v/v. The bottles were left for at least 12 hours in the anaerobic atmosphere before they were sealed with blue butyl rubber stoppers and thereafter sealed with aluminium clamps (Bellco Biotechnology, Bie & Berntsen, Malmö, Sweden). The bottles were then sterilised in an autoclave. All media components were added from sterile, anaerobic stock solutions and all contained 0.2 mgL^{-1} of Resazurin. Each bottle was also amended with 1 mL of a reducing solution consisting of (per litre) cysteine-$HCl{\cdot}H_2O$, 0.25 g and $Na_2S{\cdot}9H_2O$, 0.25 g. To all media, except R2A, were also added 1 mL trace element solution and 1 mL vitamin solution, as described for aerobic cultures, and glucose, lactate, acetate, pyruvate, formate, or trimethylamine (TMA) (only 1999), 8 mg (1999) or 50 mg (2000). The Fe(III)-reducer medium also contained amorphous FeOOH, 125–160 mgL^{-1} (Kostka and Nealson 1998). The manganese(IV)-reducer medium also contained MnO_2, 25–40/150–250 mgL^{-1} (1999/2000) (Kostka and Nealson, 1998). The sulphate reducer medium contained Na_2SO_4, 17/50 mgL^{-1} (1999/2000) and the nitrate reducer medium had KNO_3, 17 mgL^{-1} (1999). The fermentation medium was not amended with an external electron acceptor. The yeast/peptone media also contained (per litre) yeast extract (Difco), 17 mg (1999), and peptone (Difco), 17 mg. The R2A medium was prepared as described for aerobic media. Enrichment culture cells were sub-cultured in the respective fresh media, with 20 mL of 0.2 µm sterile-filtered groundwater from the respective sampled site added.

A.5.8 Assimilation of organic carbon sources by unattached cells (G3)

Acid-washed, sterile 50 mL serum bottles were prepared as described above for aerobic and anaerobic media. The 50 mL bottles were amended with the following radio-labelled carbon sources (all from Amersham Pharmacia Biotech, UK): D-[U-^{14}C]-glucose, 113 nM, specific activity 323 mCi/mmol; L-[U-^{14}C]-lactate, 239 nM, specific activity 152 mCi/mmol; [1,2-^{14}C]-acetate, 649 nM, specific activity 56 mCi/mmol; [^{3}H]-acetate, 1.1 nM, specific activity 970 mCi/mmol; L-[4,5-^{3}H]-leucine, 0.3 nM, specific activity 141 mCi/mmol. In addition to these bottles, during the 2000 campaign 500 mL glass bottles with butyl rubber stoppers and aluminium screw caps were prepared for aerobic and anaerobic batch assimilation tests. To the 500 mL bottles were added 16 mL of a D-[U-^{14}C]-glucose solution, 1130 nM, specific activity 323 mCi/mmol. For each 500 mL bottle, 16 aerobic or anaerobic 50 mL bottles were prepared for subsequent uptake tests as described below.

To sets of eight 50 mL bottles amended with each of the radio-labelled carbon sources, 10 mL groundwater was added from the respective IV bag. The groundwater was transferred using a sterile 10 mL syringe and needle. Groundwater from all sites was combined with carbon sources in discrete assimilation tests. The contents of two bottles from each combination were killed simultaneously with formaldehyde (3.4% final concentration v/v) at the start of each assimilation time series, as shown in the results section (5.4). To the 500 mL bottles 160 mL of groundwater was added from the same IV bag that was used for cultivations. Two 11 mL aliquots of the isotope/groundwater mixture were removed from the batch bottles with sterile 20 mL syringes and added to 50 mL serum bottles containing 1 mL formaldehyde (3.4% final concentration v/v). This procedure was repeated in a time series, as shown in the Results section. The final concentration of radio-labelled glucose in this batch of 50 mL bottles was 113 nM, and the specific activity was 323 mCi/mmol.

The samples were first transported from the field sites and stored at room temperature at the University of Jordan, Amman. They were then shipped to the analysis laboratory by

air cargo and arrived at Göteborg University on 28 December 1999 and 22 May 2000, respectively. All cultures were stored at room temperature.

A.5.9 Assimilation of organic carbon sources by attached cells (G4)

Assimilation studies of various organic carbon sources by attached microbes were performed as for unattached microbes, with the following modifications. To sterile 50 mL screw-capped polypropylene tubes, isotope solutions were added in the laboratory. The final concentrations of the radio-labelled carbon sources were similar as to the assimilation studies of unattached cells. To each such tube was added 18 mL of 0.2 µm filtered groundwater from the respective sampling site. The glass slides were removed from the FTB or FTC with a pair of tweezers and rinsed with 5 mL of 0.2 µm filtered groundwater and thereafter placed in the 50 mL tubes.

A.5.10 Scintillation procedure

The aluminium crimp seal was removed from each bottle for unattached assimilations. The bottle was vortexed and two 5.0 mL aliquots of the assimilation mixture were removed with a pipette. Each aliquot was filtered (0.2 µm), and the filters were rinsed with 2×2.5 mL of 0.2 µm filtered groundwater from the respective sampling site. The filters were subsequently placed in scintillation vials (Poly-Q Vial, Beckman Instruments, Inc., Fullerton, CA, U.S.A.) and left to dry. After drying, 15 mL scintillation cocktail for organic samples (NOCS104, Amersham Pharmacia Biotech, U.K.) was added and the vial was sealed and counted using a Beckman LS 6000LL scintillation instrument (Beckman Instruments, Inc.). Each glass slide from the attached assimilation tests was split into two or more pieces and added to a scintillation vial and allowed to air-dry. After drying, 15 mL scintillation cocktail for organic samples was added and the vial was sealed and counted as for the unattached cells. The mean assimilation per time and radio-labelled carbon source was calculated and subtracted from the control counts obtained from the killed controls at time 0. For all radioactive isotopes, 1 dpm = $1/2.22 \times 10^6$ µCi. Using this expression, the counts obtained were converted from dpm to µCi. As the specific activities of the isotopes used were known, the assimilation was calculated in molar units. Finally, the mean assimilation per cell and hour was calculated from obtained data on the total number of cells in each bottle.

Appendix 6

Khushaym Matruk Analytical Methods

A6.1 Mineralogy and Petrology of Some Opaline Phases

Opaline samples associated with the Daba marble and Khan Az Zabib travertine were collected from central Jordan (D and K samples). These samples were compared with opaline samples collected from the metamorphic zone (Analogue Cement Zone) in Maqarin (M-samples).

Table A6.1 summarises the results of microscopic analysis and of XRD before and after DTA treatment. Opal-C to -CT is strongly disordered cristoblaite or cristobalite/tridymite. According to increasing degree of stacking disorder, a differentiation between opal-C (C = cristobalite) and opal-CT (cristobalite/tridymite) can be made. Opal-CT is abundant in the studied samples. It shows only three major reflections in the XRD pattern (at 4.3, 4.10 and 2.50 A^{o}).

Further differentiation can be made with the polarizing microscope. Chalcedony and quartzine are fibrous quartz (Figure A6.1a-c). Chalcedony has a negative optical character of fibre elongation (length-fast). The fibre axis is one of the trigonal a-axis. Quartzine is a length-slow chalcedony and has a positive character of elongation. The fibre axis is the trigonal c-axis. Microcrystalline opal occurs essentially as massy opal-CT_m or lussatite (opal-CT_L) in the studied samples. Lussatite is fibrous (Figure A6.1c) with a positive character of elongation (fibre axis <101> using indices of tetragonal low cristobalite). Lussatite can vary from opal-C to opal-CT. It exhibits comparatively strong birefringence. Massy opal-CT_m does not show texture that is resolved with the polarized microscope. The birefringence is very low.

Due to the structural disorder and small crystal size, most microcrystalline silica varieties do not show noticeable DTA effects on heating. All silica minerals described here (including noncrystalline opal-A) are transformed to more or less disordered cristobalite in DTA runs going up to 1400^{o}C and being held there for one hour. After this treatment the sample shows an exothermic effect on cooling and an endothermic effect on reheating. The transformation termperatures vary from 270 to approximately 220^{o}C decreasing with increasing degree of structural disorder due to displacive high-low-transformation of the cristobalite formed.

Hyslop (1998) reported significant concentrations of U up to 160 ppm and, here, U levels in silica are particularly enhanced adjacent to open voids. Matrix carbonate has lower and more variable U contents, and levels up to 40 ppm U are present in patches commonly associated with inclusions of fine volkonskoite and phosphates.

Table A6.1 Microscopic and XRD results before and after DTA

Sample No.	Macroscopic appearance	XRD	Microscopy of the silica phases	XRD after DTA
K_1	white light green green	calcite, gypsum (tr); opal-CT, calcite, quartz + 3F, opal-CT, quartz (tr) + (1F)	opal-CT and lussatite, lussatite occurs as the thin rind.	portlandite, bassanite, calcite, disordered cristobalite, other phases
M_6		quartz + (1F)	chalcedony	–
M_{13}	white grey	micro-and noncrystalline opal quartz and noncystalline opal	noncrystalline opal and lussatite	–
M_{15}	grey	calcite, ettrignite, tobermorite 11 A^o, other phases	few quartzine spherulites	–
M_{16}	grey	Calcite, ettringite, other phases	Noncrystalline opal-A.	–
D_4	white green brown	calcite, other phases calcite, ettringite, tobermorite, other phases calcite	Noncrystalline opal	–
D_6	green white brown	opal-CT, calcite calcite calcite, apatite	opal-CT, lussatite rind, few chalcedony spherulites	cristobalite, $CaSiO_3$, disoposide, portlandite, other pahses
D_{36}	white green glassy	calcite calcite calcite, opal-CT (tr)		portlandite, calcite (tr) diopsite (tr), other phases
D_{41}		calcite	few quartzine spherulites	–
D_{42a}	glassy light brown red	calcite apatite, calcite calcite, haematite		–
D_{42b}	white sandy red	opal-CT, quartz calcite, quartz (tr) + 4F opal-CT, quartz, calcite + 1F	opal-CT with chalcedony spherulites	disordered cristobalite
D_{45}	white grey light brown yellow	calcite, aragonite, opal-CT (tr) quartz, calcite calcite, apatite opal-CT, calcite, quartz (tr)	opal-CT	disordered cristobalite and other phases
D_{66}	yellow red grey	opal-CT, quartz (tr) opal-CT, quartz (tr), calcite (tr) calcite	opal-CT with some chalcedony spherulites	–

M = Maqarin

D = Daba tr = traces

K = Khan Az Zabib nF = number of unidentified lines

Figure A6.1a Photomicrograph of banded opal-CT from Daba (X-nicols, field of view =2.2mm)

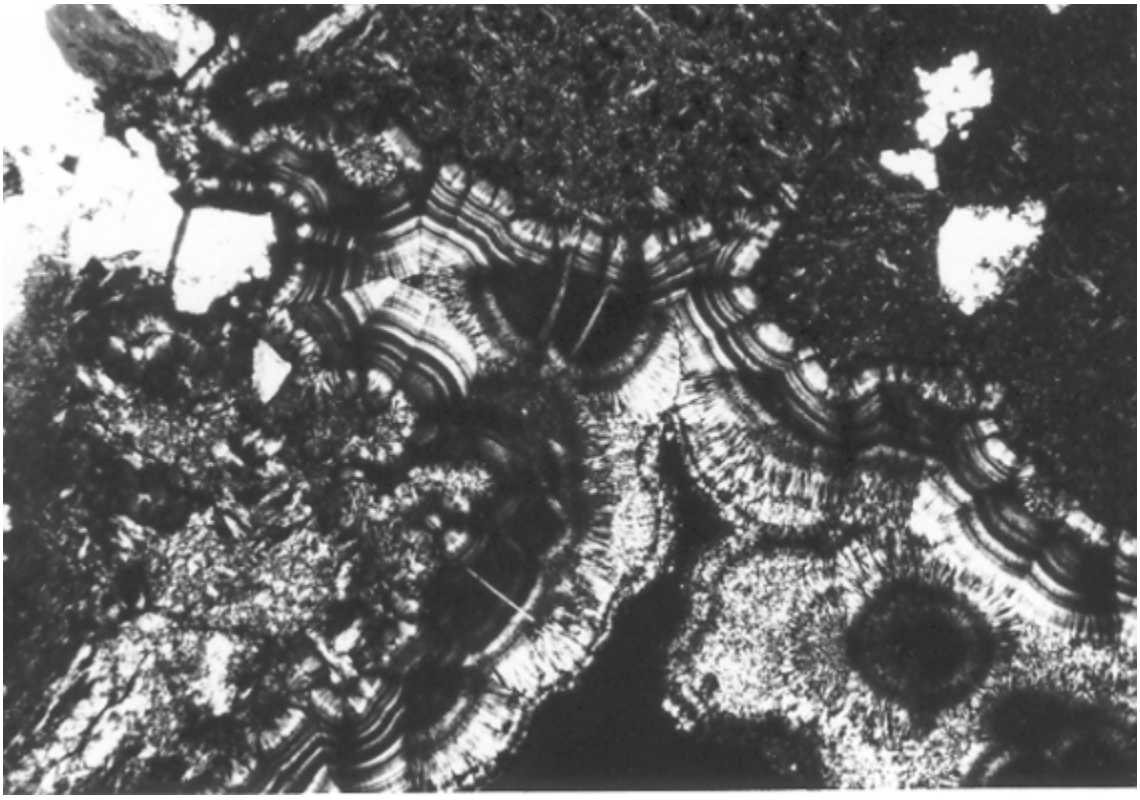

Figure A6.1b Photomicrograph of quartzine embedded in a opal-CT cement from Daba; scale as above

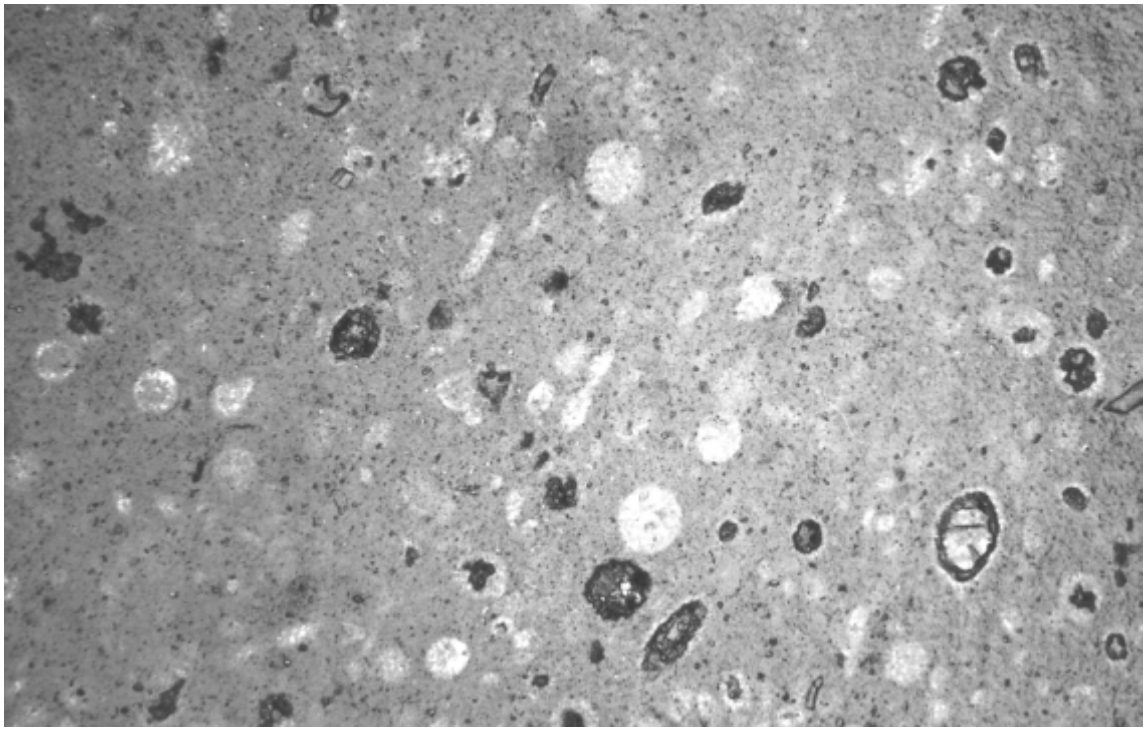

Figure A6.1c Photomicrograph of lussatite spherules in non-crystalline opal from Maqarin (x-nicols, scale as above)

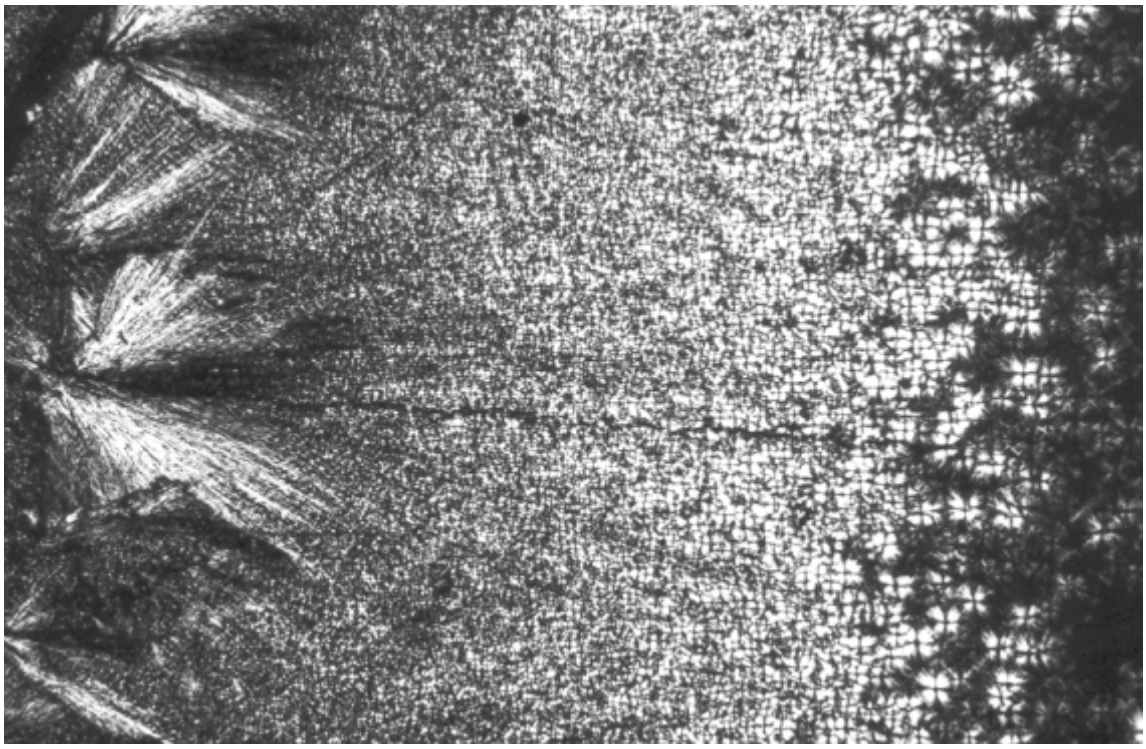

A6.2 Travertine and the Associated Volkonskoite

Travertine overlying the marble zone in central Jordan are thick and are widely distributed (see Figure A6.2). Most of these travertines are buff brown to cream in colour with a lot of opaline phases, but some are green colored as a result of secondary precipitation of the clay mineral volkonskoite. High chromium, high magnesium and iron-free volkonskoite were reported in central Jordan for the first time by Khoury et al. (1984).

Figure A6.2 Distribution of travertine in central Jordan

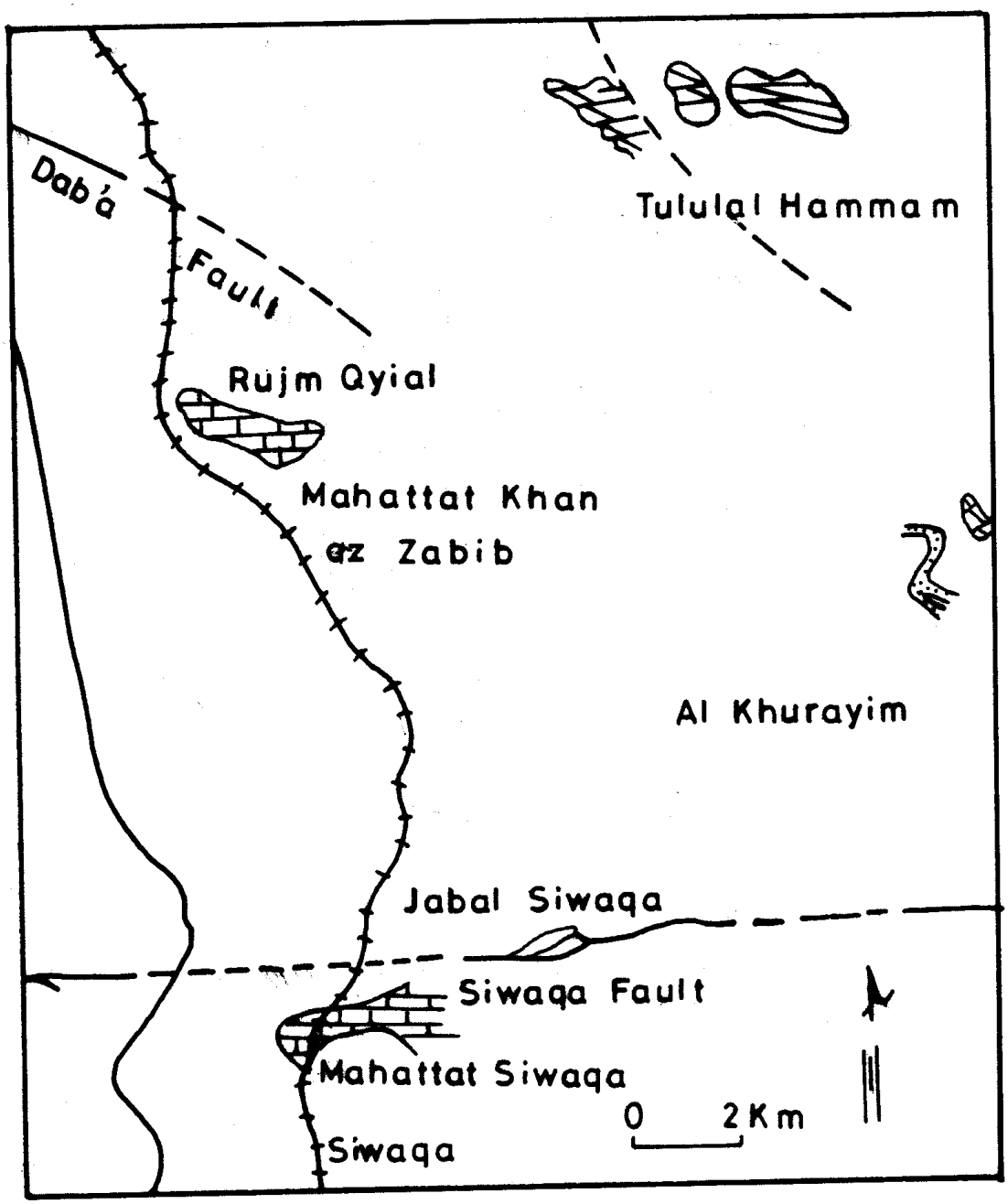

Clark et al. (1992a) showed that the travertines were precipitated from hyperalkaline groundwater containing calcium hydroxide through the uptake of atmospheric CO_2 and subsequent precipitation of calcite. Opaline phases, however, occur within the travertine in the lower part and within some casts of vegetation. They are interpreted as a late diagenetic process. Stable isotopes of the travertine are depleted from equilibrium values as a result of CO_2 uptake and calcite precipitation. An age has been estimated at 700-900 Ka before present for the travertine (Clark et al., 1992a).

The Jordanian volkonskoites have cellular, ball-like and cornflakes texture that resulted from continuous growth of micro-aggregates in cavities and fissures associated with idiomorphic calcite and quartz crystals (Figure A6.3a-c).

Figure A6.3a SEM image of volkonskoite with calcite

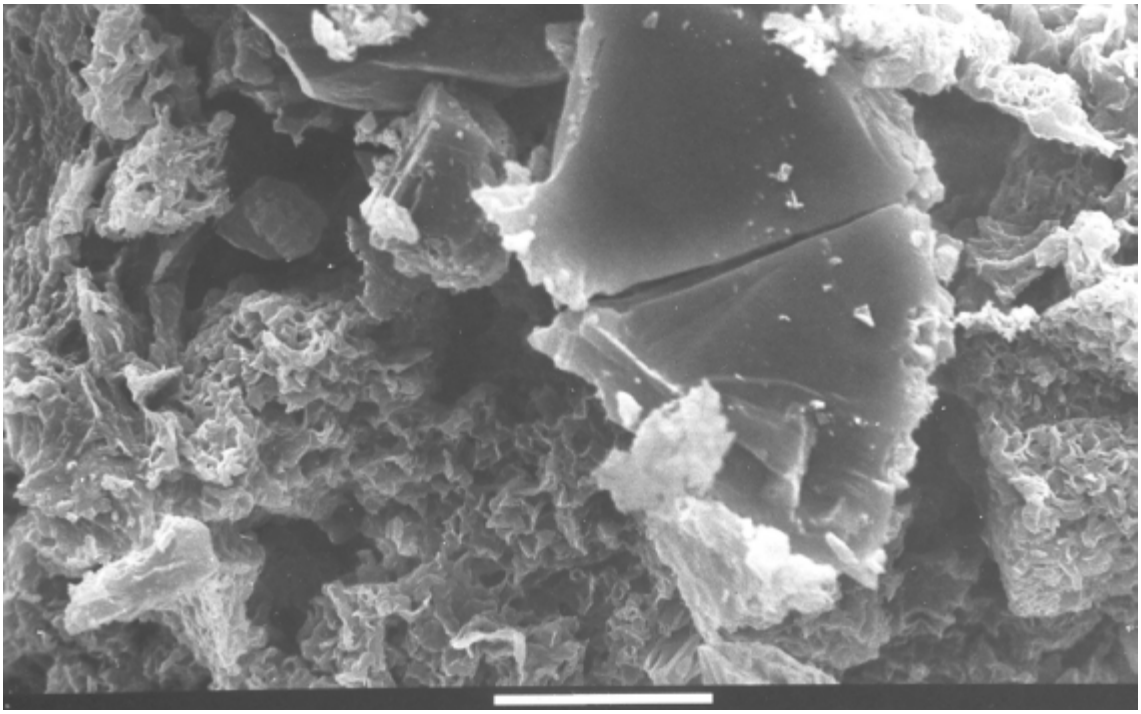

Figure A6.3b SEM image of volkonskoite

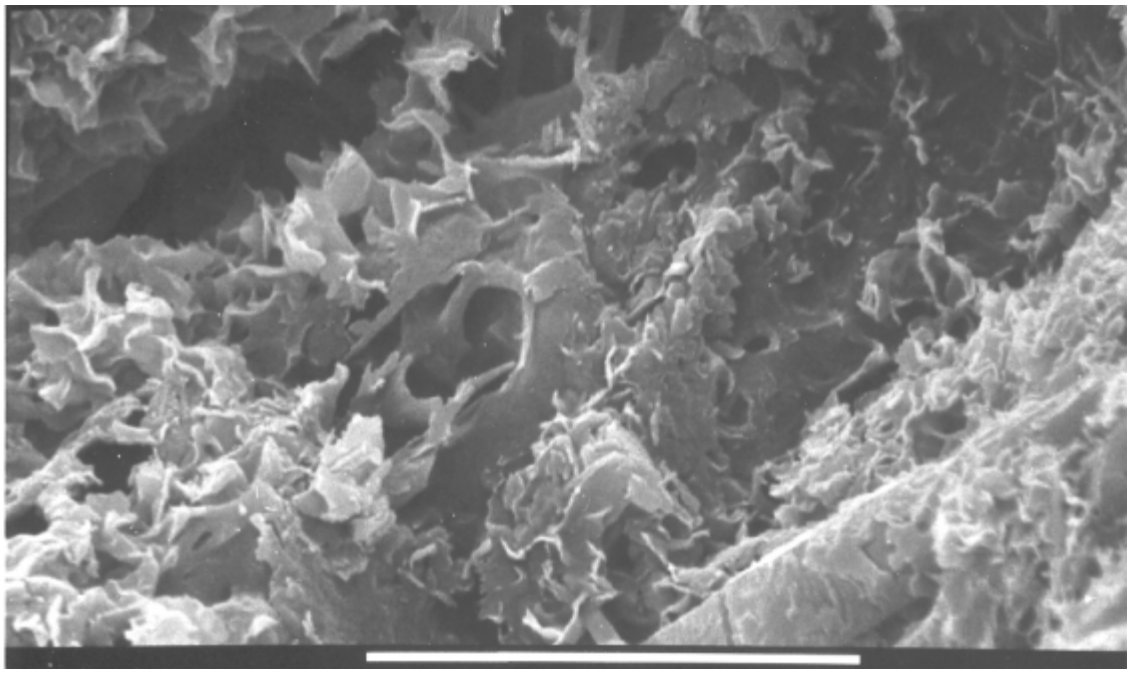

Figure A6.3c SEM image of volkonskoite with calcite and quartz

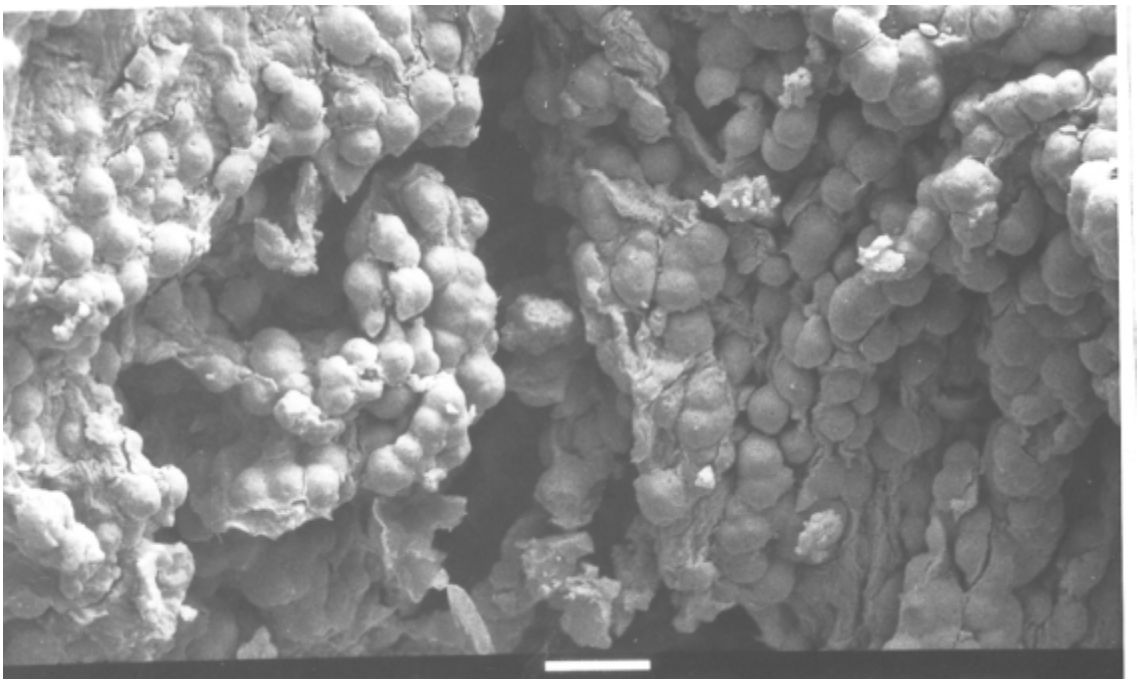

Figure A6.4 illustrates a typical X-ray diffractogram of central Jordan volkonskoite and the behavior of volkonskoite upon heating and glycolation. The X-ray patterns of the oriented samples from the four localities are typical of montmorillonite. A sample from the Siwaqa area, for example, has a basal (001) reflection of 17A^{o} on glycolation, which collapses to 10A^{o} on heating to 550^{o}C for two hours. On saturation, the montmorillonitic clay from the different localities show two major affinities for the interlayer cation as Li > Mg > Ca > K > Sr > Ba > Na for the Siwaqa sample and Ca > Mg > Ba > K. Li > Sr > Na for the Tulul El Hammam sample.

Figure A6.4 A typical X-ray tracing (air-dried, glycolated and heated) of volkonskoite from central Jordan

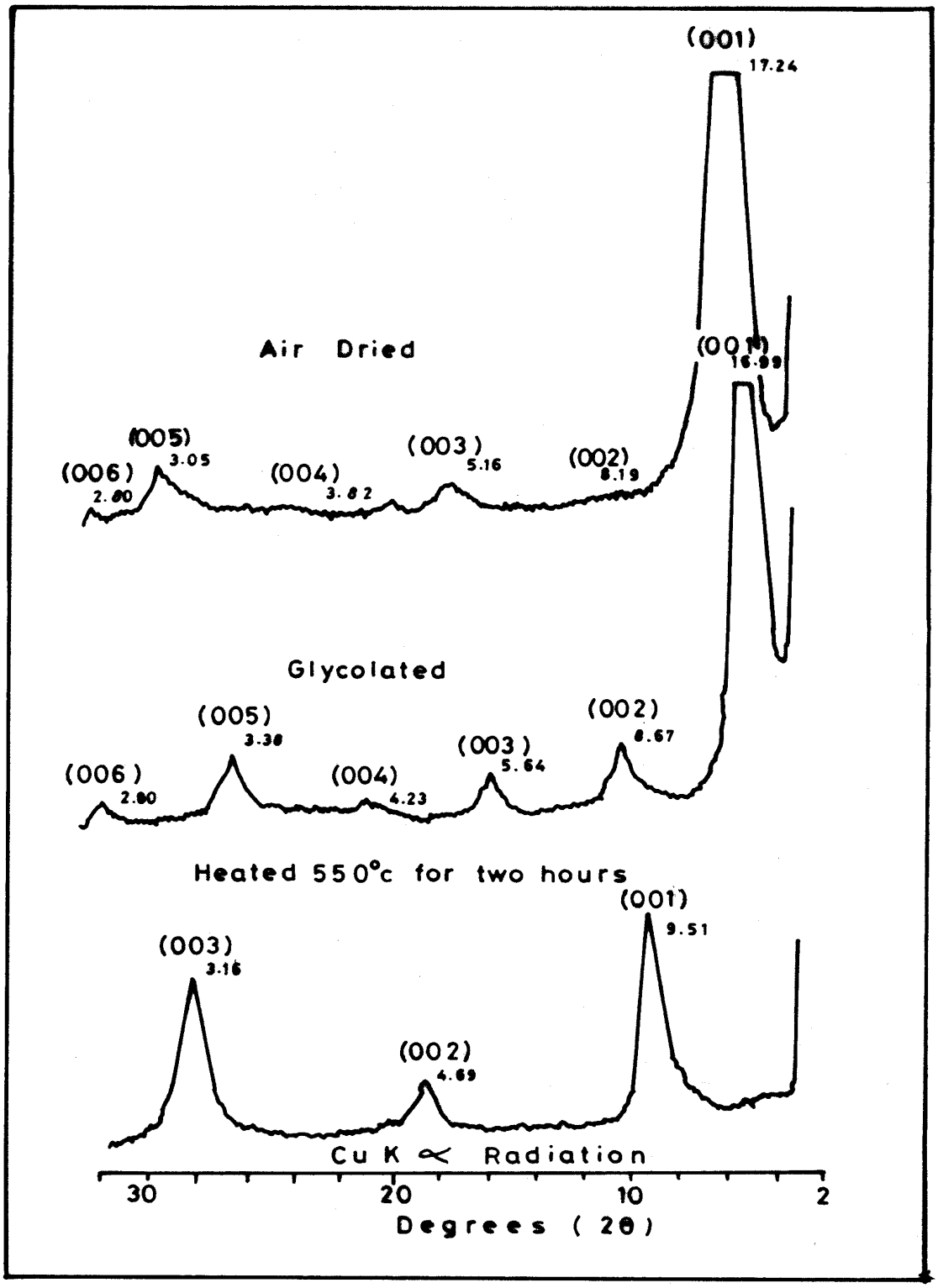

The structural formulae (calculated from the AAS chemical analysis) for this clay mineral is based on a half unit cell after correction for the opaline phases. The formulae are as follows:

Khan Az-Zabib:

$$(Ca_{0.21}\ Na_{0.03}\ K_{0.02})\ (Si_{3.64}\ Al_{0.036})\ (Al_{0.08}\ Ti_{0.02}\ Fe_{0.08}\ Cr^{3+}_{0.75}\ Mg_{1.24})\ O_{10}\ (OH)_2$$

Tulul Al-Hammam:

$$(Ca_{0.35}\ Na_{0.02)}\ (Si_{3.71}\ Al_{0.29})\ (Al_{0.29}\ Ti_{0.01}\ Fe^{3+}_{0.03}\ Cr_{1.17}\ Mg_{0.53})\ O_{10}\ (OH)_2$$

Siwaqa:

$$(Ca_{0.44}\ Na_{0.03}\ K_{0.02})\ (Si_{3.40}\ A_{l0.6})\ (Al_{0.44}\ Ti_{0.04}\ Fe^{3+}_{0.30}\ Cr_{0.34}\ Mg_{0.61})\ O_{10}\ (OH)_2$$

Jabal Al-Khurayim:

$$(Ca_{0.22}\ Na_{0.03})\ (Si_{3.69}\ Al_{0.31})\ (Al_{0.44}\ Ti_{0.04}\ Fe^{3+}_{0.23}\ Cr_{0.53}\ Mg_{1.07})\ O_{10}\ (OH)_2$$

The XRD basal reflections were constant although the structural formulae show variation in the Cr content in the octahedral sheets and specimens from different sites have different affinities to interlayer cations. This may be attributed to compositional variations and/or differences in the layer-charge distribution. The negative charge in the tetrahedral and octahedral sheets is not equally distributed. The differential substitution would result in the variation of the total negative charge within the layers and, accordingly, would lead to the variation in the adsorption capacities of the interlayer cations.

Volkonskoite associated with the travertines and marbles in central Jordan has precipitated from ascending hyperalkaline solutions, following the combustion of the original Cr-rich Bituminous Marl and limestone. Hydration and alteration of the calcined products occurred through reaction with recirculating meteoric waters. Volkonskoite free crystal growth as indicated by the SEM results (Figure 6.3a-c), suggest that its crystallisation occurred after the precipitation of calcite. The water chemistry after the removal of CaO was ideal for the crystallization of volkonskoite, and was followed by the precipitation of the remained silica.

A6.3 Clay Mineralogy

Petrographic studies were performed to characterise the rock types and fracture/joint fillings. This was supplemented by scanning electron microscopy (SEM), energy dispersive analysis (EDS) and X-Ray Diffraction (XRD).

After this preliminary study, eleven representative samples along the profile were analysed in detail (red arrows in Figure 6.3.4). The carbonate content was measured using a Bernard calcimeter. The clay fraction (< 2 μm) was then extracted from crushed bulk rock by centrifugation. Previous to separation, samples were treated with hydrogen peroxide (H_2O_2 at 70°C) to destroy the organic matter and with hydrochloric acid at 50°C to remove carbonates. Characterisation of clay minerals was performed by XRD using standard methods. The ClayXR computing program was used for automatic identification of the diffraction patterns (Bouchet, 1992). Further information (mostly relating to interstratified clay minerals) was obtained by comparing experimental results with theoretical diffraction patterns calculated with the NEWMOD© calculation program. Chemical analysis of major elements was performed by flame photometry (Na and K) and atomic absorption spectroscopy. The cation exchange capacity (CEC) was measured on the basis of the MgCl method set (ERM specific methodology, QM MO-07). The concentration of the exchangeable cations was also determined after extraction from samples by the method described by Jackson (1964). The quantification of mineralogical phases in clay fraction was obtained with the integration of chemistry of sample, XRD mineralogical data, carbonate content and CEC value.

A6.4 Isotopic Analysis

A6.4.1 Carbon and oxygen isotopes analyses

Carbon and oxygen isotopic compositions were investigated both on whole rocks and on the carbonate material filling up the fractures. The sample of baked biomicrite A3-6, located 0.5 m beneath the contact, was carefully investigated on a smaller scale because it displayed a heterogeneous colour pattern (from dark grey to light grey) and also different carbonate-bearing veins (Fig. A6.4.1a). Early veins more or less parallel to the sediment layering, with later oblique fractures cross-cutting the previous ones. Accordingly, chips corresponding to light and dark areas and fracture infillings were extracted from that sample (Fig. A6.4.1b). Only sample A3-6 was studied by small-scale *in situ* analysis of C isotopic ratios (foraminifera, microveins, matrix; Figure A6.5c) since attempts to obtain perfectly polished sections on biomicrite samples located deeper in the profile were unsuccessful (these rocks were too porous and friable).

Bulk rock samples correspond to a few cm^3 of powdered material, but this amount was reduced to *ca.* $1/20^{th}$ of a cm^3 for sub-sample A3-6. Fracture infillings were extracted by micro-drilling and scratching out material. The carbonate fraction (1-10 mg) was reacted with 100% orthophosphoric acid at 25°C (McCrea, 1950) assuming α(O) $CO_2/CaCO_3$ (extraction) = 1.01025. Selected samples of biomicrites were enriched in their organic matter component by reaction with excess diluted HCl, then washed with distilled water, centrifugated and dried. After degassing, OM-enriched samples were reacted with purified CuO in sealed tubes (silica glass) at 900°C.

Figure A6.5 *(a) View of indurate biomicrite sample A3-6 with (b) a sketch showing the location of analysed matrix and vein sub-samples and (c) a microscopic view of the polished area studied using ion-microprobe and the corresponding C isotopic compositions ($\delta_{13}C$ vs. PDB). In 3c, calcite appears with a white colour while the dark material in the large vein is zeolite*

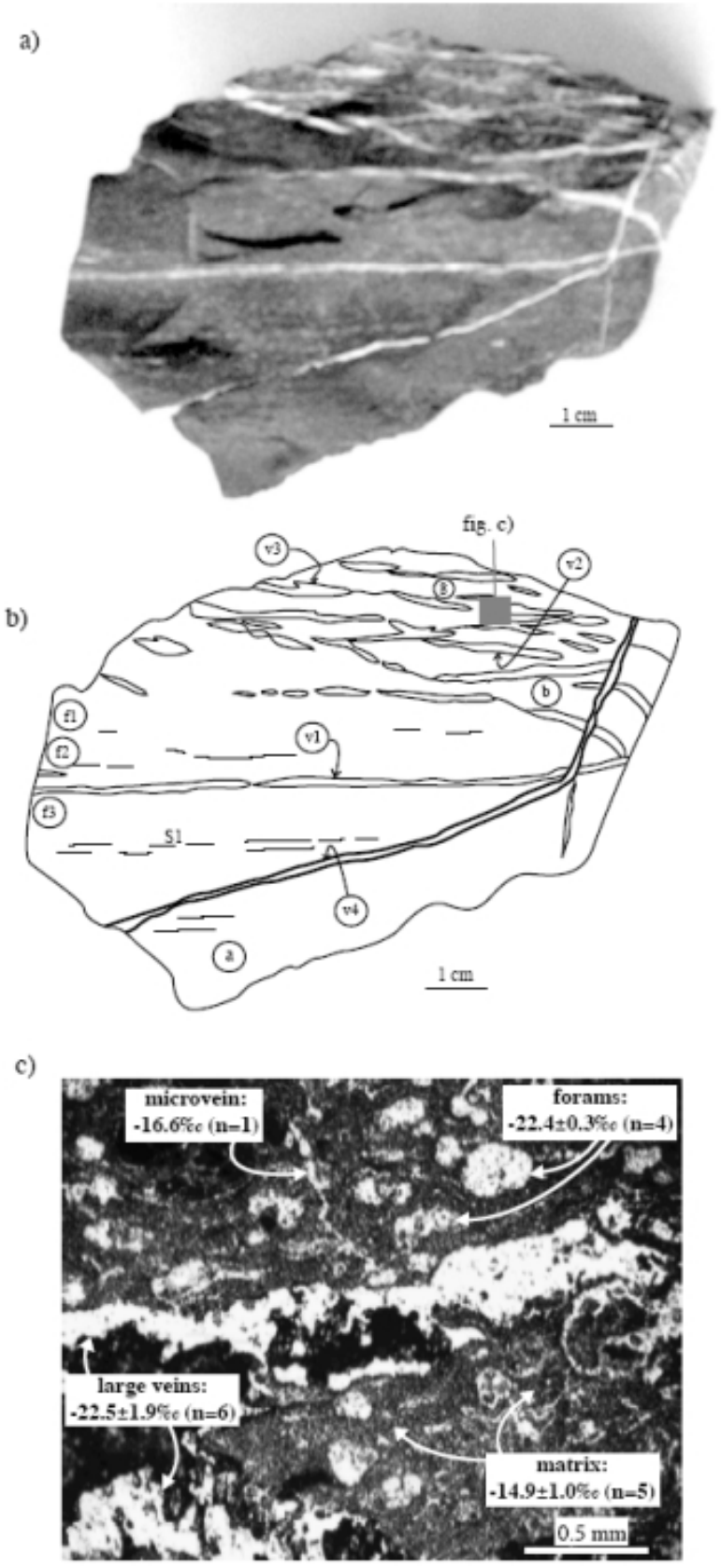

Isotopic analyses were carried out on CO_2 gas using a VG SIRA 10 mass-spectrometer at Géosciences Rennes, France, and expressed using internal carbonate standards and the USGS 24 graphite and the NBS 19 reference material, with the conventional δ notation vs. SMOW (O) and PDB (C). The average uncertainties on C and O analyses are estimated to be < 0.1‰ (C) and *ca.* 0.1‰ (O). The carbonate content of bulk rocks was also measured during CO_2 extraction with a manometer.

In situ carbon analysis of calcite cements in the microscopic matrix of sample A3-6 was performed by secondary ion mass-spectroscopy (SIMS) on the Caméca IMS1270 at CRPG, Nancy (France). Measurements were done on standard polished thin sections coated with gold by use of 25 nA defocused primary ion beam of Cs+ (impact energy of 10 keV) following the method of Rollion-Bard et al. (2003). Sub-circular ablation craters of 30 µm were produced by the analysis. Mass resolution of 5000 was used for C isotopes analyses. C isotopes were measured in multicollection mode using one off-axis Faraday cup (L'2) and the central electron multiplier. Typical ion intensities of 2.10^7 counts per second (cps) were obtained on the $12C^-$, so that an internal 1σ error of ±0.1 to 0.2 ‰ was reached after a few minutes of counting. The average external reproducibility, as estimated from replicate measurements of carbonate standards, was ±0.4‰. Instrumental mass fractionation was corrected considering the isotopic values of the calcite standards known by conventional analysis. Isotopic compositions are reported in Figure A6.5c.

In addition, for the purpose of comparison, the C and O isotopic compositions of selected carbonate stalactites from concrete structures were also analysed. Sampling areas were carefully chosen so that anthropogenic (e.g. fuel combustion exhausts or respiration) or plant (photosynthesis, respiration) contributions to the budget of local atmospheric CO_2 were minimal. Stalactites hanging on rural bridges over rivers and in other well-vented rural situations were found to be adequate for that purpose.

A6.4.2 Strontium isotopes analyses

Sr contents in whole rock powders were measured by inductively coupled plasma mass spectrometry (ICP–MS) with an analytical uncertainty of 2%. The Sr isotopic composition ($^{87}Sr/^{86}Sr$) was determined for whole rocks (WR) after crushing and dissolution in hot purified acids (HNO_3, HCl and HF) and for the carbonated phase (cp) extracted from the whole rock powders by a quick leaching with acetic acid (1 M). Separation of Sr was conducted according to Birck's method (Birck and Allegre, 1978) using Teflon FEP columns containing 0.814 ml of AG50WX12 resin (200–400 mesh). Sr was loaded on a Re filament with a Ta activator. The $^{87}Sr/^{86}Sr$ ratios were measured using a solid-source thermal-ionisation mass spectrometer TRITON TI at the GIS laboratory, Nîmes, France. A mean analytical error of 1 to 5.10^{-6} (2σ) was ensured by measuring the $^{87}Sr/^{86}Sr$ ratio about 90 times. The external reproducibility of the isotopic measurements was controlled by periodic analysis of the NBS 987 standard providing a mean $^{87}Sr/^{86}Sr$ ratio of 0.710238 ± 4.10^{-6}.

A6.4.3 U-Th disequilibrium

Carbonates from micro-cracks were picked up under a binocular lens and crushed for dating by the U–Th radioactive disequilibrium method. About 200 to 500 mg of carbonate powders were totally dissolved in hot acids (HNO3, HF and HClO4 acids) before adding a mixed 229Th–233U spike. A Fe-precipitate was formed in NH4OH and was introduced on an anionic AG1-X8 resin for U and Th separation. U and Th were deposited on single Re filaments. Measurements were performed on a VG54 mass spectrometer equipped

with a Retardation Potentiel Quadrupole (RPQ) at Cerege, Aix en Provence, France. The external reproducibility of the isotopic measurements was controlled by analysis of the SRM-U standard providing a 233U/238U ratio of 1.0685 ± 2.10-4 and a 234U/238U ratio of 0.05300 ± 3.10-5.

A6.4.4 Cathodoluminescence observations

Polished thin sections of biomicrite were examined by optical microscopy (OM) and scanning electronic microscopy (SEM, JEOL 5600) after C coating. The SEM (Cambridge S360-LEO) was equipped with an energy-dispersive system (EDS) system for semi-quantitative overall or localised analyses. Cathodoluminescence (CL) observations of polished thin sections of filled-veins were also performed under a Nikon optical microscope equipped with a Technosyn luminescence stage (8200 MkII model) and a Nikon camera, at Orsay-Terre, France. Observations were made with a beam intensity of around 400–600 µA.

A.6.4.5 Porosity measurements

Porosity parameters were measured on five selected samples across the profile at the University of Caen, France, using mercury injection. Data (total connected porosity, average pore diameter) are given in Table A6.2.

Table A6.2 Porosity parameters obtained by mercury injection on a few representative samples o the Khushaym Matruk profile

Sample	Metre mark	Type	Porosity (%)	Mean pore diameter (µm)
A 1-1	9,1	clayey biomicrite	49,27	0,135
A 2-2	8,1	clayey biomicrite	47,60	0,123
A 3-1	2,7	baked clayey biomicrite	21,91	0,047
A 3-4	1,4	baked clayey biomicrite	20,82	0,023
KHM 13	2,0	baked clayey biomicrite	15,63	0,015

A.6.4.6 Analysis of Zn

Bulk samples of the rocks collected along the trench profile were ground in an agate mortar and then mineralised using standard methods (e.g. alkaline fusion, acid dissolution). Analyses of the solutes were carried out with a Jobin-Yvon ICP-AES spectrometer. The relative error on Zn concentrations is estimated at 10 %.

A6.5 Organic Matter Analysis

A.6.5.1 Samples

Fifteen biomicrite and three ACZ samples were collected at the GIS laboratory for this research project aims to characterise the organic of the Khushaym Matruk site, Jordan. These samples were sent to BaselineDGSI for kerogen isolation and Rock-Eval analysis. The weight of samples sent for these treatments are reported on Table A6.3.

Table A.6.3 Reference, nature and distance from contact zone of the studied samples

Reference	Nature	Distance from metamorphic rock (meters)
A2-1	Bituminous biomicrite - 2nd level - ERM sample	8.2
A2-3	Bituminous biomicrite - 2nd level - ERM sample	8.0
A2-4	Bituminous biomicrite - 2nd level - ERM sample	7.9
A2-5	Bituminous biomicrite - 2nd level - ERM sample	7.8
KHM08A	Bituminous biomicrite between the 2nd and 3rd level - GIS sample	6.0
KHM08B	Bituminous biomicrite between the 2nd and 3rd level - GIS sample	6.0
A2-12	Bituminous biomicrite between the 2nd and 3rd level - ERM sample	3.1
A3-2	Bituminous biomicrite - 3rd level - ERM sample	2.6
A3-3	Bituminous biomicrite between the 3rd level and the contact zone with marbles-cements - ERM sample	2.1
KHM13	Bituminous biomicrite between the 3rd level and the contact zone with marbles-cements - GIS sample	2.2
KHM14	Bituminous biomicrite between the 3rd level and the contact zone with marbles-cements - GIS sample	2.1
KHM15	Bituminous biomicrite between the 3rd level and the contact zone with marbles-cements - GIS sample	2.0
A3-5	Bituminous biomicrite between the 3rd level and the contact zone with marbles-cements - GIS sample	1.0
A3-6	Bituminous biomicrite between the 3rd level and the contact zone with marbles-cements - GIS sample	0.5
KHM06	Bituminous biomicrite between the 3rd level and the contact zone with marbles-cements - GIS sample	0.25
KHM18	Marbles-cements from the summit zone of the ridge. GIS sample	0.0
KHM19	Marbles-cements from the summit zone of the ridge. GIS sample	0.0
KHM21	Marbles-cements from the summit zone of the ridge. GIS sample	0.0

A6.5.2 Kerogen isolation

Kerogen was isolated from rock powder using the standard HCl/HF procedure, washed with distilled water and freeze-dried at Baseline DGSI (Texas, USA). The concentrated kerogens were washed with distilled water and freeze-dried. Samples A3-6, KHM 13 and KHM 08A yielded very small amounts of kerogen and no kerogen was recovered from KHM 21 and KHM 19. The latter sample yielded a white precipitate. The KHM 06 and KHM 18 samples yielded a light grey precipitate that could be a mixture of kerogen and white precipitate similar to KHM 19 (Table A6.4). X-ray diffraction analysis of samples KHM06 and A3-5 revealed no acid-soluble minerals but ralsonite-like fluorides (Na, Mg, Al, (F, OH), H_2O) which are formed during kerogen isolation (Figure A6.6).

Table A6.4 List of samples sent to BaselineDGSI for kerogen isolation and RE analysis.

Reference	Weight of rock sent for kerogen isolation (g)	Kerogen description	RE Analysis Requested
KHM 21	70	Nothing	NO
KHM 18	127	Light grey precipitate	X
KHM 19	113	No kerogen but white unidentified precipitate	NO
KHM 06	<50	Light grey precipitate	X
A3-6	<50	Very small yield	NO
A3-5	<50	Black kerogen- Reasonable yield	X
KHM 13	<50	Very small yield	NO
KHM 14	90	Black kerogen- Reasonable yield	X
KHM 15	<50	Black kerogen- Reasonable yield	X
A3-3	50	Black kerogen- Reasonable yield	X
A3-2	<50	Black kerogen- Reasonable yield	X
A2-12	<50	Black kerogen- Reasonable yield	X
KHM 08A	<50	Very small yield	NO
KHM 08B	<50	Black kerogen- Reasonable yield	X
A2-5	<50	Black kerogen- Reasonable yield	X
A2-4	<50	Black kerogen- Small yield	X
A2-3	<50	Black kerogen- Small yield	X
A2-1	<50	Black kerogen- Reasonable yield	X

Figure A6.6 X-ray diffractograms of samples A] KHM06 and B] A3-5

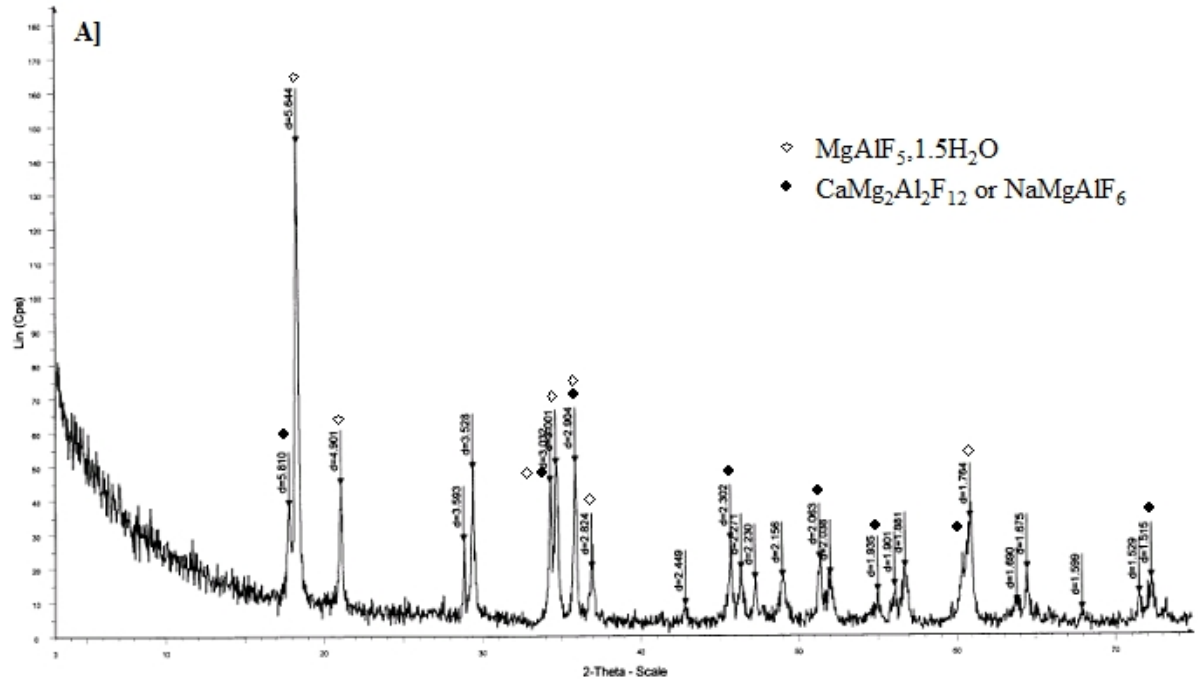

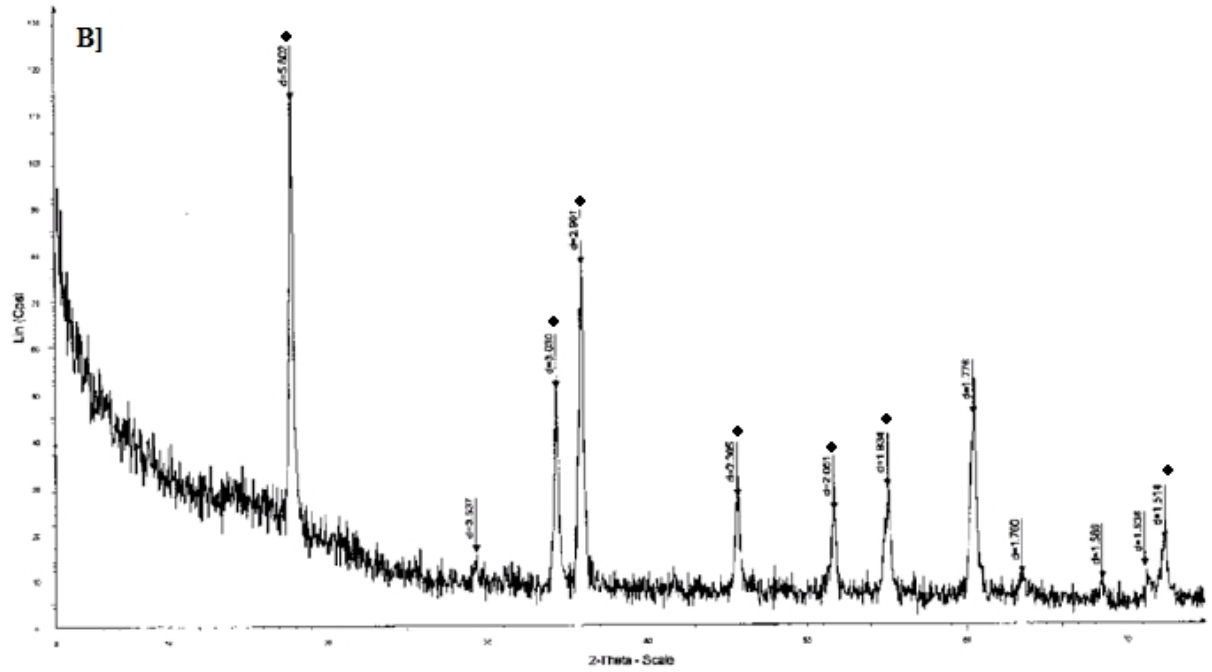

A6.5.3 Rock-eval pyrolysis

A6.5.3.1 Whole rocks

Rock-Eval pyrolysis is used in the petroleum field for a rapid screening of source rocks and allows useful information to be obtained on the structure and thermal maturity of organic matter. Briefly, the sample is heated in a oven at 30°C min^{-1} from 25°C to around 650°C, and the generated compounds can be visualised by a Rock-Eval pyrogram. The organic compounds are detected by a flame ionisation detector (FID). The first peak (S1 in mg hydrocarbons g^{-1} of rock) represents the amount of free hydrocarbons that can be thermally distilled from a rock, the second peak (S2 in mg hydrocarbons g^{-1} of rock) the amount of hydrocarbons generated by pyrolytic degradation of the kerogen in the whole rock. The third peak (S3 in mg CO_2 g^{-1} of rock) represents the amount of CO_2 generated during a Rock-Eval run, and is analysed using a thermal conductivity detector. The hydrogen index (HI) corresponds to the quantity of pyrolysable organic compounds from S2 peak relative to the total organic carbon (TOC) in sample (in mg HC g^{-1} TOC). The oxygen index (OI) corresponds to the quantity of carbon dioxide from S3 peak relative to TOC (mg CO_2 g^{-1} TOC). The production index is the ratio S1/(S1+S2), and the Rock-Eval T_{max} (°C) is the temperature at which the maximum amount of S2 hydrocarbons is generated. Aliquots of powdered sediment were sent to ISTO (Orléans) and subjected to standard Rock-Eval pyrolysis using a Rock-Eval 6 (Vinci Technologies®). The whole rocks analysed by this technique are: KHM21, KHM13, KHM15, A3-3, A3-2, A2-12, KHM08A, KHM08B, A2-5, A2-4, A2-3 and A2-1.

A6.5.3.2 Isolated kerogens

Rock-Eval pyrolyses (Rock-Eval 2) were performed on the isolated kerogens to prevent any interference with mineral matrix. Only 13 kerogens were analysed because either no kerogen or such a small amount of kerogen was obtained for some samples (Table A6.4). In a typical run, around 8 mg of sample were used when analysing kerogens but the response for these samples is very low. Samples with larger amounts of recovered kerogen were therefore re-analysed with a larger sample charge (30 mg) to obtain better data. Samples with small amounts of recovered kerogen cannot be re-run. Several samples were analysed repeatedly and the Rock-Eval parameters S2 and S3 were

determined. 10 of the concentrated kerogens were re-analysed on the Rock-Eval 6 instrument to determine TOC values. Hydrogen index (HI mg HC g^{-1} TOC) and oxygen index (OI mg CO_2 g^{-1} TOC) were calculated for them.

A6.5.4 Transmission infrared microspectroscopy

Kerogens were analysed by FT-i.r. microscopy in the near IR region (wave numbers: 4000–600 cm^{-1}). The main use of this technique is chemical characterisation *in situ* of the different components of organic matter. Demineralised kerogen aliquots were placed between the two diamond cells (2 mm diameter, 1 mm thickness) of a compression cell (7.5x5.1 cm^2, Spectra-Tech Int.). After compression of the sample by screwing, the top window was removed. The visible light x10 objective gives an enlarged image of the sample and allows the selection of the area to be analyzed. The micro-Fourier transform infrared (FTIR) analysis was performed on a Brucker IFS-88 equinox spectrometer coupled to a Brucker multi-purpose infrared microscope which was fitted with a 250 µm narrow band MCT detector cooled to 77 K. The standard analytical conditions were x15 infrared objective, 40–60 µm diameter infrared spot, 128 scans (60 s) and spectral resolution of 4 cm^{-1}. Spectra were ratioed to the background collected on a clean diamond cell under the same analytical conditions. The assignments of the main infrared bands were determined by reference to previous works.

A6.6 Cement Mineralogy

A 2 x 4 cm^2 thin slab was sawn from the rock mass in order to select a region with well-preserved fractures. This slab was then polished with water-free diamond suspensions (9, 3 and 1 µm). The sample was then observed under the binocular microscope. Finally the sample was coated with an evaporated layer of carbon in order to perform SEM/EDX investigations (Philips XL 30 and Oxford/Link EDX system, 20 kV, working distance 10 mm) . In addition, several XRD spectra were recorded on powdered fractions of the different parts of the sample.

A6.7 Raw Data

The raw data and sample list are collated in Appendix 6.2.